R-09-17

ÄSPÖ Hard Rock Laboratory

Studies of factors that affect and controls the Excavation Damaged/Disturbed Zone

Martin Jonsson, Ann Bäckström, Quanhong Feng
ÅF – Berg & Mätteknik

Johan Berglund, Vattenfall Power Consultant

Malin Johansson, Diego Mas Ivars
Itasca Geomekanik AB

Mats Olsson, SweBefo

Maj 2009

Svensk Kärnbränslehantering AB
Swedish Nuclear Fuel
and Waste Management Co

Box 250, SE-101 24 Stockholm
Phone +46 8 459 84 00

ISSN 1402-3091
SKB Rapport R-09-17

ÄSPÖ Hard Rock Laboratory

Studies of factors that affect and controls the Excavation Damaged/Disturbed Zone

Martin Jonsson, Ann Bäckström, Quanhong Feng
ÅF – Berg & Mätteknik

Johan Berglund, Vattenfall Power Consultant

Malin Johansson, Diego Mas Ivars
Itasca Geomekanik AB

Mats Olsson, SweBefo

Maj 2009

Summary

A tunnel was developed at the Äspö Hard Rock Laboratory (HRL) in 2003 purposely for a large in-situ rock mechanics experiment, the Äspö Pillar Stability Experiment (APSE). The tunnel had a large height/width ratio with a circular floor, primarily to control the stress situation around the tunnel and concentrate the stresses under the floor. An extensive set of data for understanding the **Excavation Damaged Zone (EDZ)** was collected within section 47 of the tunnel. It consist of the blast design, blast sequences, convergence measurements during excavation, geological mapping of tunnel and cores, 3D-laser scanning of the tunnel geometry etc. Furthermore, in 2006, ultrasonic measurements along eight boreholes were carried out in order to estimate the extent of the EDZ in the tunnel.

The collection of all these different information provides an opportunity to evaluate the mechanical damages caused by the excavation work. The overall aim with this project is to give feed-back to future planning of tunnelling on issues of importance for requirements with respect to minimising the EDZ in crystalline rock from the drill and blast method. A combination of the mapped geological features (tunnel and cores) and the geometry of the blasted tunnel obtained from the 3D-laser scanning were used to build a 3D model of the geology with emphasis on the geometry of the natural fractures. The rock mechanic response to the tunnelling was evaluated in a numerical model including the as-built geometry in combination with the 3D model of the geology. The modelling of the rock mechanical processes of importance for the EDZ could be calibrated against actual measurements.

From observed changes in the ultrasonic wave velocity along the boreholes it was found that the locations of the velocity changes corresponded well with the location of the mapped fractures in the drillcores. This indicates that EDZ can be detected using the ultrasonic method with high accuracy. Furthermore, the measurements indicate that the EDZ was larger in the left than in the right tunnel wall. This observation could partly be explained when studying the calculated stress situation around the tunnel, which shows that pre-existing fractures in the vicinity of the left tunnel wall induced zones of higher compressive and tensile stress which then can increase the damage initiated by the blasting.

When studying the results from the numerical simulations, it was concluded that fractures in the study area generate heterogeneous stress redistribution around the excavation at different tunnel sections. The uneven as-built geometry of the tunnel generated from blasting also contributes to the heterogeneous stress redistribution close to the contour. These variations in stresses are local and differ strongly between nearby sections, which could induce local fracturing and asymmetry in the EDZ. This shows that the extent and damage of the EDZ is highly local and influenced in a broader scale by the local geometry of natural fractures, and in the small scale by the local stress concentration on the tunnel perimeter. This study also indicates the importance of high precision contour control during drilling of the blast holes as a measure to minimize the EDZ.

Tools for a controlled modelling and verification of the mechanical behaviour of the EDZ exist. In this study, the modelling of the stresses developed in the tunnel walls were divided into one model containing the fractures, without the geometry of the tunnel wall and one with the geometry of the tunnel wall which was lacking the geometry of the fractures. These two geometries should be combined in the same model in a future work, to provide a possibility to assess their combined effect on the stress situation around the tunnel.

Sammanfattning

Den här rapporten är en utvärdering av sprängskadezonen i en välundersökt sektion av Q-tunneln i Äspölaboratoriet. Det övergripande målet med detta projekt är att ge rekommendationer för framtida planering av tunnlar och krav med syfte att minimera skadorna från sprängning i bergrund med kristallina bergarter.

År 2003 byggdes en tunnel på Äspölaboratoriet för ett stort bergmekaniskt in-situ experiment, Äspö Pillar Stability Experiment (APSE). I detta projekt behövdes spänningsbilden runt tunneln vara väl avgränsad. För att koncentrera spänningarna under golvet utformades tunneln så att höjden var större än bredden och med ett rundat golv. För att undersöka sprängskadezonen (EDZ) har flertalet undersökningar genomförts i sektion 47. Informationen som samlats in består av sprängdesign, sprängsekvenser, konvergensmätningar under sprängning, geologisk tunnelkartering och kärnkartering, tunnelgeometrin fångad med 3D-laserskanning osv. Dessutom genomfördes under 2006 ultraljudsmätningar längs åtta borrhål för att uppskatta sprängskadezonen runt tunneln.

Sammanvägningen av alla insamlad kunskap ger oss en möjlighet att utvärdera de mekaniska skadorna orsakade av tunneldrivningen. Genom att kombinera den karterade geologiska strukturerna (från både tunneln och kärnor) och den sprängda tunnels geometri (från laserskanningen) skapades en 3D-modell av geologin för att studerade de naturliga sprickornas läge. Den bergmekaniska responsen med hänsyn till berguttaget utvärderades genom numerisk modellering som inkluderade den verkliga geometrin i kombination med en modell med den framtagna 3D-modellen av geologin. Modelleringen av de bergmekaniska processerna av betydelse för EDZ kunde således kalibreras mot verkliga mätningar.

Ultraljudsmätningarna längs borrhålen kunde identifiera läget för genomgående sprickor. Detta resultat indikerar att EDZ kan detekteras med hjälp av ultraljudsmätningar. För just det här fallet visar mätningarna av EDZ att de är större i den vänstra väggen än i den högra. Detta kan delvis förklaras då man studerar den beräknade spänningssituationen runt tunnel. Den visar att existerande sprickor i den västra väggen inducerar zoner med högre tryck och dragspänningar som i sin tur kan öka skadorna som initieras av sprängningarna.

Genom att studera resultaten från genomförda numeriska beräkningar kunde det konstateras att sprickorna genererar en heterogen spänningsomlagring runt tunnelns olika sektioner. Tunnelns ojämna geometri visar sig dessutom bidra till en heterogen spänningsomlagring runt tunnels periferi. Variationerna är lokala och förändras kraftigt mellan närliggande sektioner vilket kan initiera lokal sprickbildning och orsaka en asymmetri i EDZ. Därmed kan slutsatsen dras att storleken på EDZ är lokal och att den dessutom beror på den storskaliga geometrin hos nätverket av naturliga sprickor samt på de småskaliga spänningskoncentrationerna i närheten av tunnelns periferi. Den här analysen påvisar också betydelsen av en hög precision vid borrningen av konturhålen för sprängningen för att minimera sprängskadezonen.

Spänningsmodelleringen av tunneln delades upp i två delar för den här studien: en med sprickor men utan den korrekta geometrin, och en utan sprickor men med den korrekta geometrin. Dessa två kan i framtiden kombineras i samma modell för att ge en möjlighet att utvärdera den kombinerade effekten av sprickor och tunnel geometri på spänningsbilden runt tunneln.

Contents

1 Background

A tunnel was developed at the Äspö (Hard Rock Laboratory HRL) 2003 purposely for a large in-situ rock mechanics experiment, the Äspö Pillar Stability Experiment (APSE) /Andersson 2007/. The tunnel is located at the 450-m level close to the shaft, see Figure 1-1. The tunnel is 70 m long and had a large height/width ratio with a circular floor, primarily because of the need to concentrate high stresses in the circumfencial of the tunnel, especially under the floor. Unique was the approach with a circular cross-section in the floor.

The HRL provide good opportunities to conduct various in-situ experiments as well as to demonstrate and test equipments for various purposes. The area is very well characterized from a geological and a rock mechanics point of view /Staub et al. 2004/. The blast design, blast sequences and follow-up with the in-depth investigation of slots cut in the tunnel wall and the floor of the **Excavation Damaged Zone (EDZ)** was reported by /Olsson et al. 2004/. In 2005, a part of the geometry was captured using the 3D laser-scanning technique for the DECOVALEX IV project. Furthermore, in 2006, the BGR borehole seismic equipment was tested in a section (eight boreholes were drilled in a profile) of the tunnel with the aim to estimate the extent of the EDZ in the tunnel /Schuster 2007/. All of these activities were performed in the vicinity or in section 47 and due to this; the current study was performed in this section with the aim to estimate the extent of the EDZ in the tunnel.

An extensive set of information of interest for understanding the EDZ was of various reasons collected within a limited area of the tunnel, see Table 1-1. This set of data provides an extensive set of information of interest for understanding the EDZ and to evaluate the different methods used to characterize the EDZ. In order to increase the understanding of the factors, which affects and controls the EDZ, based upon the already existing information, this project was initiated (Studies of factors that affect and controls the Excavation Disturbance/Deformation Zone).

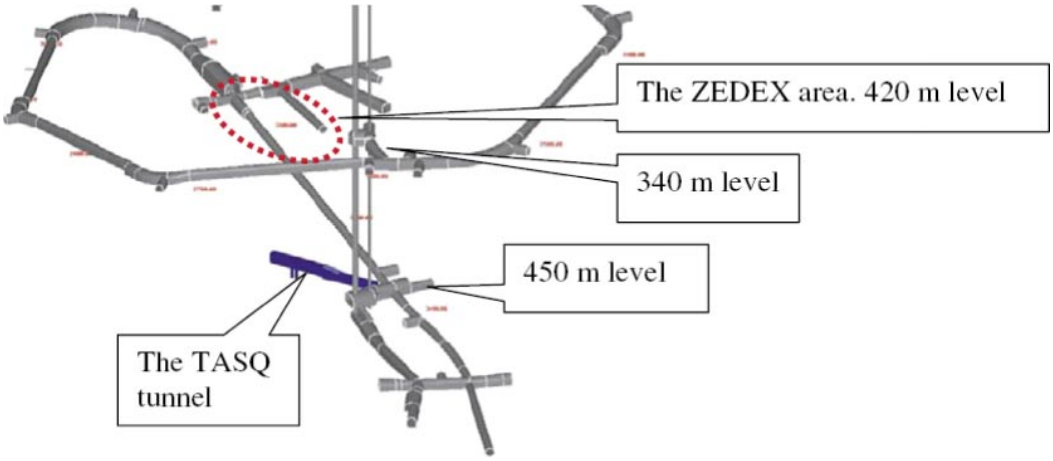

Figure 1-1. *Location of the TASQ-tunnel. Picture reprinted from /Olsson et al. 2004/.*

Table 1-1. Overview of available information from the TASQ tunnel of interest for evaluation of the EDZ.

Type of data	Chainage	Reference
Mechanical properties of intact rock and fractures	064–066	/Staub et al. 2004/
Convergence measurements during tunnelling	049	/Staub et al. 2004/
Back analysis of rock mass deformation modulus and in-situ stresses	049	/Staub et al. 2004/
Blast record	Whole tunnel	/Olsson et al. 2004/
Studies of the EDZ	048, 066–071, 080 (walls) 069 (floor)	/Olsson et al. 2004/
Ultrasonic borehole measurements in eight boreholes (floor, walls and roof)	047	/Schuster 2007/

1.1 Objectives

The generation and evolution of the EDZ involves many factors, as illustrated in Figure 1-2. The objectives of this study are by means of modelling, study the geometrical and mechanical factors of importance to the development of the EDZ in the TASQ tunnel and to evaluate the effectiveness of the various methods used for characterization of the EDZ in the actual tunnel. In order to restrict this study, only the highlighted paths in Figure 1-2 are investigated within this study.

By means of modelling of the geology and the rock mechanic response to the tunnelling, the modelling capability of the mechanical processes of importance for the EDZ could be tested against actual set of data. Thus, the aim is to give feed-back to future planning of tunnelling on issues of importance for requirements on tunnelling with respect to minimising the EDZ from the drill and blast method in crystalline rock.

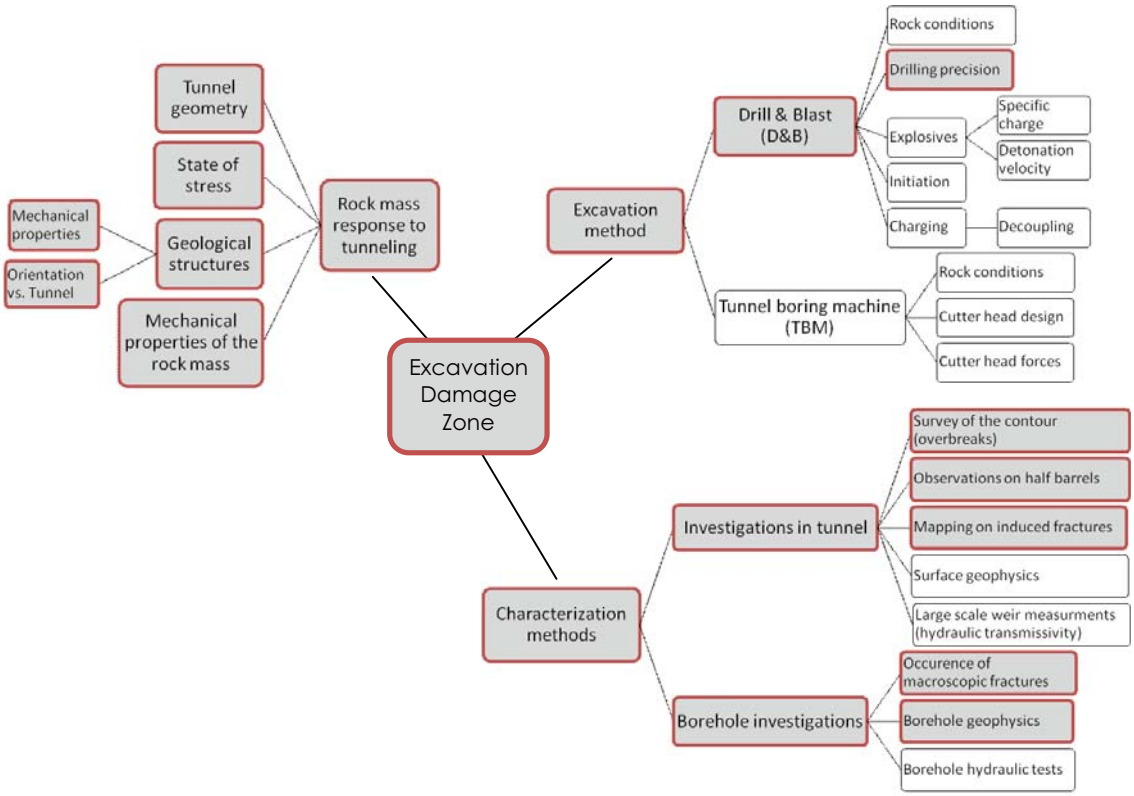

Figure 1-2. *Summary of the factors relating to the rock mass response to tunnelling, the excavation method, and characterisation methods. The highlighted paths are investigated within this study. Picture reproduced from /Hudson et al. 2008a/*

1.2 Outline

In order to introduce the reader to the **Excavation Damaged Zone (EDZ)**, the conventional definition of EDZ is first given (Chapter 2). Thereafter follows a comprehensive summary of previous EDZ studies performed at Äspö HRL (Chapter 3). The geology of the Simpevarp region and the local geology of the TASQ tunnel are then presented (Chapter 4). To brief the reader of two investigations, which are of major importance for this study, a summary of both the drill and blast operations around section 47 (Chapter 5) and the ultrasonic borehole measurements (Chapter 6) are then given.

For this project, laserscanning of the floor and the slot was performed in order to guaranty the highest possible accuracy for the numerical modelling (Chapter 7). For the purpose of this project, a model of larger fractures in the TASQ tunnel in the study area was created. The model should function as input data for the modelling of stresses in the area. In order to incorporate the original 2D tunnel mapping into the new model, the identified fractures have been transposed to its correct location using the laser data available in the tunnel (Chapter 8). Finally, based on the geometric model obtained from the laserscanning and the latest geological model of the TASQ-tunnel, the conceptual model of the study volume could be assembled and simulations could be conducted in order to understand the role and relative influence of several different parameters (Chapter 9).

2 Definition of EDZ

The damage around tunnels is different depending on rock type and the description of this zone in the literature has therefore been different depending on the rock type involved /McEwen 2003/. In crystalline rocks, a distinction between the **Excavation Disturbed Zone (EdZ)** and the **Excavation Damaged Zone (EDZ)** were made /Martino and Chandler 2004, Bäckblom and Martin 1999/. As these zones do not contemporarily exist in all types of rock or are manifested with different responses, a division using a general description of the most dominant properties for each zone is used in today's literature proposed by /Tsang et al. 2005/ and others.

- The EdZ is a zone with hydromechanical and geochemical modifications, without major changes in flow and transport properties.
- The EDZ is a zone in which hydromechanical and geochemical modifications induce significant changes in flow and transport properties. These changes are irreversible.

In crystalline rock, the EdZ is the region where only reversible (recoverable) elastic deformation has occurred; the EDZ is the region of irreversible deformation with fracture propagation and/or development of new fractures. In, among others, the ZEDEX experiment /Emsley et al. 1997/, the change in rock properties and rock stress has been found to be gradual from the damaged zone to the disturbed zone and further on to the virgin rock. A schematic of the EDZ is presented in Figure 2-1.

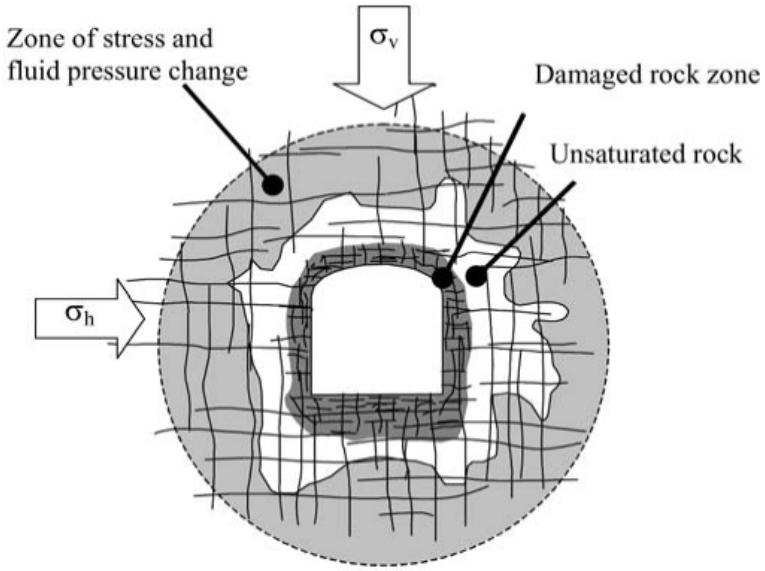

Figure 2-1. *Schematic of the EDZ around a tunnel /Rutqvist and Stephansson 2003/.*

3 Previous EDZ studies at ÄSPÖ

Four large investigations of the Excavation Damage Zone have been performed in Sweden. These project are presented in a table added as Appendix A to this report; inspired by the table by /Bäckblom and Martin 1999/. Three of these projects have been hosted by the Äspö HRL. The Stripa project was performed at the Stripa mine 1980–1992 where the two main objectives were: i) to develop techniques to characterize potential repository sites in granite and; ii) examine engineered barrier materials and designs that could enhance the long-term safety of the repository. This project has been reported in several publications but as the main focus is on projects at the Äspö HRL the reader is referred to /Pusch 1989/, /Olsson 1992/ and /Börgesson et al. 1992/ for further information of the Stripa project.

The three projects that has been performed at the Äspö HRL are: i) Blasting damage investigation in access ramp section 0/526–0/565 m; ii) Zone of Excavation Disturbance Experiment (ZEDEX); iii) investigations in the TASQ tunnel which here is divided into two parts a) Experience of blasting and b) DECOVALEX-THMC IV.

This chapter will mainly concentrate on the mechanical effects reported in these three projects.

3.1 The blasting damage investigation

During the blasting damage investigation of three different blasting configuration for 60 m of the access ramp (Figure 3-1) the questions to be answered were; how to identify the distribution and character of the blasting damage around the tunnel contour using three different blasting schemes and measuring it with: i) geophysical logging; ii) TV borehole logging; iii) hydraulic testing; iv) geological mapping in boreholes and tunnel wall and floor; v) vibration measurements in boreholes; vi) tests for Kaiser effect and microcracks. The three different configurations were called Siab 1 to 3 (from the name of the contractor) and were differentiated into:

- Siab 1, (Cautious blasting (CB)) the configuration used during the blasting of the access tunnel defined by SKB, creating a nominal damage zone of 0.3 m in the walls and 1.7 m in the floor. The advance of this blasting was sometimes poor, about 92% of the advance of Siab 3. There seems to be a tendency for the rock to be left un-blasted in walls and abutments with this blasting configuration. The extent of the EDZ is concluded to be about 1 m in the center of the floor and around the upper limit of 0.3–0.6 m in the walls.
- Siab 2, (Very cautious blasting (VCB)) configuration, nominally damaging 0.3 m in the walls and 0.6 m in the floor. This blasting failed, due to detonation problems that happened in two of the explosives used as well as problems in difference in diameter of the drill hole and explosive cartridge, causing a pressure wave which propagates along the hole and shuts off the detonation. The rock was mainly left in the roof, abutment and floor. Despite these problems it was found that the frequency of induced fractures was significantly lower in the floor of Siab 2 compared to Siab 1 and 3. Also here the short induced fractures runs sub-parallel to natural fractures and occur close to contour holes with a large deviation. The conclusions of the extent of the EDZ are that at the center of the floor it is about 1 m and around the lower limit of 0.3–0.6 m in the walls.
- Siab 3, (Normal blasting (NB)) a blasting configuration normally used in tunnelling, creating a nominal damage extending 0.5 m in the walls and 2.1 m in the floor. The rock that did not brake in these rounds was mostly found in the walls and the floor and is generally put down to orientation of drilling and geological conditions. Compared to the other two blasting techniques, the amount of fractures induced at the contour holes are larger for this blasting configuration. This is the most violent blasting with the largest advance per round. The conclusions of the extent of the EDZ are that at the center of the floor it is about 1.7 m and around the upper limit of 0.3–0.6 m in the walls.

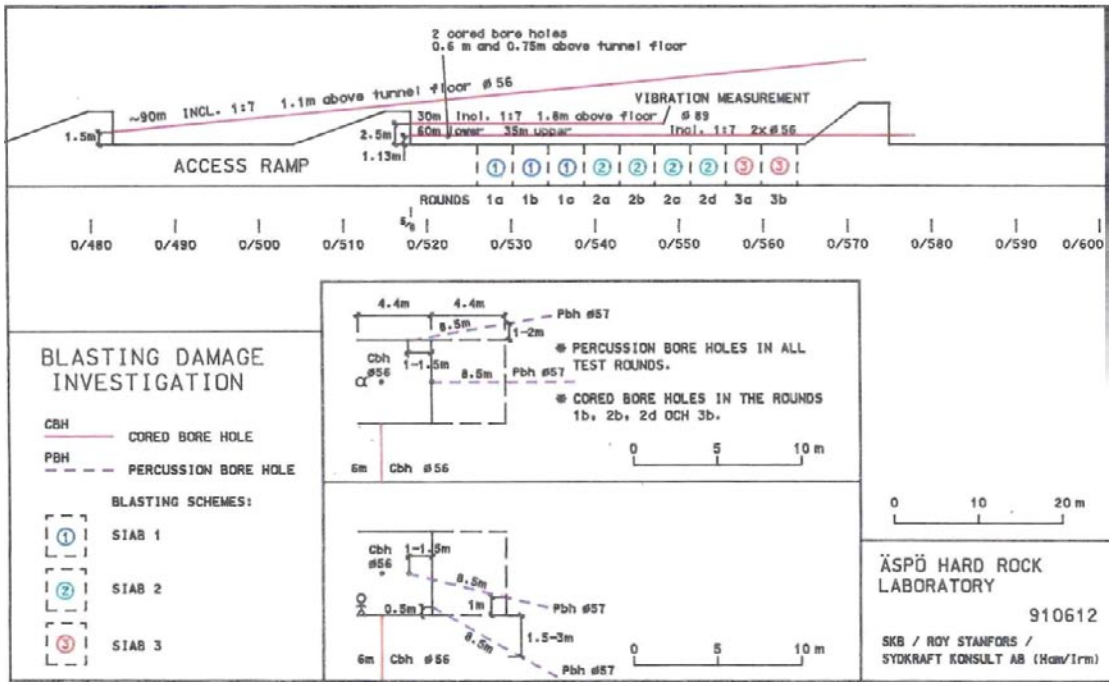

Figure 3-1. *Plan view of the test site for the blast damage investigation /Christiansson and Hamberg 1991/.*

Totally nine blasting rounds were performed in this study (3 for Siab 1, 4 for Siab 2, and 2 for Siab 3). The Siab 2 blasting failed, thus the main body of information about the EDZ is generated from Siab 1 and 3 blasting. No significant difference in the observed damage in the Siab 1 and 3 blasting were found. The fractures induced could be divided into two main groups; i) parallel to the tunnel axis, showing radial propagation from the contour hole and ii) controlled by the geology, either concentrated to particular blocks or perpendicular to long natural fractures. The distribution of induced fractures in the contours was mainly controlled by two parameters; the precision in contour drilling and the local geology. It was found that drilling accuracy was very important for achieving successful rounds.

3.1.1 Conclusions

In the blast damage project a large amount of information was gathered and several methods of measuring the EDZ were used. Some general conclusions are gathered here. The results of the investigation of the EDZ in the different blasting configurations are found in Table 3-1. Some general conclusions are listed below. From the fracture characteristics the main conclusions were that the different configurations are significant for the damage in the floor, whereas the damage in the walls is mainly due to local variations rather than blasting configuration. The distribution of induced fractures is to a large extent related to boreholes on the contour. They emanate radially from the bore hole.

Table 3-1. The EDZ extent identified from the geophysical methods in the different blasting configurations.

The Siab 1	1 m	in the center of the floor
(CB)	the upper limit of 0.3–0.6 m	in the walls
The Siab 2	1.4 m	in the center of the floor
(VCB)	the lower limit of 0.3–0.6 m	in the walls
The Siab 3	1.7 m	in the center of the floor
(NB)	the upper limit of 0.3–0.6 m	in the walls

3.2 The ZEDEX project

For the ZEDEX project, the objectives were: i) to understand the mechanical behaviour of the Excavation Disturbed Zone (EDZ) with respect to its origin, character, magnitude of property change, extent and its dependence in excavation method; ii) to perform supporting studies to increase understanding of the hydraulic significance of the EDZ and; iii) to test equipment and methodologies for quantifying the EDZ.

The two drifts in which these investigations was made is located at about 420 m depth in the Äspö HRL, one tunnel was drilled with a tunnel boring machine (TBM) and the blasted tunnel consists of a tunnel blasted with two different methods normal smooth blasting and low shock blasting (Figure 3-2). Around both the drifts there were several drill holes where core logging and geophysical instruments were installed. In this summary we will concentrate on the results from the drill and blast tunnel. The drift was planned to be driven through the relatively homogenous Äspö diorite as it was found from the earlier study of the blasting damage investigation that the pre-existing geological structures have a large influence on the damage surrounding the tunnel.

The parameters measured and evaluated for the understanding of the EDZ in this project are:

- input energy during excavation,
- elastic and non elastic properties of the rock mass and their response to excavation,
- hydraulic conductivity,
- natural and induced fracturing,
- acoustic energy release,
- stress state,
- temperature.

Several methods, both direct (fracture observations) and indirect (geophysical measurements of different parameters were used. Some of them are listed here, *(methods used in the near-field close to the tunnel wall is written in italic)*:

- *Mapping of the cores of short radial holes, distinguishing between induced and natural fractures.*
- Seismic tomography to map P- and S-wave velocity in several planes around the tunnel to identify fractures.
- *Mapping of half barrels.*
- *P-wave seismic velocity and acoustic resonance measurements on short radial holes.*
- *Seismic velocity anisotropy studies.*
- Far-field stress was measured prior to the project, and through the entire HRL. After the excavation stress measurements were made in the pillar between the two drifts (Figure 3-2).
- The hydraulic properties were measured using build-up tests in several boreholes distributed in the drift after the excavation to determine the transmissivity.
- Radar and seismic reflection were used to identify and orient fractures. The radar measurements could also be used to estimate the water content of the rock mass.
- Measurements of vibrations or acceleration during excavation were made to estimate the magnitude of the energy released into the rock mass during the excavation.
- *High resolution permeability measurements in short radial holes with packer distances of 50 mm.*
- *Detailed laboratory studies of specimens to examine crack damage.*
- Acoustic emission monitoring was used to detect the temporal and spatial distribution of micro crack activity associated with the excavation (both near-field and far-field).
- Convergence measurements in the near-field and extensometers in boreholes extended the measurements into the far-field. These two measurements measure the displacement on different scales.
- Geological and fracture mapping was made in the tunnel and on cores from the bore holes. Bore hole imaging BIPS was also used in all the boreholes.

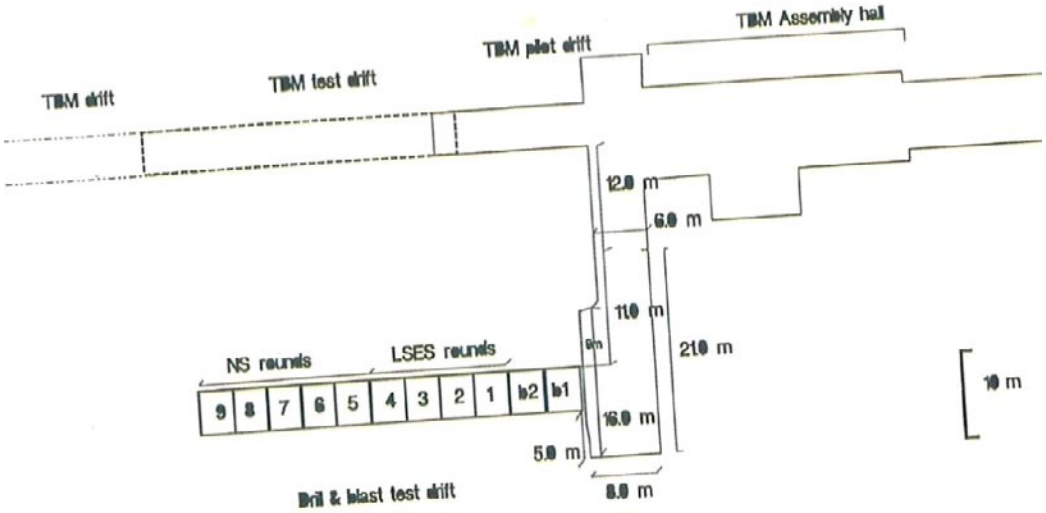

Figure 3-2. *Layout of test drift located at the 420 m depth level, the blasted tunnel show numbered rounds where NS is the normal smooth blasting rounds and the LSES is the rounds where the low-shock explosives are used.*

3.2.1 Conclusions

The most sensitive method to detect the extent of the EDZ is the detection of the Acoustic Emission (AE) events. The AE events detected within the first 8 hours after excavation showed that the AE events occurred at deviatoric stress levels of about 25 MPa, well below the typical range of crack initiation stress of the rock in this area. It was concluded that the AE events were generated by slipping pre-existing fractures /Emsley et al. 1997/. For the Drill and blast tunnel the event density was about 10 times higher than that for the TBM drilled tunnel, and the density was high out to 1 m from the tunnel wall.

All the seismic methods used, indicate a reduction of the seismic wave velocity close to the tunnel wall, in the EDZ. This method is thus useful for detecting the extent of the EDZ.

A larger EDZ was found in the floor of the drill and blast tunnel, for example the dye penetration test performed in the slots cut from the floor show an extent of macro fracturing to about 0.5 m depth in the floor.

As seen in Figure 3-3, the extent of the EDZ is larger around the Drill and blast tunnel compared to the TBM drilled tunnel. The extent of the damage zone is about 0.3 m in the wall and about 0.8 m in the floor in the drill and blast drift. The damage zone is characterized by irreversible changes in property due to excavation induced macro and micro fracturing in decreasing seismic velocity and increased permeability.

The disturbance zone does not seem to be affected by excavation method. This conclusion is derived from the similar AE event activity around both drifts. The AE events suggest shear-slip on already existing fractures in the disturbed zone, thus no new fractures forming. The hydraulic tests performed before and after excavation does not show any change in hydraulic properties in the disturbed zone and the seismic velocity show no change in this zone. This induce the project group to draw the conclusion that the disturbed zone is characterized by changes in state, considered to be reversible /Emsley et al. 1997/.

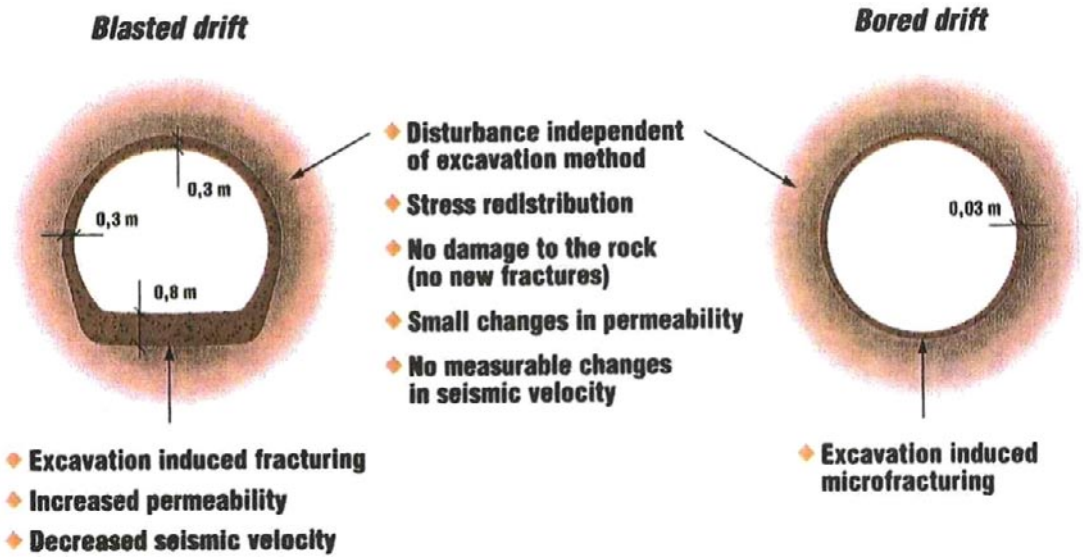

Figure 3-3. *Summary of the main findings of the ZEDEX project. The extent of the damage zone is significantly greater in the drift excavated by the blasting compared to the drift excavated by a tunnel boring machine. Reproduction from /Emsley et al. 1997/.*

3.3 EDZ projects in the TASQ tunnel

The project in the EDZ investigations at Äspö was performed in the TASQ-tunnel divided into a primary investigation which was afterwards followed by a Ph. D. project performed by Ann Bäckström for the Royal Institute of Technology (KTH) in Stockholm. One of the objectives of the Ph. D. project was to provide the DECOVALEX-THMC project with input data for the evaluation of the development of the excavations zone by modelling using coupled Thermo-Hydro-Mechanic-Chemical processes /Hudson et al. 2008a/.

During the primary investigation, the objects were to: i) study the possibility to control the development of an Excavation Damage Zone; ii) could the lessons learned from 8 years ago produce a less pronounced EDZ; iii) investigation of drilling precision through manual mapping of half-pipes and geological mapping of cut out of slots in the wall and the floor. The open fractures in the surfaces of the cut-outs were enhanced with a penetrative dye. The blast cracks, induced cracks and natural cracks were mapped. The blast cracks are identified as cracks emanating from a trace of a blast hole whereas the induced cracks are cracks not directly associated to a blast hole. The induced fractures are assumed to be a response to either the blasting or be stress induced. The natural fractures can be opened or extended as a result of the blasting.

In the investigation of the half-pipes it was found that 95% of all half-pipes fulfilled the demands which is defined as the hole ending less than 0.30 m outside of the nominal tunnel section and no hole deviation exceeding 10 mm/m /Olsson et al. 2004/. The total amount of visible half-pipes in the TASQ-tunnel was high and indicated a successful smooth blasting. Several measurements of the tunnel profile was made and shown in Figure 3-4. The “undulating” contour of the left hand wall in section 0/070 is visible on the wall show that the contour drilling was not aligned for that round. It is also indicative that there is a tendency for over-break in the left abutment in several sections.

Soon after the tunnel was completed, 13 cores were drilled in the floor for detailed planning of the APSE experiment, and for instrumentation. The bore holes were 6–7 m deep and primarily located around sections 0/064 to 0/066 m. The core were logged and sonic velocities were measured /Staub et al. 2004/. Possible induced fracturing was found to a depth of normally not more than 0.3 m. However, it is not possible to determine if observed fractures in the 51 mm cores are induced, or if they consists of natural horizontal fractures that are somewhat sheared because of the elevated stresses in the floor.

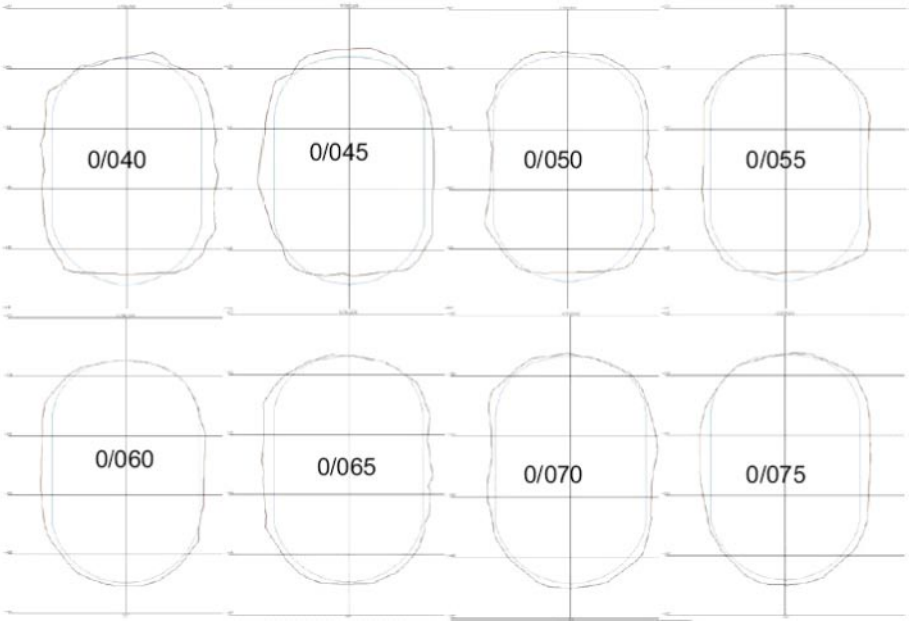

Figure 3-4. *Reproduction of tunnel profiles measured with a 2D laser compared to the designed tunnel profile /Olsson et al. 2004/.*

Earlier studies have shown that water in the blast hole can increase the length of blasting cracks along the blast hole by a factor of 3–4 times /Olsson and Ouchterlony 2003/ and as the drill rig uses water to flush away the cuttings and several of the blast holes cut in the slot for the EDZ observation were dipping 1–3° down it is highly likely that they were partly filled with water /Olsson et al. 2004/.

The conclusions regarding the EDZ from the report by /Olsson et al. 2004/ are reproduced here:

- Unexpectedly long crack lengths were obtained from holes simultaneously initiated with electronical detonators (Table 3-2). This is unexpected due to the contrary results found in the great number of tests in quarries and tunnels, performed by SveBeFo /Fjellborg and Olsson 1996, Olsson and Ouchterlony 2003/, which have very obviously shown that simultaneous detonation with electronic detonators always creates shorter cracks than Nonel-initiation when the same conditions apply. Water in holes strongly affects the crack length which is a plausible explanation why electronical detonators seem to cause longer cracks compared to holes initiated with Nonel.
- Unexpectedly short crack lengths were obtained from holes initiated with Nonel detonators (Table 3-2). See comment above.
- Shorter cracks and fewer cracks were created in the left hand wall than in the right wall.
- Most of the induced cracks in the vertical slots seem to have a diagonal direction (pointing upwards) in the lower part of the wall. The largest number of induced and natural cracks seems to point in the direction 60–120 degrees. In the vertical slots most of the induced cracks therefore have a diagonal direction (pointing upwards) as shown in Figure 3-5. The cracks originating from blast holes point in all directions.
- Most of the induced and natural cracks seem to be in the direction 60–120 degrees relative to the vertical walls.
- Fewer cracks were observed to be derived from the bench than from the tunnel (due to stress, hole straightness, water and perhaps confinement).
- No cracks originating from blast holes in the floor.
- No evidence of a continuous damage zone parallel to the tunnel wall was found.

Table 3-2. Blast induced crack length in tested sections and from different initiation.

Explosive	Section	Initiation	Crack length in cm		
			Minimum	Maximum	Average
Dynotex 17	Tunnel	Electronic	0	22	14
Dynotex 17	Tunnel	Nonel	0	0	0
Dynotex 17	Bench	Nonel	0	10	5
Dynotex 17	Floor	Nonel	0	0	0

Some more general conclusions were also drawn from this investigation such as:

- There is a demand for new drilling equipment with a better guidance control to increase the drilling accuracy.
- Electronic detonators have very good accuracy and a high potential to reduce cracks from blasting. However, they must be more easy to use.
- It is possible to minimize the damage zone in the floor by using top heading and bench. However, there is a demand for more development in order to minimize the damage zone in the floor without a separate bench.
- Water in bore holes increases the damage zone in terms of length and frequency of induced fractures. This could be avoided by drilling the holes pointing slightly upwards.
- The look-out angle and distribution of specific charge along each round causes a discontinuous EDZ along the tunnel. It is therefore indicated that the impact of the EDZ on hydraulic conductivity along the tunnel has very limited impact.
- During similar conditions it is believed that the extent of the EDZ is manageable through D&B design and QA control during excavation.

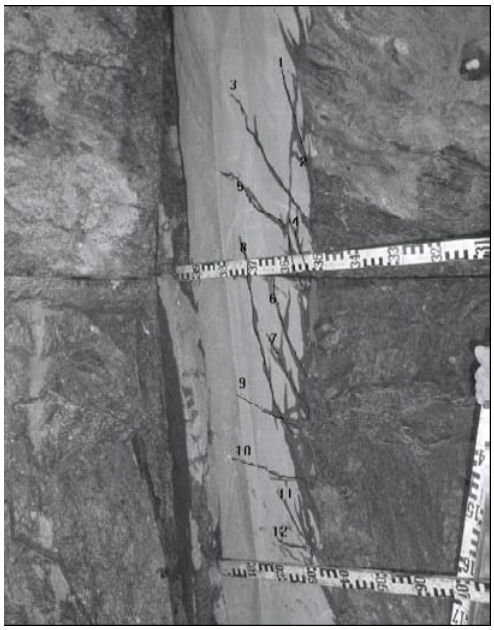

Figure 3-5. *An example of the measurements of fractures in the cut-out at section 47. Reproduced from /Olsson et al. 2004/.*

3.4 DECOVALEX-THMC

The DECOVALEX-THMC project addressed the nature of and potential for thermo-hydro-mechanical-chemical modelling of the Excavation Damaged Zone (EDZ) around the excavations for an underground radioactive waste repository. The DECOVALEX-THMC project was divided into several phases (Figure 3-6).

The target for the Ph. D. study within the DECOVALEX-THMC project was the optimization of the parameter acquisition from an in-situ case study to be used for numerical modelling of coupled T-H-M-C processes in the EDZ. Furthermore, the development of strategies for the characterisation of the EDZ from tunnels and improvement of the quality assessment (QA) program used during the construction of a deep repository will also be carried out. Deeper understanding of the EDZ will be achieved through investigation of the formation processes with emphasis on the coupling between the mechanical evolution of the EDZ and chemical processes.

The project started with a study of the failure behaviour of the Ävrö granite under different hydro-chemical environments. The results from these tests were distributed to four research teams using different modelling tools. The capabilities of the four models were compared to each other. The results generated by each model were compared with the experimentally determined complete stress-strain curves for the Swedish Ävrö granite for different porewater conditions /Bäckström et al. 2008b/. A further investigation of the fracture generation and propagation in these specimens were conducted. It was found that a pre-existing fracture set was present in all the specimens used in this study. This pre-existing fracture set was found to be oriented in the direction of major principal stress in the rock mass from which the specimens were retrieved. The close to perpendicular orientation to the specimen axis of these pre-existing fractures is found to influence the propagation of the fractures induced by the uniaxial compressive stress during the tests.

A 3D-laser-scanning measurement of the TASQ tunnel was performed in November 2005 /Bäckström et al. in prep/. The 3D-laser-scanning method was used as a tool for measuring and evaluating the geometrical results of the blasting rounds for the excavation of a tunnel. By combining information on the overbreak and underbreak with the orientation and visibility of drill holes and fractures in three dimensions, much more information than what is generally available can be gained to improve the performance of the drill-and-blast method. The 3D-laser-scanning method was tested as a tool for diagnosing the effect of the blasting operation and the possibility to identify the damage around tunnels.

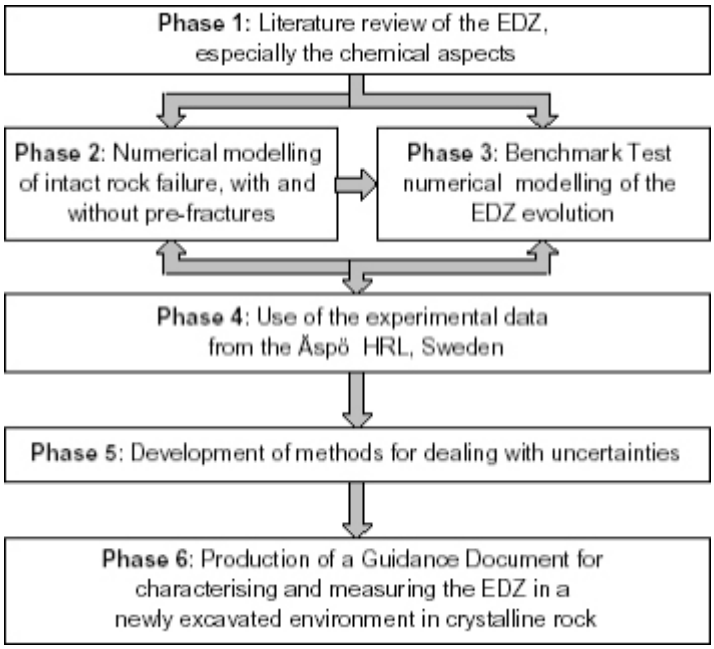

Figure 3-6. *Overview of the different phases of DECOVALEX-THMC, Task B.*

3.4.1 Failure behaviour with different pore fluids

Twenty specimens were subjected to waters with different salinity and their behaviour during uniaxial compressive tests /Fairhurst and Hudson 1999/ was identified /Jacobsson and Bäckström 2005/. These rocks have a strong Class II behaviour /Wawersik and Fairhurst 1970/, see Figure 3-7. Class II behaviour is failure of rocksamples under uniaxial compression that cannot be controlled in axial strain even by a perfectly stiff testing machine, i.e. self-sustaining failure behaviour. This type of behaviour can be controlled by using alternative feedback to the axial strain, such as the radial strain, which was used in this study. In this study, the effect of weak saline water on Young's modulus and the compressive strength increased with the immersion time (Figure 3-8). Our experiments also suggest that there is an effect of salinity on the post-failure behaviour of brittle rocks. With high saline water, the specimens act more in a more ductile manner than those with low salinity water (Figure 3-8). Future studies need to be conducted to provide more information and confirm the general trends reported here because it was only possible to test a limited number of samples. In particular, more attention should be paid to:

- long immersion time,
- triaxial and tensile tests,
- fracture toughness,
- mineral weathering in saline environments.

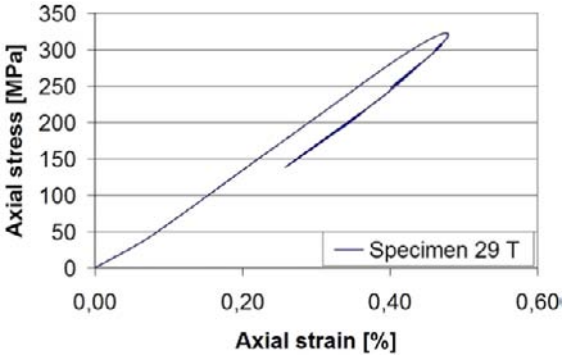

Figure 3-7. *Class II stress-strain curve for specimen 29T where T stands for dry. Note that the Ävrö granite is ultra-brittle, this being an extreme example of Class II behaviour.i.e self-sustaining failure behaviour under axial strain control in uniaxial compression tests, in this case controlled by using radial strain as feedback.*

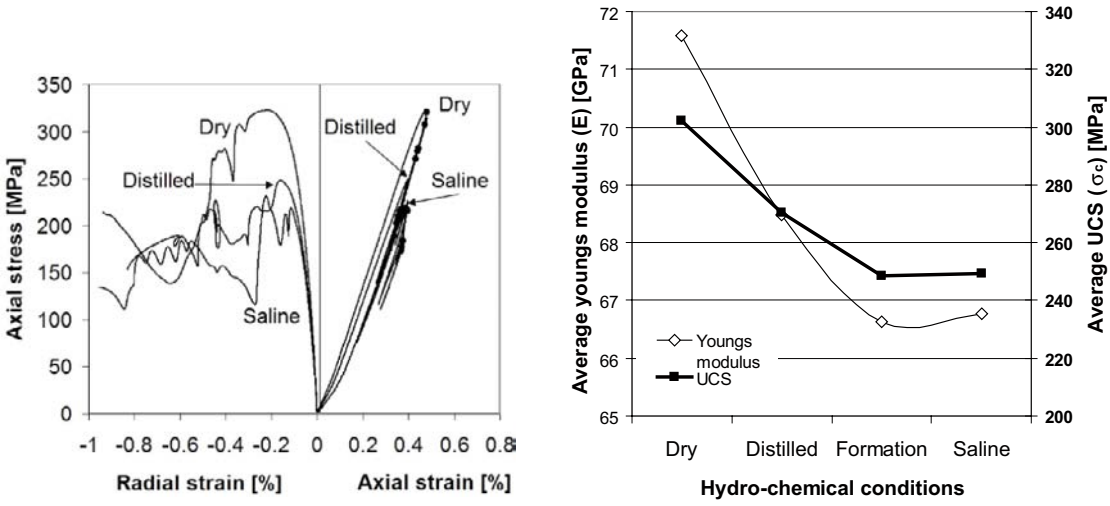

Figure 3-8. *(a) Class II stress-strain curves for three individual specimens subjected to the separate conditions of dry, distilled and saline water following 90 days immersion each. (b) Average Young's modulus and UCS of the specimens for the same four saturation conditions. (The Young's moduli values are indicated by hollow diamonds with the axis shown on the left and the UCS values are the filled squares with the axis shown on the right).*

3.4.2 Modelling of the failure behaviour

An inter-comparison of results from four different models and direct comparison between models and experimental results in an exercise to model the uniaxial compressive failure of intact rock with and without saline porewater using different numerical models is presented in /Bäckström et al. 2008b/. Representatives of both continuum-based and discontinuum-based modelling tools are presented. The continuum approach is based on the application of fundamental models such as the elasto-plastic/elasto-viscoplastic models /e.g. Adachi et al. 2005/ and damage mechanics models /e.g.Goshani et al. 2005/. The two discontinuum based models used in this simulation is either developed from empirical observations of the behaviour of rocks, like FRACOD /Shen et al. 2005/ with pre-existing cracks, or via particle mechanics, such as the Particle Flow Code /e.g. Potyondy and Cundall 1996, 2004, Potyondy 2007, Itasca Consulting Group 2003/, involving a series of discrete elements. Two of the four models could reproduce the stress-strain curve of the Class II behaviour as seen in Figure 3-9 where the simulated of the Ävrö granite is presented. Although the exact test conditions and results could not be faithfully simulated, the general trends in mechanical behaviour were apparent from the models. The Class II behaviour was not simulated by the PFC model at this stage in its current form, but such behaviour can be simulated by using proper numerical control techniques. The Damage Expansion Model was able to be adapted through the extraction of strain energy to approximate the Class II behaviour in the uniaxial compressive test.

All these models were useful in characterising and illustrating the trends in mechanical behaviour during the rock's microstructural breakdown. Moreover, all the models were eminently suitable for sensitivity studies to evaluate the influence of their respective supporting parameters. The different models operate on different constitutive basis and the laboratory testing still needs to be developed to identify the damage and failure mechanisms of the intact Ävrö granite. The reproduction of the Class II behaviour that was achieved by several of the models must be regarded as a starting point for further development of the understanding of this phenomenon.

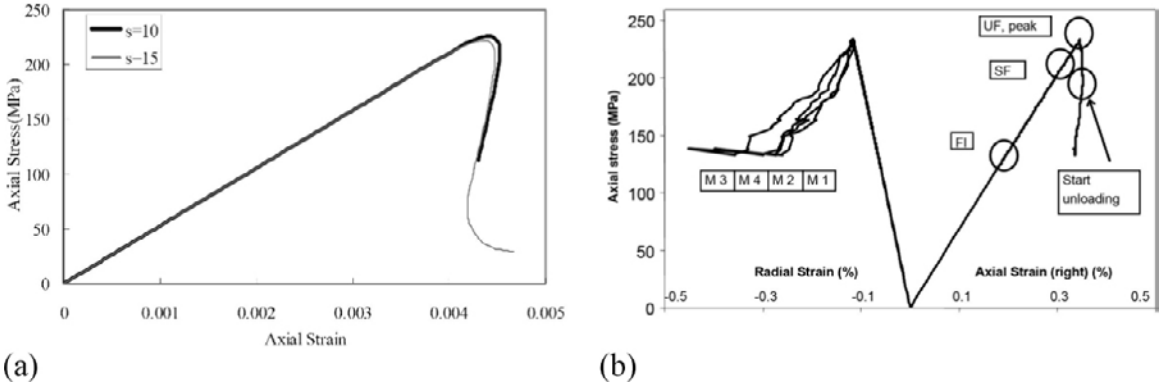

Figure 3-9. *The stress-strain curve for the simulation of the Class II behaviour of the Ävrö granite using: a) the Elasto-Plastic cellular Automaton method (where s is the randomness of the parameter distribution in the cells /Pan et al. 2006/) and b) the DDM technique represented by the FRACOD model where M represents four different points on the specimen /Hudson and Jing 2007/.*

3.4.3 Laser scanning of the TASQ tunnel

Detailed laser scanning geometric data were used to provide basic audit data for comparing the "as-designed" tunnel with the "as-built" tunnel. The information of the verbreak and underbreak together with a 3D model with the location and orientation of the fractures and visible drill holes provide a basis for further evaluation. The tunnel was about three years old when this investigation took place, thus the roof was supported with shotcrete and scaling of the walls have been performed regularly. For a more detailed description of this study see /Bäckström et al. 2008a/. In this study, it was shown that there is about 20% of overbreak in the section between 44.5–55.5 m in the tunnel (not including the floor) (Figure 3-10). Additionally, two large areas of overbreak was identified in the walls. The damage in the area of extreme overbreak (> 0.5 m) at chainage 44.8 m in the TASQ tunnel is located about half-height on the tunnel wall. This overbreak area is rather limited in lateral extension but elongated in vertical direction (Figure 3-11). The drill-hole traces in this area are scarce while the fractures are numerous. From the geological mapping of the tunnel, it was found that a mylonite zone is located here, and it is likely that this geological structure is the cause of the overbreak. Contrary to this, the overbreak about 0.5 m at chainage 54.3 to 55.1 m is probably caused by the orientation of many drill holes converging towards this area (Figure 3-11). This is an overbreak caused by poor drill hole orientation. The 3-D laser scanning method has also been used to compare different blasting initiation systems (electric detonators versus non-el detonators). The electric detonators were used in the last three rounds of the top heading blasting, with a drilling length of about 4 m. They can be compared to the rounds where chemical ignition, so called, non-electric detonators was used. Only the rounds with similar drilling length were used. It was found that the electric detonators have a better blasting performance than the non-electric detonators because the accuracy of the blasting is larger, but it should be kept in mind that this conclusion is drawn from a very small number of samples.

A more detailed investigation of the fractures of the EDZ zone was made in the cut-out at chainage 47 m called AQ0047A01. This detailed mapping was performed for the in-put to a Bench Mark Test (BMT) called "Near-field model 2" for simulations of the development of the EDZ during 100,000 years using four different modelling tools in section 3.4.4. A more detailed account of the proceeding to retrieve the fracture network can be found as an appendix to /Rutqvist et al. 2008/.

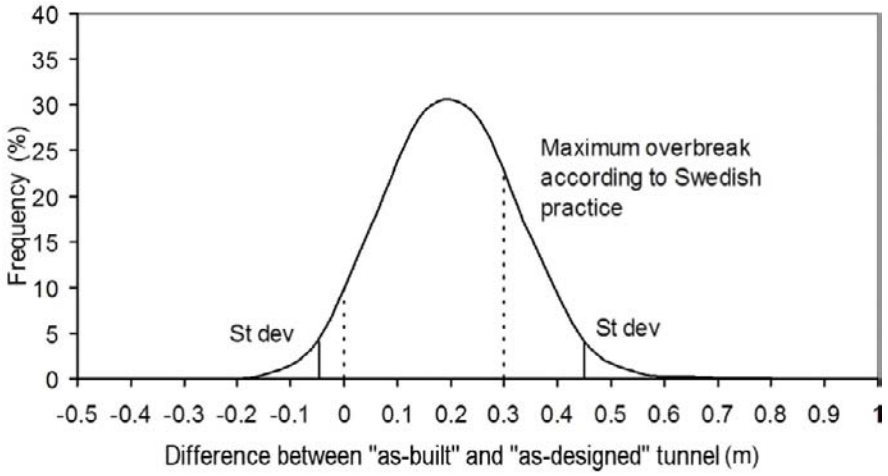

Figure 3-10. *The distribution of the difference between "as-built" and "as-designed" from the 3D-laser scanning between section 44.5–55.5 m (point-distance 1–3 mm) for about 65,335 values. The overbreak larger than 0.3 m is about 20%.*

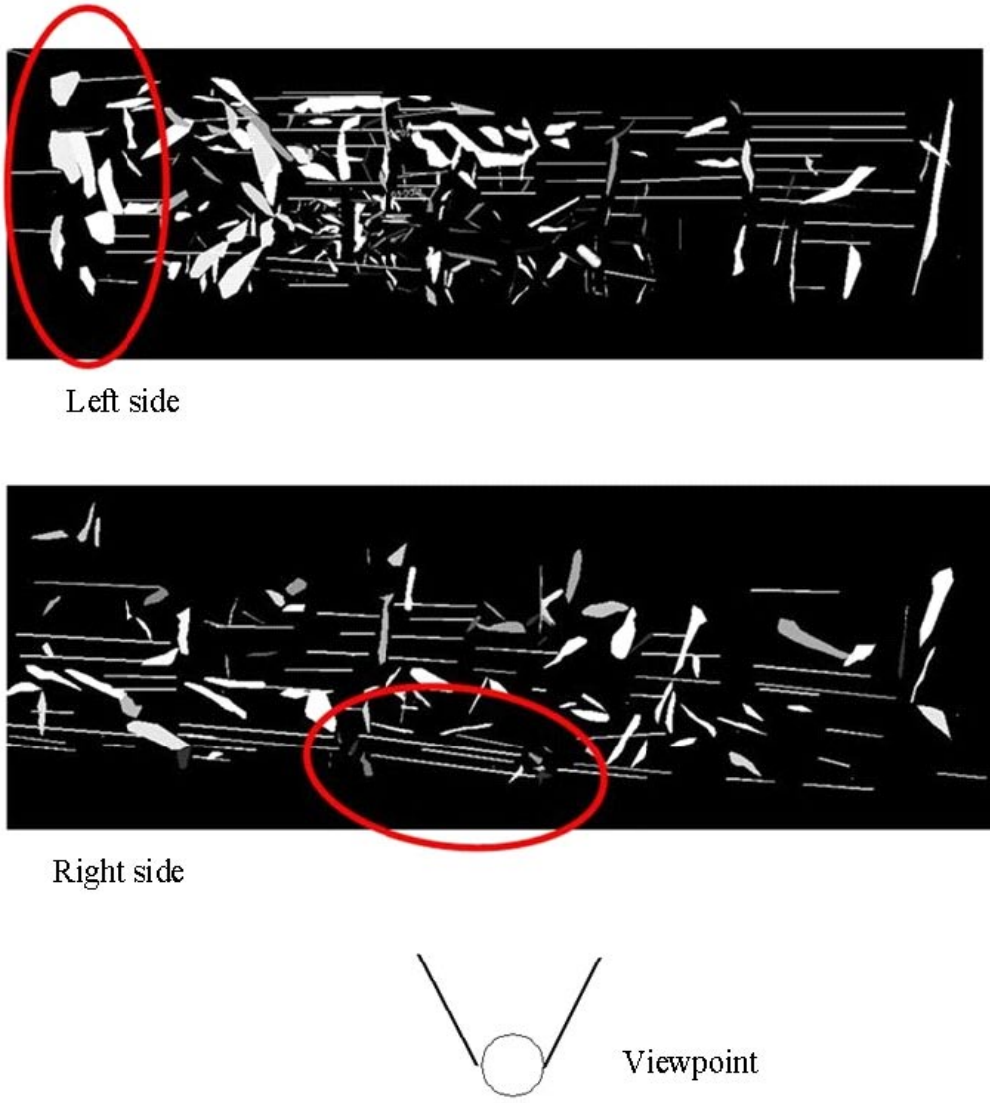

Figure 3-11. *Mapping results from laser scanning data of the two tunnel walls between about 40 to 60 m with 3-D fracture surfaces and drill holes. The red ellipses show the cause of the extreme overbreak at these locations.*

The cut-out in the wall, which is a part of the tunnel that is about 2 m high and about 0.5 m wide perpendicular to the tunnel wall (Figure 3-5). This area is a small part of the TASQ tunnel wall and is located in the lower part of the sidewall. There is no information about fractures further into the wall than about 0.5 m depth, but the fracture network from the cut-out has been combined with fracture data from the tunnel wall. A section of already existing fracture mapping is selected from the tunnel wall. The fracture pattern from the cut-out can then be traced onto the model (Figure 3-12). An area from the tunnel wall is selected to make a detailed fracture map (about 3.42 m by 3.42 m) to put into the model. Several simplifications due to the symmetry conditions in the model compared to the tunnel are made. The final fracture map has been assembled as shown in Figure 3-13, including the geometry and property distribution of the matrix rock in the EDZ.

From the raw data a normal projection (orthophoto), instead of perspective projection (like a normal photograph) is obtained. Thus the picture is not distorted in different areas, which allows for detection of "true" trace length of each fracture (Figure 3-14b). This 2D grey-scale image is generated from both 3D co-ordinates and corresponding reflectance intensity. Based on this 2D grey-scale image a trace map of fractures exposed on the tunnel wall can be created. In this trace map the location and distribution of fracture trace lines can be determined exactly (Figure 3-14c). In Figure 3-15, the orthophoto used for the fracture network for the EDZ can be seen. The fracture network used for the "background" fracture network can be seen in Figure 3-14c.

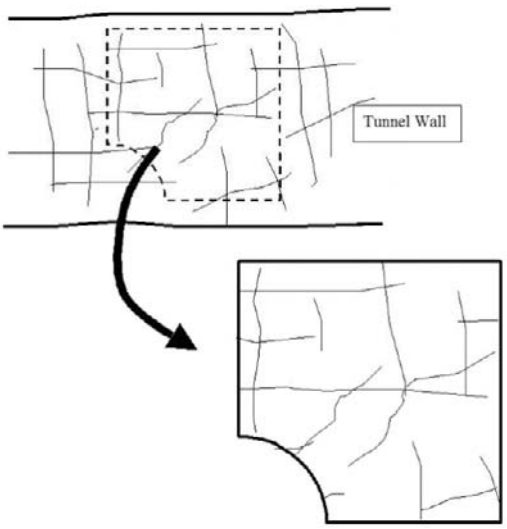

Figure 3-12. *Model of pre-existing fractures from tunnel wall traces.*

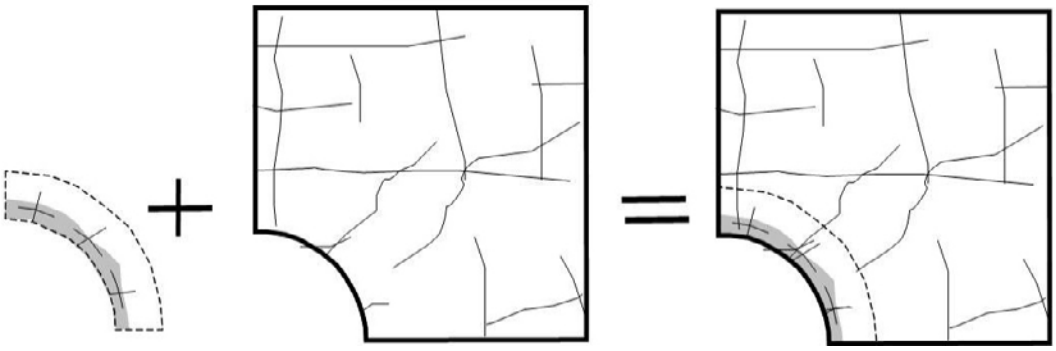

Figure 3-13. *Assembling complete fracture and disturbed zone map.*

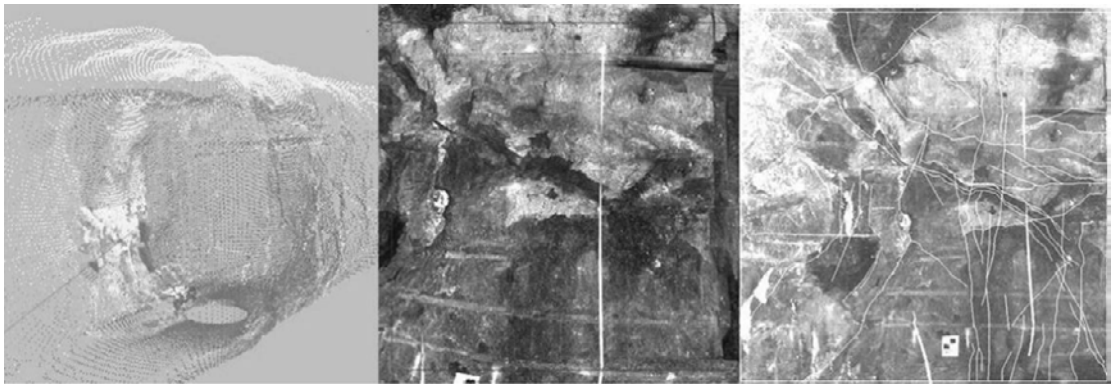

Figure 3-14. *a) A part of 3D digital model of tunnel is selected for the fracture mapping and b) creating a laser orthophoto c) 2D fracture trace map from the laser orthophoto.*

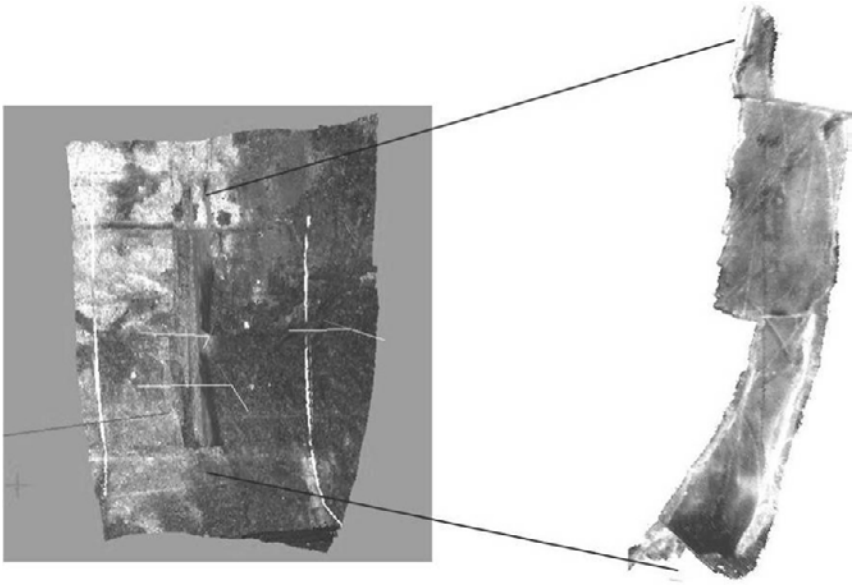

Figure 3-15. *The orthophoto used for the fracture network used for the EDZ mapping.*

The fracture network obtained from the EDZ surface can be seen in Figure 3-16a where the filled fractures are included in green colour and the pre-existing open fractures (although perhaps not opened before blasting) is seen as light blue traces. The open fractures where no mineral coating can be seen are traced in red. The fracture network of the background surface was obtained from an area of the tunnel wall juxtaposed to the cut-out. The combined fracture network used in the simulations can be seen in Figure 3-16c. The geometry of the area and the resulting fracture network from the merging of the two areas can be found in Figure 3-16c. Together with a collection of the mechanical properties measured on fractures and rock mass, this fracture network used in the Near-Field model 2 used in the simulations.

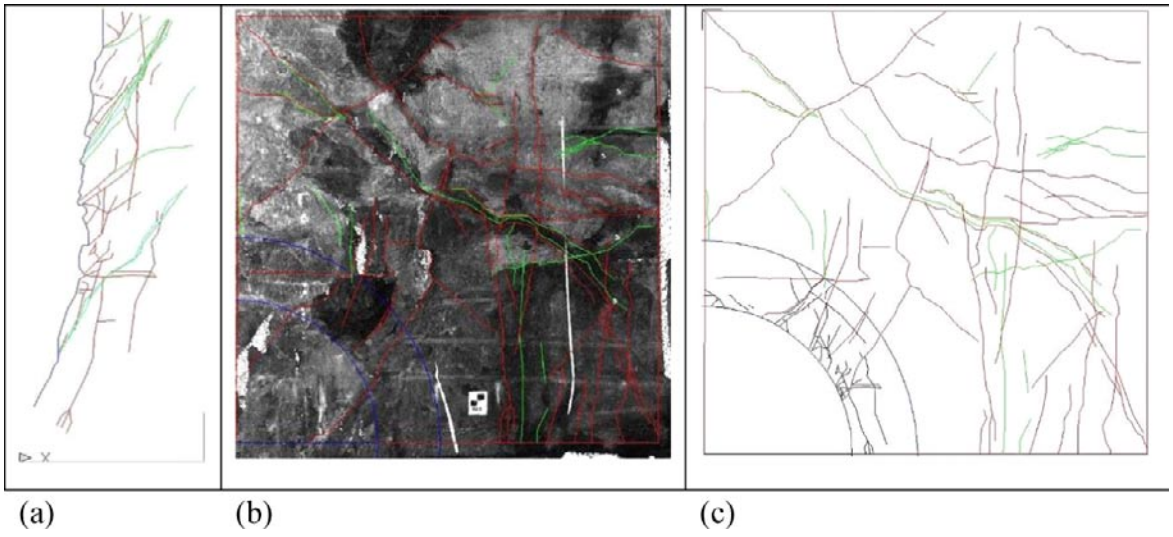

Figure 3-16. *a) The mapped cut-out area of the EDZ. b) Area mapped from orthophoto of the intensity data, for the background surface. c) The combined fracture network for the EDZ, where the red fractures are open fractures, the two light blue are natural fractures, they are surrounded by green fractures that are filled fractures.*

3.4.4 Previous modelling of the EDZ

During the DECOVALEX-THMC project, several simulations of the mechanical behaviour of the rock mass were performed using different modelling programs. A summary of the results from the DECOVALEX-THMC project can be found in /e.g. Hudson et al. 2008a, Hudson and Jing 2007, Rutqvist et al. 2008/.

The Bench Mark Simulation Study of Coupled THMC Processes in the EDZ focuses on mechanical responses and long-term chemo-mechanical effects that may lead to time-dependent changes in mechanical and hydrological properties in the EDZ. This includes processes such as creep, subcritical crack growth, and healing of fractures that might cause "weakening" or "hardening" of the rock over the long term. He main objective of this report was to investigate the change in mechanical properties. Five research teams were studying this Bench Mark Test (BMT) using a wide range of modelling approaches, including boundary element, finite element, finite difference, particle mechanics, and cellular automata methods (Table 3-3). An important part of this BMT was to investigate how different approaches could be adapted and developed to model the evolution of the EDZ and to include time-dependent processes to model the complex coupled Thermo-, Hydro-, Mechanical, and Chemical (THMC) processes at various scales around an emplacement tunnel. Thus, this BMT was not a strictly defined problem for code-to-code comparison, but was rather designed to promote innovative model developments towards simulation of chemo-mechanical interactions, with a future goal of fully coupled THMC modelling.

Two different sizes of model domains close to an emplacement tunnel were simulated: (1) a near-field model domain and (2) a wall-block model domain (Figure 3-17). The near-field model domain extended a few meters into the rock from the drift wall and allowed analysis of both the evolution and extent of the EDZ. The smaller sized wall-block model was used for detailed analysis of THMC processes within the EDZ.

The fracture pattern to be used for Near-Field Model 2 was derived from fracture mapping from the TASQ tunnel by A. Bäckström seen in Figure 3-16c /Bäckström 2006/.

In this BMT, the excavation was assumed to occur instantaneously, whereupon the pre-emplacement, or operational, period begins. The initial pre-excavation conditions were represented by in-situ stresses, temperature, and fluid pressure at a depth of 500 m in crystalline rocks. Specifically, data representing conditions at the Äspö Hard Rock Laboratory corresponds to an initial vertical stress of 13.2 MPa, a horizontal stress of 32.1 MPa, a temperature of 25°C, and a fluid pressure of 5.0 MPa /Rutqvist et al. 2008/. After modelling of excavation of the drift, a transient analysis of the pre-emplacement period was to be conducted for 10 years. For this simulation, stress, thermal, and hydrologic boundary conditions were kept constant throughout the preclosure period.

Table 3-3. Research teams and numerical simulators.

Research Team	Numerical Simulator/Approach
DOE: U.S. Department of Energy's Research Team: Lawrence Berkeley National Laboratory (LBNL)	TOUGH-FLAC simulator using finite difference method (FDM) ROCMAS finite element (FEM) code
CAS: Chinese Academy of Sciences' Research Team	Elasto-Plastic Cellular Automata (EPCA)
FRACOM: FRACOM Ltd, Finland	FRACOD boundary element discontinuity displacement code (BEM/DDM) with discrete fracture propagation
JAEA: Japan Atomic Energy Agency's Research Team, including Kyoto University	THAMES finite element (FEM) code
SKI: Swedish Nuclear Power Inspectorate's Research Team: Royal Institute of Technology, Stockholm	PFC distinct element particle flow code

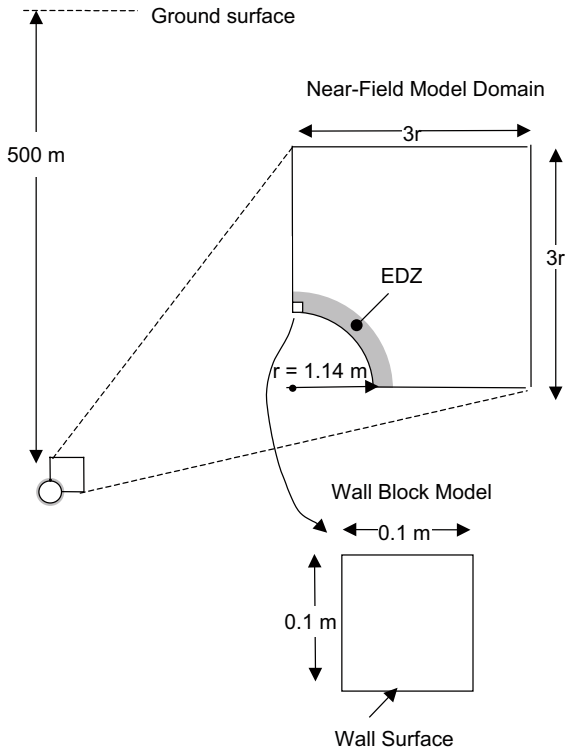

Figure 3-17. *Two model domains considered for detailed analysis of coupled THMC processes in the EDZ of a drift.*

The postclosure environment was simulated using a time-varying temperature, fluid pressure, and boundary stress. The simulation of postclosure environment was to be conducted for over 100,000 years. For more information on the development of the environment please refer to /Rutqvist et al. 2008/. The questions addressed during these simulations were:

1) How much the hydrological properties change and what is the magnitude of permanent change after cool-down?
2) How much the mechanical properties change and what is the likelihood for mechanical failure in the EDZ?
3) What are the most likely failure mechanisms in the EDZ?
4) How important are the time-dependent chemo-mechanical effects in this case?
5) How can the EDZ be properly characterized for predicting the evolution of the EDZ?

The conclusions presented here are summarized from the SKI report /Rutqvist et al. 2008/. Some tentative assessments of the model results as to the questions asked during the project have been presented in /Rutqvist et al. 2008/ where different models contribute with results. This study show that the permeability outside the excavation disturbed zone decline during the first 100 years after emplacement. Inside the excavation disturbed zone, the permeability may increase or decrease due to stress redistribution around the drift. From models based on the BEM method with discrete fracture propagation, local increases at fracture intersections are identified; this could lead to additional permeability changes that are permanent. In another simulation of the mechanical effect on the hydraulic properties in fractures around a deposition hole indicate only small changes /Hökmark et al. 2006/.

In-elastic rock failure was predicted near the tunnel wall by many research teams, but only if fractures or scale dependent strength parameters are considered. Most of the models predicted very limited rock failure with fractures included in the model, and none in the cases calibrated against small scale laboratory tests. The zone of failure largely coincides with a zone of high deviatoric stress, whereas some tensile failure may also play a role, especially near the spring line of the drift.

The analysis of the specific BMT presented in /Rutqvist et al. 2008/ indicated that increased differential stresses near the top of the emplacement tunnel during the first 100 years may cause additional failure and permeability changes. Time dependency may play only a small role during the first 100 years of loading, which is a relatively short time for chemically mediated processes. Without the heat load, the maximum principal stress is about 60 MPa (about 20% of the small-scale peak strength), which may be too small to induce significant time-dependent mechanical changes. However, predictions of chemically mediated time-dependent mechanical change over a 100,000-year period are still very uncertain, but could be conservatively bounded. The importance of the time-dependent chemo-mechanical effects on the evolution of the excavation disturbed zone is still unclear because of lack of sufficient data and models to evaluate such changes.

3.5 General conclusions

The tunnels are about the same size and the EDZ in the walls are about the same extent in all three tunnels presented here (about 0.3 m). The different excavation configurations between the tunnels, causes a difference in extent of EDZ in the floor. In the three different blasting configurations in the blasting damage investigation: siab 1 (defined by SKB) cause 1 m damage in the floor; siab 2 (cautions blasting, so cautious that it need reblasting) cause 1.4 m damage in the floor whereas the siab 3 (normally used in tunnelling, larger charges than Siab 1 and 2) cause 1.7 m damage in the floor. In the ZEDEX project the EDZ in the floor was about 0.8 m. In the visual observation of the slots in the floor of the TASQ tunnel few cracks were observed, and no cracks originating from blast holes were found in this investigation. The seismic investigation in the TASQ tunnel (summarized below) identifies the extent of the EDZ in the floor to about 0.75 m, although, this is results from one borehole in the floor.

- The misfires and required reblasting of these contours as well as deviations of the contour holes cause larger EDZ in the wall. This was seen as unexpected high frequency of new fractures observed for the sections where reblasting was necessary in the damage project and as newly connected cracks introduced by the excavation process in the ZEDEX project. Examples of larger overbreak due to deviation of the contour holes have been identified from the laserscanning results in the DECOVALEX project. A quantification of the damage caused by the deviation of the contour holes was made in this study.
- The conclusion that the excavation method needed modification to limit the amount of misfiring and thus reblasting and limit the deviations of the contour holes has resulted in the modified blasting method used in the TASQ tunnel and the testing of electric detonators in the three last blasting contours. In the model of the contour holes in the tunnel, generated from laser scanning data of the tunnel, a comparison between the number of traces of drill holes in the rounds with electronic detonators and the ones with non-electronic detonators was done. It was found that there were about 23% more traces found in the rounds in which electric detonators were used. The average length of the visible traces of drill holes for the electronic detonators were longer than the average length of the non-electronic detonators: 2.24 m compared to 2.05 m. The conclusion of this comparison is thus that the electric detonators have a better blasting performance than the non-electric detonators because the accuracy of the blasting is larger, but it should be kept in mind that this conclusion is drawn from a very small number of samples.

4 Geology

4.1 Regional geology in the Simpevarp region

The Precambrian bedrock of southeastern Sweden was formed between ca 1,850 and 1,650 Ma, i.e. during the Svecokarelian orogeny. The predominating rock types are mainly magmatic rocks that belong to the Transscandinavian Igneous Belt (TIB). In the Simpevarp region they were emplaced at ca 1,810–1,760 Ma /e.g. Kornfält et al. 1997/. The dominating rocks are granitoids to dioritoids and gabbroids and related rocks of possible volcanic origin, though the latter are not positively identified in the area. The dominating felsic portions of the granitoids to dioritoids are by tradition collectively referred to as "Småland granites", although the latter comprise a variety of rock types regarding texture, mineralogy and chemical composition. To the local variants of Småland granites in the Simpevarp the so-called Äspö diorite and Ävrö granite belongs. For magmatic rocks in this region magma-mingling and mixing processes are typical, exemplified by the occurrence of enclaves, hybridization and diffuse transitions between different lithologies etc. At a local scale, such as an outcrop or a short section in a tunnel, these processes often result in a more or less inhomogeneous rock mass. However, if larger rock volumes of rocks are considered the Småland granites can be regarded as rather homogeneous, despite their internal variations. Locally, fine-grained granitic or aplitic dykes and minor massifs are frequent. Although volumetrically subordinate, these dykes locally constitute essential inhomogeneities of the bedrock in the Simpevarp region. These rocks are considered to be roughly coeval with the TIB host rock /Kornfält et al. 1997/, but have intruded at a late stage in the magmatic process. At Äspö felsic dykes of this type is common. TIB-related doleritic dykes and composite dykes are sparse.

A somewhat later period of rockfoming magmatism in the Simpevarp region occurred when local emplacement of granitic magmas took place at ca 1,450 Ma. This magmatism is exemplified by the occurrence of the Götemar, Uthammar and Jungfrun granites. Except for the occurrence of TIB-related felsic dykes described above, fine-grained granitic dykes and pegmatites related to the ca 1,450 Ma granites occur as well, e.g. in the Götemar granite and the surrounding TIB rocks. However, these dykes are inferred to occur only within the granite proper and in the immediate surroundings.

The bedrock at Äspö consists exclusively of magmatic rocks belonging to the ca 1.81–1.76 Ga generation of the Transscandinavian Igneous Belt as described above. The predominating rock types in this generation are:

1) a medium-grained, equigranular granite to granodiorite, including subordinate quartz monzonite and monzodiorite (local name: "Ävrö granite"),
2) a medium-grained, sparsely to strongly porhyritic intrusive rock that varies in composition between granite and quartz diorite, including tonalitic, granodioritic, quartz monzonitic and quartz monzodioritic varieties. (local name: "Äspö diorite"). Quatz-monzonitic-grandioritic composition dominate,
3) a grey, fine-grained, at places slightly porphyritic, intermediate rock,
4) dykes of fine-grained granite and pegmatite,
5) mafic rocks. These are undifferentiated amphibolites, but most of them are considered to be genetically related to the granitoids and dioritoids of Transscandinavian Igneous Belt. These rocks have normally been mapped as "greenstones" at Äspö HRL.

4.2 Local geology in the TASQ tunnel

4.2.1 Mapping procedure

Since the tunnel mapping and the different kinds of core logging are made in different ways they are not fully comparable, which must be regarded as a bias in the input data. The major biases in this respect are the fact that different cut-off levels and procedure when performing the mapping are used.

SKB utilizes systems that partly have been developed in-house, for documentation (mapping/logging) of geology in tunnels and boreholes. For Tunnels this is the so called Tunnel Mapping System (TMS) that is used for all geological mapping at Äspö HRL. It is based on 2D mapping templates in paper format in the tunnel, transformed via digitalization to CAD environment (Microstation) at the office. A database connection to the assigned characters of each mapped object is set up during the digitising process. The TMS database is stored on a local server at Äspö. The logging of cores from boreholes is done in the so called Boremap system, utilising not only the core itself but normally also a photographic image of the borehole walls. The latter has been produced via a video image system known as BIPS (Borehole Image Processing System), in which the orientation of mapped objects is calculated by the system software, provided that the borehole geometries and orientation is known. Data from the mapping is stored in a database known as SICADA.

The lower cut-off level for mapped fractures is different for tunnel mapping than for geological logging of cores. The cut-off level in the tunnel mapping is normally about 1 m. Fractures shorter than that is thus not mapped. When cores are logged, on the other hand, virtually every visible fracture could be recorded, both sealed fractures and fractures that break the core. This means that the cut-off level in this case will be dependent of the core width.

Mapped fractures in a core either break ("broken fractures") or do not break the core (i.e. "sealed fractures"). However, many of the broken fractures may have been initially sealed in the intact rock. This is explained by that some breaks occur during the drilling, or during the following handling of the core. During the mapping procedure of cores, a standardized procedure is used, based on the fracture surface characteristics, resulting in judgment weather the 'in-situ' fracture was sealed or open. This is not a straightforward procedure, and may lead to a bias in the sealed/open relation and in the amount of open (or sealed) fractures. Apertures visible in the core (rare in TASQ) are always measured and noted during mapping, whereas obvious apertures in the BIPS image are measured in the video image.

During tunnel mapping, fractures are observed at several locations along the course, although large parts may be obscured or difficult to examine due to e.g. unsatisfactory light condition, superficial cover etc. Nevertheless, the mapped character of fractures in a tunnel generally is a representative average. In summary, the orientation and other characteristics of fractures from core mapping should be regarded as detailed samples with high resolution, but the documented characters of individual fractures may not be important on a larger scale. Fractures from tunnel mapping on the other hand are for practical reasons normally mapped in a more generalized way. A single line representing a fracture in the tunnel mapping is normally a simplification of what in a more detailed scale actually may represents an undulating, splaying and/or stepping fracture. The degree of generalization of fracture distribution is a function of in which scale the mapping is carried out.

Regarding fractures caused by the blasting, these can normally not be mapped during regular geological mapping of the tunnel. Normally the fractures are too small to be identified with the unaided eye, or else they part a previously sealed fracture. At some locations new fractures are formed in the intact rock, but when found in drillcores they can rarely be separated from fractures formed during the drilling process or during the proceeding handling of the core. However, in the tunnel it may be possible to locate and map the latter kind of fractures if the cut-off level permits.

4.2.2 Rock types

The geological description here is valid for the whole tunnel but focus on the RVS model volume. The geology in the model volume is thus not anomalous to the surrounding geology.

About 80% of the mapped areas in the tunnel are composed of Äspö "diorite", which means that it is the predominating rock type in the TASQ tunnel. Pegmatite and fine-grained granites make up ca 5% of the mapped area. The Äspö diorite in TASQ is very heterogeneous with respect to e.g. frequency and size of feldspar megaclasts, alteration intensity and degree of ductile deformation overprint. The prime alteration found is oxidation, revealed by red staining (sub-microscopic hematite) of minerals and particularly along their boundaries. Epidotization and minor chloritization can also be found. In particular the local shear zone that runs along the tunnel is strongly associated with oxidation and some chloritization.

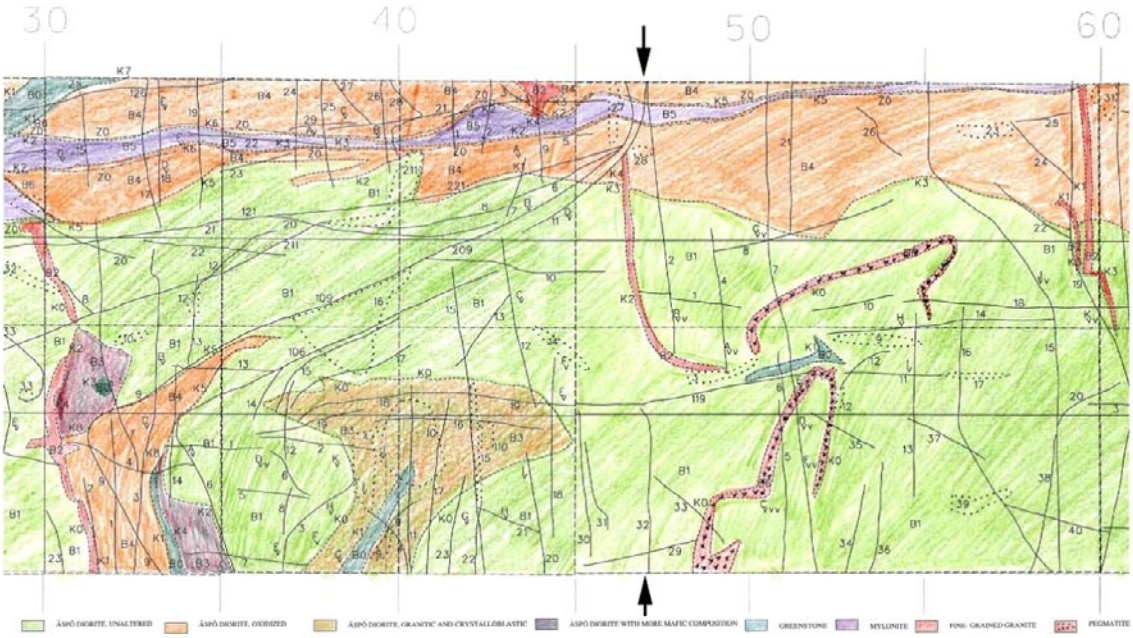

Figure 4-1. *Original mapping of the sections relevant for this project /Magnor 2004/. The left wall (top part), roof (central part) and right wall (lower part) are here projected to a planar surface. The tunnel chainages are shown at the top. Arrows marks section 47 in the tunnel.*

The shear zone (marked in bluish purple in upper part of Figure 4-1) varies in width from locally ca 0.1 m to over 1 m. It undulates slightly along its course but more notably it splays and there are a number of minor shear zones that splay off from the main zone, particularly to the northwest into the left wall of the tunnel. Most of these minor splays were too narrow to be represented in the mapping. The foliation in the zone is to a large extent mylonitic or proto-mylonitic and is composed of a mixture elongated grains of brittle minerals on the one hand (such as quartz, feldspar and epidote) and softer phyllosilicates (such as white mica and biotite/chlorite) on the other hand. The amount of these two major components varies although the brittle components generally seem to dominate. Evidence of brittle reactivation is ubiquitous (Figure 4-2).

The shear zone runs along a major part of the modelled volume in the left wall and at several places the foliation in the zone is aligned with the drillpipes from the blasting of the tunnel. It appears that the blasting energy have caused an extra volume of rock to fall out at several places, outside the nominal tunnel profile (see Figure 4-3).

4.2.3 Input data for the 3D model (RVS)

The geology in the TASQ tunnel has been mapped during the regular mapping program at Äspö HRL /Magnor 2004/. In the current project, mapping has been made in the Boremap system of the following cores; KQ0047A001, KQ0047A002, KQ0047A003, KQ0047B001, KQ0047B002, KQ0047G001, KQ0047H001 and KQ0047I001. An image of these boreholes has been made using the BIPS, which is used in the Boremap system to semi-automatically generate the true orientation of the mapped objects.

The tunnel mapping data is stored in the TMS database at Äspö, whereas Boremap data are stored in SICADA. When comparing data from these two sources it is important to note that all orientations in TMS are stored with values given in magnetic north, but in SICADA the local coordinate system (Äspö96) is being used. In this report, all data are given in Äspö96 and values from the TMS database have thus been adjusted.

Figure 4-2. *Close up photo of a local part of the shear zone running along TASQ. The strong foliation in the zone can be seen aligned with minor fractures filled with calcite /Magnor 2004/.*

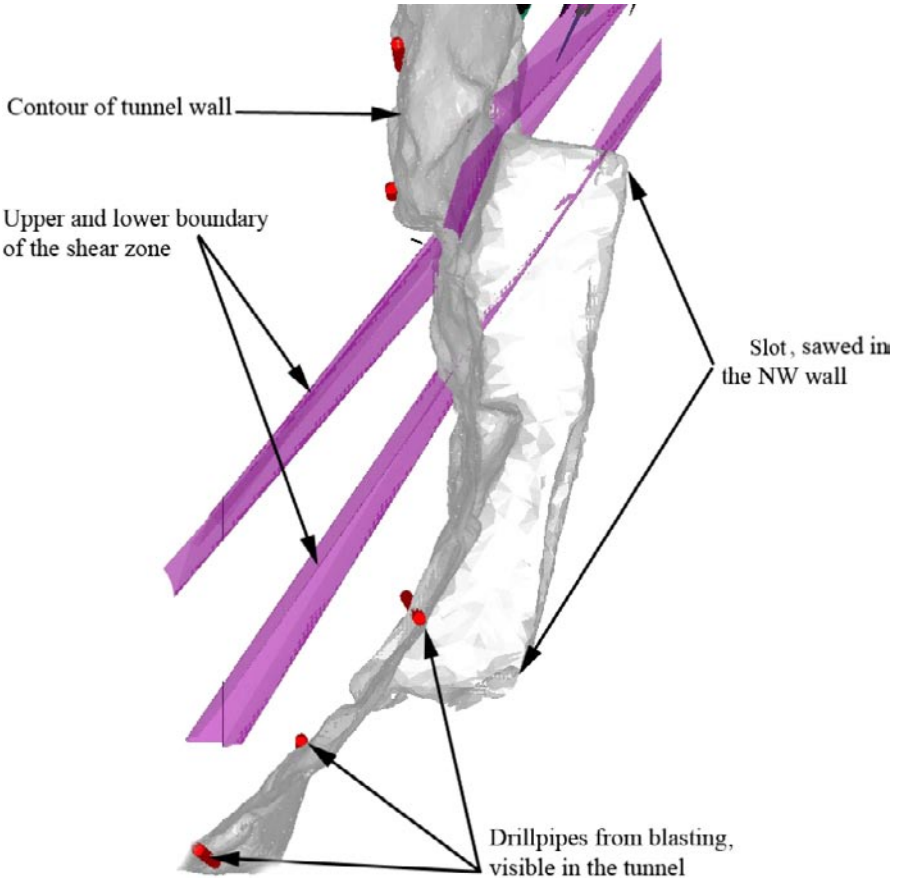

Figure 4-3*. A local image from the minor 3D model around section 47, seen towards the southwest.*

Earlier mappings of cores in the area include boreholes KQ0053A001, KQ0053A002, KQ0053A003, KQ0053A004 and KQ0048G001, and may be found in SICADA. There also exists a core from a short borehole, KQ0055A001, which is apparently not mapped. None of these boreholes have been logged by BIPS, and thus the orientations of objects (such as fractures, rock contacts and other structures) cannot be used for analysis without careful considerations. In the four KQ0053-boreholes the mapping has been made in a similar way as in the Boremap system, but without BIPS. This data can be used with respect to location along the borehole and for general statistical purposes. In KQ0048G001, only partial mapping has been performed earlier and data from fractures has not been found. From the KQ0055A001, no geological data exists. To complement these data, an overview mapping of fractures in the two latter boreholes was performed so the data can be used and compared with the data from the KQ0053 boreholes. The data from this simplified mapping is given in Appendix B. An overview of the input data to the RVS-model can be seen in Figure 4-4.

4.3 Fracture characteristics

To get a detailed picture of the fracture characteristics in the investigated part of the TASQ tunnel, a compilation has been made of the geology in the nearby boreholes and in the tunnel itself. Fractures in section 34–60 in the tunnel and the boreholes located within the model volume (listed in Table 4-1) are primarily used. These are also compared to fractures in more distant parts of the tunnel, to check if the selected rock volume is anomalous from the surrounding rock. Fractures in sealed networks are not included in the fracture characterization.

4.4 Fracture orientation

The acquisition of the fracture orientation data is derived from the boreholes given in Table 4-1 and from data in the TMS database. The orientation of objects (strike) taken from this database have been compensated for the fact that they are measured in magnetic north, in order to compare it with data from the boreholes, which are given in the local coordinate system (Äspö96).

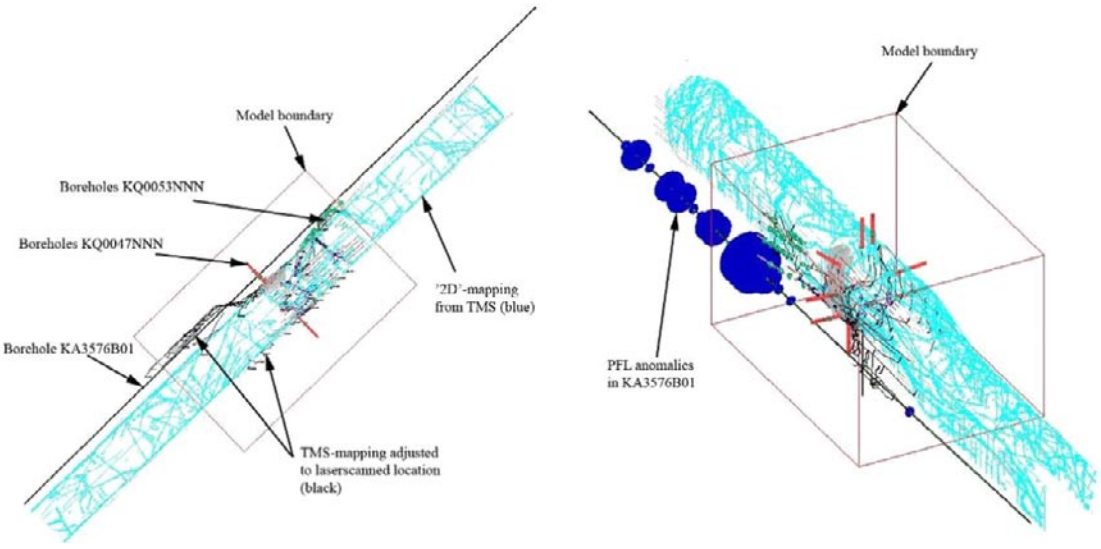

Figure 4-4. *Input data to RVS. This is a graphical view from RVS, visualising the components that have been used when the RVS modeling was created. The character of the geological features, such as fractures, rock contacts and ductile structures, are partly visualized, but generally acquired from the database (TMS or SICADA).*

Table 4-1. Boreholes in the model volume, with data in SICADA.

Borehole	Borehole length (meters)	Borehole direction (azimuth/inclination)	Comment
KA3376B01	Ca 80		Most parts outside the model boundary
KQ0047A01	3.2	316.3/2.5	
KQ0047A02	3.1	316.2/4.1	
KQ0047A03	3.1	316.7/40	
KQ0047B01	3.2	136/3	
KQ0047B02	3.1	136.5/3.9	
KQ0047G01	3.2	286.8/–89.8	
KQ0047H01	3.1	275.2/89.4	
KQ0047I01	3.1	161.6/89.5	
KQ0048G01	7.05	290.2/–89.9	Reduced data in SICADA
KQ0053A01	7.6	36.2/–1.5	No orientation of data
KQ0053A02	7.5	36.3/–0.9	No orientation of data
KQ0053A03	7.4	37.8/–0.7	No orientation of data
KQ0053A04	7.1	42.0/–1.7	No orientation of data

The eight boreholes at KQ0047 are situated centrally in the model volume. These are drilled around the tunnel perimeter, at right angle to the tunnel drift (Figure 4-5). For this reason, the capture of fractures in these holes underestimates the number of fractures orientated at high angle to the tunnel. Since they also are fairly short, a correction for this bias /e.g. Terzhagi 1965/ would still not give a correct picture of the fracture orientation in the area. However, the borehole KA3376B1 may be used to compensate for this bias, since it has an orientation parallel to the tunnel.

The orientations of measured fractures in the model volume and in the TASQ tunnel are shown in Figure 4-6. It is notable that the predominating fracture set at Äspö, i.e. fractures oriented NW-SE, appears to be less common in the model volume than outside (Figure 4-6, b–d).

The total approximate lengths of the boreholes, measured in three orthogonal directions within the model volume, are as follows:

- Vertical 11.4 metre
- Parallel to the tunnel 27 metre
- At right angle to the tunnel 14.8 metre

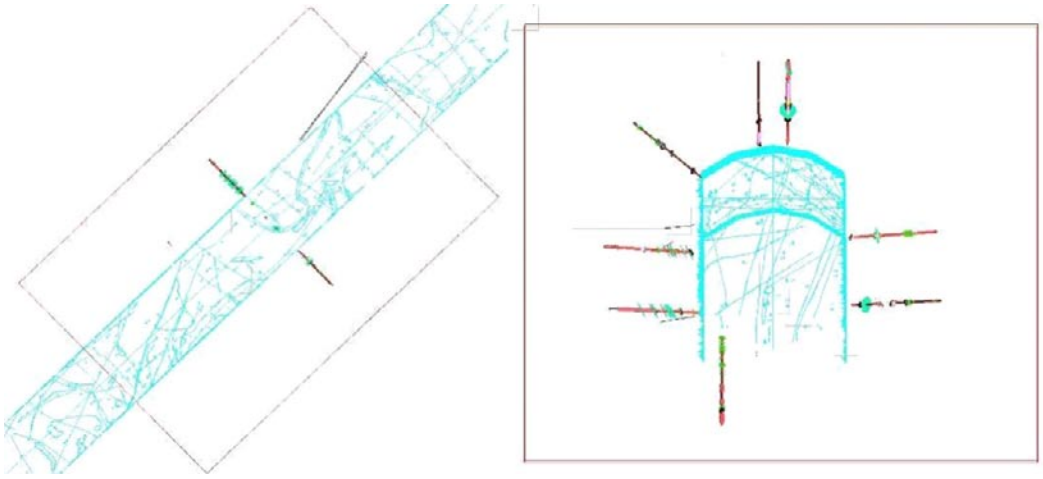

Figure 4-5*. The model volume (main model) with TMS mapping and boreholes at section 47. A top view to the left and seen along the tunnel to the right.*

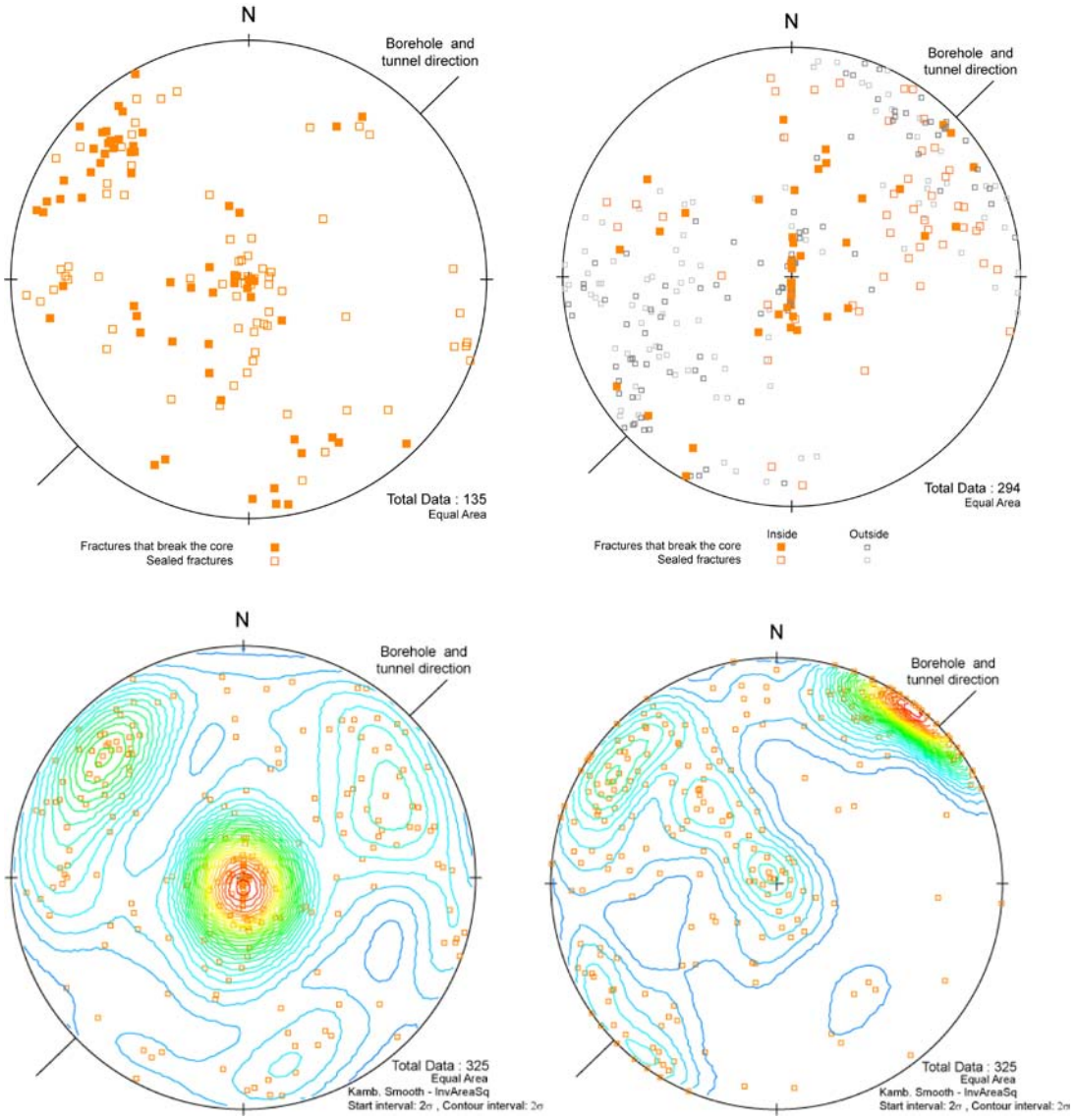

Figure 4-6. *Stereographic projection of fractures in the model volume. a) fractures from all eight boreholes at KQ0047, b) fractures in KQ3376B01 inside and outside the model volume, c) all fractures from BIPS boreholes in the model volume and d) all fractures mapped in the tunnel (TMS data). Data represent poles to fracture planes plotted in the lower hemisphere in Äspö 96 coordinate system. Contour levels in c and d are given below each figure, with red nuances starting at about 50.*

There is a particular high frequency of sub-horizontal fractures, sealed and broken (Figure 4-6). A total of 38 fractures, i.e. ca 30% of all fractures in the KQ0047 boreholes, have dips less than 20 degrees. A majority of the fractures are found in boreholes KQ0047G01 and KQ0047I01. This is not surprising, since they are drilled vertically and thus by default transects more gently dipping than steep fractures. In addition, many of the fractures are located close to the tunnel contour. Initially sealed fractures close to the contour may, however, have become broken during blasting since they normally are weaker than the intact rock. This is further discussed in the subsequent chapter.

4.5 Fracture frequency

For this project, it is relevant to investigate how the broken fracture frequency varies as a function of distance from the tunnel wall. As discussed in section 4.2.1, the broken fractures can be divided into several groups on the basis of their character. In this report, only fractures mapped in the different cores in the model volume are considered. Broken fractures may either have been broken initially (in the intact rock) or may have broken during drilling, during blasting or during the succeeding

handling of the cores. Of special interest in this report is whether fractures close to the tunnel wall have broken during the blasting of the tunnel or if they already existed. Indications of such processes may be found if a decrease of the fracture frequency can be seen away from the tunnel face or if the frequency of fractures lacking internal fracture minerals is higher close to the tunnel.

The Borehole KA3376B01 was drilled parallel to the left wall and mapped prior to the blasting of the TASQ tunnel and will give the best picture on the fracture frequency prior to excavation, although fractures sub parallel to the borehole will be strongly underrepresented. On the other hand, the amount of broken fractures is probably overrepresented, because of the bias of fractures being broken during or after the drilling. There are 50 broken fractures in KA3376B01 (Figure 4-7). This amounts to 1.85 fractures per metre. However, there is a distinct anomaly at around 44 m, where a set of gently dipping fractures appears.

Of the 135 fractures in the KQ0047 boreholes, 66 are broken (Figure 4-8). As these boreholes all lie at an approximate right angle to the tunnel wall, the number of fractures at high angle to the tunnel is underestimated as discussed in section 4.2.1. The broken fracture frequency in these holes amounts to 2.63 fractures per meter or 0.26 fractures per decimetre. There is generally no higher frequency of broken fractures close to the tunnel face looking at the KQ0047NNN boreholes (Figure 4-8). One exception is the borehole KQ0047A01 that has a peak of 3 fractures at around 0.4 meters. However, this peak has a natural cause since it is situated along the upper boundary to the shear zone (marked in purple in Figure 4-2) and represent fractures with weak, chlorite sealing. They may or may not have become broken during the blasting.

In borehole KQ0047I01, only two broken fractures close to the tunnel face exist, but rather many sealed fractures. 7 fractures are mapped in the first 1.1 m and 3 fractures within the first 0.4 m to the tunnel wall. These sealed fractures are all gently dipping and contain only minor amounts of chlorite and possibly calcite, but have oxidized walls. Sealed fractures have generally lower tensile strength than the intact rock and since none of these fractures have broken during blasting, this may indicate a shallow EDZ in this area.

The four boreholes at KQ0053 are drilled at low angle to the tunnel direction and although the boreholes are over 7 m long their low inclination, all parts of the boreholes in fact lye within about one metre from the tunnel face. This also means that every metre in each borehole very roughly represents 1 decimetre of distance away from the tunnel face.

The fractures are not oriented but the frequency may still be useful information for this project. A total of 114 broken fractures have been mapped in these four boreholes. This must be regarded as an unusual high fracture frequency, averaging at 3.8 fractures per meter distributed according to Figure 4-9 (upper part). This may be attributed to its proximity to the tunnel or to actual higher frequency of fractures in the in-situ rock in this area. 50 of these fractures have a rough, fresh surface and may thus have been broken during the blasting. Looking at the distribution of these 50 fractures (lower part of Figure 4-9) it can be seen that all fractures in KQ0053A03 are fractures of this type, but otherwise they seem to be fairly evenly distributed along the boreholes.

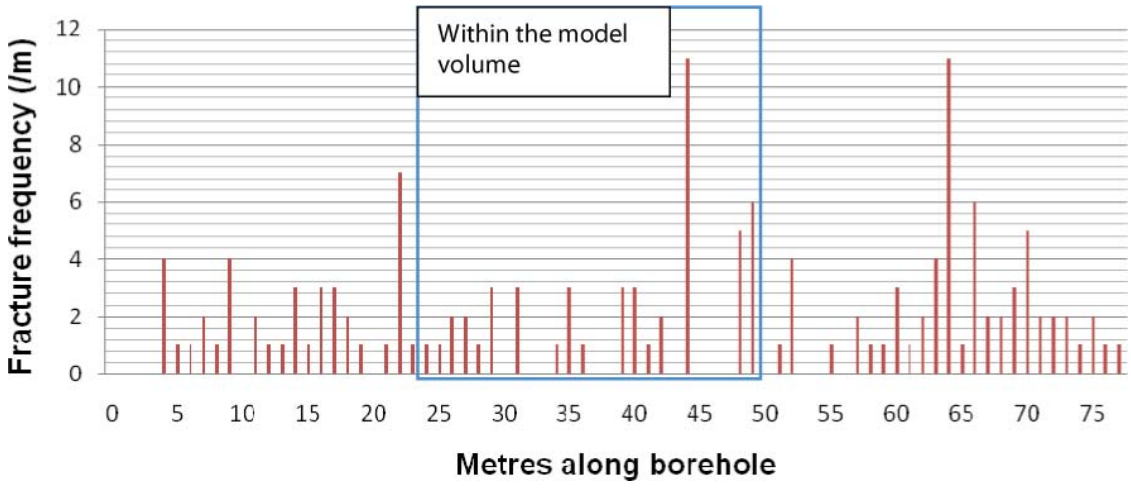

Figure 4-7. *The fracture frequency in borehole KA3376B01, in fractures per meter. The part of the borehole that lies in the main model volume is enclosed in blue.*

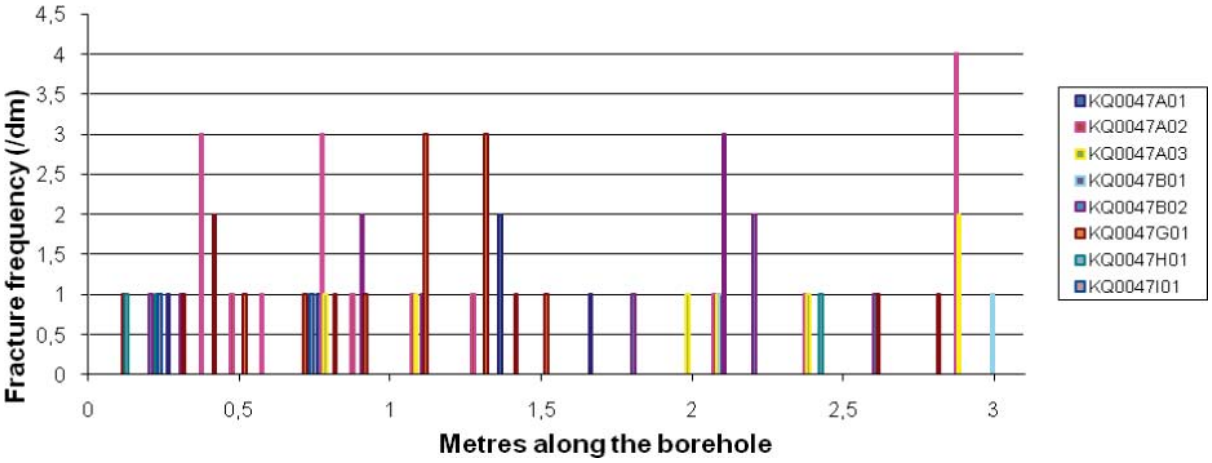

Figure 4-8. *The average fracture frequency per decimetre in the eight boreholes at KQ0047.*

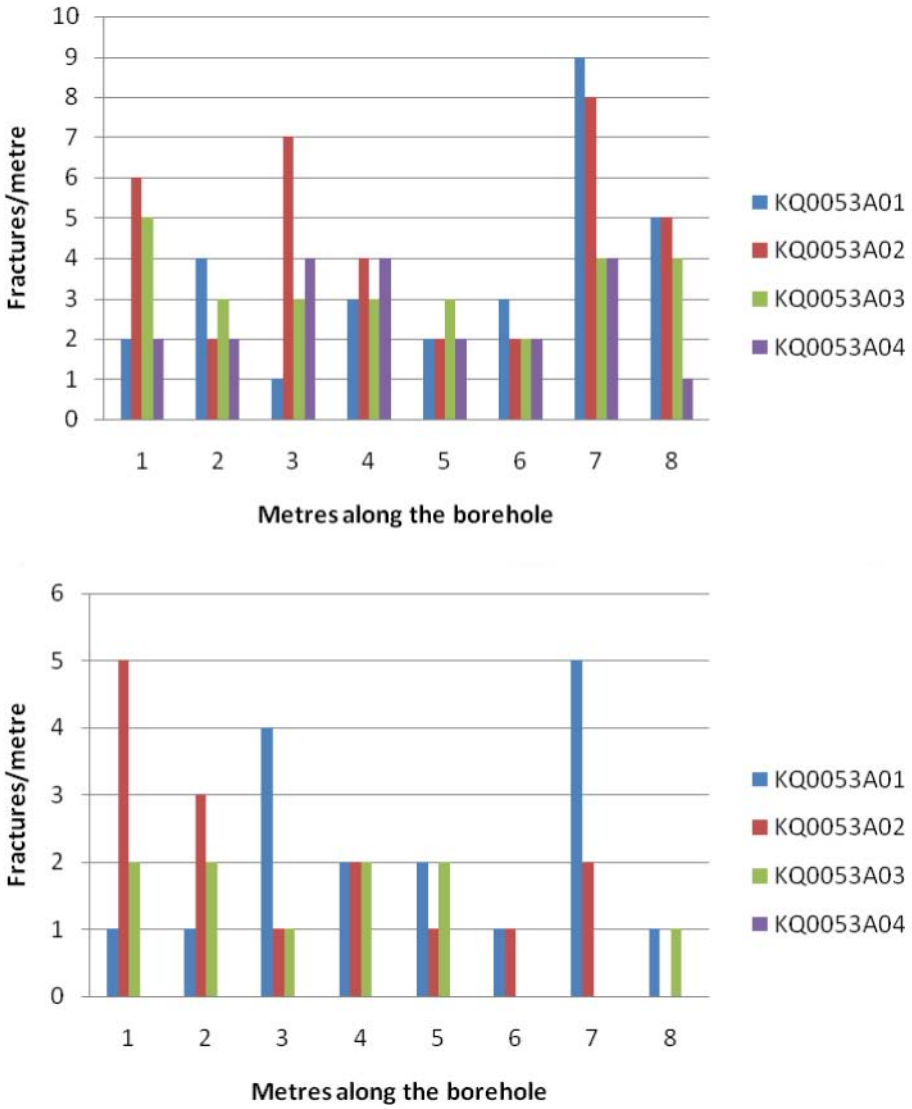

Figure 4-9. *Fracture frequencies along the boreholes at KQ0053. Above the total frequency of broken fractures per metre and below the frequency of fractures with rough, fresh surfaces.*

5 Drilling and blasting in section 47

The excavation of the 70 m long TASQ-tunnel was divided in two different sequences. The first sequence was ordinary tunneling by top heading and then, from approximately 30 m from the start section, the second sequence bench blasting. The top heading sections were tunnels of 26 m^2 and the total area (tunnel+bench) was 33 m^2. Figure 5-1 shows a length section of the tunnel and Figure 5-2 shows the tunnel and bench section. This report will focus on drilling and blasting of section 0/47 in the TASQ-tunnel (marked with red lines) as several of the reported investigations highlighted in this report are conducted within this limited area of the tunnel. The blast design, blast sequences and the vibrations measurements are originally reported by /Olsson et al. 2004/.

Section 47 of the TASQ-tunnel consists of one tunnel round and one bench round. The tunnel round starts at section 0/046 and ends at section 0/050. The bench round starts at section 0/045 and ends up at section 0/049.

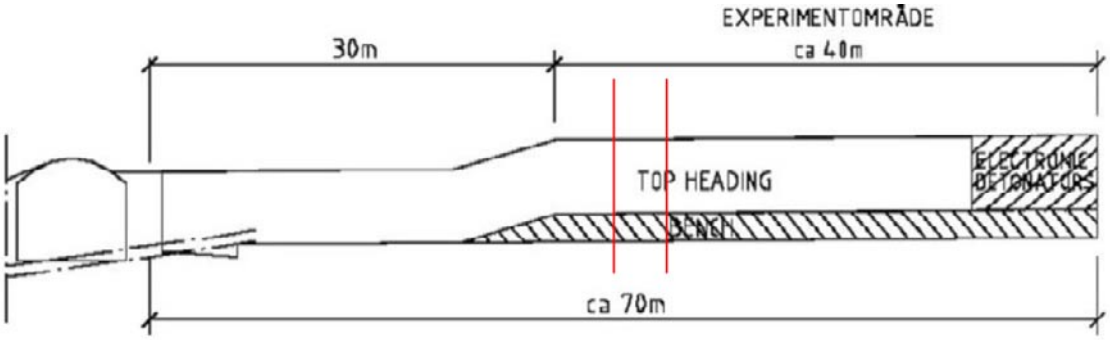

Figure 5-1. *Length section of the TASQ-tunnel and approximate location of section 0/47. Reprint from /Olsson et al. 2004/.*

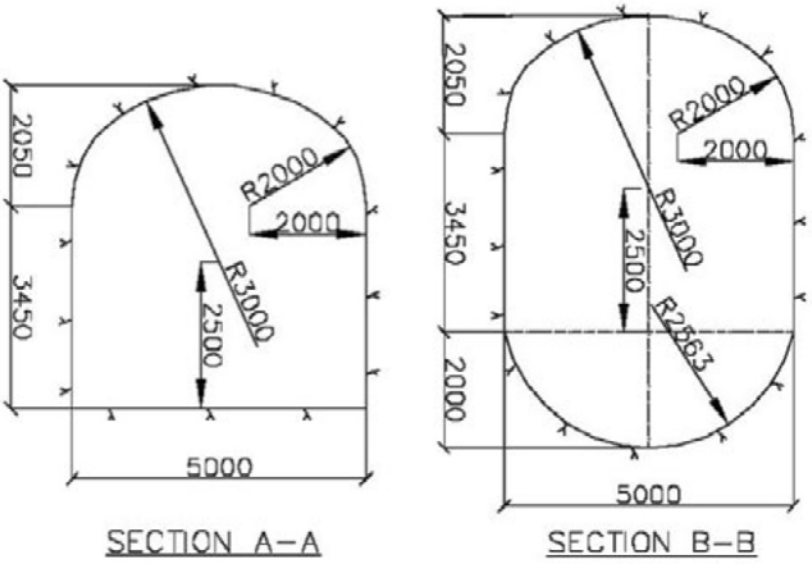

Figure 5-2. *The top heading section and the total section. Reprint from /Olsson et al. 2004/.*

5.1 Tunnel rounds – top heading

The tunnel round here was round number 24. This round was blasted 26th May 2003 at 01:55. The round consisted of 125 blasting holes of 48 mm and four 102 mm uncharged open cut holes, see Figure 5-3. The lookout angle was 0.3 m. The bore holes were reported free from water.

The drill length was 4 m and totally 516 m was drilled. The holes were charged with cartridged explosives with a total amount of 256 kg of explosives. The largest number of holes on the same interval was 16. The maximum co-ordinated charge due to initiation was 2.95 kg. In Table 5-1, the used charges are shown.

All of the charged holes were initiated with Nonel. The initiation plan is shown in Figure 5-4.

Table 5-1. Charge explosives.

Charged holes	Type of explosive in a hole		Total charge (kg/hole)
	Bottom charge (mm)	Column charge (mm)	
Opening cut	2 Dynomit 30×380	3 Dynorex 25×1,110	2.95
Stoping holes	2 Dynomit 30×380	2.5 Dynorex 25×1,110	2.59
Helpers	1 Dynomit 30×380	4 Dynotex 22×1,000	1.82
Contour holes	2 Nobelprime 15×150	9 Dynotex 17×460	0.92
Lifters		4 Dynorex 25×1,110	2.92

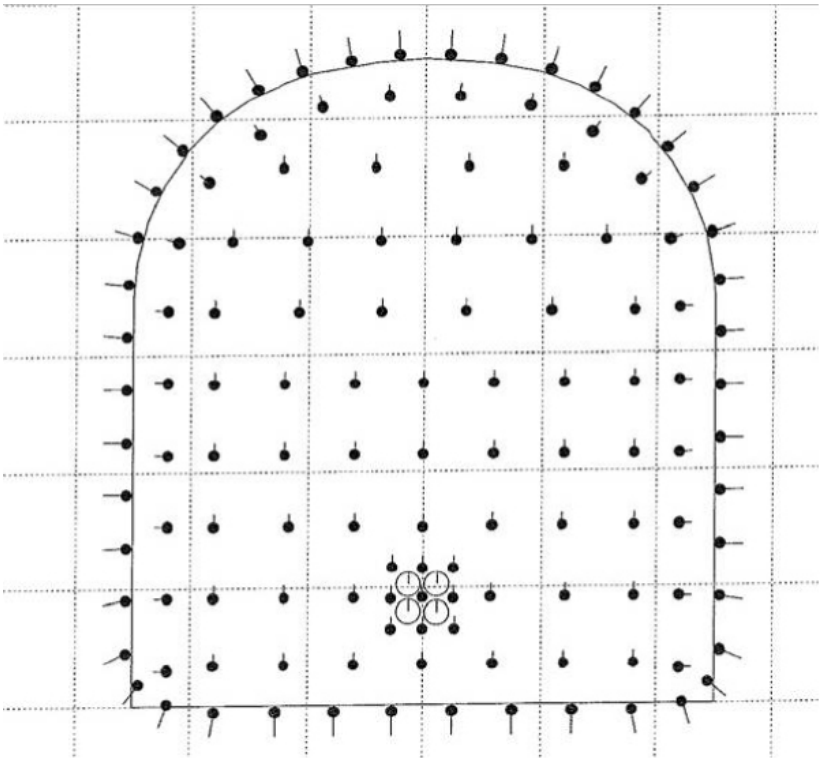

Figure 5-3. *Drilling plan for tunnel round 24, section 0/46–0/50.*

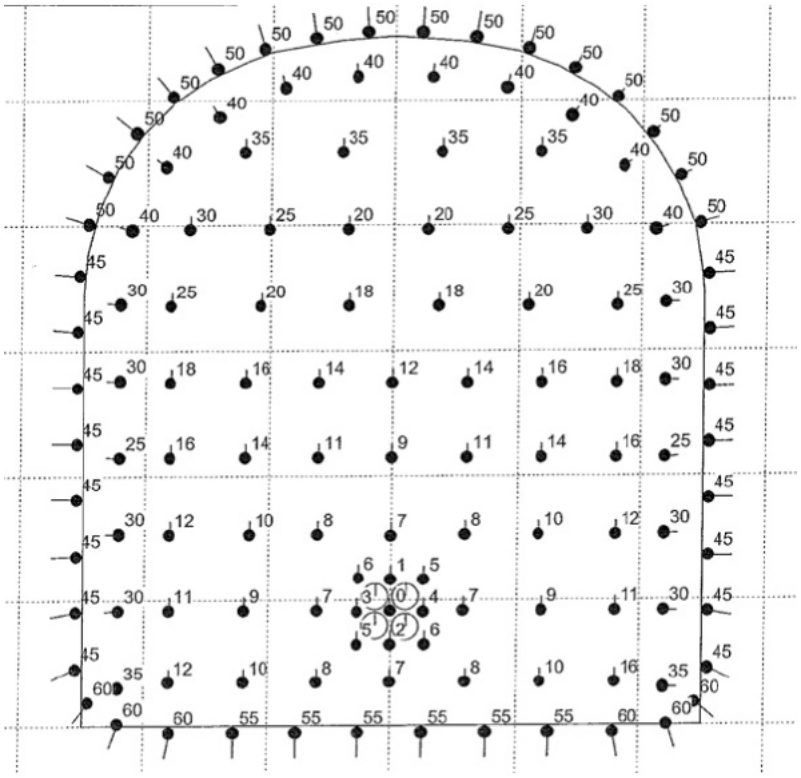

Figure 5-4. *Initiation plan for round 24, section 0/46–0/50.*

There was no log for this round as the drill rig computer was out of order. Therefore, the figures above only show the planned drilling and initiation. However, all the measured vibrations, air blast and fly rock were within the stipulated levels. The highest level of vibration was measured to 32.4 mm/s at a transformer 16 m from the tunnel portal. In the same point, the maximum acceleration was measured to be 15.9 m/s^2, which is under the stipulated level of 30 m/s^2 according to the tender dossier. In order to understand the evidentially effect of vibrations to damage zone, the measurements of the vibration must be considerably closer to the blasted area then these performed measurements. The damage zone obtained from a hole charged like these contour holes is estimated to be less than 0.3 m.

5.2 Tunnel rounds – bench blasting

The actual bench round was round 37 and this was blasted 7th of December 2003 at 16:05. The round consisted of 32 blast holes with a diameter of 48 mm. The drilling length for each hole was 4.4 m and totally 139 m were drilled in this round. The actual logged drilling plan is shown in Figure 5-5. Three holes seem to have a longer look out angle then the planned 0.3 m. From the round log, these three holes seem have a look out angle of roughly 0.5 m. No detailed investigation was done to quantify whether or not the boreholes were free from water. However, the contractor reported that they were free from water.

The holes were charged with cartridged explosives with a total amount of 40.5 kg of explosives. The largest number of holes on the same interval was 10. The maximum co-ordinated charge due to initiation was 1.81 kg (in Table 5-2).

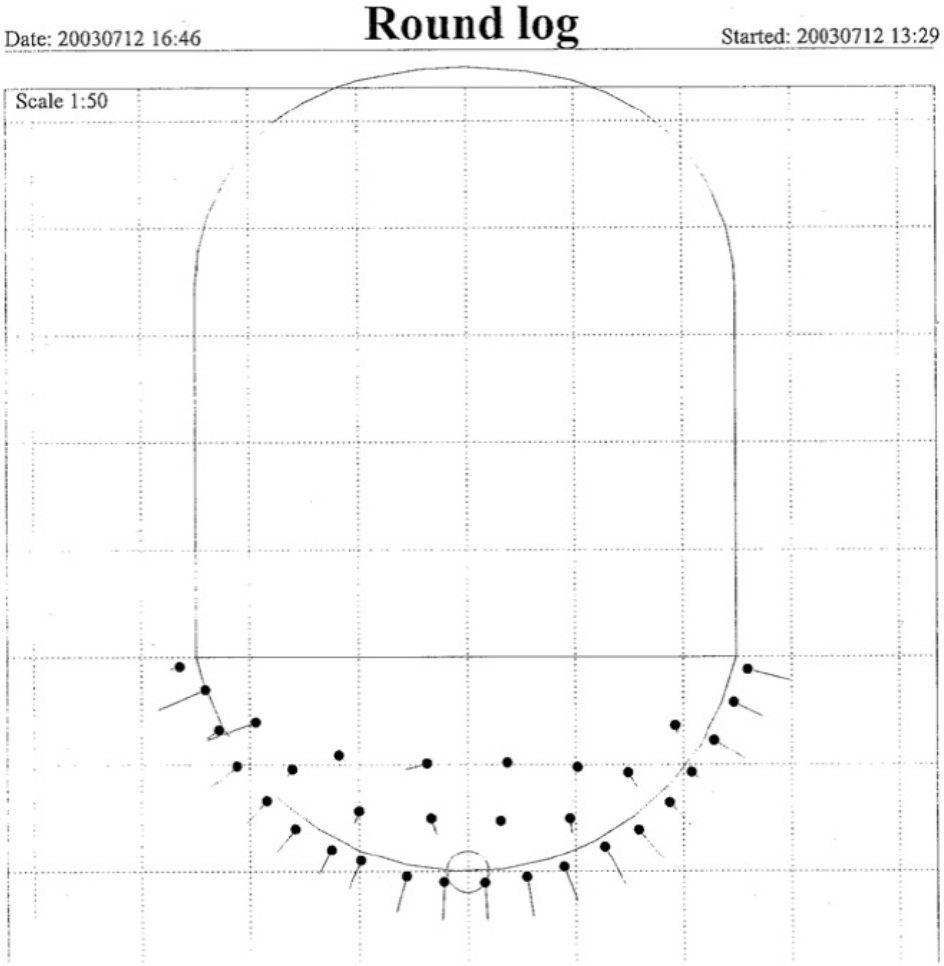

Figure 5-5. *Actual drilling plan of bench round 37, section 0/45–0/50.*

Table 5-2. Charged explosives.

Charged holes	Type of explosive in a hole Bottom charge (mm)	Column charge (mm)	Total charge (kg/hole)
Stoping holes	0.5 Dynorex 25×1,100	4 Dynotex 22×1,000	1.81
Helpers	0.25 Dynorex 25×1,100	4 Dynotex 22×1,000	1.62
Contour holes	2 Nobelprime 15×150	10 Dynotex 17×460	1.01

All of the charged holes were initiated with Nonel. The initiation plan is shown in Figure 5-6.

All performed measurements of vibration; air blast and fly rock were within the stipulated levels. The highest measured vibration level was 13.3 mm/s. In the same point, the acceleration was measured to 5.3 m/s^2 which is far below the permitted value of 30 m/s^2.The damage zone obtained from a hole charged like these contour holes is estimated to be less than 0.3 m.

5.3 Conclusions

When studying the results from the tunnel round and the bench round, nothing abnormal could be seen. The drilling, charging and initiation plans were performed as planned and the stipulated limits for vibration, air blast and fly rock were not exceeded. Furthermore, there are no reported misfires in this section and all of the holes were reported free from water. The damage zone in this section should therefore be less than 0.3 m

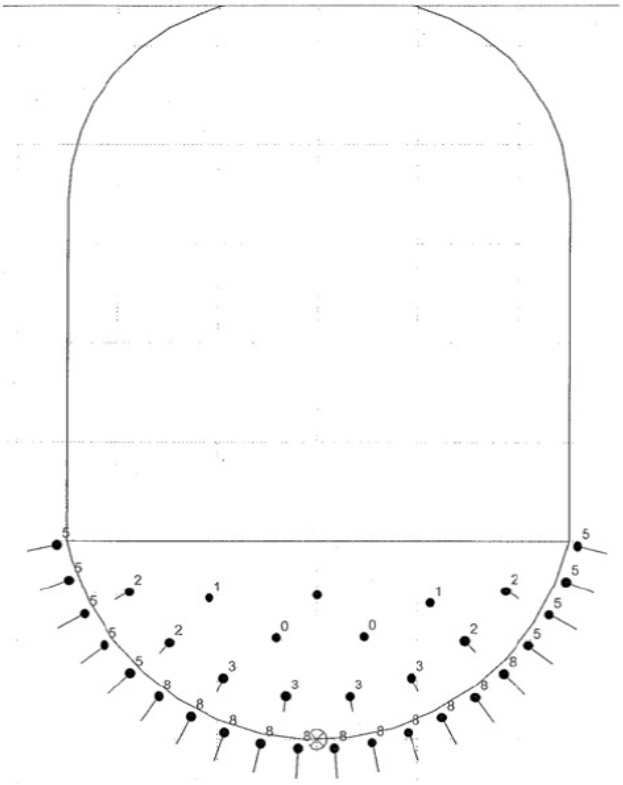

Figure 5-6. *Initiation plan for bench round 37, section 0/45–0/50.*

6 Seismic measurements in the TASQ tunnel

6.1 Method

In November 2006, a study of the ultrasonic velocity was performed in the TASQ tunnel at Äspö HRL by Bundesanstalt für Geowissenschaften und Rohstoffe (BGR). A profile of eight boreholes was drilled in section 47 in the TASQ tunnel /Schuster 2007/. Each borehole was about 3 m deep. The study was performed with the aim to estimate the extent of the excavation damaged zone (EDZ) in the tunnel. In other studies, the ultrasonic method has also been used /Meglis et al. 2005/. In this study the location of "large" fractures crossing the borehole was detected. A further study, was initiated where the detection rate of fractures crossing the boreholes were evaluated together with an investigation of the sensitivity of the ultrasonic velocity to the stress situation in different directions out from selected boreholes. These "rotational measurements" were made to investigate the anisotropy of the rock mass.

According to /Schuster 2007/, the quality of the measured data is very clear. P- and S_V-wave onsets were determined and different parameters were derived from the data, including seismic P- and S_V-wave velocities. The travel time for the seismic wave is used in the identification of the extent of the EDZ. Besides the travel time information also absolute and relative amplitude information were extracted from all datasets, mainly for the estimation of the degree and extent of the EDZ/EdZ. It is also used in order to get information about dynamic elastic parameters like in-situ dynamic pseudo elastic parameters such as Poisson's Ratio and Young's Modulus. They could be of interest for geo-mechanical modelling and comparison with parameters derived from core measurements at the laboratory. The following seismic parameters were derived from all data sets:

- P- and S_V-wave (vertical polarised) velocities,
- absolute amplitudes of first arrival (P-wave) and S_V-wave onset phases,
- normalised amplitudes of first arrival (P-wave) and S_V-wave onset phases,
- apparent frequency of first arrival phases (P-wave) and S_V-wave onset phases,
- in-situ dynamic pseudo elastic Poisson's ratio,
- in-situ dynamic pseudo elastic Young's modulus and
- in-situ dynamic pseudo elastic modulus of rigidity.

6.2 Results

For the identification and determination of the extent of the EDZ/EdZ, reduced P- and SV-wave velocities as well as reduced normalised amplitudes are good indicators /Schuster et al. 2001, Schuster and Alheid 2002/. These parameters change in general gradually within the EDZ/EdZ until the parameters reach values which stay almost constant with increasing borehole depth (an example from the report by Schuster can be seen in Figure 6-1). These values are seen as representative for the undamaged and undisturbed rock. In Table 6-1 the results from the analysis of the different parameters derived from the ultrasonic measurements in the TASQ tunnel are listed. With the help of different seismic parameter criteria the extents of the EDZ/EdZ were estimated. However, the determination of the extent of EDZ could only be estimated roughly with an accuracy of ± 10 cm. According to these derived parameters the extents of the EDZ/EdZ determined in the horizontal boreholes (KQ0047B01, KQ0047B02) at the side wall are about 0.25 m at the ESE side of the tunnel and 0.35 m and 0.30 m at the opposite side (WNW side, KQ0047A01, KQ0047A02). In the floor the extent reaches 0.75 m (measured from the concrete slab, KQ0047G01) and in the roof 0.75 m (KQ0047H01) and 0.30 m (KQ0047I01).

The comparison of results from interval velocity and crosshole measurements in the same holes (KQ0047B01, KQ0047B02) shows similarities in the extent of the EDZ. Fractures/cracks or hints for their existence could be detected in all boreholes, except for boreholes KQ0047B01 and KQ0047B02 (ESE side of the tunnel).

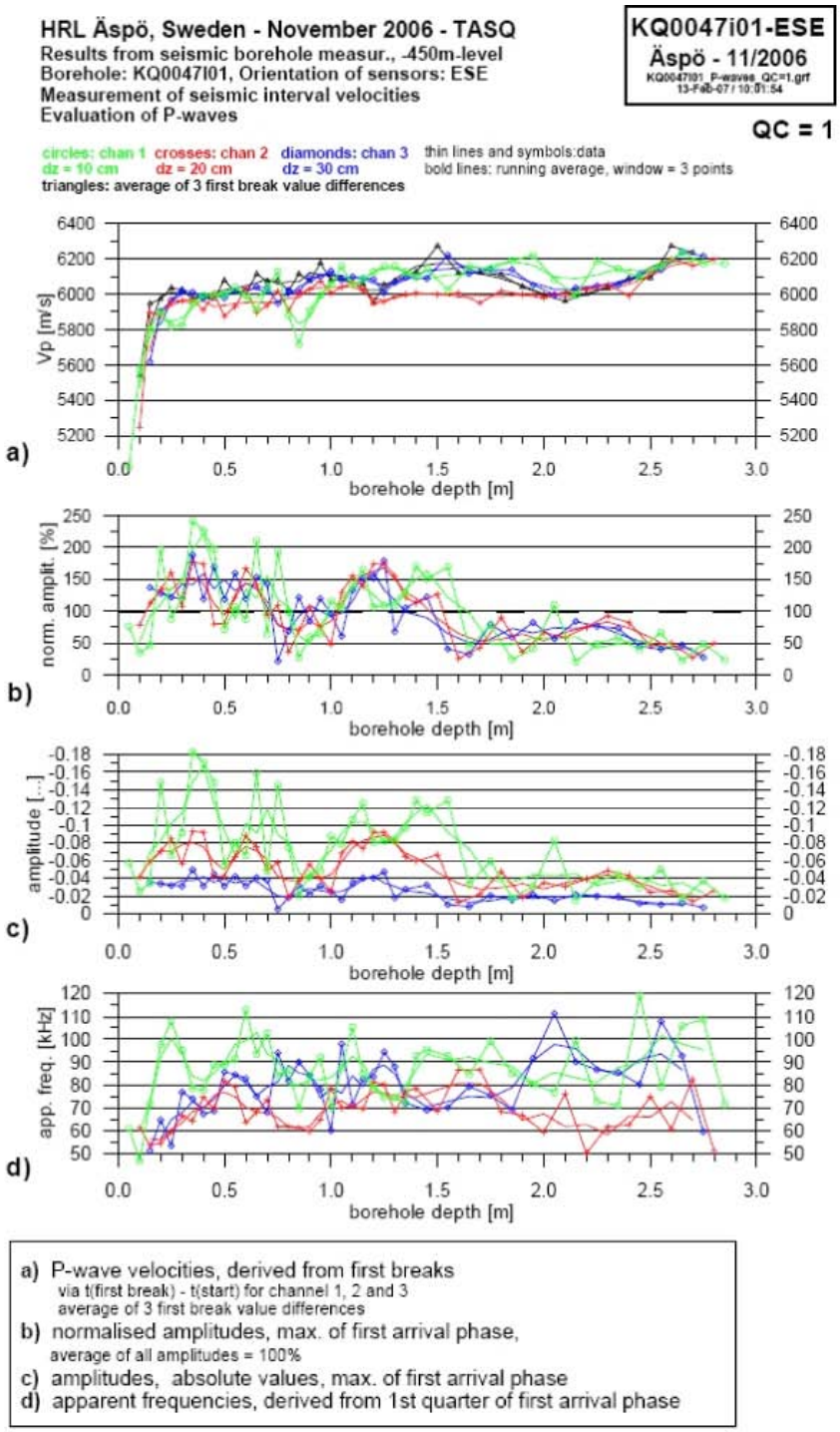

Figure 6-1. *Example of the results from the ultrasonic investigation of borehole KQ0047I01 /Schuster 2007/.*

Table 6-1. Different parameter and the analysis results of the extent of the EDZ in m, from the report /Schuster 2007/.

Borehole KQ0047...	Vp	Norm. amp. P-waves	Seismogram sections	Vs	Norm. amp. S-waves	Estimate
...A01	–	0.35	0.3	–	0.35	0.35
...A02	–	–	0.3	–	–	0.30
...A03	–	0.25	0.35	–	–	0.30
...B01	–	0.25	0.25	–	–	0.25
...B02	0.2	0.25	0.25	0.35	–	0.25
...G01	0.75	0.85	0.65	–	–	0.75
...H01	0.15	0.85	0.65	0.35	0.9	0.75
...I01	0.25	0.25	0.3	0.6	–	0.30

The result obtained when comparing the measurement of the ultra sonic wave velocity and the mapping of fractures from the drillcores is reported in /Bäckström 2008/ and a summary is presented in this report. A further analysis of the rotational measurements used to estimate the usefulness of the ultrasonic method in the context of characterising the rock mass surrounding the tunnel is also done. The results show that the ultrasonic method can detect and predict the location of open fractures crossing the borehole in crystalline rocks (Table 6-2). Fractures are distinguished as more abrupt changes in the ultra sonic wave propagation (indicated as certain in the seismic investigation). The changes in rock type have been identified as less distinct changes in the ultra sonic wave propagation (indicated as uncertain in the seismic investigation). The change in elastic properties when changing rock type gives a response in the elastic properties that is less abrupt than fractures.

Table 6-2. Identified fractures or other structural features that can be distinguished in the seismic interval velocity data as well as from the drillcores and the BIPS. The parenthesis and the question marks denote uncertain fracture indication from the seismic investigation.

Borehole name	Suggested section with fractures from seismic (m)	Fractures indicated in the drillcore and in BIPS (m)
KQ0047A01	0.20–0.25	0.248 – open in the core and visible in BIPS
KQ0047A01	0.7–0.75	0.743 – open fracture in the drillcore and visible in BIPS
KQ0047A02	0.55–0.6	0.592 – open in the core and visible in BIPS
	0.7–0.8	0.734 – open in the core and visible in BIPS (actually two fractures exist in this section)
	1.2–1.25	1.212 – open in the core and visible in BIPS
KQ0047A03	(1.55–1.65)?	No fracture found at this location but a change in mineral content can be observed in the core
KQ0047B01	No	No obvious open fracture indication found in the BIPS image from the borehole
KQ0047B02	No	No obvious open fracture indication found in the BIPS image from the borehole
KQ0047G01	(0.15–0.4)?	Several fractures found in both the core and BIPS
	0.4	0.394 – open in the core and in BIPS
	(2.05–2.15)?	No fracture found at this location, however a closed fracture network containing chlorite is observed in the core
KQ0047H01	(0.1–0.2)?	0.199 – open fracture in the core but not in BIPS
	(170)?	No fracture found at this location but a change in mineral content can be observed in the core
KQ0047I01	(0.85–0.9)?	No fracture found at this location but a change in rock type can be observed in the core

In three boreholes; one in the side wall (KQ0047B01), one in the roof (KQ0047H01) and one in the floor (KQ0047G01) rotational measurements at different depth has been made (Figure 6-2). In each hole, the seismic array with the source and the three receiving channels were kept at one specific depth and rotated 360° in about 30° steps in order to identify how the seismic velocity varied in different direction (Figure 6-3). These measurements were made at different depth in the different holes. The locations of fractures and changes in geological structures crossing the borehole were avoided as much as possible. By identifying and avoiding changes in rock type and fractures in the drill core the optimal locations for these measurements were located.

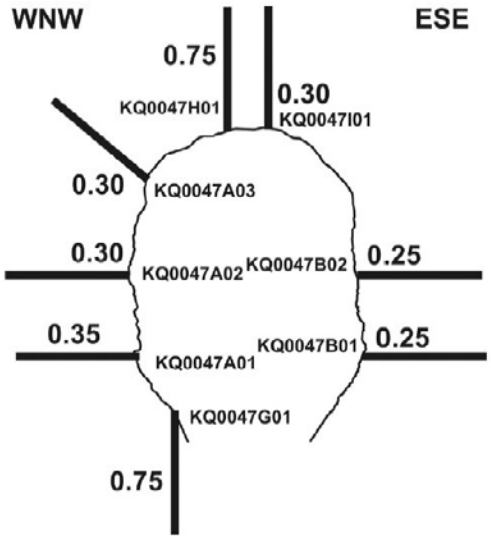

Figure 6-2. *The locations of the eight boreholes used for the investigations. Depth of EDZ (in m) in the cross section of the TASQ tunnel at about 47 m along the tunnel /Schuster 2007/. View from the entrance (SSW) towards the heading face of the tunnel (NNE).*

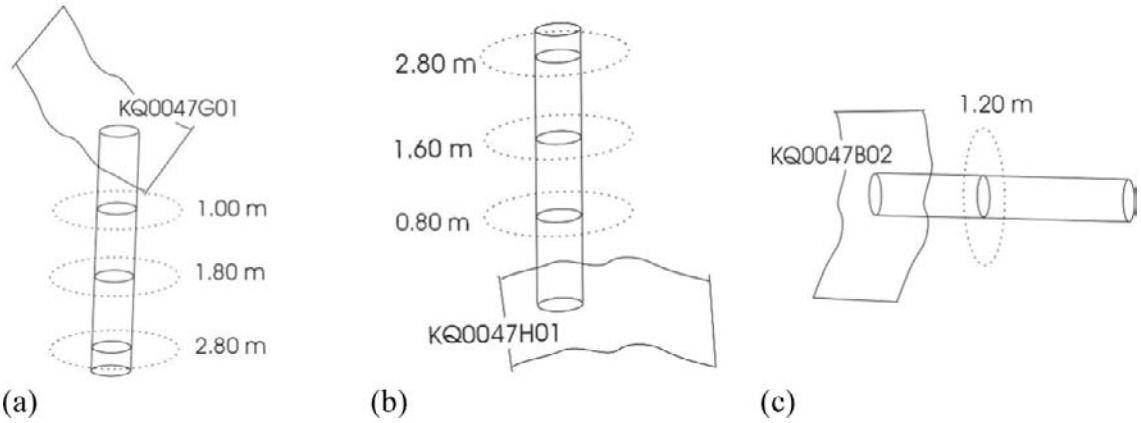

Figure 6-3. *Sketch of the rotational measurements performed in the three boreholes a) KQ0047G01, b) KQ0047H01, and c) KQ0047B02.*

The results from the rotational measurements presented in /Schuster 2007, Bäckström 2008/ are reproduced here. In KQ0047G01, the P-wave and S-wave velocity is largest in the NE to the SW and smallest in the NW to SE direction (Figure 6-4). At 1 m depth, a strong anisotropy with highest velocity in the tunnel axis direction is found at this depth. The results at 1.8 m depth are quite scattered and non-uniform with the highest P-wave velocity to the W-SW and the lowest orthogonally to the E. The deepest measurement is rather isotropic, at 2.8 m depth. In the S-wave velocity the effect of the stress field can be observed. Similar to the shallow measurement in borehole KQ0047G01, the P-wave velocity of the rotational measurement in the 0.8 m deep measurement of KQ0047H01 show a higher velocity in the NE-SW direction. This can also be seen in the S-wave velocity at the 1.6 m depth. This is the same direction as the tunnel axis.

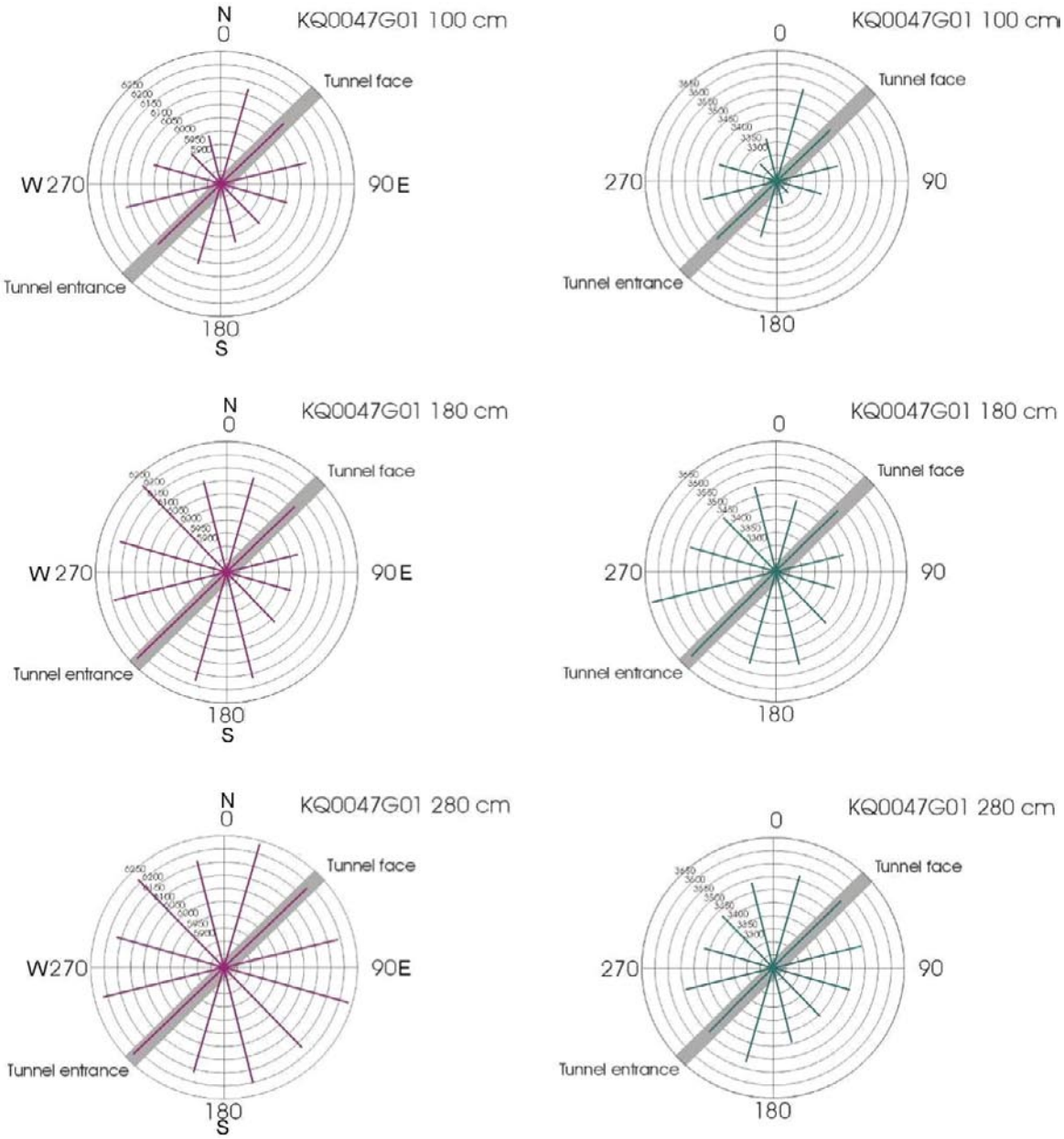

Figure 6-4. *Results from the velocity measurements in borehole KQ0047G01 (in the floor) where the velocity is represented by bars in a 360° circular plot. Longer bars indicates higher velocity. Left: Compressional wave (P-wave) results, the scale varies between 5,900–6,300 m/s. Right: Shear wave (S-wave) results, the scale varies between 3,300–3,650 m/s.*

At a depth of 1.6 m, the P-wave velocity is non-uniform, however this measurement shows a more pronounced 180°-periodicity than the measurement 1.8 m under the floor (Figure 6-5, middle row). The highest velocity in the E-W direction is directed about 60° to the east compared to the highest velocity in the 0.8 m measurement. At largest depth in the roof (2.8 m), the P-wave velocity is quite homogenously dispersed although the velocity is generally lower at 2.8 m compared to 1.6 m. A very small velocity increase can be discerned in the ESE direction. This could indicate a rotation of the velocity as one move away from the tunnel into the rock mass. The measurement in KQ0047B02 is a vertical measurement in the ESE wall of the tunnel at 1.2 m depth from the tunnel wall. Here the 0° is in the up-wards direction. In this borehole only one rotational measurement was performed, at depth 1.2 m as seen in Figure 6-3. This measurement indicates a high disparity in different directions which does not indicate any preferred direction of velocity increase. This disparity prevents any conclusions to be drawn from this measurement.

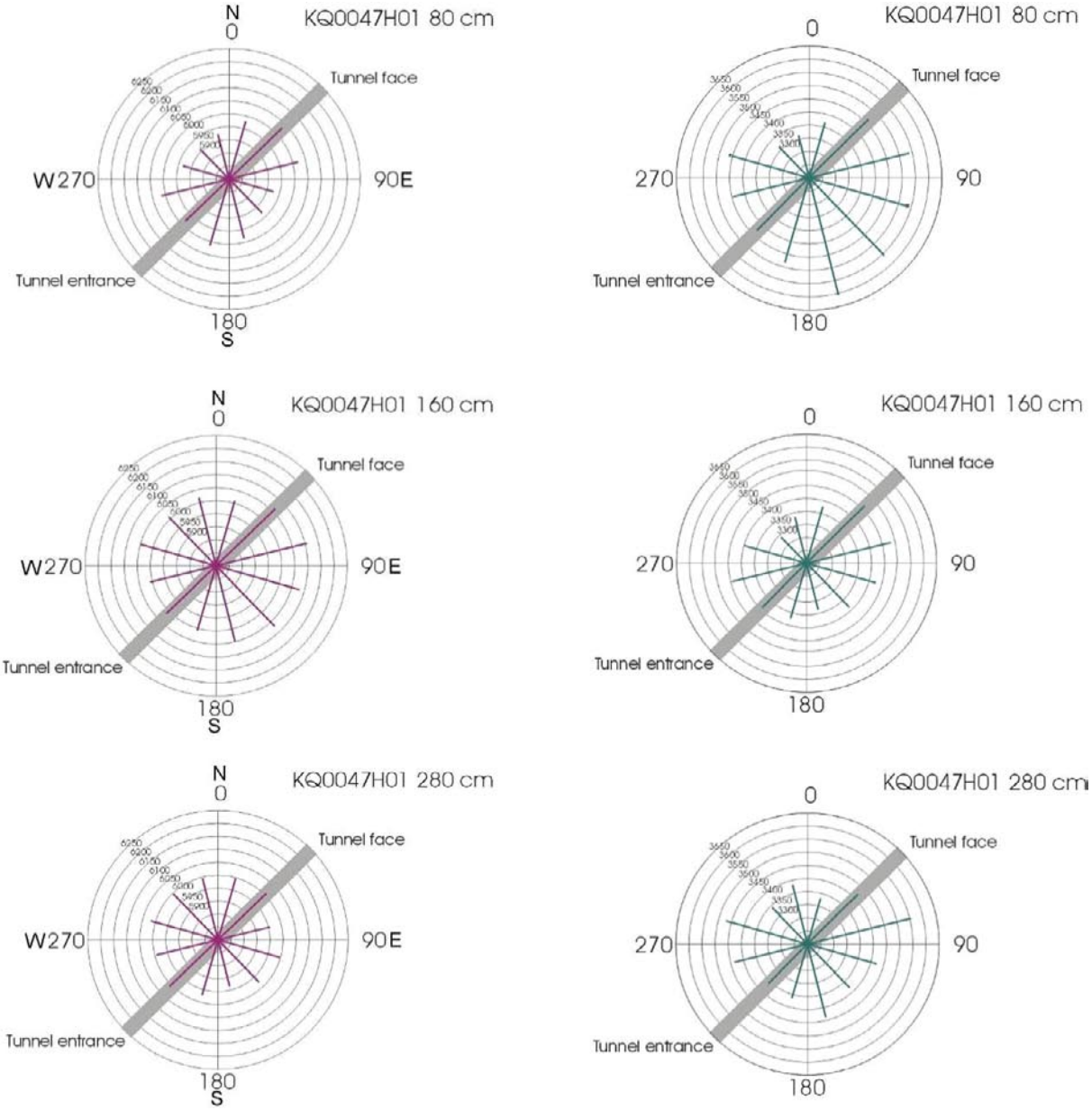

Figure 6-5. *Results from the velocity measurements in borehole KQ0047H01 (in the roof) where the velocity is represented by bars in a 360° circular plot. Longer bars indicates higher velocity. Left: Compressional wave (P-wave) results, the scale varies between 5,900–6,300 m/s. Right: Shear wave (S-wave) results, the scale varies between 3,300–3,650 m/s.*

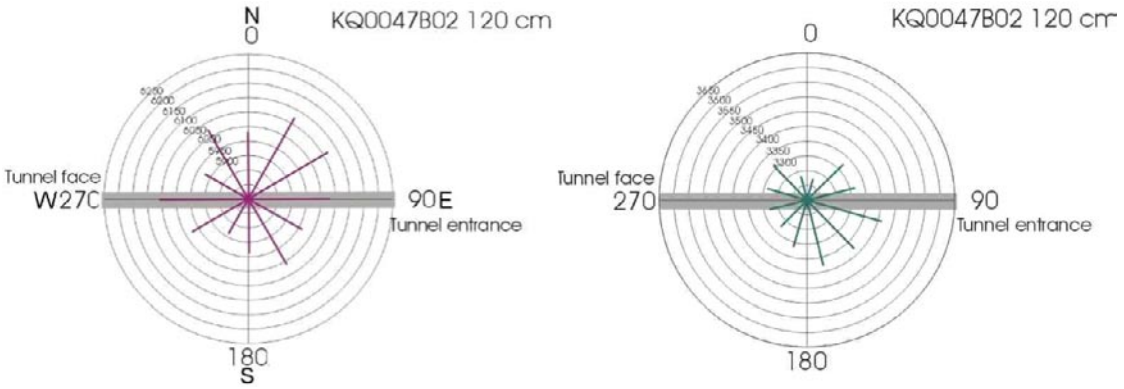

Figure 6-6. *Results from the velocity measurements in the borehole KQ0047B02 (in the ESE wall) where the velocity is represented by bars in a 360° circular plot. Longer bars indicates higher velocity. Left: Compressional wave (P-wave) results, the scale varies between 5,900–6,300 m/s. Right: Shear wave (S-wave) results, the scale varies between 3,300–3,650 m/s.*

6.3 Conclusion

From the results of the comparison of the ultra sonic wave velocity and the mapping of the fractures from the drillcores, it can be concluded that the certain suggestions of fractures from the ultra sonic measurements really indicated fractures. For the uncertain suggestions (within parenthesis, followed by question marks) indicated by /Schuster 2007/ no explanations were given. However when comparing these uncertain indications, it was seen that they coincide with mineral changes in rock type, or other disturbances like the deformation zone with its sealed fractures /Bäckström 2008/.

The stress situation in the rock mass will adapt to the free surface of the borehole but also to the tunnel which will have a large effect on the seismic velocity. The orientation of the tunnel amplifies the stress situation in the vertical boreholes, thus the P-wave and S-wave minima can be seen in the direction of the maximum far-field stress. Although the TASQ tunnel was built with the stress situation in mind, a small misalignment of the tunnel-axis to the principal stress tensor can be seen in the ultrasonic measurements from boreholes KQ0047G01 and KQ0047H01. For KQ0047G01, Figure 6-4, the P-wave and S-wave velocity is largest in the NE to the SW and smallest in the NW to SE direction at shallow depths similar to the results in the roof (KQ0047H01). In the measurements furthers out from the tunnel a stronger response to the far-field stress can be seen in the S-wave velocity than the P-wave velocity.

7 Geometry of the tunnel

3D terrestrial laser scanning technique was applied in this project in order to obtain the real geometric model of the TASQ tunnel for further numerical modelling. The following parts are presented in this chapter:

- 3D laser scanning system used in this project
- Laser scanning in the field
- Geometric modeling of the tunnel
- Conclusion and discussion

7.1 3D laser scanning system

7.1.1 Scanning principle

The different laser scanning systems, which exist on the market are designed based upon three different scanning principles, e.g. triangulation, pulse-based and phase-based techniques and are suitable for different applications. One of the phase-based scanning systems, Leica HDS4500 (or Z+F Imager 5003), with the following specifications was used in this project

- high scanning speed at the rate of up to 625,000 points per second,
- wide scanning field with the rotation of 360 degrees in horizontal and 310 degrees in vertical,
- high resolution and accuracy within mm levels,
- no need for lighting during the scanning due to the infrared laser used,
- obtaining both point clouds and intensity laser images,
- scanning distance up to 53.5 meters.

The scanning device consists of two major components: the single-point laser measurement system and the mechanical beam deflection system (Figure 7-1). The point-sensor laser measurement system comprises the laser head, the high frequency unit and the signal processing unit for data pre-processing. This part controls the emitting, receiving and processing of the laser beam. By using the dual frequency AMCW (amplitude-modulated, continuous-wave) method in conjunction with a coaxial transmitter/receiver design, the receiver measures the phase difference between the original and returned laser signal at both modulation frequencies and the power of the reflected laser light. In this way, both range and reflectance of a target point can be obtained and thus the measurement accuracy (within mm-range) can be achieved.

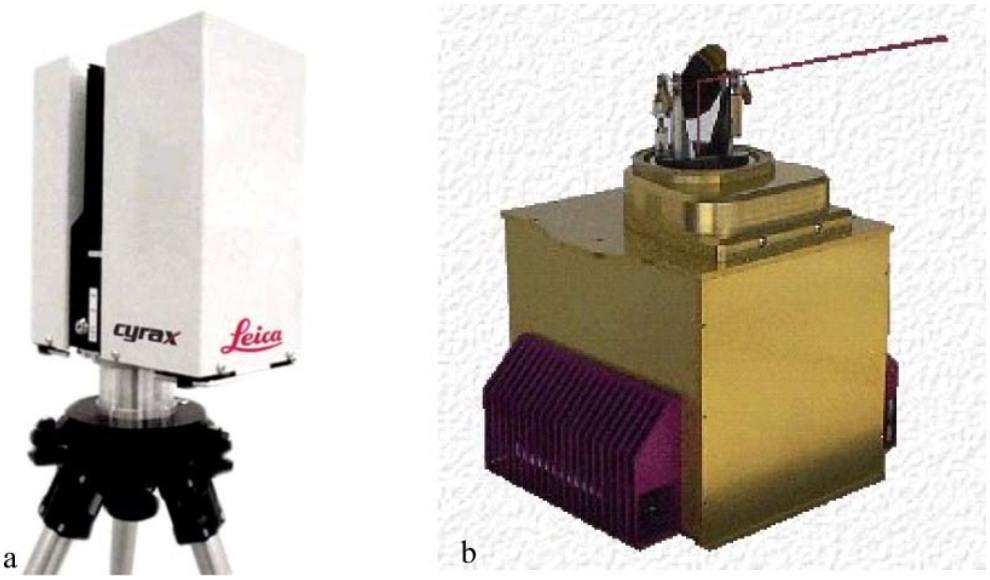

Figure 7-1. *Leica HDS4500 3D laser scanner (a) and its scanning head (b).*

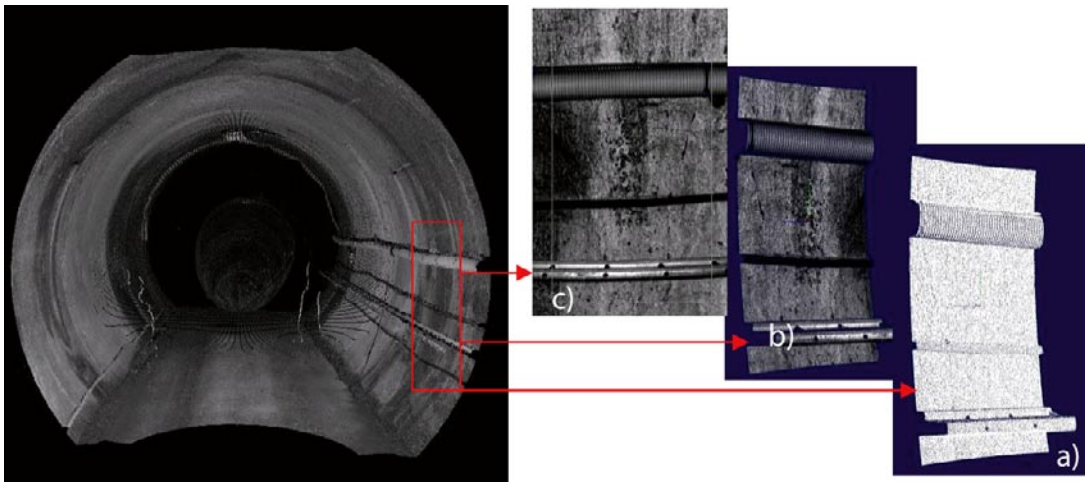

Figure 7-2. *Presentation of raw scanning data in different formats: a) 3D point cloud, b) 3D laser image and c) 2D laser image.*

The scanning distance (also called Ambiguity Interval) is in the range of 0.4–53.5 m /Mettenleiter et al. 2000/. However, the accuracy depends on the distance and can with optimal conditions (incident angle, reflectivity of the object surface etc) be as good as 3–5 mm. The mechanical beam deflection system consists of a special mirror and the motor control unit. The mirror is used for deflecting the emitted laser beam generated from the laser head at the bottom, and collecting the back-scattered laser light cone. The motor controls the mirror rotation in the horizontal and vertical direction, which can make a scanning field overview of 360 degrees in azimuth and 310 degrees in elevation. Each scan takes about 1–6 minutes (depending on the resolution) with the high sampling speed up to 625,000 points per second.

7.1.2 Raw scanning data

As mentioned above, the presented scanner was intentionally designed to measure the position and the reflectance intensity of each point simultaneously. Compared to other 3D laser scanning systems, the raw data can be recorded with x-y-z coordinates and reflex intensity for each point, and then displayed in three different formats: i) 3D point clouds with 3D co-ordinates (Figure 7-2a); ii) 3D grey-scale image generated from both 3D co-ordinates and corresponding reflectance intensity values (Figure 7-2b); iii) 2D grey-scale image created from reflectance intensity (Figure 7-2c). The different ways of visualising the laserscanning data are useful for geological mapping and documentation.

7.2 Scanning in the field

Field scanning was carried out in November 14–15, 2007. Although most parts of the tunnel have been scanned in 2005 for another SKB project, some parts were missing at the beginning of this project. This includes the slot between 30–45 m, which was not excavated 2005 and the part under the bench from section 45 until the end of the tunnel which was covered during the scanning 2005. According to the requirement of this project, the new-excavated slot and the section between 45–60 m should be scanned.

The terrestrial 3D laser scanner, Leica HDS4500 (Figure 7-3) was used to perform the field scanning /Leica 2008/. In order to obtain the geometric model and the measurement of the tunnel with the highest accuracy and full coverage, each scanning was performed with 3–5 mm distance between scanning points. It is often discovered that some parts are missing or scanned with a lower resolution due to the undulation of the tunnel wall and the small incidental angle of the laser beam. In order to avoid these problems, an overlap between each scan is necessary. The distance between each scanning station was in this project set to 6 m, which quarantined a sufficient overlap between each scan.

Figure 7-3. *Field scanning in the TASQ tunnel at ÄSPÖ.*

Totally, 11 scans were performed during this project. At least three reference points must be captured in each scan in order to transform all the scanning data into the same coordinate system. Totally, 22 reference points have been set and measured with Total Station, with an accuracy of ± 3 mm.

7.3 Geometric modelling

The geometric model of the tunnel was used as input data for the numerical modelling of the stress situation around the tunnel during the excavation. Based on the requirements of the numerical modelling, the following geometrical models and measurement was created from the scanning data in this project:

1) 3D mesh model of TASQ tunnel in section 29–64 m,
2) 3D mesh model of the front surface for each blast round in section 34–60 m,
3) flat plane for each blast round in section 34–60 m,
4) 2D Cross-section at three different locations, sections 047, 048 and 048.7.

7.3.1 Transformation of raw scanning data into Äspö 96

The raw scanning data from each separate scan was originally captured in a local coordinate system. Using this approach, it is necessary to transform all the local scanning data into the Äspö96 coordinate system. In this way, the scanning data can be compared with other input data from different measurement as well as integrated with the numerical modelling.

In order to transform the raw scanning data into the requested coordinate system, the three reference points must be marked and scanned in the local coordinate system, and then measured by Total Station within the requested global coordinate system, i.e. Äspö96. When the reference points are known, the transformation was performed using the software Light Form Modeler (LFM), which gives an accuracy of about 8 mm. After transforming the raw data, a 3D digital model of TASQ tunnel was created (Figure 7-4a and b).

7.3.2 3D mesh model of tunnel geometry from scanning data

In section 29 to 64 m of TASQ tunnel, a 3D mesh model of the top heading and the bench was created with the resolution of 0.2 m as input for numerical modelling (Figure 7-5). Although the resolution of the scanning data can be as high as 3–5 mm, it is difficult to run a three-dimensional numerical model with this high resolution due to the limitations of the software.

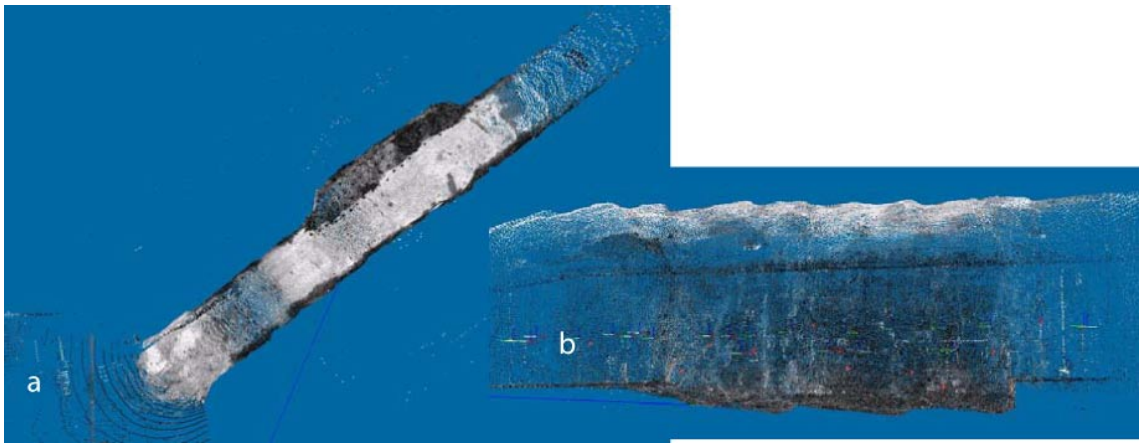

Figure 7-4. *3D digital model of TASQ tunnel transformed from each separated scan into Äspö96 coordinate system with top view (a) and side view (b).*

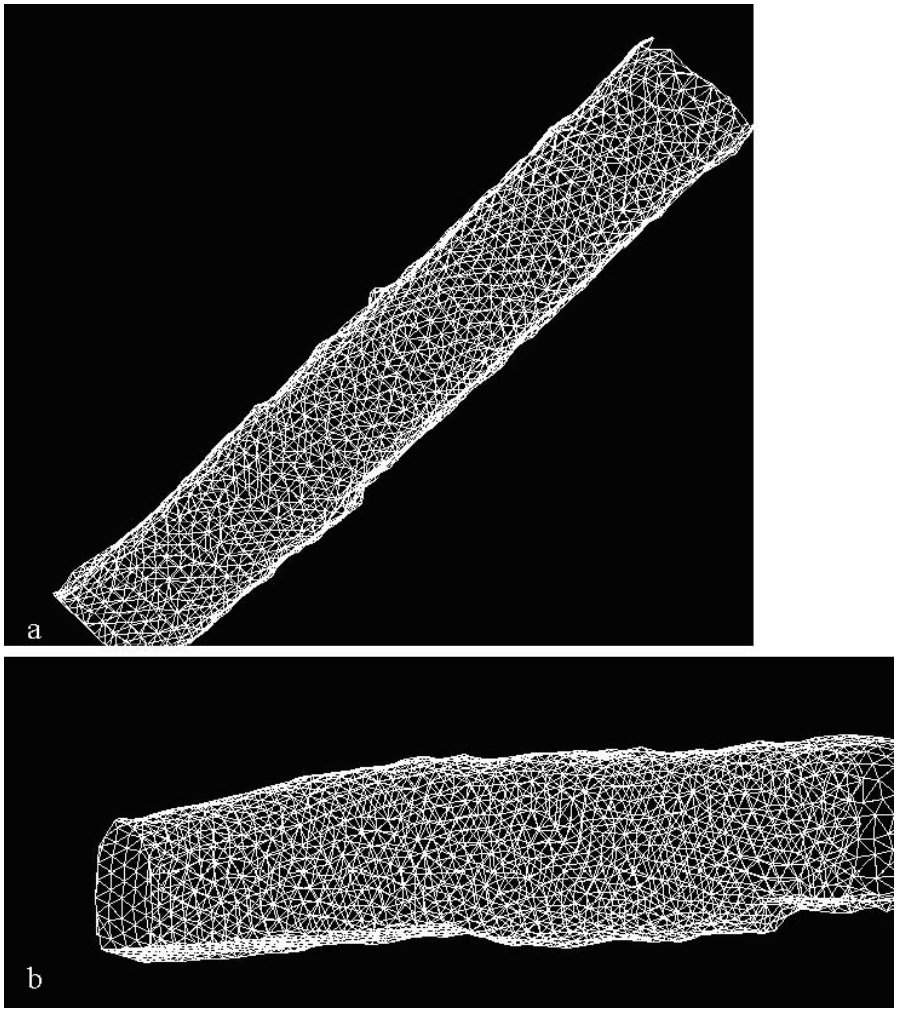

Figure 7-5. *Mesh model in the section of 29–64 m with top view (a) and side view (b).*

7.3.3 Creation of 3D model of the tunnel face for each blast round

In order to characterize the response of the tunnel for each blasting round by the numerical modelling, the geometric model of each tunnel face must be known. However, no scanning data was recorded for the faces as each face was removed when performing the blasting of the subsequent round. In this way, the exact shape as well as the exact location of each face must be recreated as close possible to the reality.

In this project, an approach in four steps was used in order to recreate the faces for each round. In the subsequent sections, the procedures used to obtain these geometric features are explained:

1. The only face that was scanned in the TASQ tunnel was the face from the last blasting round. Thus, for this face, the correct shape and curvature can be determined. Although this face is different than the other ones, it is closer to the real face than an ideal model. Therefore, this face was used as a reference to create the face model for the intermediate blast rounds (Figure 7-6).

2. The location of each face along the tunnel was determined from the position of the halfpipes and from existing documentation capturing the blasting procedure in the TASQ tunnel. Some visible halfpipes existed in the tunnel walls and in the ground but not in the roof as it was covered with reinforced shotcrete. The 3D model of those halfpipes was rebuilt from the scanning data. The start and the end of each blasting round with are marked with different colours and can be seen in Figure 7-7. When using the location of the halfpipes as an indicator for the position of the tunnel face, the location of each blasting face can be estimated with a tolerable accuracy. However, it must be mentioned that this method cannot replace a laser scanning of every tunnel face while blasting.

3. As the dimension (shape and curvature) of the tunnel face at the end of the tunnel differs from the intermediate ones, the tunnel face used as a reference must be scaled in order to fit the actual dimension of the tunnel. In order to get the boundary to which to scale the reference face, a cross-section created from scanning data at the location of each front had to be created (Figure 7-8).

4. Based upon the above-presented procedure, a 3D mesh model of the tunnel face for each blasting round was created (Figure 7-8). The red part is the reference model taken from the tunnel face at the end of the tunnel and the blue part was created by taking the cross-section (white dot-line) at the location of the tunnel face for the boundary of the new mesh model. By using the same technique, the geometry of all the front faces in the section of 34–60 meters could be created, and then located at the position according to the distribution of the blasting boreholes, and the blasting record notes (Figure 7-9).

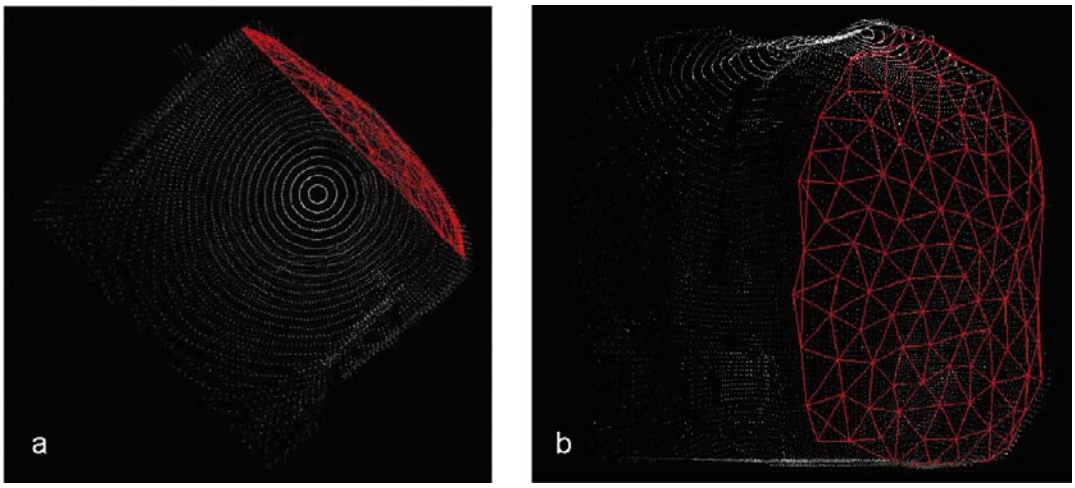

Figure 7-6. *3D mesh model of the tunnel face at the end of TASQ tunnel showing a) top view and b) side view.*

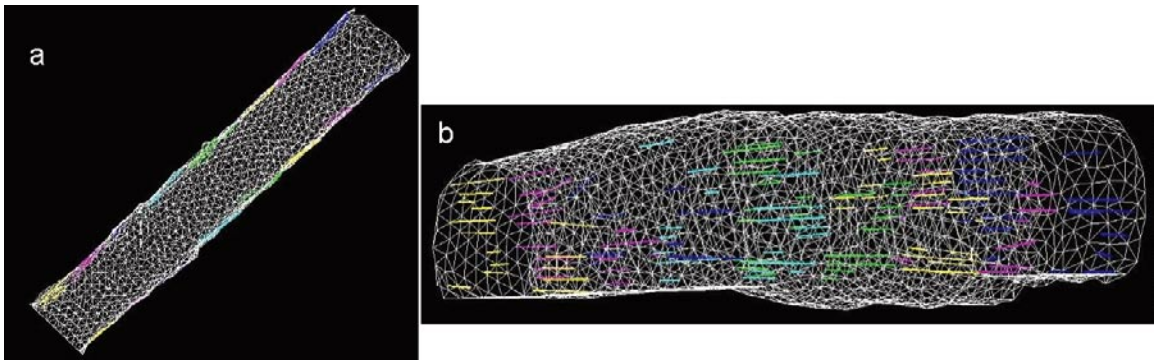

Figure 7-7. *3D model of boreholes for each blast round in the section of 29–64 m of the TASQ tunnel a) top view b) side view).*

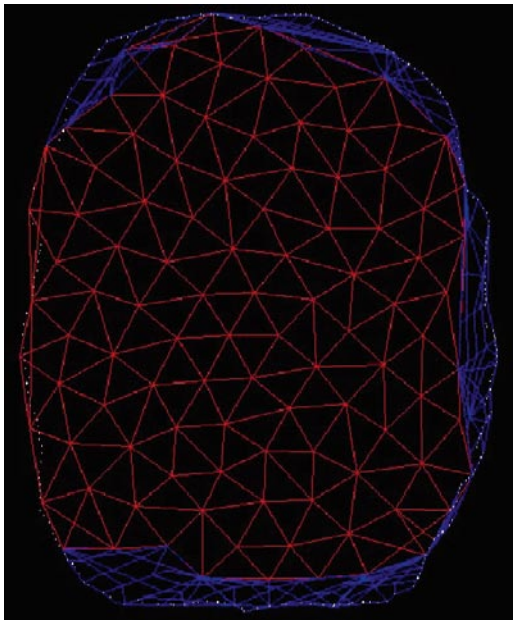

Figure 7-8. *Adjustment of the mesh mode for each tunnel face by the tunnel face at the end of the tunnel (red) and the cross-section (white dot line) located at each blast round. The new created 3D mesh model of the face can be seen in blue.*

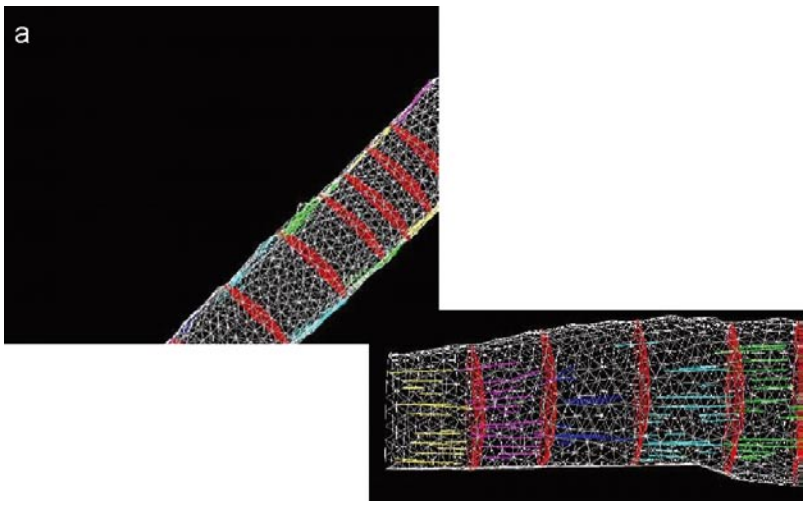

Figure 7-9. *3D mesh model of the tunnel faces (red parts) in section 34–60 m: a) top view and b) side view.*

7.3.4 Creation of a flat plane for each blast front

Two of the factors identified to influence EDZ are the tunnel shape and blasting round face shape. In order to investigate the tunnel response when using a different geometry for the tunnel faces, it was decided during the project to investigate the influence of a flat tunnel face. Each flat plane was located at the beginning of each round as indicated in Figure 7-10.

7.3.5 Creation of 2D cross-sections for UDEC

In order to perform a more accurate modelling of the stress situation around the tunnel, it was decided to perform UDEC simulations, which is a 2D simulation tool (this is further described in section 9.4). The advantage using UDEC is that a much higher accuracy of the tunnel profile can be obtained. When creating the desired geometry, the highest possible resolution was used (less than 5 mm).

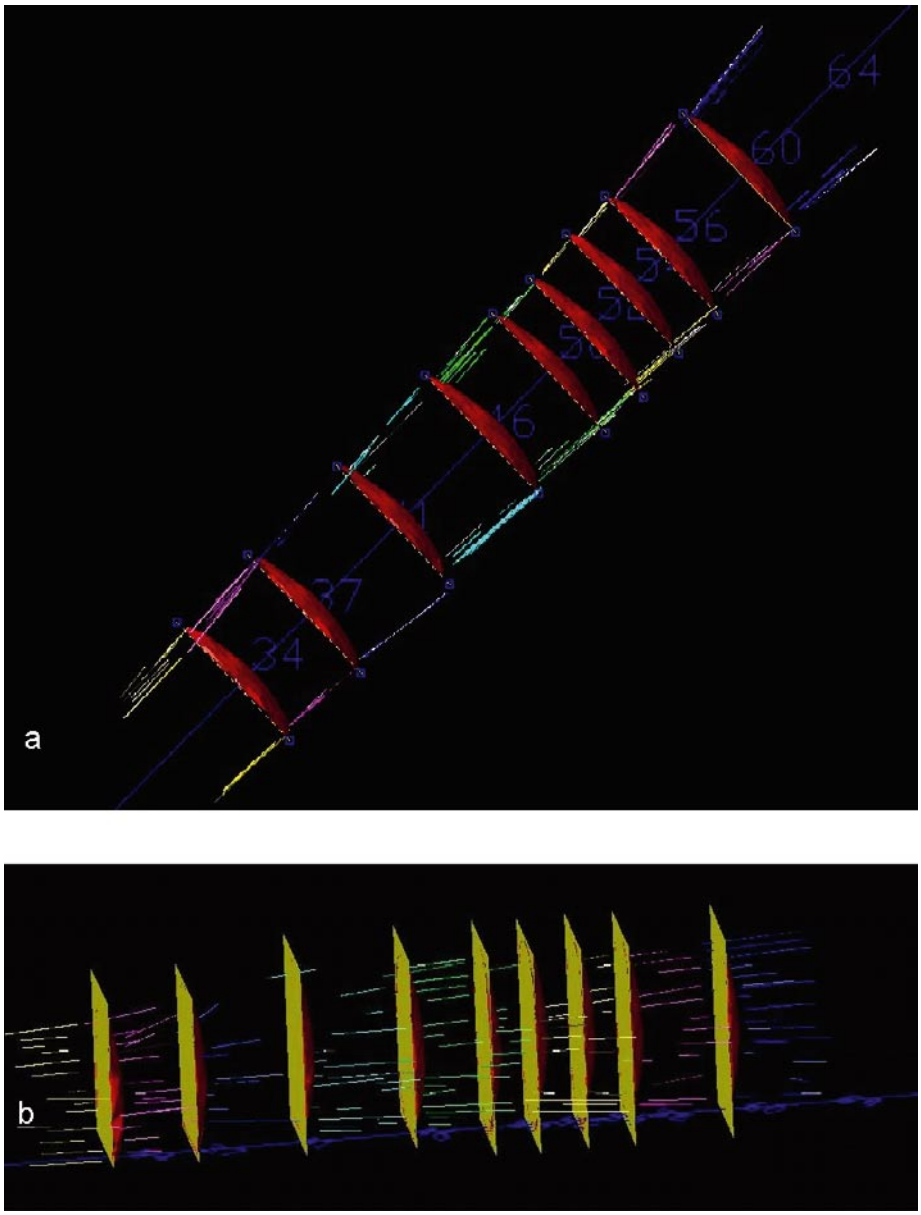

Figure 7-10. *3D model of both idea flat plane (yellow) and curved tunnel face (red) for each blast round in section 34–60 m with top view (a) and side view (b).*

Furthermore, these simulations were performed for cross-section located at position determined to be of special interest with respect to EDZ. Thus, for this purpose, the following geometric models and the location were selected:

(1) cross-section-1 (Figure 7-11) is located at section 47.38 m which is the location of the seismic boreholes (see Figure 6-2),

(2) cross-section-2 (Figure 7-11) is located outside of the slot at section 48.31 m,

(3) cross-section-3 (Figure 7-11) is located at section 48.61 m, which is the location of the convergence measurement.

7.4 Integration of different models for numerical modeling

In order to compare and visualize the scanning data together with other input data such as tunnel fracture mapping, geophysical measurement, blasting measurement, and design all data must be integrated into the same system. A further advantage using this approach is that all the different measurements can easily be integrated into the numerical modelling tool. As the numerical simulations consist of both the tunnel geometry and the fracture mapping, it was necessary to incorporate all the different data into one single model in order to run the numerical simulations as efficient as possible. For this project, the following geometric features were assembled into a single model as shown in Figure 7-12:

1) tunnel geometric model in 3D mesh,
2) tunnel face of each blast round in both flat plane and 3D mesh,
3) simplified fracture model in 3D defined block (the modelled fractures are indicated in Table 8.3),
4) theoretic tunnel axis and bench lines.

7.5 Conclusion and discussion

The presented results show that 3D laser scanning techniques can be used as a tool for providing the real geometric features required for an accurate numerical modelling of the tunnel excavation. In this way, an improved prediction of the tunnel response during excavation can be obtained.

When using laser image and 3D points, laser scanning data can also be used for documentation and visualization. For example, outgoing from the laserscanning data, the overbreak could be calculated to about 10% for section 29–64 in the TASQ-tunnel. As the overbreak was about 20% in the section 44.5–55.5 m it can be concluded that the amount of overbreak depends on the scale for which the results are evaluated.

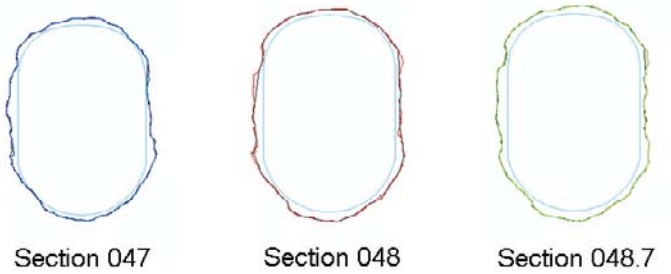

Figure 7-11. *Planned and as-built geometry in the shady area. Compare group a) in Figure 9-22.*

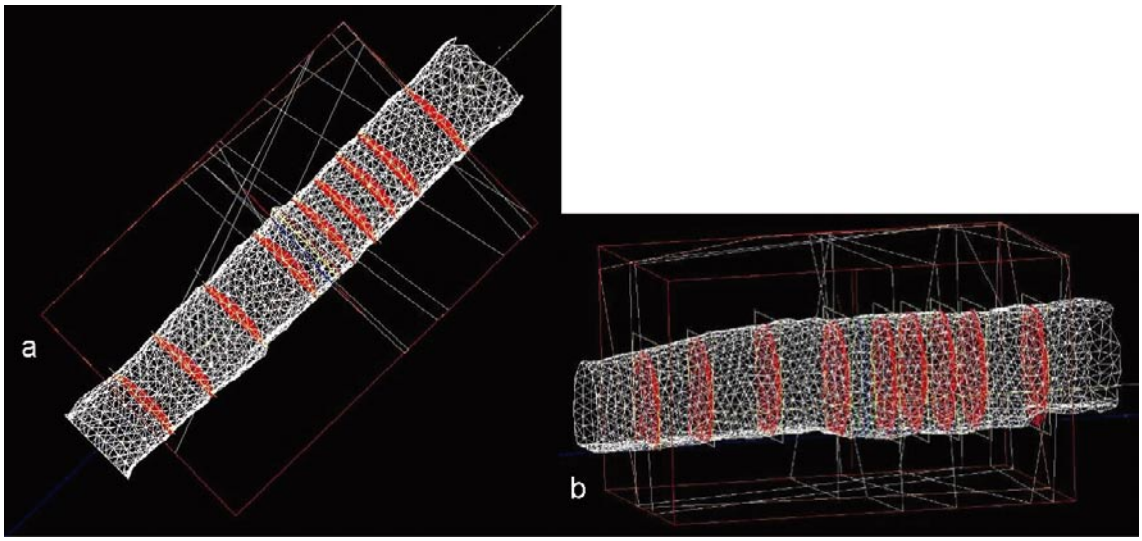

Figure 7-12. *Integrated model for numerical modelling: top view (a) and side view (b).*

In addition, the laser scanning data can be transformed into the same coordinate system as for other measurements such as tunnel mapping and design models, which means that the model created, can be easily integrated into a numerical modelling tool for example. Furthermore, it is important to capture the scanning data as soon as possible after the tunnel is excavated as otherwise; some parts will be hidden by the ventilation pipes or covered by the reinforced shotcrete, or even removed as the face will be blast away during the next round. When no geometrical information exists, an extra effort to rebuild the real geometric model is needed. However, it is impossible to achieve a good accuracy for the geometric models. A typical example is the uncertainty of the tunnel faces when creating the geometric model of each blast front. As no scanning data of the tunnel face was recorded after each blasting round, the geometry of each blast front was rebuild using the approach explained in section 7.3.3. In this way, the following uncertainties are obtained:

- The shape and curvature are the same for all front faces in the model. As each tunnel face had to be scaled to fit the actual tunnel geometry differences exist. However, no effort was done within this project to outline the effect of this geometric feature.
- The location of each tunnel face along the tunnel was determined from the position of the halfpipes and from existing literature capturing the blasting procedure in the TASQ tunnel. Using this approach, the exact location is unknown. This will then introduce some bias in the tunnel response when simulating the excavation process as the length of each round will affect the stress situation around the tunnel.

As mentioned above, several factors causing uncertainties in the tunnel geometry are introduced in the model as no exact measurement (position, shape, and curvature) of the tunnel faces are done. It is therefore recommended to perform measurements of each tunnel front when planning to use them in a numerical simulation like in this project. In this way, the above mentioned uncertainties can be quantified and, it can be determined whenever or not the estimation of the front locations and its shape has an influence on the tunnel response.

Furthermore, due to some limits of the numerical modelling software, it is difficult to run a 3D model of the full tunnel with higher resolution than 0.2 m even though the lasers canning equipment can provide resolution up to approximately 3 mm. However, as future project might find the need to access old data and reanalyse them for another application, it is always recommended to perform the scanning with the highest possible resolution. In this way, a new field scanning might not be necessary.

8 RVS model

For the purpose of this project, a model of larger fractures in the TASQ tunnel in the study area was made in RVS (Rock Visualization System). The model should function as input data for the modelling of stresses in the area, as described later in this report.

The model volume was selected in order to incorporate the area of interest, which is centred at about section 47 meter where a clustering of information was available from e.g. boreholes and a sawed wedge in the west wall. It was decided to model the tunnel from ca 32.5 m to 59.5 m length to incorporate the rice of the floor level that starts at about 32.5 m and to include an approximately similar size of rock volume also on the inner part of tunnel, with respect to section 47. The model was selected to be wide enough to include the borehole drilled in the tunnel, but not too wide in order to avoid to incorporating rock volume with unknown character.

8.1 Complementary TMS tunnel mapping

No new objects (fractures or rock boundaries) have been added, but the original 2D TMS-mapping has been transposed to its correct location, using the laser data available in the tunnel. This work was done in the tunnel using two computers, one with the graphics from the TMS-mapping on the screen (with ODBC-link to the database) and one with the laser data visible on the screen. Selected geology was correlated between TMS-data and "reality", i.e. the tunnel walls. The same geology was then drawn in the laser scan software, using images from laser data as a template.

8.2 Existing RVS models

Several RVS models exist at Äspö. Most of these are project related and of local extent only. However, one model for the whole laboratory exists, but it involves primarily larger deformation zones detected, none of which is modelled through the RVS model volume for this project. One zone of larger extent, called NE-2 exists fairly close and have similar characteristics as the shear zone mapped in TASQ /Wanne et al. 2004/.

An RVS model was made during the Pillar Stability Experiment in TASQ /Staub et al. 2003/. The model of the shear zone in the present work has been refined, but uses the input data from this earlier model.

8.3 RVS models

A new RVS model has been produced within this project (Figure 8-1). The model is created using strictly planar surfaces with no thickness in order to fulfil the needs from the rock mechanical modelling tools (see Chapter 9). At a more local scale, a provisional modelling of the upper and lower boundary to the shear zone was made by triangulation to match observed locations in a better way around the slot in the left wall at section 47 (see Figure 4-3 and Figure 8-2).

Table 8-1. Origin and extent of the RVS main model. The Y/X-axes of the model is rotated 46 degrees in Äspö96 coordinate system in order to align the with the tunnel direction.

	Origin	Extent
Easting	2098.000	18.000
Northing	7304.000	27.000
Elevation	–450.000	16.000

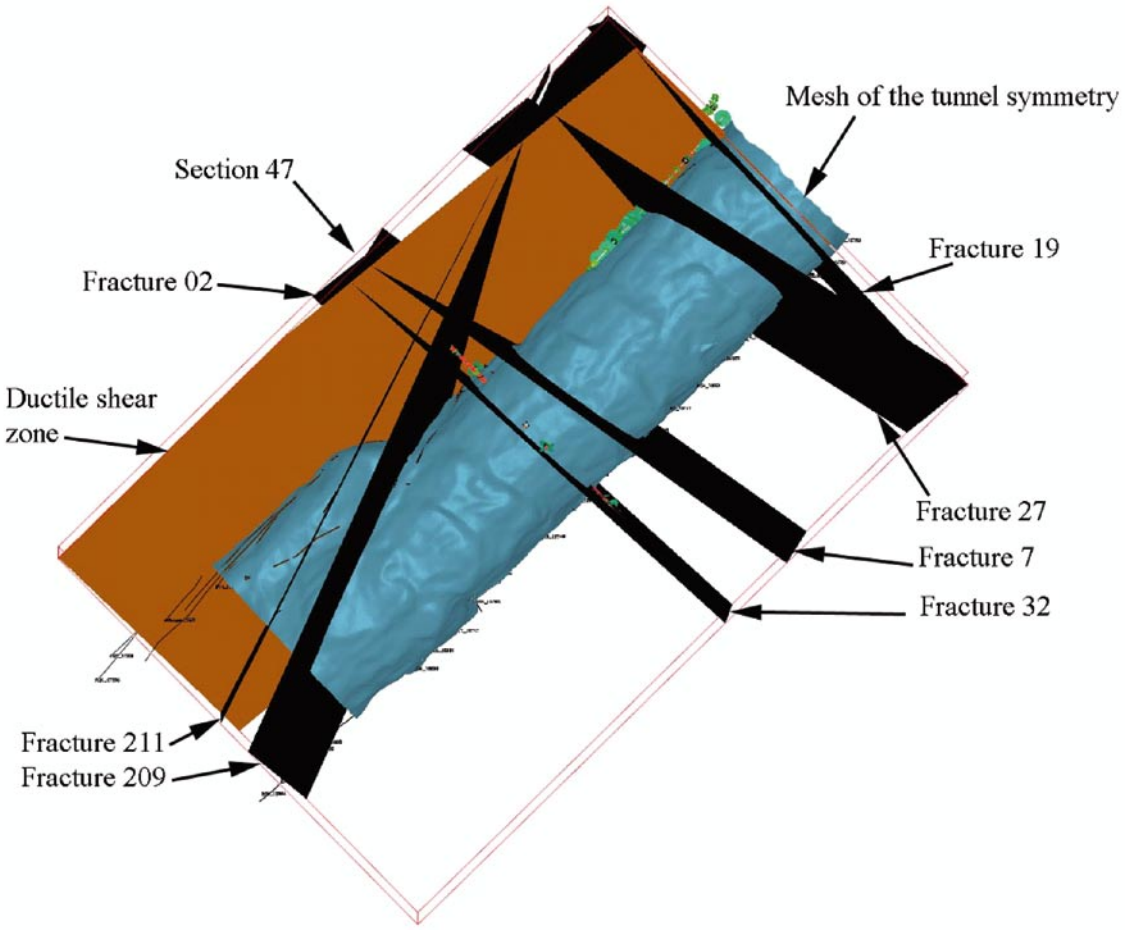

Figure 8-1. *Main model with topview (left) and isometric view (right). Modelled fractures are illustrated in black and the shear zone in brown.*

Table 8-2. Origin and extent of the minor model. The Y-axis parallels that of the main model.

	Origin	Extent
Easting	2110.000	3.000
Northing	7310.000	4.000
Elevation	–446.000	8.000

8.4 Modelled objects

In total, eight fractures and one shear zone has been modelled in the main model. Coordinates for the model, including boundary box and modelled objects are given in Table 8-3 together with the characteristics of the objects. The Information in column two in the table is derived from the TMS database stored at Äspö, where also the naming of the fracture can be found. “sectID” refers to the mapped section in the tunnel (eg. sectID 60 means the mapped section ending at 60 metres length in the tunnel and correspondingly named so in the database). The information in column three gives the orientation of the fracture in the RVS model and in column four the orientation found in the TMS database (several values may occur here).

Table 8-3. Modelled objects and their characteristics.

Modelled object name	Fractures from TMS	Orientation of modelled object (strike/dip)	Orientation of mapped fractures (strike/dip)	Characteristics of mapped fractures
Fracture02_w	Left wall: Fracture 02 sectID 60	133/79	121/79	Sealed with epidote and grout Sealed with calcite
	Floor: Fracture 45 sectID 59		128/90	
Fracture32_e	Right wall: Fracture 32 sectID 60	313/89	125/90	Sealed with chlorite and calcite Sealed with calcite
	Floor: Fracture 04 sectID 59		323/90	
Fracture19	Left wall and roof: Fracture 19 sectID 60	137/86	93/80; 278/90	Waterbearing with cacite and grout
	Right wall: Fracture 15 sectID 60			Waterbearing with grout
Fracture209	Fracture9 sectID:s 35, 40, 45, 60	25/80	25/72	Sealed with epidote, chlorite, calcite and quartz
Fracture211	Right wall and roof: Fracture 11 sectID:s 30, 35, 40	27/90	28/72; 28/82	Sealed with chlorite and epidote Sealed with chlorite, calcite and with oxidized walls
	Left nisch: Fracture 15 and 5, sectID NASQ 44			
Fracture27	Left wall: Fracture 15 sectID 60	123/79	291/90; 100/90; 110/90; 95/90; 100/90	Waterbearing and some grout Sealed with epidote, chlorite and calcite
	Floor: Fracture 51, 66, 30, 27, sectID 59			
Fracture7	Left wall, roof and right wall: Fracture 7	306/86.5	303/90; 123/80; 128/90	Waterbearing with calcite and grout
	Floor: Fracture 17 and 18			Sealed with chlorite and calcite
TASQ_SZ		51/58	27/58; 42/57; 53/60	Partly undulating brittle-ductile shear zone
				Width ca 0.1 to 1.5 metre

Fracture02 and Fracture32 were initially modelled as on fracture crosscutting the whole model volume. The fractures characteristic does however indicate that it steps or runs ‘en echelon’. Only in the upper part of the left wall and in the roof there are indications that the fracture has been initially open, where grout has been mapped and a water leakage is found close to the fracture. The structure was thus separated into two model fractures, Fracture02_w and Fracture32_e, both ending to the shear zone and with slightly different orientation. Several fractures do in fact end at the shear zone in the mapping of the floor in this area.

A cross-section through the tunnel where the KQ0047 boreholes are located (Figure 8-2) shows the principal major fractures in the model volume. Except for the steep fractures 209 and 211 that run at low angle to the tunnel, the brittle-ductile shear zone, that runs sub-parallel to the tunnel, affects the geology in a large part of the left wall and the floor in the model volume. The fracture32e represents the steep northwest-southeast fracture set, which is the most common set not only in the model volume, but also in the whole Äspö facility. In this case it has been modelled to end at the shear zone, which was indicated in the tunnel floor for a few fractures at this location, but often this set of fractures seem to crosscut the shear zone.

In the boreholes in the left wall (see Figure 8-2) the majority of the fractures are either steep or runs almost parallel to the shear zone.

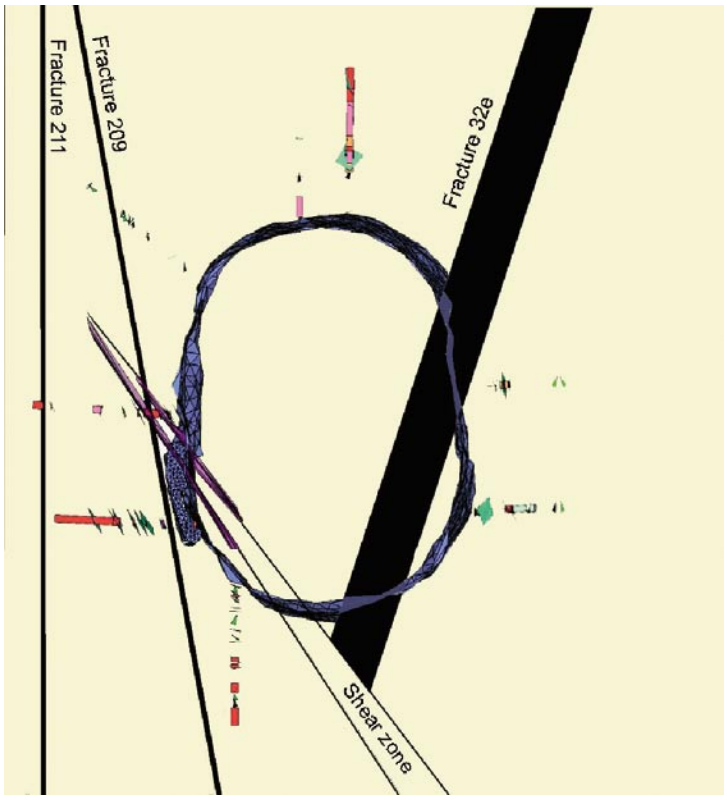

Figure 8-2. *A narrow section at right angle to the tunnel at length section 47, viewed towards the northeast. Visualized parameters in the eight boreholes at KQ0047 are seen. Large discs represents open fractures, and small discs sealed fractures. Dark purple is mylonites and breccias, light purple represents fine-grained granite and orange represent deformed "Äspö diorite" and sealed fracture networks.*

9 Numerical modelling using 3DEC and UDEC

The main objective of this project is to understand what the main factors causing the EDZ are. A number of rock mechanics aspects which could influence the initiation, development and extent of the EDZ have been identified:

- Tunnel shape: as-planned shape vs. as-built shape.
- Blasting round face: planar (as-planned) and concave (as-built).
- Rock mass elastic behaviour.
- In-situ stress field (magnitude and orientation).
- Major fractures in the TASQ tunnel according to the geological mapping.

In order to understand the role and relative influence of each one of these aspects on the EDZ, a numerical study using 3DEC /Itasca 2007/ and UDEC /Itasca 2004/ has been conducted. These codes are suited to simulate the behaviour of rock masses containing multiple, intersecting discontinuities in three dimensions and two dimensions respectively.

The numerical study has included three different phases:

1. A calibration exercise in which the elastic properties of the rock mass and the in-situ stress in 3DEC models of the as-built tunnel considering concave blasting round faces have been calibrated to match the convergence measurements performed during the excavation of the TASQ tunnel. This calibration was done without considering the fractures.
2. An extensive sensitivity analysis in which 3DEC models with different combinations of all the above mentioned aspects have been run.
3. UDEC models of three different sections of the TASQ-tunnel to be able to judge the influence of the actual (as-built) shape of the tunnel vs. the planned shape using the best resolution model of the tunnel based on the available laser-scanning data.

The mesh of the 3DEC models with the different tetrahedral zone sizes is shown in Figure 9-4.

9.1 Conceptual model

Based on the latest geological model of the TASQ-tunnel (Chapter 8), and the available data ranges on the in-situ stress field, rock mass and fracture mechanical properties, the conceptual model of the study volume was created.

9.1.1 Model geometry for 3DEC

From the identified factors influencing the EDZ, two of them are related to the model geometry: tunnel shape and blasting round face shape.

In order to assess the relative influence of each of these factors, the following three-dimensional models were generated using 3DEC /Itasca 2007/:

1. A model with the planned tunnel shape and flat blasting round faces (see Figure 9-1).
2. A model with the as-built tunnel shape and flat blasting round faces (see Figure 9-2). The tunnel shape was obtained from the three-dimensional laser-scanning model of the TASQ-tunnel (section 7.3.2).
3. A model with the as-built tunnel shape and actual (concave) blasting round faces (see Figure 9-3). The tunnel shape was obtained from the three-dimensional laser-scanning model of the TASQ-tunnel. The actual blasting round faces are all the same and were obtained from the laser-scanning representation of the front of the tunnel and extrapolated to each of the blasting round faces positions (Figure 7-6).

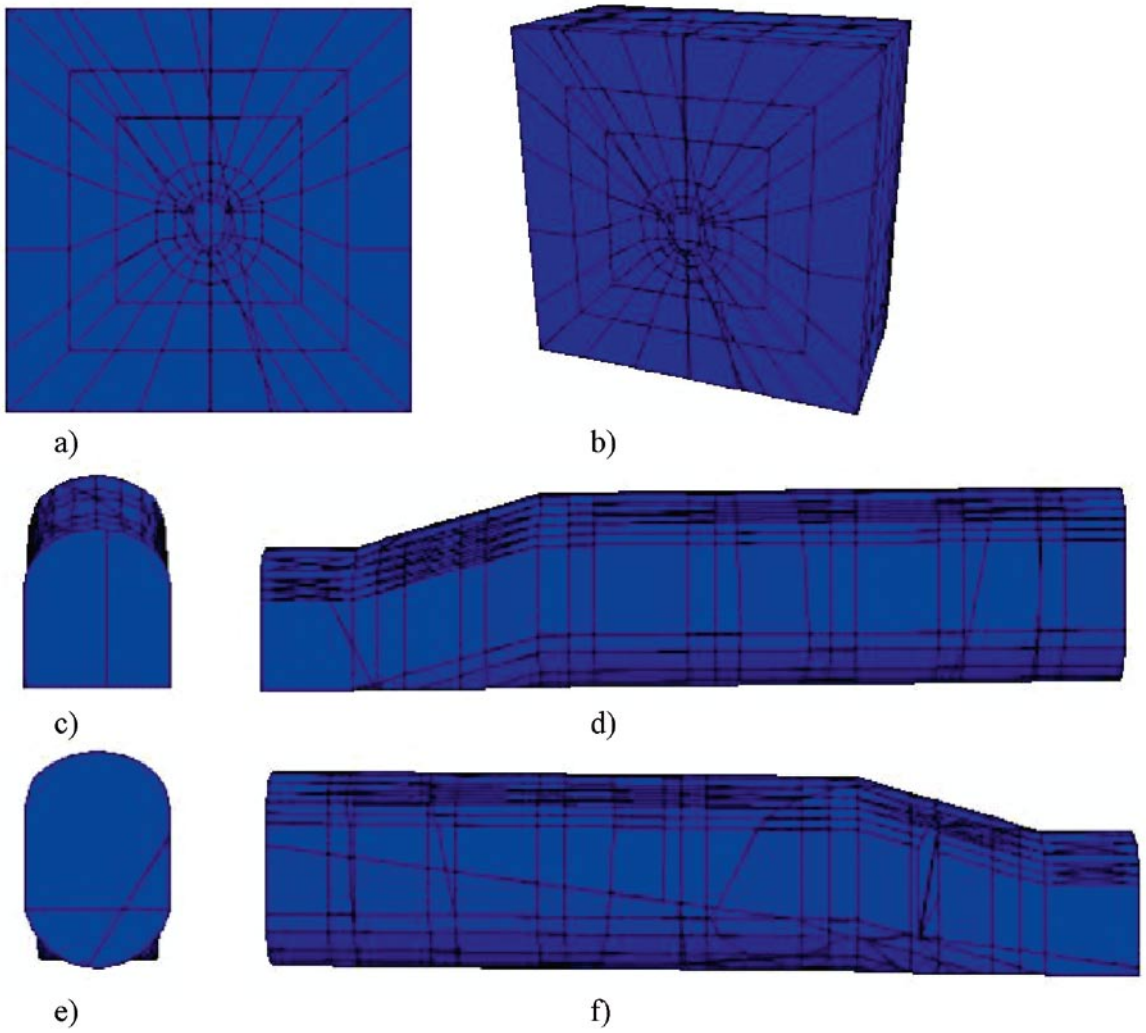

Figure 9-1. *The 3DEC tunnel geometry for the* ***as-planned tunnel shape*** *with flat blasting round faces and* ***without fractures****; a) model block b) rotated view of model block c) front view of the entrance to the tunnel, d) right side of the tunnel, e) end of modelled tunnel and f) left side of the tunnel.*

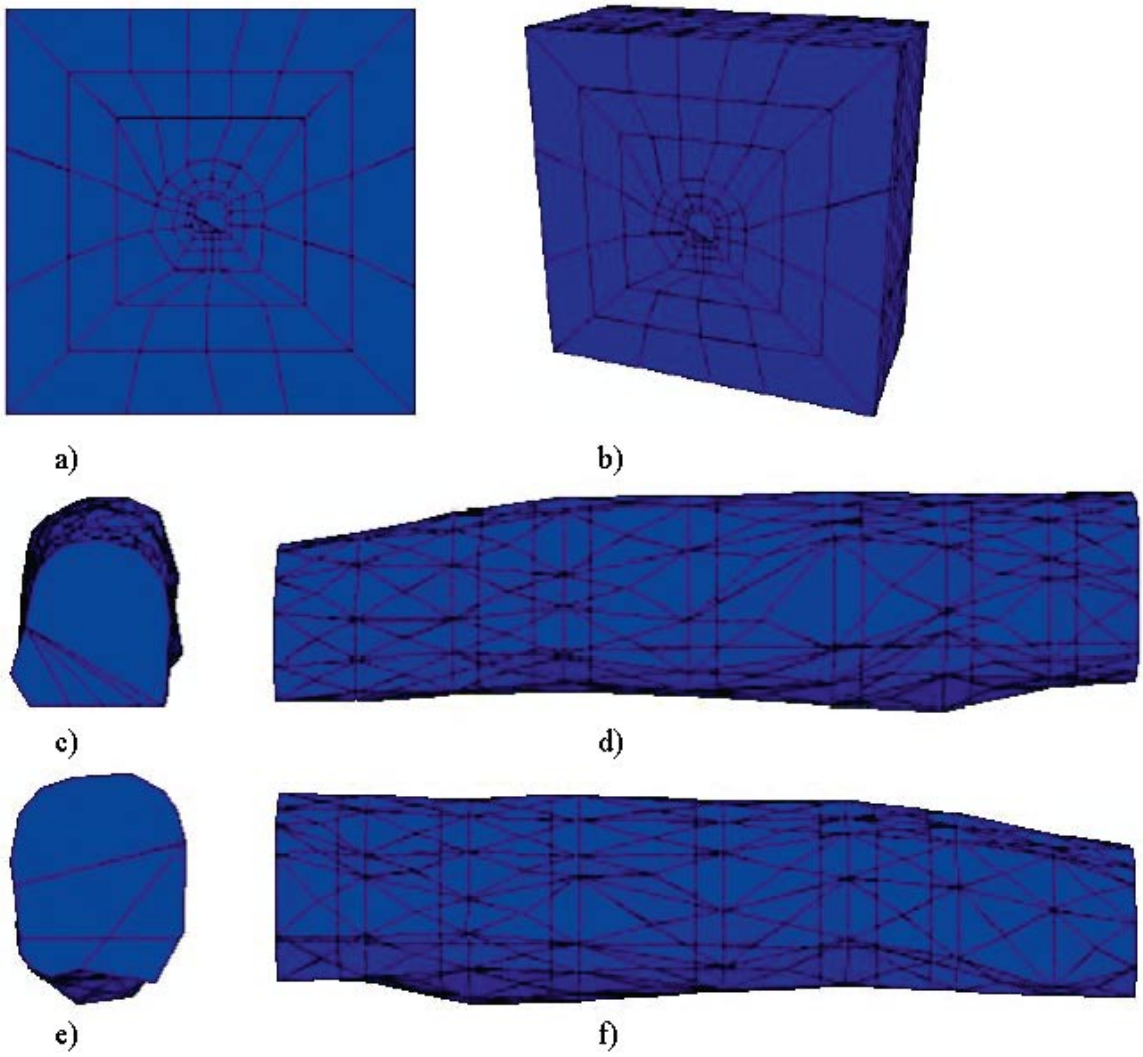

Figure 9-2. *The 3DEC tunnel geometry for the* ***as-built tunnel shape*** *with flat blasting round faces and* ***without fractures****; a) model block b) rotated view of model block c) front view of the entrance to the tunnel, d) right side of the tunnel, e) end of modelled tunnel and f) left side of the tunnel.*

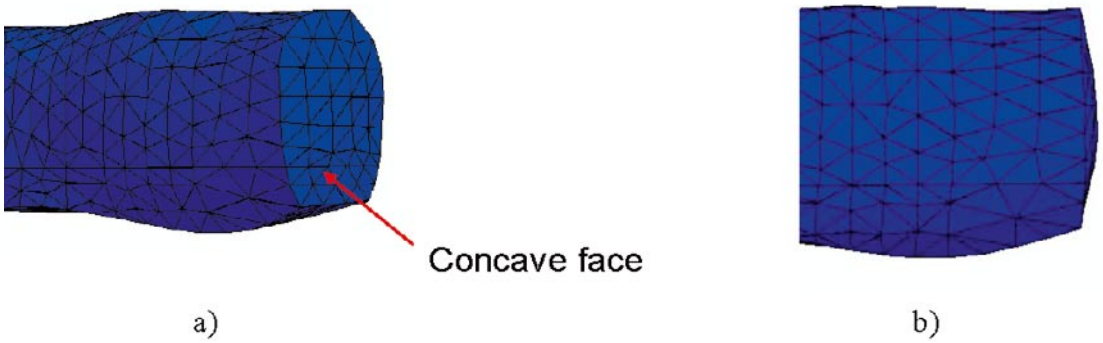

Figure 9-3. *Part of the 3DEC tunnel geometry for the as-built tunnel shape showing one concave blasting round face a) rotated and b) perpendicular to the tunnel axis.*

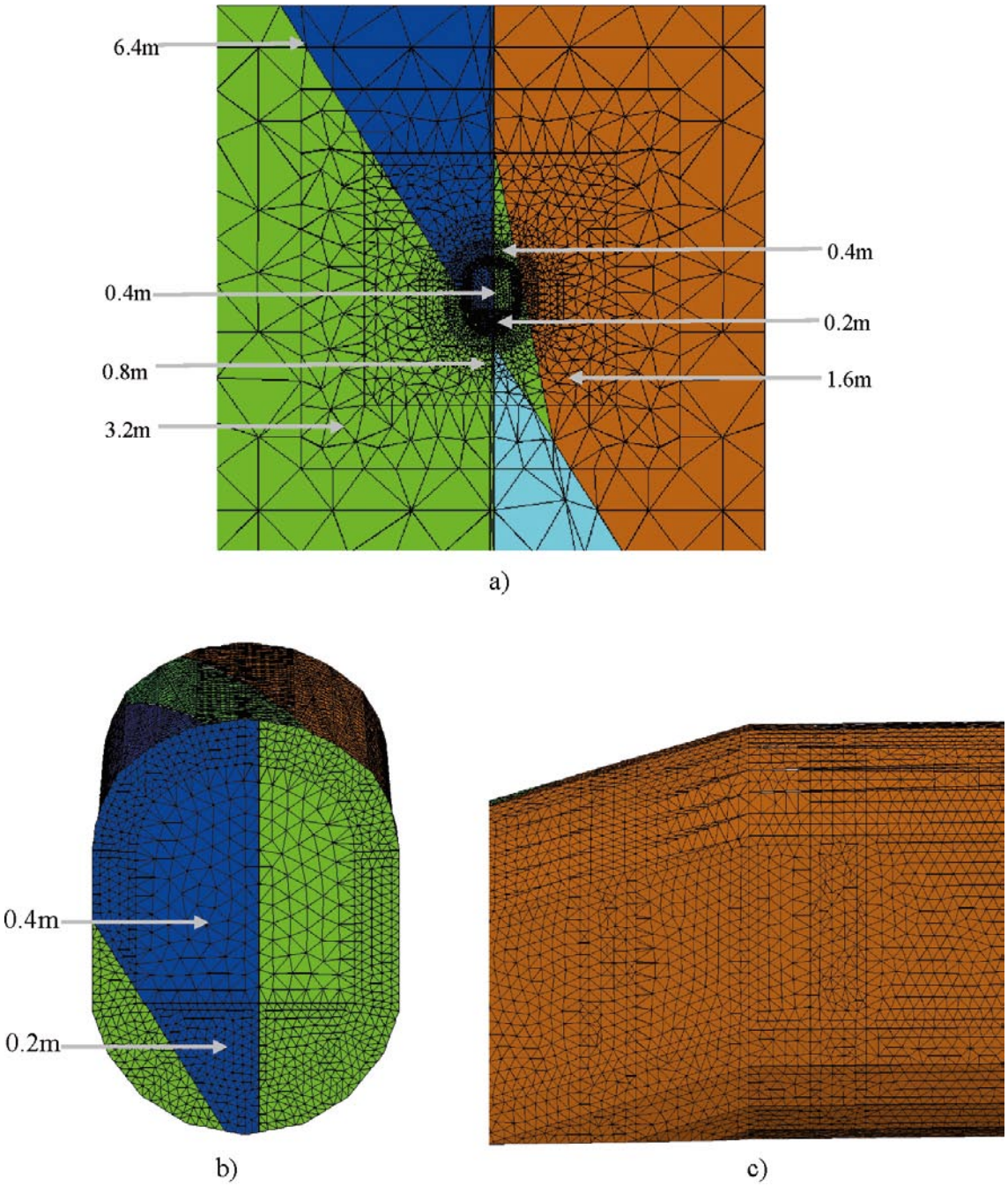

Figure 9-4. *The mesh in the 3DEC model with the different tetrahedral* ***zone sizes****; a) the model block with the size of the tetrahedral zones outlined, b) the tunnel and the closest surrounding rock and c) the tunnel wall mesh.*

9.1.2 In-situ and boundary conditions for 3DEC

The in-situ and boundary conditions considered in the 3D models are as follows:

- Hydrostatic water pore pressure (4.5 MPa at the depth level considered) was applied in the fractures when present.
- Based on the in-situ stress tensors used in previously reported simulations /Fredriksson et al. 2004, Rinne et al. 2004, Wanne et al. 2004/ and in the stress tensor obtained from the back-calculation of the convergence measurements made during the excavation of the TASQ tunnel /Andersson 2004/, the ranges considered for the in-situ stress tensors applied to the models in this study are as shown in (Table 9-1). A scheme showing the approximate range of orientations of the major and minor principal stress relative to the TASQ-tunnel axis is shown in Figure 9-5.

- In the lateral boundaries, no displacement in the normal direction to their respective surfaces was allowed. They may move freely in the other directions.
- In the lower boundary, no displacement in any direction was allowed.
- In the upper boundary, the vertical principal stress (σ_2) was applied as boundary condition.

9.1.3 Rock mass properties and behavior

The rock mass in the 3DEC model was modelled as isotropic linear elastic. A range of values was assigned for the Young's modulus in the three-dimensional sensitivity and calibration studies. Ranges were chosen according to available published data /Andersson 2004, Hakami et al. 2008/ and cover a range from 45 GPa to 75 GPa. The values for each particular model are shown in Table 9-6, Table 9-7 and Table 9-9. The Poisson's ratio considered was 0.26 and the density was considered (2,731 kg/m^3) for all the cases simulated /Andersson 2004/.

9.1.4 Selected fractures and their behavior

The fractures in the 3DEC model were chosen to represent the major fractures and shear zones intersecting the TASQ tunnel according to the last version of the available geological mapping (Chapter 8). The two major fracture sets in the TASQ tunnel have a sub-vertical dipping nature and are trending NE and NW respectively. The NW trending fractures are mainly perpendicular to the TASQ-tunnel axis and the NE trending fractures are sub-parallel to it, see Figure 9-5 and Figure 9-6. The fractures and fracture zones included in the 3DEC model are listed in Table 9-2.

The fractures follow a Coulomb slip model in which zero tensile strength was assumed. The ductile shear zone, due to its thickness and rock mass like nature (see section 4.2.2), was simulated in three different ways: purely elastic fracture, strong Coulomb slip fracture, very strong Coulomb slip fracture (see Table 9-5).

Table 9-1. In-situ stress in 3DEC models.

	Magnitude of stress (MPa)	Plunge (deg)	Trend (Äspö 96) (deg)
σ_1	25, 30	0	310, 316, 322
σ_2	15	90	90
σ_3	10	0	220, 226, 232

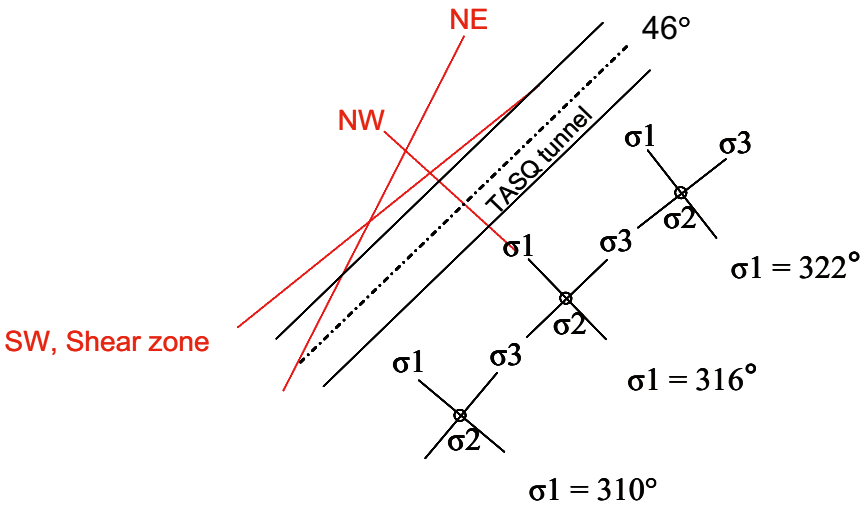

Figure 9-5. Schematic figure showing the three different in-situ principal stress orientations relative to the TASQ tunnel axis (orientations given in ÄSPÖ96 coordinate system) used in the simulations. The major fracture sets trends are also included in the figure.

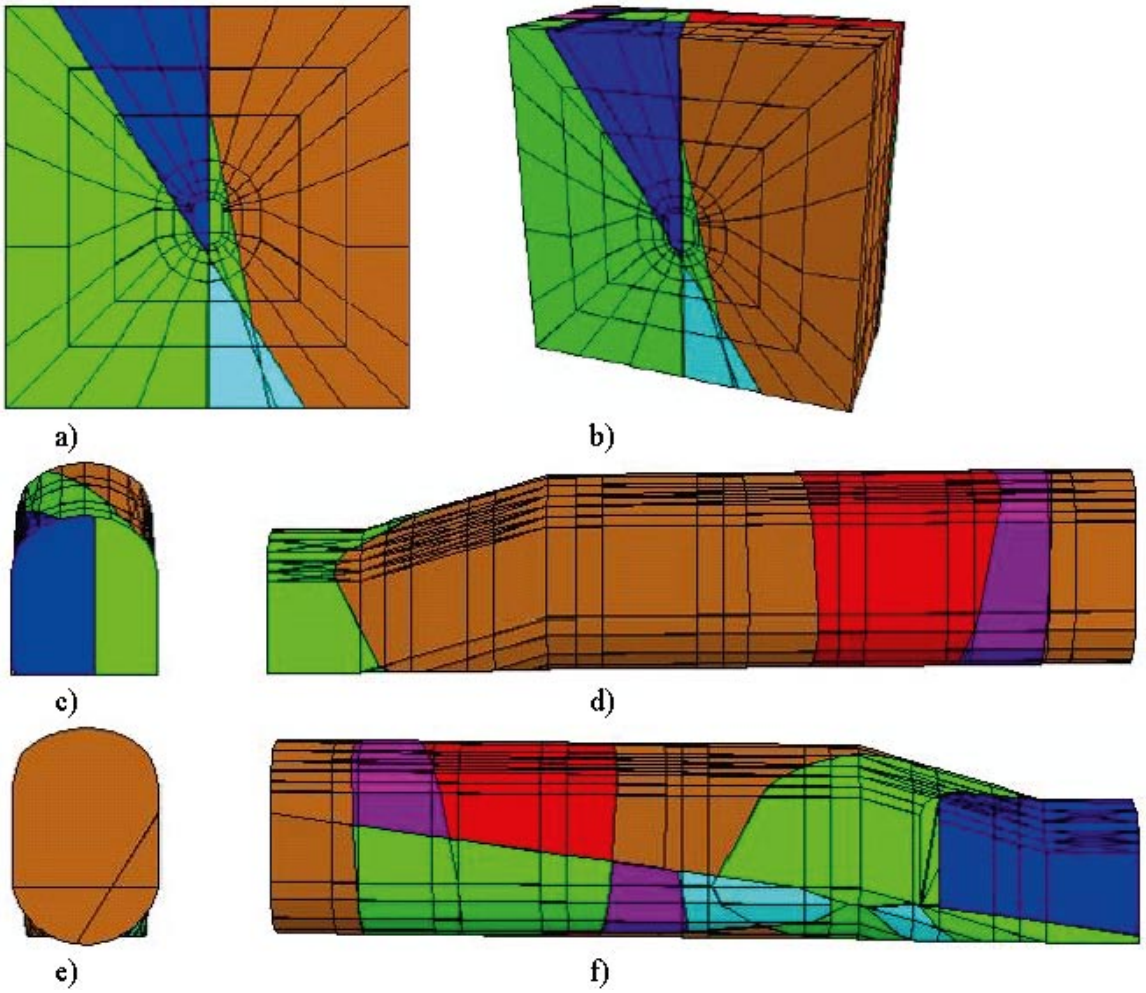

Figure 9-6. *The 3DEC tunnel geometry using the* ***as-planned tunnel shape with fractures****; a) model block b) rotated view of model block c) beginning of the tunnel, d) right side of the tunnel, e) end of tunnel and f) left side of the tunnel.*

Table 9-2. **Fractures included in the 3DEC model.**

	Dip (deg)	Dip direction[1] (deg)	Comments
Fracture32_e	88.8	356.9	NW trending
Fracture02_w	79.0	176.8	NW trending
Fracture7	86.6	350.1	NW trending
Fracture27	79.0	167.0	NW trending
Fracture19	86.4	181.4	NW trending
Fracture209	79.3	68.5	NE trending
Fracture211	90.0	81.8[2]	NE trending
TASQ_SZ	58.0	94.0	Ductile shear zone represented as a single planar feature in 3DEC. Its actual thickness varies from about 0.1 m to 1.5 m.

[1] The dip direction refers to the local coordinate system of the model, which is transformed 46 degrees.

[2] The fracture plans were created in an early stage of the project when only a preliminary dip direction was available. The dip direction of fracture 211 should be 75 degree. However, fracture 211 is about 1 m away from the tunnel wall and therefore, should not affect the stress distribution (see appendix H and I).

The fracture parameters are shown in Table 9-3 to Table 9-5**.** The fractures have been grouped into their respective fracture set and values for the base-line case fractured model have been chosen from available published data /Staub et al. 2003, 2004, Jacobsson and Flansbjer 2005, Olofsson et al. 2007, Hakami et al. 2008/. Furthermore, a range of values for stiffness and strength properties has been selected for each fracture set taking into account the fact that laboratory properties are often not representative of in-situ properties due to scale effect /Fardin 2003/, difference in boundary conditions (laboratory tests having often stress boundary conditions while there are stiffness boundary conditions in-situ), the fact that laboratory tests derived properties are usually taken at large displacements while the displacements in-situ are relatively small (friction angles are typically much larger for small displacements), fractures in-situ are not perfectly planar, they are undulated to a higher or lower degree, etc.

Table 9-3. Fracture properties for the NE trending fractures in the different simulation cases of the fracture sensitivity study.

Fracture model case	kn (GPa/m)	ks (GPa/m)	friction (deg)	cohesion (MPa)	dilation (deg)
baseline case	200	100	36	1.2	2.0
weak	100	50	30	1.2	2.0
strong	200	100	50	1.2	2.0
stiff	1,000	500	36	1.2	2.0
stiff and weak	1,000	500	30	1.2	2.0
stiff and strong	1,000	500	50	1.2	2.0
stiffer	2,000	1,000	36	1.2	2.0
stiffer and weak	2,000	1,000	30	1.2	2.0
elastic TASQ_SZ	200	100	36	1.2	2.0
strong TASQ_SZ	200	100	36	1.2	2.0

Table 9-4. Fracture properties for the NW trending fractures in the different simulation cases of the fracture sensitivity study.

Fracture model case	kn (GPa/m)	ks (GPa/m)	friction (deg)	cohesion (MPa)	dilation (deg)
baseline case	200	100	40	0.9	3.0
weak	100	50	35	0.9	3.0
strong	200	100	50	0.9	3.0
stiff	1,000	500	40	0.9	3.0
stiff and weak	1,000	500	35	0.9	3.0
stiff and strong	1,000	500	50	0.9	3.0
stiffer	2,000	1,000	40	0.9	3.0
stiffer and weak	2,000	1,000	35	0.9	3.0
elastic TASQ_SZ	200	100	40	0.9	3.0
strong TASQ_SZ	200	100	40	0.9	3.0

Table 9-5. Fracture properties for the shear zone (TASQ_SZ) in the different simulation cases of the fracture sensitivity study.

Fracture model case	kn (GPa/m)	ks (GPa/m)	friction (deg)	cohesion (MPa)	dilation (deg)
baseline case	200	100	55	1.2	4.0
weak	100	50	50	1.2	4.0
strong	200	100	65	1.2	4.0
stiff	1,000	500	55	1.2	4.0
stiff and weak	1,000	500	45	1.2	4.0
stiff and strong	1,000	500	65	1.2	4.0
stiffer	2,000	1,000	55	1.2	4.0
stiffer and weak	2,000	1,000	45	1.2	4.0
elastic TASQ_SZ	200	100	–	–	–
strong TASQ_SZ	200	100	65	1.2	4.0

9.2 Calibration of the 3DEC model against convergence

Tunnel convergence was measured with the help of convergence pins located at different positions in the contour of section 048.7 of the TASQ-tunnel while different sections of the tunnel were excavated /Andersson 2007, Staub et al. 2004/. Using these convergence measurements, a numerical calibration study has been performed in order to obtain the best fitting in-situ stress and elastic rock mass properties. The different ranges for the Young's modulus and the magnitude and orientation of the major principal stress used in this study are listed in Table 9-6.

The main body of the simulations was performed using the as-built tunnel shape as well as concave (actual) blasting round faces. Additional simulations were performed using the as-planned tunnel shape with planar blasting round faces and the as-built tunnel shape with planar blasting round faces in order to consider the effect of tunnel shape and blasting round face shape (cases with E = 45 GPa and σ_1 = 30 MPa and E = 65 GPa and σ_1 = 25 MPa). No fractures were considered in the calibration study. The simulation of the excavation of the heading of the TASQ-tunnel was performed in stages, according to the actual blasting round stages in order to simulate the correct tunnel convergence sequence.

Figure 9-7 shows some of the results of the calibration back-analysis. The rest of the calibration results can be found in Appendix J.

Table 9-6. Rock mass properties and σ_1 magnitude and trend for each of the cases for the calibration (without fractures).

Tunnel shape	Blasting round face shape	Young's modulus (GPa)	Trend of σ_1 (deg)	Magnitude of σ_1 (MPa)
As-planned	Plane	45	316	30
As-built	Plane	45	316	30
As-built	Concave	45	310	25
As-built	Concave	45	310	30
As-built	Concave	45	316	25
As-built	Concave	45	316	30
As-built	Concave	45	322	25
As-built	Concave	45	322	30
As-built	Concave	50	310	25
As-built	Concave	50	310	30
As-built	Concave	50	316	25
As-built	Concave	50	316	30
As-built	Concave	50	322	25
As-built	Concave	50	322	30
As-built	Concave	55	310	25
As-built	Concave	55	310	30
As-built	Concave	55	316	25
As-built	Concave	55	316	30
As-built	Concave	55	322	25
As-built	Concave	55	322	30
As-built	Concave	65	310	25
As-built	Concave	70	316	25
As-built	Concave	75	316	25
As-built	Concave	75	316	30

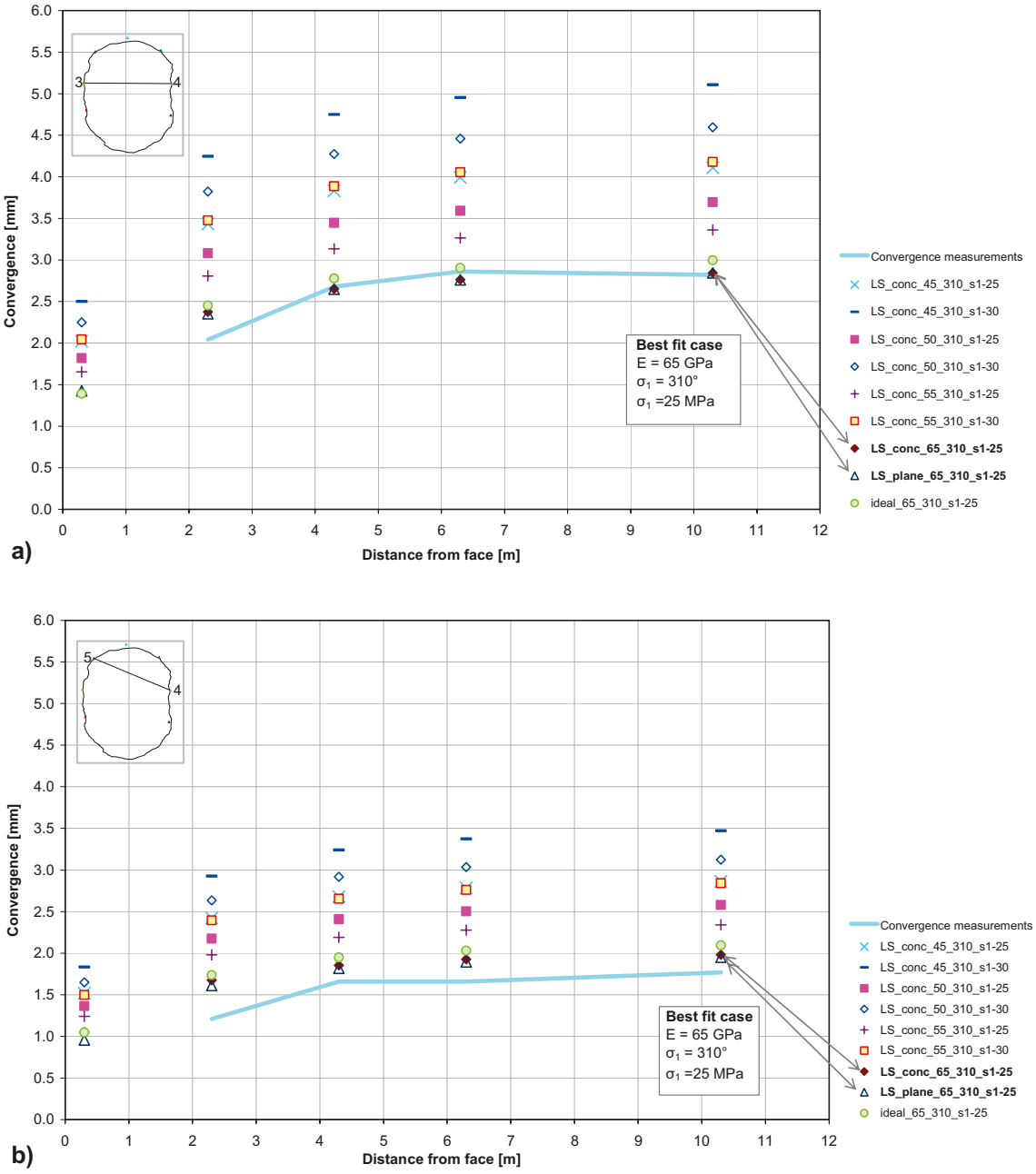

Figure 9-7. *Simulated vs. field convergence measurements between a) pin 3 and 4, and b) pin 4 and 5; "LS" indicates laser-scanned (as-built) tunnel shape and "ideal" indicates the as-planned tunnel shape. "conc" indicates concave blasting round faces. 45, 50, 55 and 65 are the rock mass Young's modulus in GPa used in the simulations. 310 indicate the trend of the major in-situ principal stress. "s1-25" and "s1-30" indicate the magnitude of major in-situ principal stress in MPa (see Appendix J).*

Figure 9-8 and Figure 9-9 contain major and minor principal stress scanlines of the best fit calibration case (E = 65 GPa, σ_1 = 25 MPa) showing the difference between the model with as-planned tunnel shape with planar blasting round faces, the model with as-built tunnel shape with planar blasting round faces and the model with as-built tunnel shape with concave blasting round faces at cross section 048.7 (convergence pins location) in the TASQ tunnel when the heading of section 049 is excavated. The scanlines are approximately at the same place in the tunnel as the boreholes in the BGR section, which is section 047 (Figure 9-12). The stress scanlines after excavation of other head sections are shown in Appendix K.

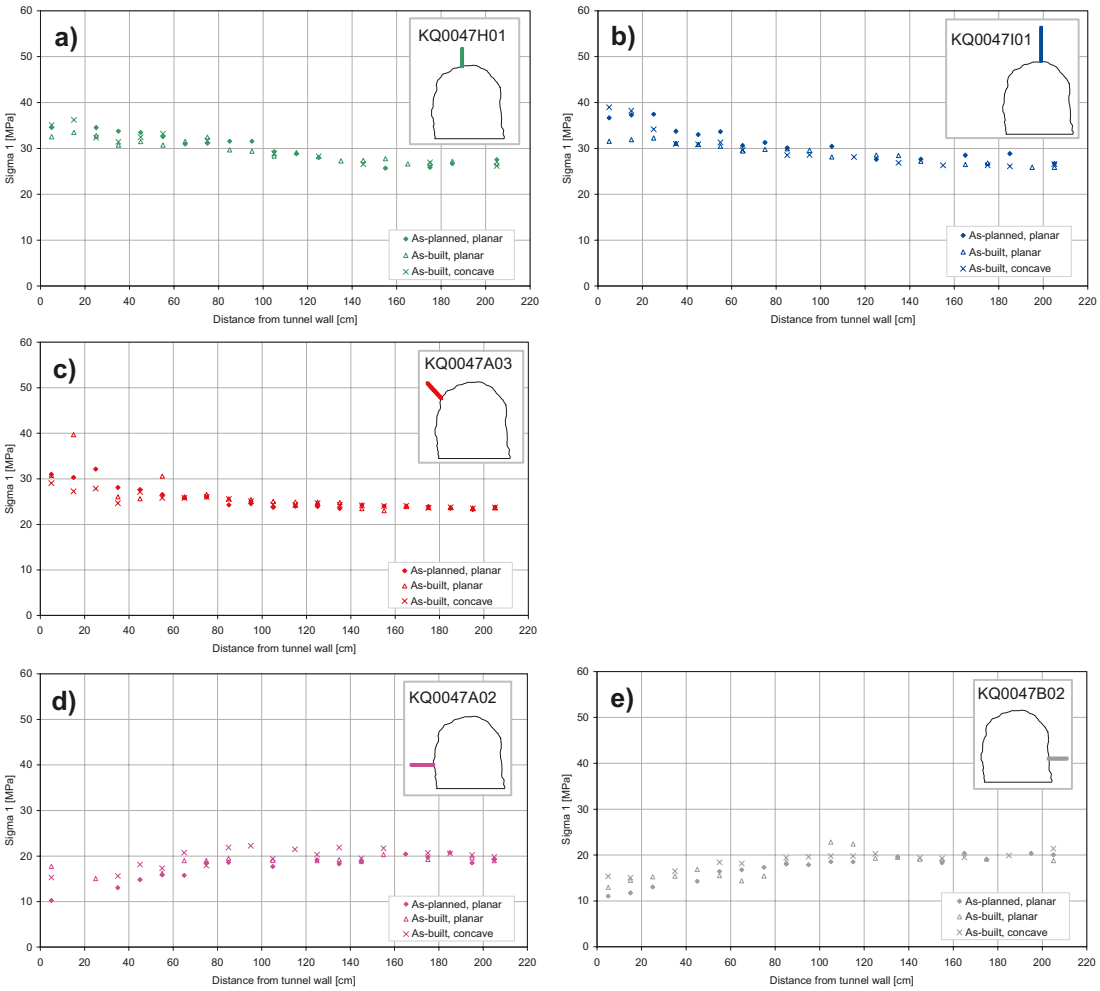

Figure 9-8. *Plots of* ***major principal stress*** *scanlines showing the difference between the model with* ***as-planned*** *tunnel shape with planar blasting round faces, the model with* ***as-built*** *tunnel shape with* ***planar*** *blasting round faces and the model with* ***as-built*** *tunnel shape with* ***concave*** *blasting round faces at cross section 048.7 (convergence pins location) in the TASQ tunnel when the heading of section 049 was excavated. The scanlines are approximately at the same place in the tunnel as the boreholes in the BGR section (E = 65 GPa, sigma 1 = 25 MPa, see Appendix K).*

The main conclusions from the 3DEC calibration back-analysis are:

- The lateral convergence is best fitted with a rock mass Young's modulus of 65 GPa and a magnitude of σ_1 of 25 MPa (see Figure 9-7).
- The range of σ_1 orientation considered in the calibration (± 6°) has little effect on the convergence for every simulated case (see Appendix J).
- Some of the convergence measurements between different combinations of measurement pins are better fitted with rock mass Young's modulus of 70 GPa (see Appendix J). This may be due to the poor consideration of heterogeneity in rock type in the model (the model considers a homogeneous linear elastic rock mass while it is well known that the rock mass around the APSE tunnel is heterogeneous).
- The difference in convergence, when using a rock mass Young's modulus of 65 GPa and σ_1 = 25 MPa, between a model with as-built tunnel shape with concave blasting round faces and a model with as-built tunnel shape with planar blasting round faces (maximum difference is 0.099 mm, average difference is 0.032 mm) is in general smaller than the difference between a model with as-built tunnel shape with concave blasting round faces and a model with as-planned tunnel shape with planar blasting round faces (maximum difference is 0.193 mm, average difference is 0.074 mm) (see Figure 9-7 and Appendix J).

- The same type of observation can be concluded from the case with a rock mass Young's modulus of 45 GPa and σ_1 = 30 MPa, however, the rock mass being softer in this case, the differences are slightly larger than in the case with Young's modulus 65 GPa. The difference in convergence between a model with as-built tunnel shape with concave blasting round faces and a model with as-built tunnel shape with planar blasting round faces (maximum difference is 0.111 mm, average difference is 0.037 mm) is in general smaller than the difference between a model with as-built tunnel shape with concave blasting round faces and a model with as-planned tunnel shape with planar blasting round faces (maximum difference is 0.195 mm, average difference is 0.077 mm) (see Figure 9-7 and Appendix J).

9.3 Sensitivity analysis

To be able to run a fair number of cases combining the different rock mechanics aspects of interest and, at the same time, avoiding excessive computational time, the excavation of the tunnel for the sensitivity studies was performed at once. In this manner, only the state after the whole excavation of the TASQ-tunnel had taken place was compared for each case.

There were two parts on the sensitivity analysis: sensitivity to the tunnel shape, the elastic behaviour of the rock mass and the in-situ stress without fractures, and sensitivity to the presence of major fractures in the model.

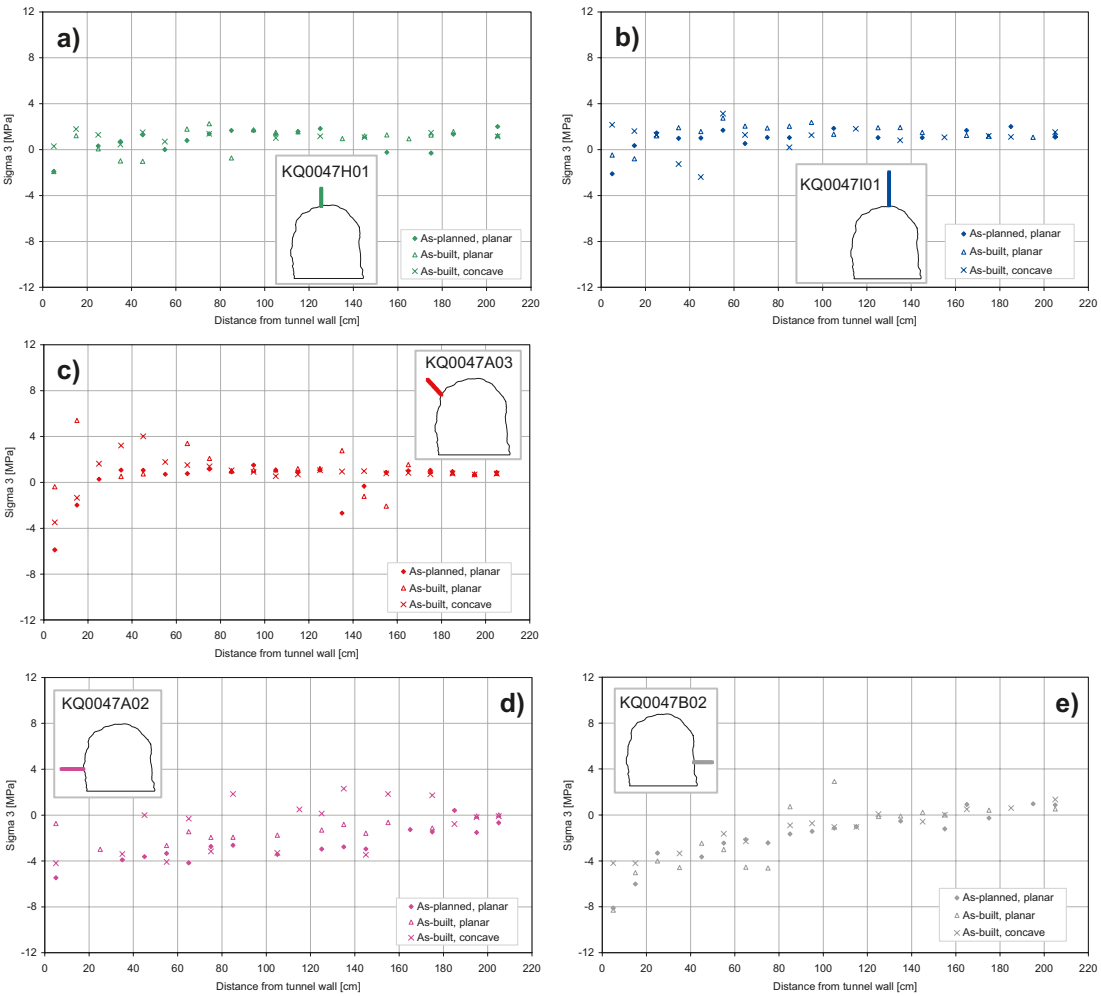

Figure 9-9. *D:o for* ***minor principal stress*** *(see Figure 9-8).*

9.3.1 Sensitivity analysis without fractures (rock mass behavior, in-situ stress and tunnel shape)

The objective of this sensitivity analysis was to assess the influence on the stress redistribution around the tunnel of the following factors:

- Rock mass Young's modulus.
- Magnitude of the major principal stress (Sigma 1).
- Orientation of the major and minor horizontal stresses (Sigma 1 and Sigma 3 respectively).
- The shape of the tunnel: as-planned vs. as-built.

As mentioned previously, only the final stage after the excavation has taken place has been used to compare the different cases analysed. The influence of the factors considered in this analysis was compared with regards to the maximum compressive stress and the principal stress redistribution plots after excavation. Major principal stress scan-lines at different locations have also been compared between different cases. The different cases analysed and their properties are shown in Table 9-7.

An analysis of the influence of the shape of the tunnel cross section on the major principal stress was performed by /Lönnqvist 2008/ (see Appendix N). For this study major principal stress on vertical scan-lines starting at the floor of the tunnel and extending about 6 m downwards were compared between two 3DEC models (one with as-planned tunnel shape and the other one with as-built tunnel shape) and corresponding Code Bright results at different tunnel segments. The results showed that the influence of the irregular shape of the tunnel on the major principal stress is very minor after a depth of 1 m under the floor of the tunnel (see Figure 9-10).

Table 9-8 summarizes the difference in maximum compressive stress in the first meter around the tunnel wall caused by different parameter ranges used in the sensitivity analysis.

Table 9-7. Rock mass properties and Sigma 1 magnitude and trend for each of the cases for the sensitivity analysis without fractures.

Tunnel shape	Blasting round face shape	Young's modulus (GPa)	Trend of σ_1 (deg)	Magnitude of σ_1 (MPa)
As-planned	Plane	45	316	30
As-planned	Plane	55	310	25
As-planned	Plane	55	310	30
As-planned	Plane	55	316	30
As-planned	Plane	55	322	30
As-planned	Plane	65	310	25
As-built	Plane	45	316	30
As-built	Plane	50	310	25
As-built	Plane	50	310	30
As-built	Plane	50	316	25
As-built	Plane	50	316	30
As-built	Plane	50	322	25
As-built	Plane	50	322	30
As-built	Plane	55	310	25
As-built	Plane	55	310	30
As-built	Plane	55	316	25
As-built	Plane	55	316	30
As-built	Plane	55	322	25
As-built	Plane	55	322	30
As-built	Plane	65	310	25
As-built	Plane	65	310	30
As-built	Plane	65	316	25
As-built	Plane	65	316	30
As-built	Plane	65	322	25
As-built	Plane	65	322	30

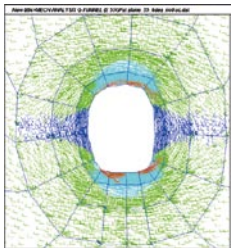

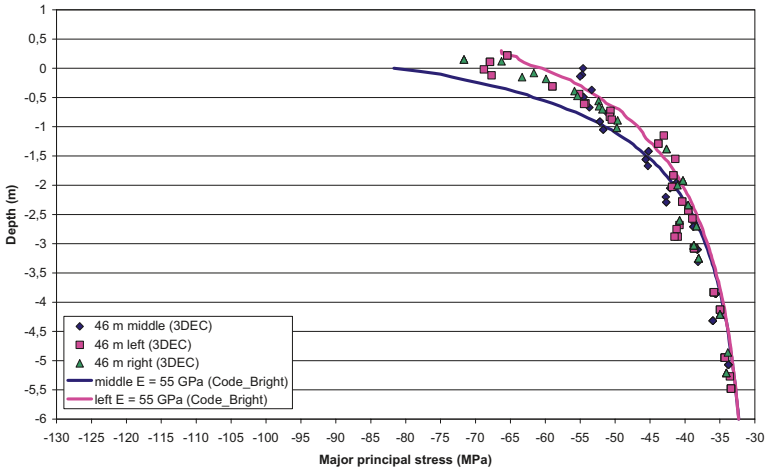

As-built tunnel shape in section 046 – Maximum compressive stress = 126.8 MPa

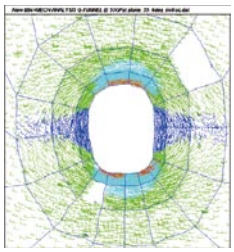

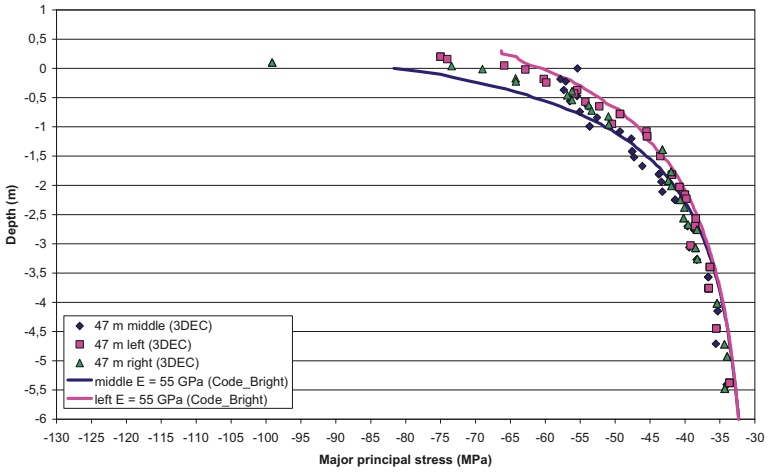

As-built tunnel shape in section 047 – Maximum compressive stress = 100.6 MPa

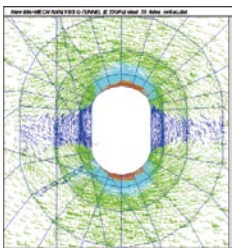

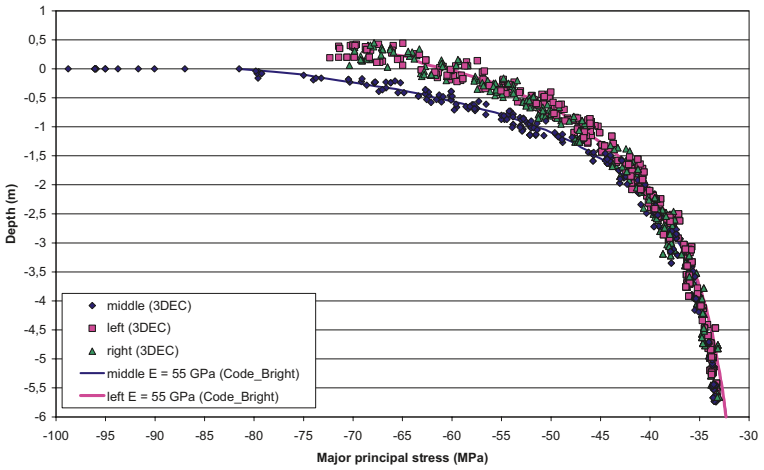

As-planned tunnel shape – Maximum compressive stress = 101.0 MPa

Figure 9-10. *Major principal stress along vertical scan lines in the floor of the tunnel segments 46 and 47 in the TASQ-tunnel with as-built shape compared with those from a model with the ideal (as-planned) tunnel shape /Lönnqvist 2008/ (see Appendix N).*

Table 9-8. Difference in maximum compressive stress in sections 046 to 055 of the TASQ-tunnel caused by different parameter ranges.

Parameter	Changes	Difference in max compressive stress (MPa) [1]
Young's modulus	45, 50, 55, 65 GPa	0 → 1.1
Magnitude of σ_1	25, 30 MPa	15 → 25
Trend of σ_1	310°, 316°, 322°	0.3 → 1.5
Fractures	With, without	1 → 95 [2]
Tunnel shape	As-planned, as-built	1 → 29

[1] This applies only to the first meter around the tunnel wall.

[2] This range varies significantly from section to section along the tunnel as the effect of the fractures is very local (see Figure 9-13 and Figure 9-14). These values range from 1 to 107 MPa if the results from the softest and weakest fracture properties are considered.

The main conclusions from the sensitivity analysis (without fractures) are:

- The magnitude of the maximum compressive stress close to the wall of the tunnel is always equal or smaller for the simulations of the as-planned tunnel than for the as-built ones (see Figure 9-10 and Appendix E).
- The influence of the shape of the tunnel on the stress redistribution is relevant in the first meter around the tunnel surface, beyond that it is negligible (see Figure 9-13). Close to the tunnel wall, the difference between the maximum compressive stresses considering as-planned or as-built tunnel shape ranges from 1 MPa to 29 MPa for different tunnel sections (see Table 9-8).
- The effect of the rock mass Young's modulus on the stress field redistribution after excavation of the tunnel within the ranges considered (45 GPa to 65 GPa) is negligible (see Table 9-8 and Figure 9-11).
- Considering a magnitude of maximum principal in-situ stress (sigma 1) of 25 MPa or 30 MPa causes a difference in the maximum compressive stress close to the tunnel walls ranging between 15 MPa to 25 MPa (see Table 9-8, Appendix C and Appendix D).
- The influence of the orientation of the maximum principal stress relative to the tunnel axis (see Figure 9-5) can be considered negligible regarding stress redistribution after excavation of the tunnel. The difference in the maximum compressive stress close to the tunnel walls caused by considering a ± 6° range in major principal stress orientation is between 0.3 MPa and 1.5 MPa (see Table 9-8 Appendix C and Appendix D).

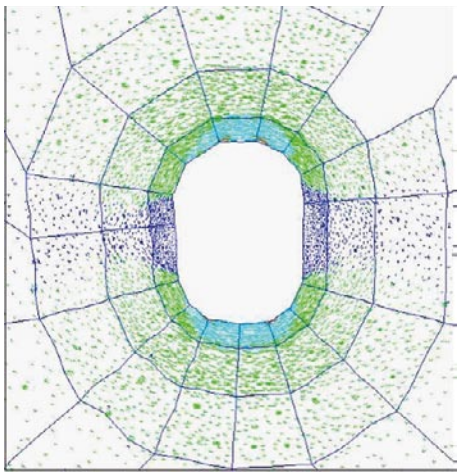

a) E=55GPa, σ_1=310°, σ_1=25MPa
Max compressive stress = 82.0 MPa

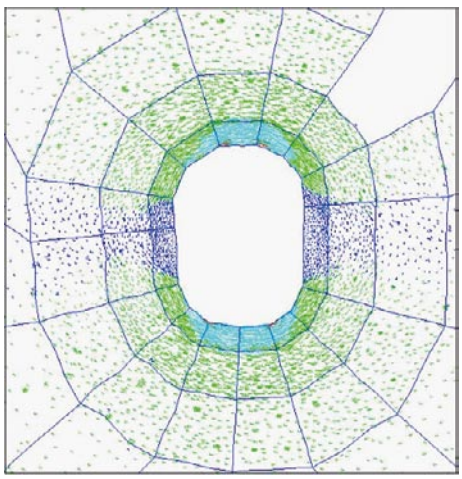

b) E=65GPa, σ_1=310°, σ_1=25MPa
Max compressive stress = 81.5 MPa

Figure 9-11. *Cross section plots showing the projection of the principal stress tensor (colour by magnitude of Sigma 1) at tunnel section 049. Note that there is almost no difference in stress redistribution when using a Young's modulus of 55 GPa or 65 GPa.*

9.3.2 Sensitivity analysis with fractures (fracture behavior)

In order to judge the importance of considering the major fractures and shear zones explicitly in the 3DEC model, a sensitivity analysis was conducted. In this sensitivity analysis the shape of the tunnel was as-planned (ideal) and it was excavated at once. Therefore, only the final state of equilibrium after excavation has been compared.

As previously mentioned the main fractures included in the model represent the major fractures and shear zones according to the geological model of the APSE tunnel (Chapter 8) and are listed in Table 9-2. The base-line case and the different ranges of properties used in the simulations are shown in Table 9-3 to Table 9-5. A pore pressure according to the hydrostatic gradient was considered in the fractures (4.5 MPa in the middle of the model).

The rock mass properties and sigma 1 trend and magnitude used for each of the cases for the sensitivity analysis with fractures are shown in Table 9-9.

The main conclusions from the sensitivity analysis on the influence of the major fractures are:

- The difference between the maximum compressive stress after excavation close to the tunnel walls in discontinuum models (with the major fractures explicitly included) and continuum models (without fractures) ranges from 1 MPa to 95 MPa, nonetheless this difference is very local (see Table 9-8). The difference depends strongly on the stiffness of the fractures (see Figure 9-13 to Figure 9-15, Appendix F and Appendix H) as well as on the distance between the fractures and the tunnel walls and the relative orientation between the fractures and the tunnel axis and between each of the fractures. Therefore the influence of the fractures varies strongly from one section of the tunnel to another (see Figure 9-17b and Figure 9-18b).
- The maximum fracture shear displacement and normal displacement (occurring in the NE trending fractures) vary strongly at each section of the tunnel depending also on the relative orientation between the fractures and the tunnel axis and between each of the fractures (see Figure 9-16 to Figure 9-18).
- The effect on the maximum compressive stress and fracture maximum shear displacement of increasing the fracture stiffness from (kn, ks) = (1,000 GPa/m, 500 GPa/m) to (kn, ks) = (2,000 GPa/m, 1,000 GPa/m) is almost negligible, the most of the effect takes place when the fracture stiffnesses are increased from (kn, ks) = (200 GPa/m, 100 GPa/m) to (kn, ks) = (1,000 GPa/m, 500 GPa/m) (see Figure 9-15 and Figure 9-16).
- The effect of fracture friction angle on the maximum compressive stress is negligible (see Figure 9-13 to Figure 9-15, Appendix F and Appendix H). However, the effect of fracture friction angle on the maximum fracture shear displacement is noticeable when comparing soft fracture cases (baseline, weak and strong) and negligible for the rest of the cases (see Figure 9-16 and Table 9-3 to Table 9-5).
- When considering the shear zone (TASQ_SZ) to be strong (high friction angle) while keeping all the other fractures in the model with baseline case properties, has minor effect on the magnitude of the principal stresses and the shear displacements (Figure 9-15, Figure 9-16, Figure 9-19 and Appendix G). However, when the shear zone is considered to behave elastically, the shear displacements become similar to those observed when using stiffer fractures (all fractures) and the stress has a different pattern than in any other case (Figure 9-15, Figure 9-16 and Figure 9-19).
- The effect of rock mass Young's modulus is relevant on the fracture shear displacement but almost negligible on the redistribution of the stress field. Considering stiff fractures with 65 GPa intact rock Young's modulus, the shear displacement is 15% smaller than with 55 GPa intact rock Young's modulus (see Figure 9-15 and Figure 9-16).
- The effect of explicitly considering the fractures in the model on tunnel wall displacements depends strongly on the tunnel section (relative orientation between fractures and tunnel axis) and fracture properties used (see Figure 9-17 and Figure 9-18).
- Figure 9-20 and Figure 9-21 show major and minor principal stress scanlines from different locations at the wall of tunnel section 047 (BGR section). The scanlines are located approximately where the boreholes for the ultrasonic measurements were drilled (see Figure 9-12 with the borehole locations). It can be seen that the maximum differences induced by the presence of fractures

on the major and minor principal stress take place along boreholes KQ0047A02 (Figure 9-20d and Figure 9-21d) and KQ0047A01 (Figure 9-20f and Figure 9-21f). There is also noticeable difference induced by the fractures along boreholes KQ0047G01 (Figure 9-20h and Figure 9-21h). The influence of the fractures is almost negligible along the rest of the scanlines. It is important to notice the high compressive and tensile stresses induced by the presence of the fractures in boreholes KQ0047A02 (Figure 9-20d and Figure 9-21d) and KQ0047A01 (Figure 9-20f and Figure 9-21f). The heterogeneous stress redistribution caused by the presence of pre-existing fractures in the left side of the TASQ tunnel (section 047) in combination with the blasting wave makes this area more vulnerable to further local fracturing and increase in EDZ.

Figure 9-12 shows the location of the boreholes drilled in section 047 of the TASQ tunnel used to make ultrasonic measurements to characterize the EDZ. The same location has been used in the 3DEC and UDEC models (section 9.4) to compare principal stress scanlines for different simulation cases.

The values of the maximum fracture shear and normal displacement and maximum compressive stress shown in the following figures are local and should only be used as a means for relative comparison between models. These maximum values are a consequence of the relative orientation between fractures and tunnel axis and between each of the fractures, as well as the behaviour of each particular fracture (see Table 9-3 to Table 9-5).

Table 9-9. Rock mass properties and Sigma 1 magnitude and trend for each of the cases for the sensitivity analysis with fractures.

Tunnel shape	Blasting round face shape	Fracture type[1)]	Young's modulus (GPa)	Trend of σ_1 (deg)	Magnitude of σ_1 (MPa)
As-planned	Plane	baseline case	55	310	30
As-planned	Plane	Weak	55	310	30
As-planned	Plane	Strong	55	310	30
As-planned	Plane	Stiff	55	310	30
As-planned	Plane	stiff and weak	55	310	30
As-planned	Plane	stiff and strong	55	310	30
As-planned	Plane	Stiffer	55	310	30
As-planned	Plane	stiffer and weak	55	310	30
As-planned	Plane	elastic TASQ_SZ	55	310	30
As-planned	Plane	strong TASQ_SZ	55	310	30
As-planned	Plane	Stiff	65	310	30
As-planned	Plane	Stiff	65	310	25

[1)] See Table 9-3 to Table 9-5 for fracture properties.

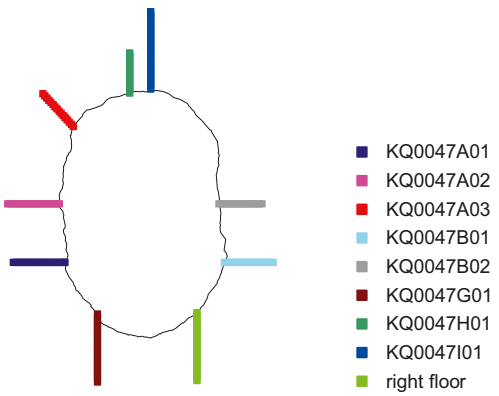

Figure 9-12. *Schematic picture showing section 047 of the TASQ tunnel using the finest resolution laser-scanning data; the locations of the boreholes for the ultrasonic measurements performed by BGR are outlined in the figure. The borehole in the right side of the floor didn't exist in the actual tunnel. It is used in the numerical analysis for comparison purposes.*

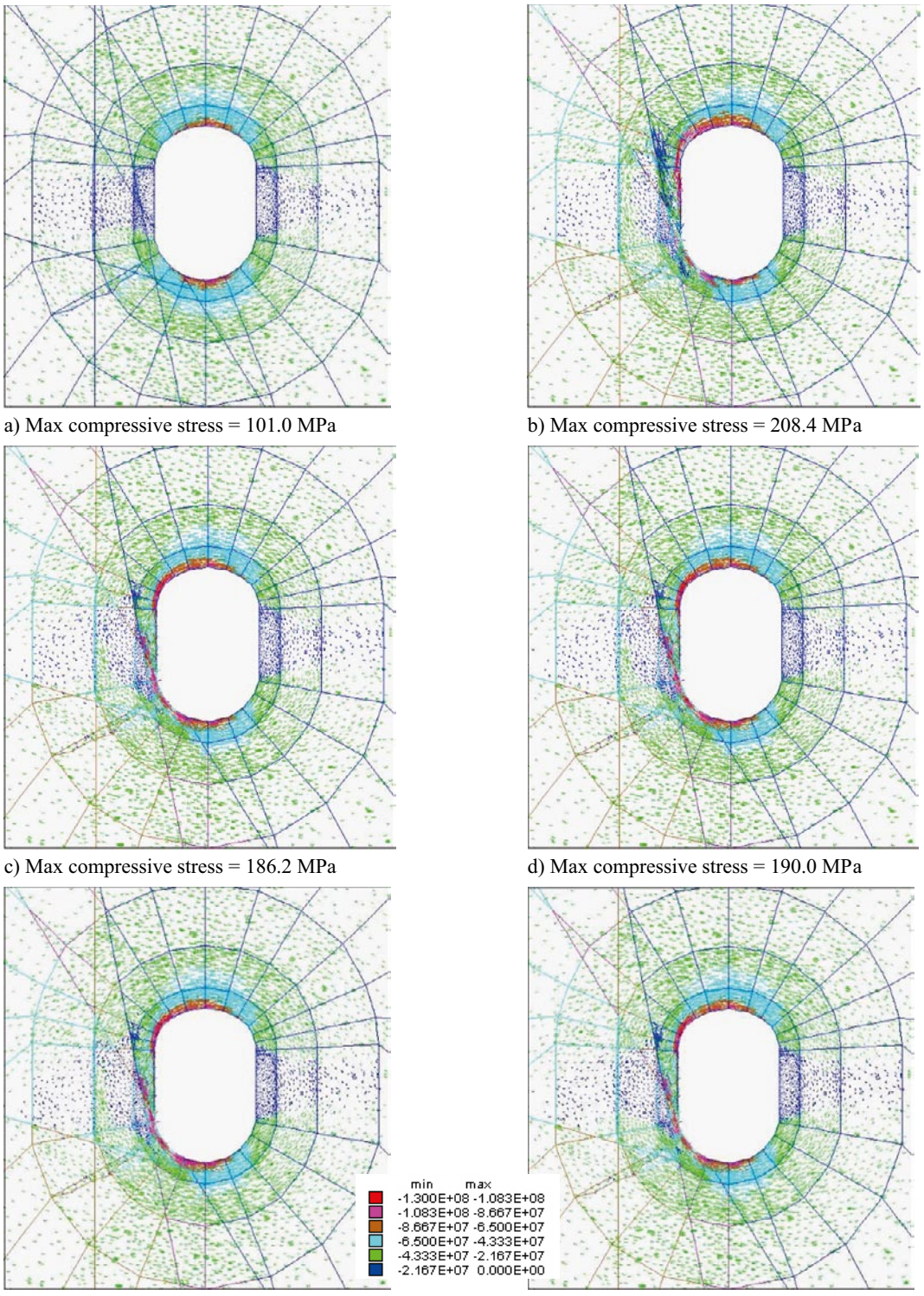

a) Max compressive stress = 101.0 MPa

b) Max compressive stress = 208.4 MPa

c) Max compressive stress = 186.2 MPa

d) Max compressive stress = 190.0 MPa

e) Max compressive stress = 188.4 MPa

f) Max compressive stress = 183.9 MPa

Figure 9-13. *Cross section plots showing the projection of the principal stress tensor (colour by magnitude of Sigma1) at section 046 in the TASQ tunnel for a) baseline case with no fractures, b) baseline case including fractures, c) stiff fractures (E=55GPa, σ_1=30MPa), d) stiff fractures (E=65GPa, σ_1=25MPa), e) stiff and weak fractures and f) stiff and strong fractures. See Table 9-3 to Table 9-5 for fracture properties and Appendix F for results from other cases.*

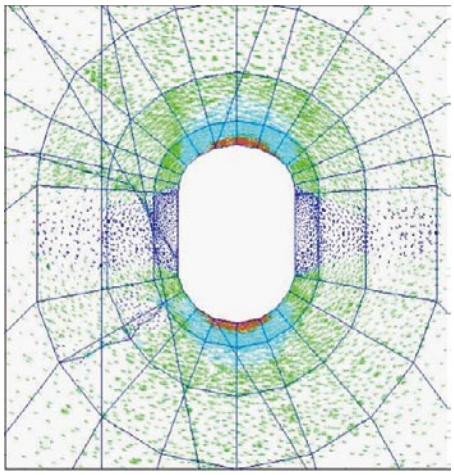

a) Max compressive stress = 98.8 MPa

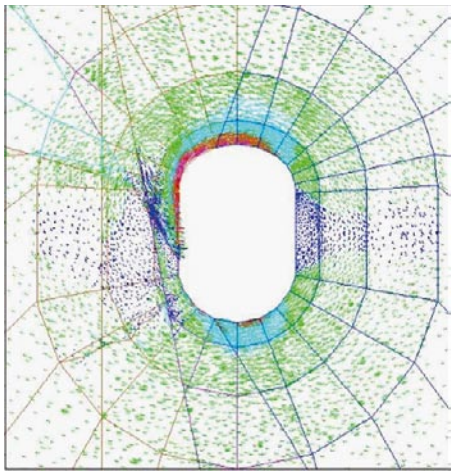

b) Max compressive stress = 145.7 MPa

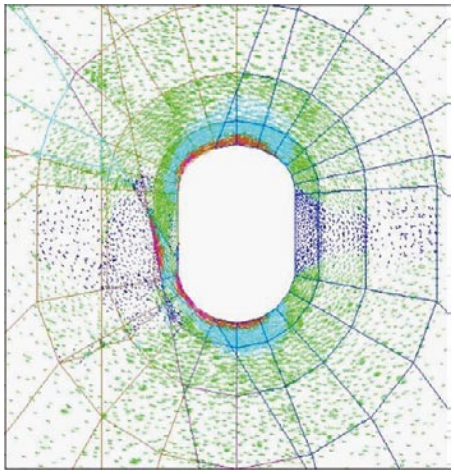

c) Max compressive stress = 120.9 MPa

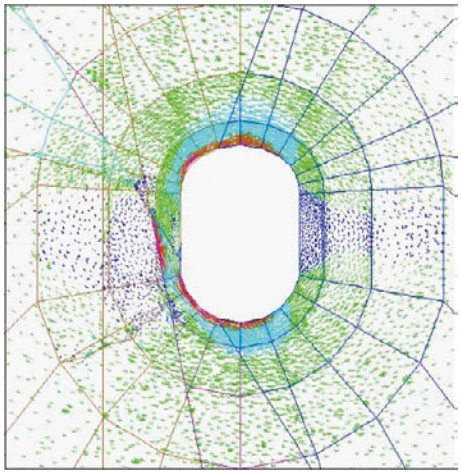

d) Max compressive stress = 122.7 MPa

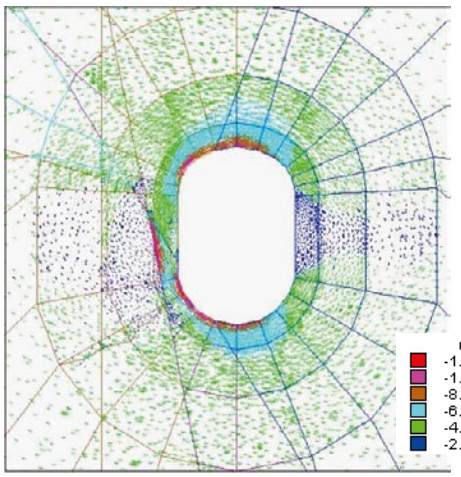

e) Max compressive stress = 121.2 MPa

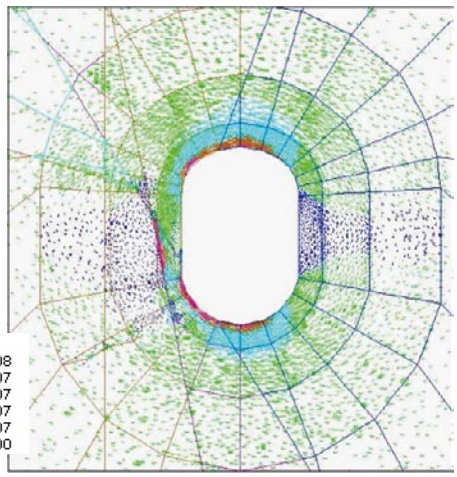

f) Max compressive stress = 121.5 MPa

Figure 9-14. *Cross section plots showing the projection of the principal stress tensor (colour by magnitude of Sigma1) at section 047 in the TASQ tunnel for a) base line case with no fractures, b) base line case including fractures, c) stiff fractures (E=55 GPa, σ_1=30MPa), d) stiff fractures (E=65GPa, σ_1=25MPa), e) stiff and weak fractures and f) stiff and strong fractures. See Table 9-3 to Table 9-5 for fracture properties and Appendix F for results from other cases.*

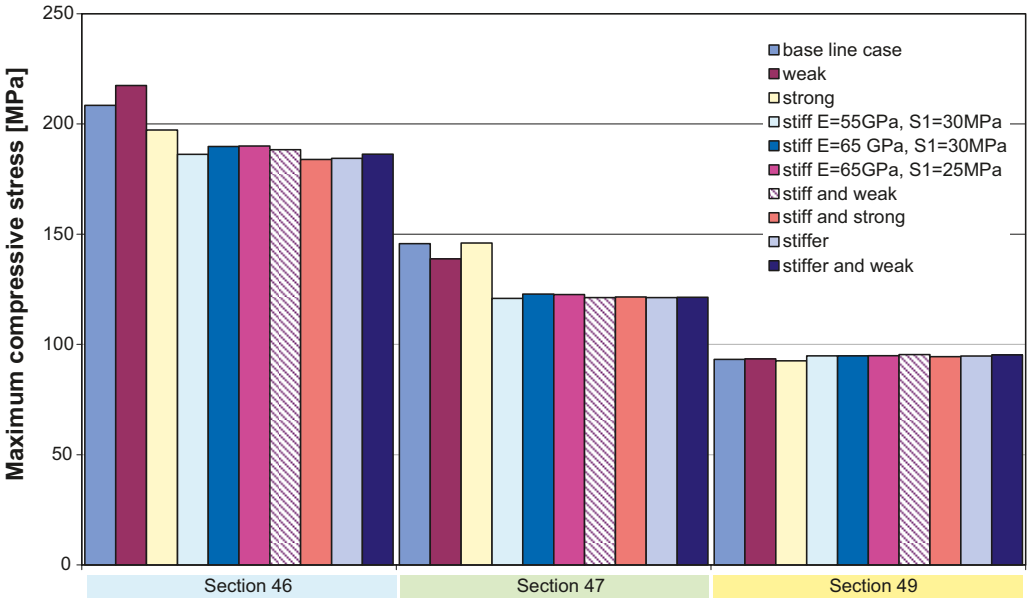

Figure 9-15. *Histogram showing the values of maximum* ***compressive stress*** *(MPa) for different fracture property cases for section 046, 047 and 049.*

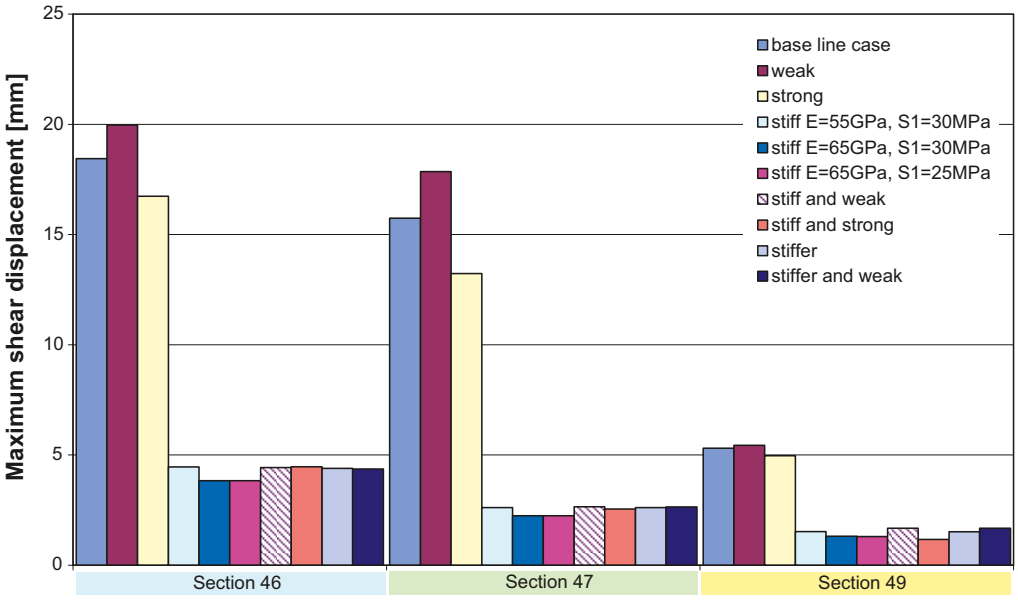

Figure 9-16. *Histogram showing the maximum* ***shear displacement*** *(mm) for different fracture property cases for section 046, 047 and 049.*

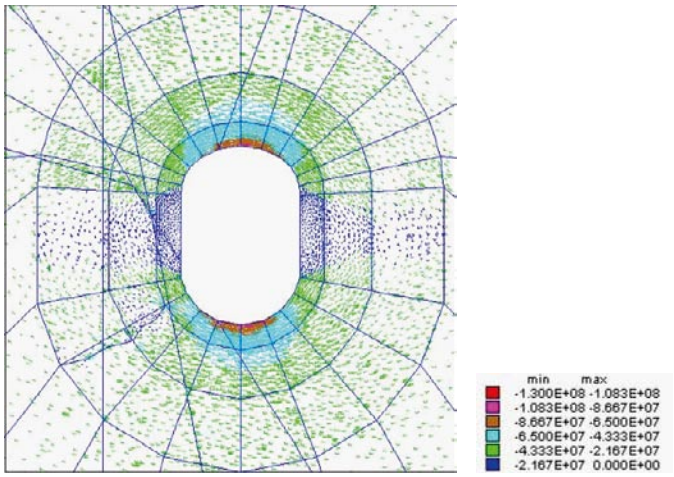

a) Maximum compressive stress = 98.8 MPa

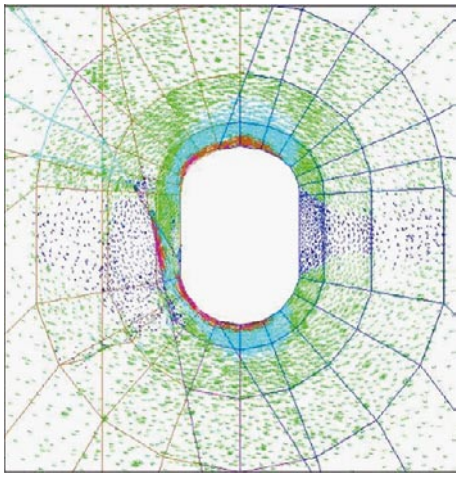

b) Maximum compressive stress = 122.7 MPa

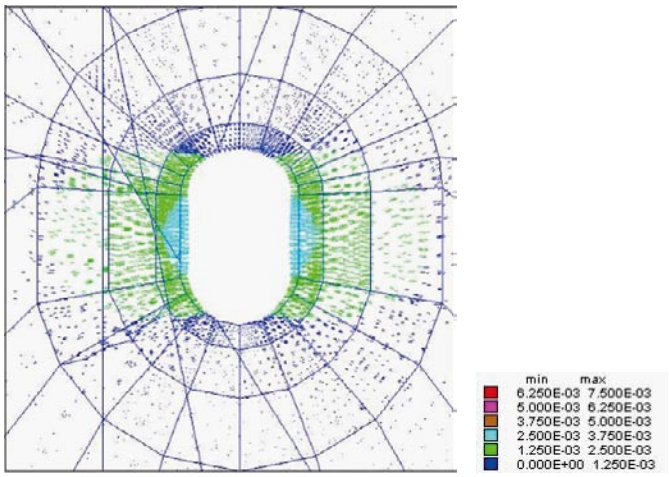

c) Maximum displacement = 2.9mm

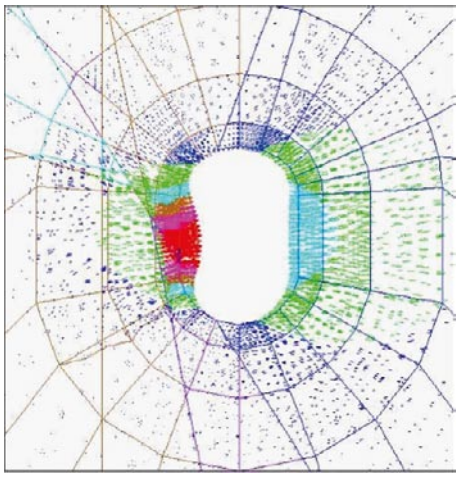

d) Maximum displacement = 7.5 mm

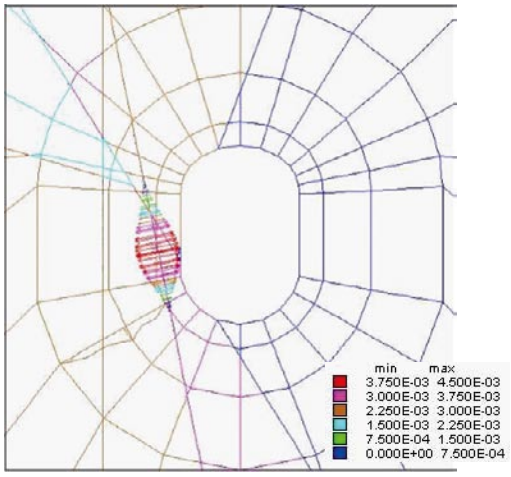

e) Max fracture normal disp. = 4. 4 mm

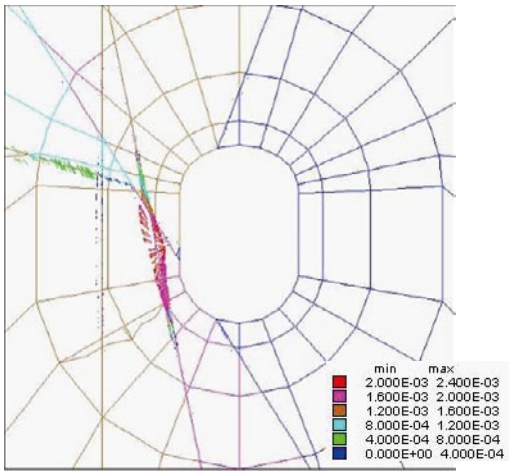

f) Max fracture shear disp. = 2.2 mm

Figure 9-17. *Cross-section plots of the as-planned tunnel shape (E = 65GPa, σ_1 = 25MPa, σ_1 trend = 310°) at the BGR section at* ***section 047*** *a) stress tensor plot (colour by magnitude of Sigma 1), without fractures, b) d:o, with stiff fractures, c) displacement vector plot without fractures, d) d:o with stiff fractures, e) normal displacement on fractures and f) shear displacement on fractures. See Table 9-3 to Table 9-5 for fracture properties.*

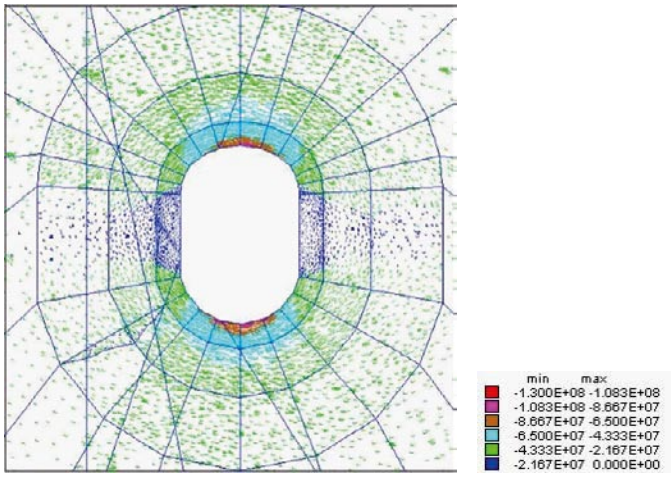

a) Maximum compressive stress = 99.2 MPa

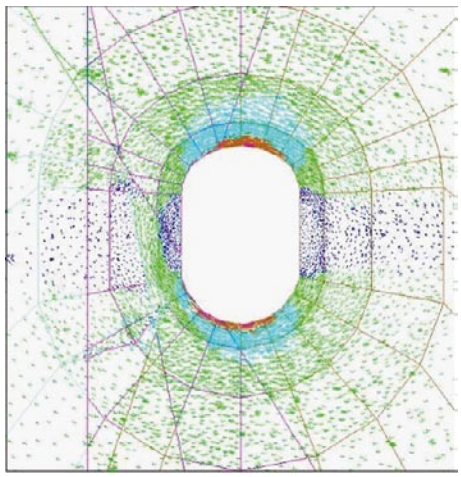

b) Maximum compressive stress = 94. 9 MPa

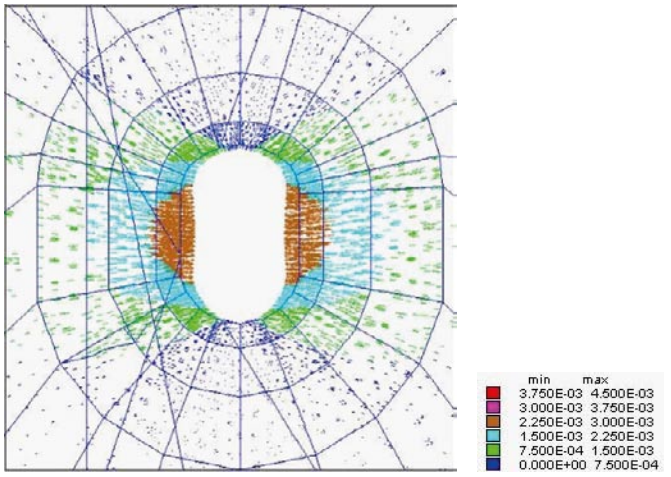

c) Maximum displacement = 2.9 mm

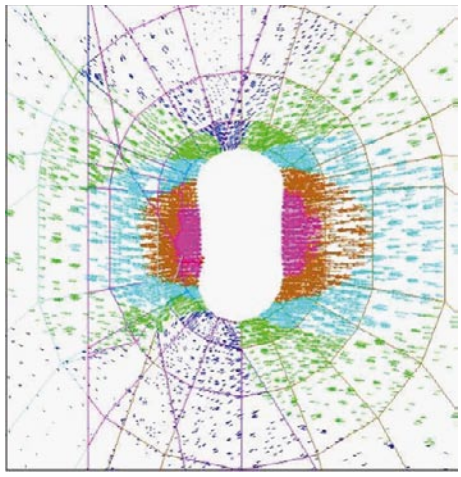

d) Maximum displacement = 4.0 mm

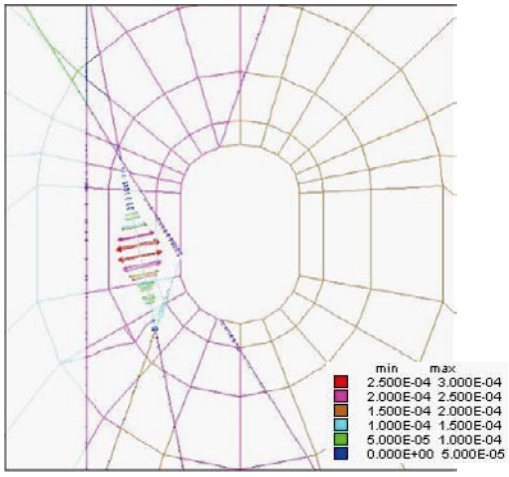

e) Max fracture normal disp. = 0.3 mm

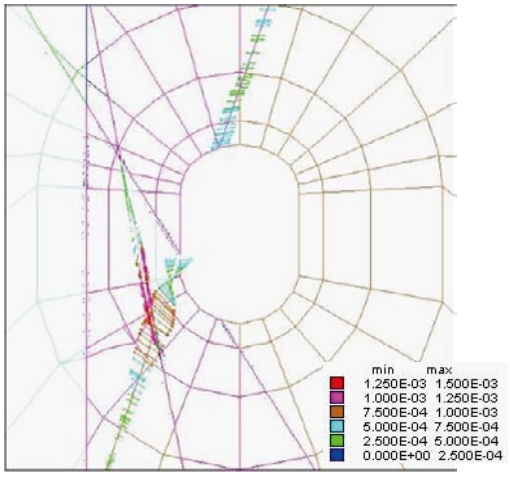

f) Max fracture shear disp. = 1.3 mm

Figure 9-18. *Cross-section plots of the as-planned tunnel shape (E = 65GPa, σ_1 = 25MPa, σ_1 trend = 310°) at* ***section 049****; a) stress tensor plot (colour by magnitude of Sigma 1), without fractures, b) d:o, with stiff fractures, c) displacement vector plot without fractures, d) d:o with stiff fractures e) normal displacement on fractures and f) shear displacement on fractures. See Table 9-3 to Table 9-5 for fracture properties.*

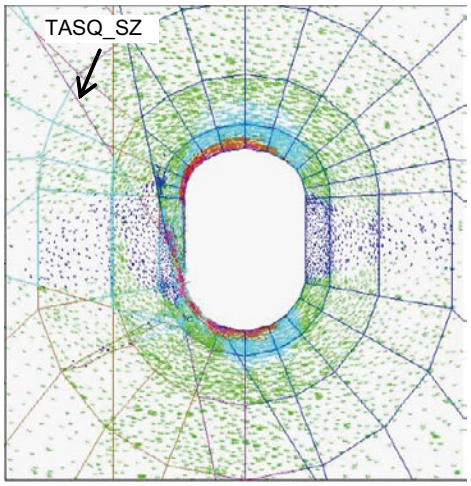

a) Elastic TASQ_SZ, section 046
Max compressive stress = 191.1MPa

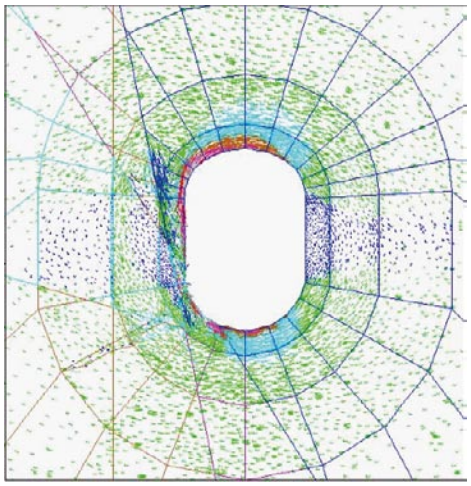

b) Strong TASQ_SZ, section 046
Max compressive stress = 206.7 MPa

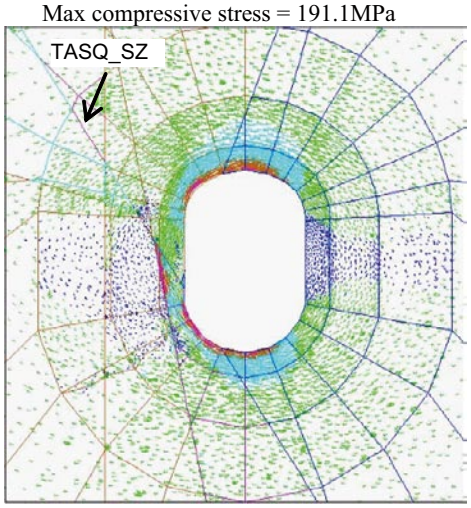

c) Elastic TASQ_SZ, section 047
Max compressive stress = 118.7 MPa

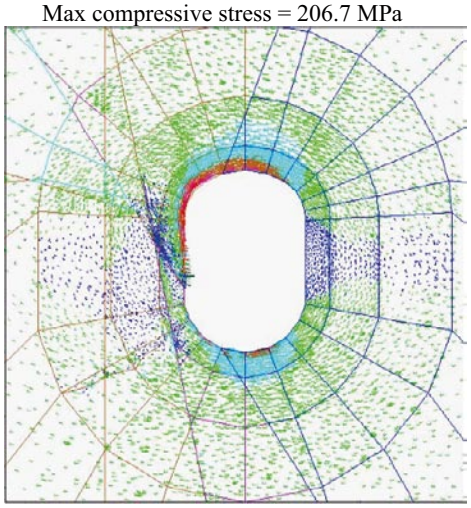

d) Strong TASQ_SZ, section 047
Max compressive stress = 147.2 MPa

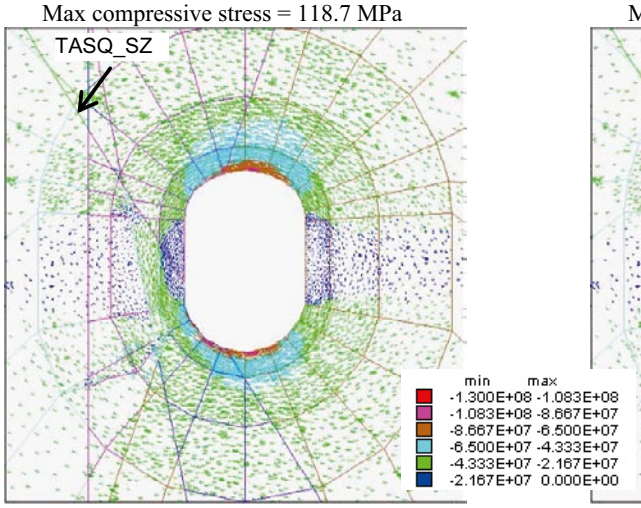

e) Elastic TASQ_SZ, section 049
Max compressive stress = 95.2 MPa

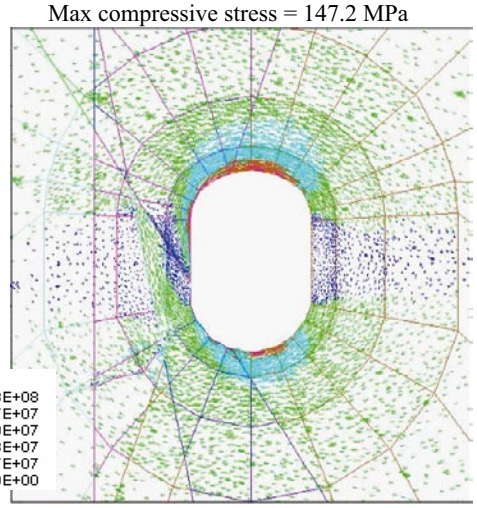

f) Strong TASQ_SZ, section 049
Max compressive stress = 92.3 MPa

Figure 9-19. *Cross section plots showing the effect that different properties for the shear zone,* ***TASQ_SZ****, (see Table 9-5) have on the stress redistribution around the tunnel (stress tensor, colour by magnitude of Sigma 1) at section 046 a) and b), section 047 c) and d) and section 049 e) and f). E = 55 GPa, σ1 = 30 MPa, σ1 =310° for both cases.*

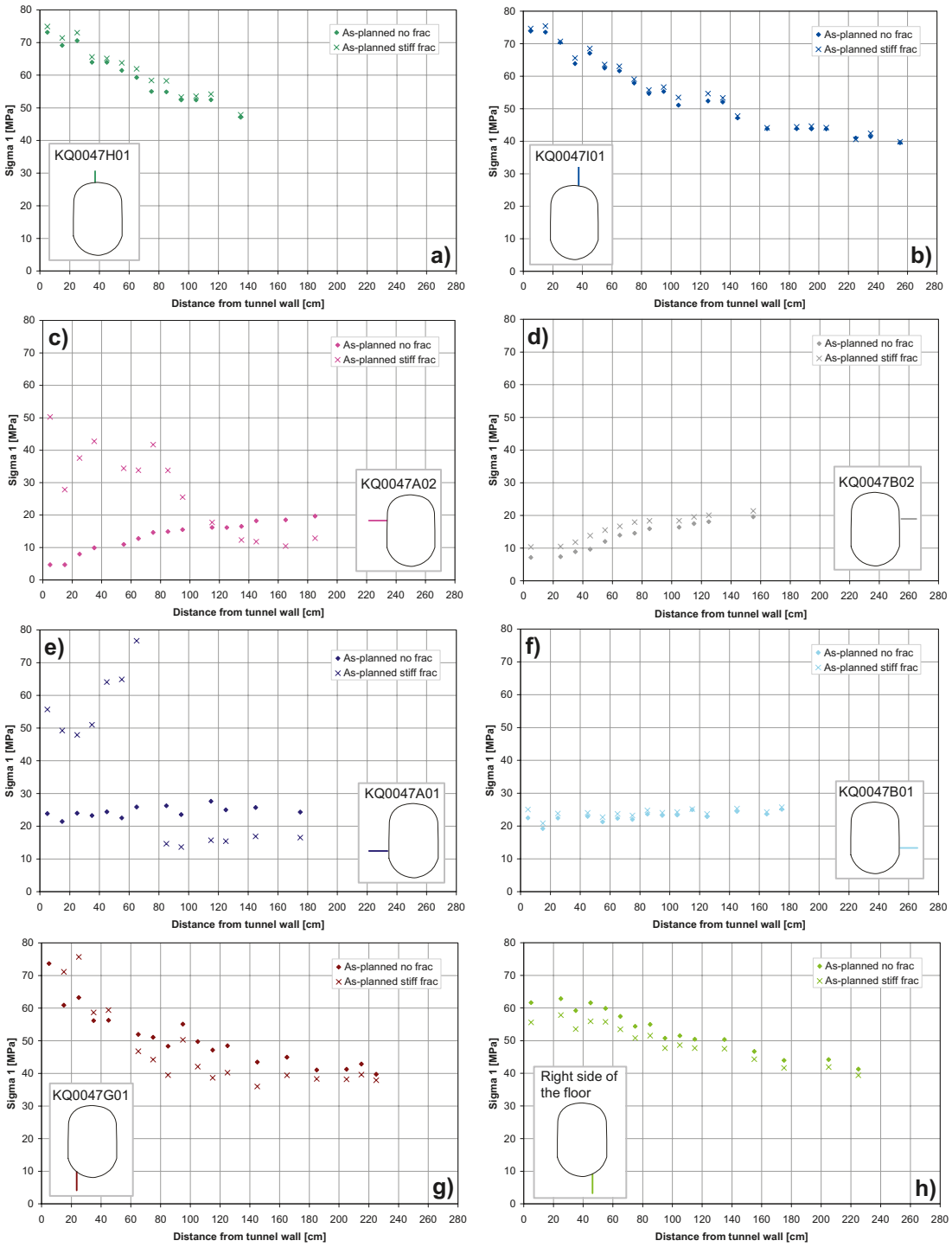

Figure 9-20. *Comparison between* ***major principal stress*** *along different scan lines from the wall of tunnel section 047 (BGR section) in the case the as-planned tunnel shape without fractures and the case with as-planned tunnel shape with stiff fractures (Rock mass E = 65 GPa, Sigma 1 = 25 MPa). For results from borehole KQ0047A03, see Appendix I.*

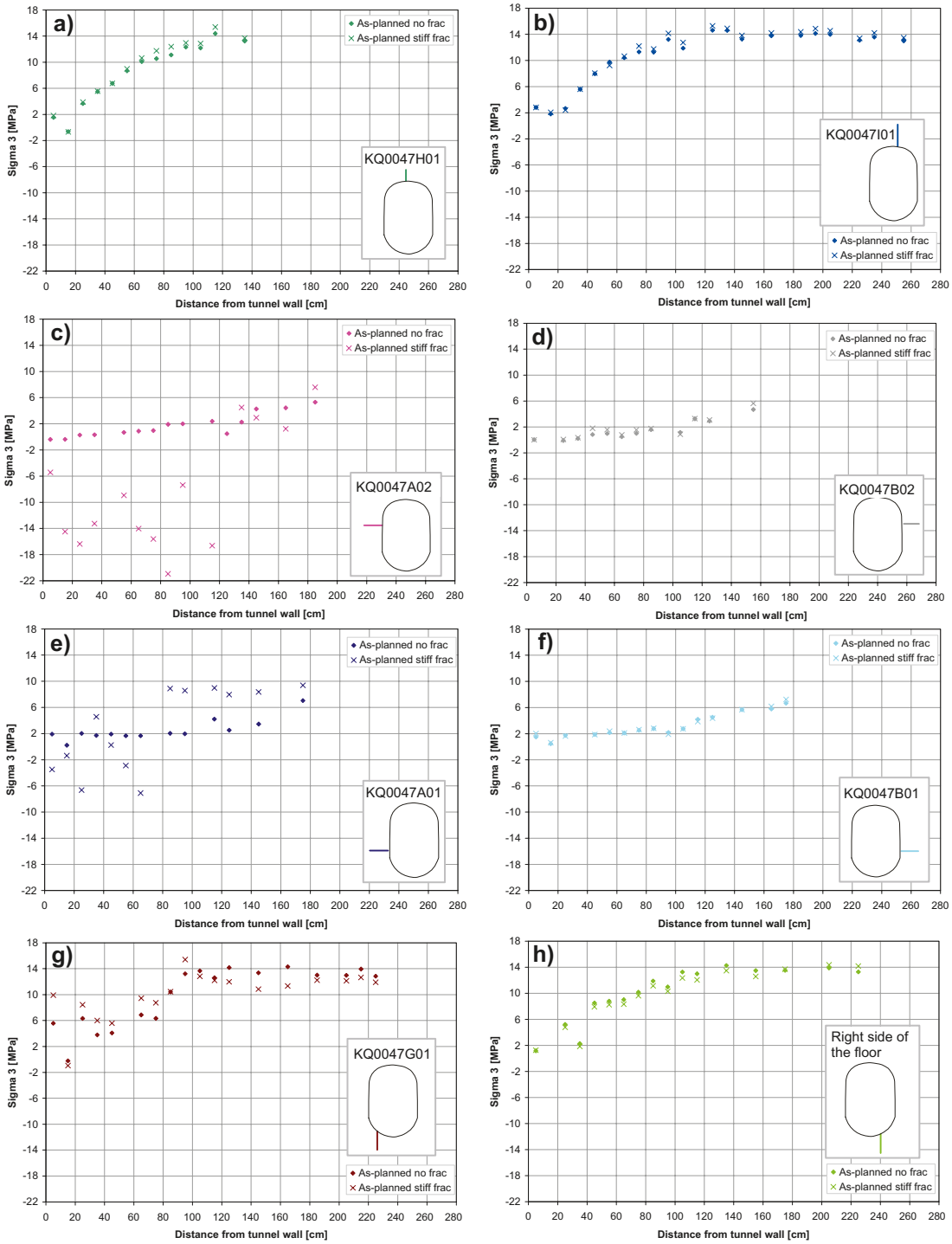

Figure 9-21. *Comparison between* ***minor principal stress*** *along different scanlines from the wall of tunnel section 047 (BGR section) in the case with as-planned tunnel shape without fractures and the case with as-planned tunnel shape with stiff fractures (Rock mass E=65GPa, Sigma 1 = 25 MPa). For results from borehole KQ0047A03, see Appendix I.*

9.4 Two dimensional analysis with UDEC

9.4.1 Model Geometry for UDEC

The three-dimensional laser-scanning model of the as-built TASQ tunnel had to be made coarser in order to be able to incorporate it in a three-dimensional 3DEC model. In this manner the point-cloud was triangulated into triangles of 0.2 m side-length (section 7.3.2). To be able to incorporate this coarser version of the tunnel as-built shape in a 3DEC model it had to be further smoothed. Although this smoothing process keeps the general shape of the as-built tunnel, it removes the small scale irregularities (roughness) on the tunnel walls (see Figure 9-22). In order to judge the influence of those irregularities in the stress redistribution around the tunnel, three two-dimensional vertical cross sections at three different locations along the as-built tunnel were modelled using UDEC /Itasca 2004/ (see Figure 9-22). Besides, an ideal model with the as-planned tunnel cross section was also modelled. The two-dimensional models could incorporate the highest resolution laser-scanned data (see Figure 9-23 and Figure 9-24).

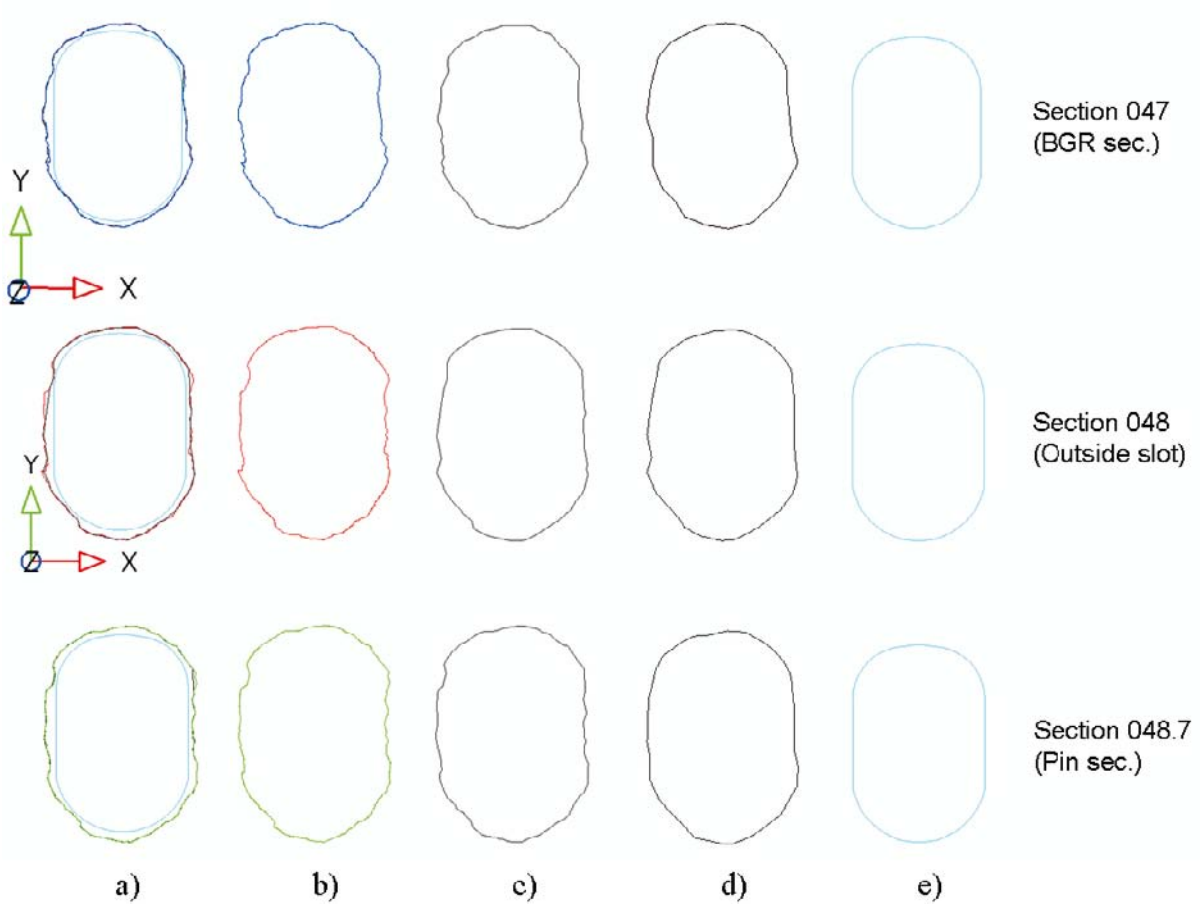

Figure 9-22. *UDEC tunnel geometry; a) a combination of the as-planned tunnel shape, the finer resolution laser-scanned shape and the coarser resolution laser-scanned shape, b) finer resolution laser-scanned tunnel shape used for the UDEC runs c) coarser resolution laser-scanned tunnel shape d) smoothed version of the coarser resolution laser-scanned tunnel shape used for the 3DEC runs and e) as-planned tunnel shape.*

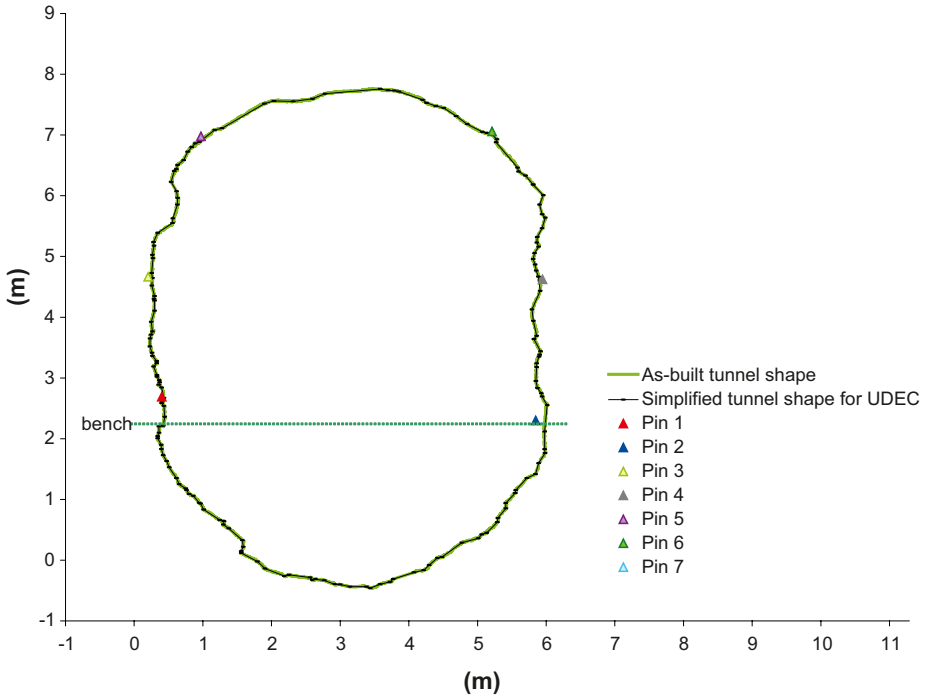

Figure 9-23. *Two-dimensional cross-section of the TASQ tunnel section 048.7, where the convergence pins were located. It is showing the best resolution laser-scanned tunnel shape, the simplification of the tunnel shape used in the UDEC model and the location of the convergence pins (1–7). The reason why pin 7 and pin 2 are not in the wall is probably due to the fact that the pins are not coplanar and they are projected in a 2D section.*

9.4.2 In-situ and boundary conditions for UDEC

The in-situ and boundary conditions considered in the 2D UDEC models are as follows:

- Based on the results from the 3D calibration of the convergence measurements, the in-situ stress tensor and the Young's modulus used in the best fit model case have been selected as in-situ stress and Young's modulus for the two dimensional UDEC models (Table 9-10). Additional 2D simulations have been performed with the lowest Young's modulus within the ranges considered for the calibration back-analysis.
- In the lateral boundaries, no displacement in the normal direction to their respective surfaces was allowed. They may move freely in the other directions (roller boundaries).
- In the lower boundary, no displacement in any direction was allowed.
- In the upper boundary, the vertical principal stress (σ_2) was applied as boundary condition.

Table 9-10. In-situ stress in UDEC models.

	Magnitude of stress (MPa)	Plunge (deg)	Trend (Äspö 96) (deg)
σ_1	25 [1], 30 [2]	0	316
σ_2	15	90	90

[1] According to best fit 3D calibration case with E = 65 GPa.

[2] Additional case with E = 45 GPa. Results reported in Appendix M.

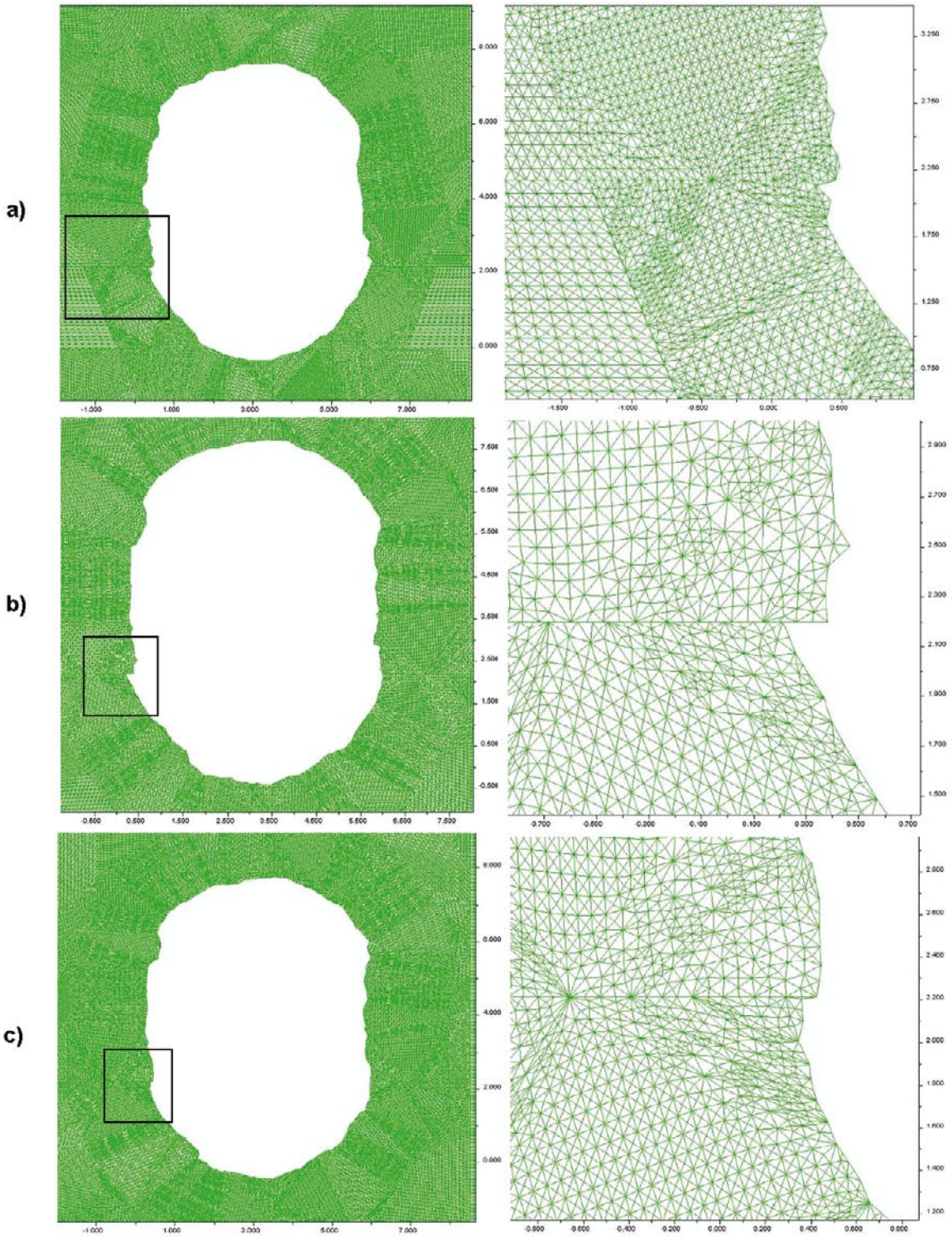

Figure 9-24. *Mesh in the UDEC models (0.1 m side length); a) BGR section (section 047) with a close-up b) section outside the slot (section 048) and c) convergence pins section (section 048.7).*

Two rock mass types were considered in the UDEC analysis; a soft case (Rock mass Young's modulus = 45 GPa) and the best fit case according to the three-dimensional calibration back-analysis in 3DEC (Rock mass Young's modulus = 65 GPa). For both of these cases three different as-built tunnel cross-sections were considered: section 047 (BGR measurements section), section 048 (outside the slot) and section 048.7 (convergence pins section). Besides, for both, soft case and best fit case, a simulation with the as-planned shape has been performed in order to judge the influence of the tunnel shape on the stress-redistribution after excavation. The excavation has been simulated in two stages: heading and bench. The rock mass properties and the in-situ stress orientation and magnitude for the simulation cases can be seen in Table 9-11.

The following discussion is based on the results from the models with rock mass Young's modulus = 65 GPa (best fit case to the convergence measurements). Similar conclusions can be achieved from the results from the simulations with Young's modulus = 45 GPa.

Principal stress scanlines have been obtained along the locations of the boreholes where the ultrasonic measurements were performed (see Figure 9-12) from all the four UDEC models: "section 047" (BGR), "section 048" (outside slot), "section 048.7" (convergence pins section) and the model with "ideal" (as-planned) tunnel geometry. The major principal stresses along the scanlines are shown after excavation of the heading and the bench in Figure 9-25 and Figure 9-26 respectively. The minor principal stress scanlines are shown in Appendix L. Some of the stress magnitudes in the as-built cross sections are significantly different from those of the as-planned cross section. This is due to the effect of the local irregularities in the tunnel wall surface. The influence of the different tunnel shape reaches at most 1 m into the tunnel wall.

Stress tensor plots showing the redistribution of the stress field after the excavation of the heading on section 047 (where BGR performed the ultrasonic measurements) are shown in Figure 9-27 to Figure 9-29. The UDEC results after excavation of the bench simulating the other tunnel sections are presented in Appendix M. The following conclusions can be drawn from this set of results:

As-planned tunnel shape

The results from the 2D simulation of the as-planned tunnel section as shown in Appendix M bring up the following observations:

- The maximum compressive stress occurs at both left and right corners of the floor when excavating the tunnel heading (Max. compressive stress at the floor 173.9 MPa and at the roof 65.5 MPa). When excavating the bench of the tunnel the maximum compressive stress is lower (Max. compressive stress at the floor 78.9 MPa and at the roof 71.3 MPa).
- The maximum tensile stress occurs also at both left and right corners of the floor when excavating the tunnel heading (Max. tensile stress at the floor 11.1 MPa and at the roof 1.5 MPa). When excavating the bench of the tunnel the maximum tensile stress is lower (Max. tensile stress at the floor 1.2 MPa and at the roof 1.6 MPa).

Table 9-11. Rock mass properties, in-situ stress magnitude and orientation for the UDEC simulations.

2D-sections	Young's modulus (GPa)	Poisson's ratio	Plunge σ_1/σ_2 (deg)	Trend (Äspö 96) σ_1/σ_2 (deg)	Magnitude of σ_1 (MPa)
BGR section (section 047)	45 [1)]	0.26	0/90	316/90	30
Outside slot section	45 [1)]	0.26	0/90	316/90	30
Convergence pins section	45 [1)]	0.26	0/90	316/90	30
Ideal tunnel shape section	45 [1)]	0.26	0/90	316/90	30
BGR section (section 047)	65	0.26	0/90	316/90	25
Outside slot section	65 [1)]	0.26	0/90	316/90	25
Convergence pins section	65 [1)]	0.26	0/90	316/90	25
Ideal tunnel shape section	65 [1)]	0.26	0/90	316/90	25

1) Most of the results from these simulations are reported in Appendix M.

As-built tunnel shape

The uneven nature of the tunnel contour (bumpiness) (see Figure 9-22 to Figure 9-24) generates zones of local stress release or stress concentration (convex or concave irregularities in the tunnel wall respectively) which could potentially initiate isolated local fracturing (Figure 9-27 to Figure 9-29).

Excavation of the tunnel heading

The stress tensor plots from section 047 (BGR ultrasonic measurements section) model results with rock mass Young's modulus = 65 GPa are shown in Figure 9-27 to Figure 9-29. The results from the other sections and with other rock mass properties can be found in Appendix M.

- The BGR tunnel section shows asymmetric stress redistribution in the tunnel walls. The maximum compressive stress is located at the lower left and right corners of the tunnel (163.4 MPa and 179.3 MPa respectively). The maximum tensile stress takes place at the same locations but it is more asymmetric (23.38 MPa and 6.54 MPa respectively) (see Figure 9-27 and Figure 9-28). The asymmetry is caused by the irregularities in the tunnel walls. "Bumpy" type irregularities (convex) tend to distress the area being able to generate high tension locally. On the contrary cavity type irregularities (concave) tend to increase the compressive stress locally. The larger the irregularity, the larger its effect on the stress field.
- The stress redistribution in the section where the pins to measure the convergence of the tunnel were located shows a similar asymmetric pattern as the one in the BGR section. The maximum compressive stress is located at the lower left and right corners of the tunnel (155.0 MPa and 160.6 MPa respectively). The maximum tensile stress takes place at the same locations but it is more asymmetric (12.71 MPa and 6.06 MPa respectively) (see Appendix M).
- In the section outside the slot, the maximum compressive stress is located at the lower left and right corners of the tunnel (184.8 MPa and 206.1 MPa respectively). The maximum tensile stress takes place at the same locations but it is more asymmetric (3.56 MPa and 6.63 MPa respectively) (see Appendix M).
- The roof does not seem to have high enough stress to initiate damage in any section (Max. Comp. Stress in all the as-built sections is 88.92 MPa and Max. Tensile stress is 5.90 MPa). However, the same general pattern can be seen, very low compressive stress or tension in the bumps and higher compressive stress in the cavities. See Figure 9-29 and Appendix M.

Excavation of the tunnel bench

- The maximum compressive stress after excavation of the bench, takes place at the rounded floor of the tunnel in every section (BGR section = 109.9 MPa, Outside slot section = 114.0 and convergence pins section = 122.8 MPa). There is also a high compressive stress state in the roof that is slightly lower than the one in the floor for every tunnel section (around 15 MPa to 30 MPa lower). The same happens to the tensile stress (BGR section; floor = 8.48 MPa and roof 6.52 MPa, outside slot section; floor = 8.98 MPa and roof = 5.66 MPa and convergence pins section; floor = 12.71 MPa and roof = 4.14 MPa) (see Appendix M).

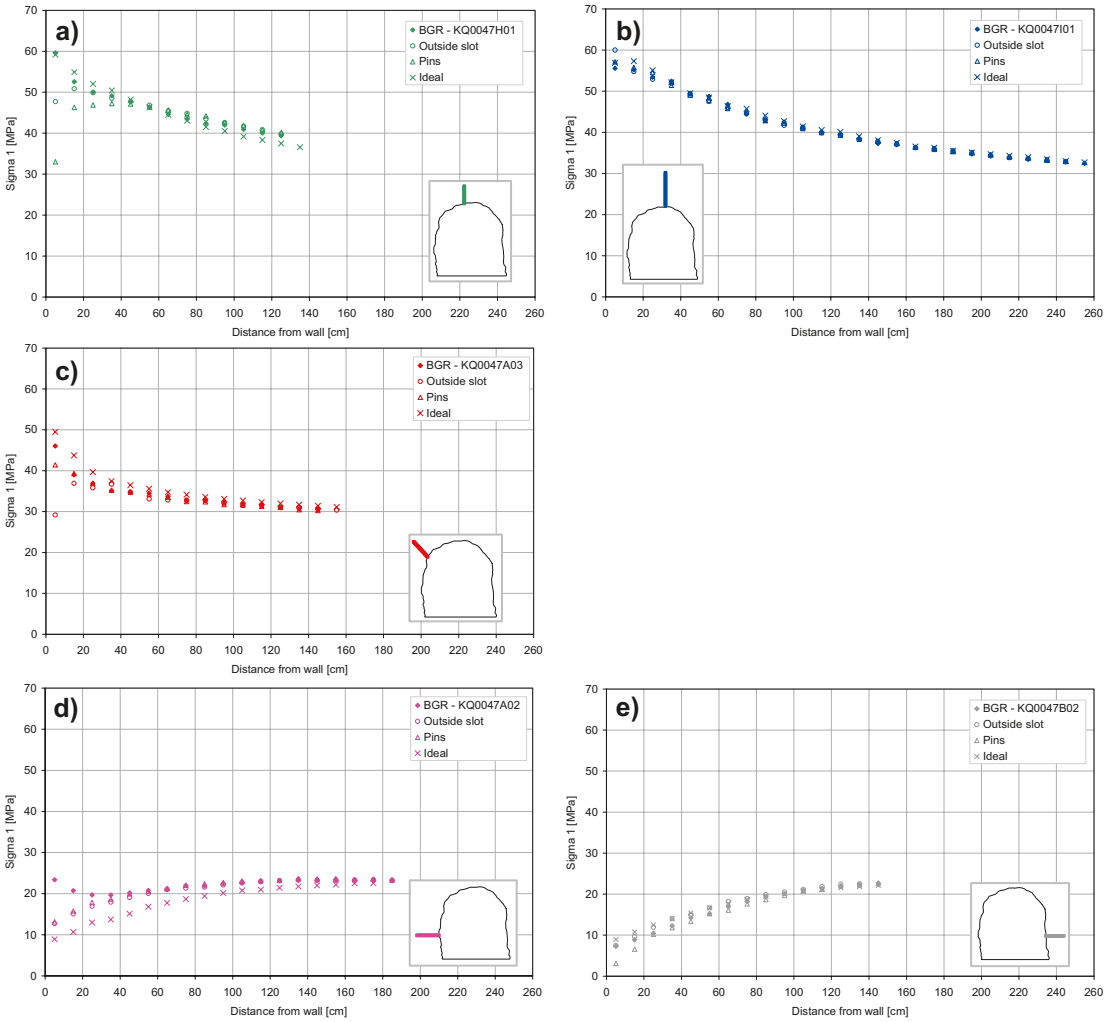

Figure 9-25. *Comparison of major principal stress when the tunnel heading is excavated, for three different sections in the as-built tunnel (section 047 (BGR), section 048 (outside slot) and section 048.7 (convergence pins)) and for the as-planned (ideal) tunnel shape. The scanlines are located at the approximate location where the boreholes for the ultrasonic measurements were placed in section 047. Models with E = 65 GPa (see Table 9-11 and Appendix L for other cases).*

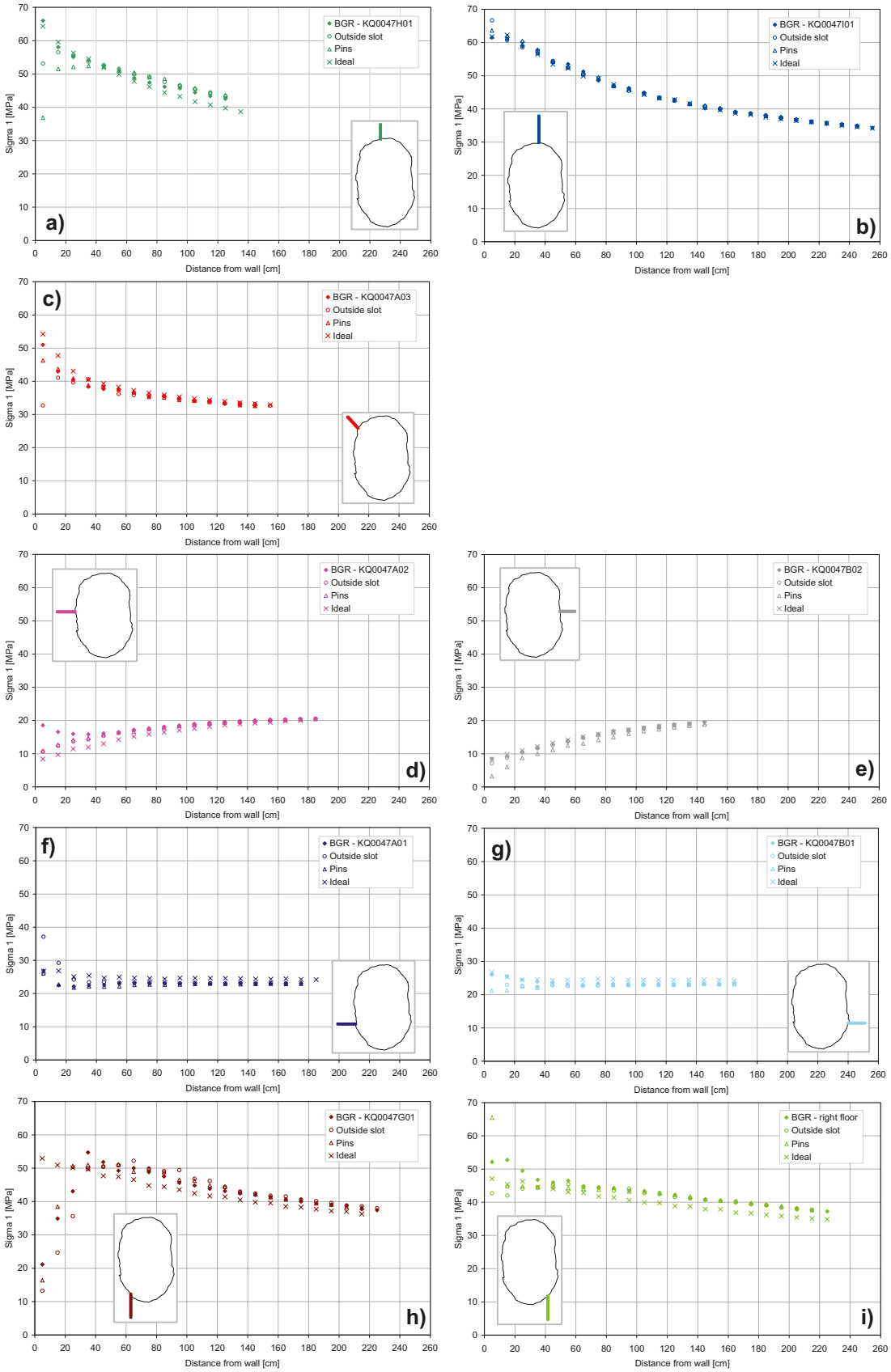

Figure 9-26. *D:o result after the tunnel bench is also excavated (see Table 9-11 and Appendix L for other cases).*

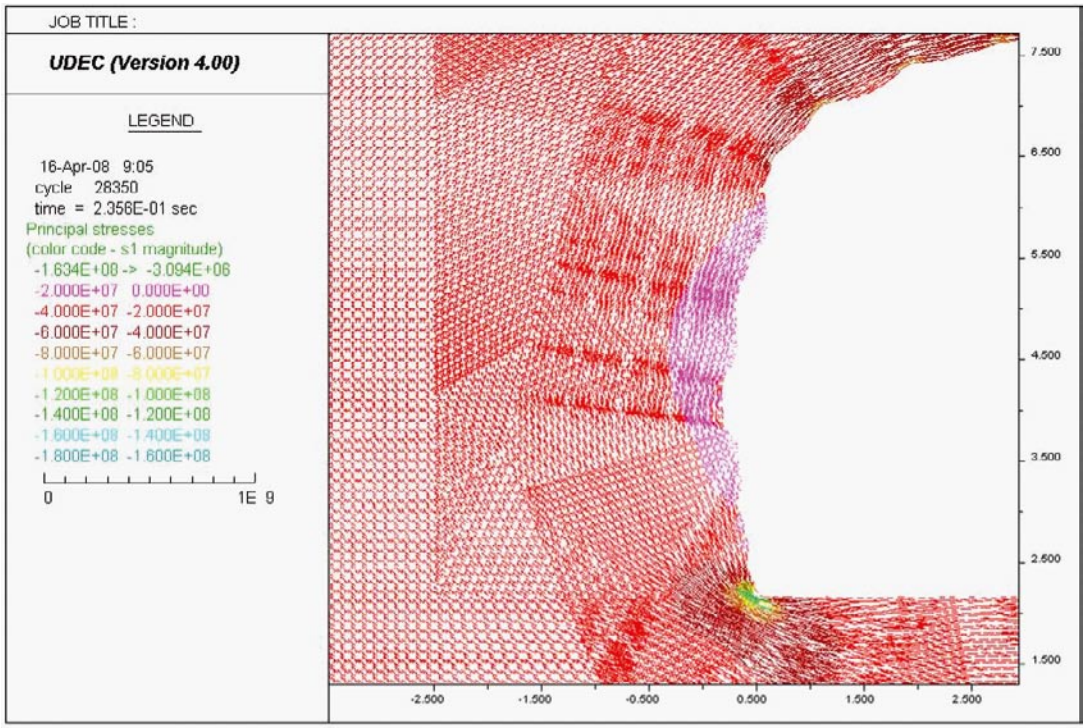

a) Maximum Compressive stress = 163.4 MPa

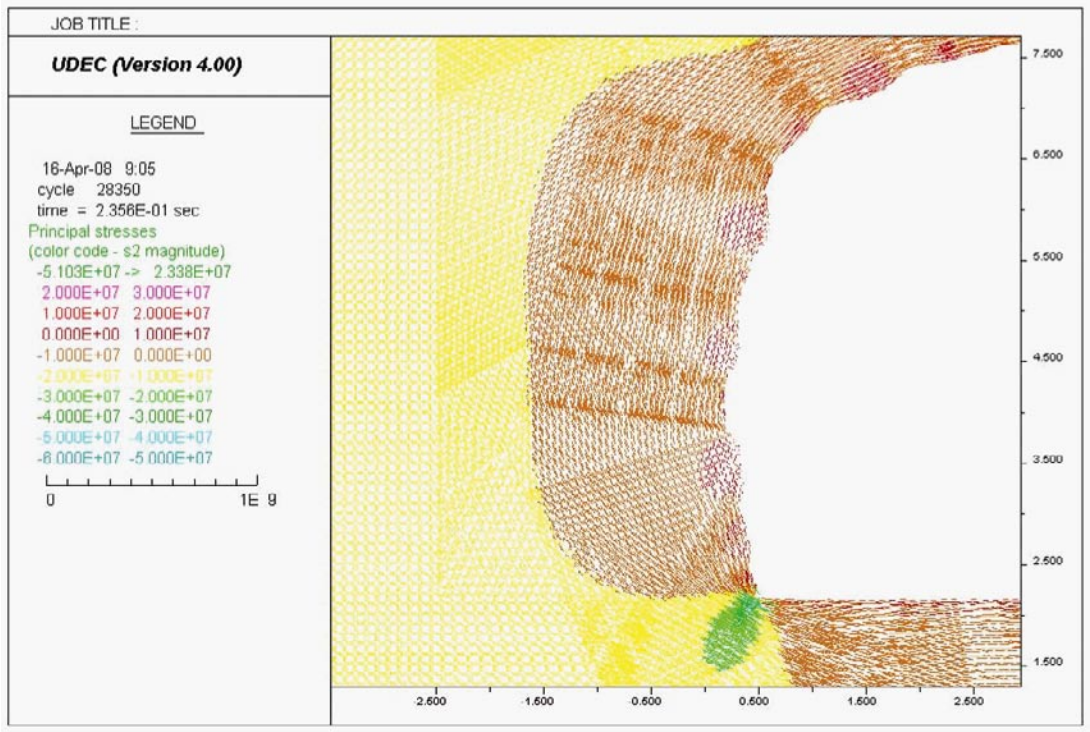

b) Maximum Tensile stress = 23.4 MPa

Figure 9-27. *Close-up images of the left side wall. Stress tensor plots at section 047 (BGR section) after excavating the heading; Colors by magnitude of a) Sigma 1 and b) Sigma 2. Model with E = 65 GPa (see Table 9-11 and Appendix M).*

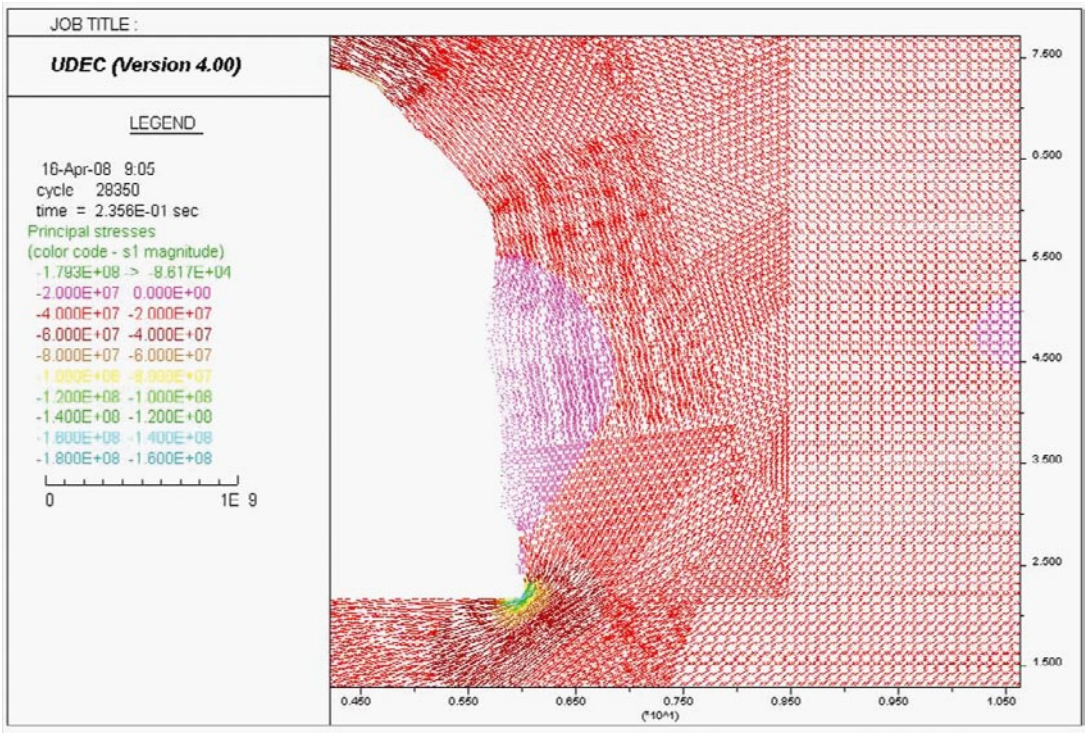

a) Maximum Compressive stress = 179.3 MPa

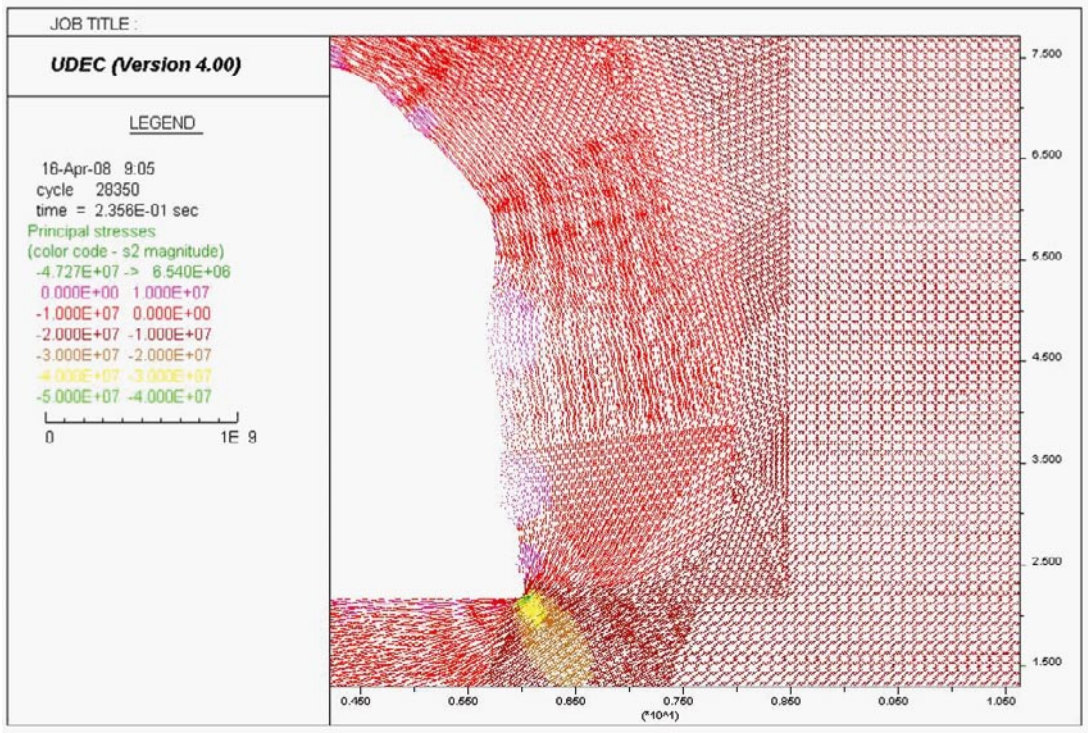

b) Maximum Tensile stress = 6.5 MPa

Figure 9-28. *Close-up images of the right side wall. Stress tensor plots at section 047 (BGR section) after excavating the heading; Colors by magnitude of a) Sigma 1 and b) Sigma 2. Model with E = 65 GPa (see Table 9-11 and Appendix M).*

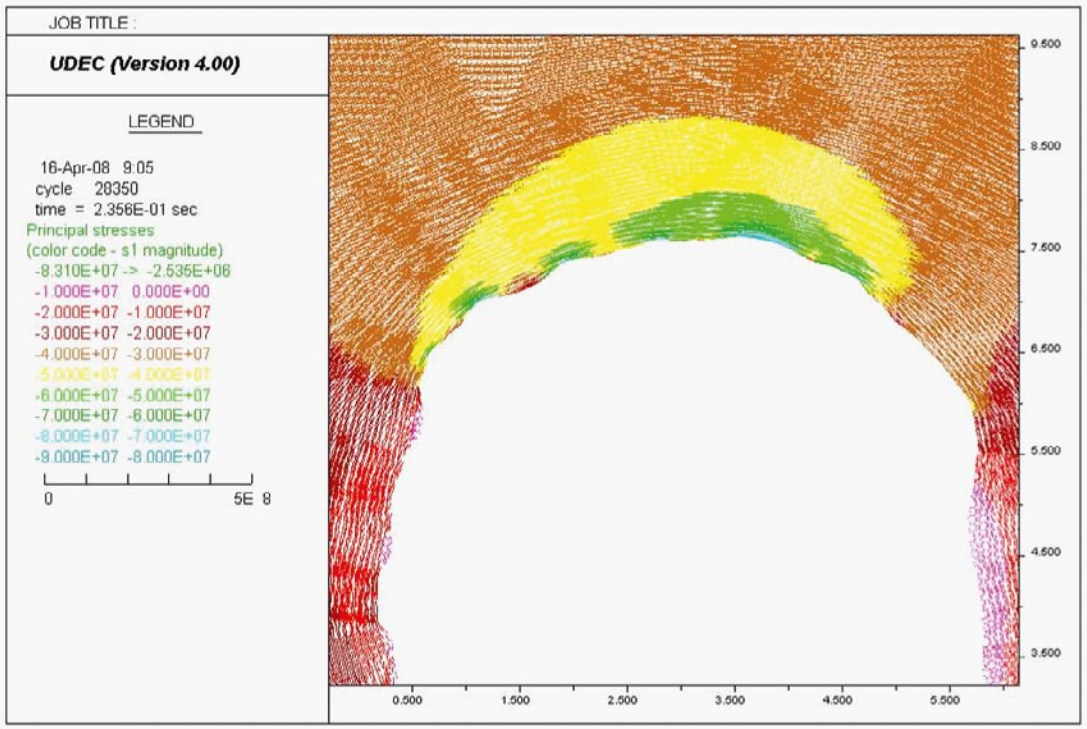

a) Maximum Compressive stress = 83.1 MPa

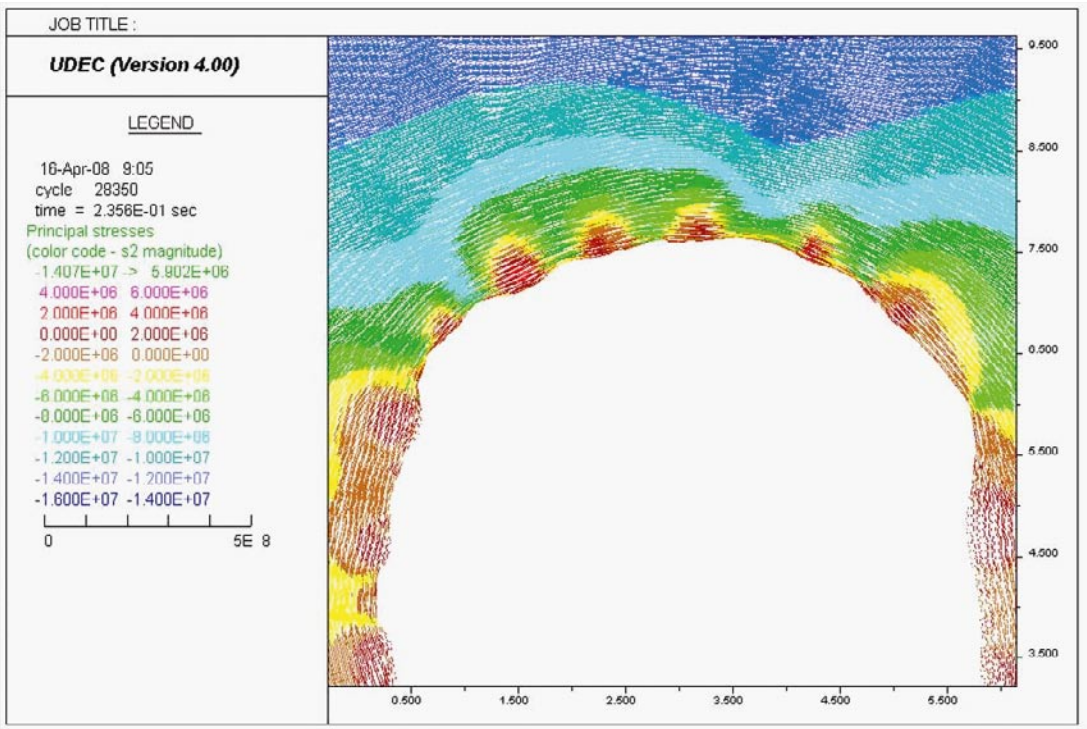

b) Maximum Tensile stress = 5.9 MPa

Figure 9-29. *Close-up images of the roof. Stress tensor plots at section 047 (BGR section) after excavating the heading; Colours by magnitude of a) Sigma 1 and b) Sigma 2. Model with E = 65 GPa (see Table 9-11 and Appendix M).*

9.5 Summary of the numerical studies

A numerical study has been performed using 3DEC (three-dimensional) and UDEC (two-dimensional) with the objective of understanding and, if possible, quantifying the relevance of different factors on the formation of the EDZ. Factors like tunnel shape, major fractures and fracture properties, shape of the blasting round face, elastic rock mass behaviour and orientation and magnitude of in-situ stress have been considered in this modelling exercise. All the simulations reported in this study considered the rock mass to be linear elastic, the only plasticity coming from the fractures (when fractures were considered), which followed a Coulomb-slip model.

9.5.1 Conclusions from the convergence calibration

Tunnel convergence measurements were taken while different sections of the tunnel were excavated. Using these convergence measurements a numerical calibration study has been performed in order to obtain the best fitting in-situ stress and elastic rock mass properties. No fractures were considered in this back-analysis exercise. The results from the calibration show that:

- The lateral convergence is best fitted with a model with rock mass Young's modulus of 65 GPa and a magnitude of σ_1 of 25 MPa (see Figure 9-7). (The total convergence in this case about 2.8 mm.)
- The range of σ_1 orientation considered has little effect on the convergence.
- Some of the convergence measurements are better fitted with E = 70 GPa. This variation may be due to the heterogeneity in rock type at the site.
- The difference in convergence between models with concave blasting round faces and planar blasting round faces is in average 0.032 mm (for the best-fit case). When comparing a model with as-built tunnel shape with as-planned tunnel shape it gives an average difference of 0.074 mm.
- According to the analysis performed in this study, it can be concluded that the tunnel shape has a roughly equal influence on the tunnel convergence as the shape of the blasting round face.

9.5.2 Conclusions from the sensitivity analysis

After the calibration back-analysis was completed, an extensive sensitivity analysis including all the above mentioned factors was conducted. In this study, the simulation of the excavation of the TASQ tunnel have been performed in one stage (all the tunnel at once), and only the final state of stress situation around the tunnel has been compared. The following paragraphs summarize the main conclusions from this sensitivity study. The conclusions are divided into two different groups; the first group refers to the results from simulations without any fractures (continuum) which considered the ideal and the laser scanned tunnel shape and the second group refers to the results from simulations with the main fractures at the APSE site (discontinuum) which only considered the ideal tunnel shape.

Conclusions from 3DEC models without fractures

- The most relevant factors affecting the stress redistribution around the tunnel, from those considered in this study within their particular ranges, are the magnitude of the in-situ major principal stress (25 MPa or 30 MPa) and the tunnel shape (as-planned vs. as built) (see Table 9-8).
- The magnitude of the maximum compressive stress close to the wall of the tunnel is always equal or smaller for the as-planned tunnel shape compared to the as-built tunnel shape. The irregular shape of the tunnel walls in the as-built case causes local stress concentrations and local stress release (convex or concave irregularities in the tunnel wall respectively) in different wall areas which can lead to local isolated fracturing.
- The influence of the shape of the tunnel on the stress redistribution exists in the first meter around the tunnel surface, beyond that it is negligible (see Figure 9-10).
- The effect on the stress field redistribution, of the ranges used for the rock mass Young's modulus and the orientation of the major principal stress, is negligible (see Table 9-8).

Conclusions from 3DEC models with fractures

- The influence of the fractures on the stress-redistribution and tunnel wall displacements varies strongly from one section of the tunnel to another (see Figure 9-17 to Figure 9-18) depending on the relative orientation between fractures and the tunnel axis.
- The difference between the maximum compressive stress close to the tunnel walls in discontinuum models (with the main fractures explicitly included) and continuum models (without fractures) ranges from 1 MPa to 95 MPa (see Table 9-8) depending mainly on the stiffness of the fractures and the studied section of the tunnel.
- The maximum fracture shear displacement and normal displacement (occurring in the NE trending fractures) vary strongly at each section of the tunnel and depend on the relative orientation between the fractures and the tunnel axis and between each of the fractures (see Figure 9-16 to Figure 9-18).
- The effect of increasing the fracture stiffness from (kn, ks) = (1,000 GPa/m, 500 GPa/m) to (kn, ks) = (2,000 GPa/m, 1,000 GPa/m) is almost negligible. Most of the effect takes place when the fracture stiffnesses are increased from (kn, ks) = (200 GPa/m, 100 GPa/m) to (kn, ks) = (1,000 GPa/m, 500 GPa/m).
- The effect of friction angle on stress is negligible (see Figure 9-13 to Figure 9-15). However, the effect of friction angle on the maximum fracture shear displacement is noticeable for cases where the fracture stiffness is low, while negligible for other cases (see Figure 9-16 and Table 9-3 to Table 9-5).
- The effect of rock mass Young's modulus is relevant on the fracture shear displacement but almost negligible on the redistribution of the stress field. When considering stiff fractures with 65 GPa intact rock Young's modulus, the shear displacement is 15% smaller than with 55 GPa (see Figure 9-15 and Figure 9-16).
- The explicit consideration of the major fractures in the study area generates different asymmetric patterns in the stress redistribution around the excavation at different tunnel sections (Figure 9-17 to Figure 9-21). This asymmetry in the stress around the tunnel can in turn induce, in combination with the effect of blasting, different EDZ in different parts of the tunnel wall.

9.5.3 Conclusions from UDEC models

The actual (as-built) shape of the TASQ tunnel differs from the ideal (as-planned) shape. Although the 3DEC models capture the 3-dimensional nature of the tunnel, they are not capable of incorporating at present the highest resolution laser-scanned data. As a consequence, the resolution of the laser-scanned tunnel model had to be decreased losing some of the lower order roughness of the tunnel walls. For this reason, to be able to evaluate the influence of the small scale "bumpiness" of the tunnel walls, it was decided to model two-dimensional sections of the TASQ tunnel using UDEC which can accommodate the highest resolution laser-scanning tunnel 2D models.

As also seen in the three-dimensional models, the results of the UDEC simulations show that the influence on the stress from the difference in tunnel shape reaches at the most 1 m inside the rock (Figure 9-25 to Figure 9-26).

Conclusions from the UDEC model with as-planned tunnel shape

The results of the 2D simulations of the as-planned tunnel shape show that any possible excavation damage (without considering the effect of any fractures and considering an ideal tunnel shape) should come from the excavation of the heading as the maximum compressive and tensile stresses at the corners of the floor of the tunnel are the highest at this stage. Once the bench is excavated, the maximum compressive and tensile stresses are lower due to the ideal smooth curvature of the floor.

Conclusions from the UDEC model as-built tunnel shape

As previously seen from the 3DEC results, the UDEC results also shows that the bumpiness of the tunnel surface (see Figure 9-22 to Figure 9-23) generates zones of local stress release or stress concentration which could potentially initiate isolated fracturing (Figure 9-27 to Figure 9-29).

Excavation of the tunnel heading

- When excavating the different sections of the heading of the TASQ tunnel, the zones of maximum compressive and tensile stresses are in the left and right corners of the floor due to its horse shoe shape (See Figure 9-27 to Figure 9-29 and Appendix M). The high compressive and tensile stress magnitudes in those areas can induce local fracturing.
- The irregular shape of the tunnel walls in each of the as-built sections, as well as their bumpiness, generates asymmetry in stress redistribution around the tunnel. “Bumpy” type irregularities (convex) tend to distress the area being able to generate high tension locally. On the contrary cavity type irregularities (concave) tend to increase the compressive stress locally. The larger the irregularity, the larger its effect on the stress field. The asymmetry tends to be higher when looking at the generated high tensile stress areas than in the case of the high compressive stress areas. The high stresses generated locally by the tunnel wall bumpiness could induce local fracturing and asymmetry in the EDZ.

Excavation of the tunnel bench

- When the bench is excavated the maximum compressive stress is located in the floor of the tunnel in each of the studied sections. The maximum compressive stress is always lower in the roof of each section.
- The bumpiness of the walls has the same effect as when excavating the heading. Local cavities increase the compressive stress and convex-type irregularities de-stress the area, being able to eventually generate tensile stresses locally.

10 Discussion and conclusion

The TASQ-tunnel was developed in 2003 at the Äspö Hard Rock Laboratory (HRL), Sweden purposely for a large in-situ rock mechanics experiment, the Äspö Pillar Stability Experiment (APSE) /Andersson 2007/. The tunnel had an unusual shape, primarily because of the need to concentrate high stresses in the circumferential of the tunnel, especially under the floor. An extensive set of data for understanding the **Excavation Damaged Zone (EDZ)** was collected within section 047 of the tunnel. It consist of the blast design, blast sequences, convergence measurements (in section 049) during excavation, geological mapping of tunnel and cores, 3D-laser scanning of the tunnel geometry, and seismic measurements of the EDZ (Figure 10-1a).

The approach used, which combine the laserscanned geometry (Figure 10-1b), fracture mapping using the as-built tunnel geometry (Figure 10-1c) and a numerical simulation of the tunnel response (Figure 10-1d), taking into account both fractures and the as-built geometry was successful. Furthermore, using this approach, all the collected data could be assembled into one single model, which then could be used to extract different model regions needed for e.g. numerical simulations and for documentation. By means of numerical modelling of the rock mechanic response when excavating the tunnel, the mechanical processes of importance for the EDZ could be compared to actual measurements and observations. In the following sections, the major conclusions drawn within this project are discussed with the aim to clarify their reliability.

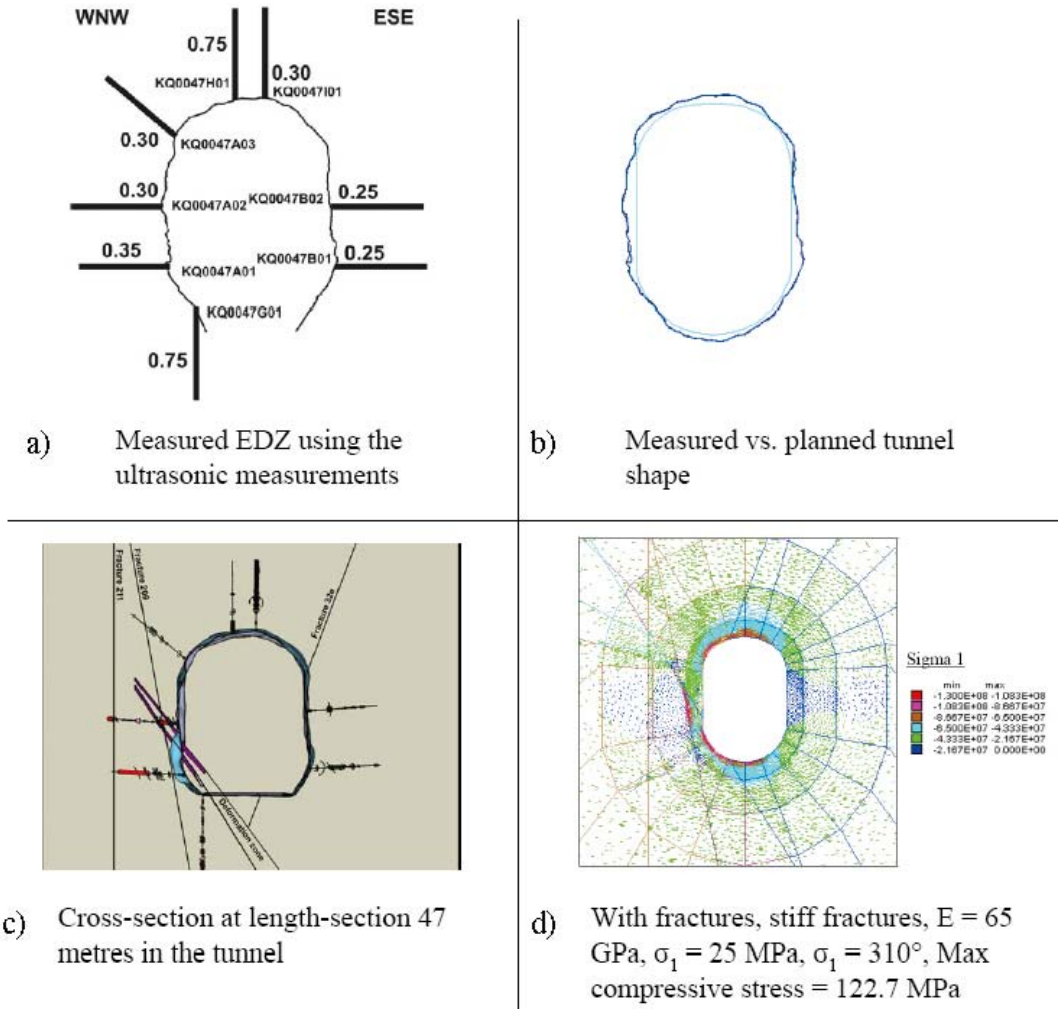

Figure 10-1. *(a) The resulting extent of the EDZ from the seismic measurements in section 47 /from Schuster 2007/. (b) Comparison between nominal and as build tunnel profile. (c) Cross-section showing the modelled fractures in the RVS model. (d) Compressive stresses around the tunnel obtained from 3DEC.*

10.1 Ultrasonic measurements and borehole mapping

When studying the wave velocity obtained from the ultrasonic measurement, a difference in the wave velocity along the drillholes was observed which indicates fractures or changed material properties such as elasticity or density. When comparing the location of the observed changes in wave velocity with the location of the mapped fractures in the drillcores, it was observed that their locations corresponded, thus indicating that the ultrasonic measurements can be used to detect damage elements such as individual fractures and the extent and location of EDZ with high accuracy (Table 6.2). The damage caused by the blasting process produce a general velocity decrease close to the tunnel wall. However, no obvious change in the observed fracture frequency with distance to the tunnel face could be detected. Thus, indicating that either micro fractures are present or that the elastic properties of the rock have changed, which then affect the velocity.

From the ultrasonic measurement of the EDZ, it was concluded that EDZ varies around the circumference of section 47 as indicated in (Figure 10-1a). For example, EDZ is 0.75 m in the left side of the roof whereas 0.3 m in the right side. An asymmetry can also be seen in the lateral walls of the tunnel. One hypothesis is that the combined effect of the pre-existing fractures and the shape could induce this asymmetry in EDZ. This hypothesis is tested in numerical simulations when including fractures in the vicinity of the tunnel left wall with a sub-parallel (acute angle) orientation relative to the tunnel axis. From these simulations it was found that zones of higher compressive and tensile stress are induced which then can increase the damage initiated by the blasting (Figures 9-23d, f and h and Figure 9-24d and f). Furthermore, the roughness of the tunnel walls caused by blasting also induce local stress concentrations (compressive and tensile) in the first 40 cm to 50 cm inside the rock (see Figure 9-29 to Figure 9-34 and Appendix M). The calculated stress situation (tension and compression) indicates a higher probability of failure in the same areas as were the ultrasonic measurements shows a large extent of the EDZ. However, according to the simulations it seems unlikely that the effect of the pre-existing fractures and the irregular shape of the tunnel wall is able to induce failure by itself (of the same magnitude as indicated by the ultrasonic measurements). To induce failure, the triggering effect of the blasting is necessary.

When studying the results from the tunnel round and the bench round, the drilling, charging and initiation plans are performed as planned and the stipulated limits for vibration, air blast and flying rock have not been exceeded, which indicates that the blasting should have produced a symmetric and a smooth tunnel shape. The disparity of the EDZ from ultrasonic measurements evaluated in the roof and the floor of the TASQ tunnel cannot be fully explained from the stress situation around the tunnel. The reason might be that some fractures are missing in the geological model or that no plasticity was considered in the numerical model (except for the pre-existing fracture). As a consequence of this elastic modelling approach, the high stresses were not allowed to propagate inside the rock.

10.2 The effect of blasting design on EDZ

In earlier investigations, it was concluded that misfires and reblasting of the contours as well as deviations of the contour holes cause larger EDZ /Christiansson and Hamberg 1991, Olsson 1991, Emsley et al. 1997, Olsson et al. 2004/. This has been observed as an unexpected high frequency of new fractures in the sections where reblasting was necessary. The blasting configurations are significant for the damage in the floor, whereas the damage in the walls is mainly due to local variations of the geology rather than blasting configuration. The more brittle lithology sustains more damage. Furthermore, during the mentioned investigation, it was found that the distribution of induced fractures to a large extent is related to boreholes on the contour /Christiansson and Hamberg 1991/.

In a model of the contour holes in the tunnel created during the EDZ investigations in the TASQ tunnel, a comparison between the number of traces of drill holes in the rounds with electronic detonators and the ones with non-electronic detonators was made /Bäckström et al. 2008a/. It was found that there were about 23% more traces found in the rounds in which electric detonators were used. The conclusion of this comparison is that the electric detonators have a better blasting performance than the non-electric detonators because the accuracy of the blasting is higher, however it should be kept in mind that this conclusion is drawn from a very small number of samples and therefore needs to be further investigated /Bäckström et al. 2008a/. Furthermore, /Olsson et al. 2004/ also report that

it is possible to minimize the damage zone in the floor by using top heading and bench. Finally, it was found that water in bore holes increases the damage zone in terms of length and frequency of induced fractures. This could be avoided by drilling the holes pointing slightly upwards.

10.3 The effect of stress concentration on EDZ

From the rock mechanics simulations, it was concluded that the influence of the tunnel shape is equally important as the influence of the shape of the blasting round face in the tunnel (Figure 9-25), thus the as-built geometry must be captured in order to predict the tunnel response accurately, for example by means of laserscanning. During the sensitivity analysis it can be concluded that the most relevant factors affecting the stress redistribution around the tunnel are the magnitude of the in-situ major principal stress, the tunnel shape (as-planned vs. as built) and the presence of unfavourably oriented fractures (sub-parallel to the tunnel axis).

Although the 3DEC models capture the 3-dimensional nature of the tunnel as well as the fractures, they are not capable of incorporating the highest resolution laser-scanned data. For this reason and to be able to evaluate the influence of the small scale "irregularities" of the tunnel walls, it was decided to model two-dimensional sections of the TASQ tunnel using UDEC which can accommodate the highest resolution laser-scanning. When studying the stress distribution around the tunnel after the excavation, the following major conclusions from the 3DEC and the UDEC simulations can be drawn:

- The influence of the fractures on the stress-distribution and tunnel wall displacement varies strongly from one section to another depending on the relative orientation between each fracture and the tunnel axis and between the fractures.
- The irregularities on the tunnel wall surfaces generate zones of local stress release or concentration which could potentially initiate local fracturing and asymmetry in the EDZ. Concave irregularities cause increase in stress in the same manner as a notch would increase the stress. Convex irregularities cause stress decrease and can induce local tensile areas. The larger the irregularity, the larger its effect on the stress field. The asymmetry tends to be higher when looking at the generated tensile stress areas than in the case of the compressive stress areas.
- The major fractures in the study area generate asymmetric patterns in the stress distribution at different tunnel sections. This asymmetry can in turn induce, in combination with the effect of blasting, different EDZ zones at different parts of the tunnel wall due to local variation of the stresses. Furthermore, an additional cause for fracture initiation could be the inhomogeneous material properties along the tunnel axis (not considered in the numerical analysis. The rock matrix in the models was homogeneous), which can create stress concentrations and thus, crack initiation /Emsley et al. 1997/.

10.4 Recommendations for future investigations of the EDZ

In order to draw any general conclusions, more measurements of EDZ along the tunnel wall must be carried out. In this way, the influence of fractures around the tunnel and the correct shape of the tunnel along its axis can be quantified.

In this study, the modelling of the stresses developed was divided into one model containing the fractures, without the geometry of the tunnel and one with the geometry of the tunnel which was lacking the geometry of the fractures. In the future, these two geometries should be combined in the same model in order to provide a possibility to assess their combined effect on the stress situation around the tunnel. The modelling tool must thus be able to accommodate both the geometries of the fractures as well as the possibility of the development of new fractures. Furthermore, depending on the volume of modelled rock mass, the cut-off length of the fractures will limit the general application of the model.

A future study of the EDZ would gain from a detailed 3D fracture network model produced from slots cut out from the wall of the tunnel. If the investigation is to be produced in the TASQ tunnel an evaluation of different stress configurations due to the modelling of the fractures and the tunnel wall geometry should be used to identify areas of interest for the validation of the EDZ. The TASQ tunnel is an "old" tunnel where several modifications to the tunnel geometry have been performed. The geometry of this tunnel is extremely complex in some areas, thus this investigation should benefit from being performed in a newly built tunnel, where no modifications from other experiments have been made.

A tool to measure the as-built geometry of the tunnel has already been developed in /Bäckström et al. 2008a/ where they suggest an analysis method to control the blasting performance using the laser-scanning method. The results from laser scanning measurements of the as-built geometry together with a model of the fractures, mapped on the tunnel wall should be combined in a preliminary model, which will serve as an identifying tool for interesting areas in which a slot should be produced. The information from the slot will then be used to verify the modelled EDZ. A less "expensive" method would be to drill boreholes at these locations instead and measure the ultrasonic wave velocity, to verify the depth of the EDZ.

When using laser image and 3D point clouds, laser scanning data can be used for both documentation and visualization and easily be integrated into a numerical modelling tool. However, it is important to capture the scanning data as soon as possible after the tunnel is excavated as otherwise; some parts will be hidden by the ventilation pipes or covered by the reinforced shotcrete, or even removed as the face will be blast away during the next round as in the case of this project. In order to avoid this problem and to obtain a more accurate geometry of the tunnel it is recommended to perform measurements after each blasting round when planning to use them for a numerical simulation like in this project.

This study would then be able to verify several questions such as the effect on the EDZ of different orientations of fractures in relation to the tunnel and the stress situation around it.

11 References

Adachi T, Oka, F, Koike M, 2005. An elasto-viscoplastic constitutive model with strain-softening for soft sedimentary rocks. Soils and Foundations;45(2):125–133.

Andersson J C, 2004. Äspö Pillar Stability Experiment. Summary of preparatory work and predictive modelling. SKB R-03-02, Svensk Kärnbränslehantering AB.

Andersson J C, 2007. Äspö Hard Rock Laboratory, Äspö Pillar Stability Experiment, Final report, Rock mass response to coupled mechanical thermal loading. SKB TR-07-01, Svensk Kärnbränslehantering AB.

Bäckblom G, Martin C D, 1999. Recent Experiments in Hard Rocks to Study the Excavation Response: Implications for the Performance of a Nuclear Waste Geological Repository. Tunnelling and Underground Space Technology; 14(3): 377–394.

Bäckström A, 2006. Details Regarding the Retrieval of the Fracture Pattern used in the Near-Field Model 2 of Phase 3, DECOVALEX IV, Task B. 25.

Bäckström A, 2008. DECOVALEX-Validation of the ultrasonic borehole investigation in the TASQ tunnel. SKB IPR report, Svensk Kärnbränslehantering AB. 84.

Bäckström A, Feng Q, Lanaro F, 2008a. Excavation Damage Zone (EDZ) at the TASQ tunnel (Äspö, Sweden) – Quantification of blasting effects on the geological settings by 3D-laser-scanning. Submitted to Engineering Geology 2008.03.12: 14.

Bäckström A, Antikainen J, Backers T, Feng X, Jing L, Kobayashi A, Koyama T, Pan P, Rinne M, Shen B, Hudson J A, 2008b. Numerical modelling of uniaxial compressive failure of granite with and without saline porewater. International Journal of Rock Mechanics & Mining Sciences, doi:10,1016/ijrmms. 2007.12.001.

Bäckström A, Feng Q, Wang G, In prep. Characterization of the EDZ in the rock mass using 3D-laser scanning of the TASQ-tunnel, Äspö, Sweden. SKB IPR report, Svensk Kärnbränslehantering AB.

Börgesson G, Pusch L, Fredriksson A, Hökmark H, Kaenland O, Sanden T, 1992. Final report of the rock sealing project – Identification of zones disturbed by blasting and stress release. Stripa Project 92-08, Svensk Kärnbränslehantering AB.

Christiansson R, Hamberg U, 1991. Blasting Damage Investigation in access ramp section 0/526-0/565 m, no 1. Tunnel excavation and geological documentation. SKB PR 25-91-12, Svensk Kärnbränslehantering AB. 38.

Emsley S, Olsson O, Stenberg L, Alheid H-J, Falls S, 1997. ZEDEX-a study of damage and disturbance from tunnel excavation by blasting and tunnel boring. SKB TR-97-30, Svensk Kärnbränslehantering AB. 198.

Fairhurst C E, Hudson J A, 1999. International Society of Rock Mechanics Commission on Testing Methods, Draft ISRM suggested method for the complete stress-strain curve for intact rock in uniaxial compression. Int. J. Rock. Mech. Min. Sci. 36: pp. 279–289.

Fardin N, 2003. The Effect of Scale on the Morphology, Mechanics and Transmissivity of Single Rock Fractures. Ph.D. Thesis, Kungliga Tekniska Högskolan, Stockholm, Sweden.

Fjellborg S, Olsson M, 1996. Large drift rounds with large cut holes at LKAB. In Swedish. SveBeFo Report no 27.

Fredriksson A, Staub I, Outers N, 2004. Äspö Pillar Stability Experiment. Final 2D coupled thermo-mechanical modelling. SKB R-04-02, Svensk Kärnbränslehantering AB.

Golshani A, Okui Y, Oda M, Takemura T, 2005. A micromechanical model for brittle failure of rock and its relation to crack growth observed in triaxial compression tests of granite. Mechanics of Materials;38:287–303.

Hakami E, Fredriksson A, Lanaro F, Wrafter J, 2008. Rock Mechanics Laxemar, Site descriptive modelling, SDM-site Laxemar. SKB R-08-57, Svensk Kärnbränslehantering AB.

Hudson J A, Jing L, 2007. DECOVALEX-THMC, Task B – Understanding and characterizing the Excavation Disturbed Zone (EDZ)-Phase 2 report. SKI Report 2007:08. 107.

Hudson J A, Bäckström A, Rutqvist J, Jing L, Backers T, Chijimatsu M, Feng X-T, Kobayashi A, Koyama T, Lee H-S, Pan P-Z, Rinne M, Shen B, 2008a. Final Report of DECOVALEX-THMC Task B. EDZ Guidance Document - Characterising and Modelling the Excavation Damaged Zone (EDZ) in Crystalline Rock in the Context of Radioactive Waste Disposal. SKI report. 68.

Hökmark H, Fälth B, Wallroth T, 2006. T-H-M couplings in rock Overview of results of importance to the SR-Can safety assessment. SKB R-06-88, Svensk Kärnbränslehantering AB. 101.

Itasca Consulting Group Inc, 2003. PFC2D User's manual, version 3.0, Minneapolis, USA.

Itasca Consulting Group Inc, 2004. UDEC version 4.0, Minneapolis, USA.

Itasca Consulting Group Inc, 2007. 3DEC version 4.0, Minneapolis, USA.

Jacobsson L, Bäckström A, 2005. Uniaxial compression tests of intact rock specimens at dry condition and at saturation by three different liquids: distilled, saline and formation water. SKB IPR-05-33, Svensk Kärnbränslehantering AB. 100.

Jacobsson L, Flansbjer M, 2005. Äspö Hard Rock Laboratory. Äspö Pillar Stability Experiment. Samples from TASQ tunnel at Äspö HRL. Normal loading and shear tests on joints. SKB IPR-05-23, Svensk Kärnbränslehantering AB.

Kornfält K-A, Wikman H, Nordlund E, Chunlin L, 1991. Blasting Damage Investigation in access ramp section 0/526–0/565 m, No 4. Optical examination of microcracks in thin sections of core samples and acoustic emission of core samples. SKB PR 25-91-15, Svensk Kärnbränslehantering AB. 30.

Kornfält K-A, Persson P-O, Wikman H, 1997. Granitoids from the Äspö area, southeastern Sweden – geochemical and geochronological data. GFF 119, 109–114.

Leica, 2008. Leica Geosystems AG. Product specification (2008-05-08). http://www.leica-geosystems.com/se/sv/lgs_51792.htm.

Lönnqvist M, 2008. On the influence of the tunnel shape on the major principal stress in the floor of the Q-tunnel. PM. Clay Technology AB.

Magnor B, 2004. Geological mapping of TASQ. Äspö Pillar Stability Experiment. SKB IPR-04-03, Svensk Kärnbränslehantering AB.

Martino J B, Chandler N A, 2004. Excavation-induced damage at the Underground Research Laboratory. International Journal of Rock Mechanics & Mining Sciences; 41: 1413–1426.

McEwen T, 2003. Review of the conclusions of previous EDZ workshops. Proceedings of a European Commission CLUSTER conference held in Luxembourg on 3–5 Nov. 2003.

Meglis I L, Chow T, Martin C D, Young R P, 2005. Assessing in situ micro crack damage using ultrasonic velocity tomography. Int. J. Rock. Mech. Min. Sci. 42: pp. 25–34.

Mettenleiter M, Härtl F, Fröhlich C, Langer D, 2000. Imaging laser for 3-D modelling of real world environments. Proceedings of the IASTED International Conference Modelling. Identification and Control, Innsbruck, Austria.

Olofsson I, Simeonov A, Stephens M, Follin S, Nilsson A-C, Röshoff K, Lindberg U, Lanaro F, Fredriksson A, Persson L, 2007. Site description modelling Forsmark, stage 2.2. A fracture domain concept as a basis for the statistical modelling of fractures and minor deformation zones, and interdisciplinary coordination. SKB R-07-15, Svensk Kärnbränslehantering AB.

Olsson O, 1991. Blast Damage Investigation in access ramp section 0/526-0/565 m, No. 2. Geophysical investigation in boreholes. SKB PR 25-91-13, Svensk Kärnbränslehantering AB. 99.

Olsson O, 1992. Site characterization and validation – final report. Stripa Project 92-22, Svensk Kärnbränslehantering AB.

Olsson M, Ouchterlony F, 2003. New formula for blast induced damage in the remaining rock. SveBeFo report No 65.

Olsson M, Niklasson B, Wilson L, Andersson C, Christiansson R, 2004. Äspö HRL, Experiences of blasting of the TASQ tunnel. SKB R-04-73, Svensk Kärnbränslehantering AB.

Ouchterlony F, Sjöberg C, Johansson S-E, Nyberg U, 1991. Blasting damage investigation in access ramp section 0/526–0/565 m, no. 3, Damage Zone assessment by vibration measurements. SKB PR 25-91-14, Svensk Kärnbränslehantering AB. 52.

Pan P-Z, Feng X-T, Hudson J A, 2006. Simulations on Class I and Class II curves by using the linear combination of stress and strain control method and elasto-plastic cellular automata. Int J Rock Mech Min Sci;43(7):1109–17.

Potyondy D O, Cundall P A, 1996. Lee CA. Modeling rock using bonded assemblies of circular particles. In: Rock Mechanics Tools and Techniques (Proc 2nd North Amer Rock Mech Symposium – NARMS96), M Aubertin et al. eds. Rotterdam: Balkema, pp 1937–1944.

Potyondy D O, Cundall P A, 2004. A bonded-particle model for rock. Int J Rock Mech Min Sci;41(8):1329–1364.

Potyondy D O, 2007. Simulating stress corrosion with a bonded-particle model for rock. Int J Rock Mech Min Sci;44(5):677–691.

Pusch R, 1989. Influence of various excavation techniques on the structure and physical properties of ”near-field” rock around large boreholes. SKB TR-89-02, Svensk Kärnbränslehantering AB.

Pusch R, Stanfors R, 1992. The Zone of Disturbance Around Blasted Tunnels at Depth. Int. J. Rock Mech. Min. Sci. & Geomech. Abstr; vol 29 (5); 447–456.

Rinne M, Shen B, Lee H-S, 2004. Äspö Pillar Stability Experiment. Modelling of fracture development of APSE by FRACOD. SKB R-04-04, Svensk Kärnbränslehantering AB.

Rutqvist J, Stephansson O, 2003. The role of hydromechanical coupling in fractured rock engineering. Hydrogeol J 11:7–40.

Rutqvist J, Bäckström A, Jing L, Hudson J A, 2008. A BenchMark Simulation Study of Coupled THMC Processes in the Excavation Disturbed Zone Associated with Geological Nuclear Waste Repositories. Final report of DECOVALEX-THMC Task B, Phase 3, Swedish nuclear inspectorate (SKI) report. 51. (In press).

Schuster K, Alheid H-J, Böddener D, 2001. Seismic investigation of the Excavation damaged zone in Opalinus Clay. Engng. Geol. 61: 189–197.

Schuster K, Alheid H-J, 2002. Engineered Barrier (EB) Experiment and Geophysical Characterisation of the Excavation Disturbed Zone (ED-C) Experiment: Seismic Investigation of the EDZ in the EB niche. Mont Terri Technical Report TR 02-03, swisstopo, Wabern, Switzerland.

Schuster, 2007. DECOVALEX. Ultrasonic borehole measurements in the TASQ tunnel (450 m level) at Äspö HRL performed by BGR in November 2006. SKB IPR-07-08, Svensk Kärnbränslehantering AB.

Shen X, Cen Z, Xu B, 1995. The characteristics of elasto-brittle-plastic softening constitutive theory and its numerical calculation. Journal of Tsinghua University (Sci. & Tech); 5(2): 22–27.

Staub I, Janson T, Fredriksson A, 2003. Äspö Hard Rock Laboratory. Äspö Pillar Stability Experiment. Geology and properties of the rock mass around the experiment volume. SKB IPR-03-02, Svensk Kärnbränslehantering AB.

Staub I, Andersson J C, Magnor B, 2004. Äspö Pillar Stability Experiment. Geology and mechanical properties of the rock in TASQ. SKB R-04-01, Svensk Kärnbränslehantering AB.

Stille H, Olsson P, 1990. Evaluation of rock mechanics. SKB PR 25-90-08, Svensk Kärnbränslehantering AB.

Terzhagi R D, 1965. Sources of errors in joint surveys. Geotechnique 15, 287–304.

Tsang C-F, Bernier F, Davies C, 2005. Geohydromechanical processes in the Excavation Damaged zone in crystalline rock, rock salt, and indurated and plastic clays – in the context of radioactive waste disposal. Int. J. Rock Mech. Min. Sci; 42; 109–125.

Wanne T, Johansson E, Potyondy D, 2004. Äspö Pillar Stability Experiment. Final coupled 3d thermo-mechanical modelling. Preliminary particle-mechanical modelling. SKB R-04-03, Svensk Kärnbränslehantering AB

Wawersik W R, Fairhurst C A, 1970. Study of brittle rock failure in laboratory compression experiments. Int. J. Rock Mech. Min. Sci. (5). 561–575.

Appendix A

Overview of EDZ field studies for hard rock at the Äspö HRL

/modified Bäckblom and Martin 1999/

Issue Site (Tunnel)	Access ramp	ZEDEX	TASQ	TASQ	Sweden, Stripa Mine
Responsible organisation(s)	SKB	ANDRA/Nirex UK/SKB	SKB	CAS/DOE/JAEA/SKI//SKB	
Project Name(s)	Blasting damage investigation in access ramp section 0/526–0/565 m.	Zone of Excavation Disturbance Experiment (ZEDEX) – A study of damage and disturbance from tunnel excavation by blasting and tunnel boring.	Experience of blasting.	DECOVALEX IV	A. Stripa Project Site Characterization and Validation Project (SCV). B. Stripa Project Buffer Mass Test and rock sealing Project (BMT).
Objectives	– Distribution and character of the blasting damage around the tunnel contour using three different blasting schemes. – Geophysical logging. – TV logging. – Hydraulic testing. – Geological mapping in boreholes and tunnel wall and floor. – Vibration measurements in boreholes. – Tests for Kaiser effect and microcrack.	– To understand the mechanical behaviour of the Excavation Disturbed Zone .(EDZ) with respect to its origin, character, magnitude of property change, extent and its dependence in excavation method. – To perform supporting studies to increase understanding of the hydraulic significance of the EDZ. – To test equipment and methodologies for quantifying the EDZ.	– Study the possibility to control the development of an Excavation Damage Zone. Could the lessons learned from 8 years ago produce a less pronounced EDZ. – High requirements on the TASQ tunnel. – Three phases of excavation. – Investigation of drilling precision. – manual mapping of halfpipes. – Geological mapping. – Cut out of slots.	– Develop a strategy for characterisation of the EDZ from tunnels. – Improve the QA program used during the construction of a deep repository. – Provide input data to the modelling teams of the DECOVALEX project.	A. Develop techniques to characterize potential repository sites in granite. B. Examine engineered barrier materials and designs that could enhance the long-term safety of the repository.
Schedule	Excavation of 0/526–0/565 1991 (1990–1993)	April 1994–July 1996	2003–2004	2005–Mars 2008	A. 1986–1992 B. 1980–1992
Main reference(s)	/Christiansson and Hamberg 1991/ /Olsson 1991/ /Ouchtelony et al. 1991/ /Kornfält et al. 1991/ /Pusch and Stanfors 1992/	/Emsley et al. 1997/	/Olsson et al. 2004/	/Hudson and Jing 2007/ /Bäckström et al. 2008b/	/Olsson 1992/ /Pusch 1989/ /Börgesson et al. 1992/

Issue Site (Tunnel)	Access ramp	ZEDEX	TASQ	TASQ	Sweden, Stripa Mine
Principal design of the studies, experiments	– Three different blasting schemes at chainage 526–565 m in the TASA tunnel. Observations of mechanical property changes and visible damage was investigated on tunnel walls, floors and in boreholes. – Nine rounds were excavated in the main access ramp. – Measurements were made prior to and after excavation. – Measurements of vibration were recorded during the blast.	– Two parallel drifts were excavated by drill-and-blast and a tunnel boring machine, respectively. Measurements were taken before, during and after excavation.	– One tunnel was excavated divided into two sections; one horseshoe shaped upper part and one lower bench, to limit the EDZ in the floor. The tunnel was built for an experiment of crack initiation at high stresses in the floor. Using investigations of the drilling precision, manual mapping of halfpipes, and geological mapping to study the possibility to control the development of an Excavation Damage Zone.	– From small scale mechanical properties of the rock type to detailed geological investigation of cut outs in the tunnel wall. – Develop a controlling method for the blasting geometry using the Laser-scanning method.	A. Extensive testing before and after drill-and-blast excavation of a test drift. B. Flow measurements in the rock at the boundary of a chamber placed and pressurized from a drift.
Rock Type	Grey granite with minor occurrences of fine-grained granite.	Granodiorite with inclusions of fine-grained granite.	Äspö diorite	Granite	Granite
Depth below surface (m)	80	420	450	450	385 360
Rock stress (MPa)	σ_1=10 MPa (// to adit); σ_2=7 MPa; σ_3~1.5 MPa (vertical) /Stille and Olsson 1990/.	σ_1~20 MPa (horizontal and $\perp$ to drift); σ_2~10 MPa (horizontal and // to drift); σ_3~4 MPa and vertical.	σ_1~30 MPa (horizontal and $\perp$ to drift); σ_2~15 MPa vertical; σ_3~10 MPa (horizontal and // to drift).	σ_1~30 MPa (horizontal and $\perp$ to drift); σ_2~15 MPa vertical; σ_3~10 MPa (horizontal and // to drift).	A. σ_1~24.4 MPa (horizontal and // to drift); σ_2~16 MPa (horizontal and $\perp$ to drift); σ_3~10 MPa (vertical). B. σ_1~20 MPa (horizontal and $\perp$ to drift); σ_2~10 MPa (horizontal and // to drift); σ_3~4 MPa (vertical, based on extrapolation).
Excavation method	Drill and blast. Area 25 m^2, advance 4 m per round, three rounds each of Normal Smooth Blasting (2.0 kg explosives per m^3), Very Smooth Blasting (1.8 kg explosives per m^3) and Normal Blasting (2.3 kg explosives per m^3). Charges in contour holes are =0.2 kg/m, except for the floor. Normal blasting is done with 0.4 kg/m, except for the floor.	The drill-and-blast diameter was 5 m, flattened in the floor. 10 rounds: two alternate blasting schemes. Normal smooth blasting and low-shock energy smooth blasting (Charges in contour holes are ~0.2 kg/m, except for the floor). TBM machine (dia. 5.03 m, area 20 m^2), ~140–190 kN per cutter.	A 80 m long tunnel was built for a stress experiment in the floor. The Drill and Blast scheme was divided in two phase. The diameter was 5 m with flat floor in the first phase. In the second a rounded floor with a height of about 2 m was excavated as a bench. The orientation was close to perpendicular to the major stress tensor in the area.	A 80 m long tunnel was built for a stress experiment in the floor. The Drill and Blast scheme was divided in two phase. The diameter was 5 m with flat floor in the first phase. In the second a rounded floor with a height of about 2 m was excavated as a bench. The orientation was close to perpendicular to the major stress tensor in the area.	A. Drill-and-blast by pilot and slash, 11mm Gurit c/c 30 cm in the contour holes, advance 3 m per round. B. Drill and blast, area ~25 m^2 advance rate 3.6 m per round. Excavation was done by pilot and slash. Charge in contour hole ~0.3 kg/m, except for the floor.

Issue Site (Tunnel)	Access ramp	ZEDEX	TASQ	TASQ	Sweden, Stripa Mine
Main Experiment and measuring items for EDZ (techniques) 1: geological observation, 2: geophysical measurement, 3: mechanical measurement, 4: hydraulic test, 5: laboratory test, 6: others. Effects that are considered: [T: thermal, H: hydraulic, M: mechanical, C: chemical]	1 2 3 Vibration measurement 4 Hydraulic conductivity (Single and double packer system) 5 Frequency of microclacks (Optical examination). The depth of damaged zone (AE/Kaiser effect in uniaxial compressive test) [M, H]	1 2 3 Vibration measurement 4 Hydraulic conductivity (Single and double packer system) 5 Frequency of microclacks (Optical examination). The depth of damaged zone (AE/Kaiser effect in uniaxial compressive test) [M, H]	1 Observed damage in core in the floor. Cut-outs in the wall and floor, fracture orientation and origin 2 3 Vibration measurement 4 5	1 Cut-outs in the wall fracture pattern used in modelling of development over time. Laser scanning of tunnel geometry drill and blast outbreak and fracture influence on outbreak 2 Seismic investigation in bore holes 3 4 5 Uniaxial compressive test with different saline porewaters [M, H]	A. 4 Hydraulic conductivity (Macro-permeability Experiment) [H] B. 4 Groundwater inflow [H]
Major results with respect to excavation effects	– The precision of drilling and local geological conditions can be as important as charging of contour holes. – Critical vibration velocity can be used to define the limit between damaged and undamaged rock. – In practical blasting, the damage zone in 0.22–0.93 m in the wall and 1.04–1.66 m in the floor. – The recorded conductivities after the blasting (10^{-8}–10^{-6} m/sec) were somewhat lower than that before the blasting (10^{-9}–10^{-7} m/sec).	– The precision of drilling and local geological conditions can be as important as charging of contour holes. – Critical vibration velocity can be used to define the limit between damaged and undamaged rock. – In practical blasting, the damage zone in 0.22–0.93 m in the wall and 1.04–1.66 m in the floor. – The recorded conductivities after the blasting (10^{-8}–10^{-6} m/sec) were somewhat lower than that before the blasting (10^{-9}–10^{-7} m/sec).		– A scheme for controlling the resulting precision of drilling and effect of geological conditions on overbreak using laser scanning.	A. The SCV experiment showed inflow to the drift to be a factor 3–7 less than expected. B. Using back calculation of measurements for the BMT site, the following results are stated: – The blast-damaged zone with 0.5 m thick and with 3 orders higher hydraulic conductivity than the undisturbed rock (~ 3–9×10^{-11} m/s). – The 2-m-thick stress-disturbed zone has axial conductivity one order higher, and radial hydraulic conductivity has the same order of conductivity as the undisturbed rock.

Appendix B

Overview mapping of drillcores KQ0048G01 and KQ0055A01

Borehole length (cm)		Alpha angle (degree)	Mineral	Comment
Start	End			
KQ0048G01				
0	0	85	Ep	rough surface
2,5	2,5	85	FeOH	
5	5	80		No mineral, fresh rough surface
9	9	75		Artificial
15	15	75	Ca	
27	74	45		Brittle-ductile shear zone
74	115			Sealed network
42	42	85		No mineral, fresh rough surface
50	50	90	Chl	Probable brake of a sealed fracture
94	94	65	Chl, Ca	
99	99	80	Ep	
137	137	80	Chl	
153	153	90		Mechanically eroded
180	180	75	Ca	Probable brake of a sealed fracture
209	209	80	Ca	Probable brake of a sealed fracture
244	244	85	Chl, Ca	Probable brake of a sealed fracture
282	282	90		No mineral, fresh rough surface
303	303	85		No mineral, fresh rough surface
335	335	60		No mineral, fresh rough surface
392	392	80		No mineral, fresh rough surface
419	419	70	Chl	
458	458	55	Chl, Ca	
485	485	60		No mineral, fresh rough surface
512	512	25	Chl	Probable brake of a sealed fracture
577	577	60	Chl	End of core
KQ0055A01				
0,1	0,1			Broken fracture
0,25	0,25			Broken fracture
0,4	0,4			Broken fracture
0,55	0,55			Broken fracture
0,5	0,75			Brittle-ductile shear zone, mylonite and protomylonite
0,75	0,75			Broken fracture
0,9	0,9			Broken fracture
1	1			Broken fracture
1,1	1,1			Broken fracture
1,3	1,3			Broken fracture
1,35	1,35			Broken fracture
1,5	1,5			Broken fracture

Appendix C

Sensitivity analysis for the as-planned tunnel shape, difference in Young's modulus and magnitude and trend of sigma 1

Sensitivity analysis. Cross section plots showing the projection of the principal stress tensor (color by magnitude of Sigma 1) for the as-planned tunnel shape without fractures and planar blasting round faces; Young's modulus (45 GPa, 55 GPa and 65 GPa), magnitude of Sigma 1 (25 MPa and 30 MPa) and trend of Sigma 1 (310°, 316° and 322°) for TASQ tunnel sections 46–51.

Section 46

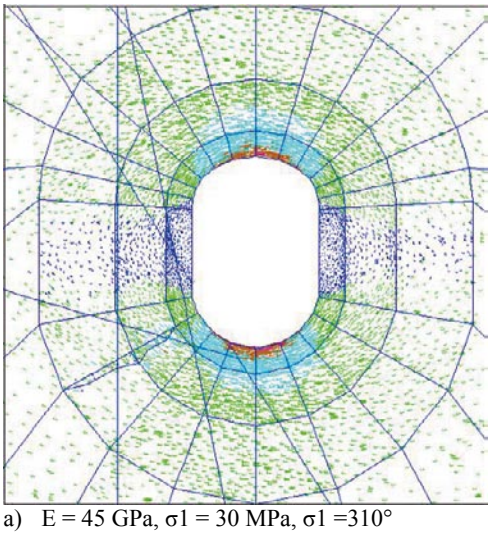

a) E = 45 GPa, σ1 = 30 MPa, σ1 =310°
Max compressive stress = 101.9 MPa

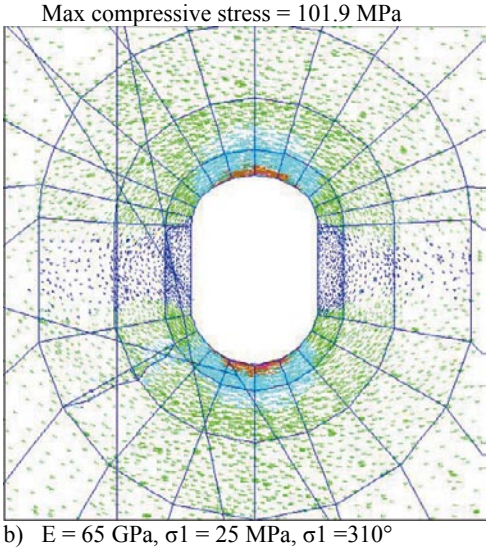

b) E = 65 GPa, σ1 = 25 MPa, σ1 =310°
Max compressive stress = 101.0 MPa

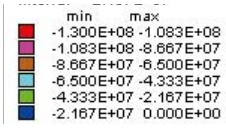

Figure C-1. *Cross section plots showing the projection of the principal stress tensor (color by magnitude of Sigma 1) for the as-planned tunnel shape without fractures and planar blasting round faces in section 46.*

Section 46

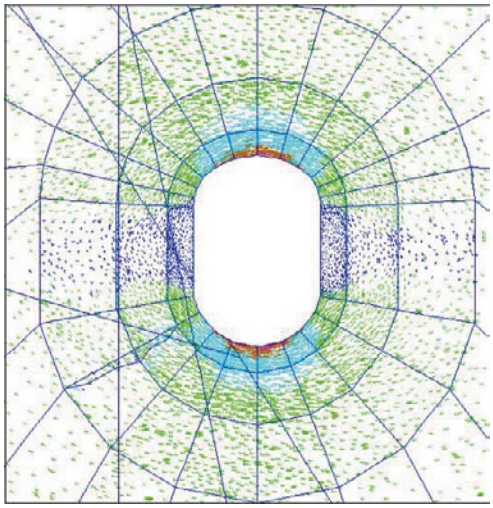

a) E = 55 GPa, σ1 = 30 MPa, σ1 =310°
Max compressive stress = 101.0 MPa

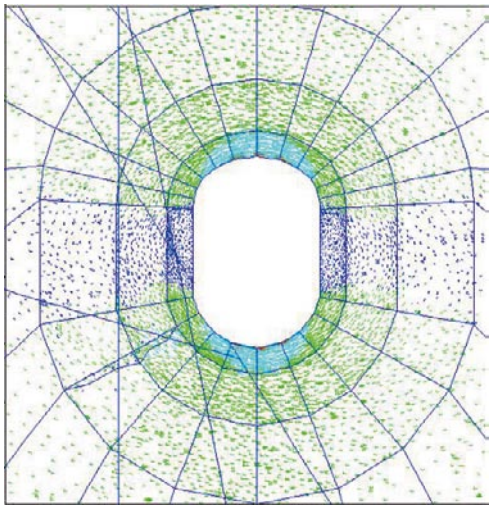

b) E = 55 GPa, σ1 = 25 MPa, σ1 = 310°
Max compressive stress = 82.87 MPa

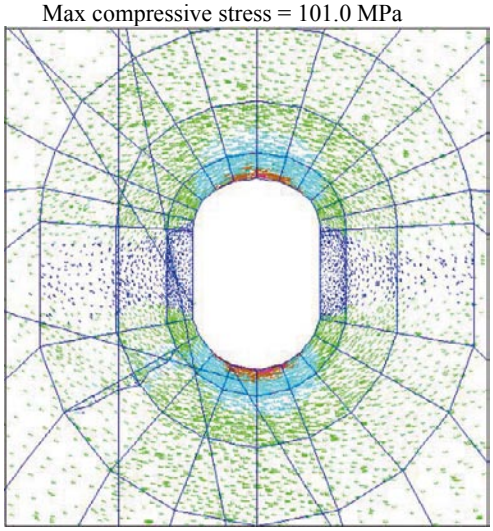

c) E = 55 GPa, σ1 = 30 MPa, σ1 = 316°
Max compressive stress = 101.9 MPa

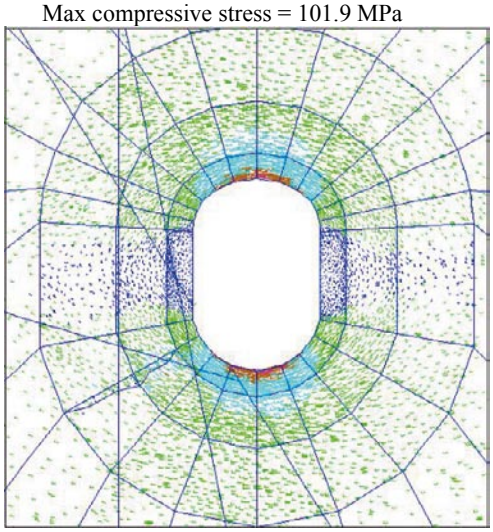

d) E = 55 GPa, σ1 = 30 MPa, σ1 = 322°
Max compressive stress = 101.1 MPa

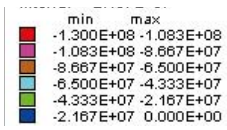

Figure C-2. *Cross section plots showing the projection of the principal stress tensor (color by magnitude of Sigma 1) for the as-planned tunnel shape without fractures and planar blasting round faces in section 46.*

Section 47

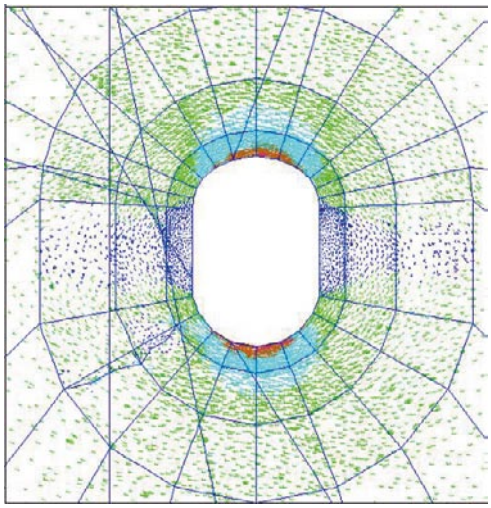

a) E = 45 GPa, σ1 = 30 MPa, σ1 =310°
Max compressive stress = 99.64 MPa

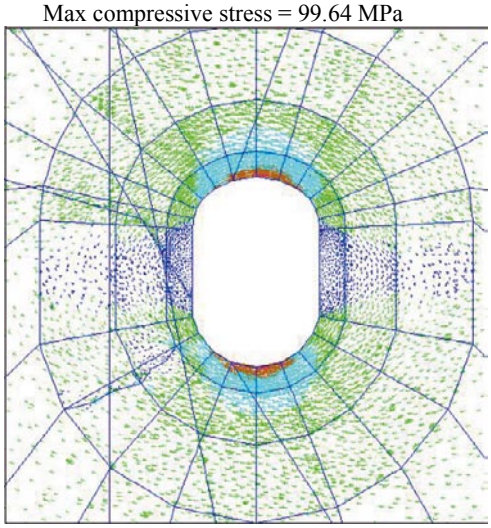

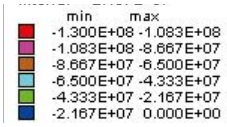

b) E = 65 GPa, σ1 = 25 MPa, σ1 =310°
Max compressive stress = 98.76 MPa

Figure C-3. *Cross section plots showing the projection of the principal stress tensor (color by magnitude of Sigma 1) for the as-planned tunnel shape without fractures and planar blasting round faces in section 47.*

Section 47

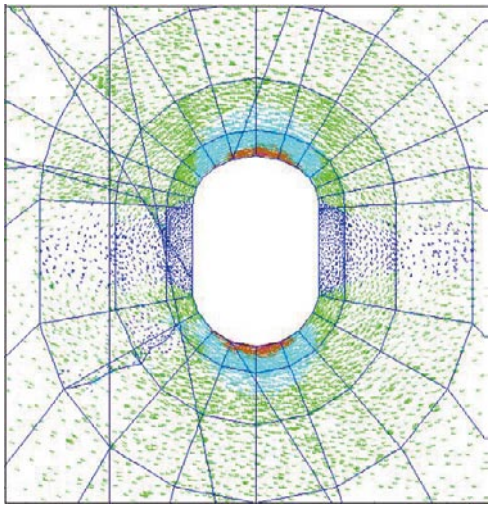

a) E = 55 GPa, σ1 = 30 MPa, σ1 =310°
Max compressive stress = 98.76 MPa

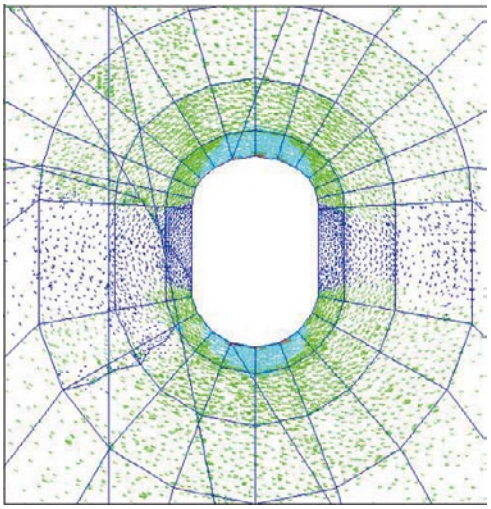

b) E = 55 GPa, σ1 = 25 MPa, σ1 = 310°
Max compressive stress = 79.76 MPa

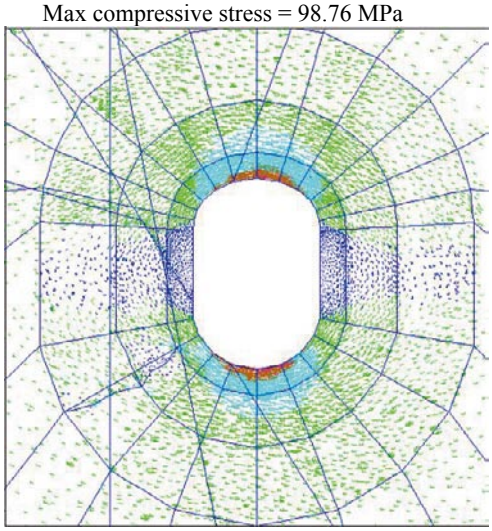

c) E = 55 GPa, σ1 = 30 MPa, σ1 = 316°
Max compressive stress = 99.65 MPa

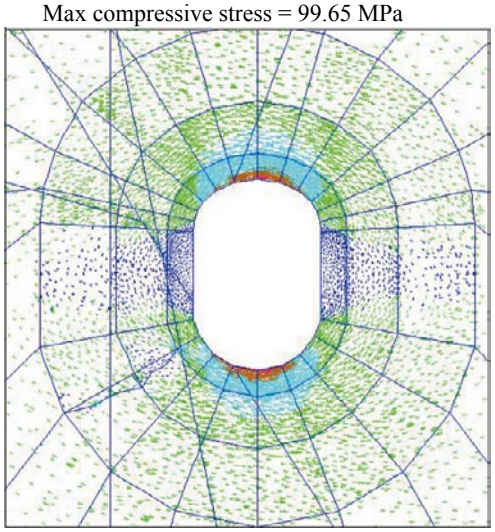

d) E = 55 GPa, σ1 = 30 MPa, σ1 = 322°
Max compressive stress = 98.95 MPa

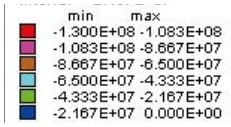

Figure C-4. *Cross section plots showing the projection of the principal stress tensor (color by magnitude of Sigma 1) for the as-planned tunnel shape without fractures and planar blasting round faces in section 47.*

Section 48

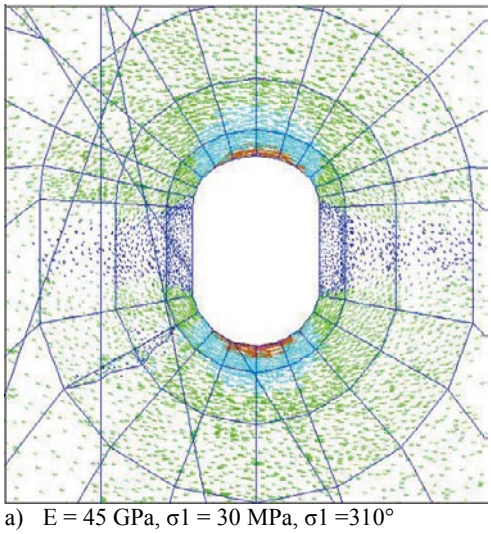

a) E = 45 GPa, σ1 = 30 MPa, σ1 =310°
Max compressive stress = 99.19 MPa

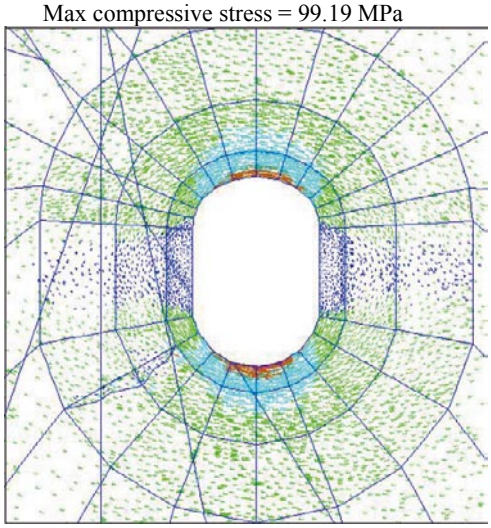

b) E = 65 GPa, σ1 = 25 MPa, σ1 =310°
Max compressive stress = 98.33 MPa

Figure C-5. *Cross section plots showing the projection of the principal stress tensor (color by magnitude of Sigma 1) for the as-planned tunnel shape without fractures and planar blasting round faces in section 48.*

Section 48

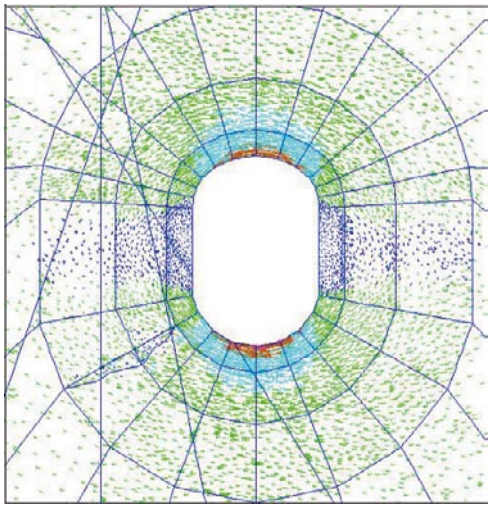

a) E = 55 GPa, σ1 = 30 MPa, σ1 =310°
Max compressive stress = 98.35 MPa

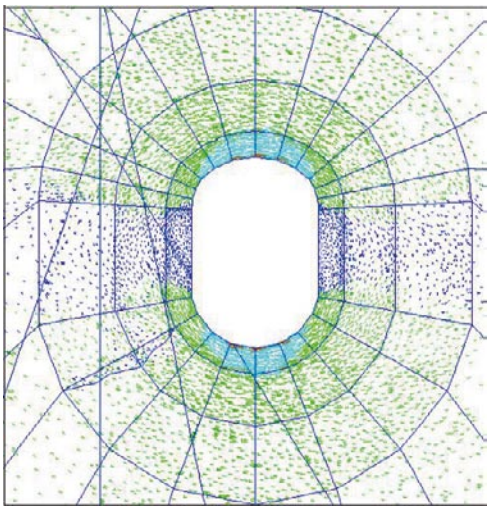

b) E = 55 GPa, σ1 = 25 MPa, σ1 = 310°
Max compressive stress = 79.47 MPa

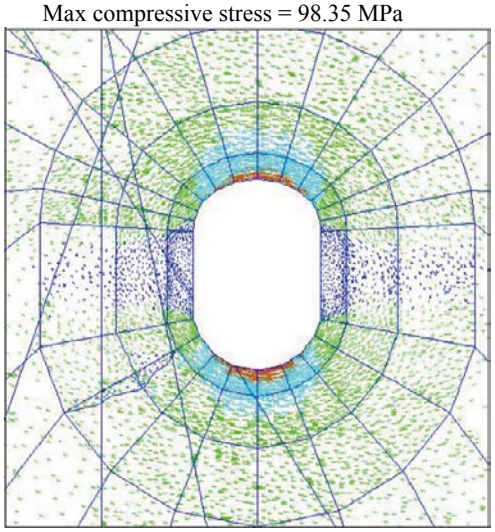

c) E = 55 GPa, σ1 = 30 MPa, σ1 = 316°
Max compressive stress = 99.19 MPa

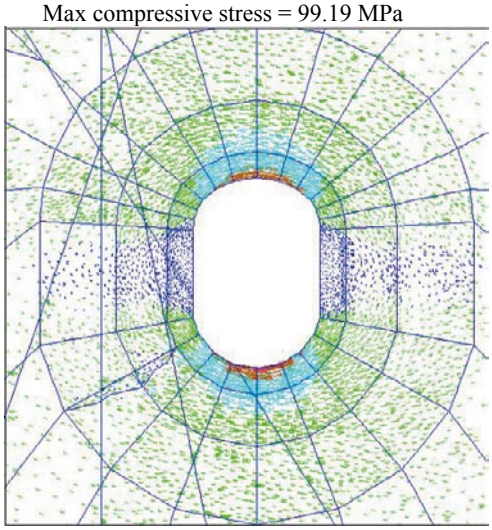

d) E = 55 GPa, σ1 = 30 MPa, σ1 = 322°
Max compressive stress = 98.49 MPa

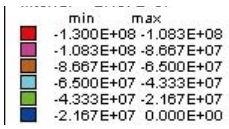

Figure C-6. *Cross section plots showing the projection of the principal stress tensor (color by magnitude of Sigma 1) for the as-planned tunnel shape without fractures and planar blasting round faces in section 48.*

Section 49

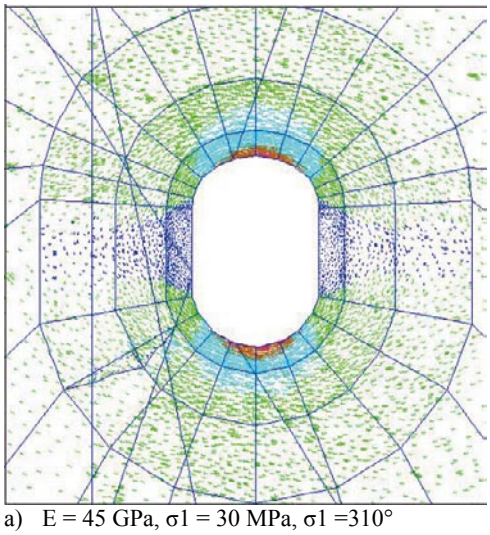

a) E = 45 GPa, σ1 = 30 MPa, σ1 =310°
Max compressive stress = 100.0 MPa

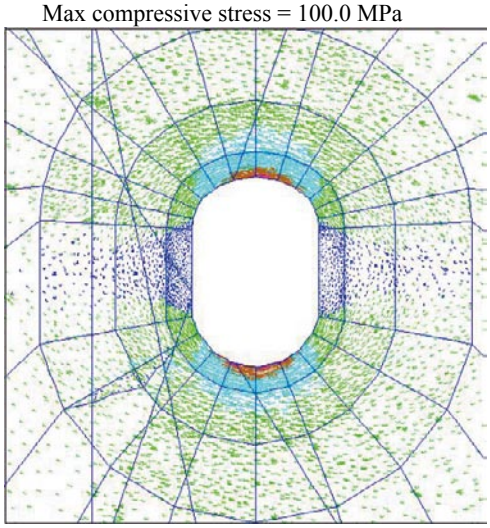

b) E = 65 GPa, σ1 = 25 MPa, σ1 =310°
Max compressive stress = 99.17 MPa

Figure C-7. *Cross section plots showing the projection of the principal stress tensor (color by magnitude of Sigma 1) for the as-planned tunnel shape without fractures and planar blasting round faces in section 49.*

Section 49

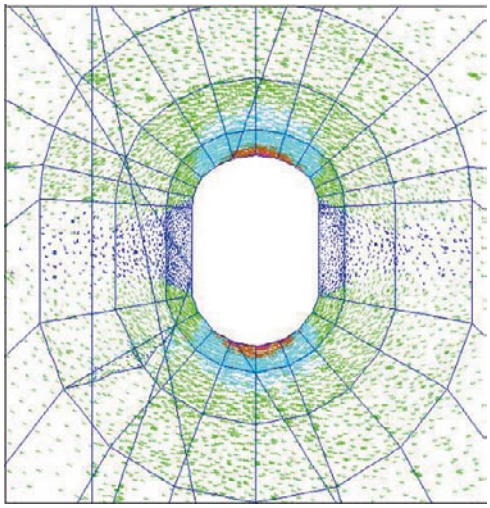

a) E = 55 GPa, σ1 = 30 MPa, σ1 =310°
Max compressive stress = 99.19 MPa

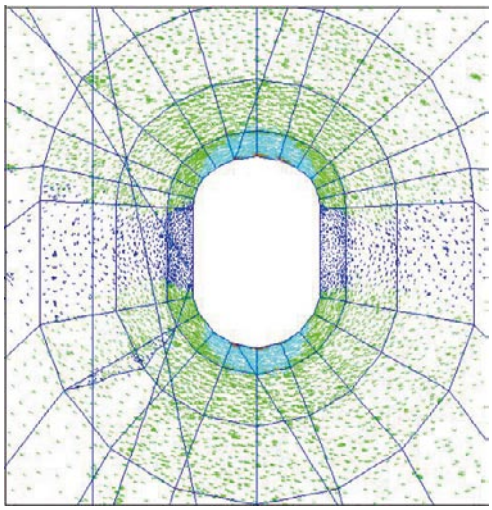

b) E = 55 GPa, σ1 = 25 MPa, σ1 = 310°
Max compressive stress = 80.12 MPa

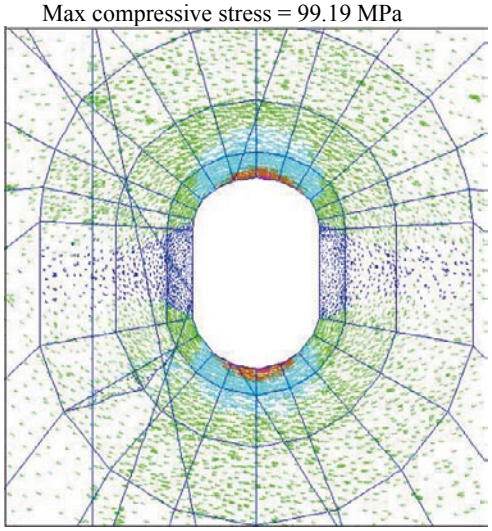

c) E = 55 GPa, σ1 = 30 MPa, σ1 = 316°
Max compressive stress = 100.0 MPa

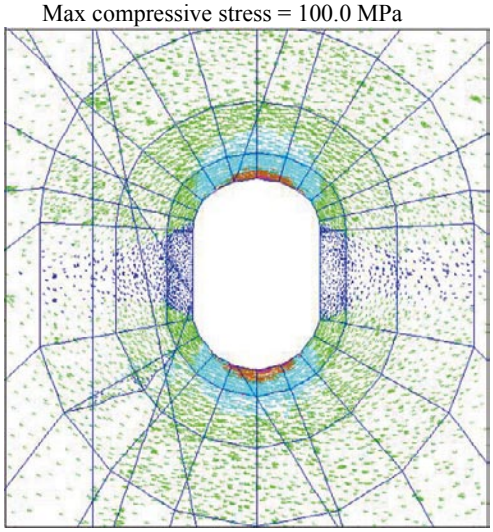

d) E = 55 GPa, σ1 = 30 MPa, σ1 = 322°
Max compressive stress = 99.23 MPa

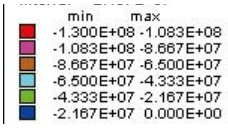

Figure C-8. *Cross section plots showing the projection of the principal stress tensor (color by magnitude of Sigma 1) for the as-planned tunnel shape without fractures and planar blasting round faces in section 49.*

Section 50

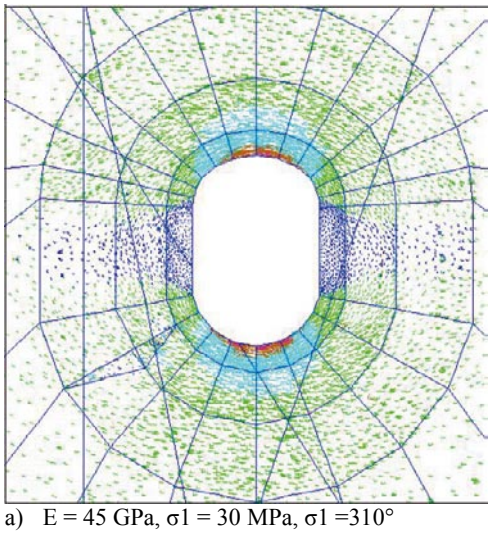

a) E = 45 GPa, σ1 = 30 MPa, σ1 =310°
Max compressive stress = 101.5 MPa

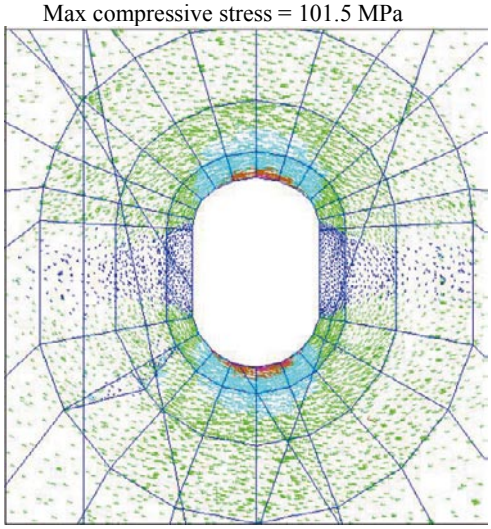

b) E = 65 GPa, σ1 = 25 MPa, σ1 =310°
Max compressive stress = 100.6 MPa

Figure C-9. *Cross section plots showing the projection of the principal stress tensor (color by magnitude of Sigma 1) for the as-planned tunnel shape without fractures and planar blasting round faces in section 50.*

Section 50

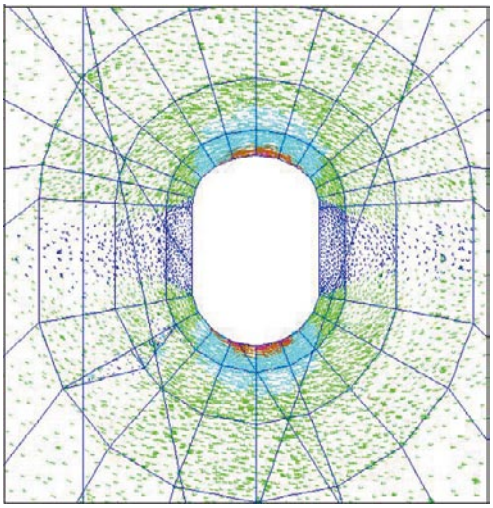

a) E = 55 GPa, σ1 = 30 MPa, σ1 =310°
Max compressive stress = 100.6 MPa

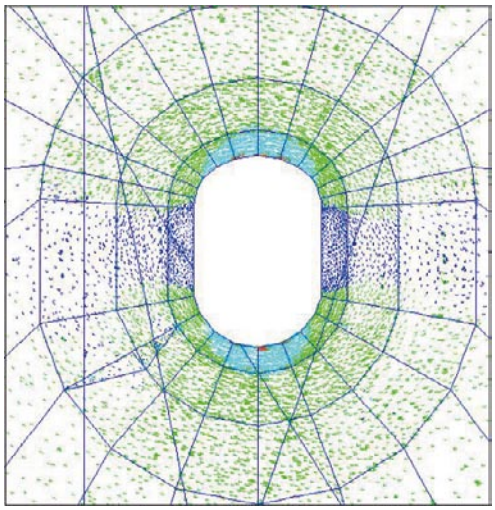

b) E = 55 GPa, σ1 = 25 MPa, σ1 = 310°
Max compressive stress = 81.22 MPa

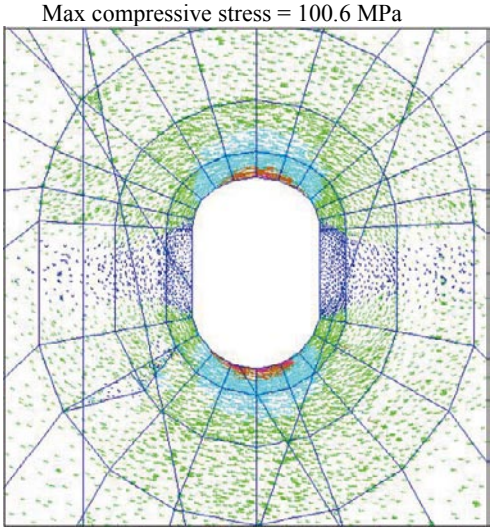

c) E = 55 GPa, σ1 = 30 MPa, σ1 = 316°
Max compressive stress = 101.4 MPa

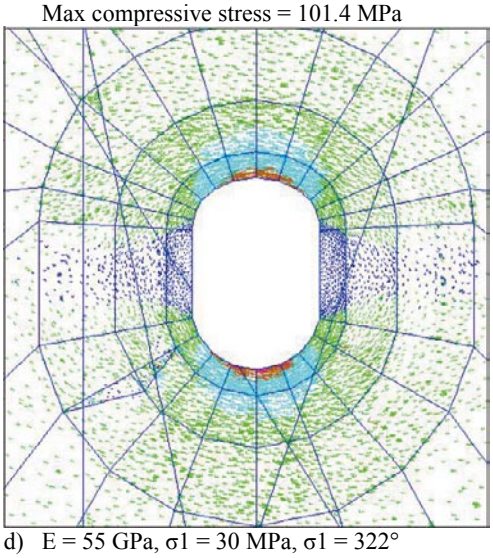

d) E = 55 GPa, σ1 = 30 MPa, σ1 = 322°
Max compressive stress = 100.6 MPa

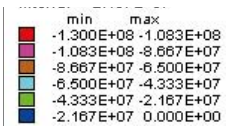

Figure C-10. *Cross section plots showing the projection of the principal stress tensor (color by magnitude of Sigma 1) for the as-planned tunnel shape without fractures and planar blasting round faces in section 50.*

Section 51

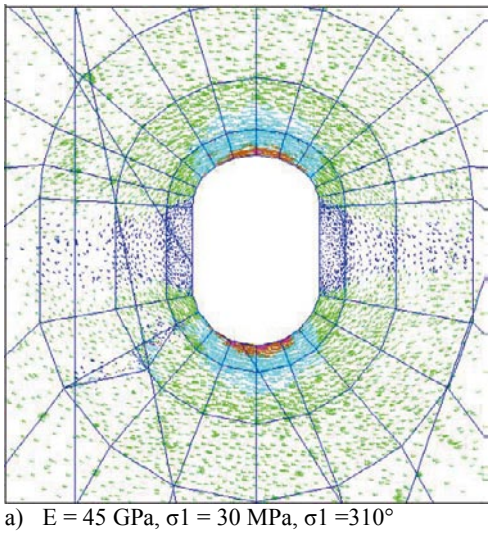

a) E = 45 GPa, σ1 = 30 MPa, σ1 =310°
Max compressive stress = 102.7 MPa

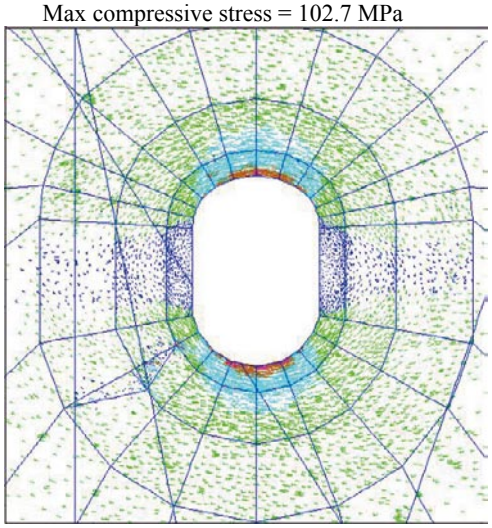

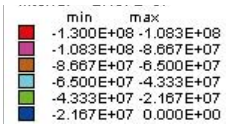

b) E = 65 GPa, σ1 = 25 MPa, σ1 =310°
Max compressive stress = 101.8 MPa

Figure C-11. *Cross section plots showing the projection of the principal stress tensor (color by magnitude of Sigma 1) for the as-planned tunnel shape without fractures and planar blasting round faces in section 51.*

Section 51

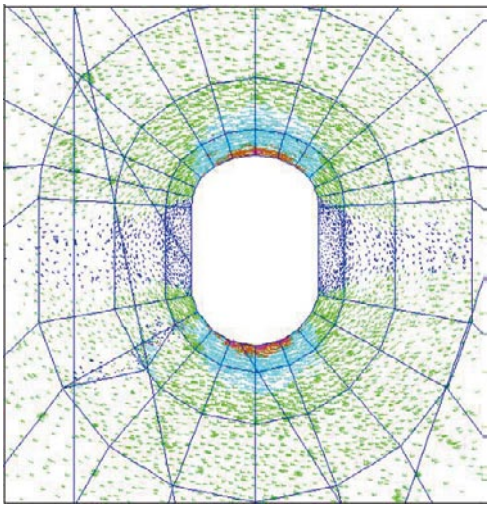

a) E = 55 GPa, σ1 = 30 MPa, σ1 =310°
Max compressive stress = 101.8 MPa

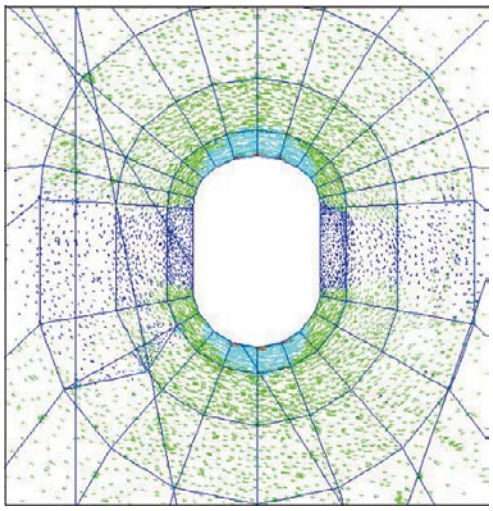

b) E = 55 GPa, σ1 = 25 MPa, σ1 = 310°
Max compressive stress = 86.83 MPa

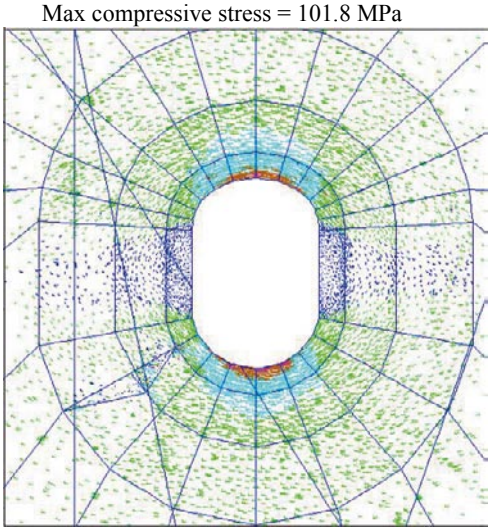

c) E = 55 GPa, σ1 = 30 MPa, σ1 = 316°
Max compressive stress = 102.6 MPa

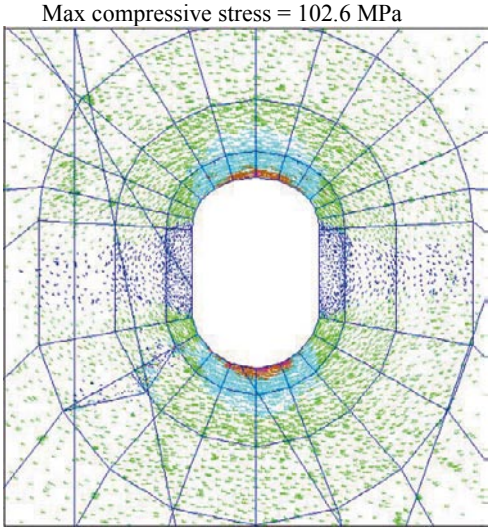

d) E = 55 GPa, σ1 = 30 MPa, σ1 = 322°
Max compressive stress = 101.8 MPa

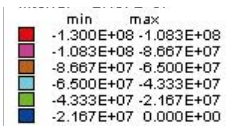

Figure C-12. *Cross section plots showing the projection of the principal stress tensor (color by magnitude of Sigma 1) for the as-planned tunnel shape without fractures and planar blasting round faces in section 51.*

Appendix D

Sensitivity analysis for the as-built tunnel shape, difference in Young's modulus and magnitude and trend of sigma 1

Sensitivity analysis. Cross section plots showing the projection of the principal stress tensor (color by magnitude of Sigma 1) for the as-built tunnel shape without fractures and planar blasting round faces; Young's modulus (45 GPa, 50 GPa, 55 GPa and 65 GPa), magnitude of Sigma 1 (25 MPa and 30 MPa) and trend of Sigma 1 (310°, 316° and 322°) for TASQ tunnel sections 46–51.

Section 46

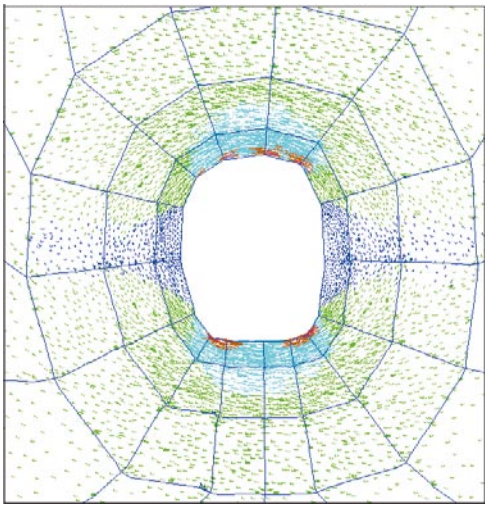

a) E = 45 GPa, σ1 = 30 MPa, σ1 =316°
Max compressive stress = -127.7 MPa

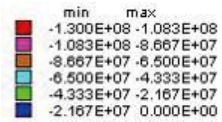

Figure D-1. *Cross section plots showing the projection of the principal stress tensor (color by magnitude of Sigma 1) for the as-built tunnel shape without fractures and planar blasting round faces in section 46.*

Section 46

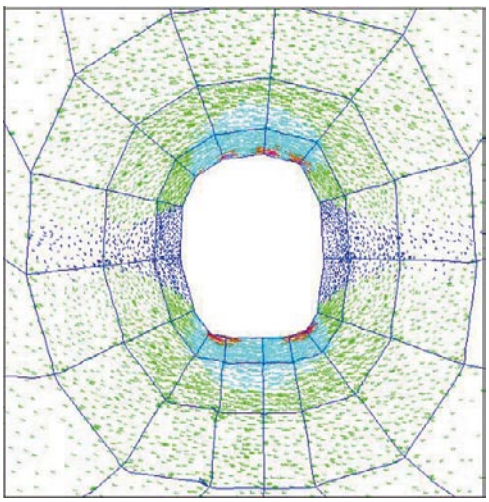

b) E = 50 GPa, σ1 = 30 MPa, σ1 =310°
Max compressive stress = 126.8 MPa

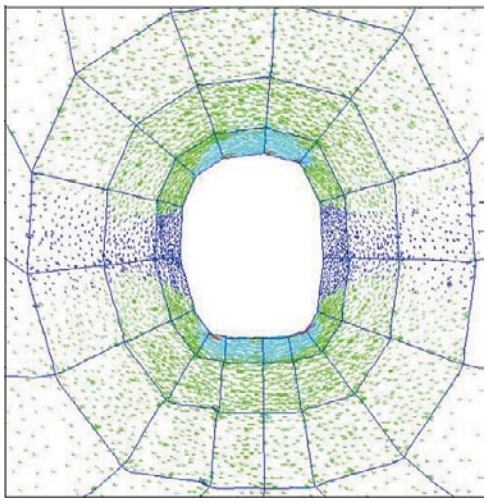

c) E = 50 GPa, σ1 = 25 MPa, σ1 = 310°
Max compressive stress = 107.4 MPa

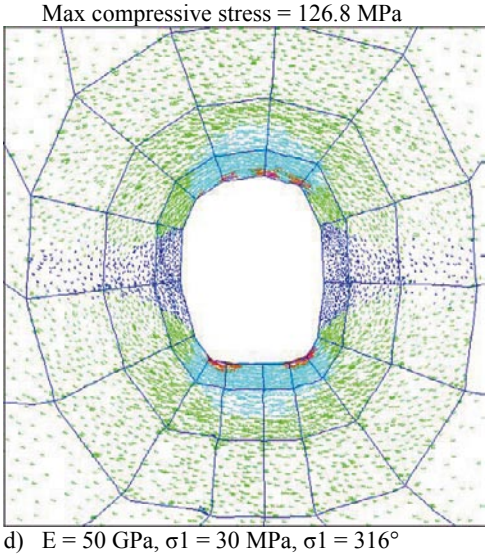

d) E = 50 GPa, σ1 = 30 MPa, σ1 = 316°
Max compressive stress = 127.7 MPa

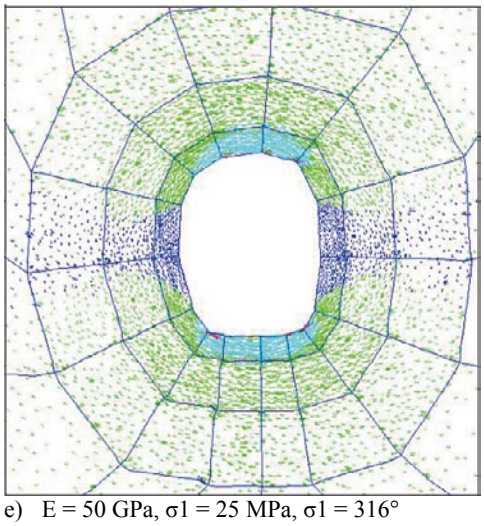

e) E = 50 GPa, σ1 = 25 MPa, σ1 = 316°
Max compressive stress = 108.1 MPa

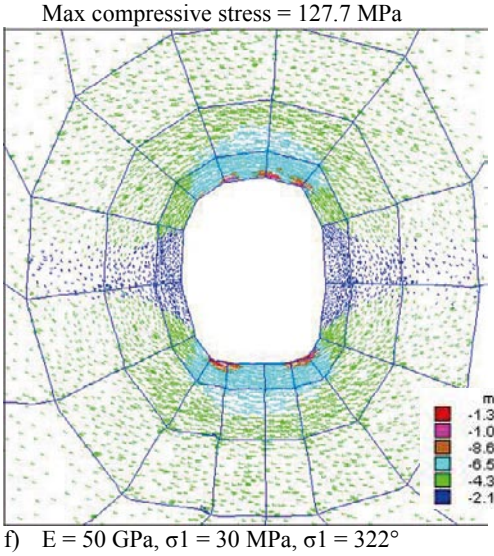

f) E = 50 GPa, σ1 = 30 MPa, σ1 = 322°
Max compressive stress = 127.0 MPa

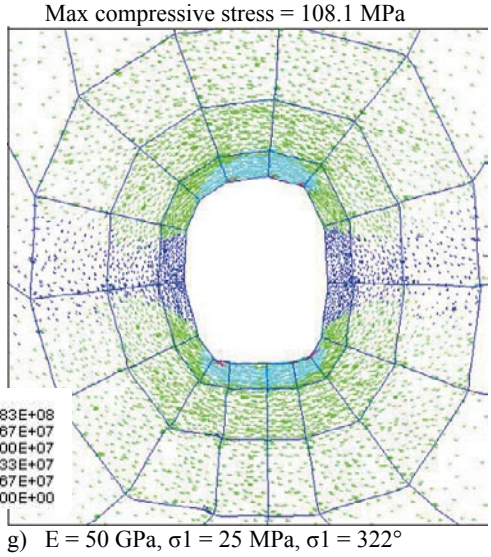

g) E = 50 GPa, σ1 = 25 MPa, σ1 = 322°
Max compressive stress = 107.6 MPa

Figure D-2. *Cross section plots showing the projection of the principal stress tensor (color by magnitude of Sigma 1) for the as-built tunnel shape without fractures and planar blasting round faces in section 46.*

Section 46

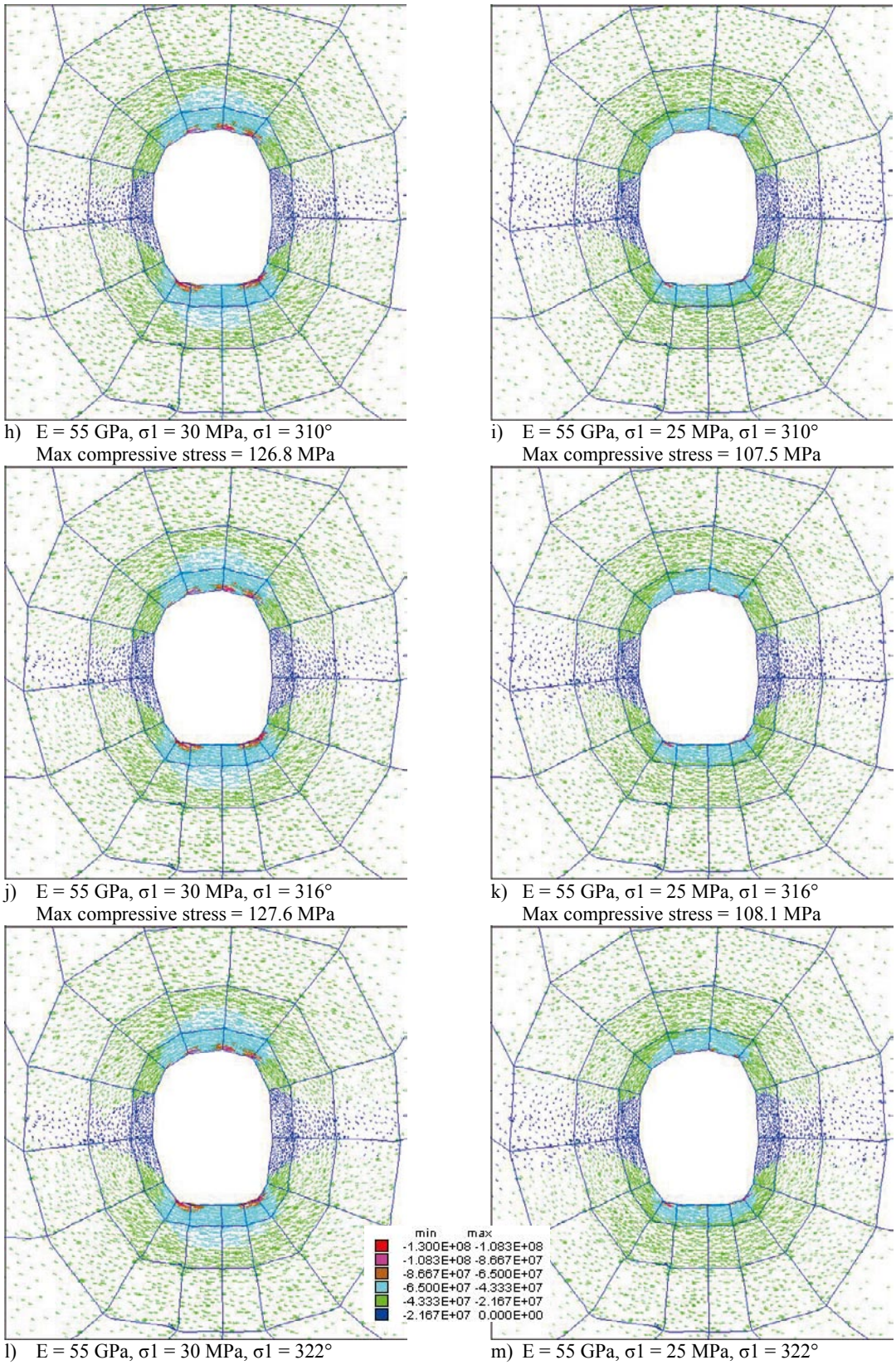

h) E = 55 GPa, σ1 = 30 MPa, σ1 = 310°
Max compressive stress = 126.8 MPa

i) E = 55 GPa, σ1 = 25 MPa, σ1 = 310°
Max compressive stress = 107.5 MPa

j) E = 55 GPa, σ1 = 30 MPa, σ1 = 316°
Max compressive stress = 127.6 MPa

k) E = 55 GPa, σ1 = 25 MPa, σ1 = 316°
Max compressive stress = 108.1 MPa

l) E = 55 GPa, σ1 = 30 MPa, σ1 = 322°
Max compressive stress = 126.9 MPa

m) E = 55 GPa, σ1 = 25 MPa, σ1 = 322°
Max compressive stress = 107.5 MPa

Figure D-3. *Cross section plots showing the projection of the principal stress tensor (color by magnitude of Sigma 1) for the as-built tunnel shape without fractures and planar blasting round faces in section 46.*

Section 46

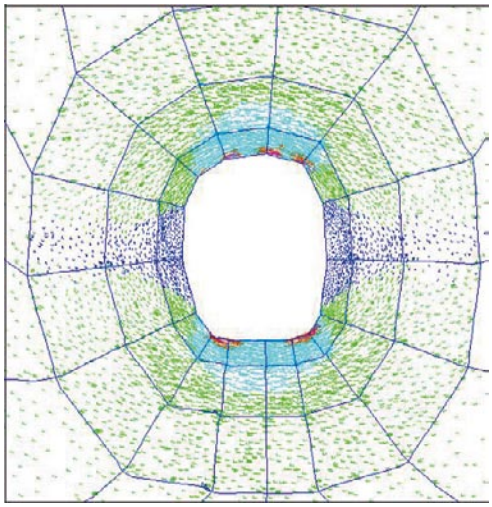

n) E = 65 GPa, σ1 = 30 MPa, σ1 = 310°
Max compressive stress = 126.7 MPa

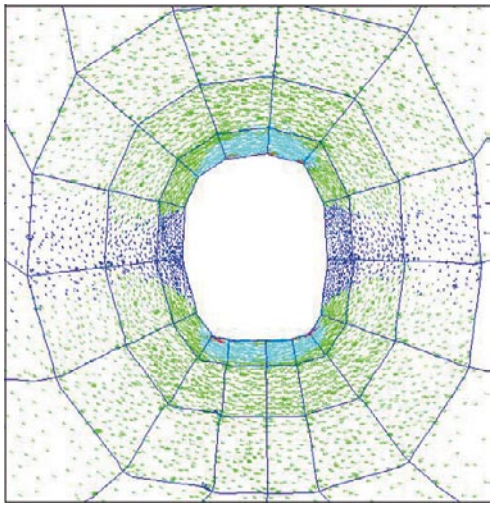

o) E = 65 GPa, σ1 = 25 MPa, σ1 = 310°
Max compressive stress = 107.4 MPa

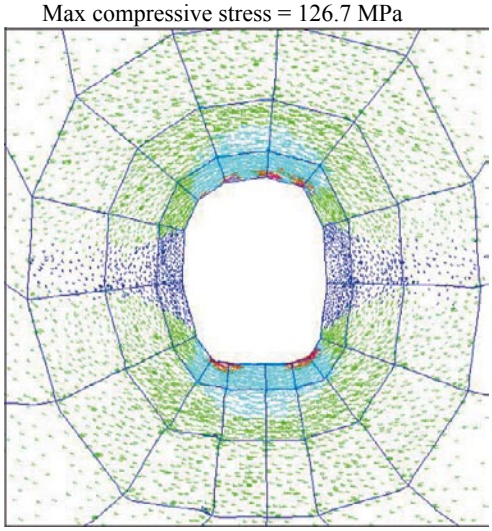

p) E = 65 GPa, σ1 = 30 MPa, σ1 = 316°
Max compressive stress = 127.6 MPa

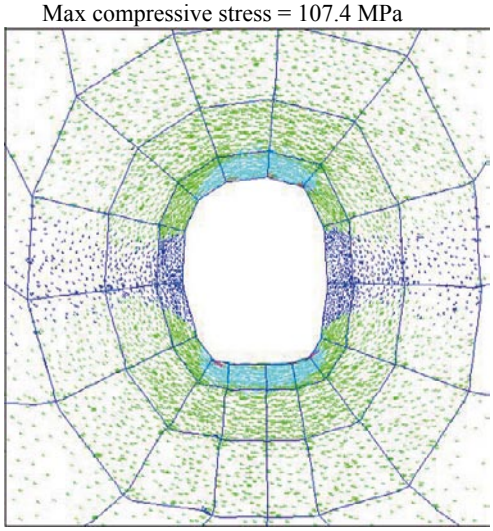

q) E = 65 GPa, σ1 = 25 MPa, σ1 = 316°
Max compressive stress = 108.0 MPa

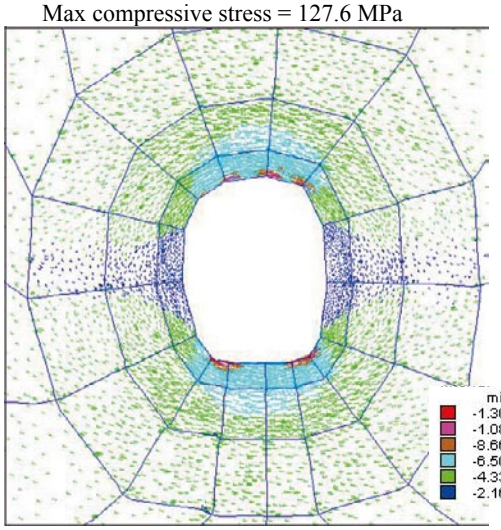

r) E = 65 GPa, σ1 = 30 MPa, σ1 = 322°
Max compressive stress = 126.9 MPa

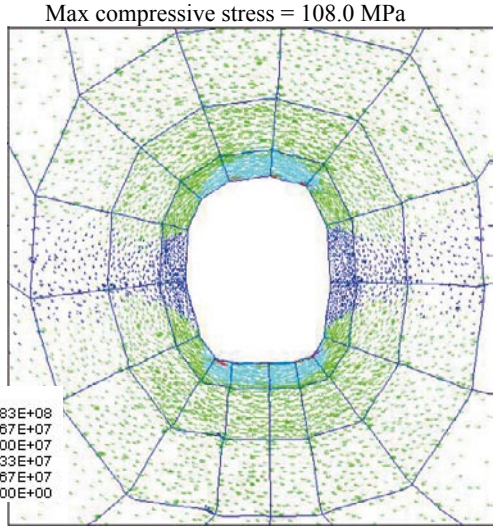

s) E = 65 GPa, σ1 = 25 MPa, σ1 = 322°
Max compressive stress = 107.5 MPa

Figure D-4. *Cross section plots showing the projection of the principal stress tensor (color by magnitude of Sigma 1) for the as-built tunnel shape without fractures and planar blasting round faces in section 46.*

Section 47

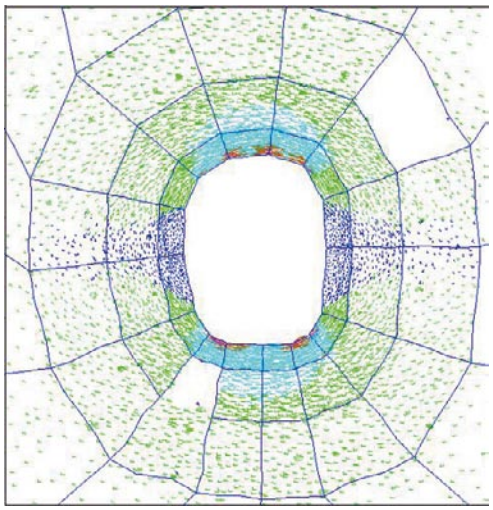

a) E = 45 GPa, σ1 = 30 MPa, σ1 =316°
Max compressive stress = 101.1 MPa

Figure D-5. *Cross section plots showing the projection of the principal stress tensor (color by magnitude of Sigma 1) for the as-built tunnel shape without fractures and planar blasting round faces in section 47.*

Section 47

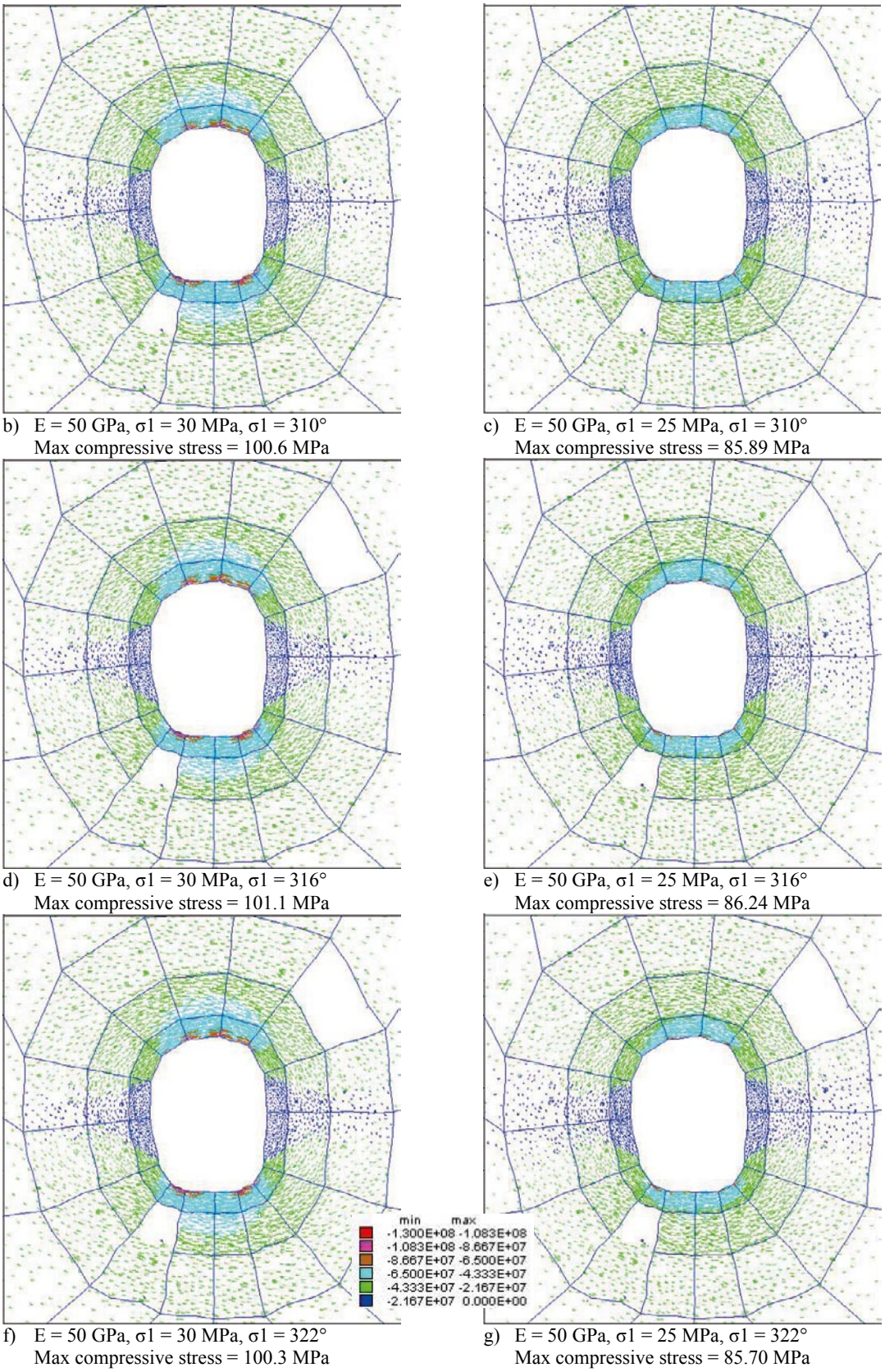

b) E = 50 GPa, σ1 = 30 MPa, σ1 = 310°
Max compressive stress = 100.6 MPa

c) E = 50 GPa, σ1 = 25 MPa, σ1 = 310°
Max compressive stress = 85.89 MPa

d) E = 50 GPa, σ1 = 30 MPa, σ1 = 316°
Max compressive stress = 101.1 MPa

e) E = 50 GPa, σ1 = 25 MPa, σ1 = 316°
Max compressive stress = 86.24 MPa

f) E = 50 GPa, σ1 = 30 MPa, σ1 = 322°
Max compressive stress = 100.3 MPa

g) E = 50 GPa, σ1 = 25 MPa, σ1 = 322°
Max compressive stress = 85.70 MPa

Figure D-6. *Cross section plots showing the projection of the principal stress tensor (color by magnitude of Sigma 1) for the as-built tunnel shape without fractures and planar blasting round faces in section 47.*

Section 47

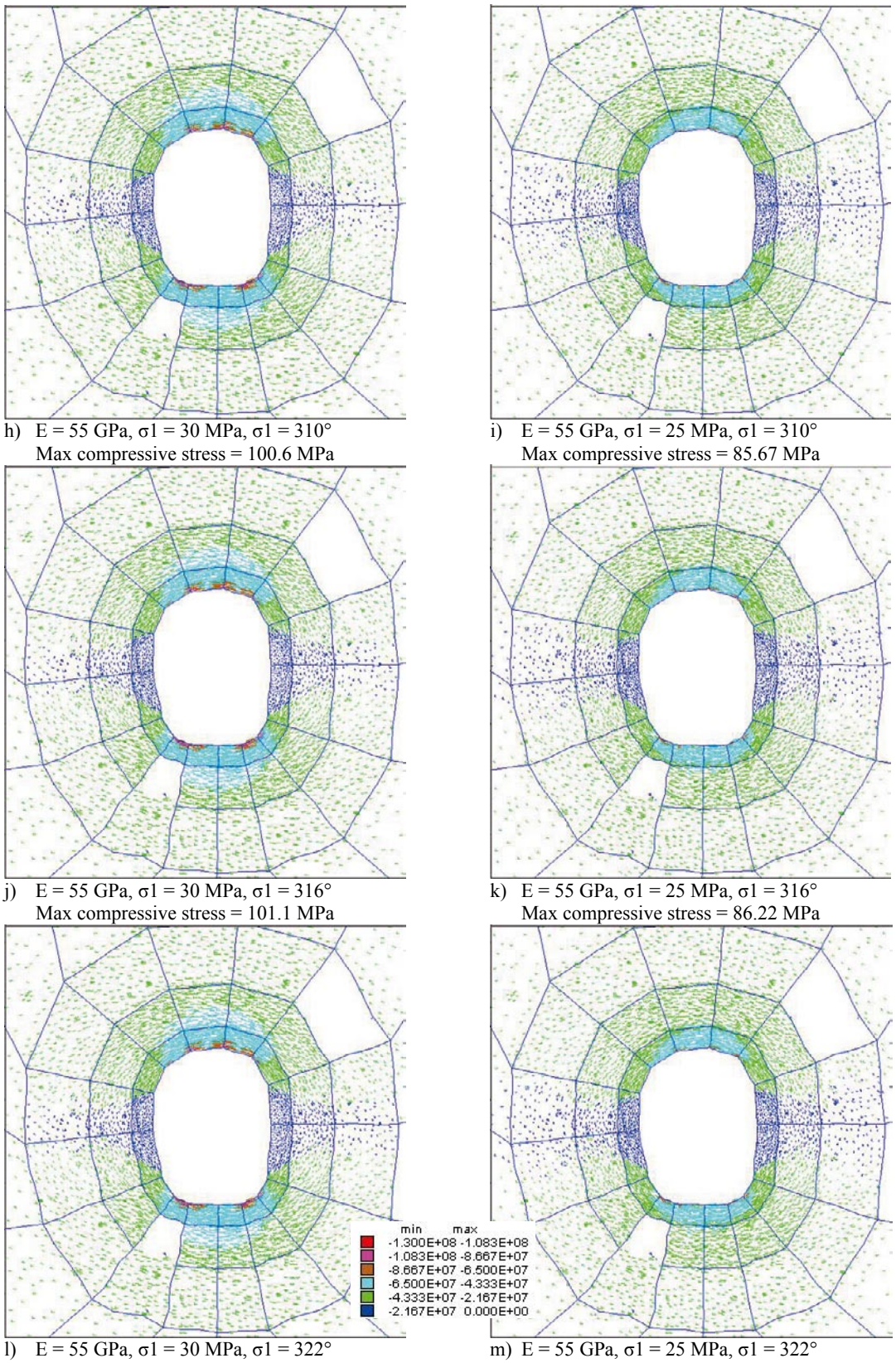

h) E = 55 GPa, σ1 = 30 MPa, σ1 = 310°
Max compressive stress = 100.6 MPa

i) E = 55 GPa, σ1 = 25 MPa, σ1 = 310°
Max compressive stress = 85.67 MPa

j) E = 55 GPa, σ1 = 30 MPa, σ1 = 316°
Max compressive stress = 101.1 MPa

k) E = 55 GPa, σ1 = 25 MPa, σ1 = 316°
Max compressive stress = 86.22 MPa

l) E = 55 GPa, σ1 = 30 MPa, σ1 = 322°
Max compressive stress = 100.3 MPa

m) E = 55 GPa, σ1 = 25 MPa, σ1 = 322°
Max compressive stress = 85.67 MPa

Figure D-7. *Cross section plots showing the projection of the principal stress tensor (color by magnitude of Sigma 1) for the as-built tunnel shape without fractures and planar blasting round faces in section 47.*

Section 47

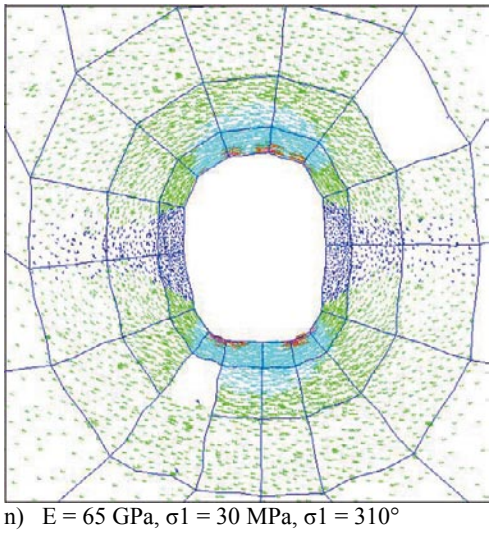

n) E = 65 GPa, σ1 = 30 MPa, σ1 = 310°
Max compressive stress = 100.6 MPa

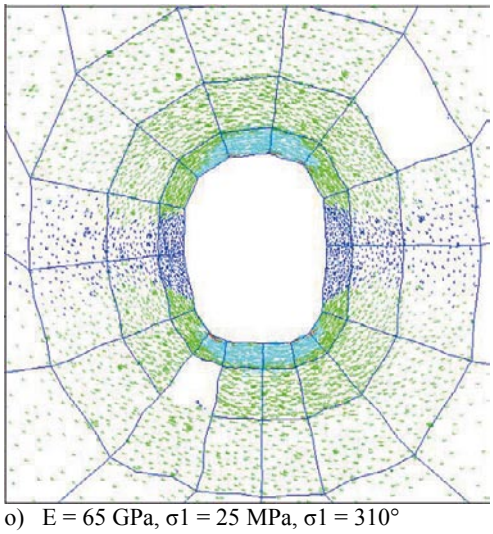

o) E = 65 GPa, σ1 = 25 MPa, σ1 = 310°
Max compressive stress = 85.86 MPa

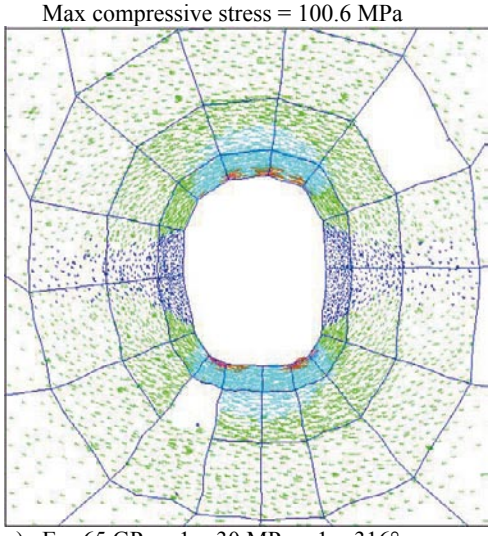

p) E = 65 GPa, σ1 = 30 MPa, σ1 = 316°
Max compressive stress = 101.0 MPa

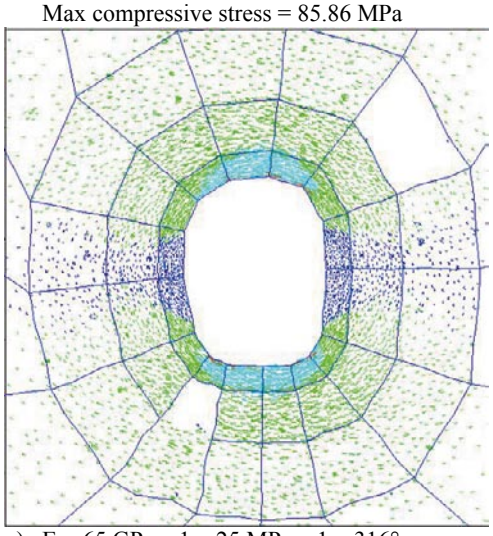

q) E = 65 GPa, σ1 = 25 MPa, σ1 = 316°
Max compressive stress = 86.19 MPa

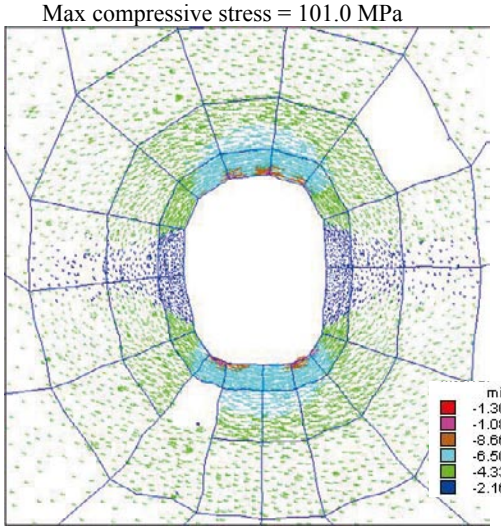

r) E = 65 GPa, σ1 = 30 MPa, σ1 = 322°
Max compressive stress = 100.3 MPa

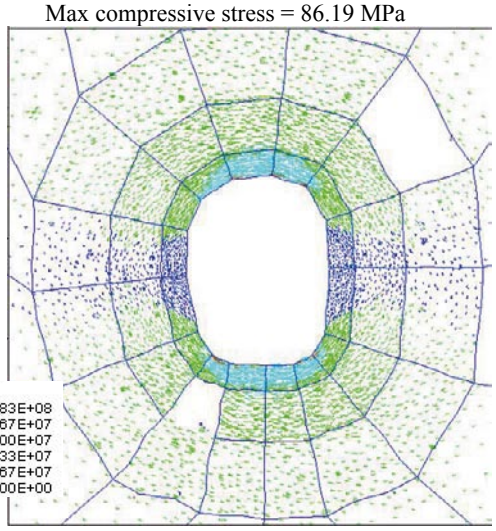

s) E = 65 GPa, σ1 = 25 MPa, σ1 = 322°
Max compressive stress = 85.66 MPa

Figure D-8. *Cross section plots showing the projection of the principal stress tensor (color by magnitude of Sigma 1) for the as-built tunnel shape without fractures and planar blasting round faces in section 47.*

Section 48

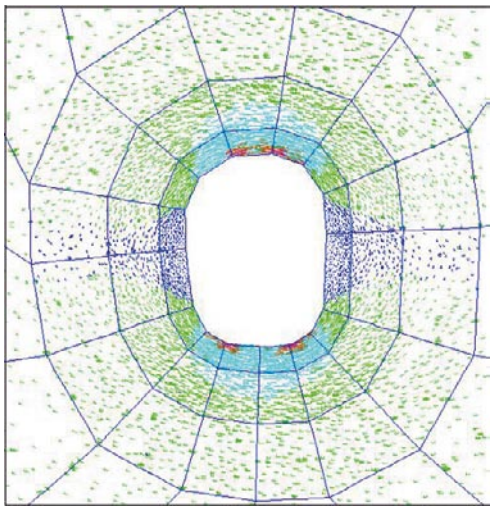

a) E = 45 GPa, σ1 = 30 MPa, σ1 =316°
Max compressive stress = 97.5 MPa

Figure D-9. *Cross section plots showing the projection of the principal stress tensor (color by magnitude of Sigma 1) for the as-built tunnel shape without fractures and planar blasting round faces in section 48.*

Section 48

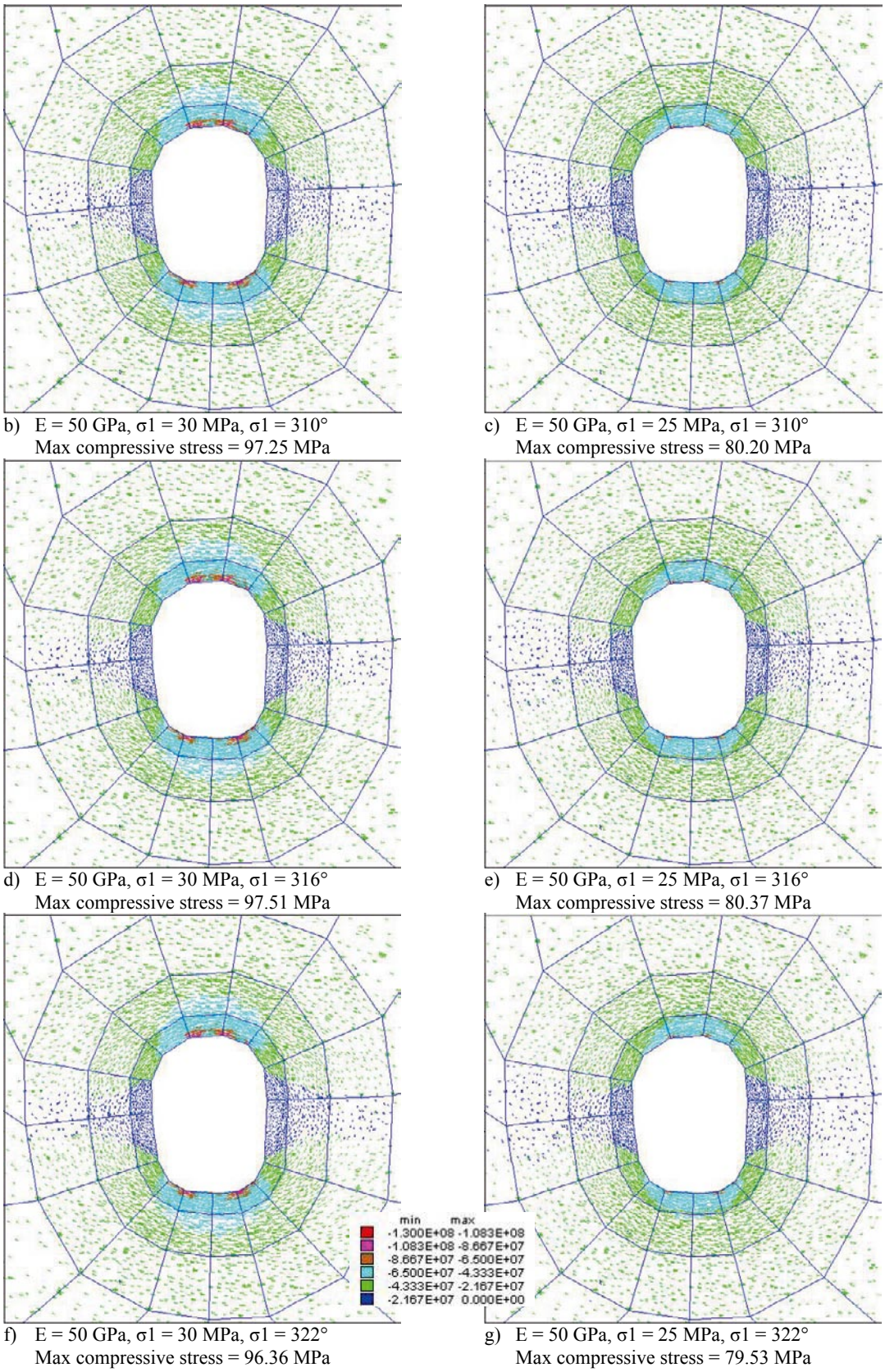

b) E = 50 GPa, σ1 = 30 MPa, σ1 = 310°
Max compressive stress = 97.25 MPa

c) E = 50 GPa, σ1 = 25 MPa, σ1 = 310°
Max compressive stress = 80.20 MPa

d) E = 50 GPa, σ1 = 30 MPa, σ1 = 316°
Max compressive stress = 97.51 MPa

e) E = 50 GPa, σ1 = 25 MPa, σ1 = 316°
Max compressive stress = 80.37 MPa

f) E = 50 GPa, σ1 = 30 MPa, σ1 = 322°
Max compressive stress = 96.36 MPa

g) E = 50 GPa, σ1 = 25 MPa, σ1 = 322°
Max compressive stress = 79.53 MPa

Figure D-10. *Cross section plots showing the projection of the principal stress tensor (color by magnitude of Sigma 1) for the as-built tunnel shape without fractures and planar blasting round faces in section 48.*

Section 48

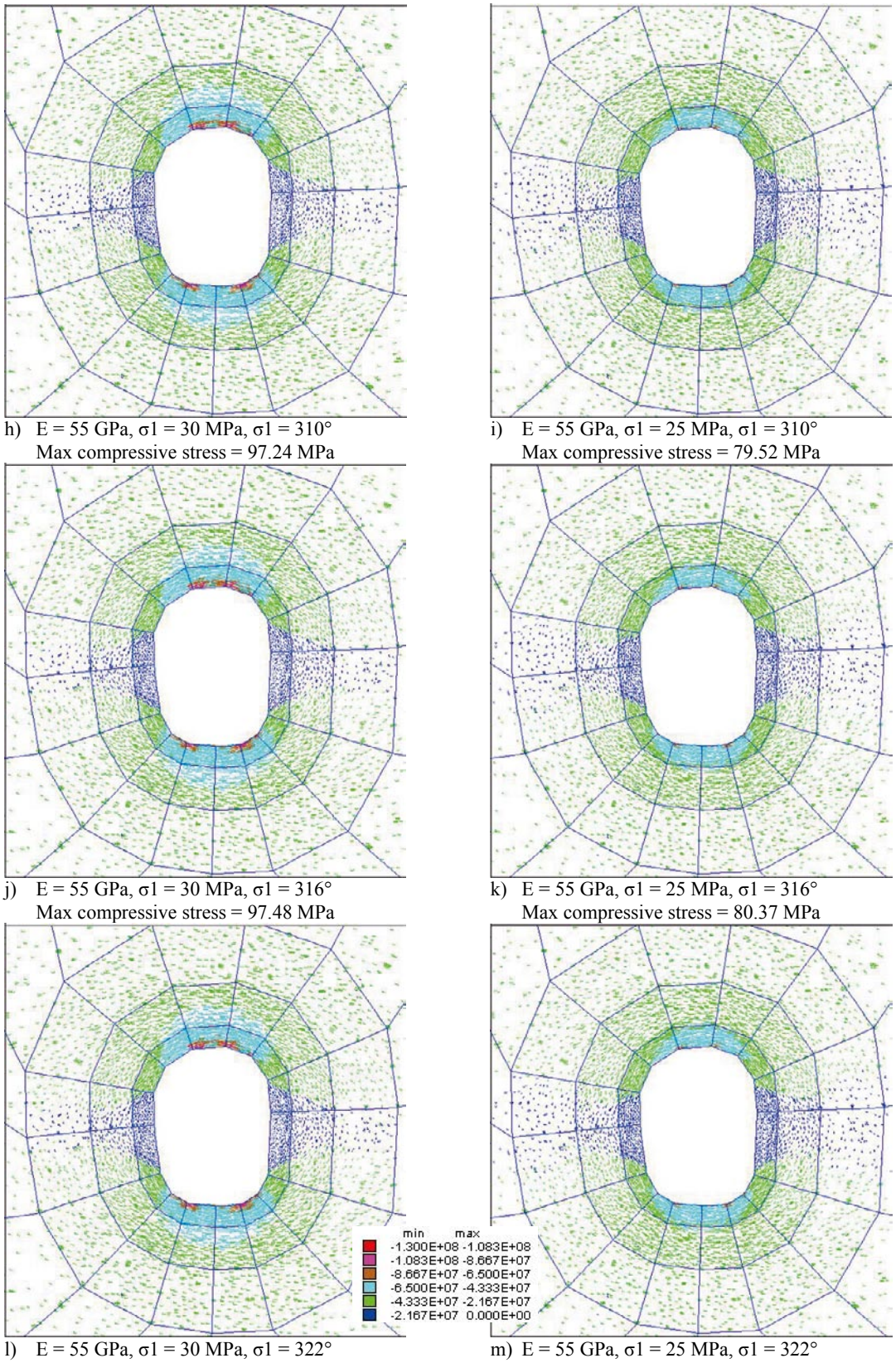

h) E = 55 GPa, σ1 = 30 MPa, σ1 = 310°
Max compressive stress = 97.24 MPa

i) E = 55 GPa, σ1 = 25 MPa, σ1 = 310°
Max compressive stress = 79.52 MPa

j) E = 55 GPa, σ1 = 30 MPa, σ1 = 316°
Max compressive stress = 97.48 MPa

k) E = 55 GPa, σ1 = 25 MPa, σ1 = 316°
Max compressive stress = 80.37 MPa

l) E = 55 GPa, σ1 = 30 MPa, σ1 = 322°
Max compressive stress = 96.34 MPa

m) E = 55 GPa, σ1 = 25 MPa, σ1 = 322°
Max compressive stress = 79.52 MPa

Figure D-11. *Cross section plots showing the projection of the principal stress tensor (color by magnitude of Sigma 1) for the as-built tunnel shape without fractures and planar blasting round faces in section 48.*

Section 48

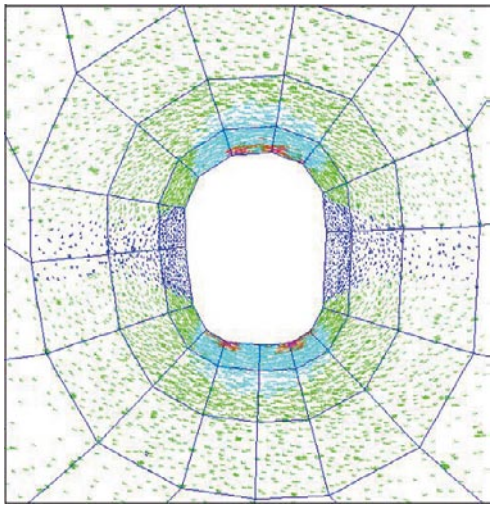

n) E = 65 GPa, σ1 = 30 MPa, σ1 = 310°
Max compressive stress = 97.21 MPa

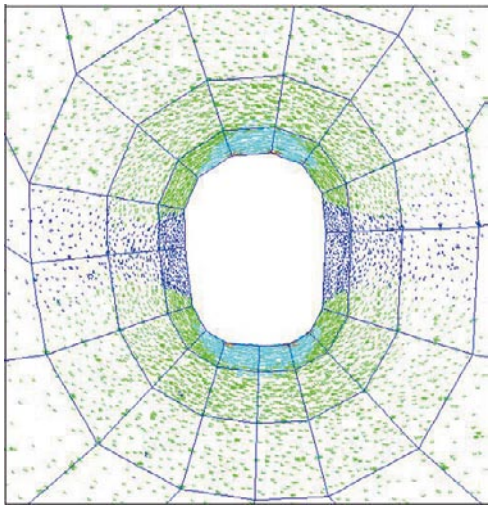

o) E = 65 GPa, σ1 = 25 MPa, σ1 = 310°
Max compressive stress = 80.17 MPa

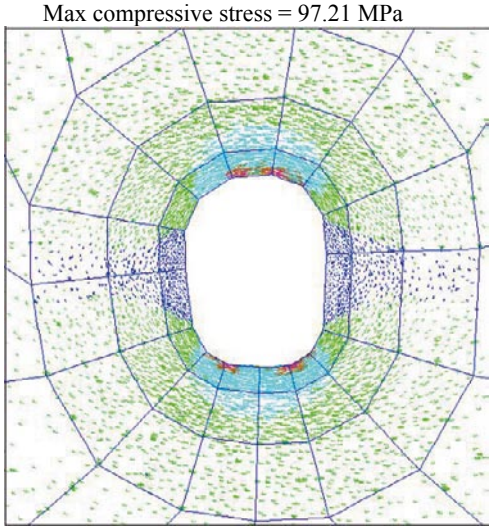

p) E = 65 GPa, σ1 = 30 MPa, σ1 = 316°
Max compressive stress = 97.47 MPa

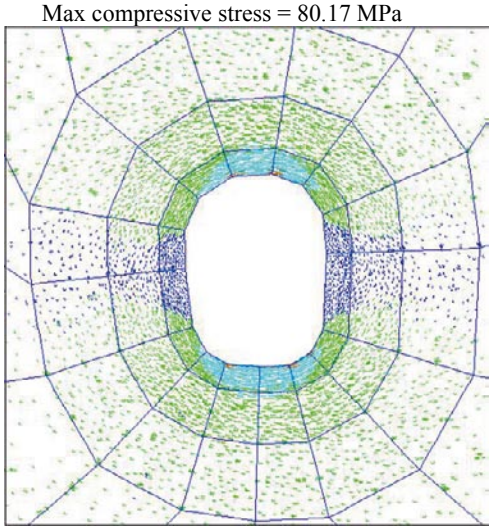

q) E = 65 GPa, σ1 = 25 MPa, σ1 = 316°
Max compressive stress = 80.35 MPa

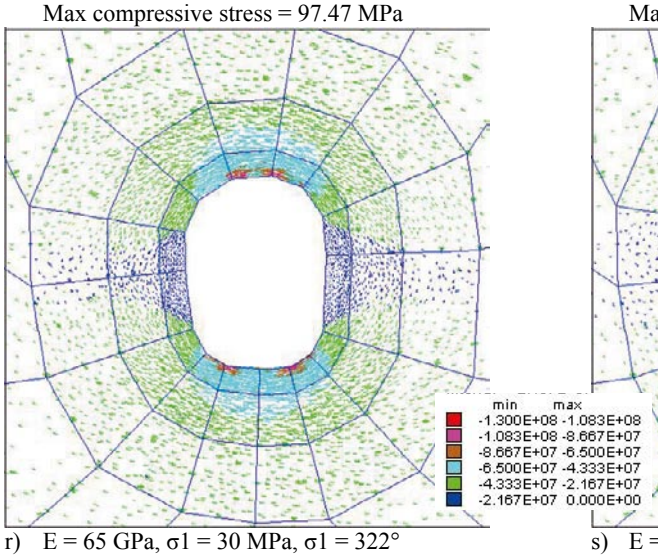

r) E = 65 GPa, σ1 = 30 MPa, σ1 = 322°
Max compressive stress = 96.32 MPa

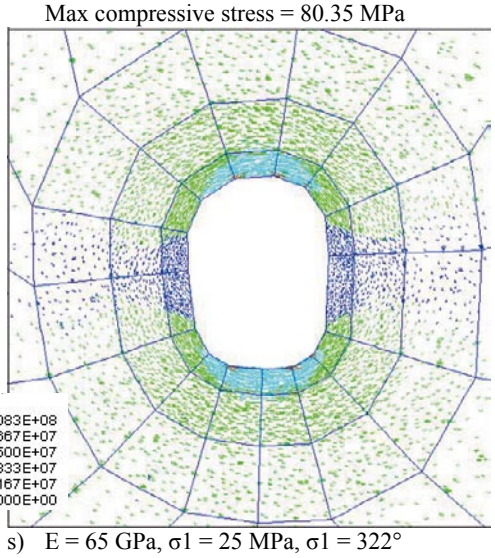

s) E = 65 GPa, σ1 = 25 MPa, σ1 = 322°
Max compressive stress = 79.50 MPa

Figure D-12. *Cross section plots showing the projection of the principal stress tensor (color by magnitude of Sigma 1) for the as-built tunnel shape without fractures and planar blasting round faces in section 48.*

Section 49

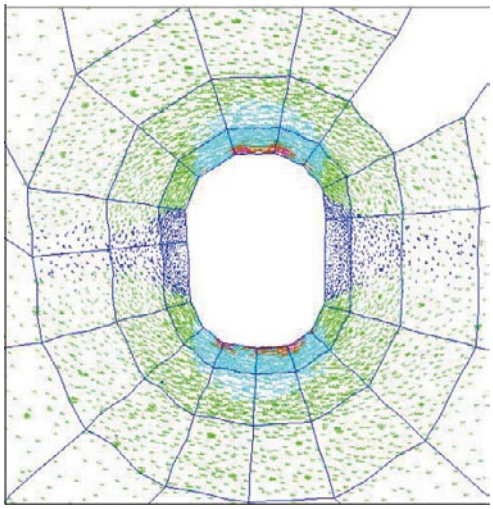

a) E = 45 GPa, σ1 = 30 MPa, σ1 =316°
Max compressive stress = 101.2 MPa

Figure D-13. *Cross section plots showing the projection of the principal stress tensor (color by magnitude of Sigma 1) for the as-built tunnel shape without fractures and planar blasting round faces in section 49.*

Section 49

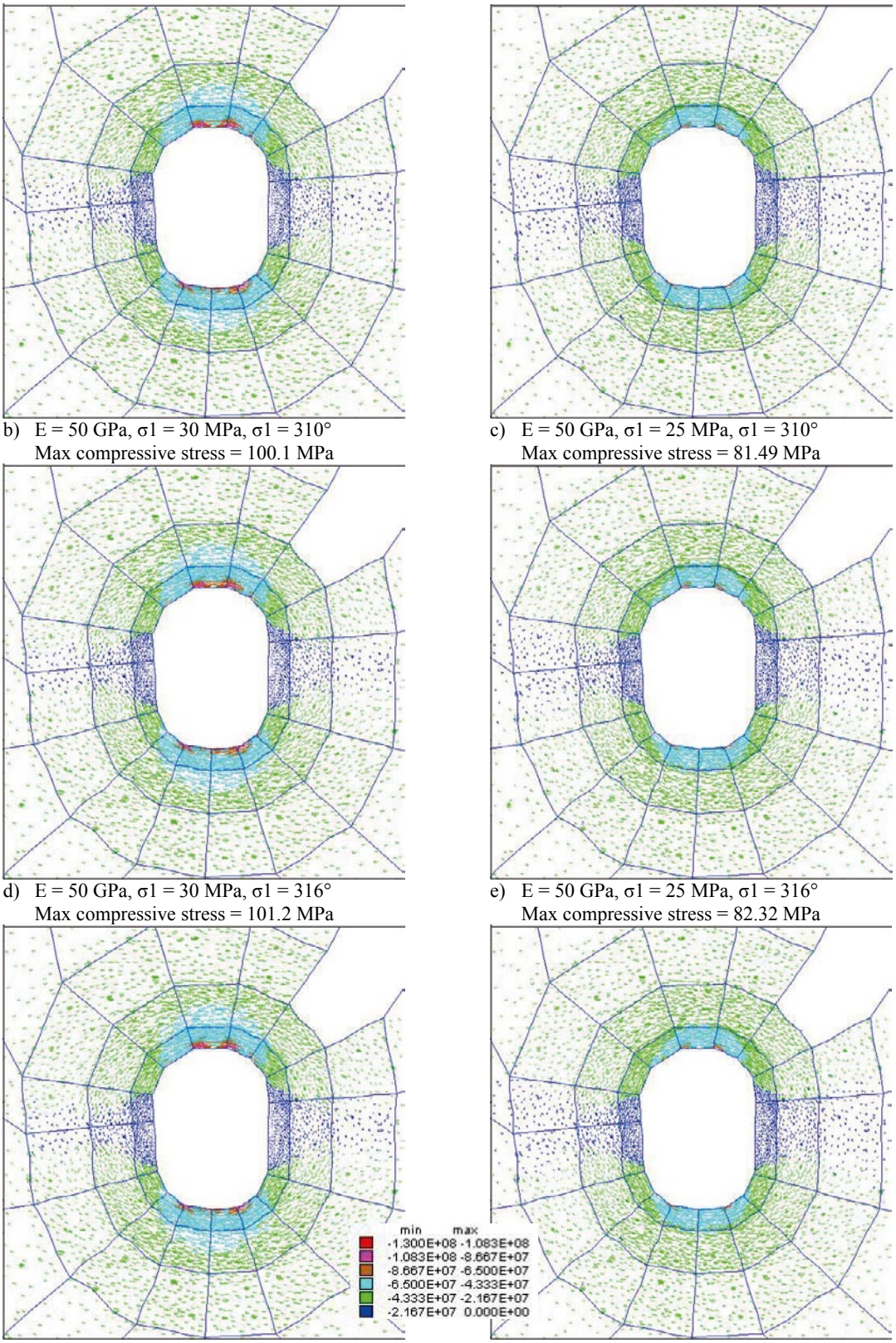

b) E = 50 GPa, σ1 = 30 MPa, σ1 = 310°
Max compressive stress = 100.1 MPa

c) E = 50 GPa, σ1 = 25 MPa, σ1 = 310°
Max compressive stress = 81.49 MPa

d) E = 50 GPa, σ1 = 30 MPa, σ1 = 316°
Max compressive stress = 101.2 MPa

e) E = 50 GPa, σ1 = 25 MPa, σ1 = 316°
Max compressive stress = 82.32 MPa

f) E = 50 GPa, σ1 = 30 MPa, σ1 = 322°
Max compressive stress = 100.8 MPa

g) E = 50 GPa, σ1 = 25 MPa, σ1 = 322°
Max compressive stress = 82.00 MPa

Figure D-14. *Cross section plots showing the projection of the principal stress tensor (color by magnitude of Sigma 1) for the as-built tunnel shape without fractures and planar blasting round faces in section 49.*

Section 49

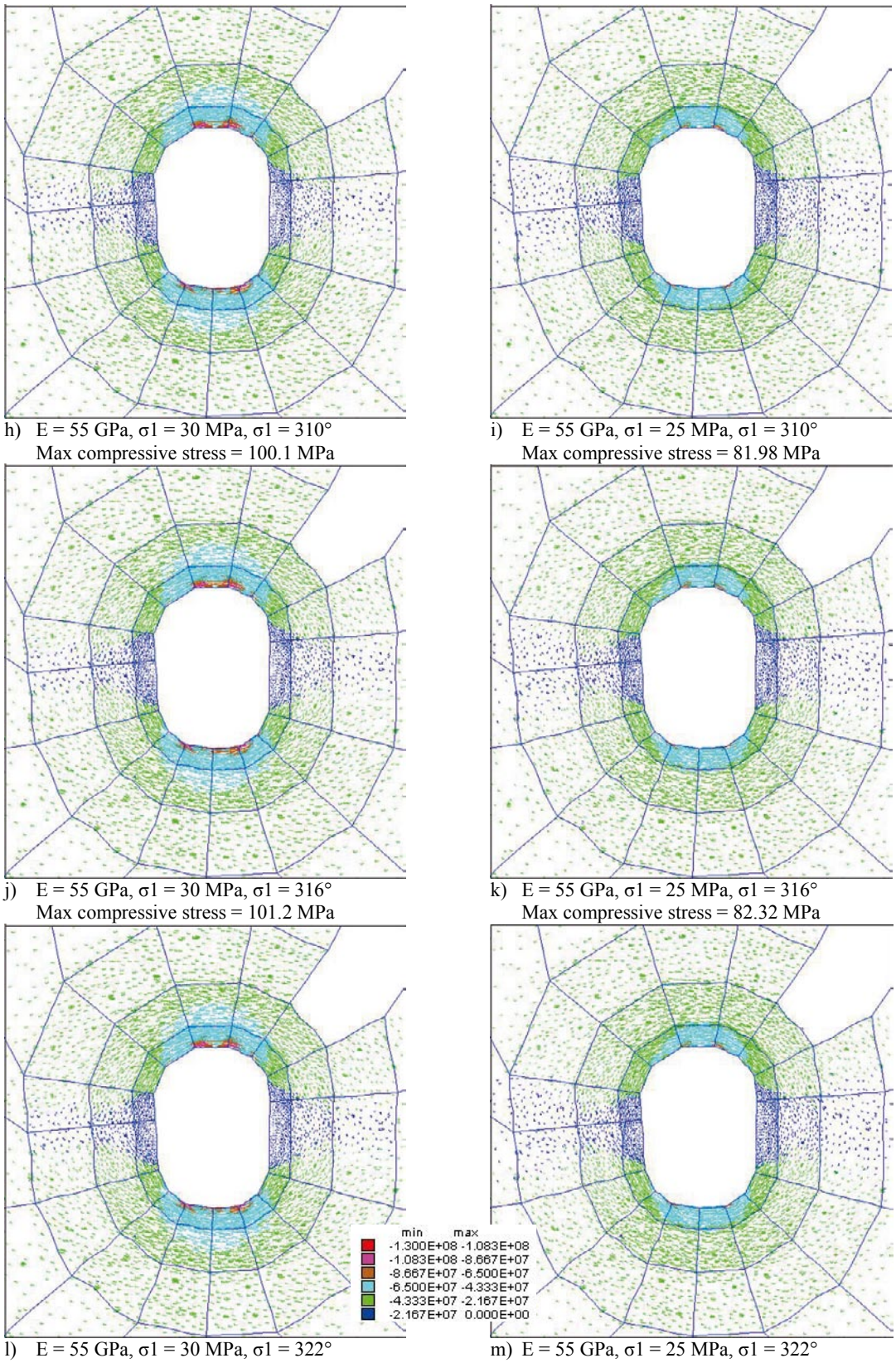

h) E = 55 GPa, σ1 = 30 MPa, σ1 = 310°
Max compressive stress = 100.1 MPa

i) E = 55 GPa, σ1 = 25 MPa, σ1 = 310°
Max compressive stress = 81.98 MPa

j) E = 55 GPa, σ1 = 30 MPa, σ1 = 316°
Max compressive stress = 101.2 MPa

k) E = 55 GPa, σ1 = 25 MPa, σ1 = 316°
Max compressive stress = 82.32 MPa

l) E = 55 GPa, σ1 = 30 MPa, σ1 = 322°
Max compressive stress = 100.7 MPa

m) E = 55 GPa, σ1 = 25 MPa, σ1 = 322°
Max compressive stress = 81.98 MPa

Figure D-15. *Cross section plots showing the projection of the principal stress tensor (color by magnitude of Sigma 1) for the as-built tunnel shape without fractures and planar blasting round faces in section 49.*

Section 49

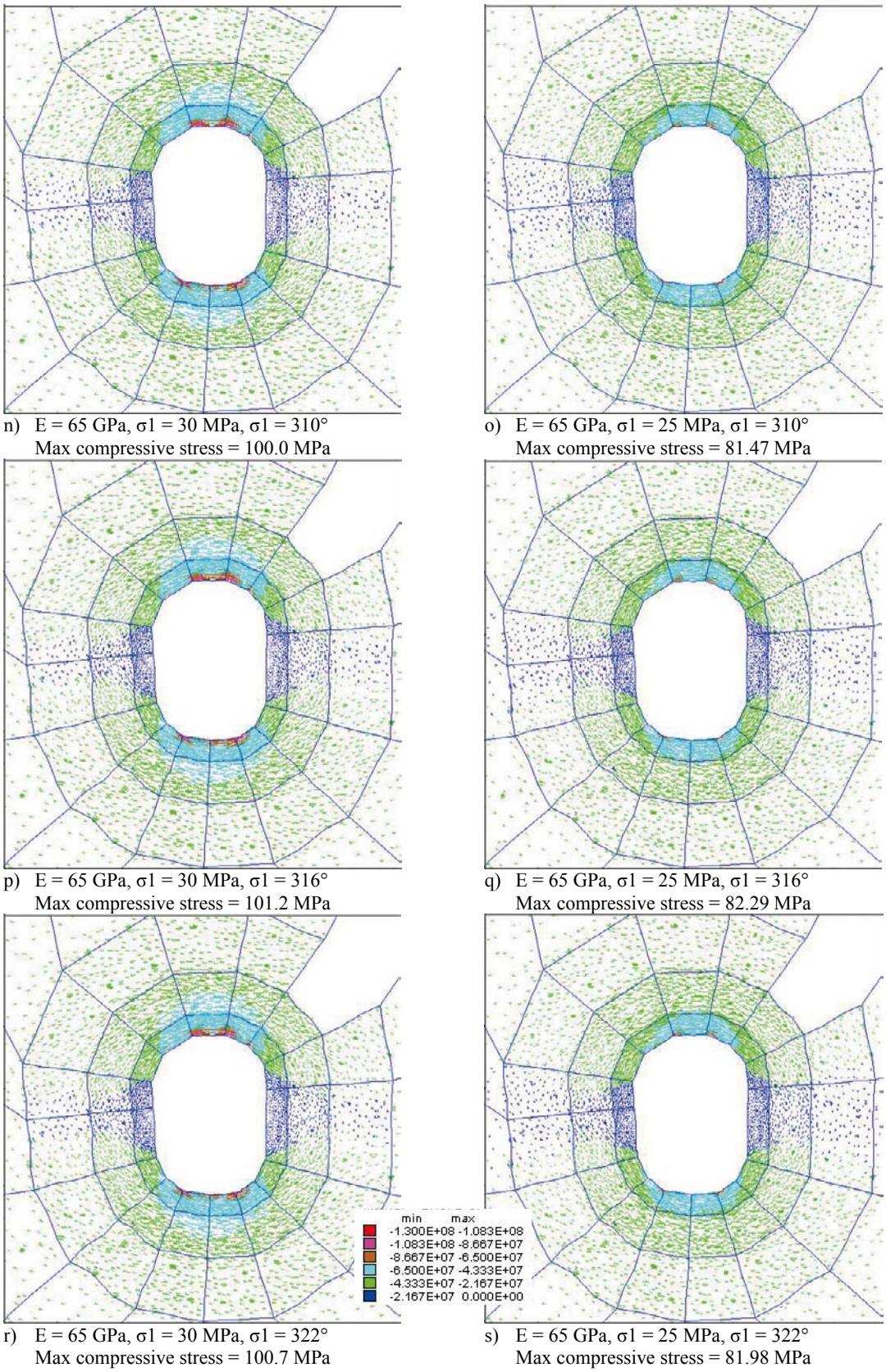

n) E = 65 GPa, σ1 = 30 MPa, σ1 = 310°
Max compressive stress = 100.0 MPa

o) E = 65 GPa, σ1 = 25 MPa, σ1 = 310°
Max compressive stress = 81.47 MPa

p) E = 65 GPa, σ1 = 30 MPa, σ1 = 316°
Max compressive stress = 101.2 MPa

q) E = 65 GPa, σ1 = 25 MPa, σ1 = 316°
Max compressive stress = 82.29 MPa

r) E = 65 GPa, σ1 = 30 MPa, σ1 = 322°
Max compressive stress = 100.7 MPa

s) E = 65 GPa, σ1 = 25 MPa, σ1 = 322°
Max compressive stress = 81.98 MPa

Figure D-16. *Cross section plots showing the projection of the principal stress tensor (color by magnitude of Sigma 1) for the as-built tunnel shape without fractures and planar blasting round faces in section 49.*

Section 50

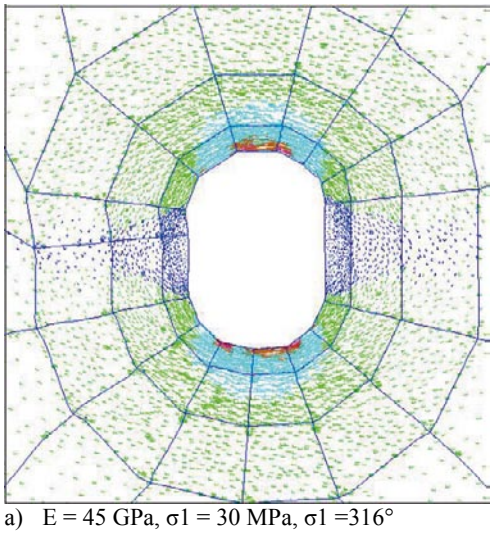

a) E = 45 GPa, σ1 = 30 MPa, σ1 =316°
Max compressive stress = 119.3 MPa

Figure D-17. *Cross section plots showing the projection of the principal stress tensor (color by magnitude of Sigma 1) for the as-built tunnel shape without fractures and planar blasting round faces in section 50.*

Section 50

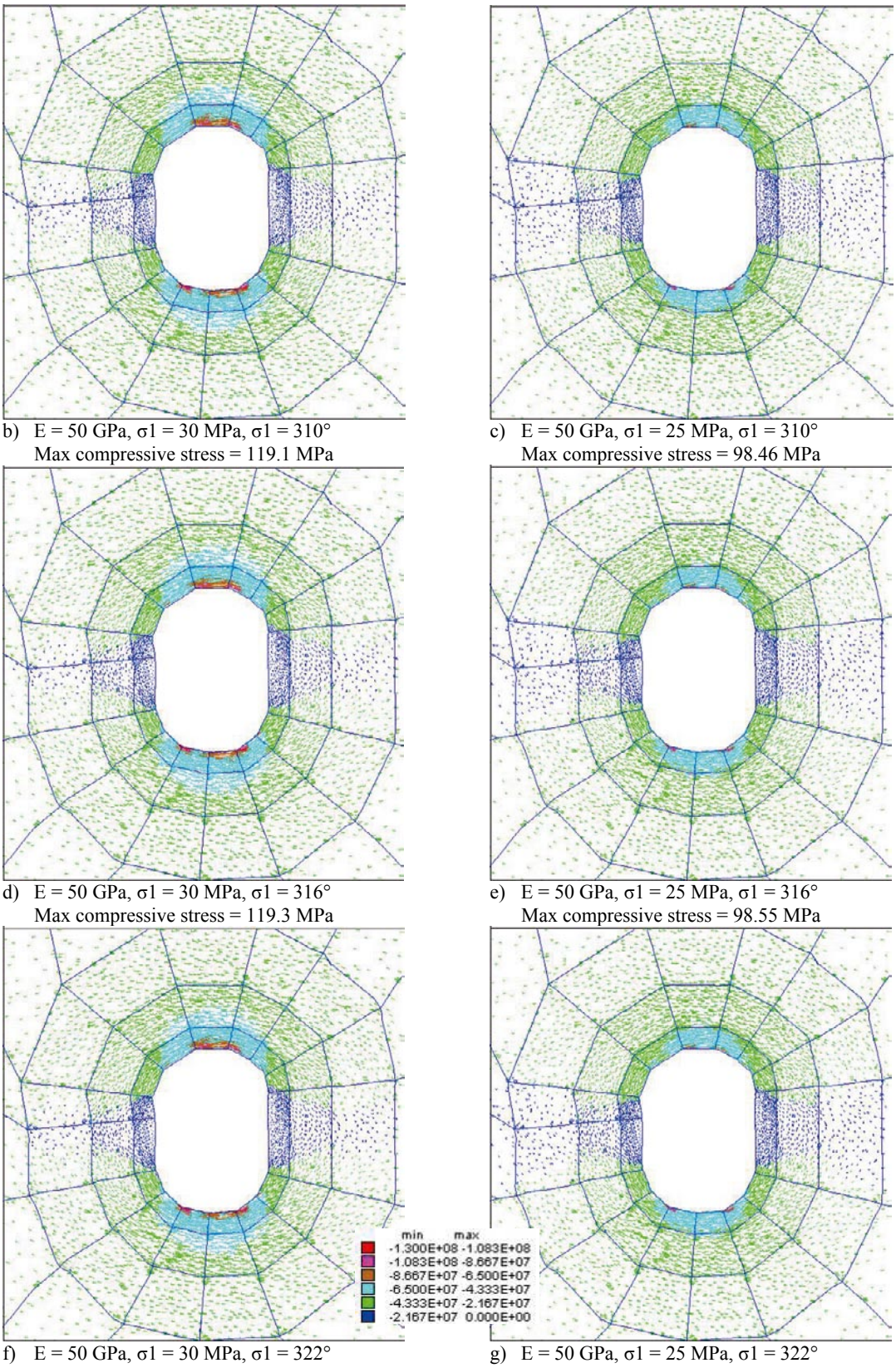

b) E = 50 GPa, σ1 = 30 MPa, σ1 = 310°
Max compressive stress = 119.1 MPa

c) E = 50 GPa, σ1 = 25 MPa, σ1 = 310°
Max compressive stress = 98.46 MPa

d) E = 50 GPa, σ1 = 30 MPa, σ1 = 316°
Max compressive stress = 119.3 MPa

e) E = 50 GPa, σ1 = 25 MPa, σ1 = 316°
Max compressive stress = 98.55 MPa

f) E = 50 GPa, σ1 = 30 MPa, σ1 = 322°
Max compressive stress = 117.7 MPa

g) E = 50 GPa, σ1 = 25 MPa, σ1 = 322°
Max compressive stress = 97.41 MPa

Figure D-18. *Cross section plots showing the projection of the principal stress tensor (color by magnitude of Sigma 1) for the as-built tunnel shape without fractures and planar blasting round faces in section 50.*

Section 50

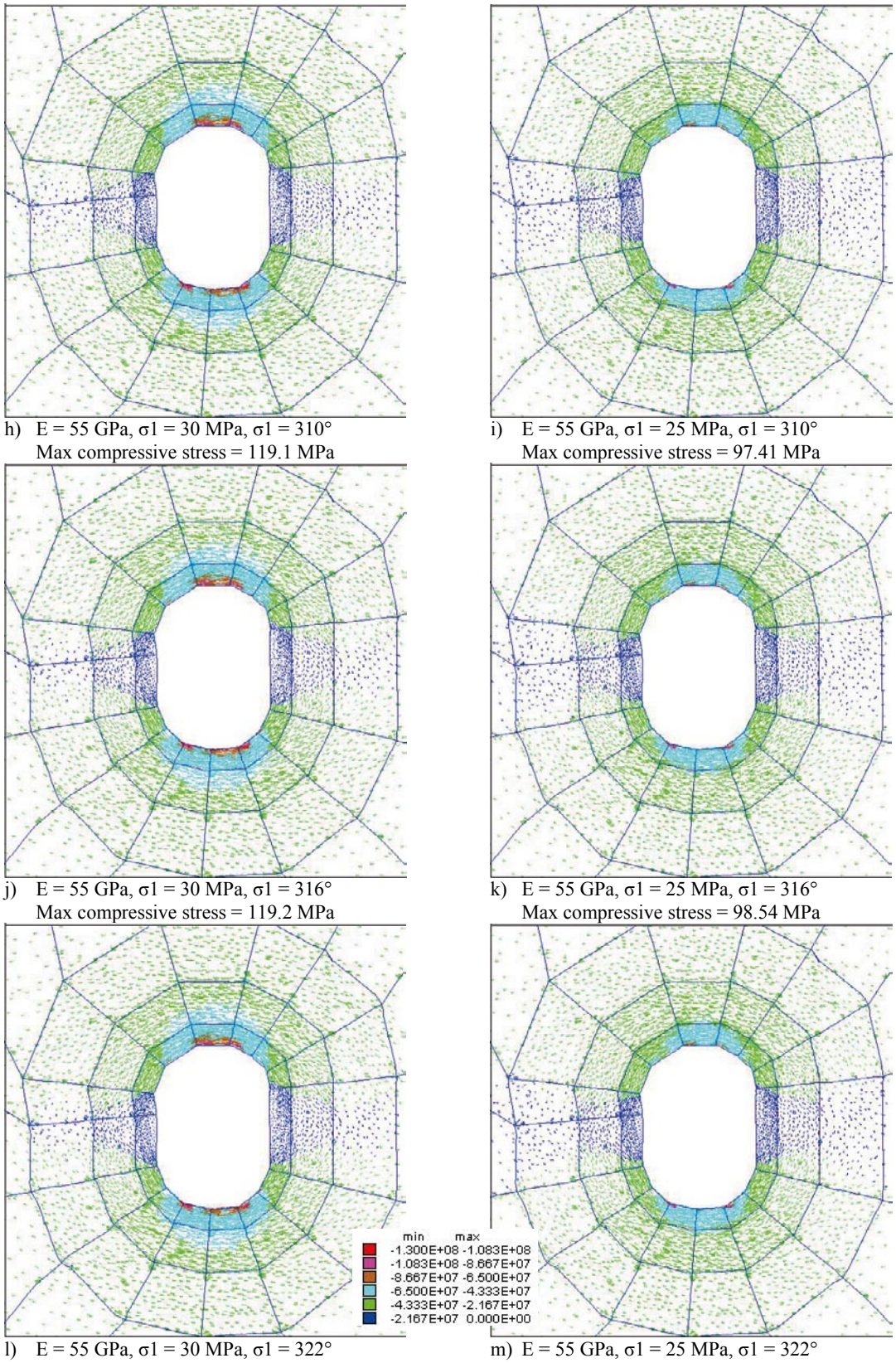

h) E = 55 GPa, σ1 = 30 MPa, σ1 = 310°
Max compressive stress = 119.1 MPa

i) E = 55 GPa, σ1 = 25 MPa, σ1 = 310°
Max compressive stress = 97.41 MPa

j) E = 55 GPa, σ1 = 30 MPa, σ1 = 316°
Max compressive stress = 119.2 MPa

k) E = 55 GPa, σ1 = 25 MPa, σ1 = 316°
Max compressive stress = 98.54 MPa

l) E = 55 GPa, σ1 = 30 MPa, σ1 = 322°
Max compressive stress = 117.7 MPa

m) E = 55 GPa, σ1 = 25 MPa, σ1 = 322°
Max compressive stress = 97.41 MPa

Figure D-19. *Cross section plots showing the projection of the principal stress tensor (color by magnitude of Sigma 1) for the as-built tunnel shape without fractures and planar blasting round faces in section 50.*

Section 50

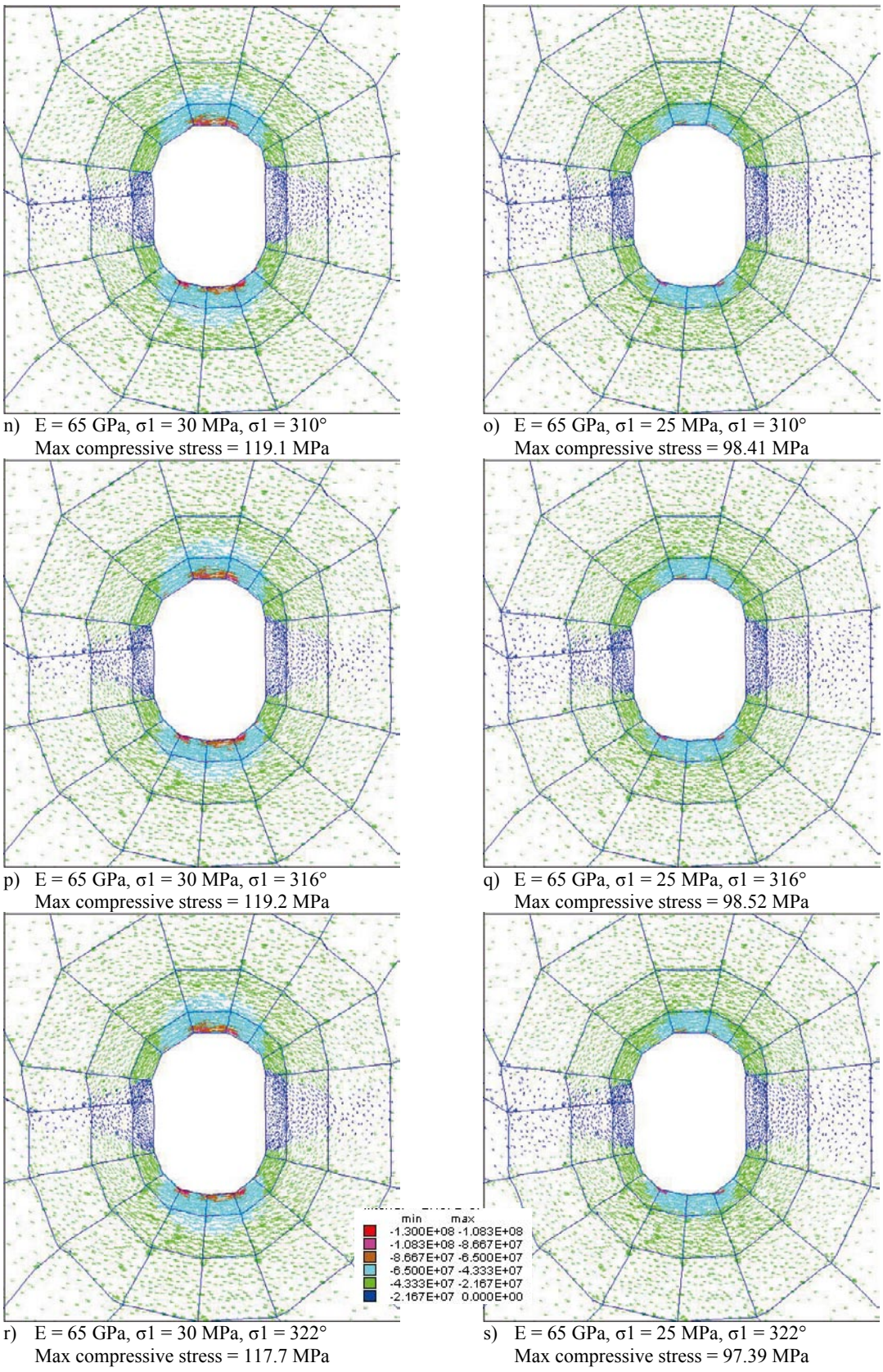

n) E = 65 GPa, σ1 = 30 MPa, σ1 = 310°
Max compressive stress = 119.1 MPa

o) E = 65 GPa, σ1 = 25 MPa, σ1 = 310°
Max compressive stress = 98.41 MPa

p) E = 65 GPa, σ1 = 30 MPa, σ1 = 316°
Max compressive stress = 119.2 MPa

q) E = 65 GPa, σ1 = 25 MPa, σ1 = 316°
Max compressive stress = 98.52 MPa

r) E = 65 GPa, σ1 = 30 MPa, σ1 = 322°
Max compressive stress = 117.7 MPa

s) E = 65 GPa, σ1 = 25 MPa, σ1 = 322°
Max compressive stress = 97.39 MPa

Figure D-20. *Cross section plots showing the projection of the principal stress tensor (color by magnitude of Sigma 1) for the as-built tunnel shape without fractures and planar blasting round faces in section 50.*

Section 51

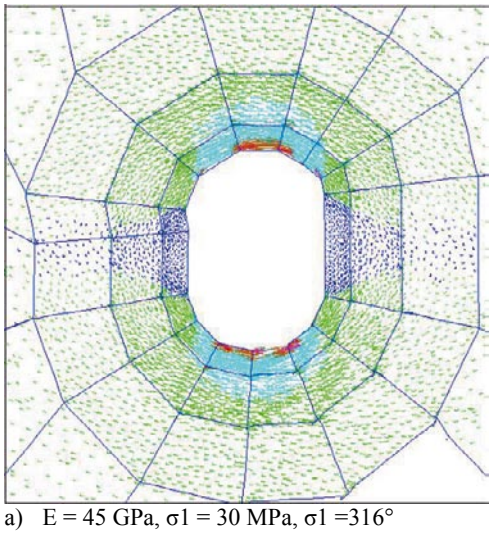

a) E = 45 GPa, σ1 = 30 MPa, σ1 =316°
Max compressive stress = 131.0 MPa

Figure D-21. *Cross section plots showing the projection of the principal stress tensor (color by magnitude of Sigma 1) for the as-built tunnel shape without fractures and planar blasting round faces in section 51.*

Section 51

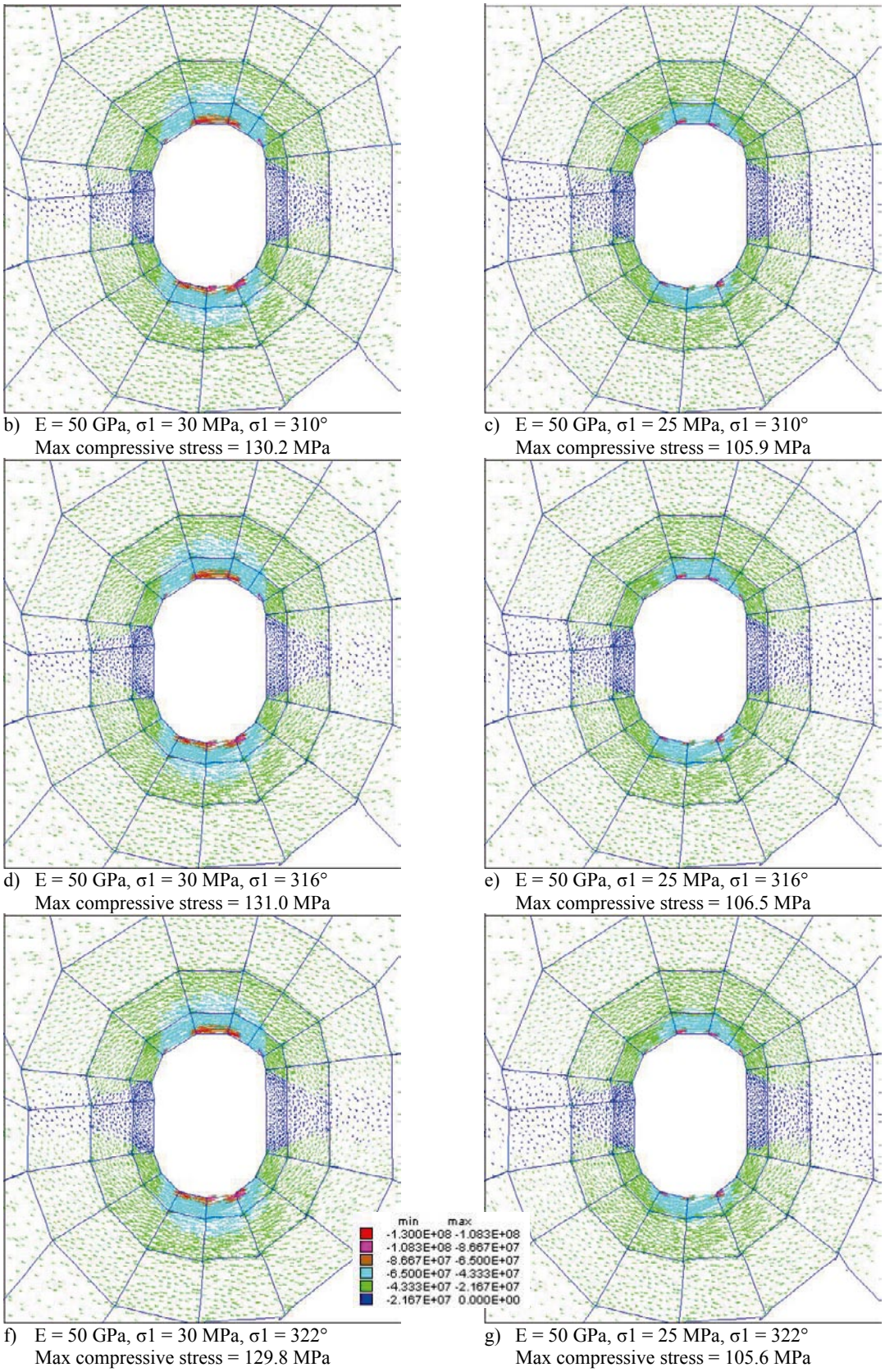

b) E = 50 GPa, σ1 = 30 MPa, σ1 = 310°
Max compressive stress = 130.2 MPa

c) E = 50 GPa, σ1 = 25 MPa, σ1 = 310°
Max compressive stress = 105.9 MPa

d) E = 50 GPa, σ1 = 30 MPa, σ1 = 316°
Max compressive stress = 131.0 MPa

e) E = 50 GPa, σ1 = 25 MPa, σ1 = 316°
Max compressive stress = 106.5 MPa

f) E = 50 GPa, σ1 = 30 MPa, σ1 = 322°
Max compressive stress = 129.8 MPa

g) E = 50 GPa, σ1 = 25 MPa, σ1 = 322°
Max compressive stress = 105.6 MPa

Figure D-22. *Cross section plots showing the projection of the principal stress tensor (color by magnitude of Sigma 1) for the as-built tunnel shape without fractures and planar blasting round faces in section 51.*

Section 51

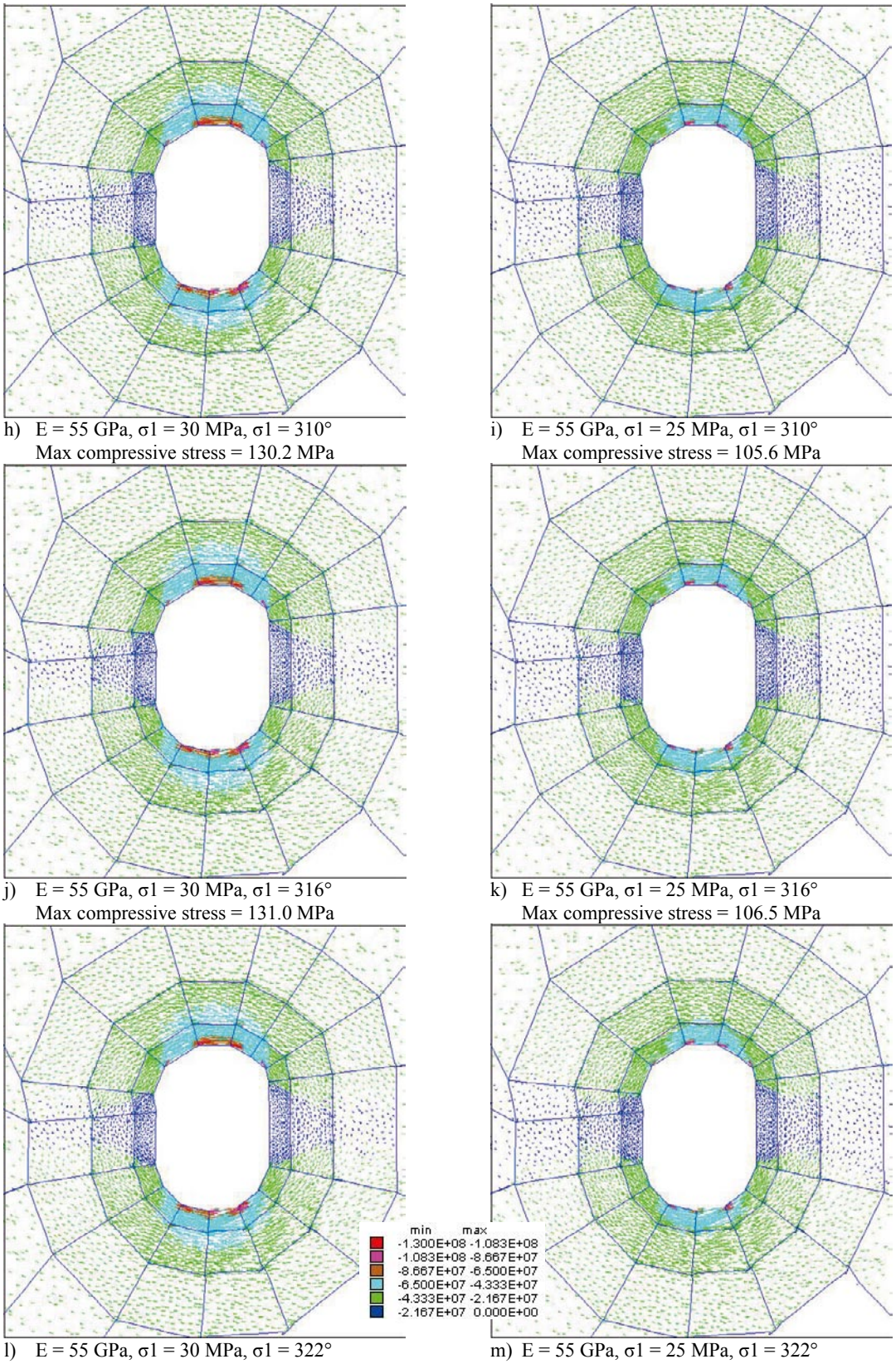

h) E = 55 GPa, σ1 = 30 MPa, σ1 = 310°
Max compressive stress = 130.2 MPa

i) E = 55 GPa, σ1 = 25 MPa, σ1 = 310°
Max compressive stress = 105.6 MPa

j) E = 55 GPa, σ1 = 30 MPa, σ1 = 316°
Max compressive stress = 131.0 MPa

k) E = 55 GPa, σ1 = 25 MPa, σ1 = 316°
Max compressive stress = 106.5 MPa

l) E = 55 GPa, σ1 = 30 MPa, σ1 = 322°
Max compressive stress = 129.8 MPa

m) E = 55 GPa, σ1 = 25 MPa, σ1 = 322°
Max compressive stress = 105.6 MPa

Figure D-23. *Cross section plots showing the projection of the principal stress tensor (color by magnitude of Sigma 1) for the as-built tunnel shape without fractures and planar blasting round faces in section 51.*

Section 51

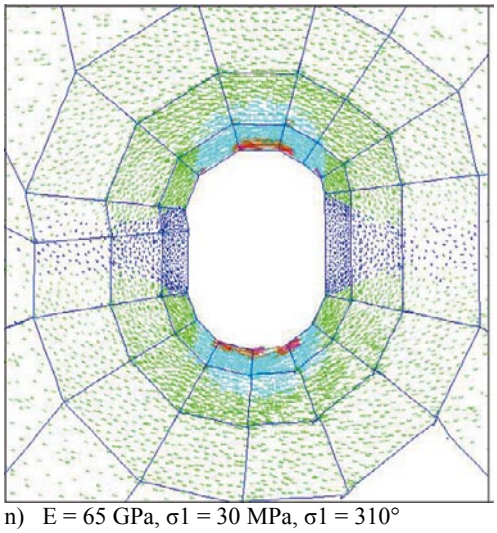

n) E = 65 GPa, σ1 = 30 MPa, σ1 = 310°
Max compressive stress = 130.1 MPa

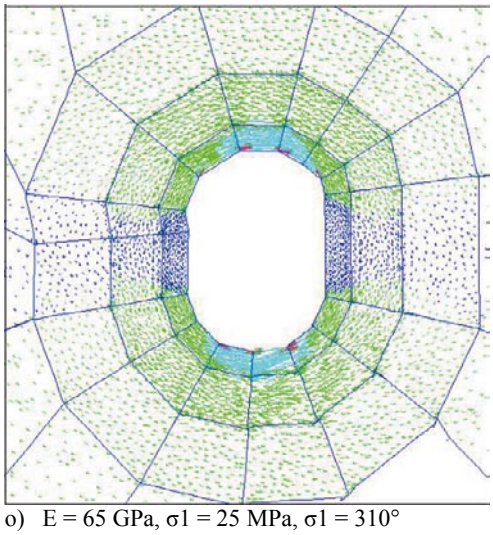

o) E = 65 GPa, σ1 = 25 MPa, σ1 = 310°
Max compressive stress = 105.9 MPa

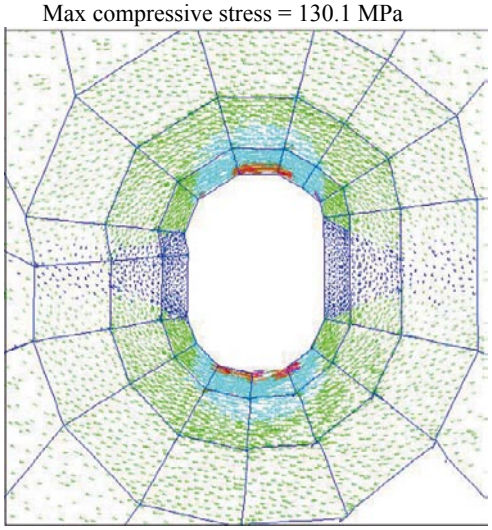

p) E = 65 GPa, σ1 = 30 MPa, σ1 = 316°
Max compressive stress = 130.9 MPa

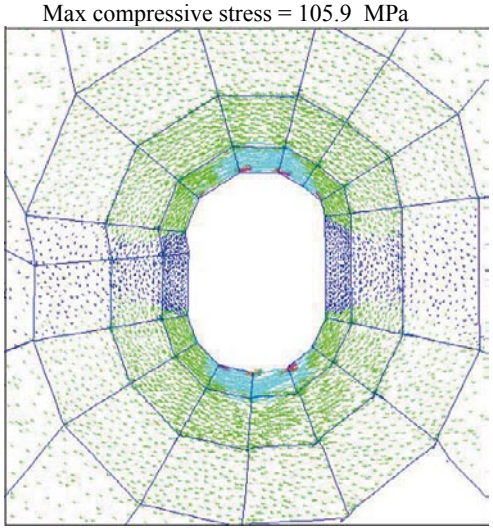

q) E = 65 GPa, σ1 = 25 MPa, σ1 = 316°
Max compressive stress = 106.5 MPa

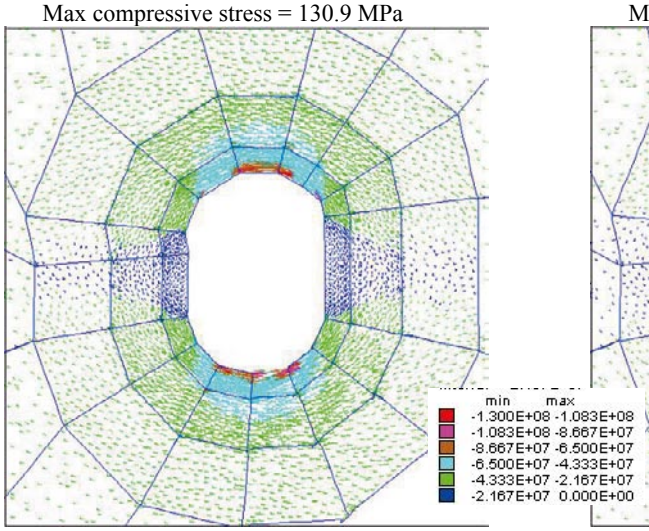

r) E = 65 GPa, σ1 = 30 MPa, σ1 = 322°
Max compressive stress = 129.7 MPa

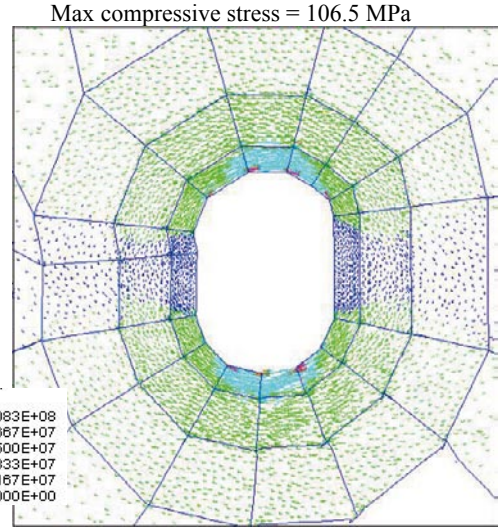

s) E = 65 GPa, σ1 = 25 MPa, σ1 = 322°
Max compressive stress = 105.6 MPa

Figure D-24. *Cross section plots showing the projection of the principal stress tensor (color by magnitude of Sigma 1) for the as-built tunnel shape without fractures and planar blasting round faces in section 51.*

Appendix E

Sensitivity analysis, As-planned vs. As-built tunnel shape

Sensitivity analysis. Comparison between cross section plots showing the projection of the principal stress tensor (colours by magnitude of σ_1, σ_2 or σ_3) for the as-planned tunnel shape (E = 55 GPa, σ_1 = 30 MPa and σ_1 = 310°) and the as-built tunnel shape (E = 55 GPa, σ_1 = 30 MPa and σ_1 = 310°) in sections 46–51 in the TASQ tunnel; a) As-planned, σ_1, b) As-built, σ_1, c) As-planned, σ_2, d) As-built, σ_2, e) As-planned, σ_3 and f) As-built, σ_3.

Section 46

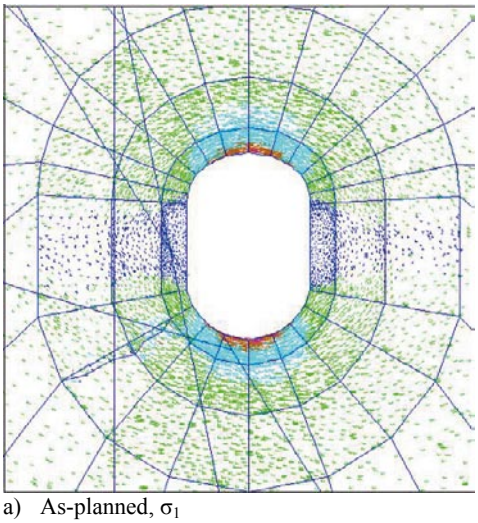

a) As-planned, σ_1
E = 55 GPa, σ1 = 30 MPa, σ1 = 310°
Max compressive stress = 101.0 MPa

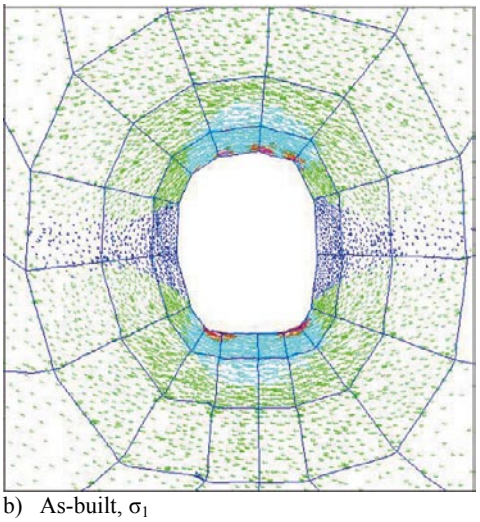

b) As-built, σ_1
E = 55 GPa, σ1 = 30 MPa, σ1 = 310°
Max compressive stress = 126.8 MPa

Sigma 1

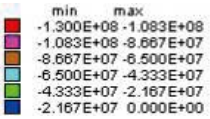

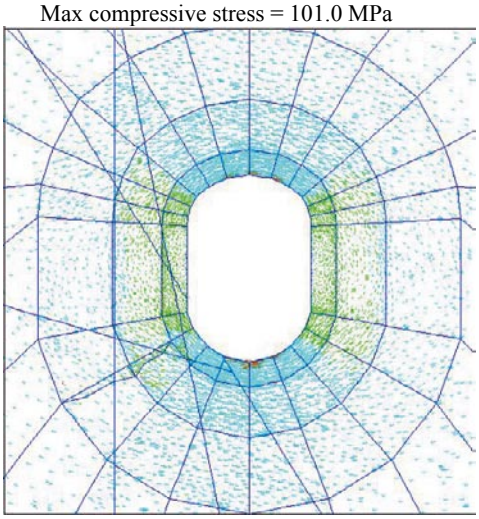

c) As-planned, σ_2
E = 55 GPa, σ1 = 30 MPa, σ1 = 310°
Max compressive stress = 101.0 MPa

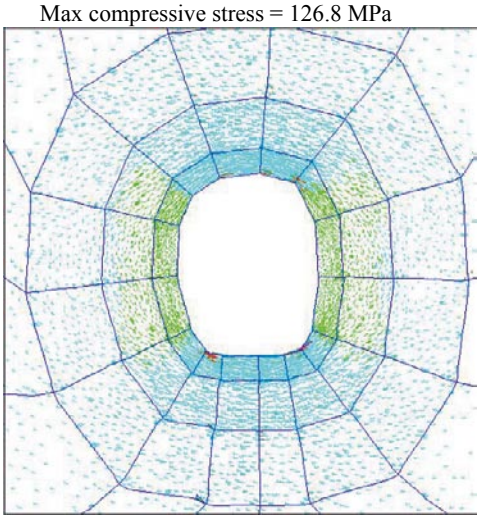

d) As-built, σ_2
E = 55 GPa, σ1 = 30 MPa, σ1 = 310°
Max compressive stress = 126.8 MPa

Sigma 2

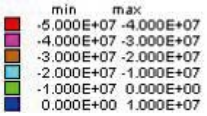

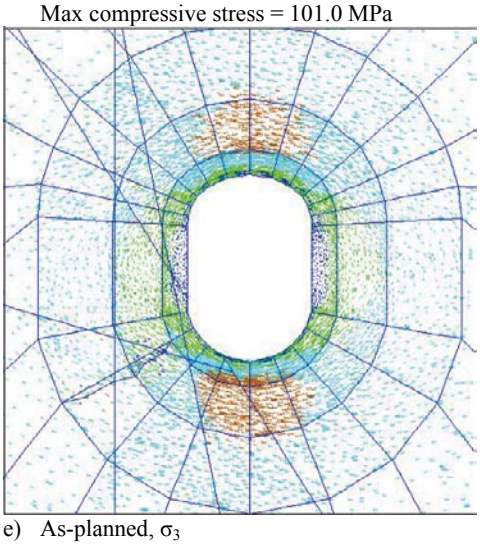

e) As-planned, σ_3
E = 55 GPa, σ1 = 30 MPa, σ1 = 310°
Max compressive stress = 101.0 MPa

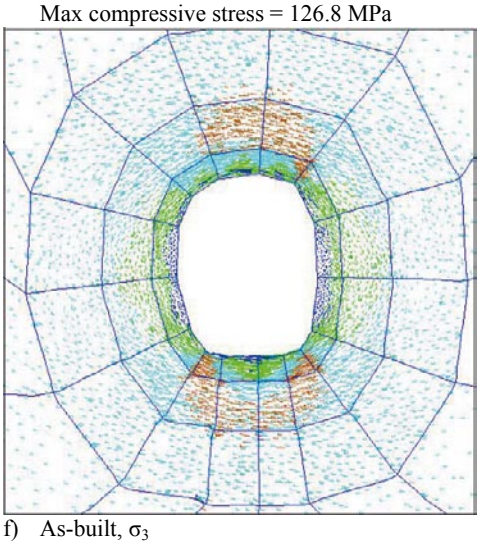

f) As-built, σ_3
E = 55 GPa, σ1 = 30 MPa, σ1 = 310°
Max compressive stress = 126.8 MPa

Sigma 3

Figure E-1. *Cross section plots showing the projection of the principal stress tensor (color by magnitude of a) and b) Sigma 1, c) and d) Sigma 2, and e) and f) Sigma 3) for the as-planned and the as-built tunnel shapes with planar blasting round faces in section 46.*

Section 47

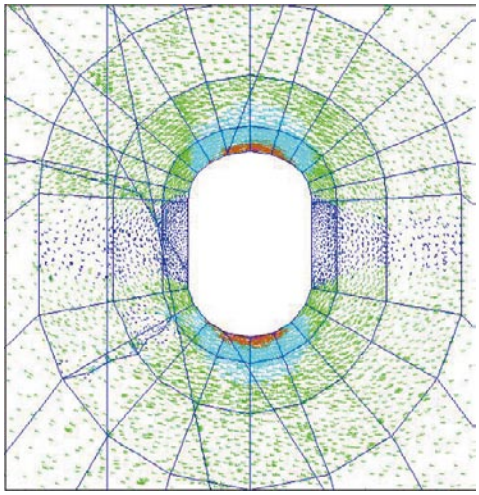

a) As-planned, σ_1
E = 55 GPa, σ1 = 30 MPa, σ1 = 310°
Max compressive stress = 98.76 MPa

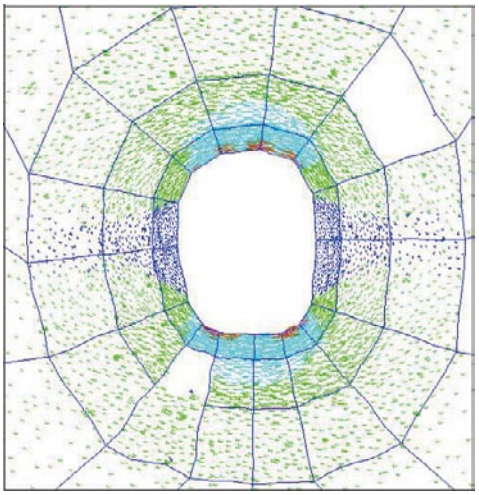

b) As-built, σ_1
E = 55 GPa, σ1 = 30 MPa, σ1 = 310°
Max compressive stress = 100.6 MPa

Sigma 1

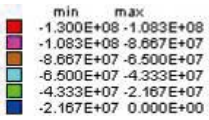

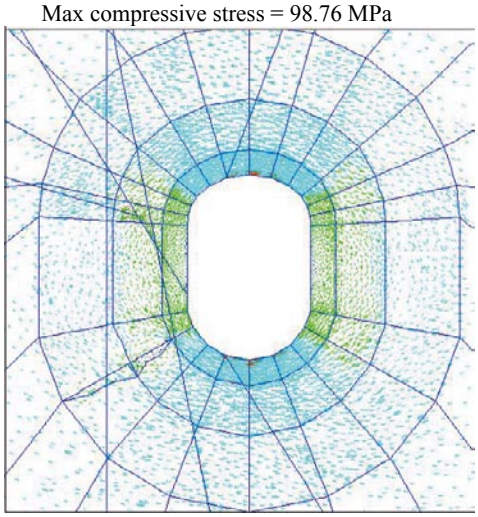

c) As-planned, σ_2
E = 55 GPa, σ1 = 30 MPa, σ1 = 310°
Max compressive stress = 98.76 MPa

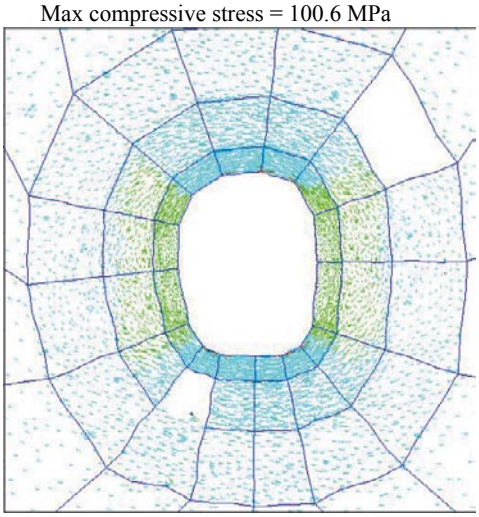

d) As-built, σ_2
E = 55 GPa, σ1 = 30 MPa, σ1 = 310°
Max compressive stress = 100.6 MPa

Sigma 2

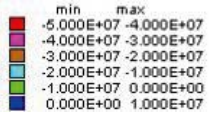

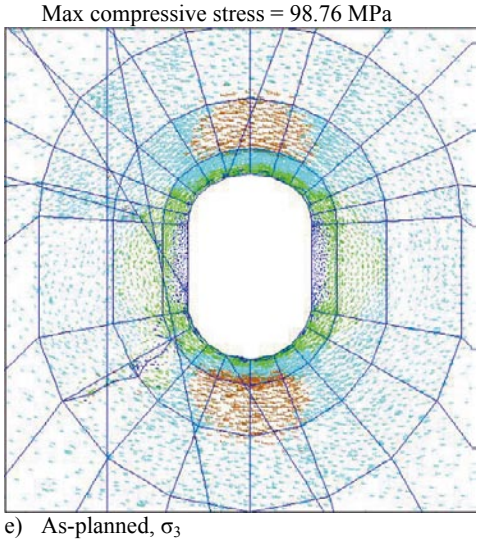

e) As-planned, σ_3
E = 55 GPa, σ1 = 30 MPa, σ1 = 310°
Max compressive stress = 98.76 MPa

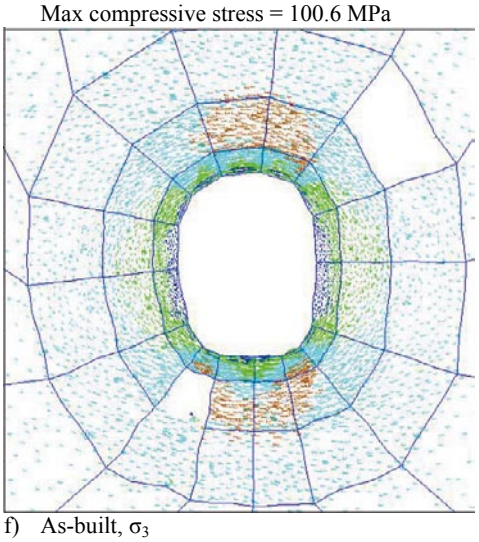

f) As-built, σ_3
E = 55 GPa, σ1 = 30 MPa, σ1 = 310°
Max compressive stress = 100.6 MPa

Sigma 3

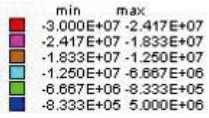

Figure E-2. *Cross section plots showing the projection of the principal stress tensor (color by magnitude of a) and b) Sigma 1, c) and d) Sigma 2, and e) and f) Sigma 3) for the as-planned and the as-built tunnel shapes with planar blasting round faces in section 47.*

Section 48

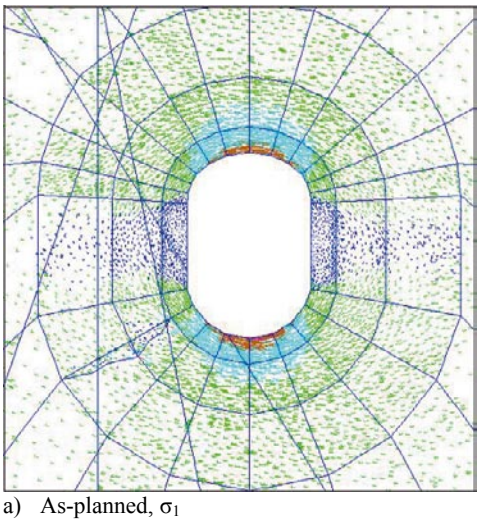

a) As-planned, σ_1
E = 55 GPa, σ1 = 30 MPa, σ1 = 310°
Max compressive stress = 98.35 MPa

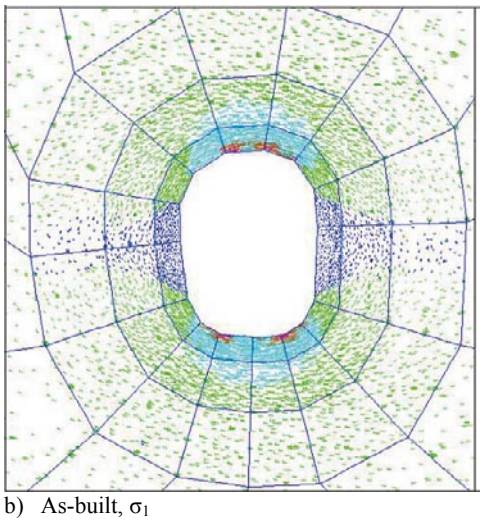

b) As-built, σ_1
E = 55 GPa, σ1 = 30 MPa, σ1 = 310°
Max compressive stress = 97.24 MPa

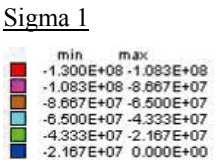

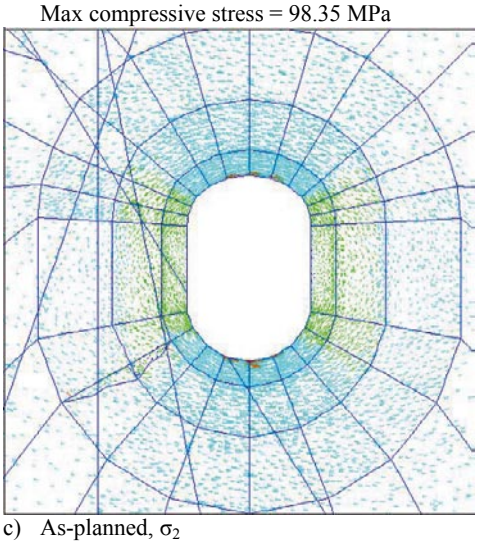

c) As-planned, σ_2
E = 55 GPa, σ1 = 30 MPa, σ1 = 310°
Max compressive stress = 98.35 MPa

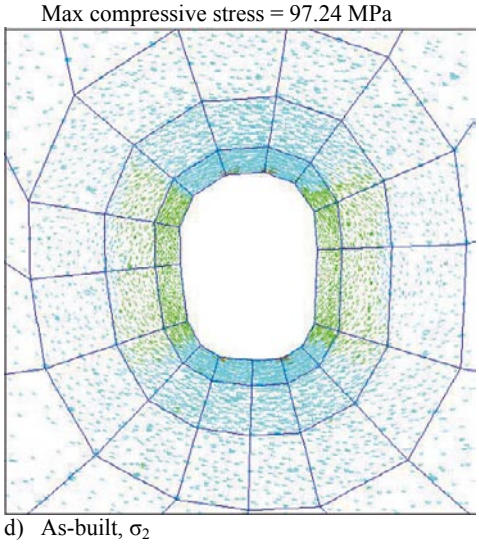

d) As-built, σ_2
E = 55 GPa, σ1 = 30 MPa, σ1 = 310°
Max compressive stress = 97.24 MPa

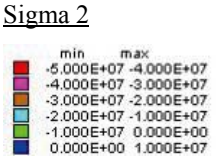

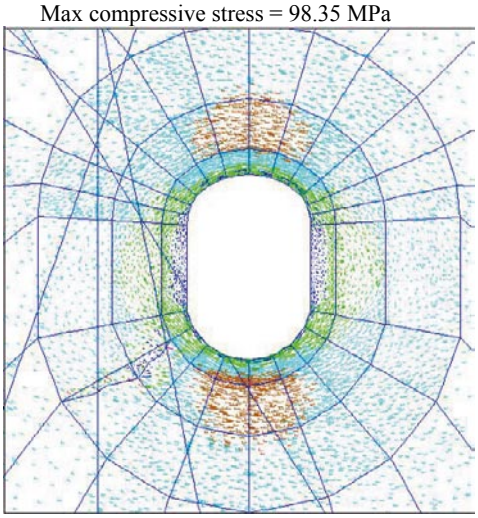

e) As-planned, σ_3
E = 55 GPa, σ1 = 30 MPa, σ1 = 310°
Max compressive stress = 98.35 MPa

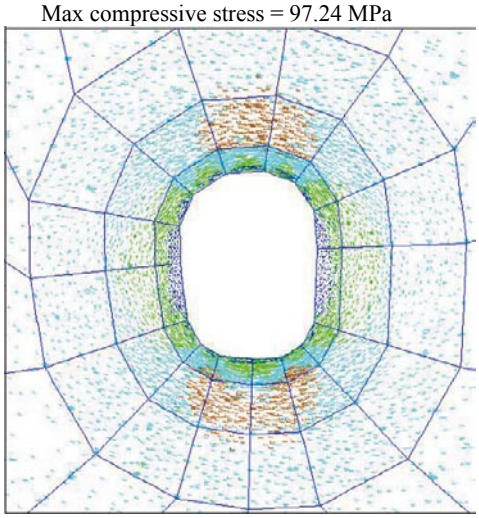

f) As-built, σ_3
E = 55 GPa, σ1 = 30 MPa, σ1 = 310°
Max compressive stress = 97.24 MPa

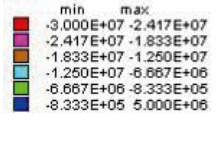

Figure E-3. *Cross section plots showing the projection of the principal stress tensor (color by magnitude of a) and b) Sigma 1, c) and d) Sigma 2, and e) and f) Sigma 3) for the as-planned and the as-built tunnel shapes with planar blasting round faces in section 48.*

Section 49

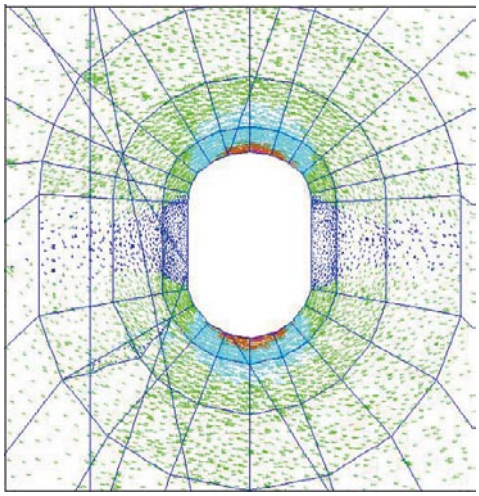

a) As-planned, σ_1
E = 55 GPa, σ1 = 30 MPa, σ1 = 310°
Max compressive stress = 99.19 MPa

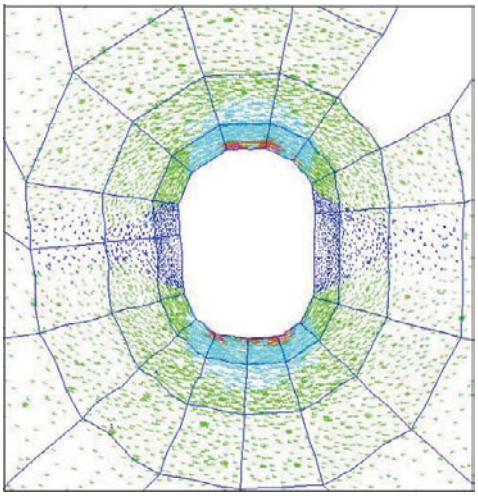

b) As-built, σ_1
E = 55 GPa, σ1 = 30 MPa, σ1 = 310°
Max compressive stress = 100.1 MPa

Sigma 1

min	max
-1.300E+08	-1.083E+08
-1.083E+08	-8.667E+07
-8.667E+07	-6.500E+07
-6.500E+07	-4.333E+07
-4.333E+07	-2.167E+07
-2.167E+07	0.000E+00

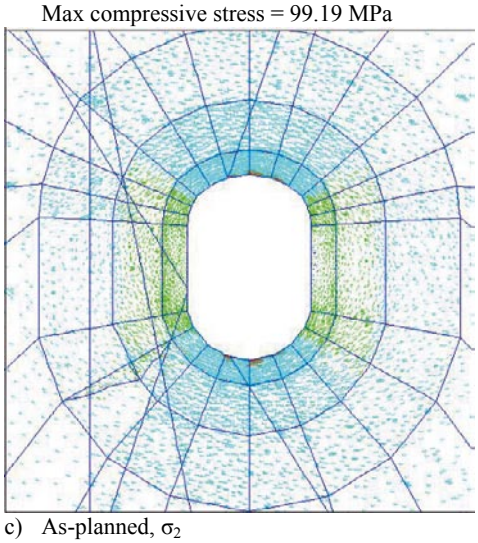

c) As-planned, σ_2
E = 55 GPa, σ1 = 30 MPa, σ1 = 310°
Max compressive stress = 99.19 MPa

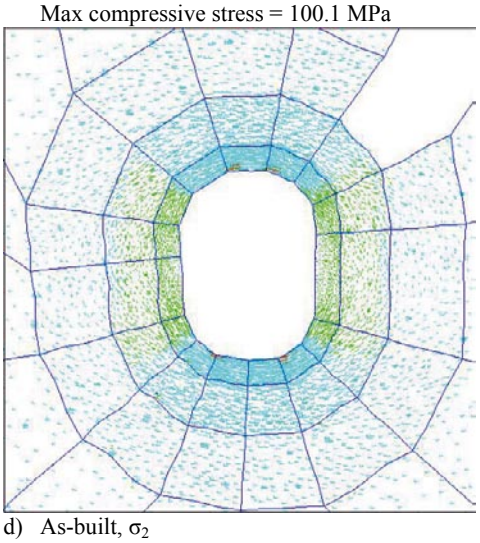

d) As-built, σ_2
E = 55 GPa, σ1 = 30 MPa, σ1 = 310°
Max compressive stress = 100.1 MPa

Sigma 2

min	max
-5.000E+07	-4.000E+07
-4.000E+07	-3.000E+07
-3.000E+07	-2.000E+07
-2.000E+07	-1.000E+07
-1.000E+07	0.000E+00
0.000E+00	1.000E+07

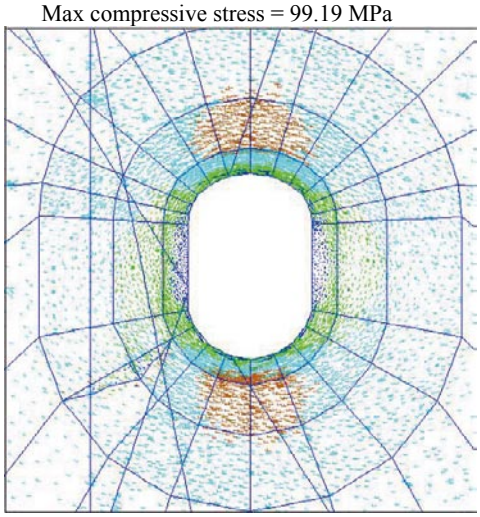

e) As-planned, σ_3
E = 55 GPa, σ1 = 30 MPa, σ1 = 310°
Max compressive stress = 99.19 MPa

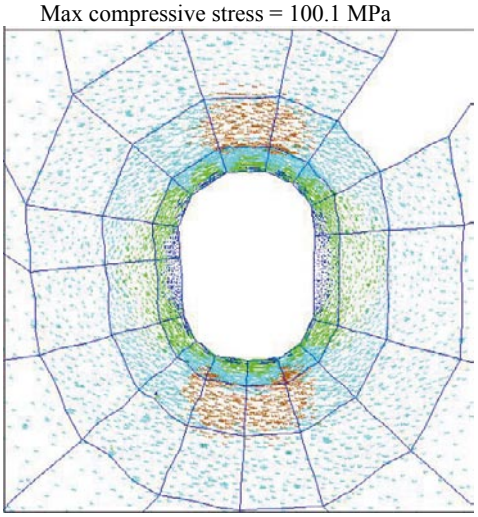

f) As-built, σ_3
E = 55 GPa, σ1 = 30 MPa, σ1 = 310°
Max compressive stress = 100.1 MPa

Sigma 3

min	max
-3.000E+07	-2.417E+07
-2.417E+07	-1.833E+07
-1.833E+07	-1.250E+07
-1.250E+07	-6.667E+06
-6.667E+06	-8.333E+05
-8.333E+05	5.000E+06

Figure E-4. *Cross section plots showing the projection of the principal stress tensor (color by magnitude of a) and b) Sigma 1, c) and d) Sigma 2, and e) and f) Sigma 3) for the as-planned and the as-built tunnel shapes with planar blasting round faces in section 49.*

Section 50

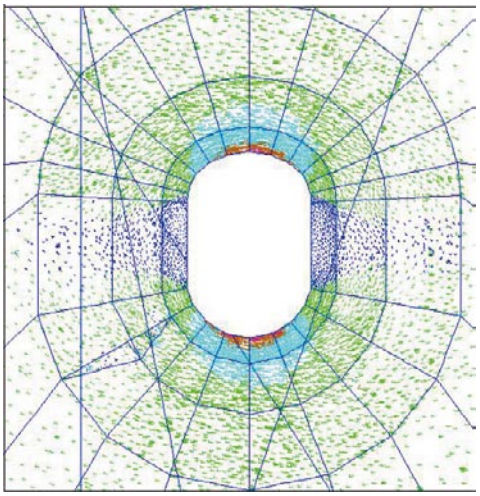

a) As-planned, σ_1
E = 55 GPa, σ1 = 30 MPa, σ1 = 310°
Max compressive stress = 100.6 MPa

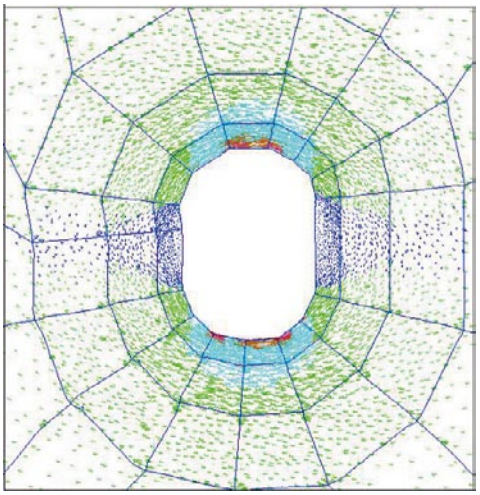

b) As-built, σ_1
E = 55 GPa, σ1 = 30 MPa, σ1 = 310°
Max compressive stress = 119.1 MPa

Sigma 1

min	max
-1.300E+08	-1.083E+08
-1.083E+08	-8.667E+07
-8.667E+07	-6.500E+07
-6.500E+07	-4.333E+07
-4.333E+07	-2.167E+07
-2.167E+07	0.000E+00

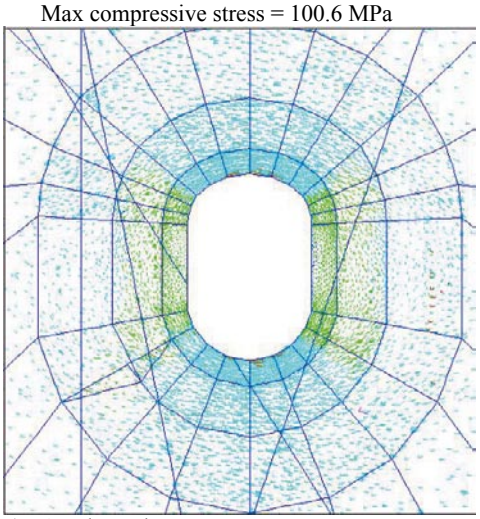

c) As-planned, σ_2
E = 55 GPa, σ1 = 30 MPa, σ1 = 310°
Max compressive stress = 100.6 MPa

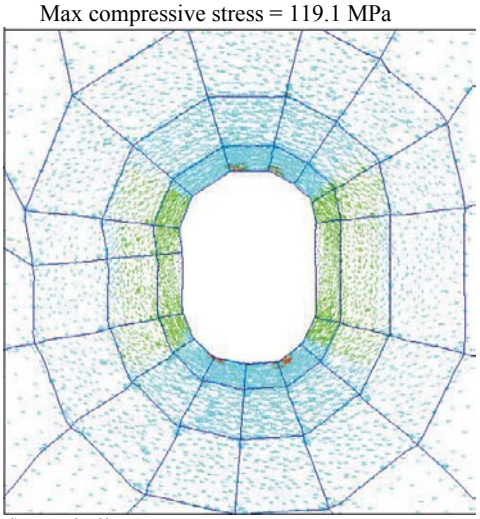

d) As-built, σ_2
E = 55 GPa, σ1 = 30 MPa, σ1 = 310°
Max compressive stress = 119.1 MPa

Sigma 2

min	max
-5.000E+07	-4.000E+07
-4.000E+07	-3.000E+07
-3.000E+07	-2.000E+07
-2.000E+07	-1.000E+07
-1.000E+07	0.000E+00
0.000E+00	1.000E+07

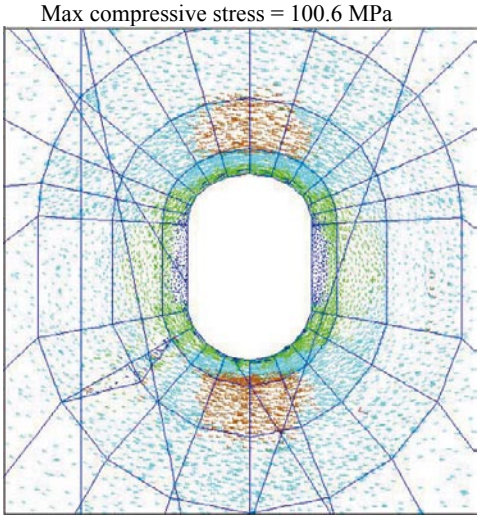

e) As-planned, σ_3
E = 55 GPa, σ1 = 30 MPa, σ1 = 310°
Max compressive stress = 100.6 MPa

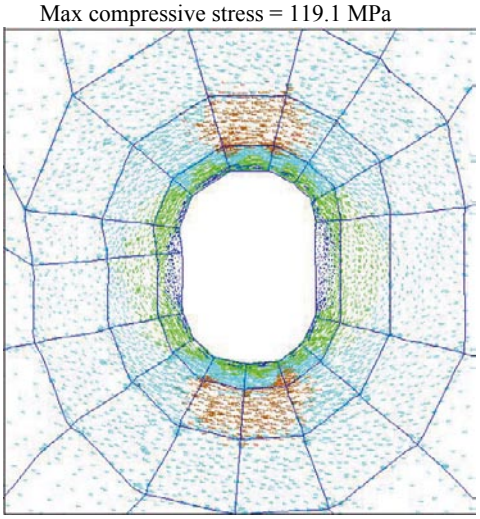

f) As-built, σ_3
E = 55 GPa, σ1 = 30 MPa, σ1 = 310°
Max compressive stress = 119.1 MPa

Sigma 3

min	max
-3.000E+07	-2.417E+07
-2.417E+07	-1.833E+07
-1.833E+07	-1.250E+07
-1.250E+07	-6.667E+06
-6.667E+06	-8.333E+05
-8.333E+05	5.000E+06

Figure E-5. *Cross section plots showing the projection of the principal stress tensor (color by magnitude of a) and b) Sigma 1, c) and d) Sigma 2, and e) and f) Sigma 3) for the as-planned and the as-built tunnel shapes with planar blasting round faces in section 50.*

Section 51

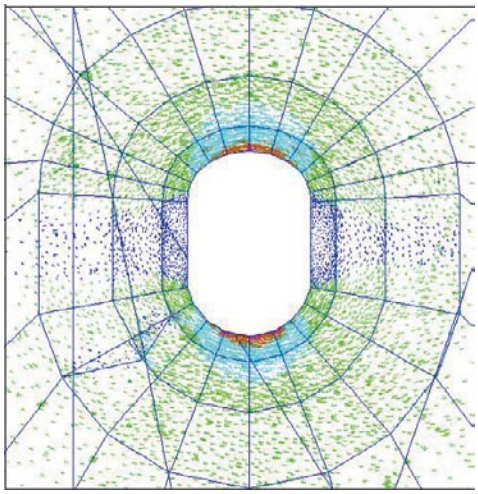

a) As-planned, σ_1
E = 55 GPa, σ1 = 30 MPa, σ1 = 310°
Max compressive stress = 101.8 MPa

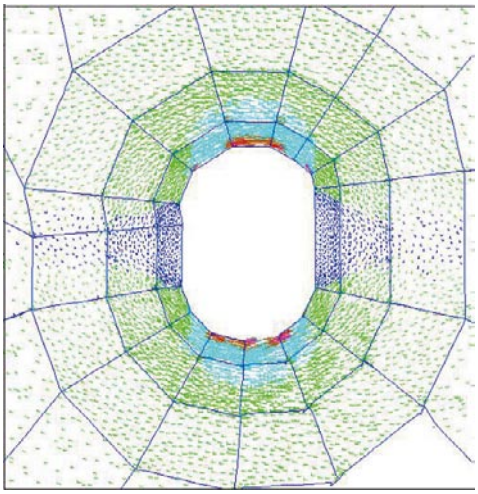

b) As-built, σ_1
E = 55 GPa, σ1 = 30 MPa, σ1 = 310°
Max compressive stress = 130.2 MPa

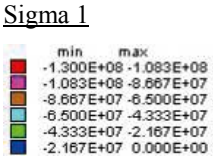

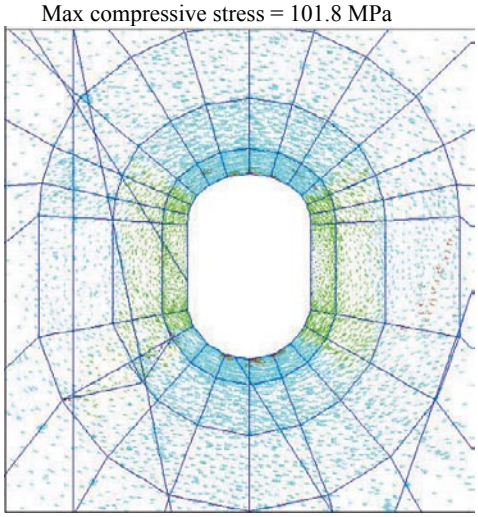

c) As-planned, σ_2
E = 55 GPa, σ1 = 30 MPa, σ1 = 310°
Max compressive stress = 101.8 MPa

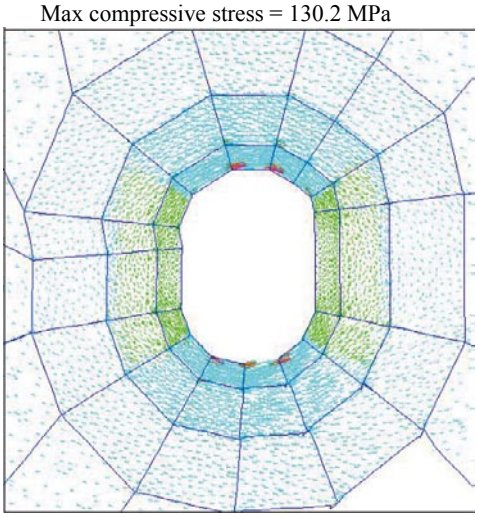

d) As-built, σ_2
E = 55 GPa, σ1 = 30 MPa, σ1 = 310°
Max compressive stress = 130.2 MPa

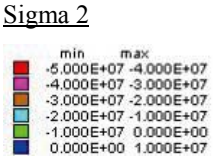

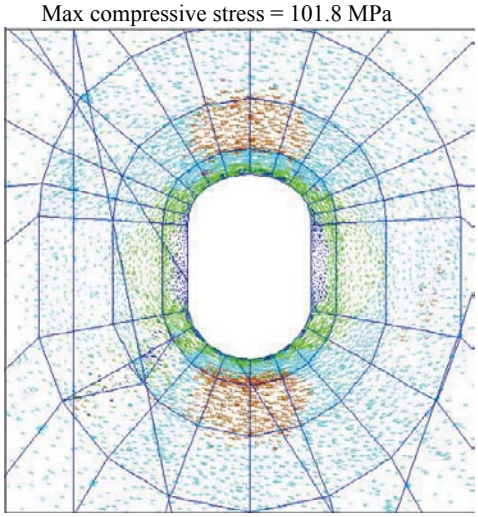

e) As-planned, σ_3
E = 55 GPa, σ1 = 30 MPa, σ1 = 310°
Max compressive stress = 101.8 MPa

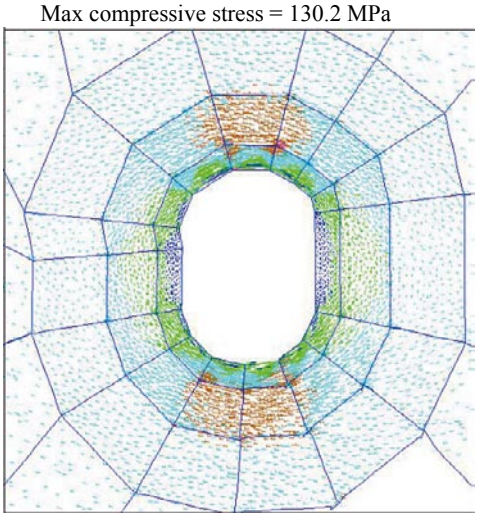

f) As-built, σ_3
E = 55 GPa, σ1 = 30 MPa, σ1 = 310°
Max compressive stress = 130.2 MPa

Figure E-6. *Cross section plots showing the projection of the principal stress tensor (color by magnitude of a) and b) Sigma 1, c) and d) Sigma 2, and e) and f) Sigma 3) for the as-planned and the as-built tunnel shapes with planar blasting round faces in section 51.*

Appendix F

Sensitivity analysis, models with fractures with different properties

Sensitivity analysis; as-planned tunnel shape including fractures and planar blasting round faces: The figures in this appendix show the difference in stress redistribution (colour by the magnitude of Sigma 1) in TASQ tunnel sections 46–51 while changing fracture properties (see Table 9-3 to Table 9-5).

Section 46

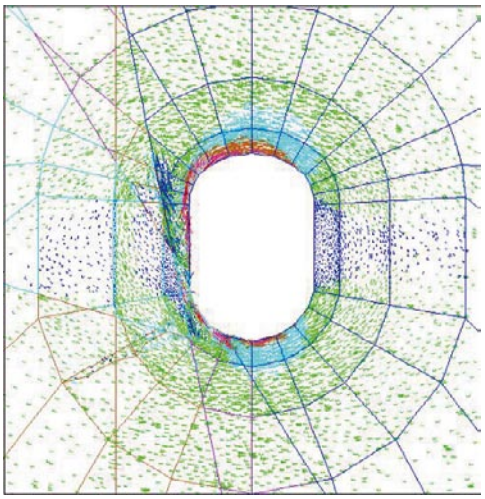

a) Baseline case
E = 55 GPa, σ1 = 30 MPa, σ1 =310°
Max compressive stress = 208.4 MPa

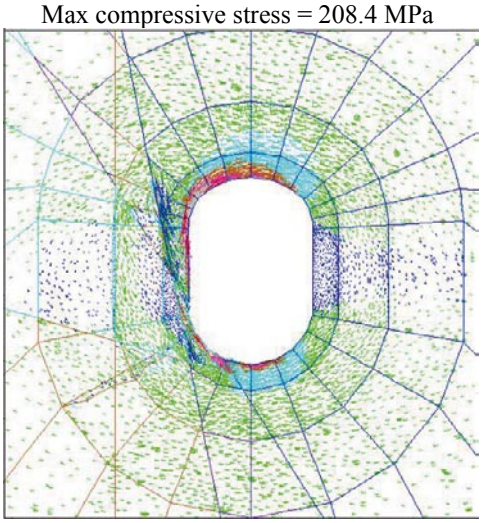

b) Weak
E = 55 GPa, σ1 = 30 MPa, σ1 = 310°
Max compressive stress = 217.5 MPa

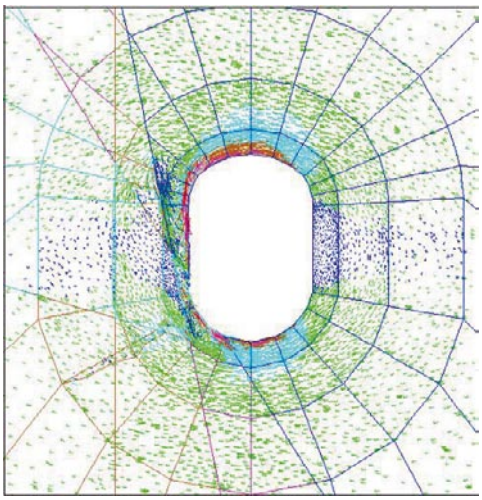

c) Strong
E = 55 GPa, σ1 = 30 MPa, σ1 = 310°
Max compressive stress = 197.3 MPa

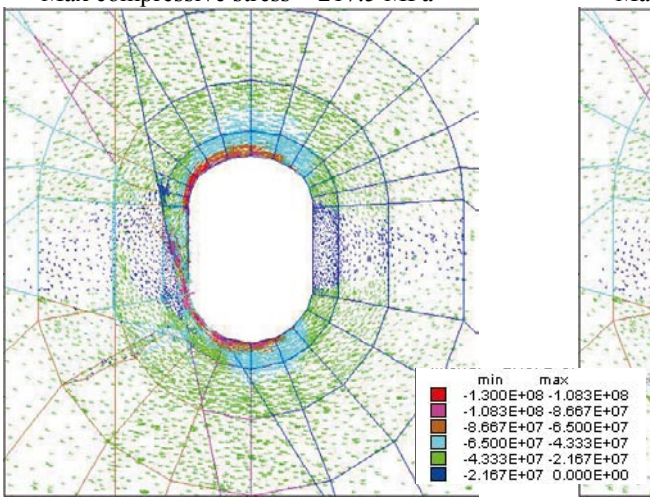

d) Elastic mylonite
E = 55 GPa, σ1 = 30 MPa, σ1 =310°
Max compressive stress = 191.1MPa

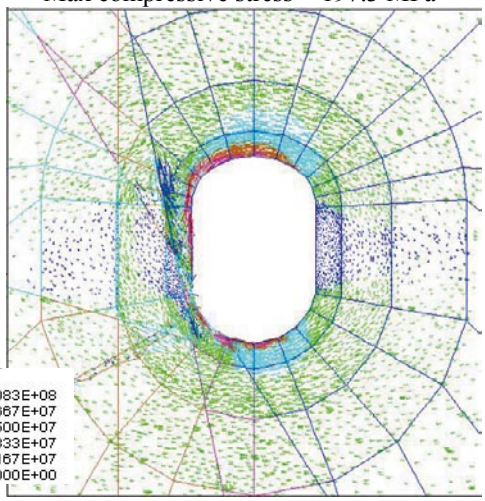

e) Strong mylonite
E = 55 GPa, σ1 = 30 MPa, σ1 = 310°
Max compressive stress = 206.7 MPa

Figure F-1. *Cross section plots showing the projection of the principal stress tensor (color by magnitude of Sigma1) at section 46. See Table 9-3 to Table 9-5 for fracture properties*

Section 46

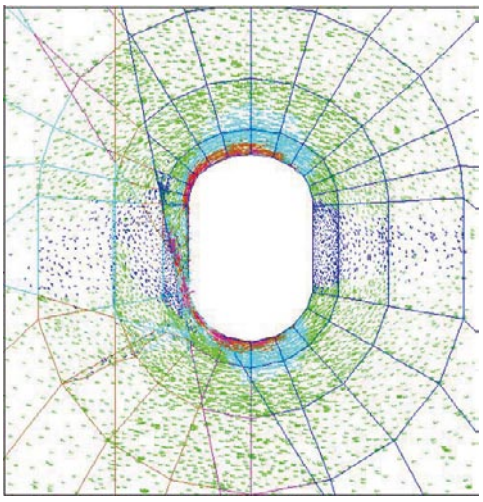

f) Stiff
E = 55 GPa, σ1 = 30 MPa, σ1 =310°
Max compressive stress = 186.2 MPa

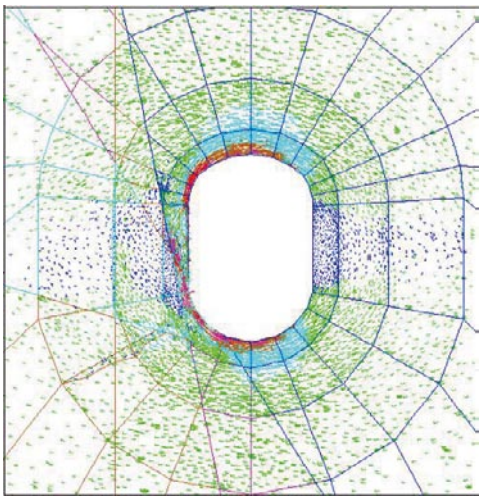

g) Stiff
E = 65 GPa, σ1 = 30 MPa, σ1 =310°
Max compressive stress = 189.8 MPa

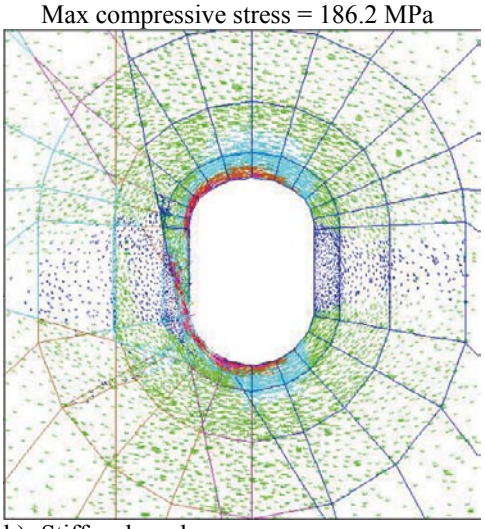

h) Stiff and weak
E = 55 GPa, σ1 = 30 MPa, σ1 = 310°
Max compressive stress = 188.4 MPa

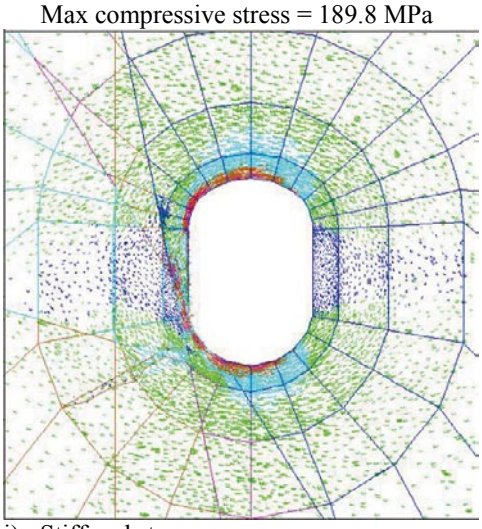

i) Stiff and strong
E = 55 GPa, σ1 = 30 MPa, σ1 = 310°.....
Max compressive stress = 183.9 MPa ....

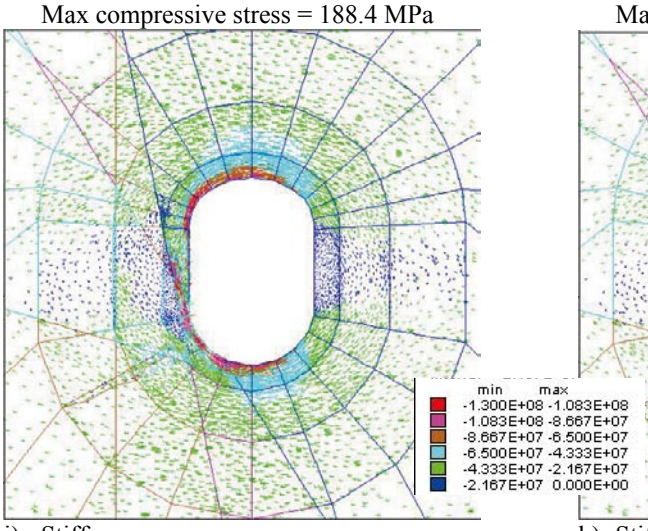

j) Stiffer
E = 55 GPa, σ1 = 30 MPa, σ1 =310°
Max compressive stress = 184.4 MPa

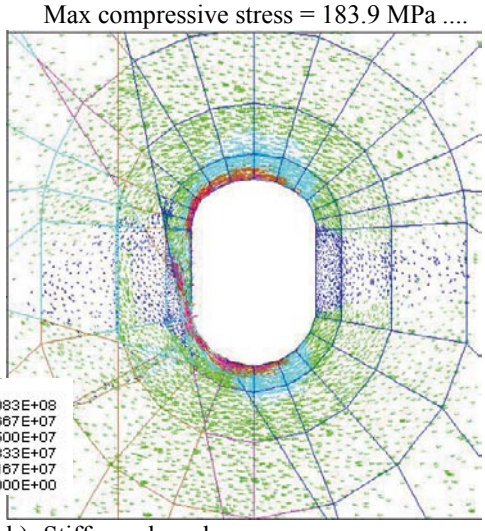

k) Stiffer and weak
E = 55 GPa, σ1 = 30 MPa, σ1 = 310°.....
Max compressive stress = 186.3 MPa

Figure F-2. *Cross section plots showing the projection of the principal stress tensor (color by magnitude of Sigma1) at section 46. See Table 9-3 to Table 9-5 for fracture properties*

Section 47

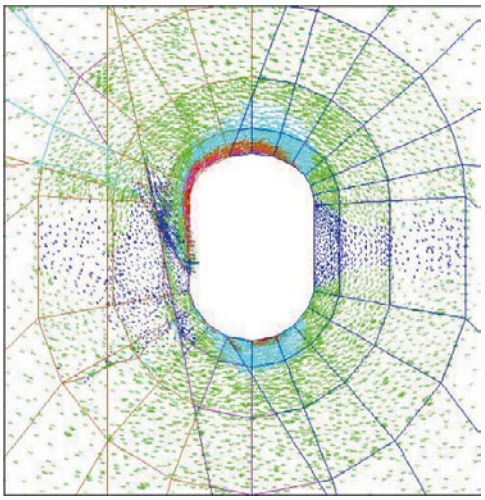

a) Baseline case
E = 55 GPa, σ1 = 30 MPa, σ1 =310°
Max compressive stress = 145.7 MPa

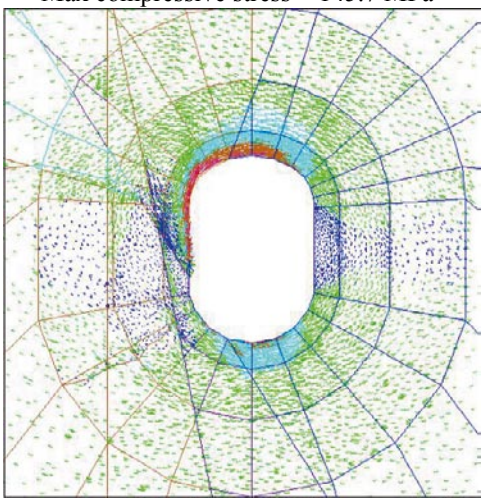

b) Weak
E = 55 GPa, σ1 = 30 MPa, σ1 = 310°
Max compressive stress = 138.8 MPa

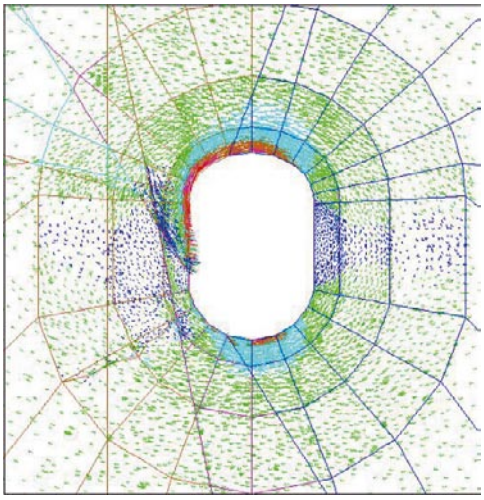

c) Strong
E = 55 GPa, σ1 = 30 MPa, σ1 = 310°
Max compressive stress = 146.0 MPa

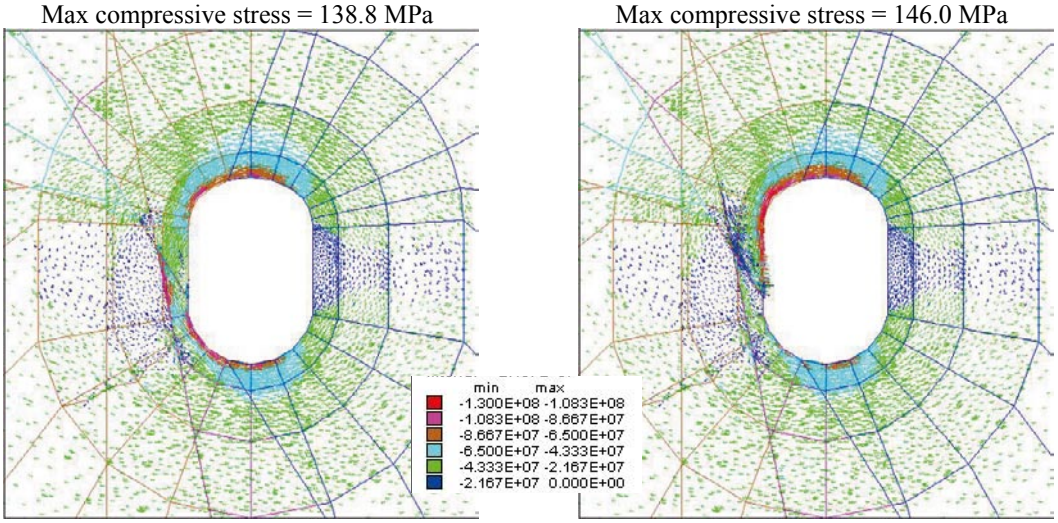

d) Elastic mylonite
E = 55 GPa, σ1 = 30 MPa, σ1 =310°
Max compressive stress = 118.7 MPa

e) Strong mylonite
E = 55 GPa, σ1 = 30 MPa, σ1 = 310°
Max compressive stress = 147.2 MPa

Figure F-3. *Cross section plots showing the projection of the principal stress tensor (color by magnitude of Sigma1) at section 47. See Table 9-3 to Table 9-5 for fracture properties*

Section 47

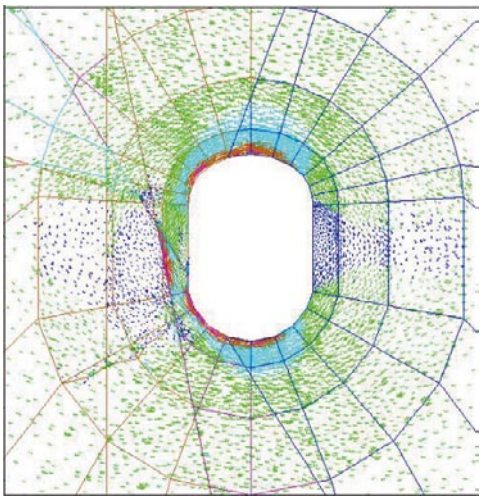

f) Stiff
E = 55 GPa, σ1 = 30 MPa, σ1 =310°
Max compressive stress = 120.9 MPa

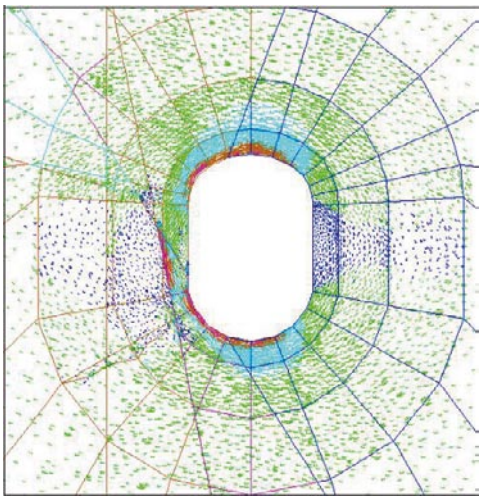

g) Stiff
E = 65 GPa, σ1 = 30 MPa, σ1 =310°
Max compressive stress = 122.8 MPa

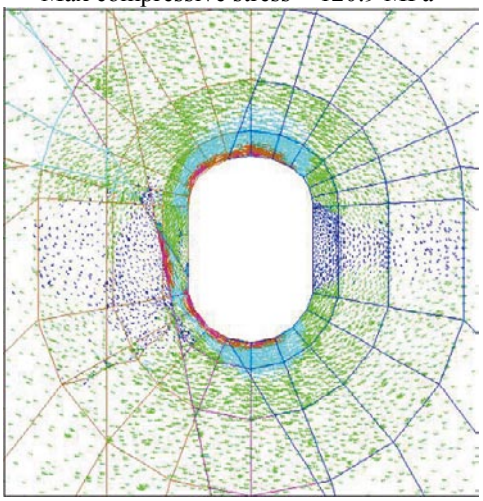

h) Stiff and weak
E = 55 GPa, σ1 = 30 MPa, σ1 = 310°
Max compressive stress = 121.2 MPa

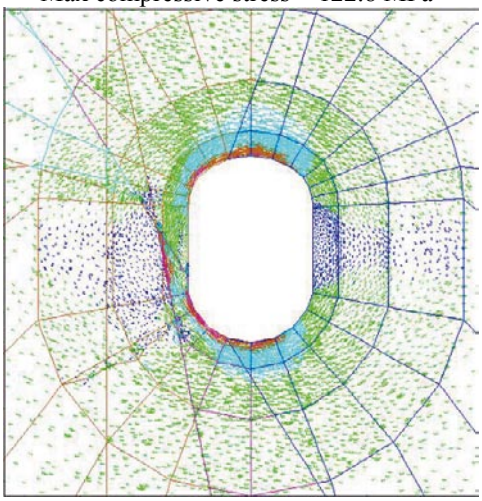

i) Stiff and strong
E = 55 GPa, σ1 = 30 MPa, σ1 = 310°
Max compressive stress = 121.5 MPa

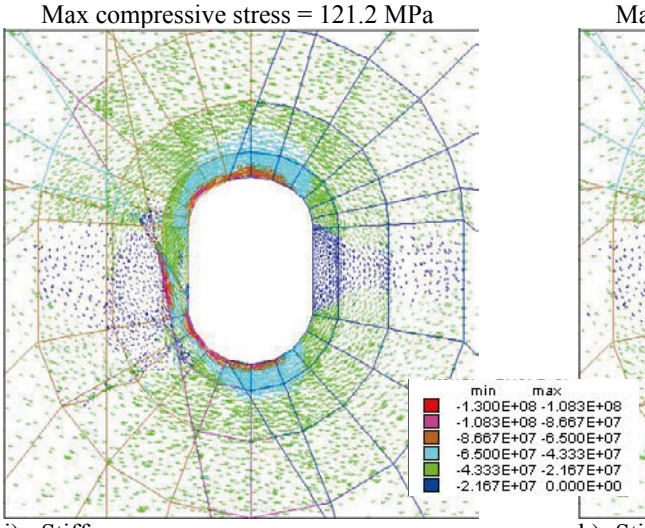

j) Stiffer
E = 55 GPa, σ1 = 30 MPa, σ1 =310°
Max compressive stress = 121.2 MPa

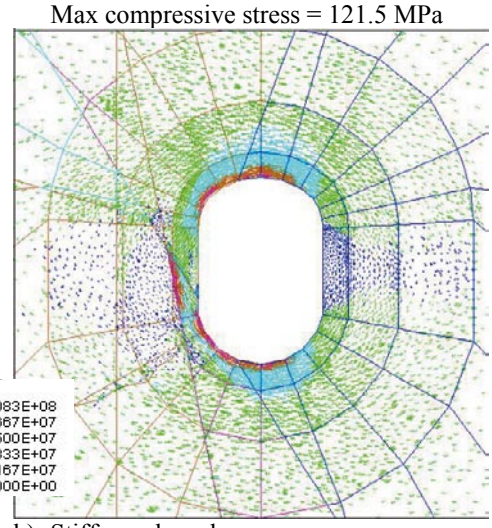

k) Stiffer and weak
E = 55 GPa, σ1 = 30 MPa, σ1 = 310°
Max compressive stress = 121.4 MPa

Figure F-4. *Cross section plots showing the projection of the principal stress tensor (color by magnitude of Sigma1) at section 47. See Table 9-3 to Table 9-5 for fracture properties*

Section 48

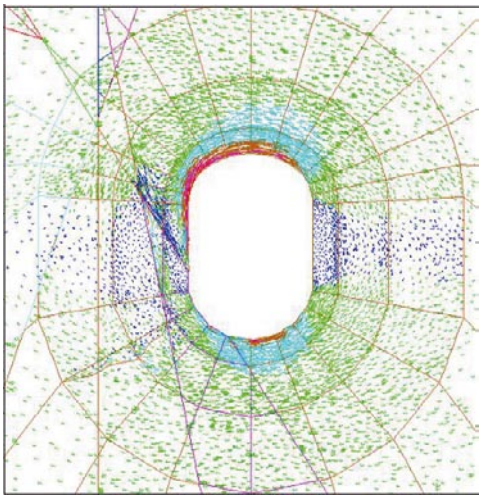

a) Baseline case
E = 55 GPa, σ1 = 30 MPa, σ1 =310°
Max compressive stress = 135.6 MPa

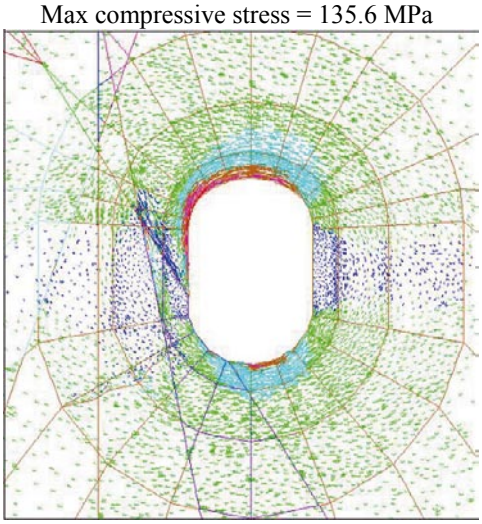

b) Weak
E = 55 GPa, σ1 = 30 MPa, σ1 = 310°
Max compressive stress = 137.1 MPa

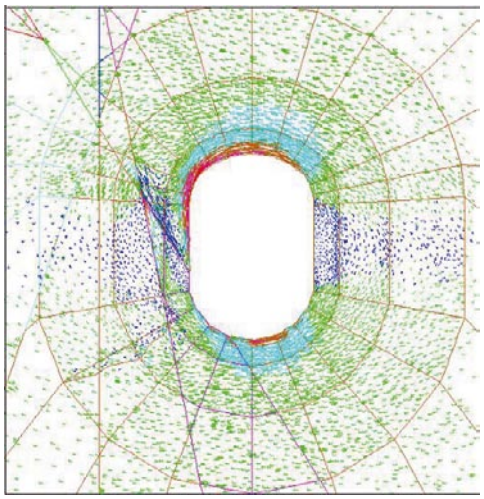

c) Strong
E = 55 GPa, σ1 = 30 MPa, σ1 = 310°
Max compressive stress = 140.0 MPa

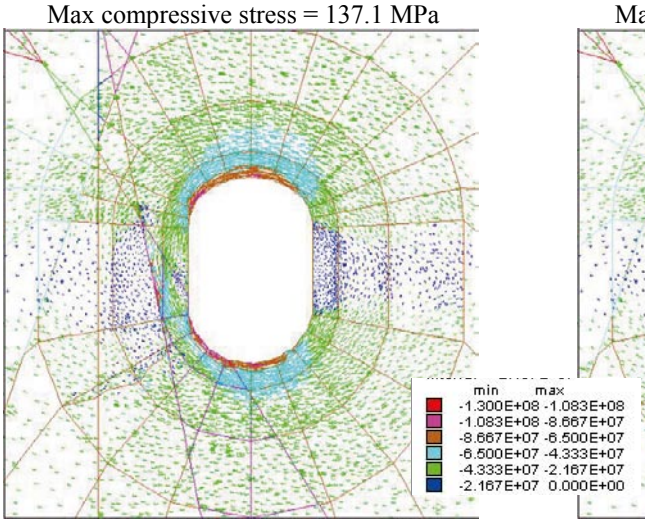

d) Elastic mylonite
E = 55 GPa, σ1 = 30 MPa, σ1 =310°
Max compressive stress = 171.7 MPa

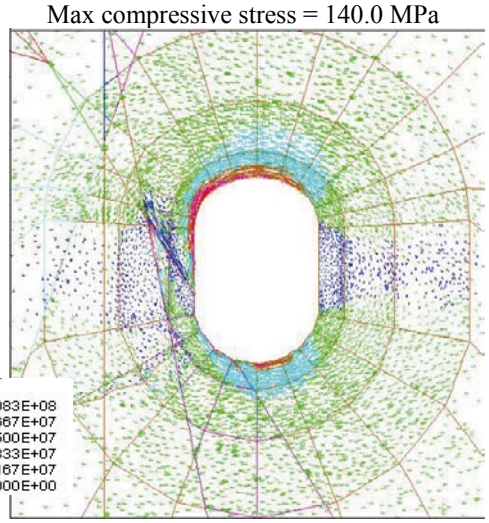

e) Strong mylonite
E = 55 GPa, σ1 = 30 MPa, σ1 = 310°
Max compressive stress = 133.7 MPa

Figure F-5. *Cross section plots showing the projection of the principal stress tensor (color by magnitude of Sigma1) at section 48. See Table 9-3 to Table 9-5 for fracture properties*

Section 48

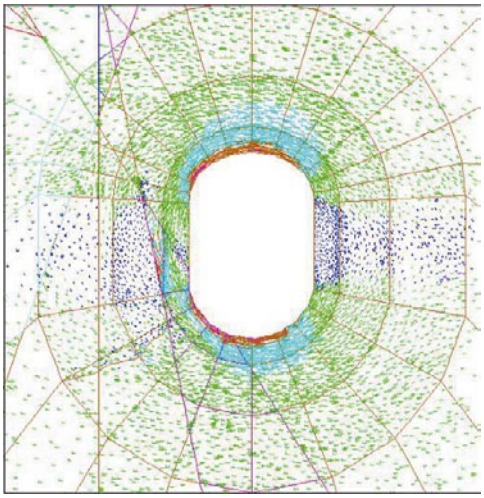

f) Stiff
E = 55 GPa, σ1 = 30 MPa, σ1 =310°
Max compressive stress = 138.7 MPa

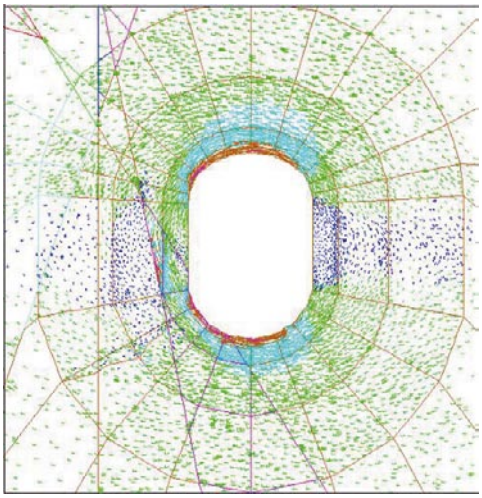

g) Stiff
E = 65 GPa, σ1 = 30 MPa, σ1 =310°
Max compressive stress = 142.1 MPa

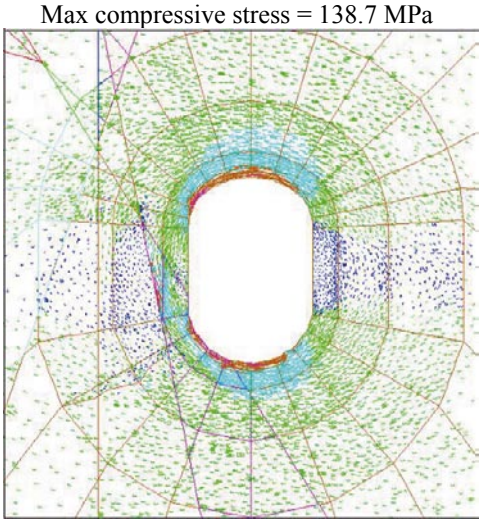

h) Stiff and weak
E = 55 GPa, σ1 = 30 MPa, σ1 = 310°
Max compressive stress = 137.8 MPa

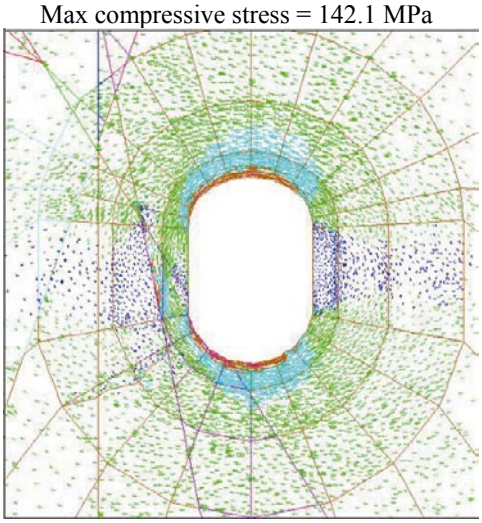

i) Stiff and strong
E = 55 GPa, σ1 = 30 MPa, σ1 = 310°
Max compressive stress = 139.9 MPa

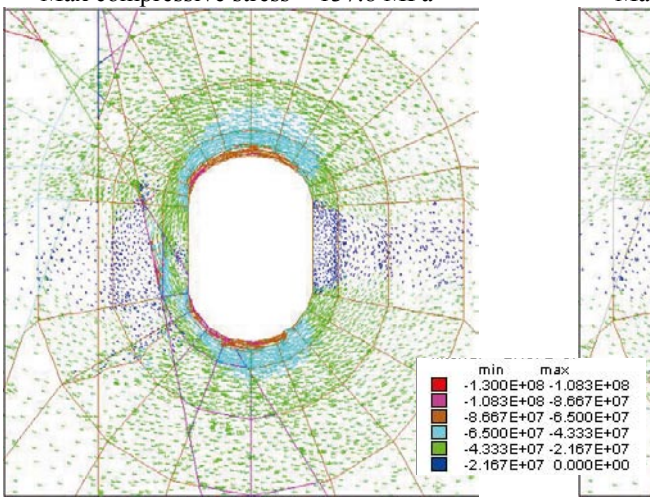

j) Stiffer
E = 55 GPa, σ1 = 30 MPa, σ1 =310°
Max compressive stress = 123.9 MPa

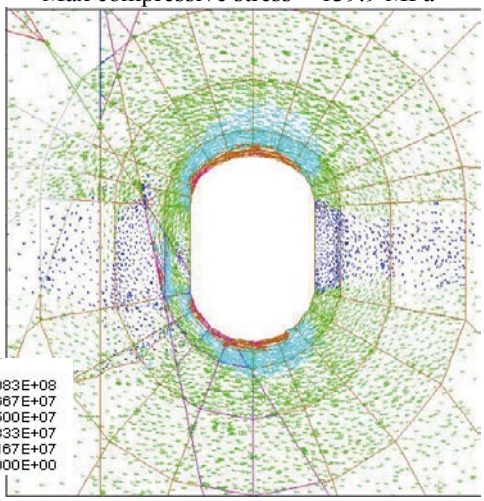

k) Stiffer and weak
E = 55 GPa, σ1 = 30 MPa, σ1 = 310°
Max compressive stress = 122.9 MPa

Figure F-6. *Cross section plots showing the projection of the principal stress tensor (color by magnitude of Sigma1) at section 48. See Table 9-3 to Table 9-5 for fracture properties*

Section 49

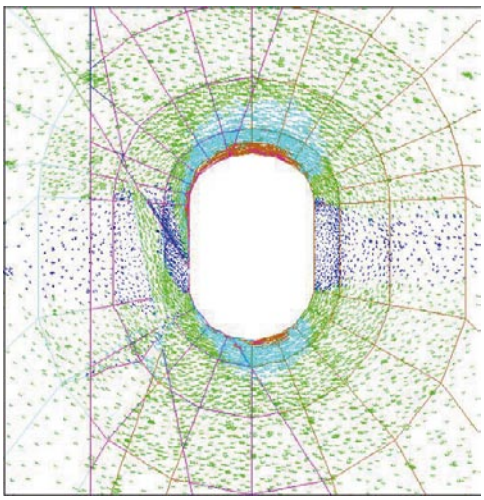

a) Baseline case
E = 55 GPa, σ1 = 30 MPa, σ1 =310°
Max compressive stress = 93.20 MPa

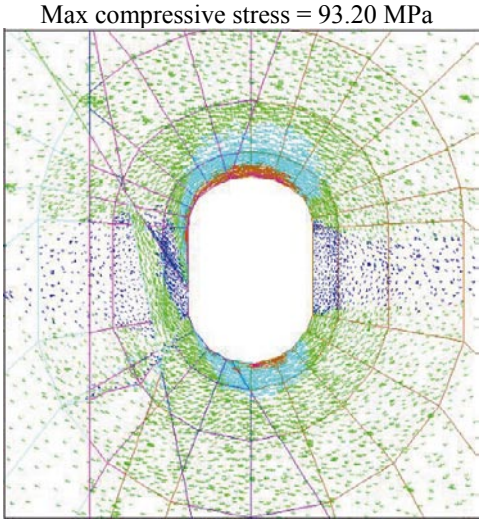

b) Weak
E = 55 GPa, σ1 = 30 MPa, σ1 = 310°
Max compressive stress = 93.47 MPa

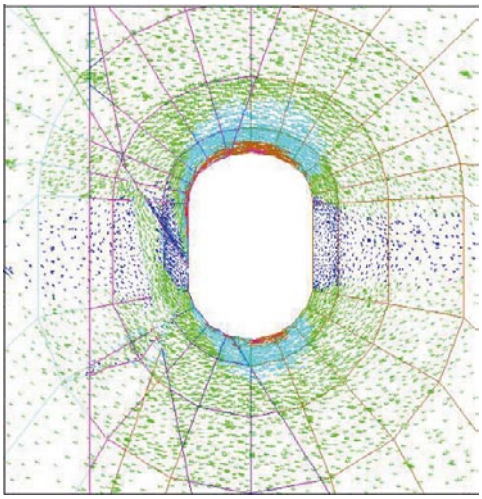

c) Strong
E = 55 GPa, σ1 = 30 MPa, σ1 = 310°
Max compressive stress = 92.56 MPa

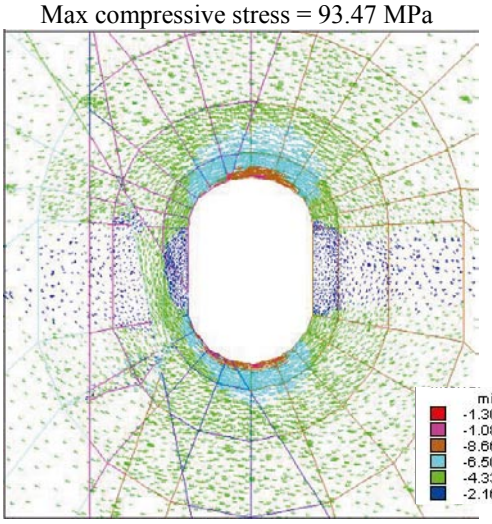

d) Elastic mylonite
E = 55 GPa, σ1 = 30 MPa, σ1 =310°
Max compressive stress = 95.19 MPa

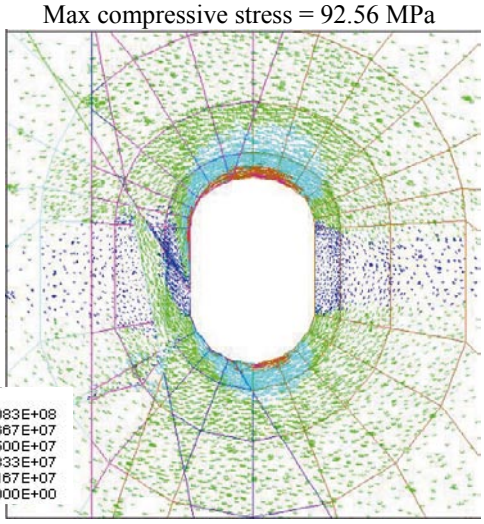

e) Strong mylonite
E = 55 GPa, σ1 = 30 MPa, σ1 = 310°
Max compressive stress = 92.34 MPa

Figure F-7. *Cross section plots showing the projection of the principal stress tensor (color by magnitude of Sigma1) at section 49. See Table 9-3 to Table 9-5 for fracture properties*

Section 49

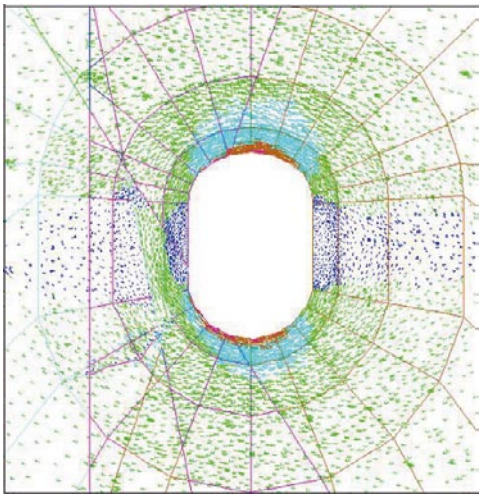

f) Stiff
E = 55 GPa, σ1 = 30 MPa, σ1 =310°
Max compressive stress = 94.82 MPa

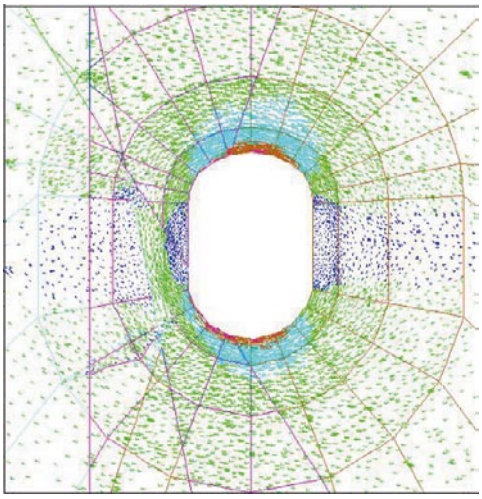

g) Stiff
E = 65 GPa, σ1 = 30 MPa, σ1 =310°
Max compressive stress = 94.81 MPa

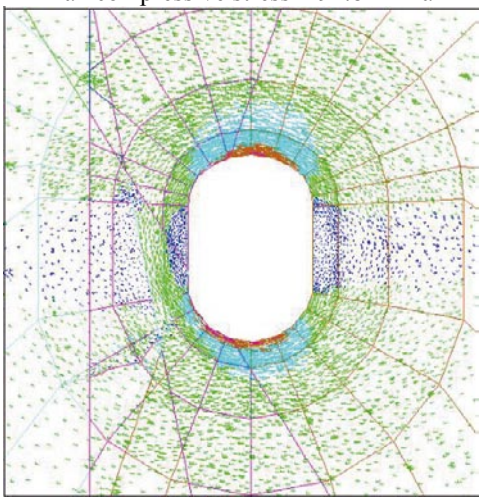

h) Stiff and weak
E = 55 GPa, σ1 = 30 MPa, σ1 = 310°
Max compressive stress = 95.45 MPa

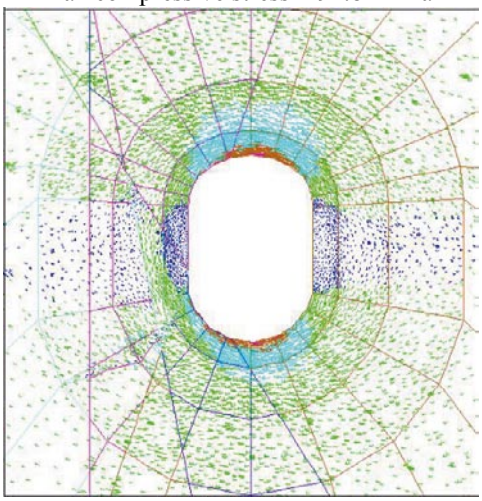

i) Stiff and strong
E = 55 GPa, σ1 = 30 MPa, σ1 = 310°
Max compressive stress = 94.48 MPa

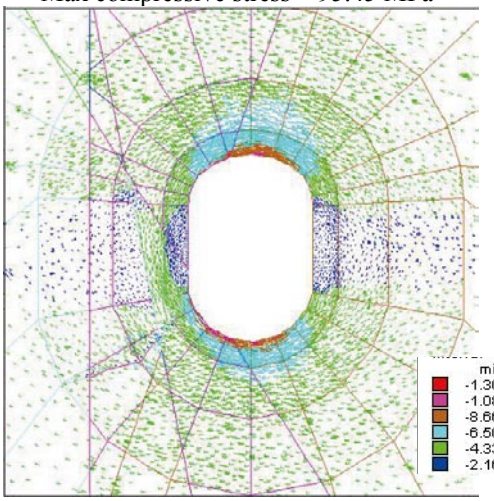

j) Stiffer
E = 55 GPa, σ1 = 30 MPa, σ1 =310°
Max compressive stress = 94.70 MPa

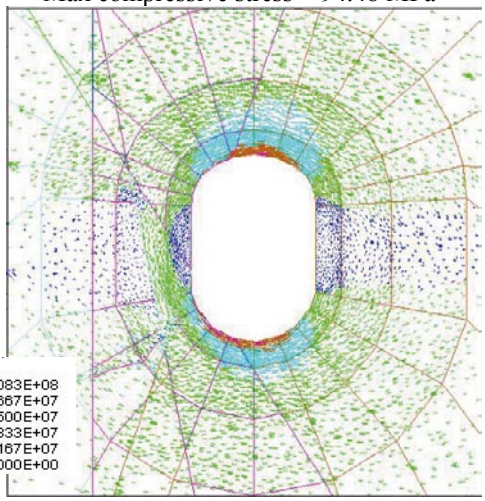

k) Stiffer and weak
E = 55 GPa, σ1 = 30 MPa, σ1 = 310°
Max compressive stress = 95.22 MPa

Figure F-8. *Cross section plots showing the projection of the principal stress tensor (color by magnitude of Sigma1) at section 49. See Table 9-3 to Table 9-5 for fracture properties*

Section 50

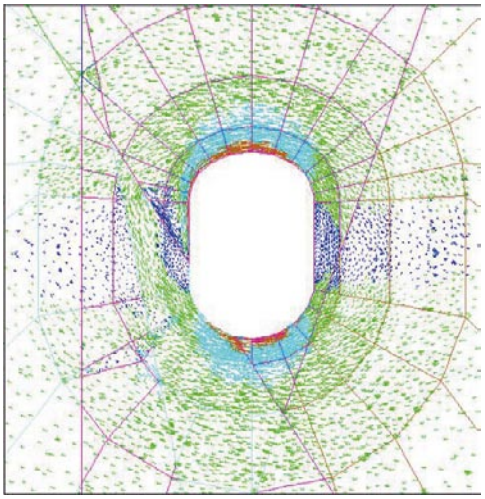

a) Baseline case
E = 55 GPa, σ1 = 30 MPa, σ1 =310°
Max compressive stress = 101.2 MPa

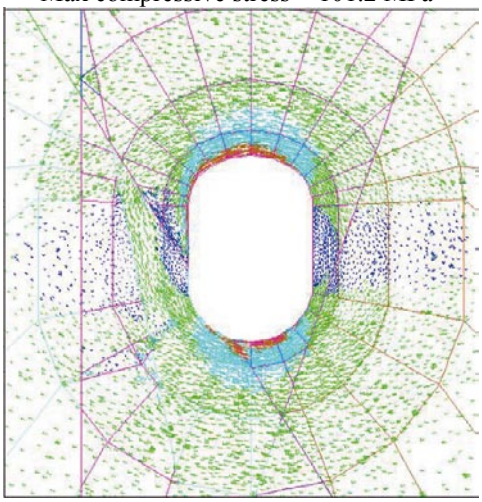

b) Weak
E = 55 GPa, σ1 = 30 MPa, σ1 = 310°
Max compressive stress = 103.7 MPa

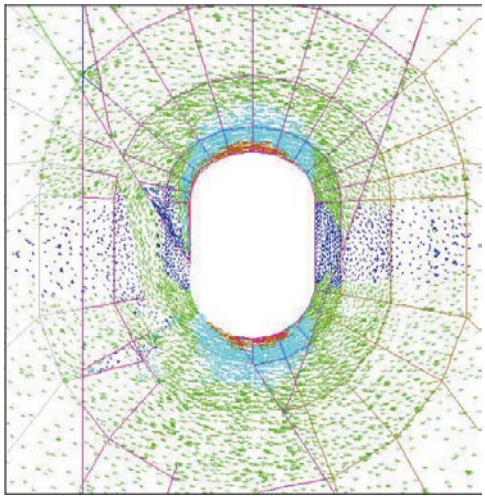

c) Strong
E = 55 GPa, σ1 = 30 MPa, σ1 = 310°
Max compressive stress = 100.7 MPa

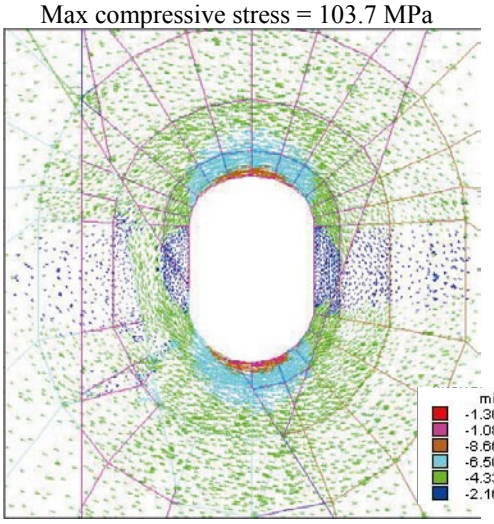

d) Elastic mylonite
E = 55 GPa, σ1 = 30 MPa, σ1 =310°
Max compressive stress = 102.2 MPa

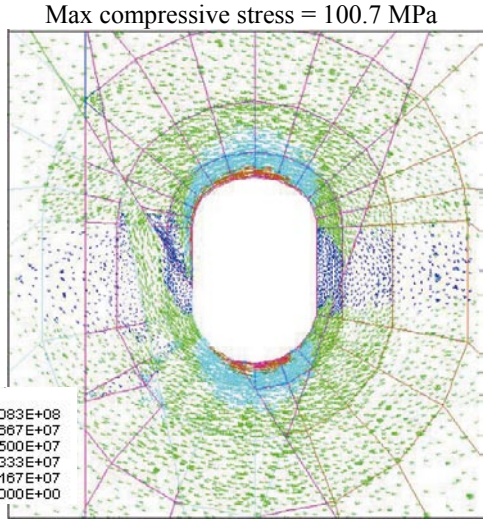

e) Strong mylonite
E = 55 GPa, σ1 = 30 MPa, σ1 = 310°
Max compressive stress = 101.1 MPa ...

Figure F-9. *Cross section plots showing the projection of the principal stress tensor (color by magnitude of Sigma1) at section 50. See Table 9-3 to Table 9-5 for fracture properties*

Section 50

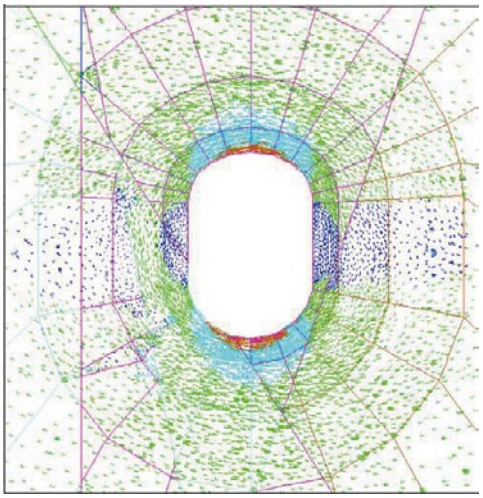

f) Stiff
E = 55 GPa, σ1 = 30 MPa, σ1 =310°
Max compressive stress = 101.8 MPa

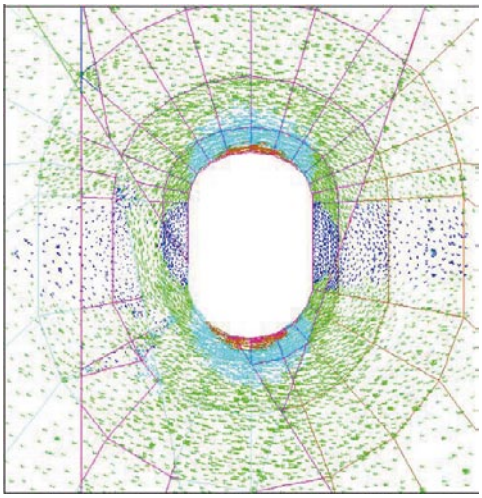

g) Stiff
E = 65 GPa, σ1 = 30 MPa, σ1 =310°
Max compressive stress = 102.0 MPa

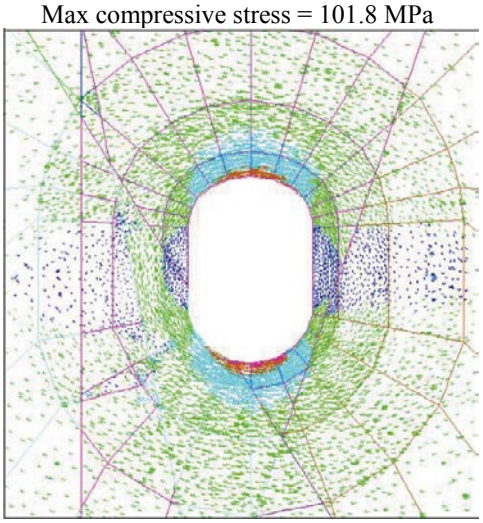

h) Stiff and weak
E = 55 GPa, σ1 = 30 MPa, σ1 = 310°
Max compressive stress = 102.5 MPa

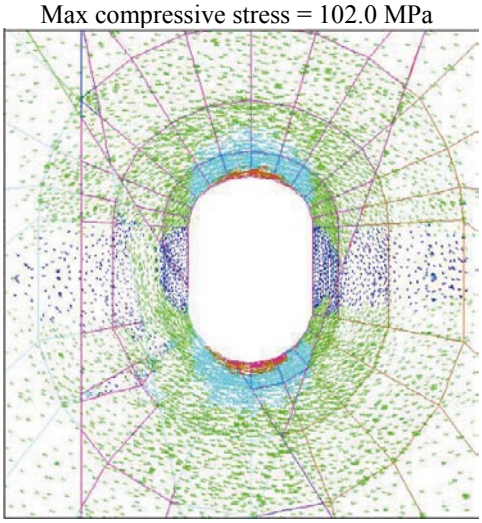

i) Stiff and strong
E = 55 GPa, σ1 = 30 MPa, σ1 = 310°
Max compressive stress = 101.6 MPa

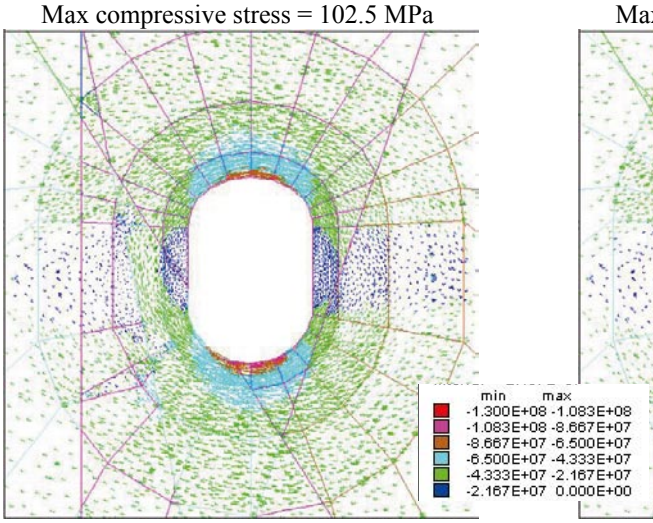

j) Stiffer
E = 55 GPa, σ1 = 30 MPa, σ1 =310°
Max compressive stress = 101.9 MPa

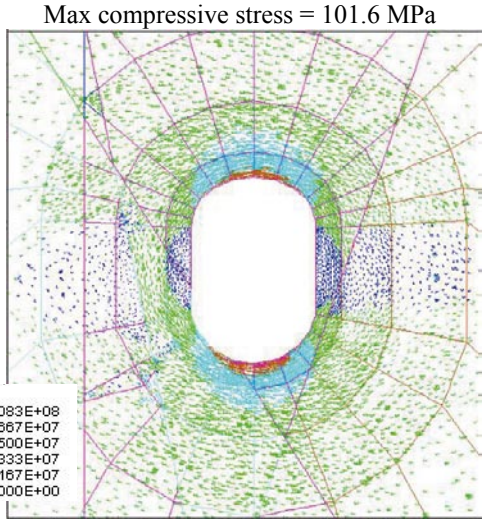

k) Stiffer and weak
E = 55 GPa, σ1 = 30 MPa, σ1 = 310°
Max compressive stress = 102.7 MPa

Figure F-10. *Cross section plots showing the projection of the principal stress tensor (color by magnitude of Sigma1) at section 50. See Table 9-3 to Table 9-5 for fracture properties*

Section 51

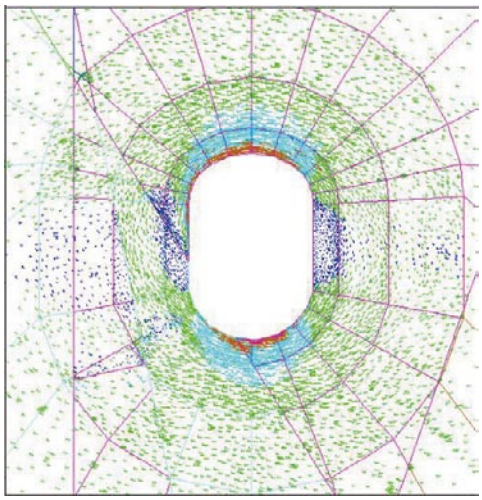

a) Baseline case
E = 55 GPa, σ1 = 30 MPa, σ1 =310°
Max compressive stress = 102.4 MPa

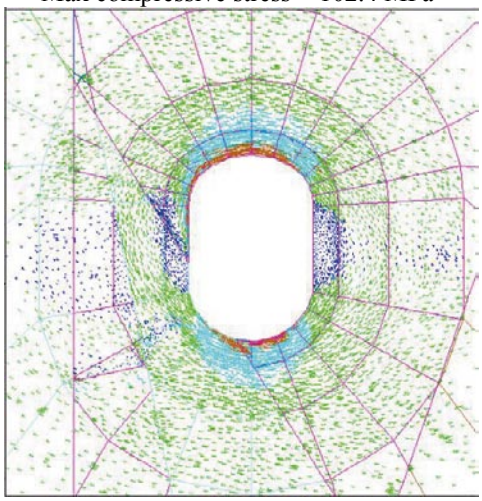

b) Weak
E = 55 GPa, σ1 = 30 MPa, σ1 = 310°
Max compressive stress = 104.4 MPa

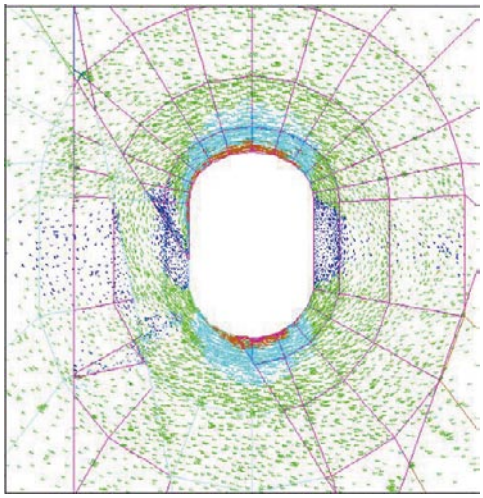

c) Strong
E = 55 GPa, σ1 = 30 MPa, σ1 = 310°
Max compressive stress = 102.5 MPa

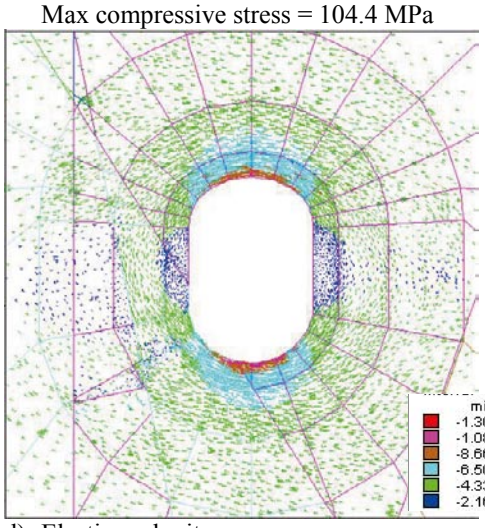

d) Elastic mylonite
E = 55 GPa, σ1 = 30 MPa, σ1 =310°
Max compressive stress = 103.4 MPa

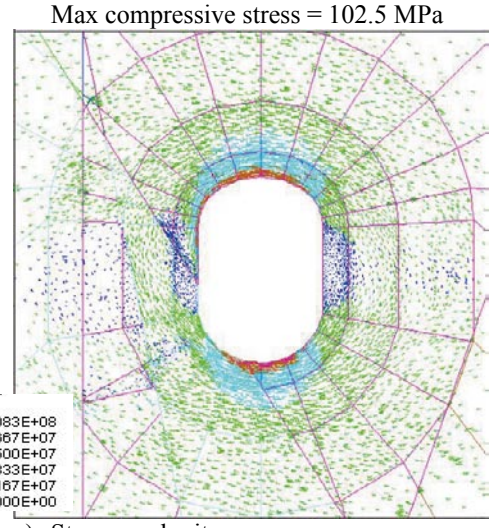

e) Strong mylonite
E = 55 GPa, σ1 = 30 MPa, σ1 = 310°
Max compressive stress = 102.6 MPa

Figure F-11. *Cross section plots showing the projection of the principal stress tensor (color by magnitude of Sigma1) at section 51. See Table 9-3 to Table 9-5 for fracture properties*

Section 51

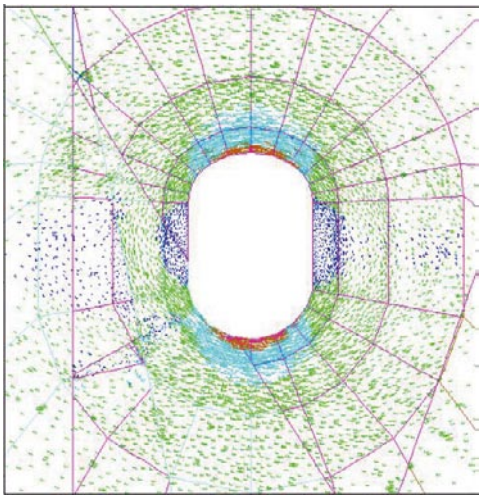

f) Stiff
E = 55 GPa, σ1 = 30 MPa, σ1 =310°
Max compressive stress = 103.3 MPa

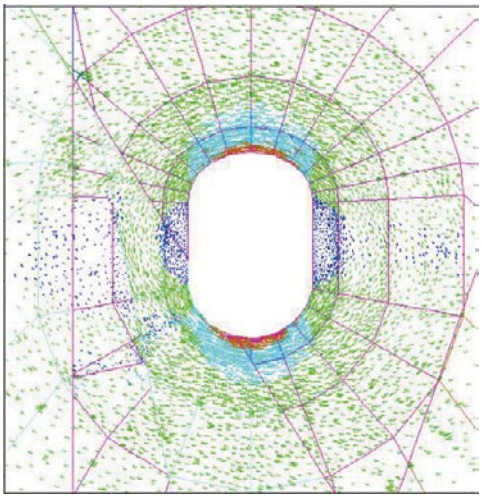

g) Stiff
E = 65 GPa, σ1 = 30 MPa, σ1 =310°
Max compressive stress = 103.4 MPa

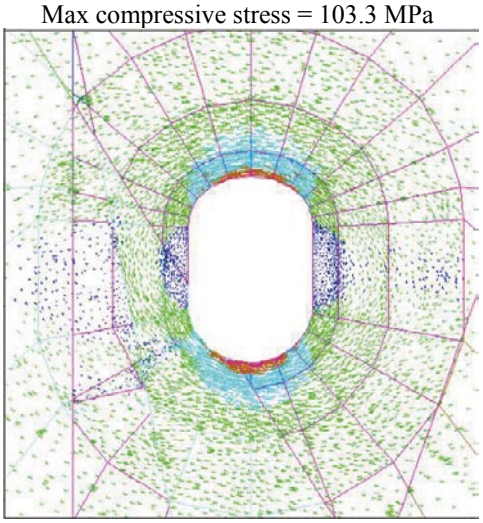

h) Stiff and weak
E = 55 GPa, σ1 = 30 MPa, σ1 = 310°
Max compressive stress = 104.2 MPa

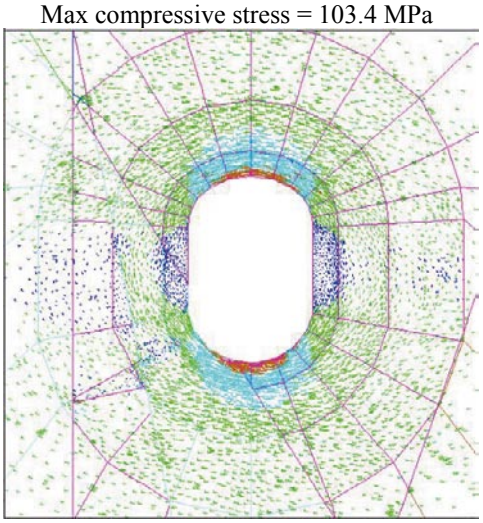

i) Stiff and strong
E = 55 GPa, σ1 = 30 MPa, σ1 = 310°
Max compressive stress = 103.3 MPa

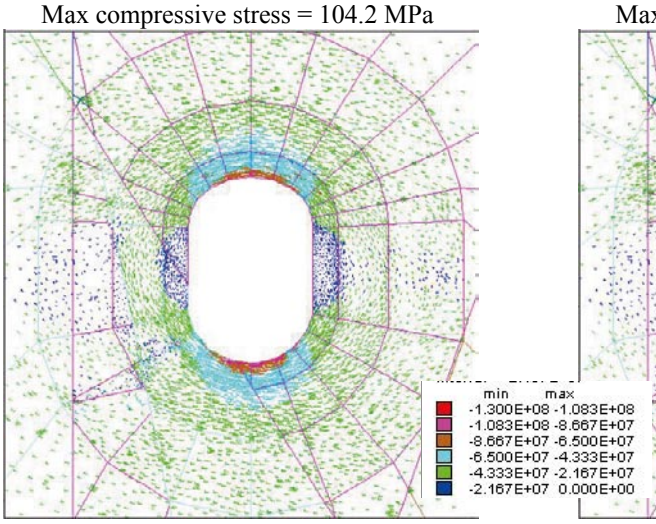

j) Stiffer
E = 55 GPa, σ1 = 30 MPa, σ1 =310°
Max compressive stress = 103.3 MPa

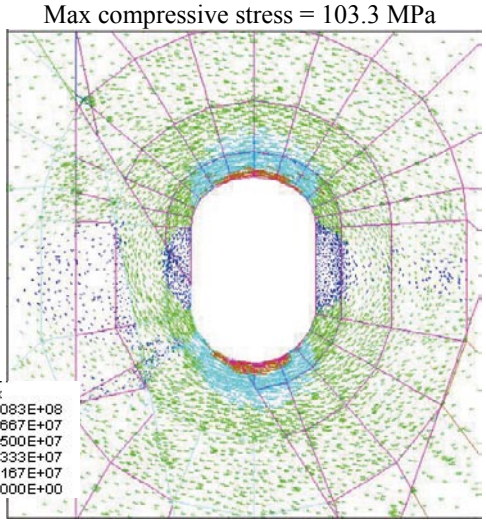

k) Stiffer and weak
E = 55 GPa, σ1 = 30 MPa, σ1 = 310°
Max compressive stress = 104.2 MPa

Figure F-12. *Cross section plots showing the projection of the principal stress tensor (color by magnitude of Sigma1) at section 51. See Table 9-3 to Table 9-5 for fracture properties*

Appendix G

Shear displacement in fractures

Cross section plots showing the maximum fracture shear displacement (as-planned tunnel shape) in TASQ tunnel sections 47 (ultra sonic measurements, BGR), 48 (slot) and 49 (close to convergence measurements). 12 cases with different fracture properties (see Table 9-3 to Table 9-5); a) Baseline case, b) Stiff fractures with E = 65 GPa and σ_1 = 25 MPa, c) Weak fractures d) Strong fractures, e) Elastic mylonite, f) Strong mylonite, g) stiff fractures with E = 55 GPa and σ_1 = 30 MPa, h) stiff fractures with E = 65 GPa and σ_1 = 30 MPa, i) Stiff and weak fractures, j) Stiff and strong fractures, k) Stiffer fractures and l) Stiffer and weak fractures.

Section 47 (Ultrasonic measurements, BGR)

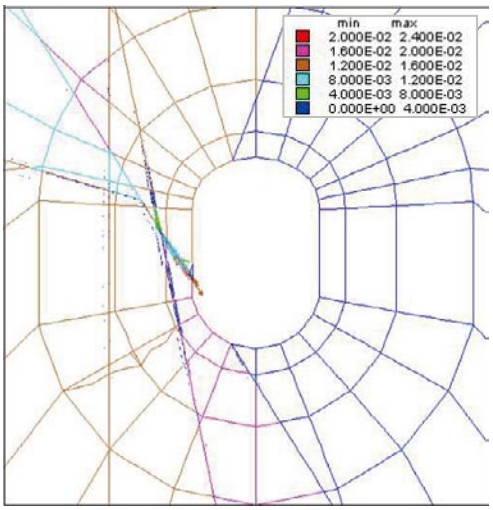

a) Baseline case
Max shear displacement = 15.75 mm

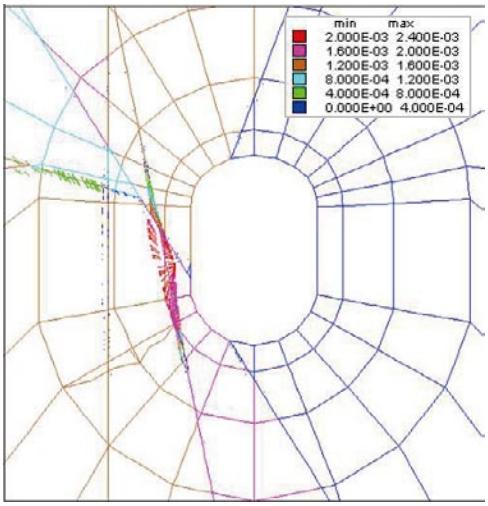

b) Stiff (E=65GPa, σ_1=25MPa)
Max shear displacement = 2.243 mm

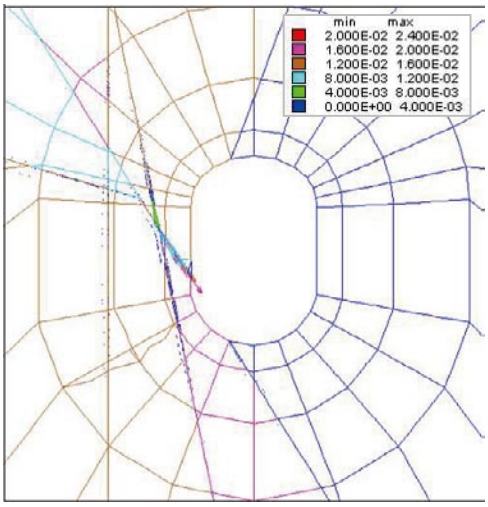

c) Weak
Max shear displacement = 17.85 mm

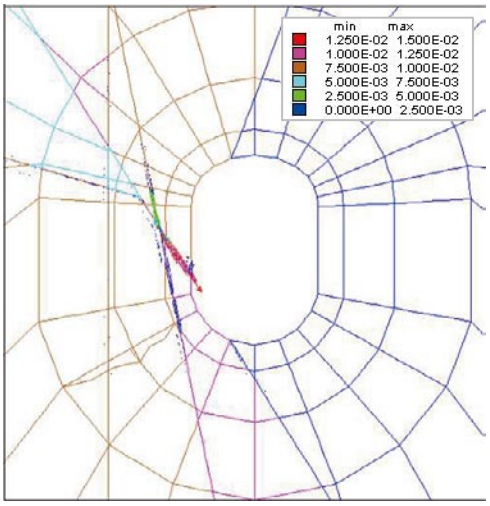

d) Strong
Max shear displacement = 13.23 mm

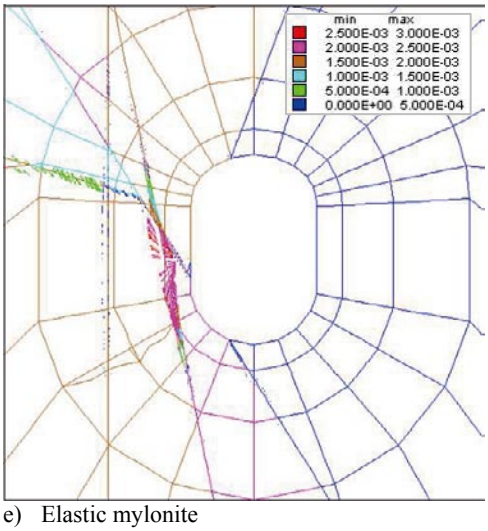

e) Elastic mylonite
Max shear displacement = 2.538 mm

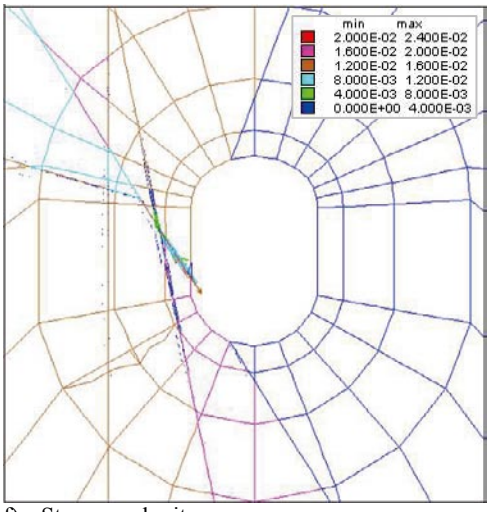

f) Strong mylonite
Max shear displacement = 15.33 mm

Figure G-1. *Cross section plots showing the maximum fracture shear displacement at section 47 for different fracture properties (See Table 9-3 to Table 9-5 for fracture properties)*

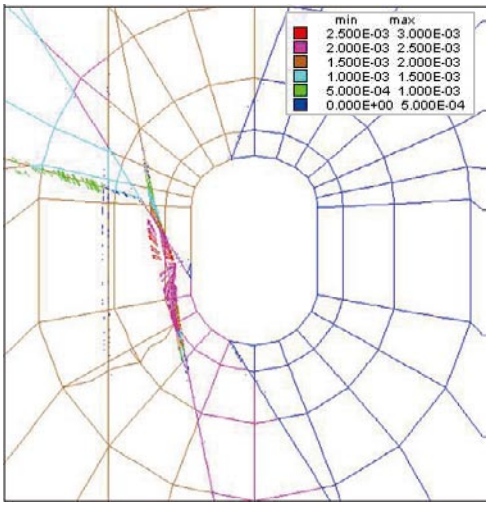

g) Stiff (E=55GPa, σ_1=30MPa)
Max shear displacement = 2.613 mm

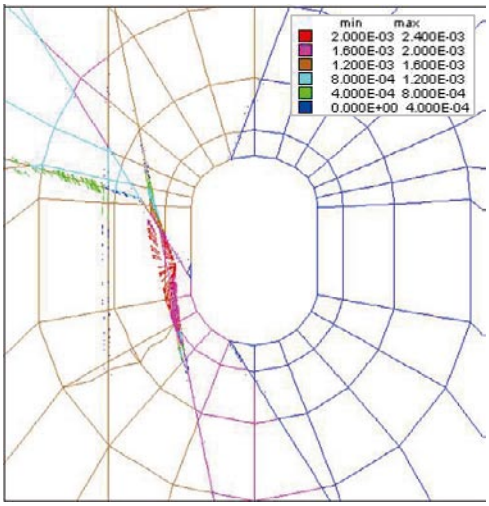

h) Stiff (E=65GPa, σ_1=30MPa)
Max shear displacement = 2.244 mm

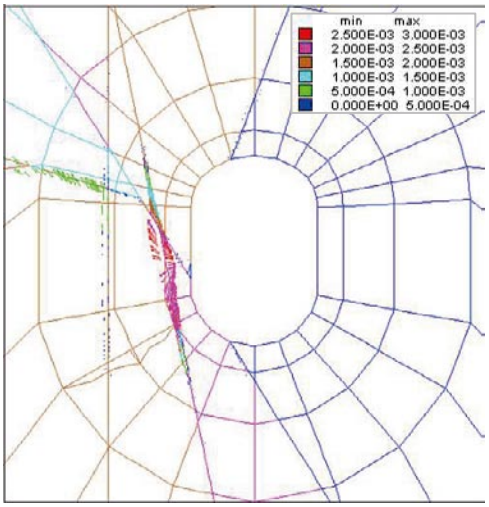

i) Stiff and Weak
Max shear displacement = 2.646 mm

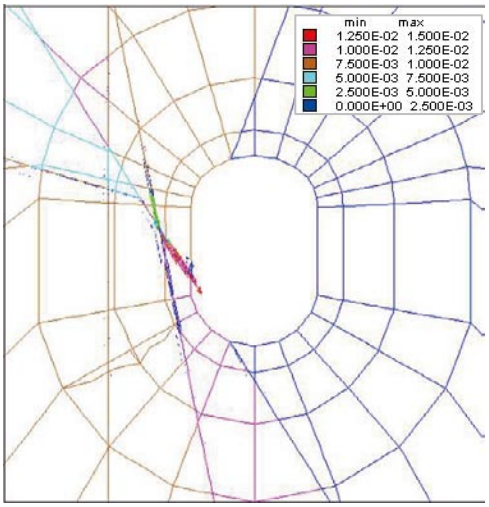

j) Stiff and Strong
Max shear displacement = 13.23 mm

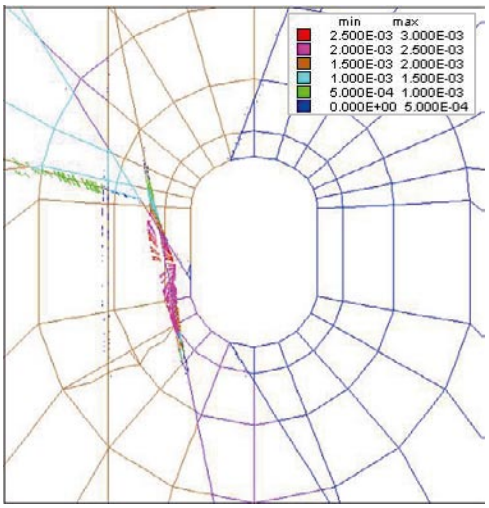

k) Stiffer
Max shear displacement = 2.613 mm

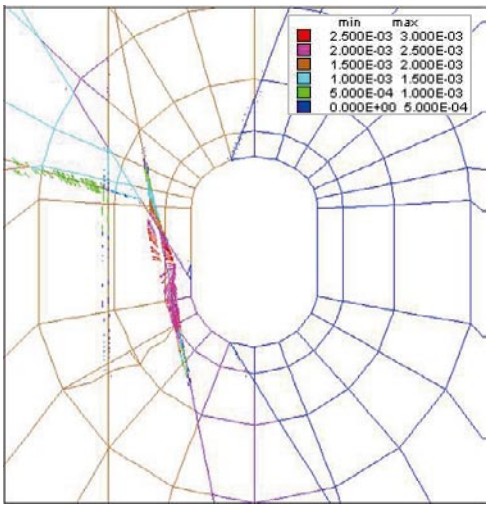

l) Stiffer and weak
Max shear displacement = 2.642 mm

Figure G-2. *Cross section plots showing the maximum fracture shear displacement at section 47 for different fracture properties (See Table 9-3 to Table 9-5 for fracture properties)*

Section 48 (Slot)

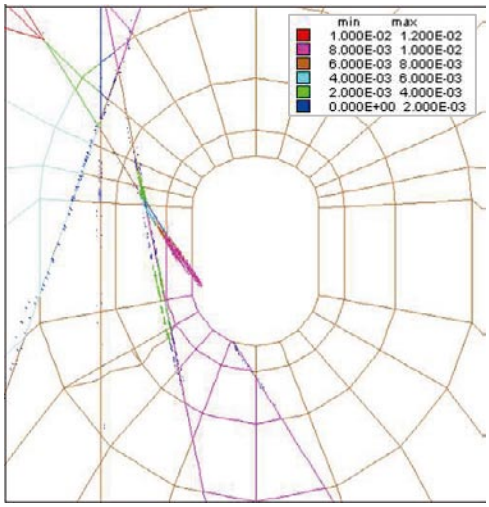

a) Baseline case
Max shear displacement = 9.253 mm

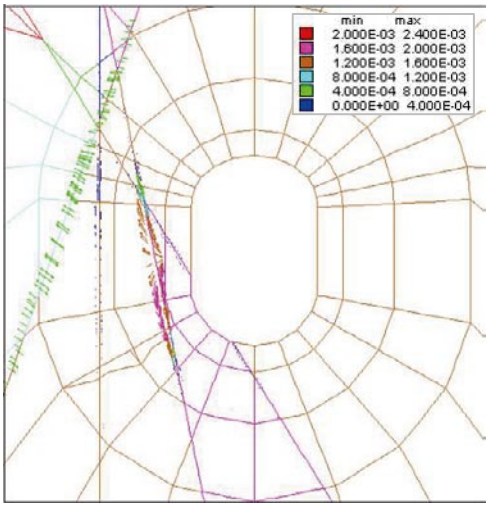

b) Stiff (E=65GPa, σ_1=25MPa)
Max shear displacement = 1.842 mm

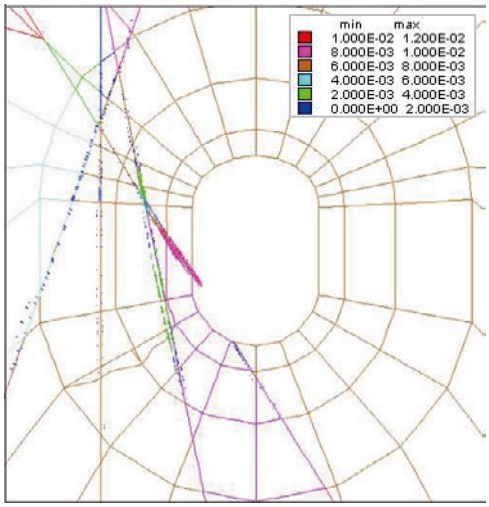

c) Weak
Max shear displacement = 9.813 mm

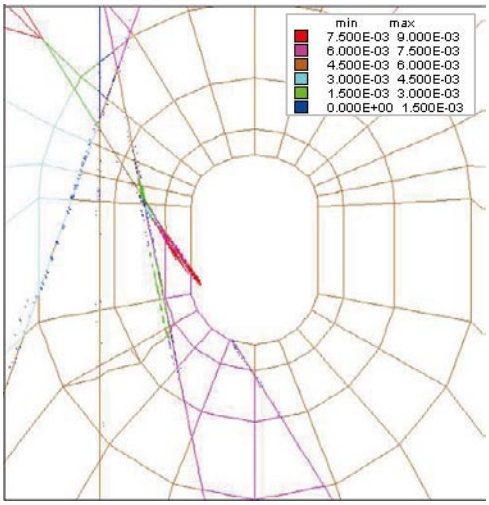

d) Strong
Max shear displacement = 8.643 mm

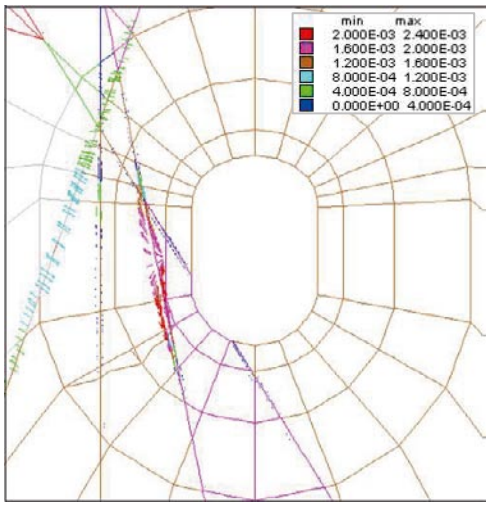

e) Elastic mylonite
Max shear displacement = 2.214 mm

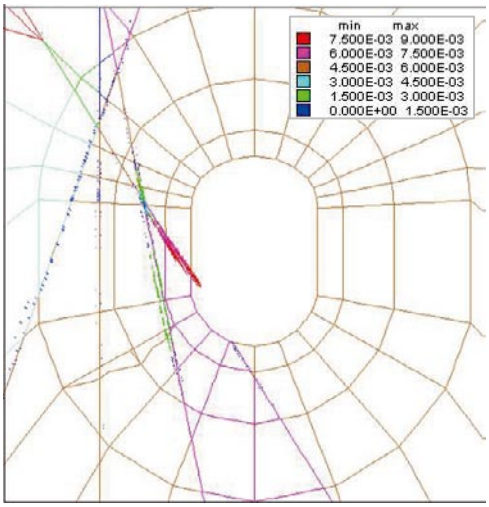

f) Strong mylonite
Max shear displacement = 8.652 mm

Figure G-3. *Cross section plots showing the maximum fracture shear displacement at section 48 for different fracture properties (See Table 9-3 to Table 9-5 for fracture properties)*

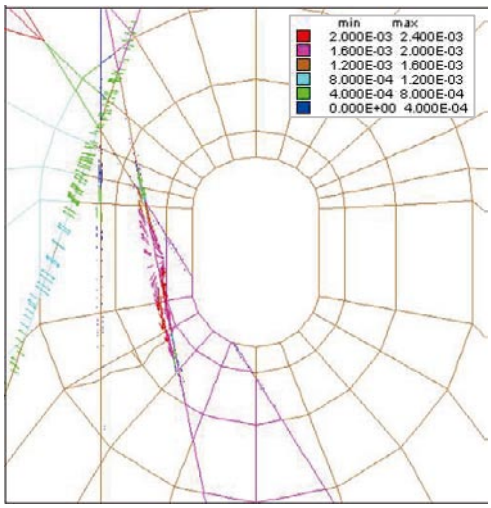

g) Stiff (E=55GPa, σ_1=30MPa)
Max shear displacement = 2.150 mm

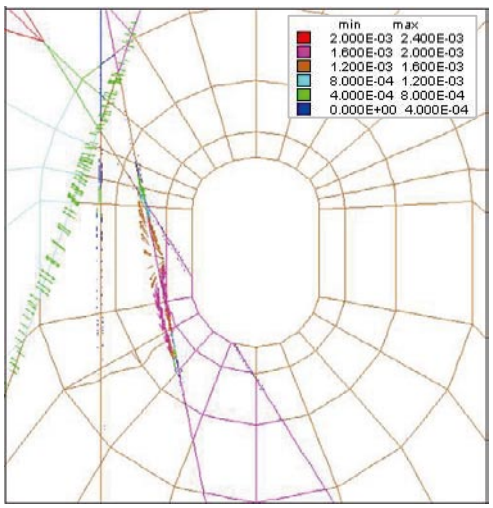

h) Stiff (E=65GPa, σ_1=30MPa)
Max shear displacement = 1.853 mm

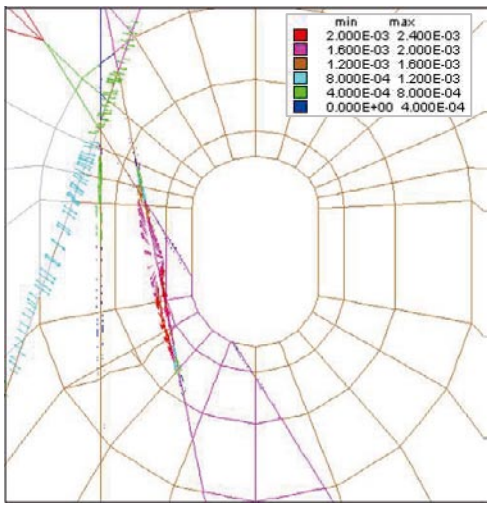

i) Stiff and Weak
Max shear displacement = 2.284 mm

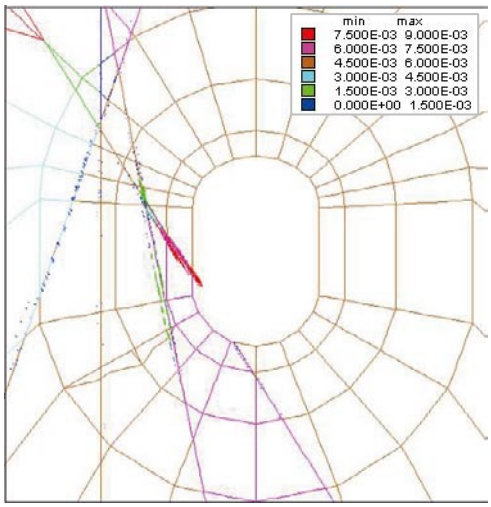

j) Stiff and Strong
Max shear displacement = 8.643 mm

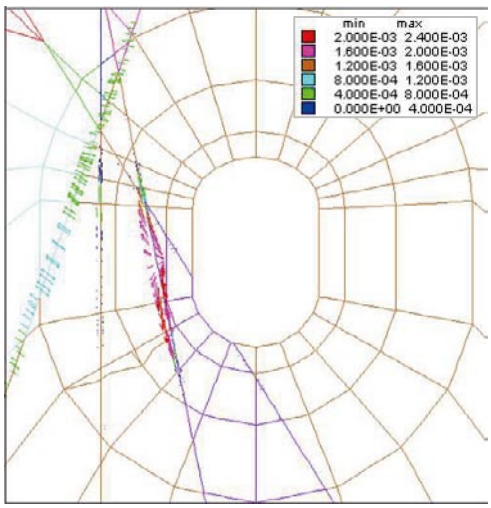

k) Stiffer
Max shear displacement = 2.147 mm

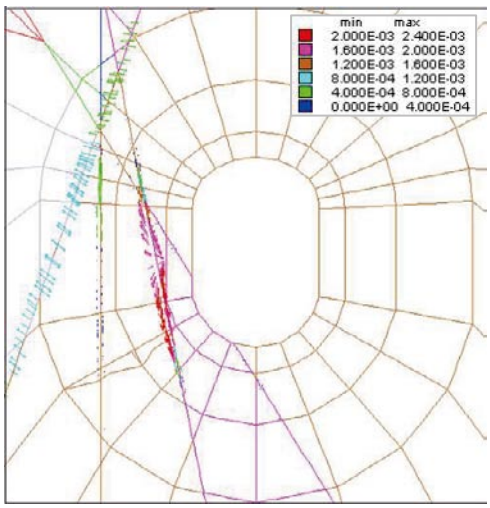

l) Stiffer and weak
Max shear displacement = 2.278 mm

Figure G-4. *Cross section plots showing the maximum fracture shear displacement at section 48 for different fracture properties (See Table 9-3 to Table 9-5 for fracture properties)*

Section 49 (close to convergence measurements)

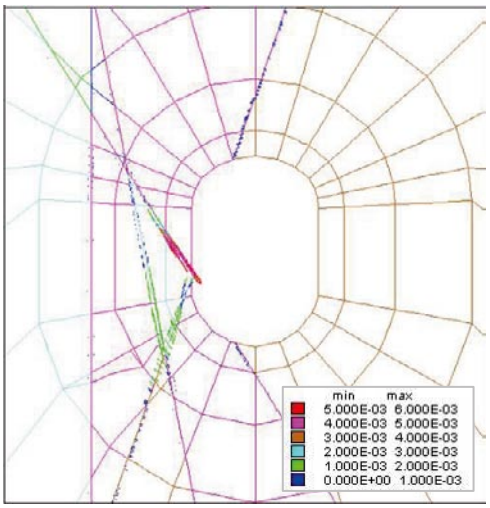

a) Baseline case
Max shear displacement = 5.309 mm

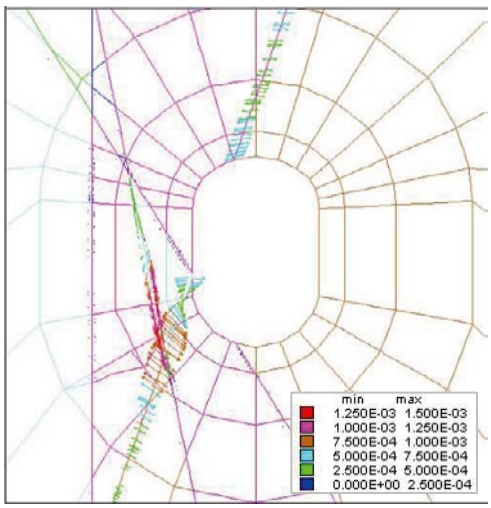

b) Stiff (E=65GPa, σ_1=25MPa)
Max shear displacement = 1.300 mm

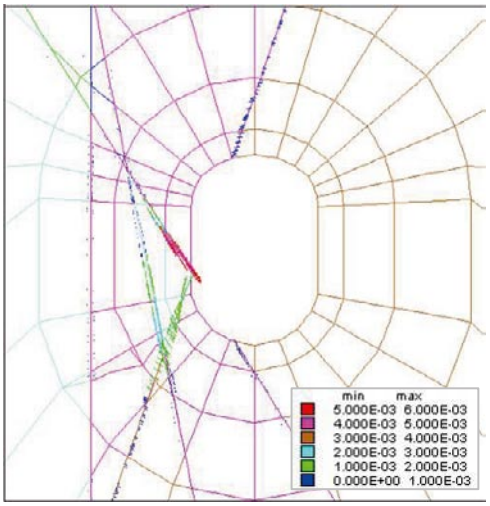

c) Weak
Max shear displacement = 5.439 mm

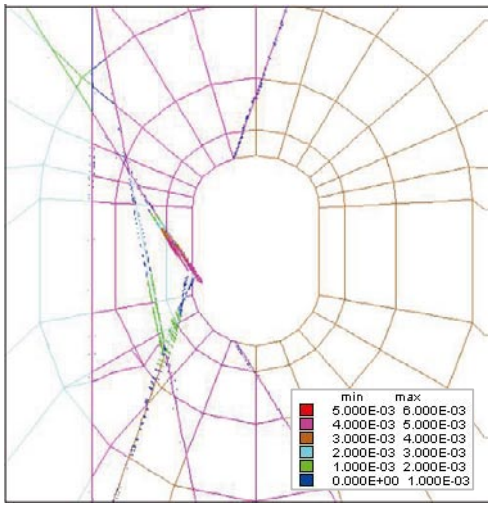

d) Strong
Max shear displacement = 4.964 mm

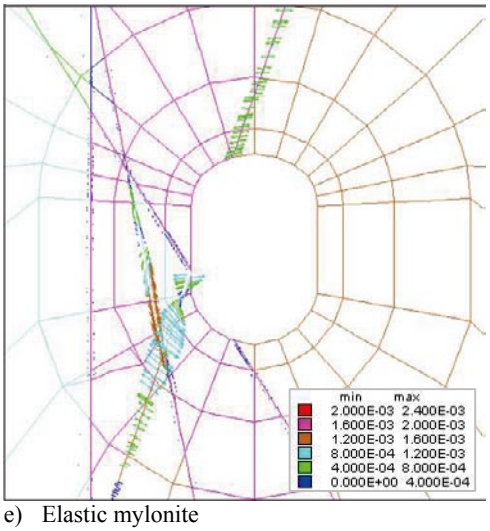

e) Elastic mylonite
Max shear displacement = 1.592 mm

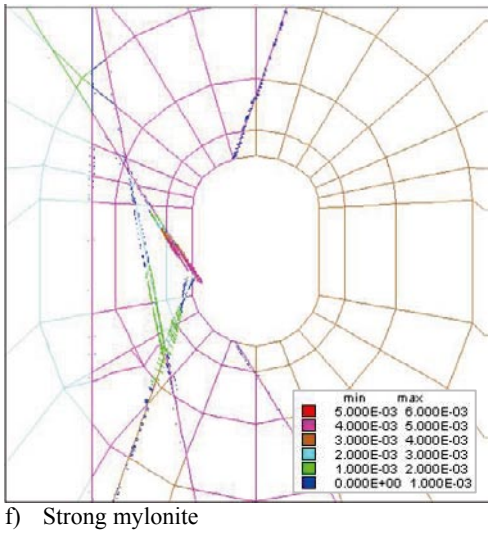

f) Strong mylonite
Max shear displacement = 4.967 mm

Figure G-5. *Cross section plots showing the maximum fracture shear displacement at section 49 for different fracture properties (See Table 9-3 to Table 9-5 for fracture properties)*

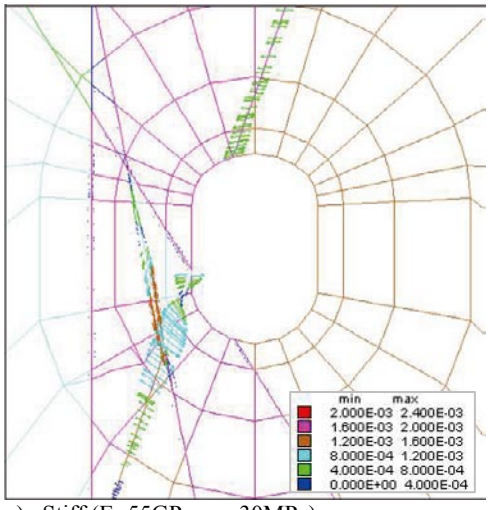

g) Stiff (E=55GPa, σ_1=30MPa)
Max shear displacement = 1.520 mm

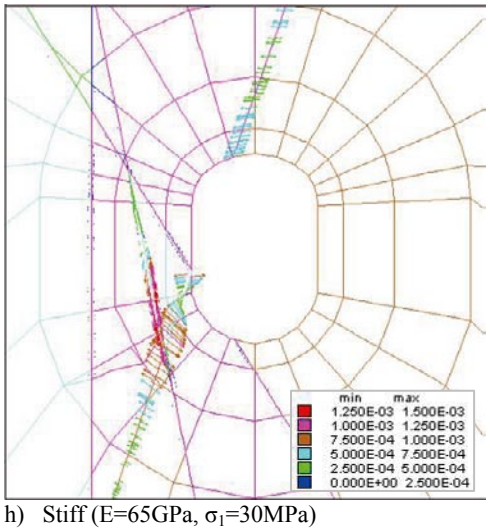

h) Stiff (E=65GPa, σ_1=30MPa)
Max shear displacement = 1.308 mm

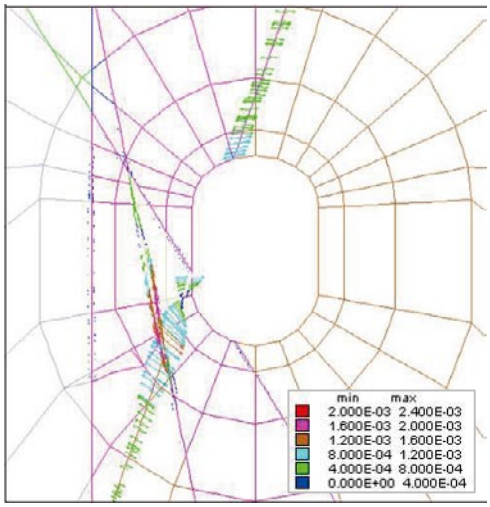

i) Stiff and Weak
Max shear displacement = 1.678 mm

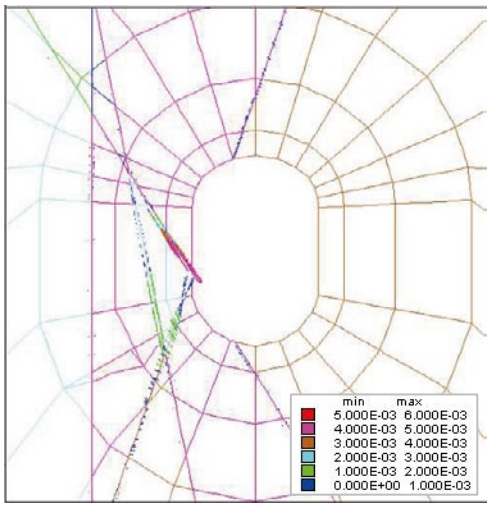

j) Stiff and Strong
Max shear displacement = 4.964 mm

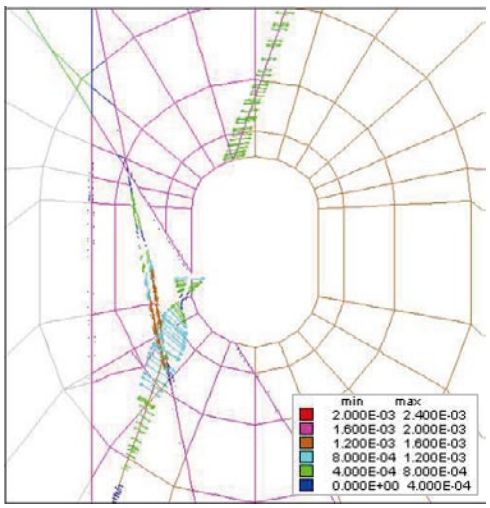

k) Stiffer
Max shear displacement = 1.516 mm

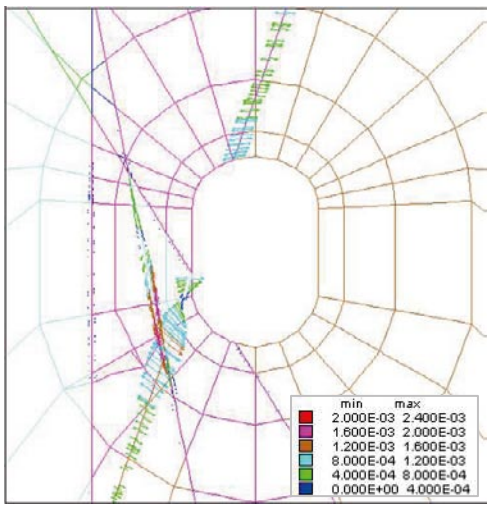

l) Stiffer and weak
Max shear displacement = 1.674 mm

Figure G-6. *Cross section plots showing the maximum fracture shear displacement at section 49 for different fracture properties (See Table 9-3 to Table 9-5 for fracture properties)*

Appendix H

Sensitivity analysis, As-planned tunnel shape with or without fractures

Sensitivity analysis. Cross section plots showing the projection of the principal stress tensor (colour by magnitude of σ_1, σ_2 or σ_3) of the as-planned tunnel without fractures and the as-planned tunnel with fractures (baseline case and stiff fractures, see Table 9-3 to Table 9-5 for fracture properties) in TASQ tunnel sections 46–51.

Section 46

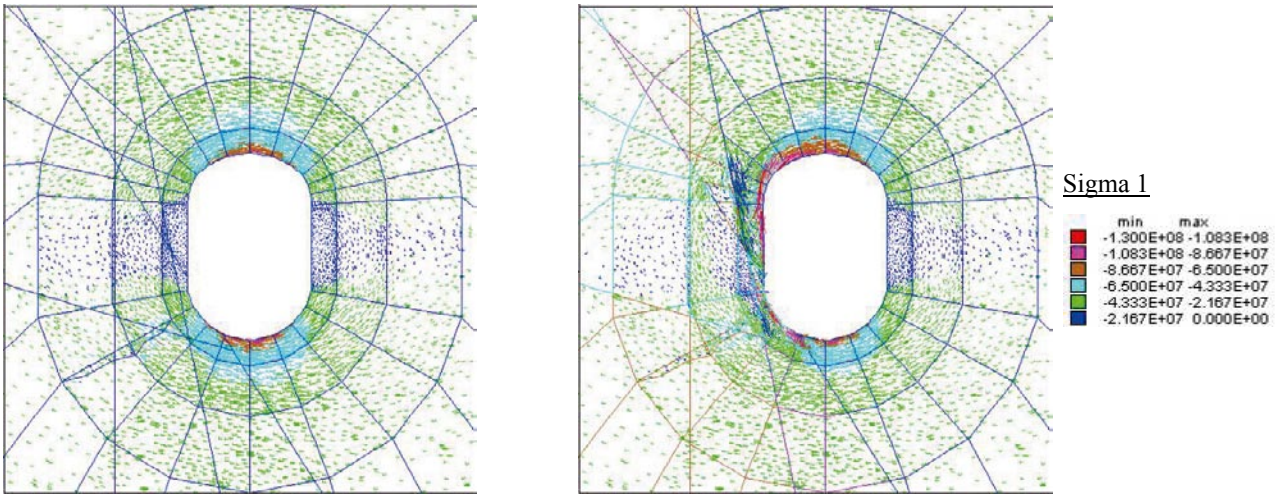

a) Without fractures
E = 55 GPa, σ1 = 30 MPa, σ1 = 310°
Max compressive stress = 101.0 MPa

b) With fractures, baseline case
E = 55 GPa, σ1 = 30 MPa, σ1 = 310°
Max compressive stress = 208.4 MPa

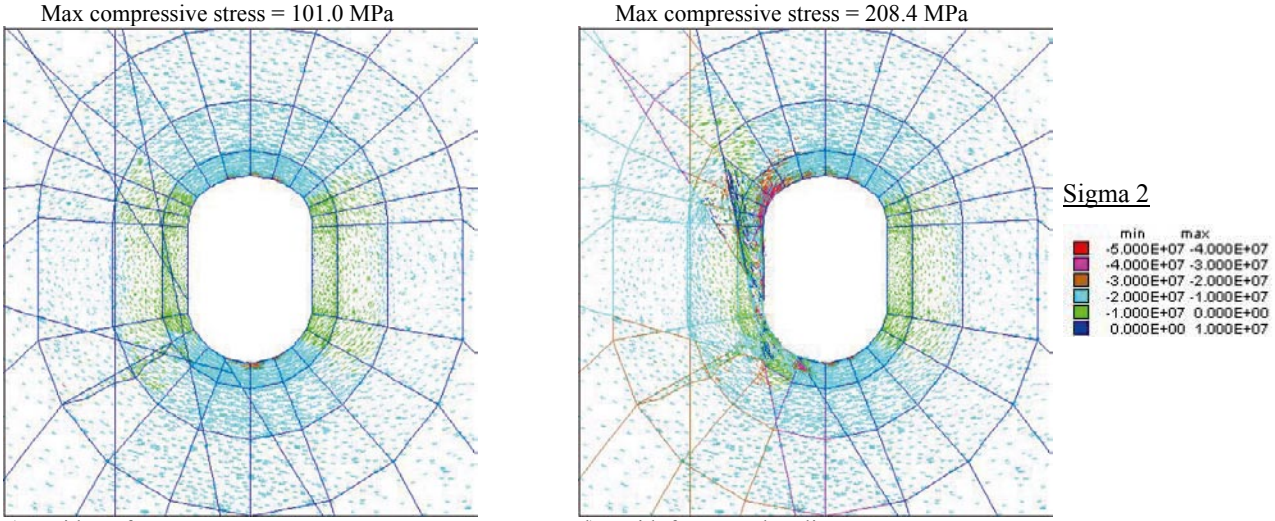

c) Without fractures
E = 55 GPa, σ1 = 30 MPa, σ1 = 310°
Max compressive stress = 101.0 MPa

d) With fractures, baseline case
E = 55 GPa, σ1 = 30 MPa, σ1 = 310°
Max compressive stress = 208.4 MPa

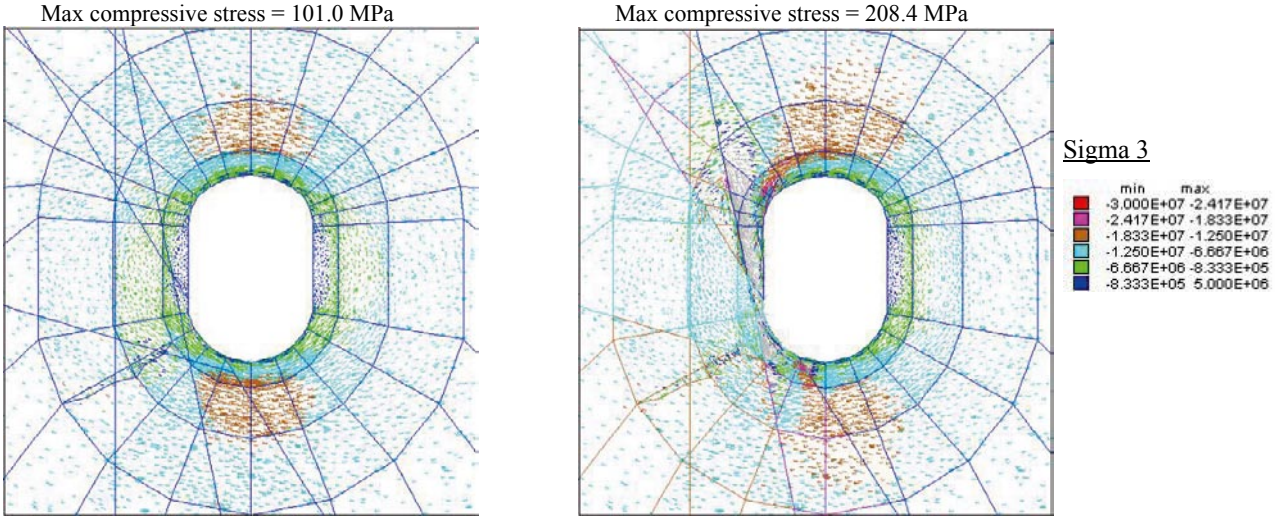

e) Without fractures
E = 55 GPa, σ1 = 30 MPa, σ1 = 310°
Max compressive stress = 101.0 MPa

f) With fractures, baseline case
E = 55 GPa, σ1 = 30 MPa, σ1 = 310°
Max compressive stress = 208.4 MPa

Figure H-1. *Cross section plots showing the projection of the principal stress tensor (color by magnitude of a) and b) Sigma 1, c) and d) Sigma 2, and e) and f) Sigma 3) for the as-planned tunnel shape without and with fractures and planar blasting round faces in section 46.*

Section 46

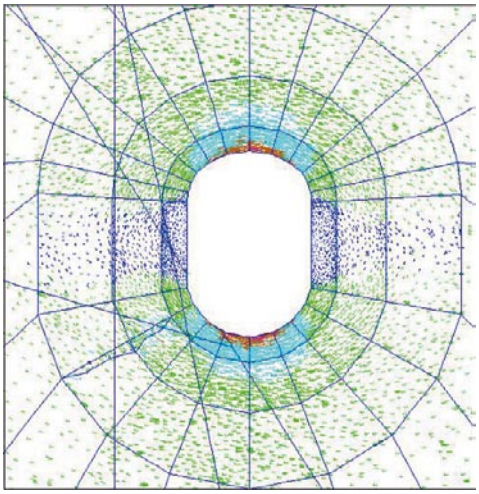

g) Without fractures
E = 65 GPa, σ1 = 25 MPa, σ1 = 310°
Max compressive stress = 101.0 MPa

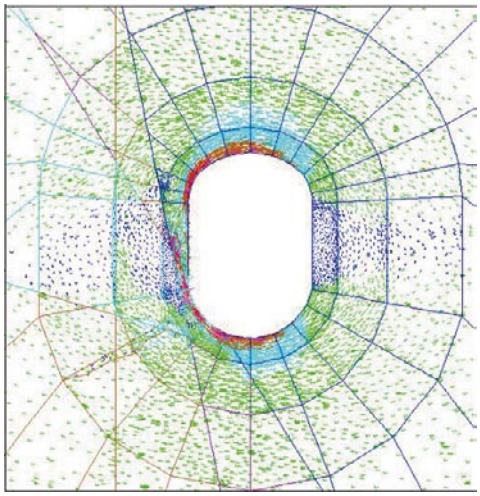

h) With fractures, stiff fractures
E = 65 GPa, σ1 = 25 MPa, σ1 = 310°
Max compressive stress = 190.0 MPa

Sigma 1

min	max
-1.300E+08	-1.083E+08
-1.083E+08	-8.667E+07
-8.667E+07	-6.500E+07
-6.500E+07	-4.333E+07
-4.333E+07	-2.167E+07
-2.167E+07	0.000E+00

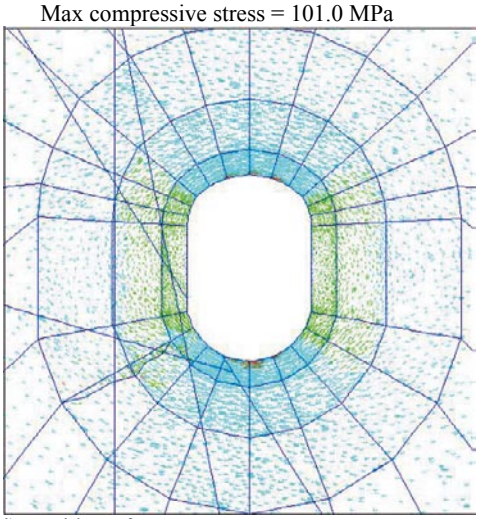

i) Without fractures
E = 65 GPa, σ1 = 25 MPa, σ1 = 310°
Max compressive stress = 101.0 MPa

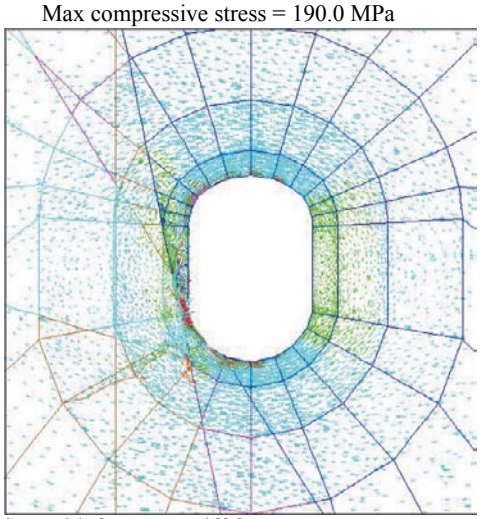

j) With fractures, stiff fractures
E = 65 GPa, σ1 = 25 MPa, σ1 = 310°
Max compressive stress = 190.0 MPa

Sigma 2

min	max
-5.000E+07	-4.000E+07
-4.000E+07	-3.000E+07
-3.000E+07	-2.000E+07
-2.000E+07	-1.000E+07
-1.000E+07	0.000E+00
0.000E+00	1.000E+07

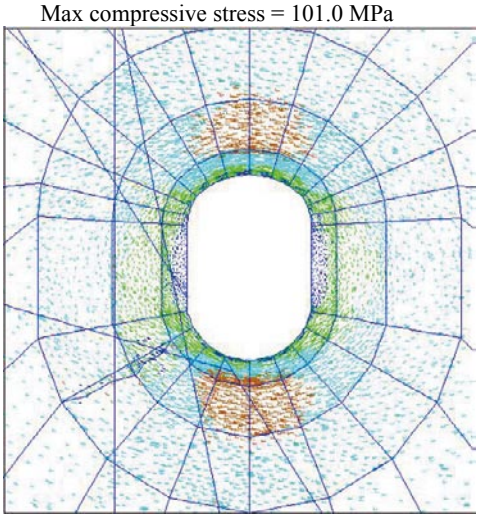

k) Without fractures
E = 65 GPa, σ1 = 25 MPa, σ1 = 310°
Max compressive stress = 101.0 MPa

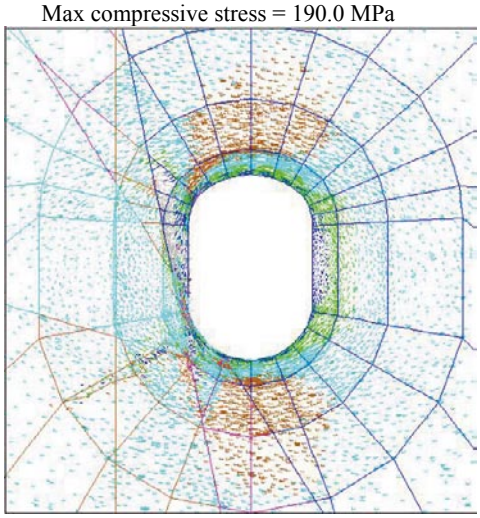

l) With fractures, stiff fractures
E = 65 GPa, σ1 = 25 MPa, σ1 = 310°
Max compressive stress = 190.0 MPa

Sigma 3

min	max
-3.000E+07	-2.417E+07
-2.417E+07	-1.833E+07
-1.833E+07	-1.250E+07
-1.250E+07	-6.667E+06
-6.667E+06	-8.333E+05
-8.333E+05	5.000E+06

Figure H-2. *Cross section plots showing the projection of the principal stress tensor (color by magnitude of a) and b) Sigma 1, c) and d) Sigma 2, and e) and f) Sigma 3) for the as-planned tunnel shape without and with fractures and planar blasting round faces in section 46.*

Section 47

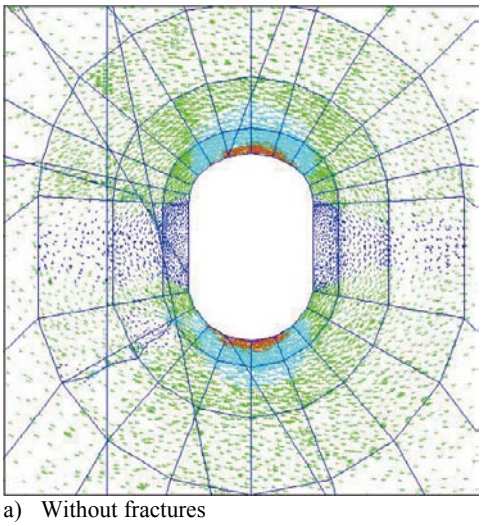

a) Without fractures
E = 55 GPa, σ1 = 30 MPa, σ1 = 310°
Max compressive stress = 98.76 MPa

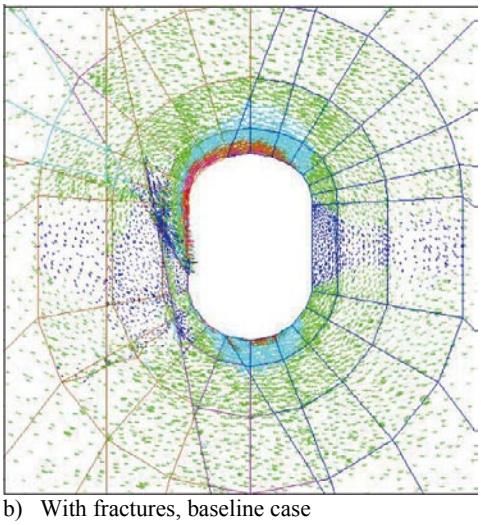

b) With fractures, baseline case
E = 55 GPa, σ1 = 30 MPa, σ1 = 310°
Max compressive stress = 145.7 MPa

Sigma 1

min	max
-1.300E+08	-1.083E+08
-1.083E+08	-8.667E+07
-8.667E+07	-6.500E+07
-6.500E+07	-4.333E+07
-4.333E+07	-2.167E+07
-2.167E+07	0.000E+00

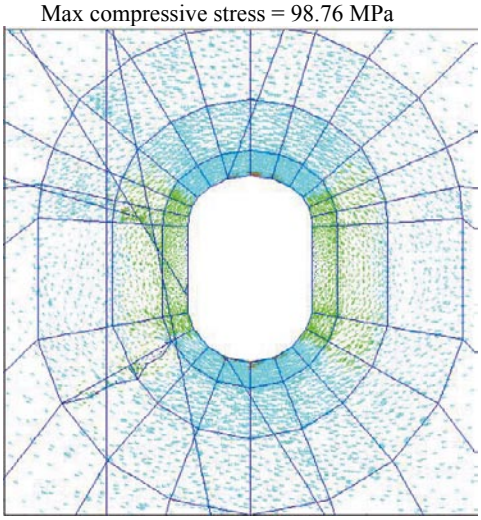

c) Without fractures
E = 55 GPa, σ1 = 30 MPa, σ1 = 310°
Max compressive stress = 98.76 MPa

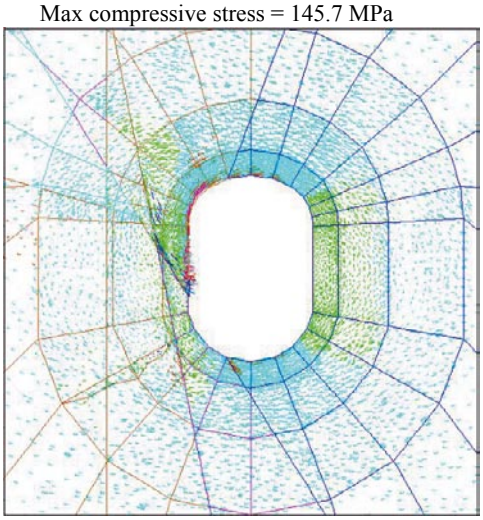

d) With fractures, baseline case
E = 55 GPa, σ1 = 30 MPa, σ1 = 310°
Max compressive stress = 145.7 MPa

Sigma 2

min	max
-5.000E+07	-4.000E+07
-4.000E+07	-3.000E+07
-3.000E+07	-2.000E+07
-2.000E+07	-1.000E+07
-1.000E+07	0.000E+00
0.000E+00	1.000E+07

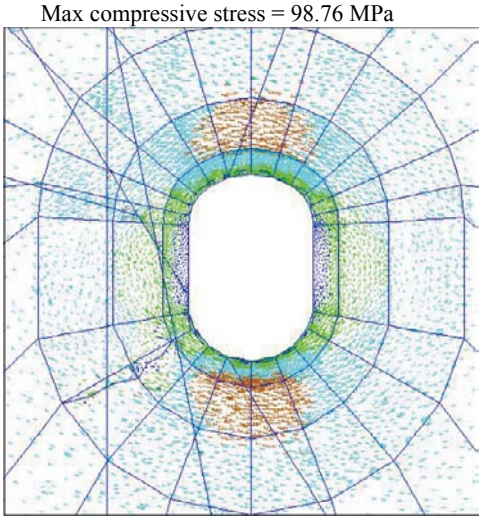

e) Without fractures
E = 55 GPa, σ1 = 30 MPa, σ1 = 310°
Max compressive stress = 98.76 MPa

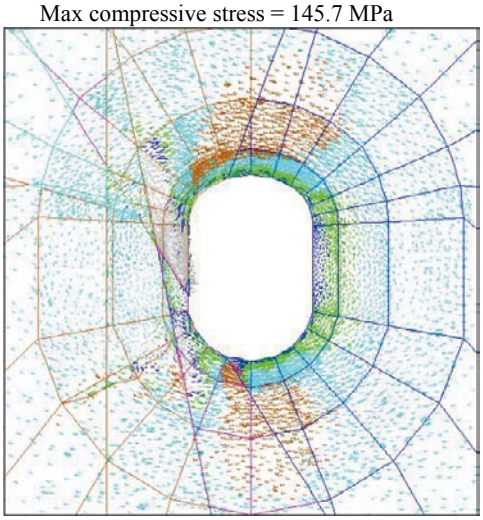

f) With fractures, baseline case
E = 55 GPa, σ1 = 30 MPa, σ1 = 310°
Max compressive stress = 145.7 MPa

Sigma 3

min	max
-3.000E+07	-2.417E+07
-2.417E+07	-1.833E+07
-1.833E+07	-1.250E+07
-1.250E+07	-6.667E+06
-6.667E+06	-8.333E+05
-8.333E+05	5.000E+06

Figure H-3. *Cross section plots showing the projection of the principal stress tensor (color by magnitude of a) and b) Sigma 1, c) and d) Sigma 2, and e) and f) Sigma 3) for the as-planned tunnel shape without and with fractures and planar blasting round faces in section 47.*

Section 47

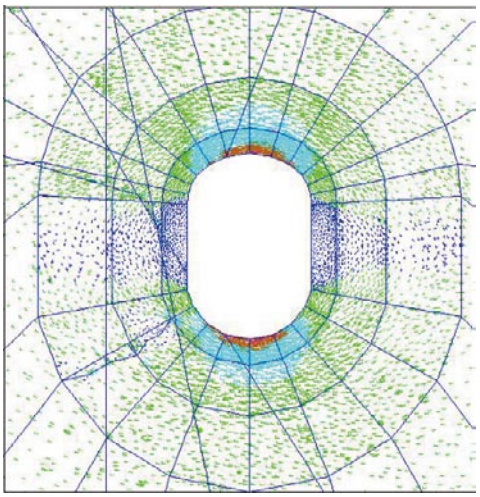

g) Without fractures
E = 65 GPa, σ1 = 25 MPa, σ1 = 310°
Max compressive stress = 98.76 MPa

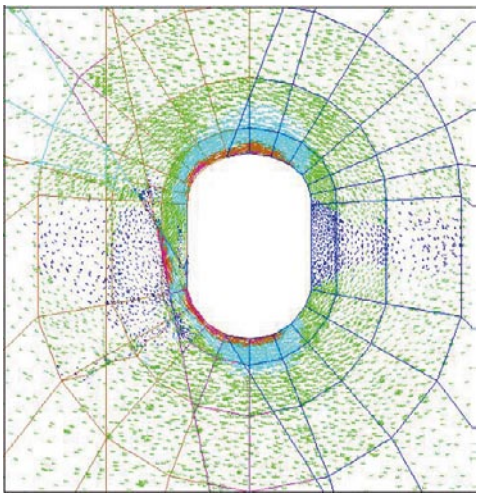

h) With fractures, stiff fractures
E = 65 GPa, σ1 = 25 MPa, σ1 = 310°
Max compressive stress = 122.7 MPa

Sigma 1

min	max
-1.300E+08	-1.083E+08
-1.083E+08	-8.667E+07
-8.667E+07	-6.500E+07
-6.500E+07	-4.333E+07
-4.333E+07	-2.167E+07
-2.167E+07	0.000E+00

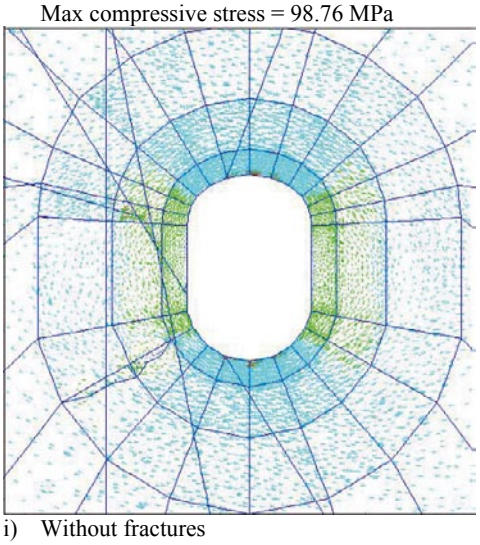

i) Without fractures
E = 65 GPa, σ1 = 25 MPa, σ1 = 310°
Max compressive stress = 98.76 MPa

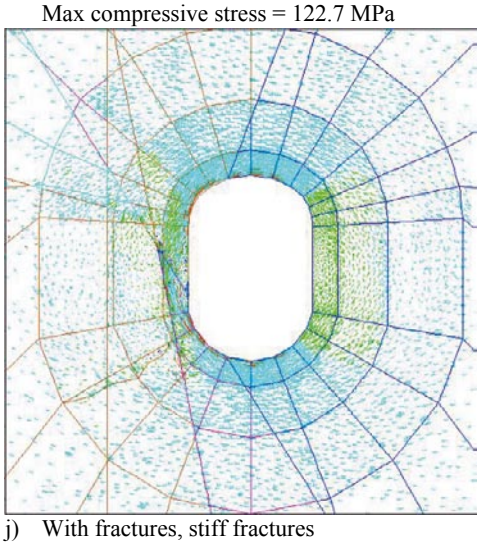

j) With fractures, stiff fractures
E = 65 GPa, σ1 = 25 MPa, σ1 = 310°
Max compressive stress = 122.7 MPa

Sigma 2

min	max
-5.000E+07	-4.000E+07
-4.000E+07	-3.000E+07
-3.000E+07	-2.000E+07
-2.000E+07	-1.000E+07
-1.000E+07	0.000E+00
0.000E+00	1.000E+07

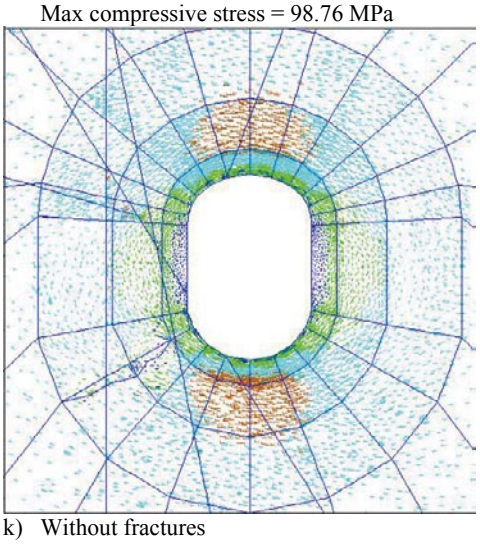

k) Without fractures
E = 65 GPa, σ1 = 25 MPa, σ1 = 310°
Max compressive stress = 98.76 MPa

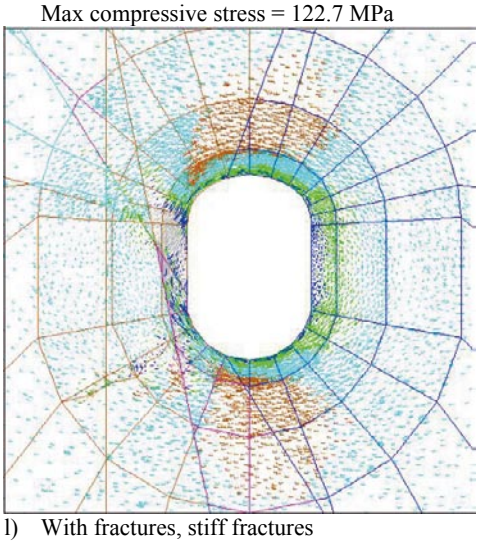

l) With fractures, stiff fractures
E = 65 GPa, σ1 = 25 MPa, σ1 = 310°
Max compressive stress = 122.7 MPa

Sigma 3

min	max
-3.000E+07	-2.417E+07
-2.417E+07	-1.833E+07
-1.833E+07	-1.250E+07
-1.250E+07	-6.667E+06
-6.667E+06	-8.333E+05
-8.333E+05	5.000E+06

Figure H-4. *Cross section plots showing the projection of the principal stress tensor (color by magnitude of a) and b) Sigma 1, c) and d) Sigma 2, and e) and f) Sigma 3) for the as-planned tunnel shape without and with fractures and planar blasting round faces in section 47.*

Section 48

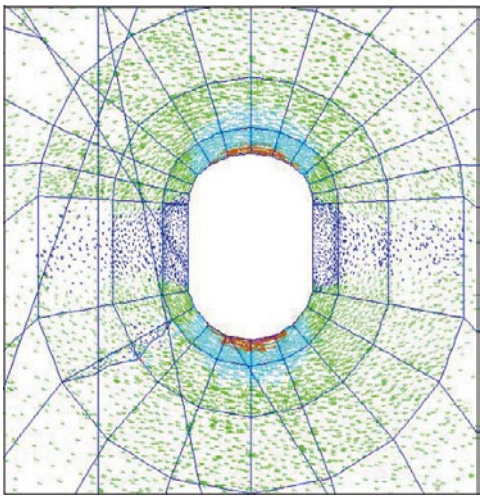

a) Without fractures
E = 55 GPa, σ1 = 30 MPa, σ1 = 310°
Max compressive stress = 98.35 MPa

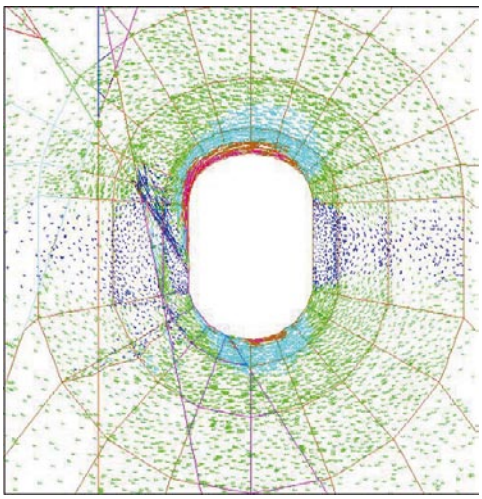

b) With fractures, baseline case
E = 55 GPa, σ1 = 30 MPa, σ1 = 310°
Max compressive stress = 135.6 MPa

Sigma 1

min	max
-1.300E+08	-1.083E+08
-1.083E+08	-8.667E+07
-8.667E+07	-6.500E+07
-6.500E+07	-4.333E+07
-4.333E+07	-2.167E+07
-2.167E+07	0.000E+00

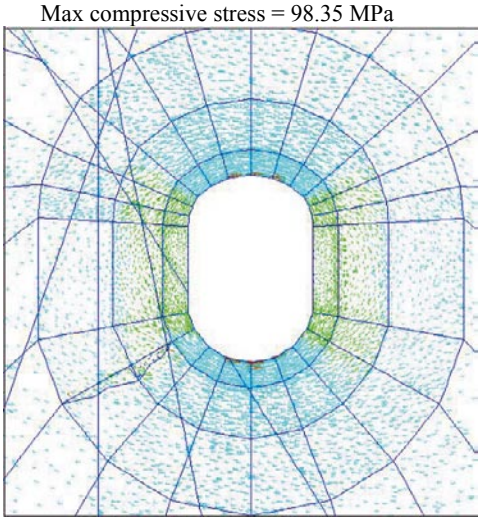

c) Without fractures
E = 55 GPa, σ1 = 30 MPa, σ1 = 310°
Max compressive stress = 98.35 MPa

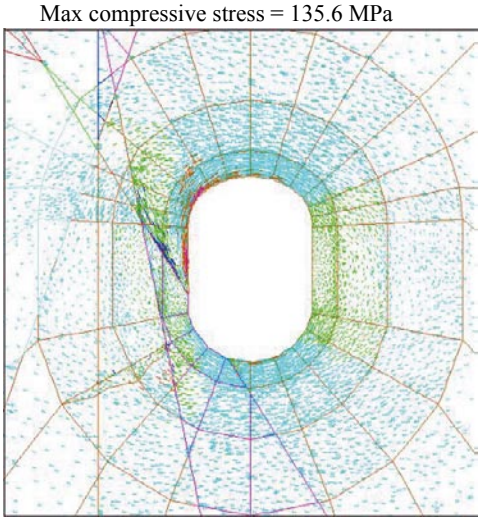

d) With fractures, baseline case
E = 55 GPa, σ1 = 30 MPa, σ1 = 310°
Max compressive stress = 135.6 MPa

Sigma 2

min	max
-5.000E+07	-4.000E+07
-4.000E+07	-3.000E+07
-3.000E+07	-2.000E+07
-2.000E+07	-1.000E+07
-1.000E+07	0.000E+00
0.000E+00	1.000E+07

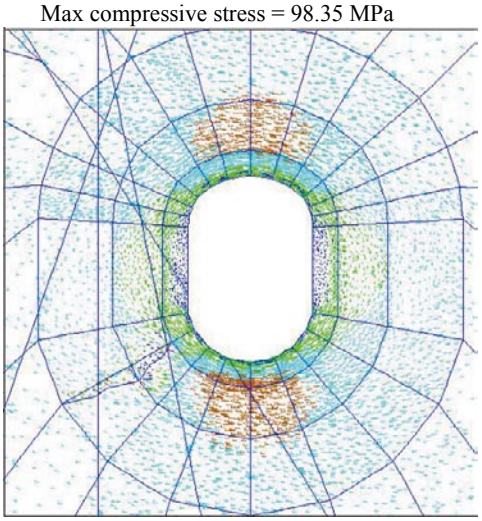

e) Without fractures
E = 55 GPa, σ1 = 30 MPa, σ1 = 310°
Max compressive stress = 98.35 MPa

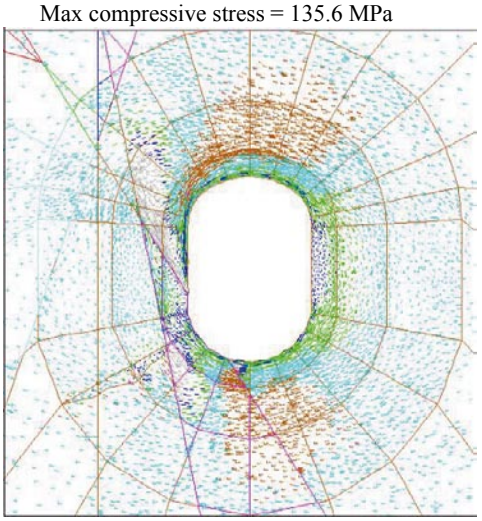

f) With fractures, baseline case
E = 55 GPa, σ1 = 30 MPa, σ1 = 310°
Max compressive stress = 135.6 MPa

Sigma 3

min	max
-3.000E+07	-2.417E+07
-2.417E+07	-1.833E+07
-1.833E+07	-1.250E+07
-1.250E+07	-6.667E+06
-6.667E+06	-8.333E+05
-8.333E+05	5.000E+06

Figure H-5. *Cross section plots showing the projection of the principal stress tensor (color by magnitude of a) and b) Sigma 1, c) and d) Sigma 2, and e) and f) Sigma 3) for the as-planned tunnel shape without and with fractures and planar blasting round faces in section 48.*

Section 48

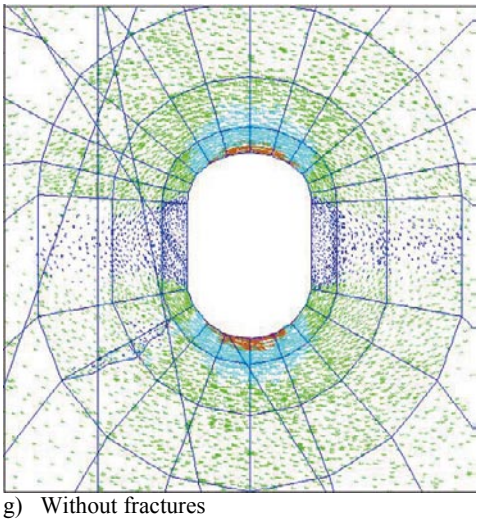

g) Without fractures
E = 65 GPa, σ1 = 25 MPa, σ1 = 310°
Max compressive stress = 98.33 MPa

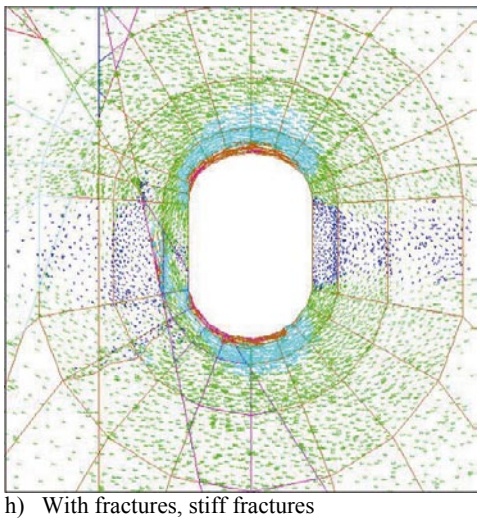

h) With fractures, stiff fractures
E = 65 GPa, σ1 = 25 MPa, σ1 = 310°
Max compressive stress = 142.7 MPa

Sigma 1

min	max
-1.300E+08	-1.083E+08
-1.083E+08	-8.667E+07
-8.667E+07	-6.500E+07
-6.500E+07	-4.333E+07
-4.333E+07	-2.167E+07
-2.167E+07	0.000E+00

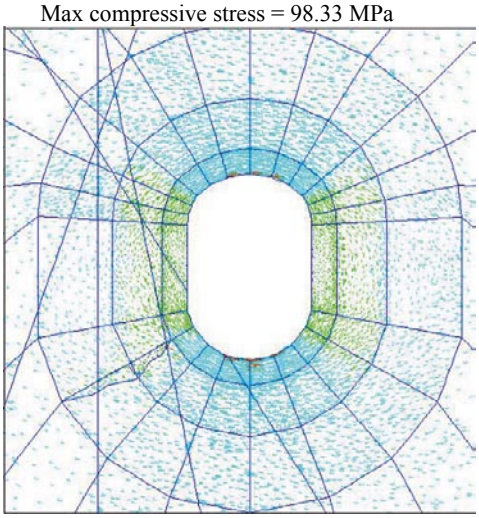

i) Without fractures
E = 65 GPa, σ1 = 25 MPa, σ1 = 310°
Max compressive stress = 98.33 MPa

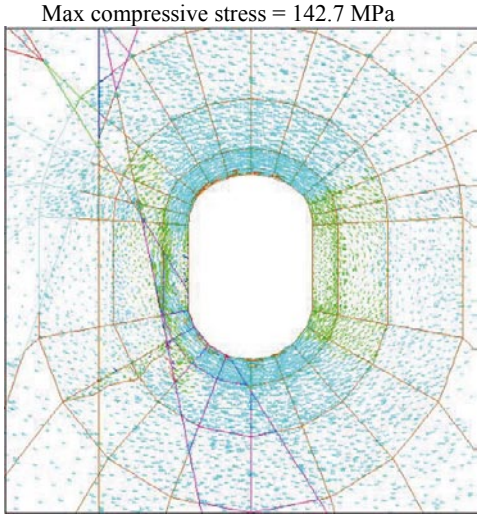

j) With fractures, stiff fractures
E = 65 GPa, σ1 = 25 MPa, σ1 = 310°
Max compressive stress = 142.7 MPa

Sigma 2

min	max
-5.000E+07	-4.000E+07
-4.000E+07	-3.000E+07
-3.000E+07	-2.000E+07
-2.000E+07	-1.000E+07
-1.000E+07	0.000E+00
0.000E+00	1.000E+07

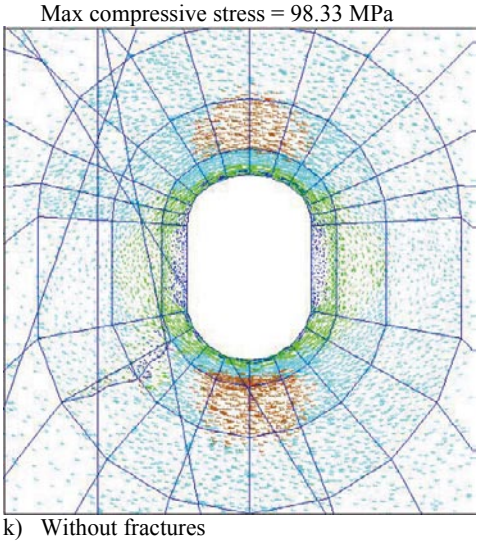

k) Without fractures
E = 65 GPa, σ1 = 25 MPa, σ1 = 310°
Max compressive stress = 98.33 MPa

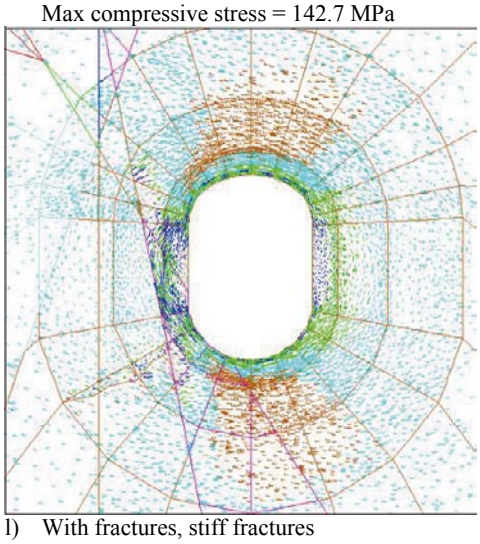

l) With fractures, stiff fractures
E = 65 GPa, σ1 = 25 MPa, σ1 = 310°
Max compressive stress = 142.7 MPa

Sigma 3

min	max
-3.000E+07	-2.417E+07
-2.417E+07	-1.833E+07
-1.833E+07	-1.250E+07
-1.250E+07	-6.667E+06
-6.667E+06	-8.333E+05
-8.333E+05	5.000E+06

Figure H-6. *Cross section plots showing the projection of the principal stress tensor (color by magnitude of a) and b) Sigma 1, c) and d) Sigma 2, and e) and f) Sigma 3) for the as-planned tunnel shape without and with fractures and planar blasting round faces in section 48.*

Section 49

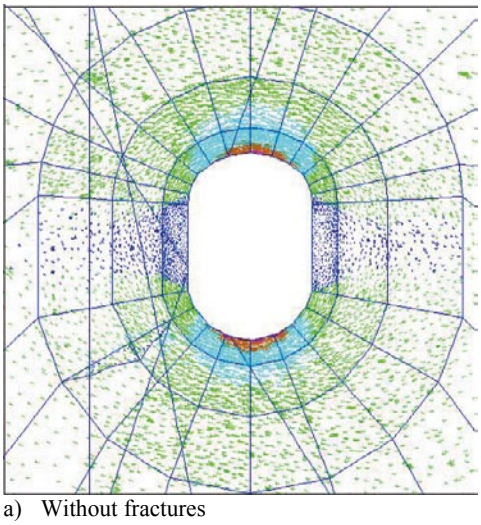

a) Without fractures
E = 55 GPa, σ1 = 30 MPa, σ1 = 310°
Max compressive stress = 99.19 MPa

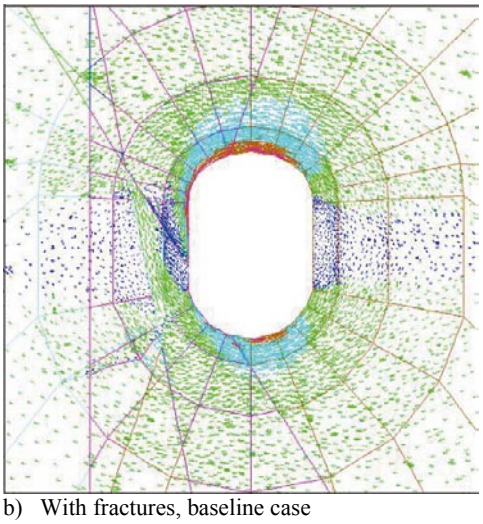

b) With fractures, baseline case
E = 55 GPa, σ1 = 30 MPa, σ1 = 310°
Max compressive stress = 93.20 MPa

Sigma 1

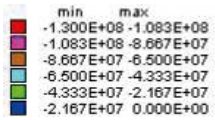

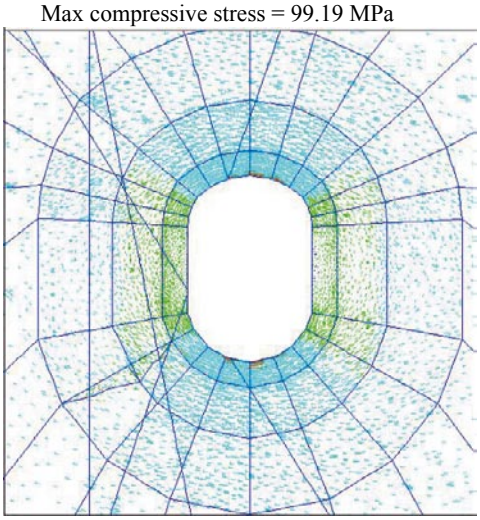

c) Without fractures
E = 55 GPa, σ1 = 30 MPa, σ1 = 310°
Max compressive stress = 99.19 MPa

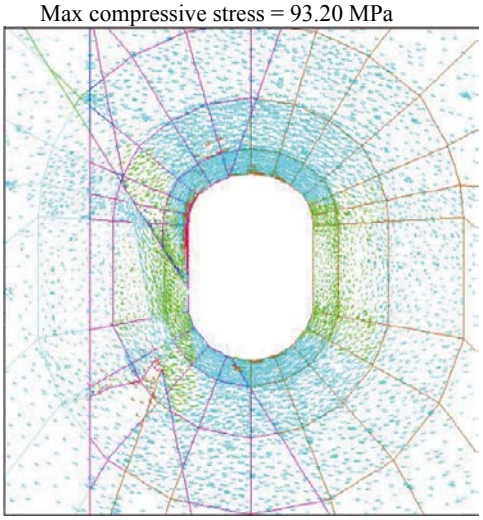

d) With fractures, baseline case
E = 55 GPa, σ1 = 30 MPa, σ1 = 310°
Max compressive stress = 93.20 MPa

Sigma 2

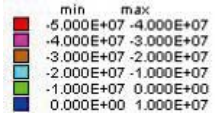

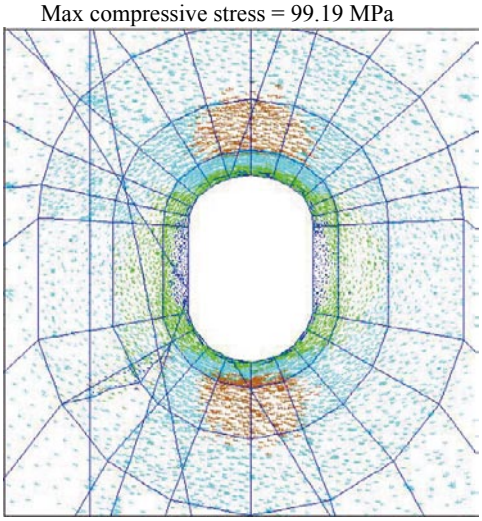

e) Without fractures
E = 55 GPa, σ1 = 30 MPa, σ1 = 310°
Max compressive stress = 99.19 MPa

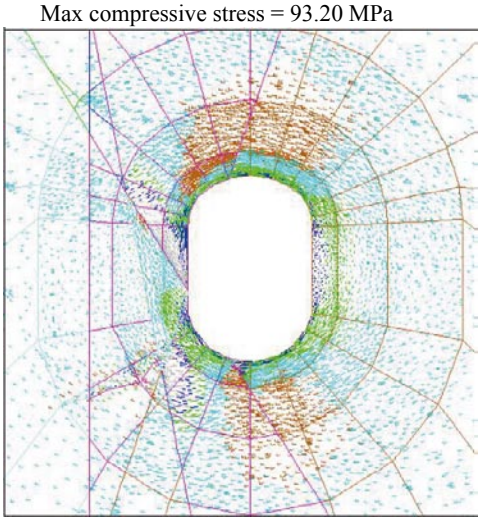

f) With fractures, baseline case
E = 55 GPa, σ1 = 30 MPa, σ1 = 310°
Max compressive stress = 93.20 MPa

Sigma 3

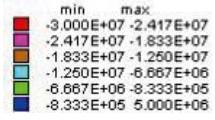

Figure H-7. *Cross section plots showing the projection of the principal stress tensor (color by magnitude of a) and b) Sigma 1, c) and d) Sigma 2, and e) and f) Sigma 3) for the as-planned tunnel shape without and with fractures and planar blasting round faces in section 49.*

Section 49

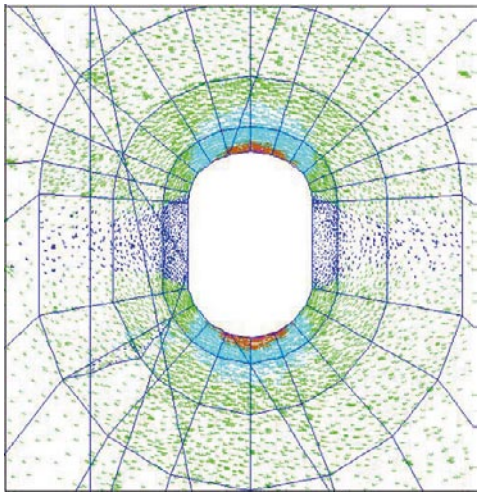

g) Without fractures
E = 65 GPa, σ1 = 25 MPa, σ1 = 310°
Max compressive stress = 99.17 MPa

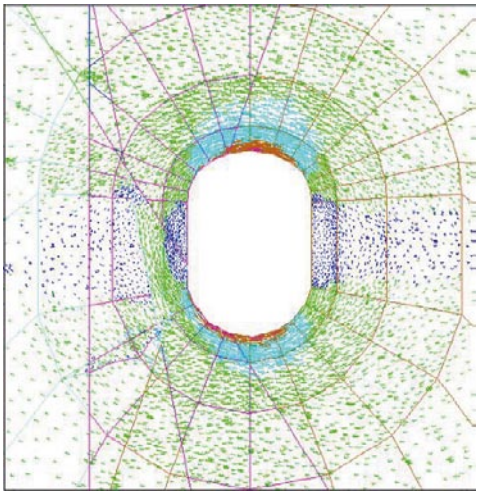

h) With fractures, stiff fractures
E = 65 GPa, σ1 = 25 MPa, σ1 = 310°
Max compressive stress = 94.89 MPa

Sigma 1

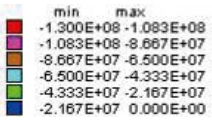

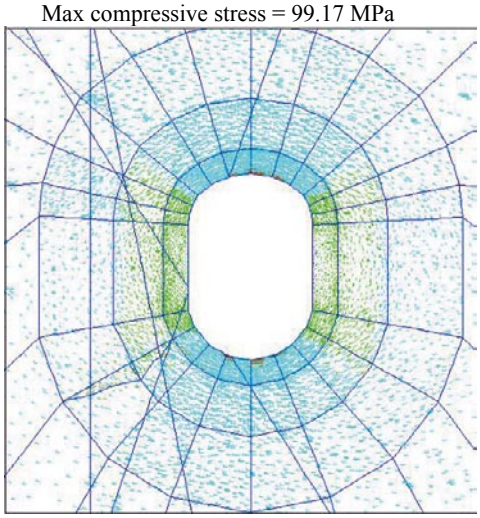

i) Without fractures
E = 65 GPa, σ1 = 25 MPa, σ1 = 310°
Max compressive stress = 99.17 MPa

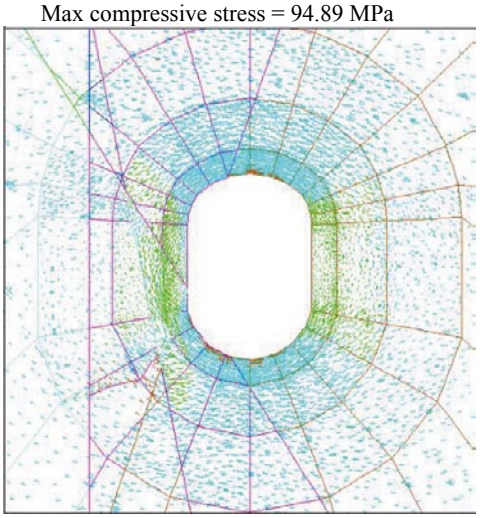

j) With fractures, stiff fractures
E = 65 GPa, σ1 = 25 MPa, σ1 = 310°
Max compressive stress = 94.89 MPa

Sigma 2

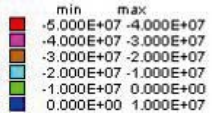

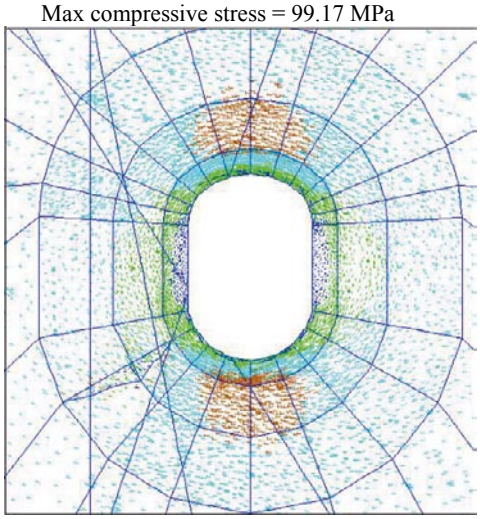

k) Without fractures
E = 65 GPa, σ1 = 25 MPa, σ1 = 310°
Max compressive stress = 99.17 MPa

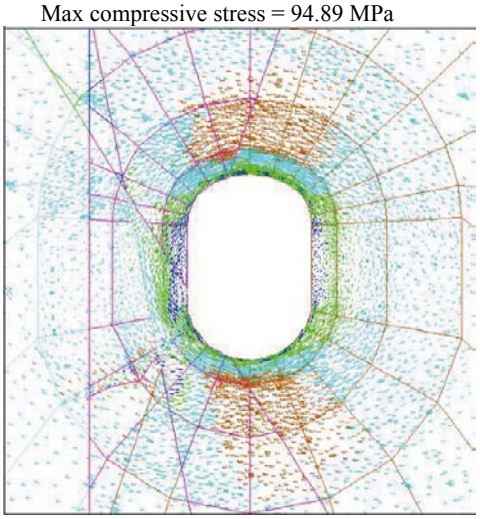

l) With fractures, stiff fractures
E = 65 GPa, σ1 = 25 MPa, σ1 = 310°
Max compressive stress = 94.89 MPa

Sigma 3

Figure H-8. *Cross section plots showing the projection of the principal stress tensor (color by magnitude of a) and b) Sigma 1, c) and d) Sigma 2, and e) and f) Sigma 3) for the as-planned tunnel shape without and with fractures and planar blasting round faces in section 49.*

Section 50

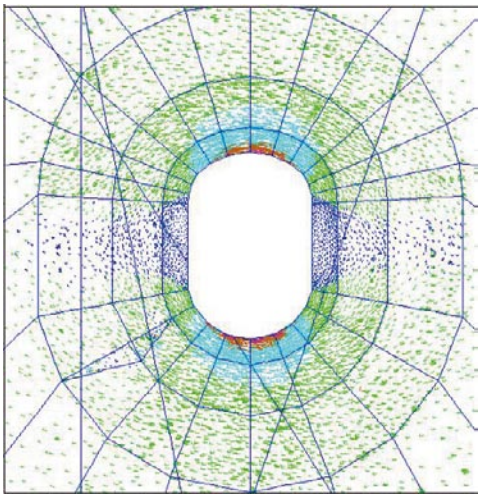

a) Without fractures
E = 55 GPa, σ1 = 30 MPa, σ1 = 310°
Max compressive stress = 100.6 MPa

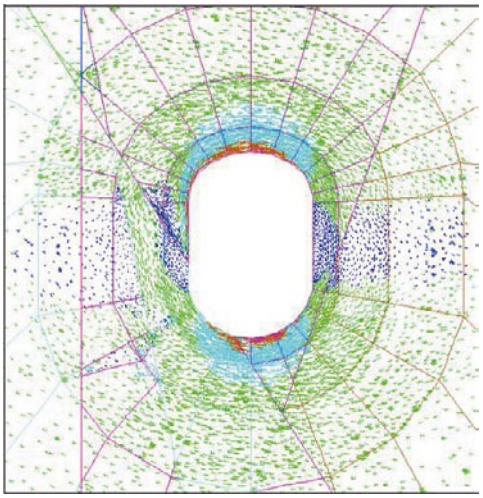

b) With fractures, baseline case
E = 55 GPa, σ1 = 30 MPa, σ1 = 310°
Max compressive stress = 101.2 MPa

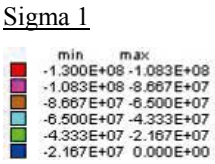

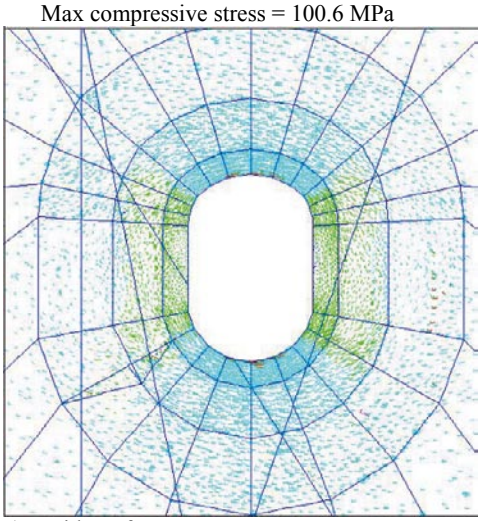

c) Without fractures
E = 55 GPa, σ1 = 30 MPa, σ1 = 310°
Max compressive stress = 100.6 MPa

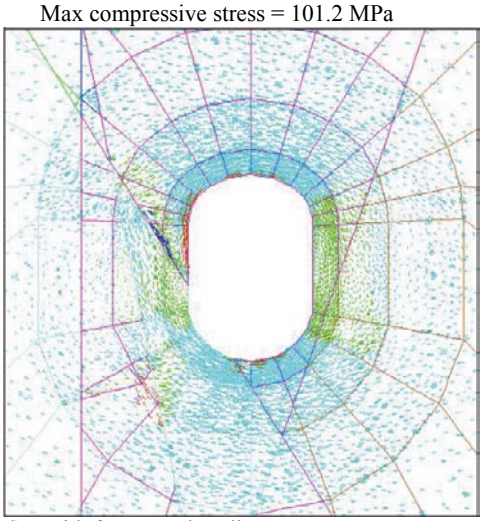

d) With fractures, baseline case
E = 55 GPa, σ1 = 30 MPa, σ1 = 310°
Max compressive stress = 101.2 MPa

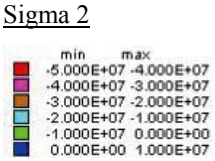

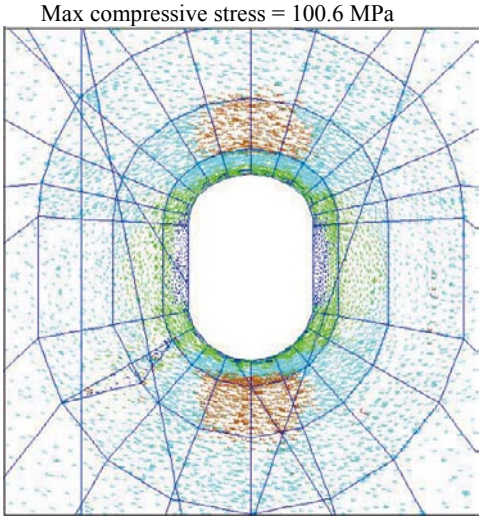

e) Without fractures
E = 55 GPa, σ1 = 30 MPa, σ1 = 310°
Max compressive stress = 100.6 MPa

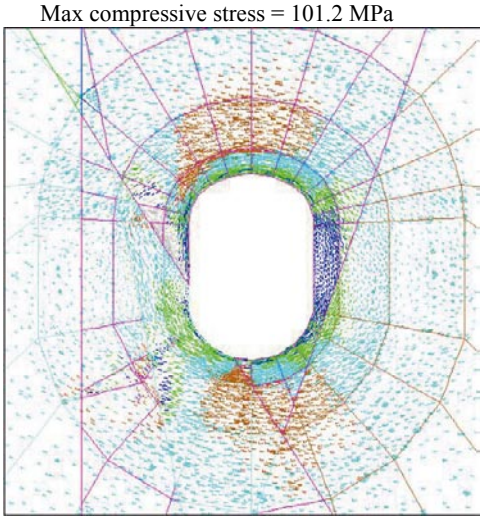

f) With fractures, baseline case
E = 55 GPa, σ1 = 30 MPa, σ1 = 310°
Max compressive stress = 101.2 MPa

Figure H-9. *Cross section plots showing the projection of the principal stress tensor (color by magnitude of a) and b) Sigma 1, c) and d) Sigma 2, and e) and f) Sigma 3) for the as-planned tunnel shape without and with fractures and planar blasting round faces in section 50.*

Section 50

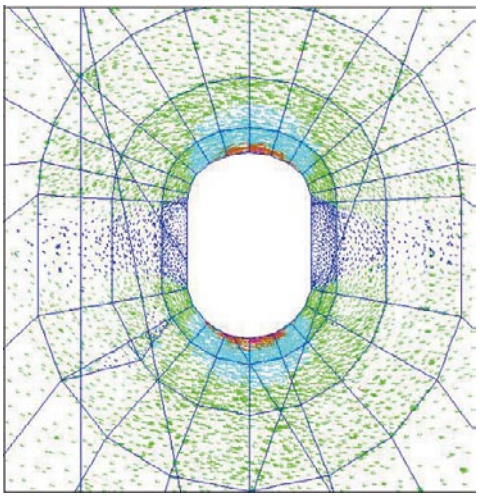

g) Without fractures
E = 65 GPa, σ1 = 25 MPa, σ1 = 310°
Max compressive stress = 100.6 MPa

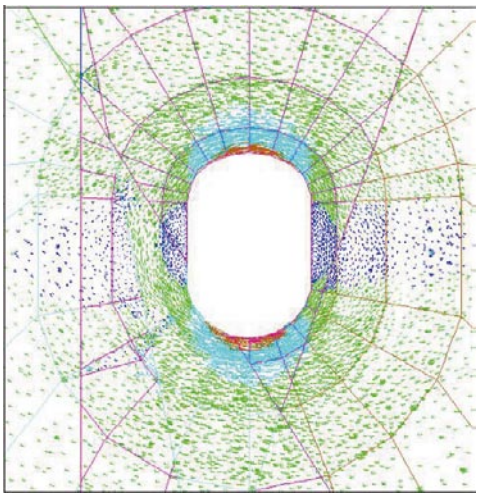

h) With fractures, stiff fractures
E = 65 GPa, σ1 = 25 MPa, σ1 = 310°
Max compressive stress = 101.8 MPa

Sigma 1

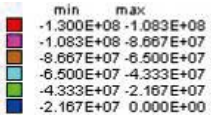

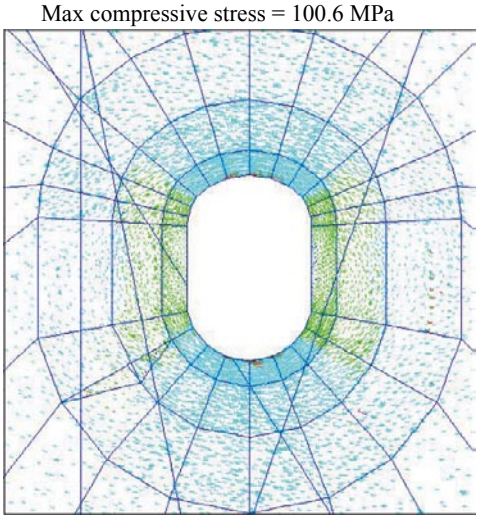

i) Without fractures
E = 65 GPa, σ1 = 25 MPa, σ1 = 310°
Max compressive stress = 100.6 MPa

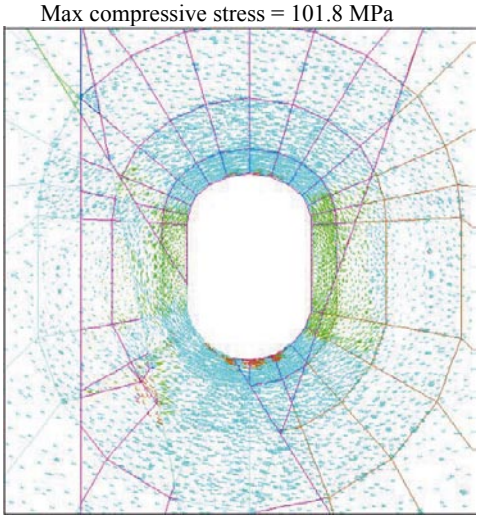

j) With fractures, stiff fractures
E = 65 GPa, σ1 = 25 MPa, σ1 = 310°
Max compressive stress = 101.8 MPa

Sigma 2

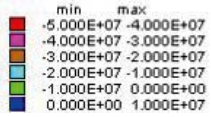

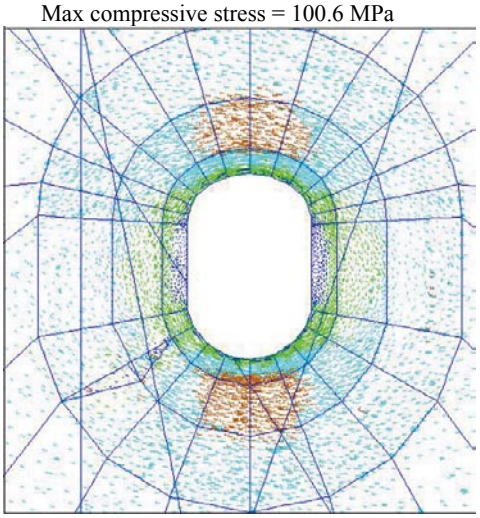

k) Without fractures
E = 65 GPa, σ1 = 25 MPa, σ1 = 310°
Max compressive stress = 100.6 MPa

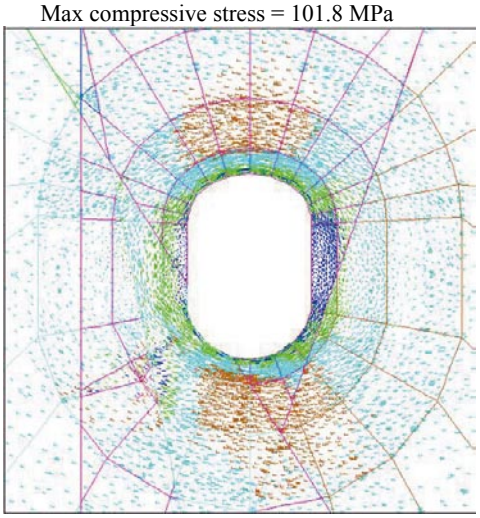

l) With fractures, stiff fractures
E = 65 GPa, σ1 = 25 MPa, σ1 = 310°
Max compressive stress = 101.8 MPa

Sigma 3

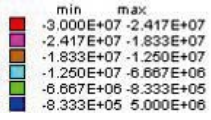

Figure H-10. *Cross section plots showing the projection of the principal stress tensor (color by magnitude of a) and b) Sigma 1, c) and d) Sigma 2, and e) and f) Sigma 3) for the as-planned tunnel shape without and with fractures and planar blasting round faces in section 50.*

Section 51

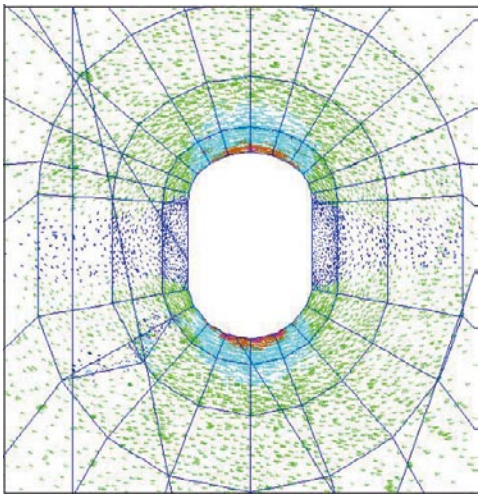

a) Without fractures
E = 55 GPa, σ1 = 30 MPa, σ1 = 310°
Max compressive stress = 101.8 MPa

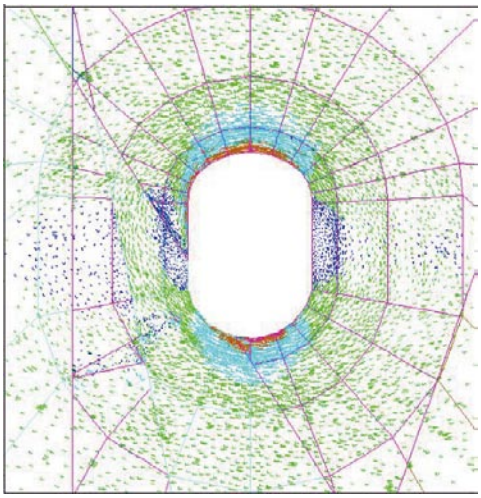

b) With fractures, baseline case
E = 55 GPa, σ1 = 30 MPa, σ1 = 310°
Max compressive stress = 102.4 MPa

Sigma 1

min	max
-1.300E+08	-1.083E+08
-1.083E+08	-8.667E+07
-8.667E+07	-6.500E+07
-6.500E+07	-4.333E+07
-4.333E+07	-2.167E+07
-2.167E+07	0.000E+00

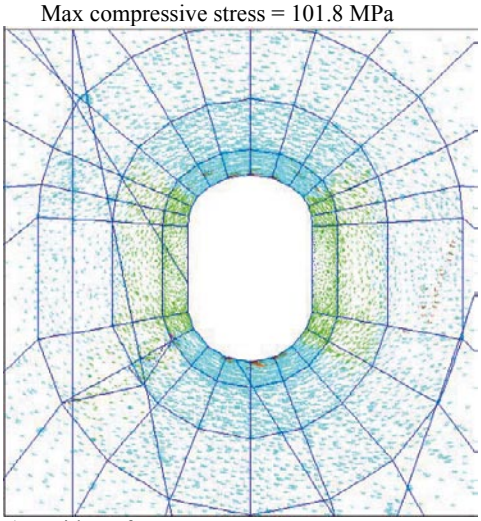

c) Without fractures
E = 55 GPa, σ1 = 30 MPa, σ1 = 310°
Max compressive stress = 101.8 MPa

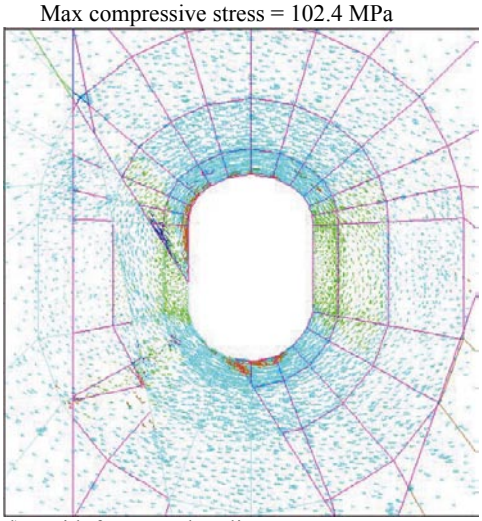

d) With fractures, baseline case
E = 55 GPa, σ1 = 30 MPa, σ1 = 310°
Max compressive stress = 102.4 MPa

Sigma 2

min	max
-5.000E+07	-4.000E+07
-4.000E+07	-3.000E+07
-3.000E+07	-2.000E+07
-2.000E+07	-1.000E+07
-1.000E+07	0.000E+00
0.000E+00	1.000E+07

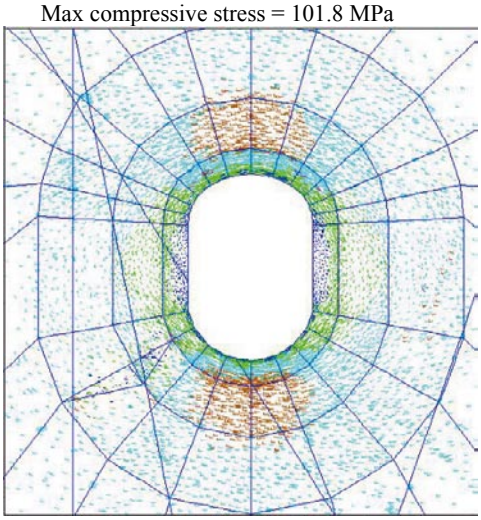

e) Without fractures
E = 55 GPa, σ1 = 30 MPa, σ1 = 310°
Max compressive stress = 101.8 MPa

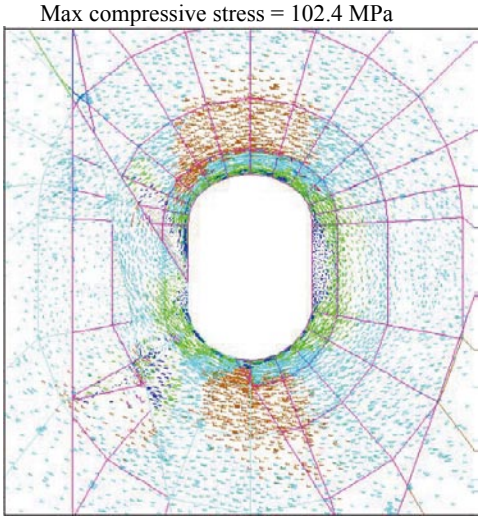

f) With fractures, baseline case
E = 55 GPa, σ1 = 30 MPa, σ1 = 310°
Max compressive stress = 102.4 MPa

Sigma 3

min	max
-3.000E+07	-2.417E+07
-2.417E+07	-1.833E+07
-1.833E+07	-1.250E+07
-1.250E+07	-6.667E+06
-6.667E+06	-8.333E+05
-8.333E+05	5.000E+06

Figure H-11. *Cross section plots showing the projection of the principal stress tensor (color by magnitude of a) and b) Sigma 1, c) and d) Sigma 2, and e) and f) Sigma 3) for the as-planned tunnel shape without and with fractures and planar blasting round faces in section 51.*

Section 51

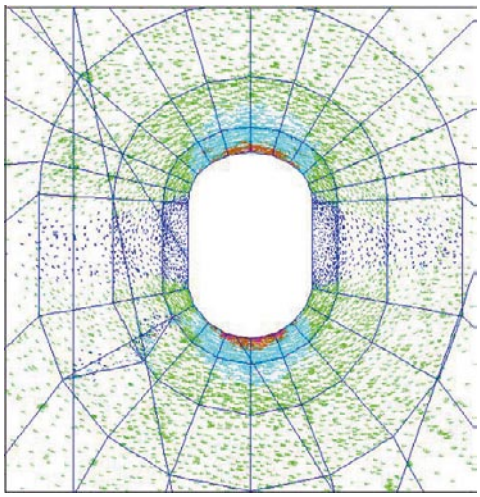

g) Without fractures
E = 65 GPa, σ1 = 25 MPa, σ1 = 310°
Max compressive stress = 101.8 MPa

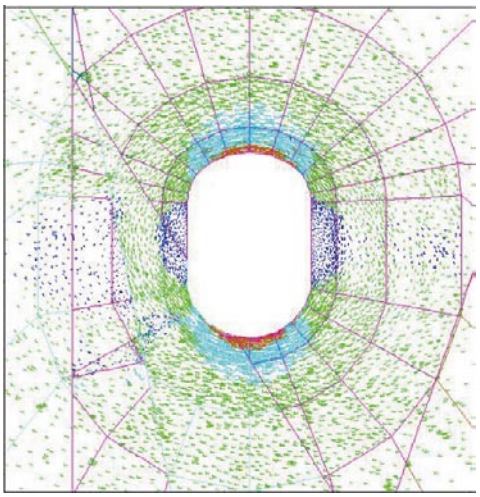

h) With fractures, stiff fractures
E = 65 GPa, σ1 = 25 MPa, σ1 = 310°
Max compressive stress = 103.3 MPa

Sigma 1

min	max
-1.300E+08	-1.083E+08
-1.083E+08	-8.667E+07
-8.667E+07	-6.500E+07
-6.500E+07	-4.333E+07
-4.333E+07	-2.167E+07
-2.167E+07	0.000E+00

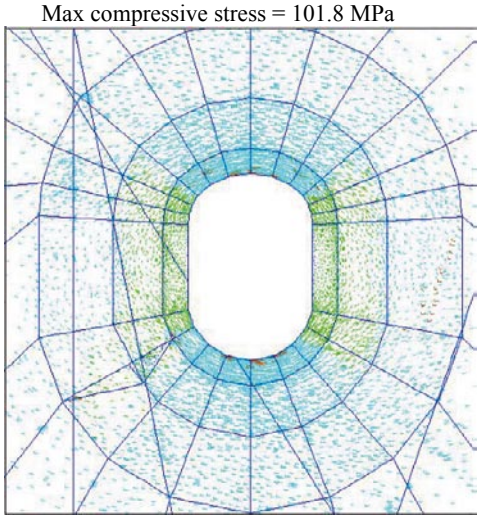

i) Without fractures
E = 65 GPa, σ1 = 25 MPa, σ1 = 310°
Max compressive stress = 101.8 MPa

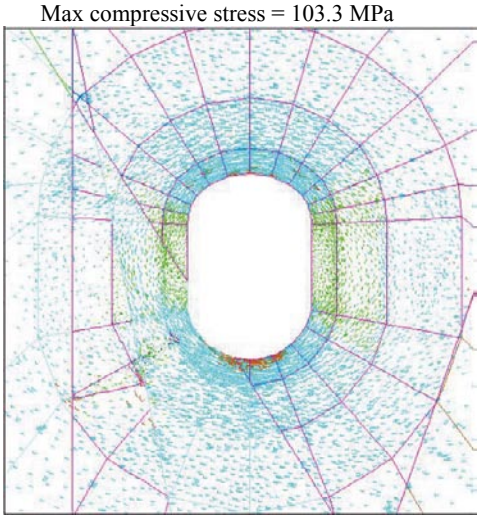

j) With fractures, stiff fractures
E = 65 GPa, σ1 = 25 MPa, σ1 = 310°
Max compressive stress = 103.3 MPa

Sigma 2

min	max
-5.000E+07	-4.000E+07
-4.000E+07	-3.000E+07
-3.000E+07	-2.000E+07
-2.000E+07	-1.000E+07
-1.000E+07	0.000E+00
0.000E+00	1.000E+07

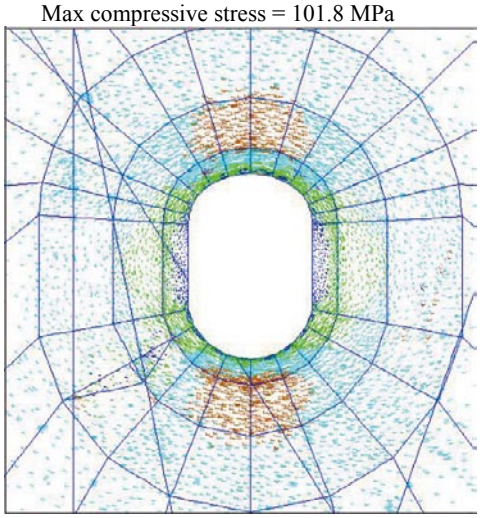

k) Without fractures
E = 65 GPa, σ1 = 25 MPa, σ1 = 310°
Max compressive stress = 101.8 MPa

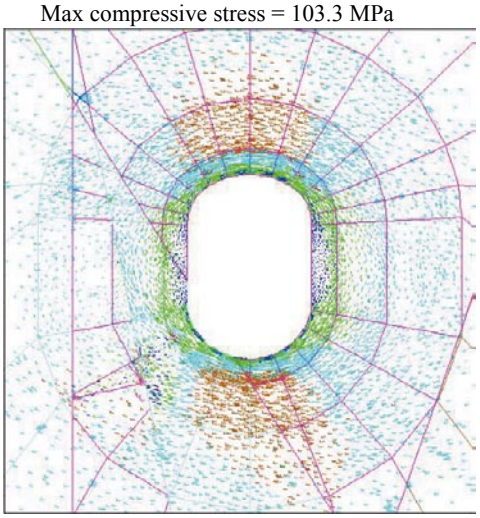

l) With fractures, stiff fractures
E = 65 GPa, σ1 = 25 MPa, σ1 = 310°
Max compressive stress = 103.3 MPa

Sigma 3

min	max
-3.000E+07	-2.417E+07
-2.417E+07	-1.833E+07
-1.833E+07	-1.250E+07
-1.250E+07	-6.667E+06
-6.667E+06	-8.333E+05
-8.333E+05	5.000E+06

Figure H-12. *Cross section plots showing the projection of the principal stress tensor (color by magnitude of a) and b) Sigma 1, c) and d) Sigma 2, and e) and f) Sigma 3) for the as-planned tunnel shape without and with fractures and planar blasting round faces in section 51.*

3DEC scanlines at section 47, with and without fractures

Scanlines of σ1, σ2 and σ3 in the location of the boreholes used for the ultrasonic measurements (boreholes KQ0047H01, KQ0047I01, KQ0047A03, KQ0047A02, KQ0047B02, KQ0047A01, KQ0047B01 and KQ0047G01 see Figure 9-14) in tunnel section 47 using the as-planned tunnel shape in 3DEC. An additional stress scanline has been obtained in the right side of the floor (see Figure 9-12).

All these simulations used a rock mass Young's modulus of 65 GPa and a magnitude of sigma 1 of 25 MPa and the fracture properties from the "stiff" case (see Table 9-3 to Table 9-5).

Sigma 1

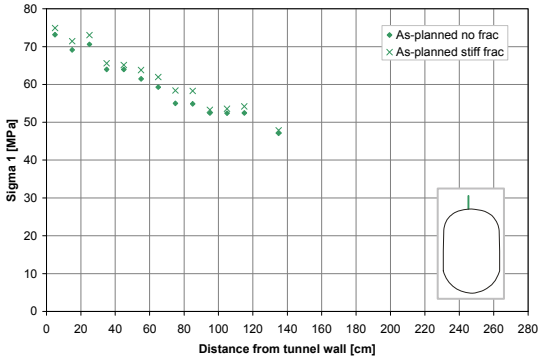

a) KQ0047H01

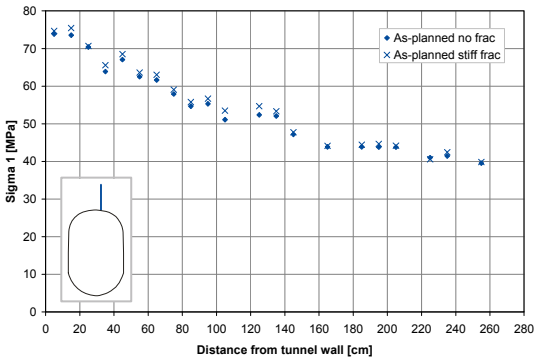

b) KQ0047I01

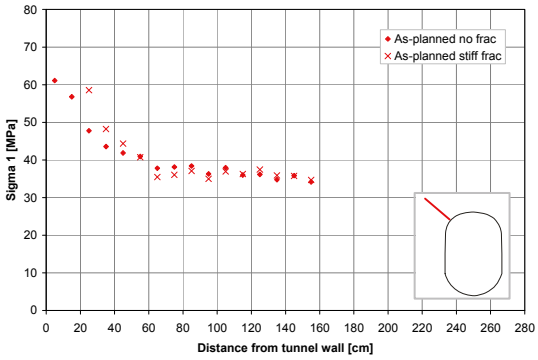

c) KQ0047A03

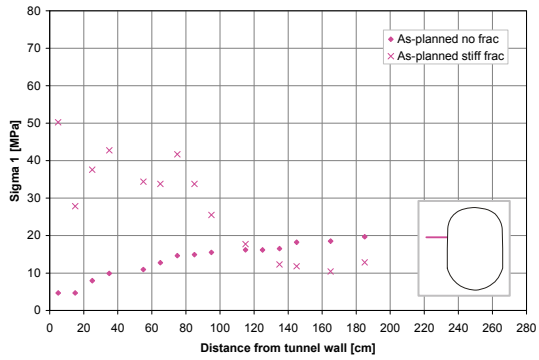

d) KQ0047A02

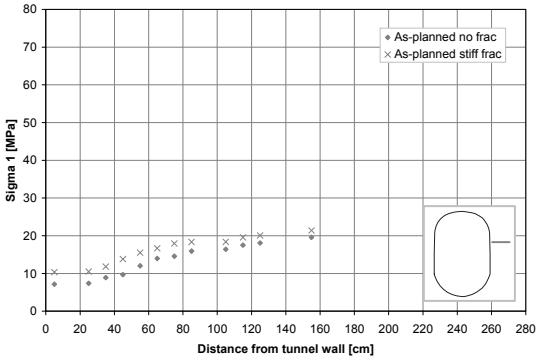

e) KQ0047B02

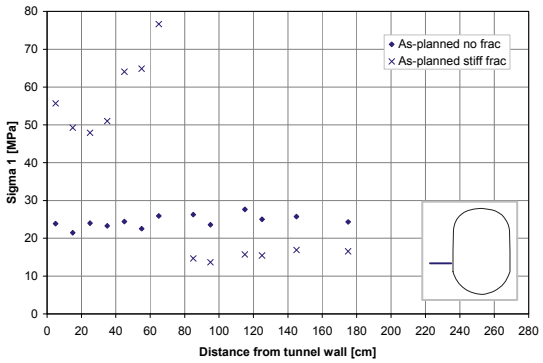

f) KQ0047A01

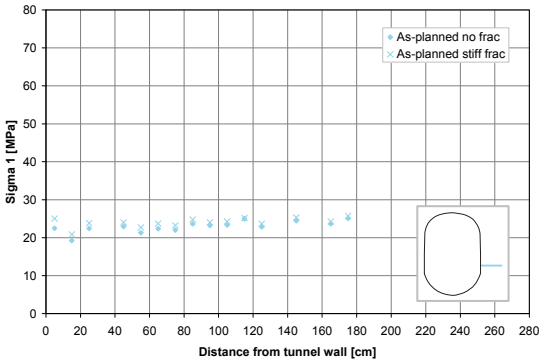

g) KQ0047B01

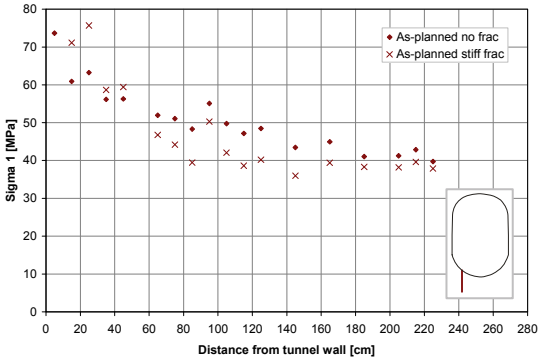

h) KQ0047G01

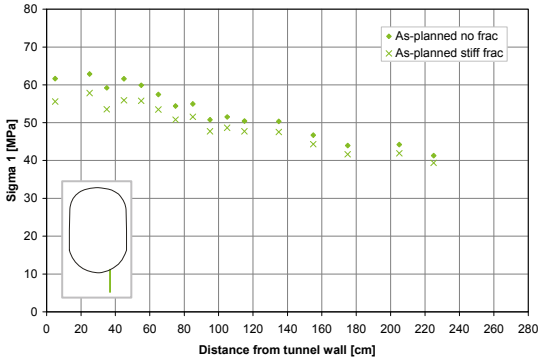

i) Right side of the floor

Figure I-1. *Comparison between major principal stress along different scanlines from the wall of tunnel section 47 (BGR section) in the case with as-planned tunnel shape without fractures and the case with as-planned tunnel shape with stiff fractures (Rock mass E=65GPa, Sigma 1 = 25 MPa); a) KQ0047H01, b) KQ0047I01, c) KQ0047A03, d) KQ0047A02, e) KQ0047B02, f) KQ0047A01, g) KQ0047B01, h) KQ0047G01 and i) right side of the floor.*

Sigma 2

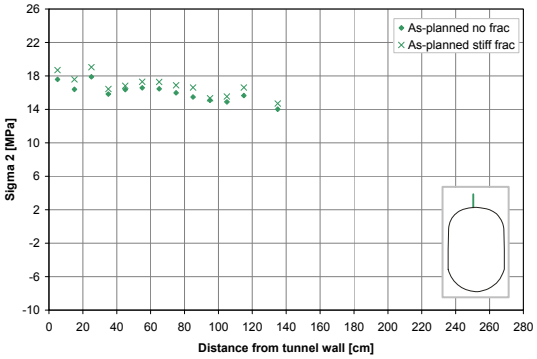

a) KQ0047H01

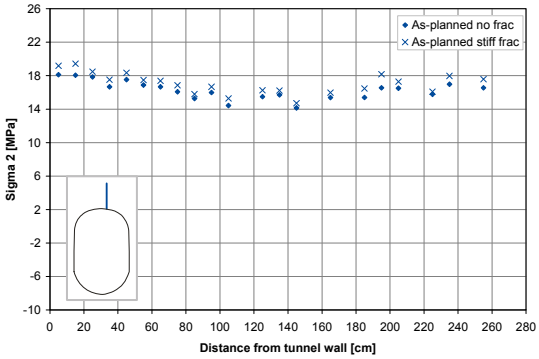

b) KQ0047I01

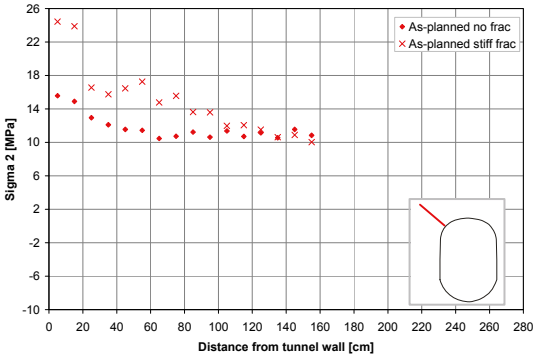

c) KQ0047A03

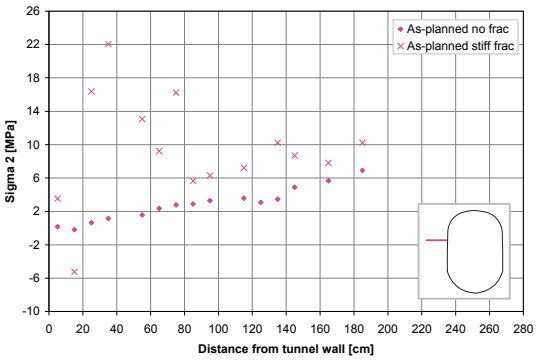

d) KQ0047A02

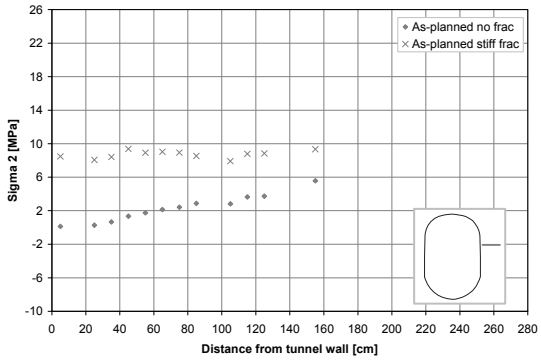

e) KQ0047B02

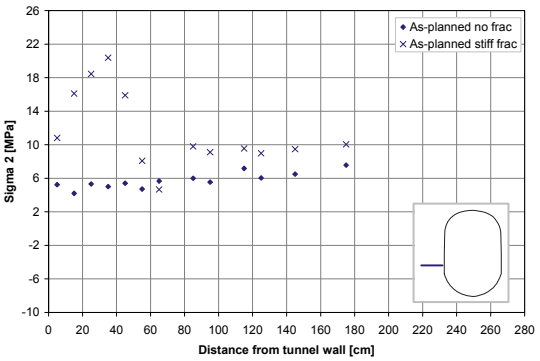

f) KQ0047A01

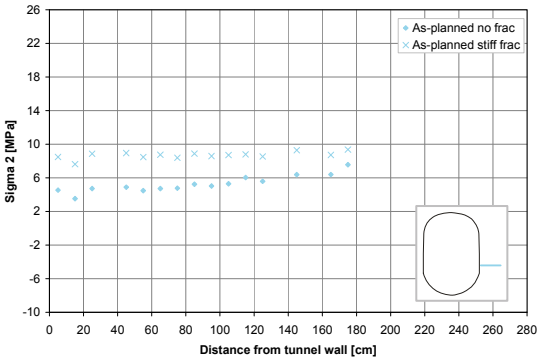

g) KQ0047B01

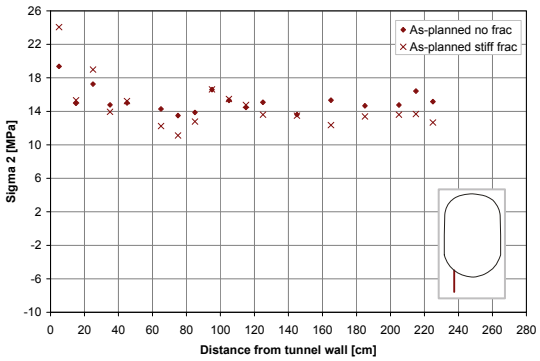

h) KQ0047G01

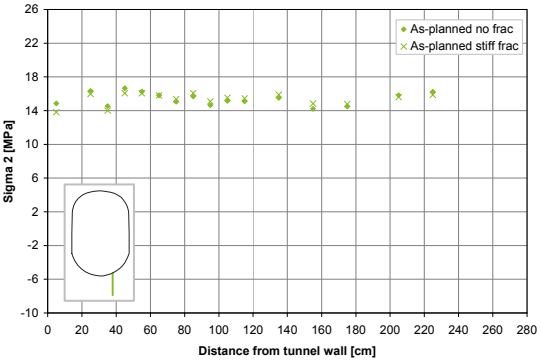

i) Right side of the floor

Figure I-2. *Comparison between intermediate principal stress along different scanlines from the wall of tunnel section 47 (BGR section) in the case with as-planned tunnel shape without fractures and the case with as-planned tunnel shape with stiff fractures (Rock mass E=65GPa, Sigma 1 = 25 MPa); a) KQ0047H01, b) KQ0047I01, c) KQ0047A03, d) KQ0047A02, e) KQ0047B02, f) KQ0047A01, g) KQ0047B01, h) KQ0047G01 and i) right side of the floor.*

Sigma 3

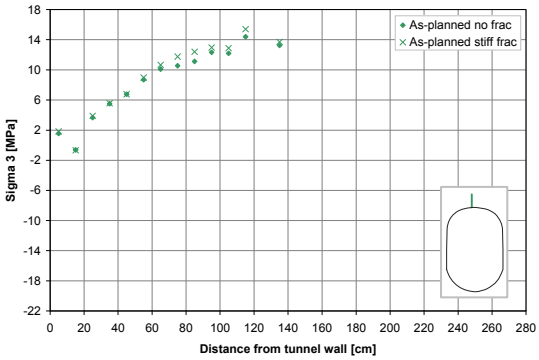

a) KQ0047H01

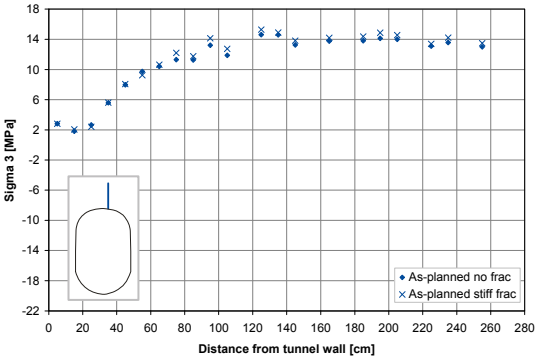

b) KQ0047I01

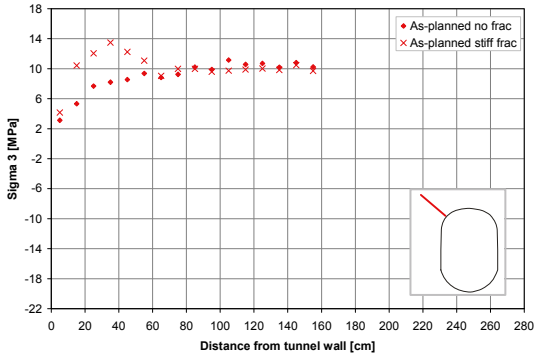

c) KQ0047A03

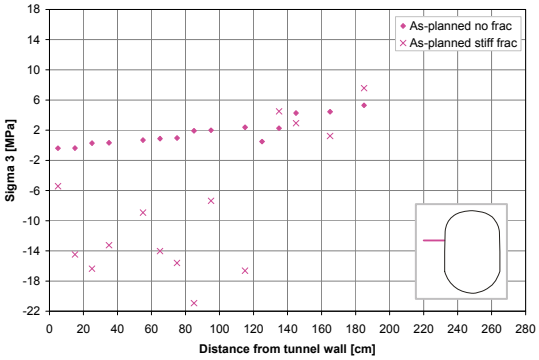

d) KQ0047A02

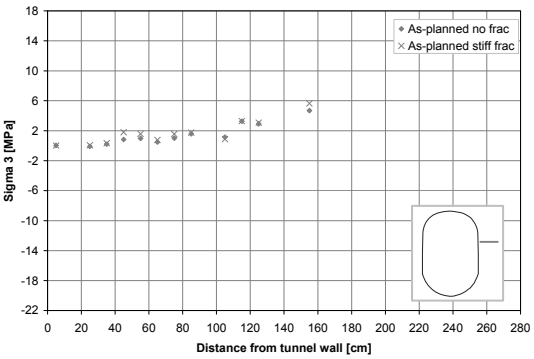

e) KQ0047B02

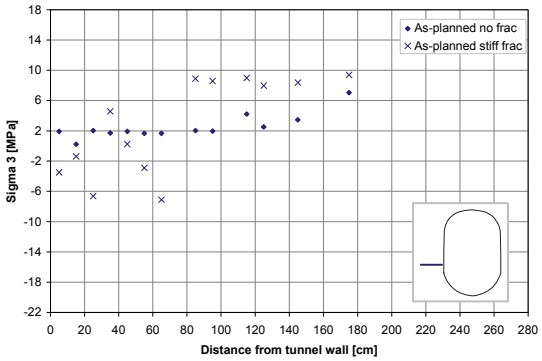

f) KQ0047A01

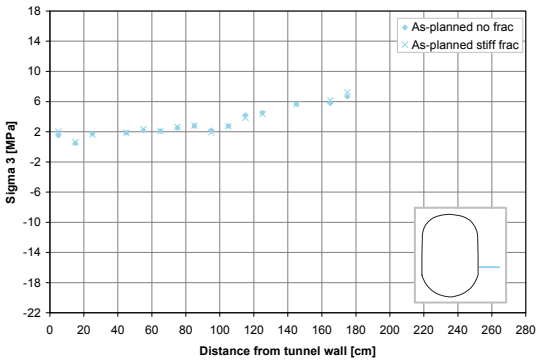

g) KQ0047B01

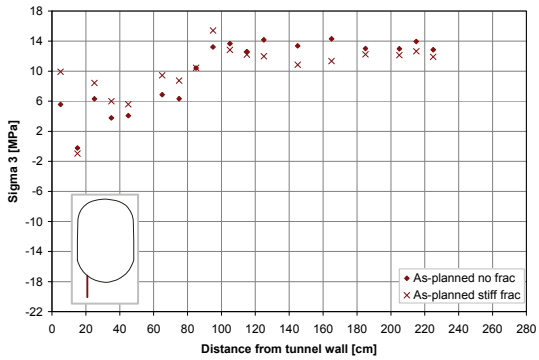

h) KQ0047G01

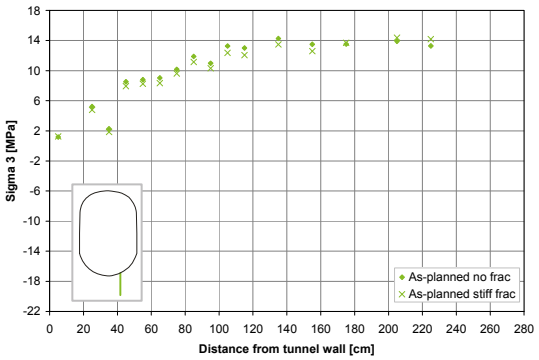

i) Right side of the floor

Figure I-3. *Comparison between minor principal stress along different scanlines from the wall of tunnel section 47 (BGR section) in the case with as-planned tunnel shape without fractures and the case with as-planned tunnel shape with stiff fractures (Rock mass E=65GPa, Sigma 1 = 25 MPa); a) KQ0047H01, b) KQ0047I01, c) KQ0047A03, d) KQ0047A02, e) KQ0047B02, f) KQ0047A01, g) KQ0047B01, h) KQ0047G01 and i) right side of the floor.*

Appendix J

Convergence calibration curves

Using the actual field convergence measurements, a numerical calibration study has been performed in order to obtain the best fitting in-situ stress and elastic rock mass properties. The different ranges for the Young's modulus and the magnitude and orientation of the major principal stress used in this study are listed in Table 9-6.

The main simulations were performed using the as-built tunnel shape as well as concave (actual) blasting round faces. Additional simulations were performed using the as-planned tunnel shape with planar blasting round faces and the as-built tunnel shape with planar blasting round faces in order to consider the effect of tunnel shape and blasting round face shape (cases with E = 45 GPa and σ_1 = 30 MPa and E = 65 GPa and σ_1 = 25 MPa). No fractures were considered in the calibration study.

The simulation of the excavation of the heading of the TASQ-tunnel was performed in stages, according to the actual blasting round stages in order to simulate the correct tunnel convergence sequence.

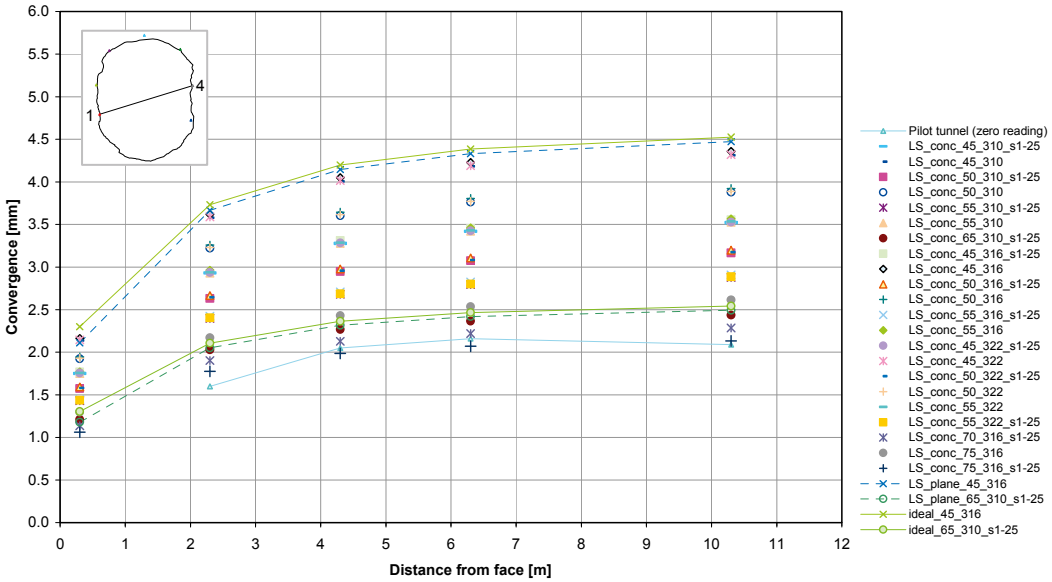

Figure J-1. *Simulated vs. field convergence measurements between pin 1 and 4; "LS" indicates laser-scanned (as-built) tunnel shape. "conc" indicates concave blasting round faces and "plane" indicates planar blasting round faces. 45, 50, 55, 65, 70 and 75 are the rock mass Young's modulus in GPa used in the simulations. 310, 316 and 322 indicate the trend of the major in-situ principal stress. "s1-25" and "s1-30" indicate the magnitude of major in-situ principal stress in MPa.*

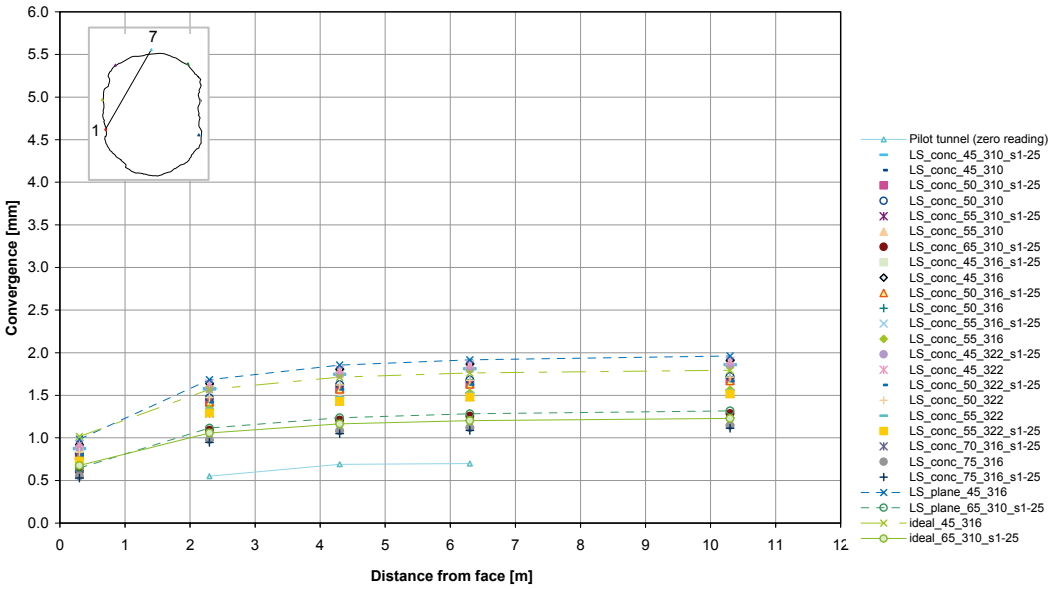

Figure J-2. *Simulated vs. field convergence measurements between pin 1 and 7; "LS" indicates laser-scanned (as-built) tunnel shape. "conc" indicates concave blasting round faces and "plane" indicates planar blasting round faces. 45, 50, 55, 65, 70 and 75 are the rock mass Young's modulus in GPa used in the simulations. 310, 316 and 322 indicate the trend of the major in-situ principal stress. "s1-25" and "s1-30" indicate the magnitude of major in-situ principal stress in MPa.*

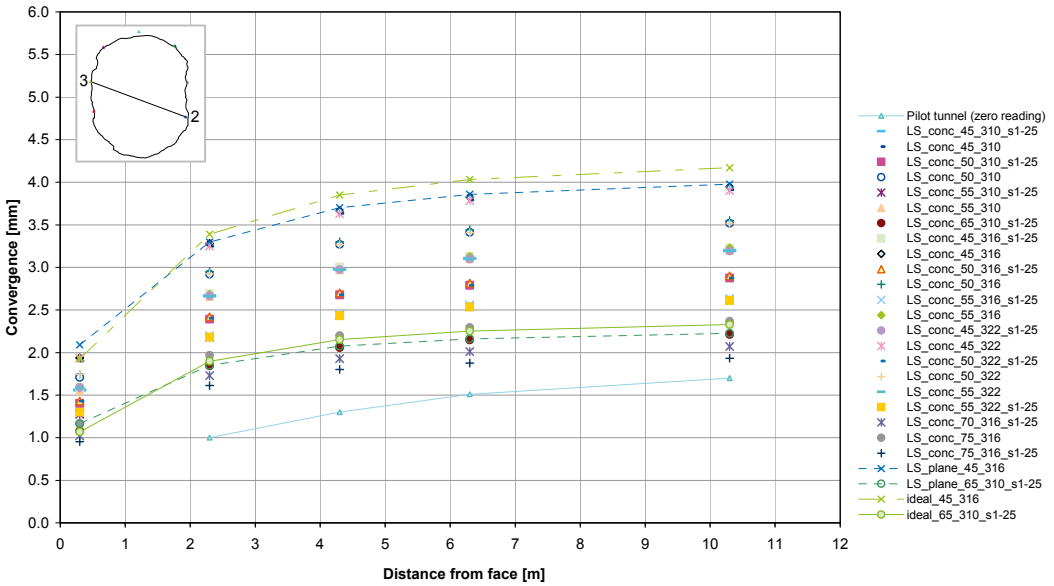

Figure J-3. *Simulated vs. field convergence measurements between pin 2 and 3; "LS" indicates laser-scanned (as-built) tunnel shape. "conc" indicates concave blasting round faces and "plane" indicates planar blasting round faces. 45, 50, 55, 65, 70 and 75 are the rock mass Young's modulus in GPa used in the simulations. 310, 316 and 322 indicate the trend of the major in-situ principal stress. "s1-25" and "s1-30" indicate the magnitude of major in-situ principal stress in MPa.*

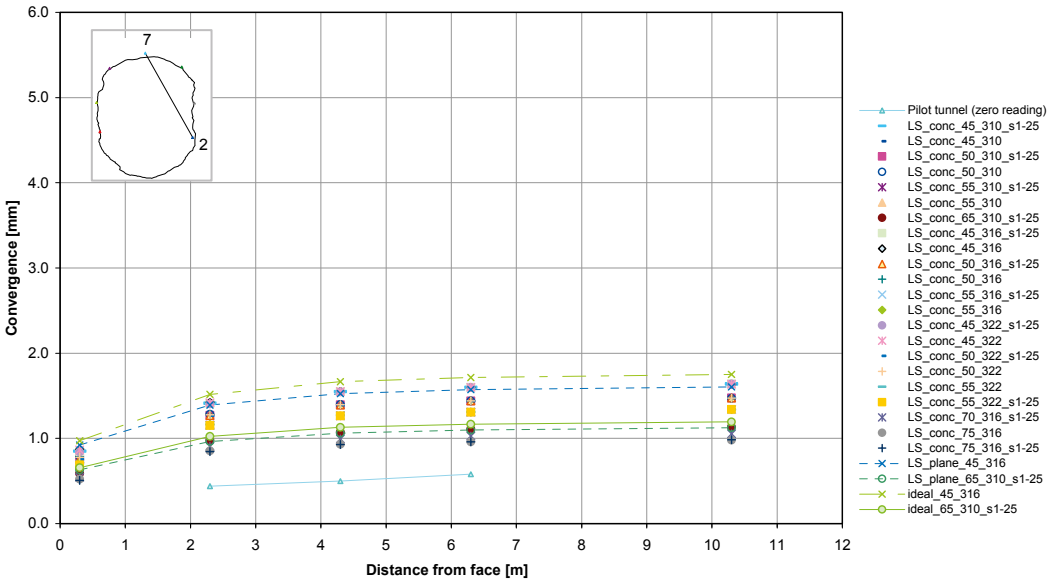

Figure J-4. *Simulated vs. field convergence measurements between pin 2 and 7; "LS" indicates laser-scanned (as-built) tunnel shape. "conc" indicates concave blasting round faces and "plane" indicates planar blasting round faces. 45, 50, 55, 65, 70 and 75 are the rock mass Young's modulus in GPa used in the simulations. 310, 316 and 322 indicate the trend of the major in-situ principal stress. "s1-25" and "s1-30" indicate the magnitude of major in-situ principal stress in MPa.*

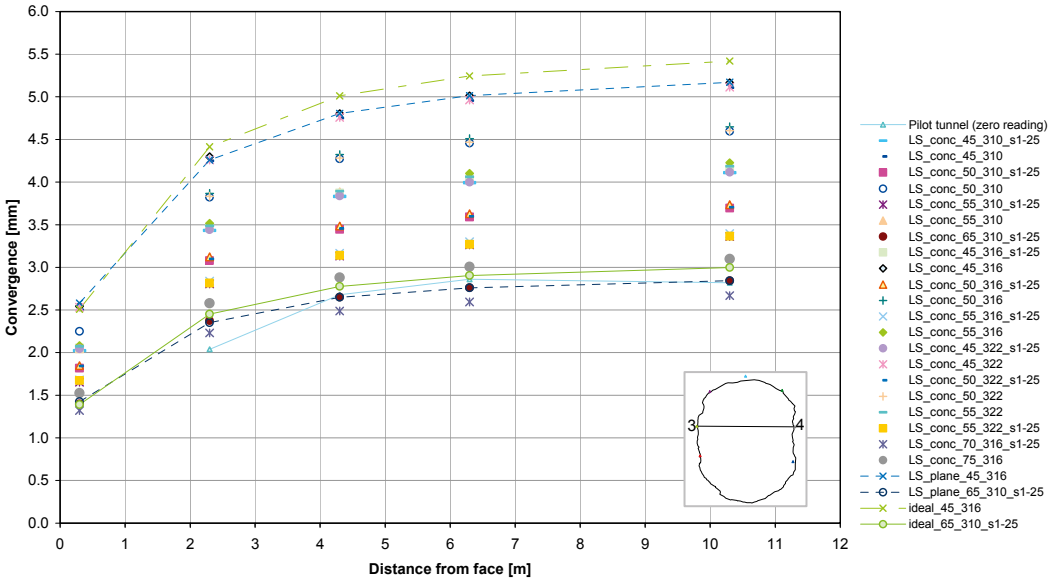

Figure J-5. *Simulated vs. field convergence measurements between pin 3 and 4; "LS" indicates laser-scanned (as-built) tunnel shape. "conc" indicates concave blasting round faces and "plane" indicates planar blasting round faces. 45, 50, 55, 65, 70 and 75 are the rock mass Young's modulus in GPa used in the simulations. 310, 316 and 322 indicate the trend of the major in-situ principal stress. "s1-25" and "s1-30" indicate the magnitude of major in-situ principal stress in MPa.*

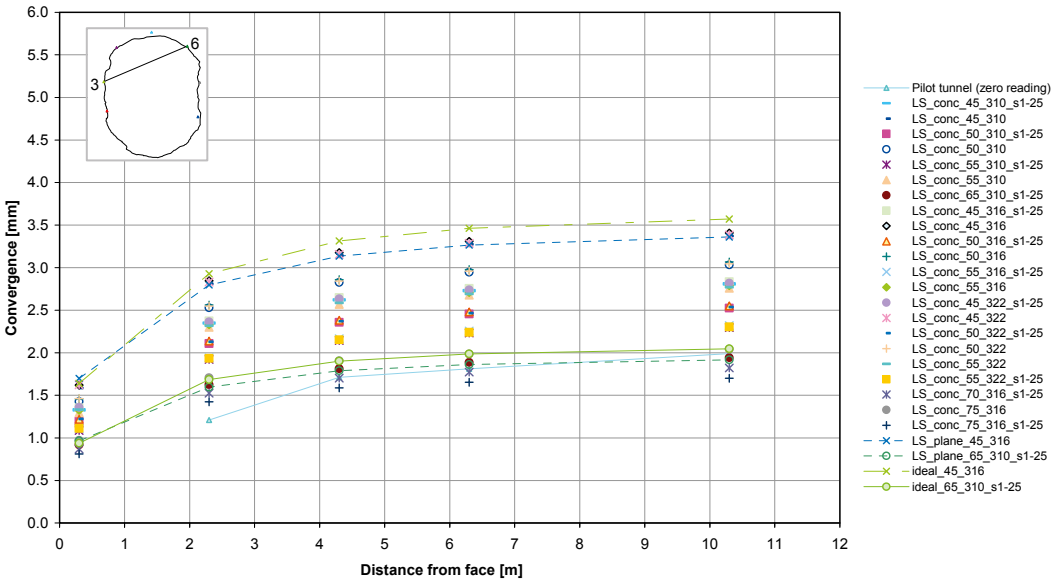

Figure J-6. *Simulated vs. field convergence measurements between pin 3 and 6; "LS" indicates laser-scanned (as-built) tunnel shape. "conc" indicates concave blasting round faces and "plane" indicates planar blasting round faces. 45, 50, 55, 65, 70 and 75 are the rock mass Young's modulus in GPa used in the simulations. 310, 316 and 322 indicate the trend of the major in-situ principal stress. "s1-25" and "s1-30" indicate the magnitude of major in-situ principal stress in MPa.*

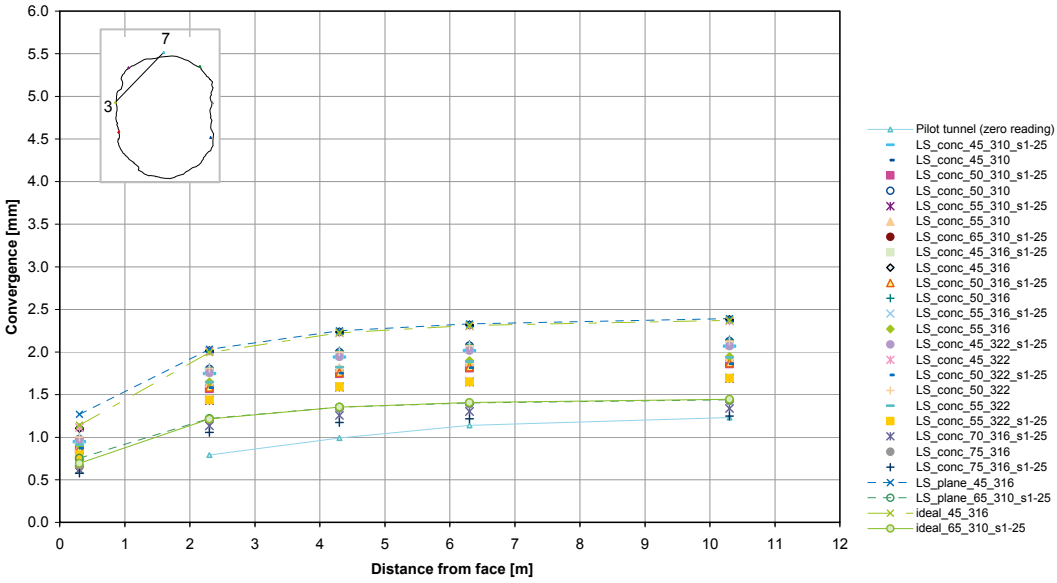

Figure J-7. *Simulated vs. field convergence measurements between pin 3 and 7; "LS" indicates laser-scanned (as-built) tunnel shape. "conc" indicates concave blasting round faces and "plane" indicates planar blasting round faces. 45, 50, 55, 65, 70 and 75 are the rock mass Young's modulus in GPa used in the simulations. 310, 316 and 322 indicate the trend of the major in-situ principal stress. "s1-25" and "s1-30" indicate the magnitude of major in-situ principal stress in MPa.*

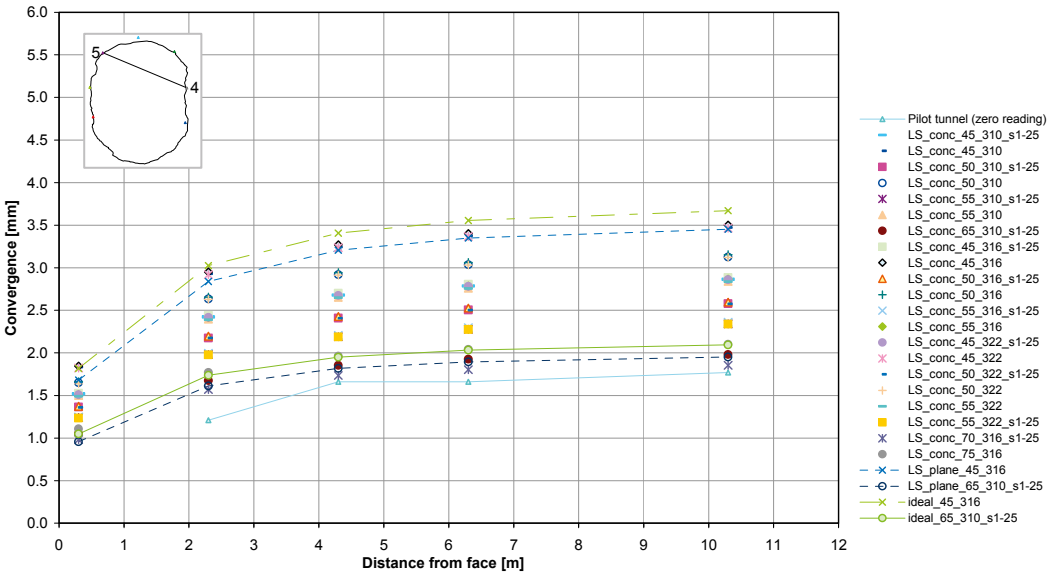

Figure J-8. *Simulated vs. field convergence measurements between pin 4 and 5; "LS" indicates laser-scanned (as-built) tunnel shape. "conc" indicates concave blasting round faces and "plane" indicates planar blasting round faces. 45, 50, 55, 65, 70 and 75 are the rock mass Young's modulus in GPa used in the simulations. 310, 316 and 322 indicate the trend of the major in-situ principal stress. "s1-25" and "s1-30" indicate the magnitude of major in-situ principal stress in MPa.*

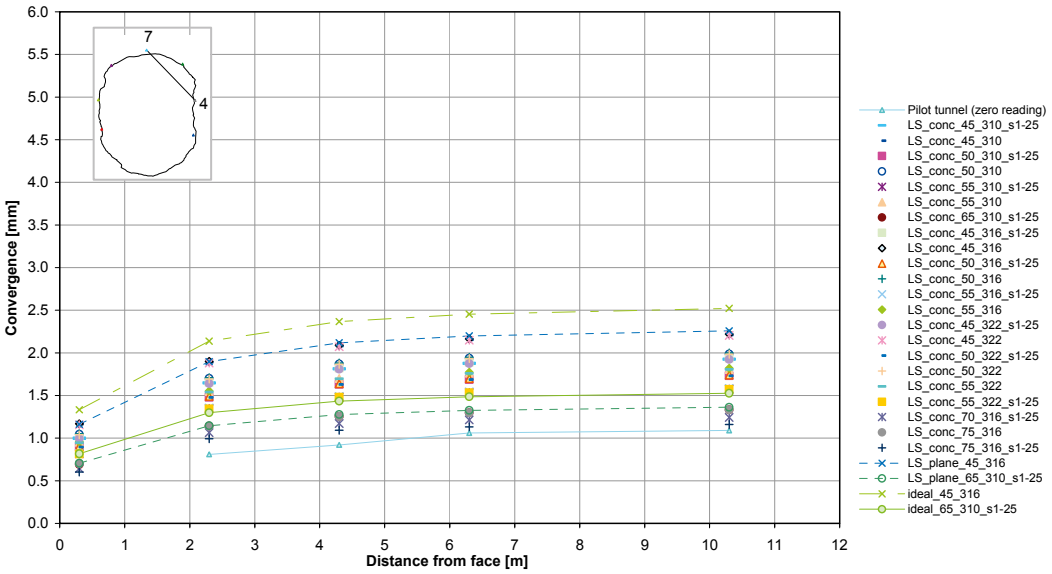

Figure J-9. *Simulated vs. field convergence measurements between pin 4 and 7; "LS" indicates laser-scanned (as-built) tunnel shape. "conc" indicates concave blasting round faces and "plane" indicates planar blasting round faces. 45, 50, 55, 65, 70 and 75 are the rock mass Young's modulus in GPa used in the simulations. 310, 316 and 322 indicate the trend of the major in-situ principal stress. "s1-25" and "s1-30" indicate the magnitude of major in-situ principal stress in MPa.*

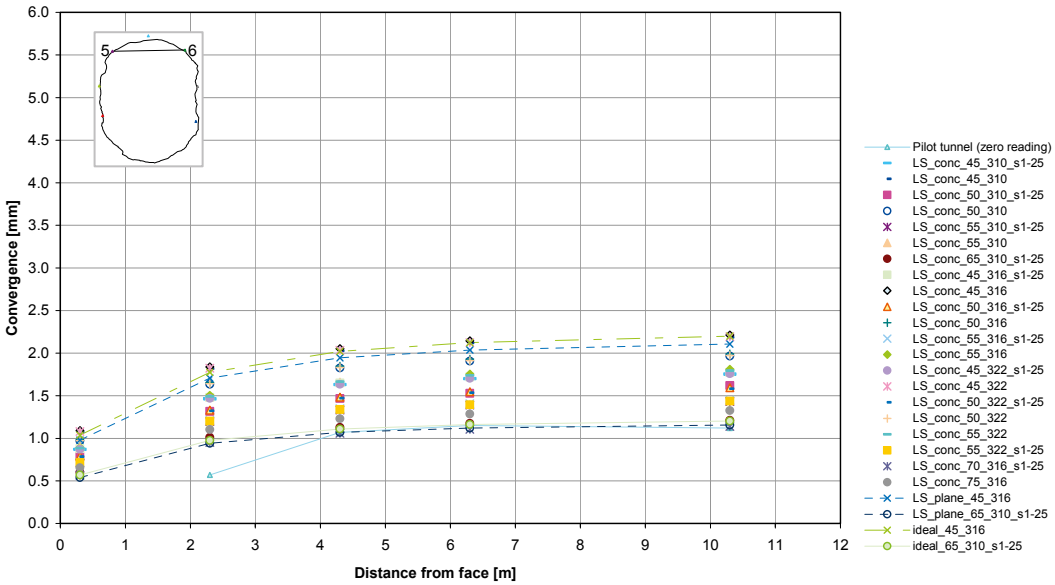

Figure J-10. *Simulated vs. field convergence measurements between pin 5 and 6; "LS" indicates laser-scanned (as-built) tunnel shape. "conc" indicates concave blasting round faces and "plane" indicates planar blasting round faces. 45, 50, 55, 65, 70 and 75 are the rock mass Young's modulus in GPa used in the simulations. 310, 316 and 322 indicate the trend of the major in-situ principal stress. "s1-25" and "s1-30" indicate the magnitude of major in-situ principal stress in MPa.*

Appendix K

Scanlines at the convergence pins section (48.7) after the excavation of each heading blasting round

Scanlines of Sigma 1 and Sigma 3 for five different heading blasting rounds (sections 49, 51, 53, 55 and 59) taken from the section where the convergence pins are located (section 48.7) for three calibration cases (see Table 9-6); 1) as-planned tunnel shape with planar blasting round faces, without any fractures, 2) as-built tunnel shape with planar blasting round faces without fractures and 3) as-built tunnel shape with concave blasting round faces without fractures. The scanlines are taken at the approximate location where the boreholes for the ultrasonic measurements were placed at section 47 (see Figure 9-12).

Section 49

Sigma 1

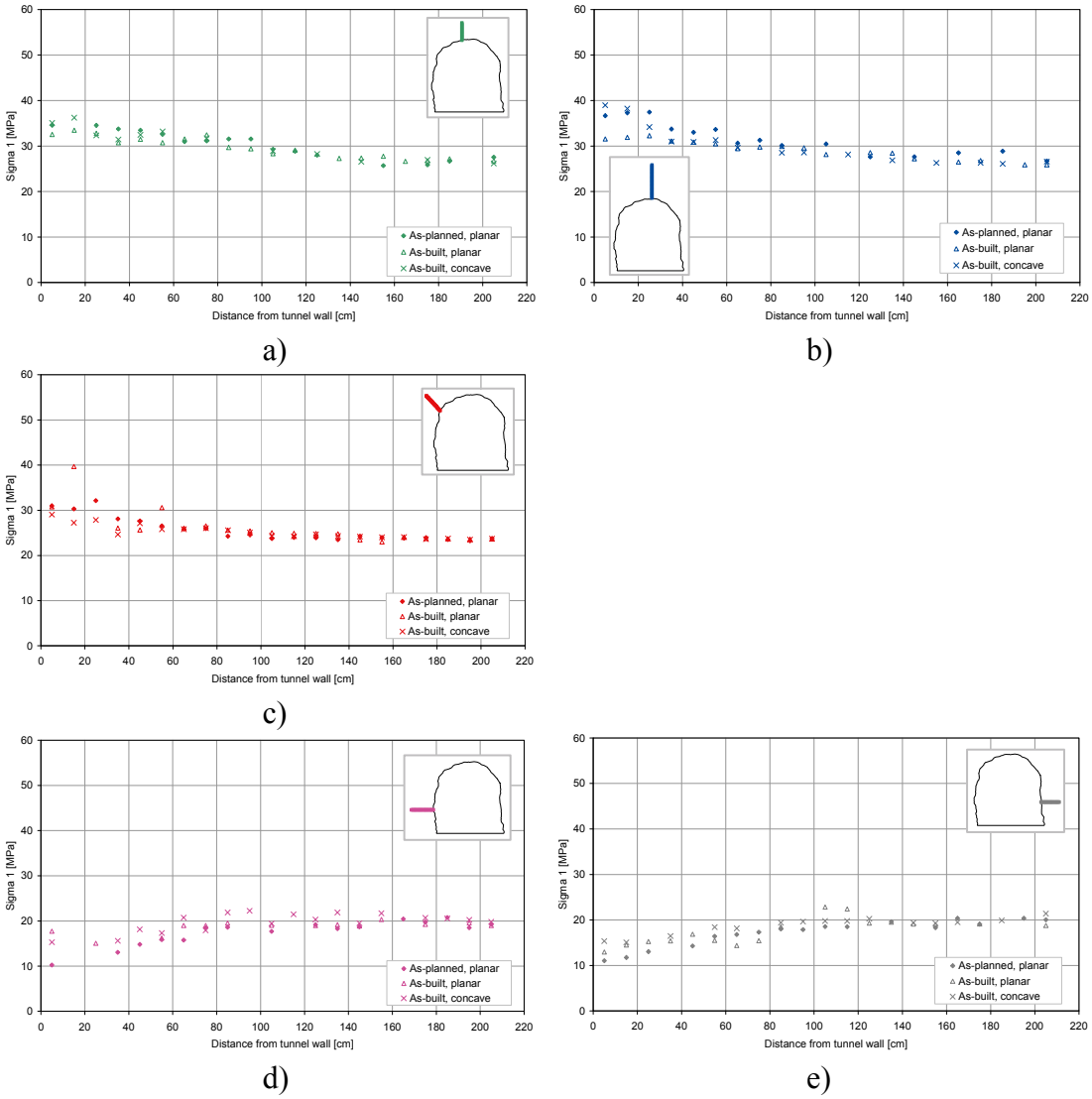

Figure K-1. *Plots of major principal stress scanlines showing the difference between the model with as-planned tunnel shape with planar blasting round faces, the model with as-built tunnel shape with planar blasting round faces and the model with as-built tunnel shape with concave blasting round faces at cross section 48.7 (convergence pins location) in the TASQ tunnel when the heading of section 49 was excavated. The scanlines are approximately at the same place in the tunnel as the boreholes in the BGR section a) left part of the roof (KQ0047H01), b) right part of the roof (KQ0047I01), c) upper left wall (KQ0047A03), d) left wall (KQ0047A02) and e) right wall (KQ0047B02). (E = 65 GPa, sigma 1 = 25 MPa).*

Sigma 3

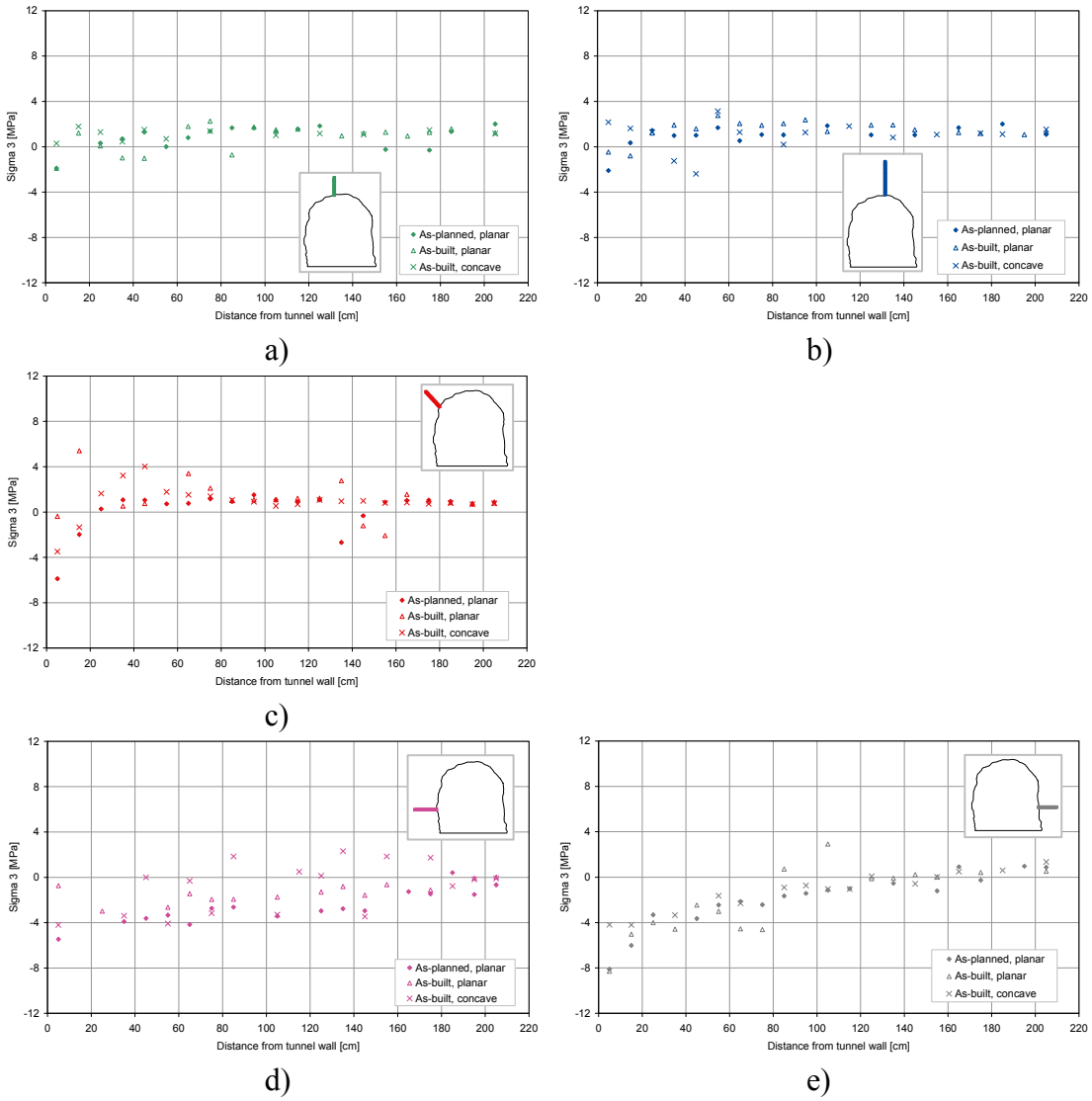

Figure K-2. *Plots of minor principal stress scanlines showing the difference between the model with as-planned tunnel shape with planar blasting round faces, the model with as-built tunnel shape with planar blasting round faces and the model with as-built tunnel shape with concave blasting round faces at cross section 48.7 (convergence pins location) in the TASQ tunnel when the heading of section 49 was excavated. The scanlines are approximately at the same place in the tunnel as the boreholes in the BGR section a) left part of the roof (KQ0047H01), b) right part of the roof (KQ0047I01), c) upper left wall (KQ0047A03), d) left wall (KQ0047A02) and e) right wall (KQ0047B02). (E = 65 GPa, sigma 1 = 25 MPa).*

Section 51

Sigma 1

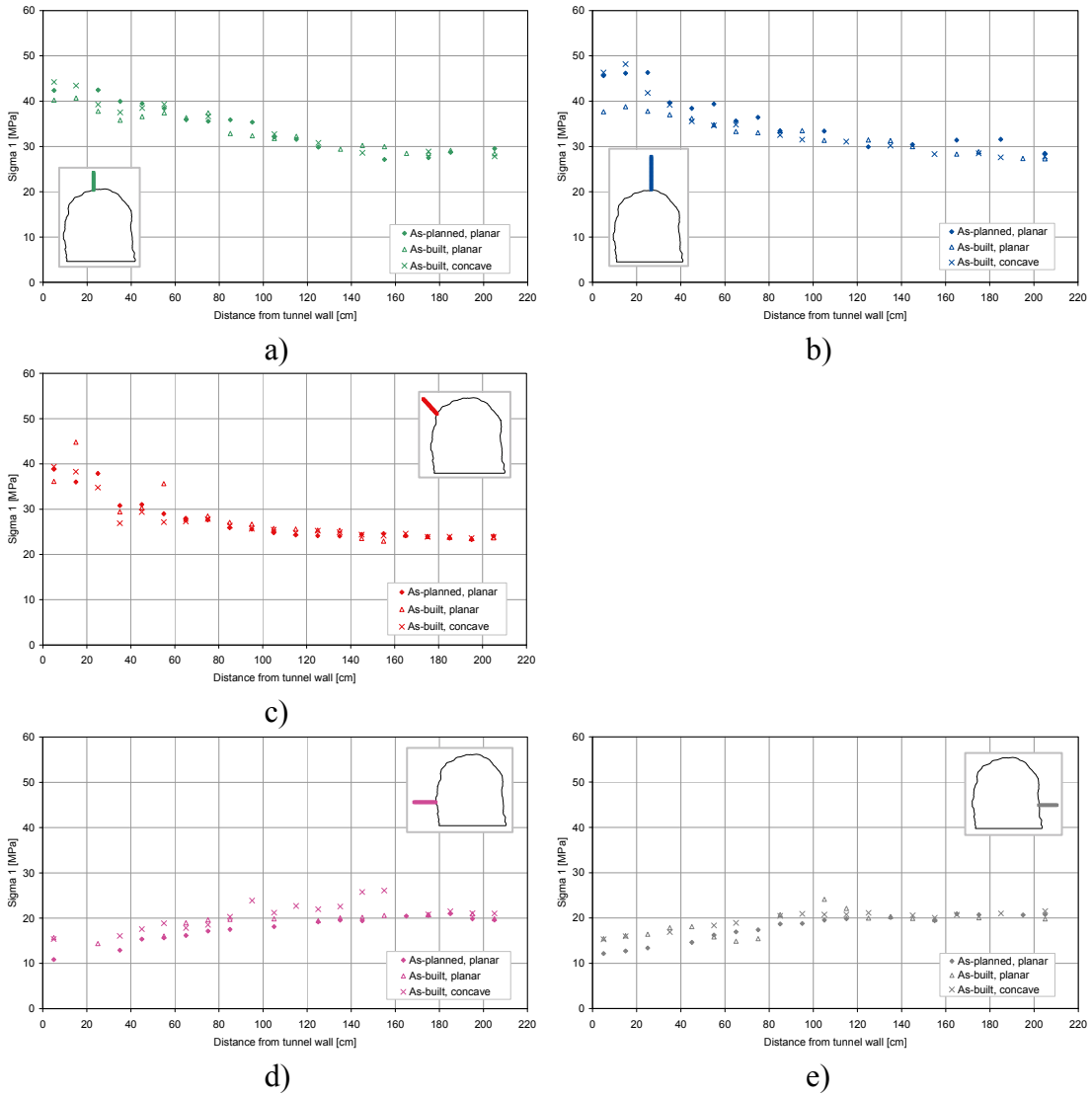

Figure K-3. *Plots of major principal stress scanlines showing the difference between the model with as-planned tunnel shape with planar blasting round faces, the model with as-built tunnel shape with planar blasting round faces and the model with as-built tunnel shape with concave blasting round faces at cross section 48.7 (convergence pins location) in the TASQ tunnel when the heading of section 51 was excavated. The scanlines are approximately at the same place in the tunnel as the boreholes in the BGR section a) left part of the roof (KQ0047H01), b) right part of the roof (KQ0047I01), c) upper left wall (KQ0047A03), d) left wall (KQ0047A02) and e) right wall (KQ0047B02). (E = 65 GPa, sigma 1 = 25 MPa).*

Sigma 3

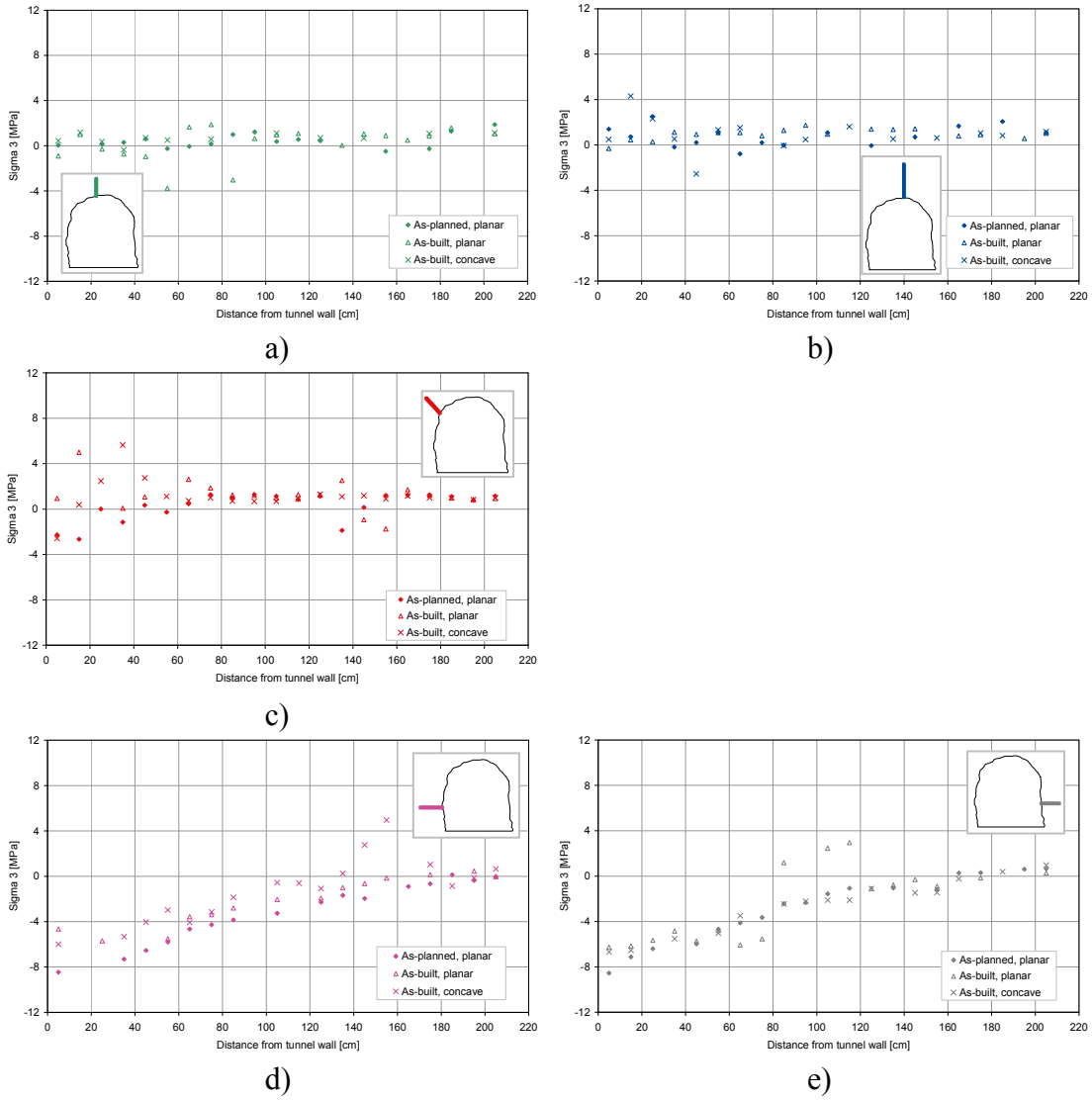

Figure K-4. *Plots of minor principal stress scanlines showing the difference between the model with as-planned tunnel shape with planar blasting round faces, the model with as-built tunnel shape with planar blasting round faces and the model with as-built tunnel shape with concave blasting round faces at cross section 48.7 (convergence pins location) in the TASQ tunnel when the heading of section 51 was excavated. The scanlines are approximately at the same place in the tunnel as the boreholes in the BGR section a) left part of the roof (KQ0047H01), b) right part of the roof (KQ0047I01), c) upper left wall (KQ0047A03), d) left wall (KQ0047A02) and e) right wall (KQ0047B02). (E = 65 GPa, sigma 1 = 25 MPa).*

Section 53

Sigma 1

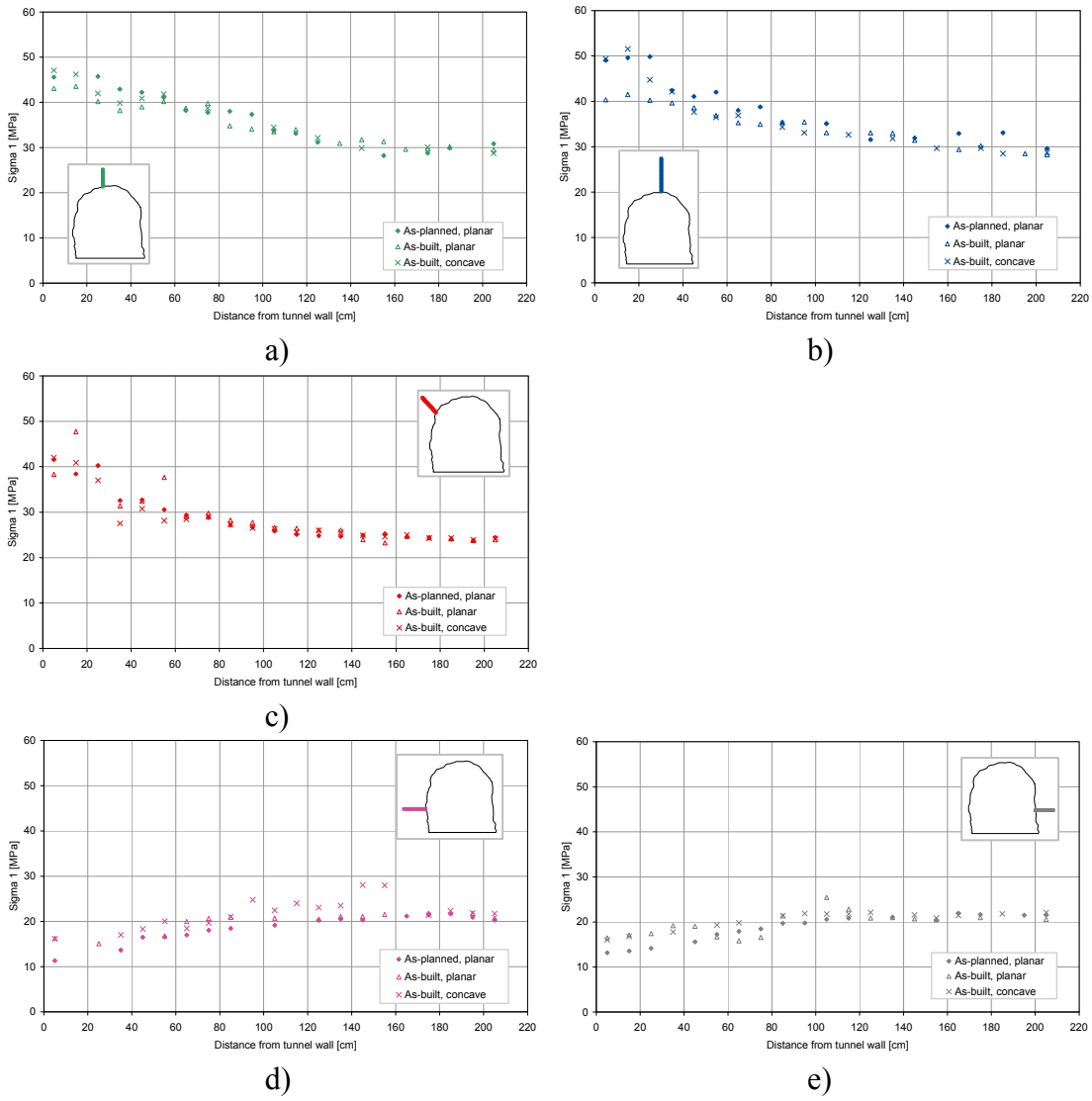

Figure K-5. *Plots of major principal stress scanlines showing the difference between the model with as-planned tunnel shape with planar blasting round faces, the model with as-built tunnel shape with planar blasting round faces and the model with as-built tunnel shape with concave blasting round faces at cross section 48.7 (convergence pins location) in the TASQ tunnel when the heading of section 53 was excavated. The scanlines are approximately at the same place in the tunnel as the boreholes in the BGR section a) left part of the roof (KQ0047H01), b) right part of the roof (KQ0047I01), c) upper left wall (KQ0047A03), d) left wall (KQ0047A02) and e) right wall (KQ0047B02). (E = 65 GPa, sigma 1 = 25 MPa).*

Sigma 3

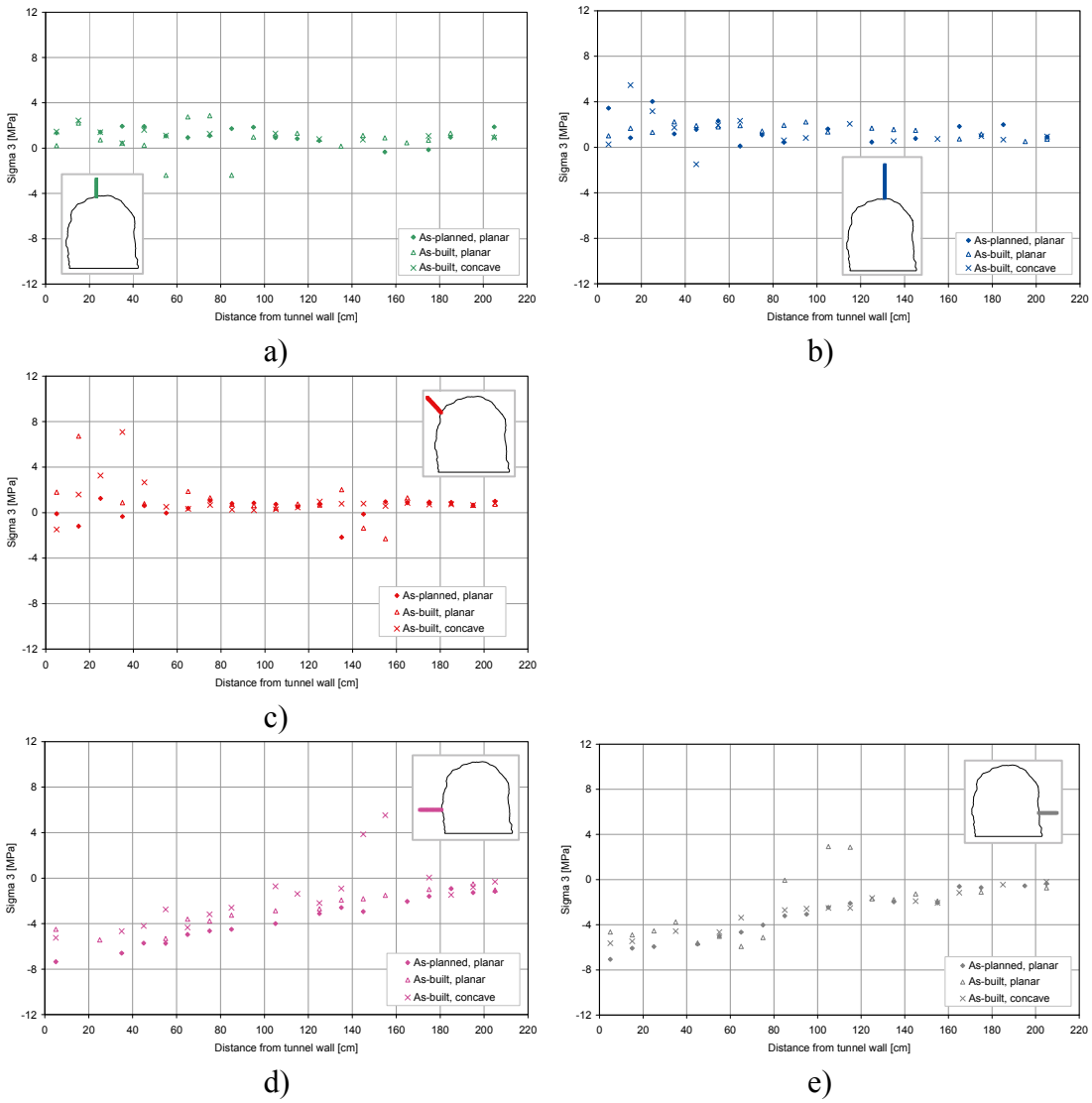

Figure K-6. *Plots of minor principal stress scanlines showing the difference between the model with as-planned tunnel shape with planar blasting round faces, the model with as-built tunnel shape with planar blasting round faces and the model with as-built tunnel shape with concave blasting round faces at cross section 48.7 (convergence pins location) in the TASQ tunnel when the heading of section 53 was excavated. The scanlines are approximately at the same place in the tunnel as the boreholes in the BGR section a) left part of the roof (KQ0047H01), b) right part of the roof (KQ0047I01), c) upper left wall (KQ0047A03), d) left wall (KQ0047A02) and e) right wall (KQ0047B02). (E = 65 GPa, sigma 1 = 25 MPa).*

Section 55

Sigma 1

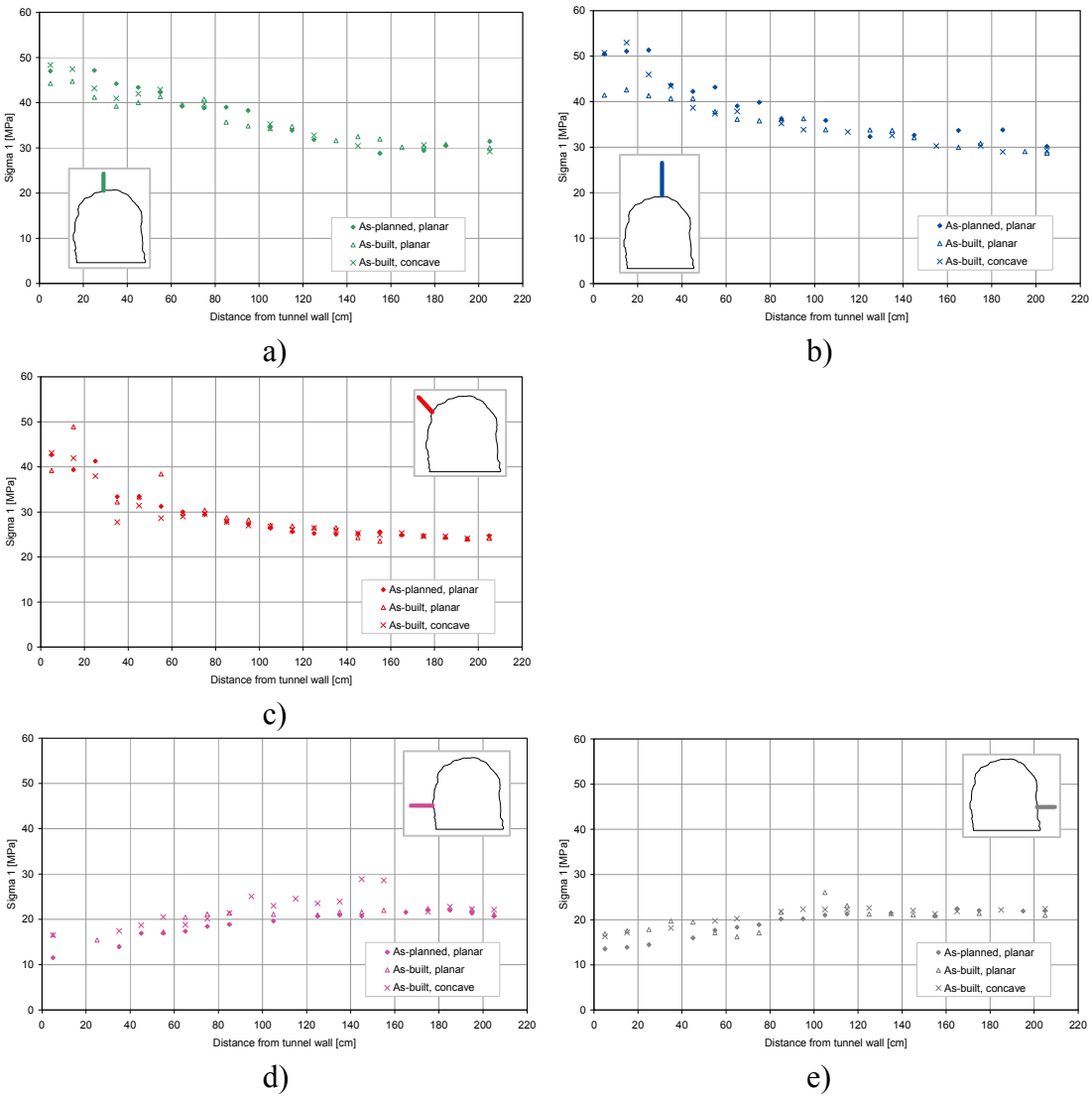

Figure K-7. *Plots of major principal stress scanlines showing the difference between the model with as-planned tunnel shape with planar blasting round faces, the model with as-built tunnel shape with planar blasting round faces and the model with as-built tunnel shape with concave blasting round faces at cross section 48.7 (convergence pins location) in the TASQ tunnel when the heading of section 55 was excavated. The scanlines are approximately at the same place in the tunnel as the boreholes in the BGR section a) left part of the roof (KQ0047H01), b) right part of the roof (KQ0047I01), c) upper left wall (KQ0047A03), d) left wall (KQ0047A02) and e) right wall (KQ0047B02). (E = 65 GPa, sigma 1 = 25 MPa).*

Sigma 3

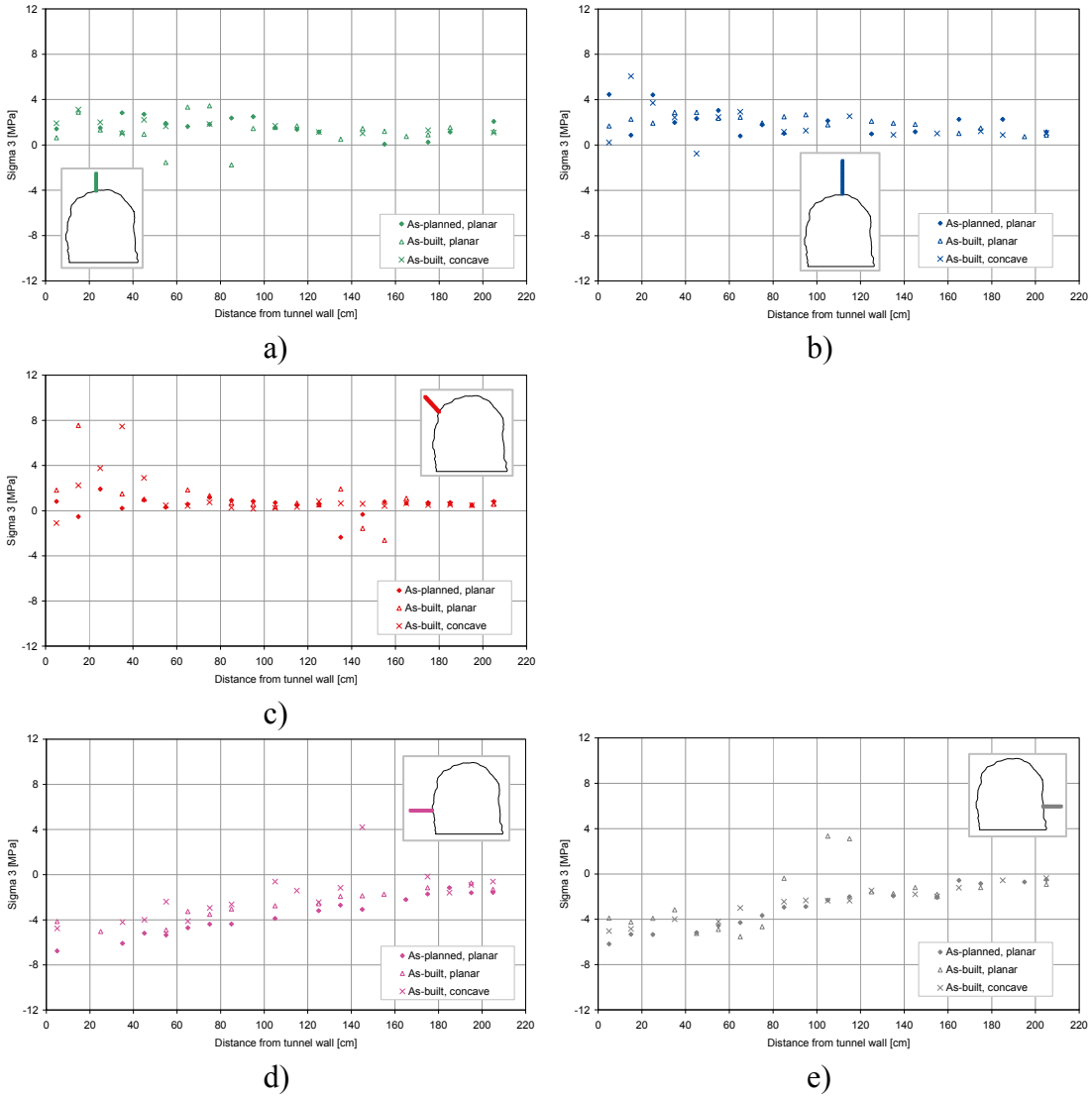

Figure K-8. *Plots of minor principal stress scanlines showing the difference between the model with as-planned tunnel shape with planar blasting round faces, the model with as-built tunnel shape with planar blasting round faces and the model with as-built tunnel shape with concave blasting round faces at cross section 48.7 (convergence pins location) in the TASQ tunnel when the heading of section 55 was excavated. The scanlines are approximately at the same place in the tunnel as the boreholes in the BGR section a) left part of the roof (KQ0047H01), b) right part of the roof (KQ0047I01), c) upper left wall (KQ0047A03), d) left wall (KQ0047A02) and e) right wall (KQ0047B02). (E = 65 GPa, sigma 1 = 25 MPa).*

Section 59

Sigma 1

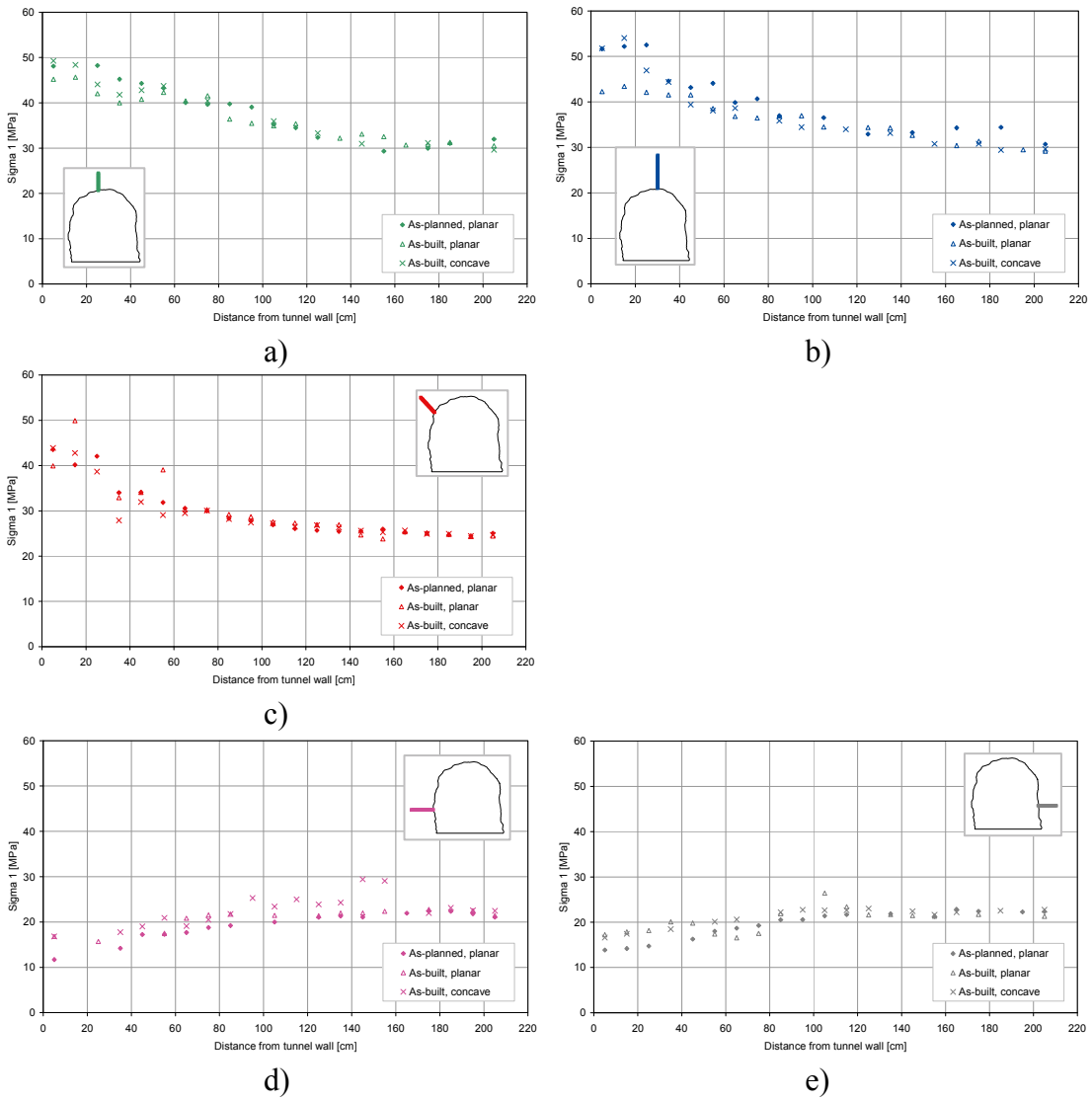

Figure K-9. *Plots of major principal stress scanlines showing the difference between the model with as-planned tunnel shape with planar blasting round faces, the model with as-built tunnel shape with planar blasting round faces and the model with as-built tunnel shape with concave blasting round faces at cross section 48.7 (convergence pins location) in the TASQ tunnel when the heading of section 59 was excavated. The scanlines are approximately at the same place in the tunnel as the boreholes in the BGR section a) left part of the roof (KQ0047H01), b) right part of the roof (KQ0047I01), c) upper left wall (KQ0047A03), d) left wall (KQ0047A02) and e) right wall (KQ0047B02). (E = 65 GPa, sigma 1 = 25 MPa).*

Sigma 3

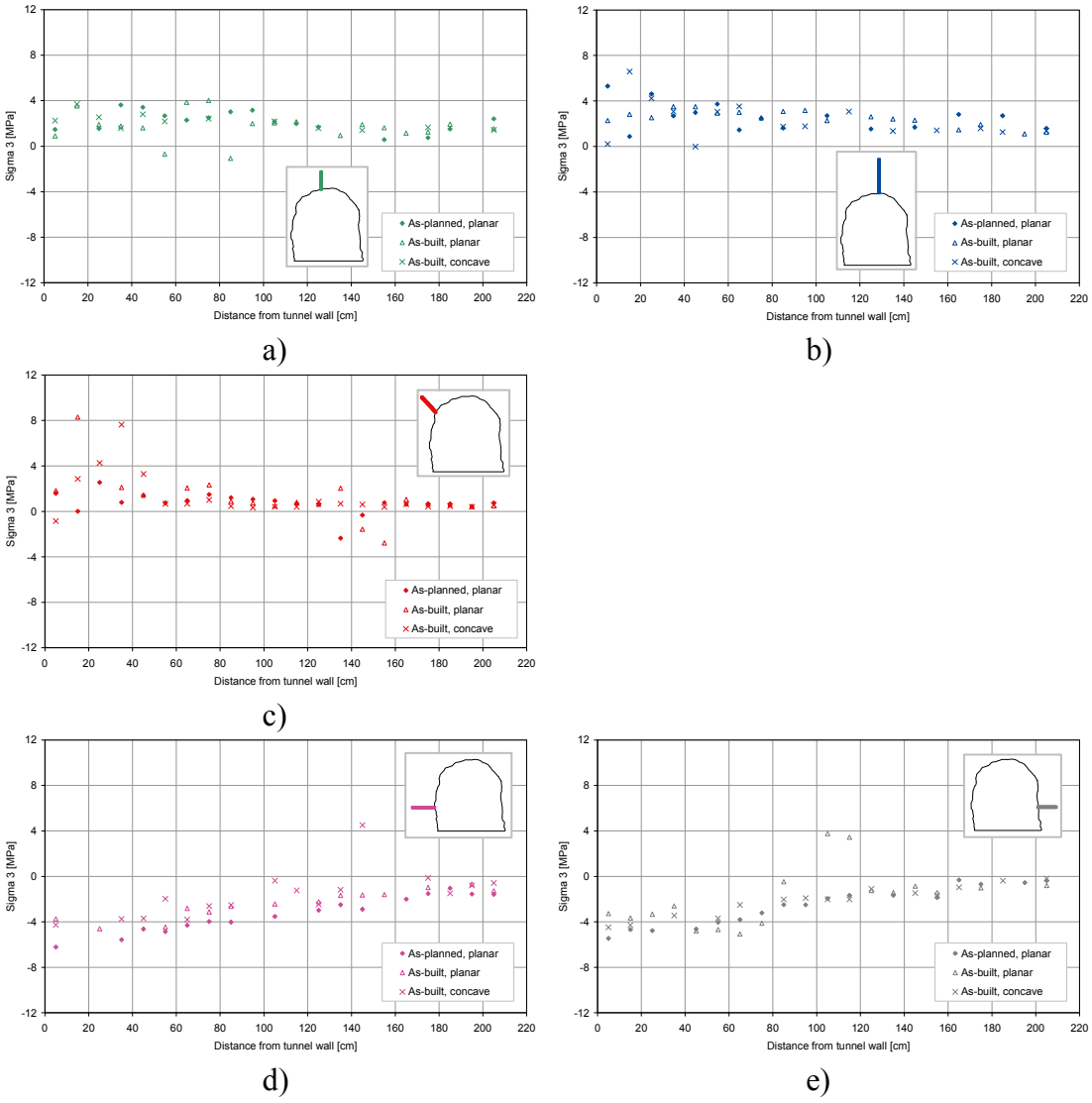

Figure K-10. *Plots of minor principal stress scanlines showing the difference between the model with as-planned tunnel shape with planar blasting round faces, the model with as-built tunnel shape with planar blasting round faces and the model with as-built tunnel shape with concave blasting round faces at cross section 48.7 (convergence pins location) in the TASQ tunnel when the heading of section 59 was excavated. The scanlines are approximately at the same place in the tunnel as the boreholes in the BGR section a) left part of the roof (KQ0047H01), b) right part of the roof (KQ0047I01), c) upper left wall (KQ0047A03), d) left wall (KQ0047A02) and e) right wall (KQ0047B02). (E = 65 GPa, sigma 1 = 25 MPa).*

Appendix L

Stress scanlines in UDEC models

Scanlines of σ_1 and σ_2 along the boreholes used for the ultrasonic measurements in tunnel section 47 (boreholes KQ0047H01, KQ0047I01, KQ0047A03, KQ0047A02, KQ0047B02, KQ0047A01, KQ0047B01 and KQ0047G01 see Figure L-1 and Figure L-4). An additional stress scanline has been obtained in the right side of the floor (see Figure L-4).

Also shown in these Figures are stress scanlines in the approximate same locations as the ones used in tunnel section 47, but for tunnel section 48 (outside the slot) and section 48.7 (convergence measurements pins). These models used the best resolution tunnel shape according to the laser scanning data (as-built tunnel shape in UDEC, see Figure 9-22 to Figure 9-25).

Stress scanlines were also obtained at approximately the same locations from a model with as-planned (ideal) tunnel geometry.

All these simulations used a rock mass Young's modulus of 65 GPa and a magnitude of sigma 1 of 25 MPa.

Comparison between scanlines of major principal stress when the tunnel heading is excavated for the as-built tunnel at section 47 (BGR), section 48 (outside slot), and section 48.7 (convergence pins) and for the as-planned tunnel shape after excavating the heading (UDEC)

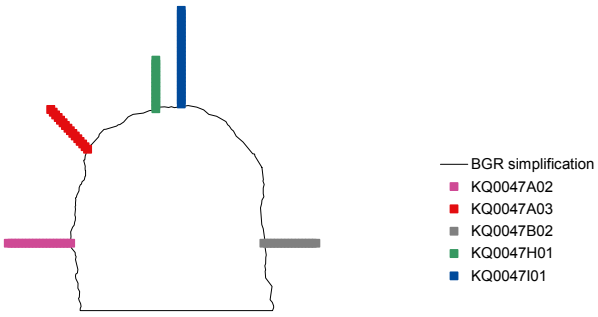

Figure L-1. *A cross section at the BGR section (as-built tunnel), when the heading was excavated, showing the location of the boreholes.*

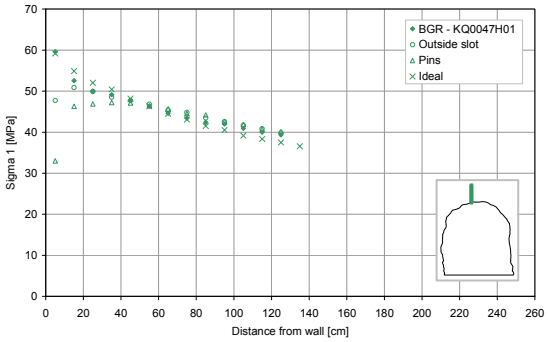

a) KQ0047H01

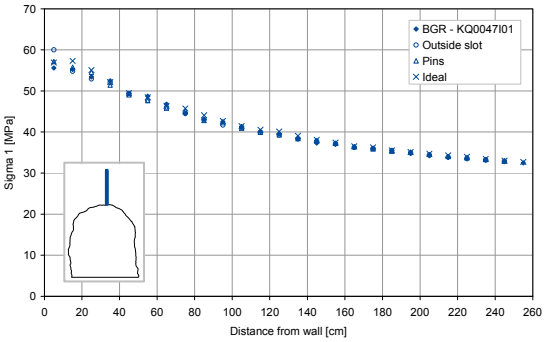

b) KQ0047I01

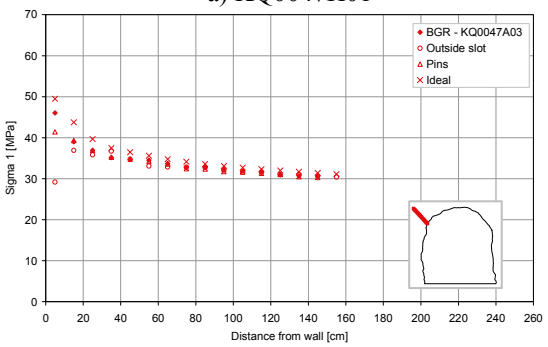

c) KQ0047A03

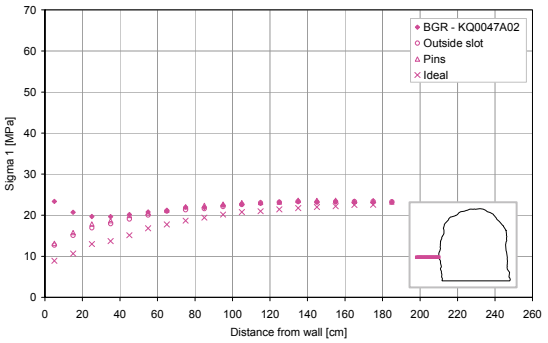

d) KQ0047A02

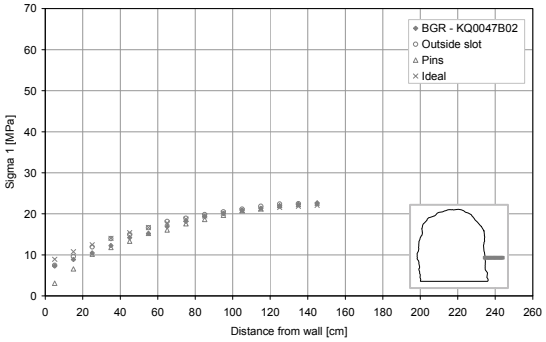

e) KQ0047B02

Figure L-2. *Comparison between scanlines of major principal stress when the tunnel heading is excavated for the as-built tunnel at section 47 (BGR), section 48 (outside slot), and section 48.7 (convergence pins) and for the as-planned tunnel shape. The scanlines are taken in each one of the simulated tunnel sections at the approximate location where the boreholes for the ultrasonic measurements were placed at section 47. Models with E = 65 GPa (see Table 9-11).*

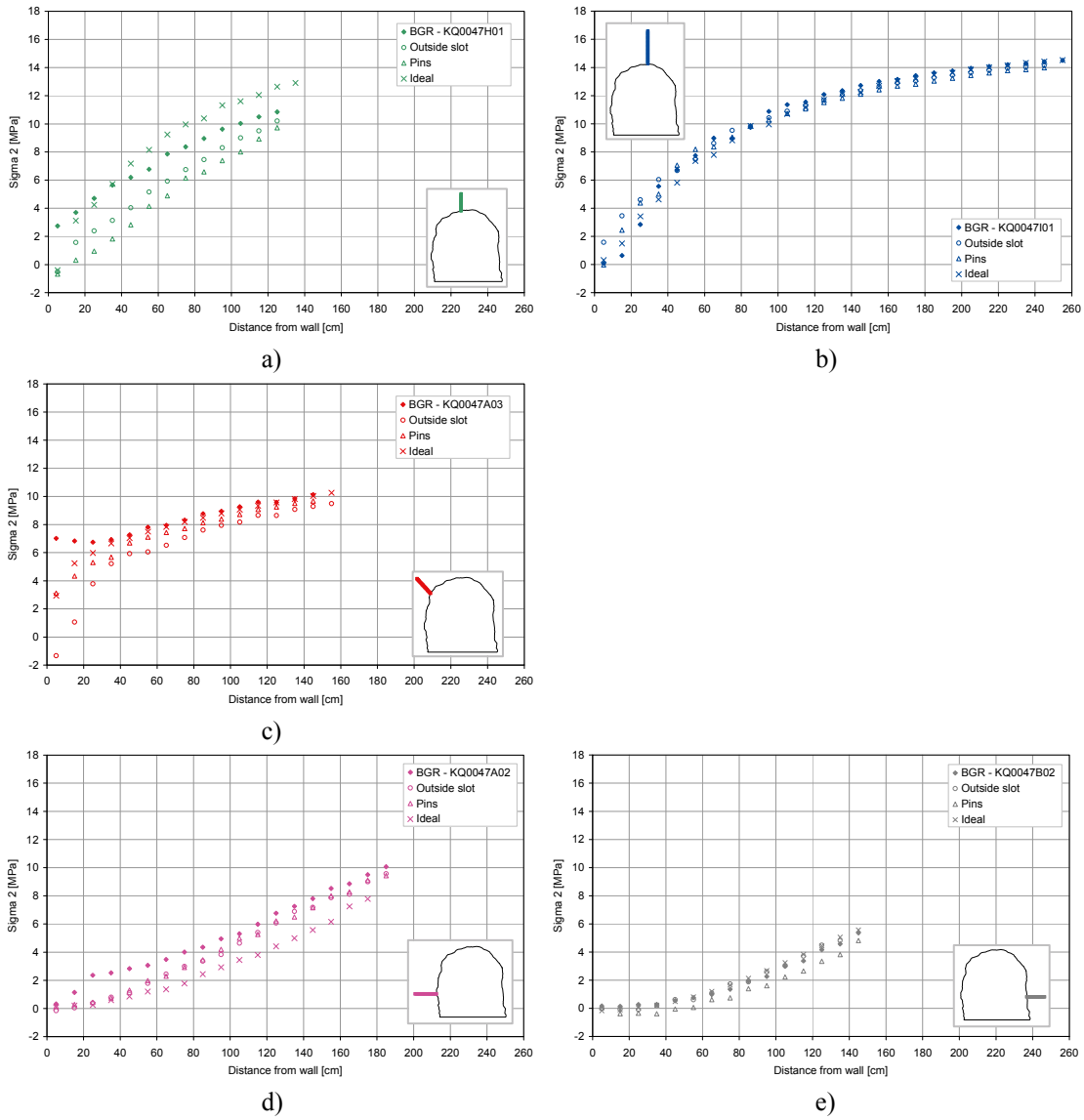

Figure L-3. *Comparison between scanlines of minor principal stress when the tunnel heading is excavated for the as-built tunnel at section 47 (BGR), section 48 (outside slot), and section 48.7 (convergence pins) and for the as-planned tunnel shape. The scanlines are taken in each one of the simulated tunnel sections at the approximate location where the boreholes for the ultrasonic measurements were placed at section 47. Models with E = 65 GPa (see Table 9-11).*

Comparison between scanlines of major principal stress when the tunnel heading is excavated for the as-built tunnel at section 47 (BGR), section 48 (outside slot), and section 48.7 (convergence pins) and for the as-planned tunnel shape after excavating the bench (UDEC)

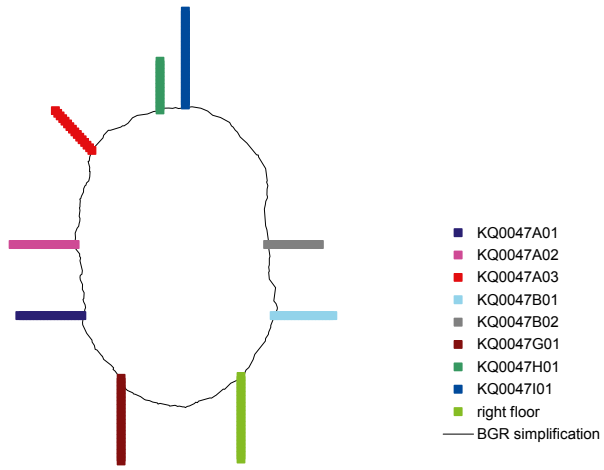

Figure L-4. *A cross section at the BGR section (section 47), when the bench was excavated, showing the location of the boreholes.*

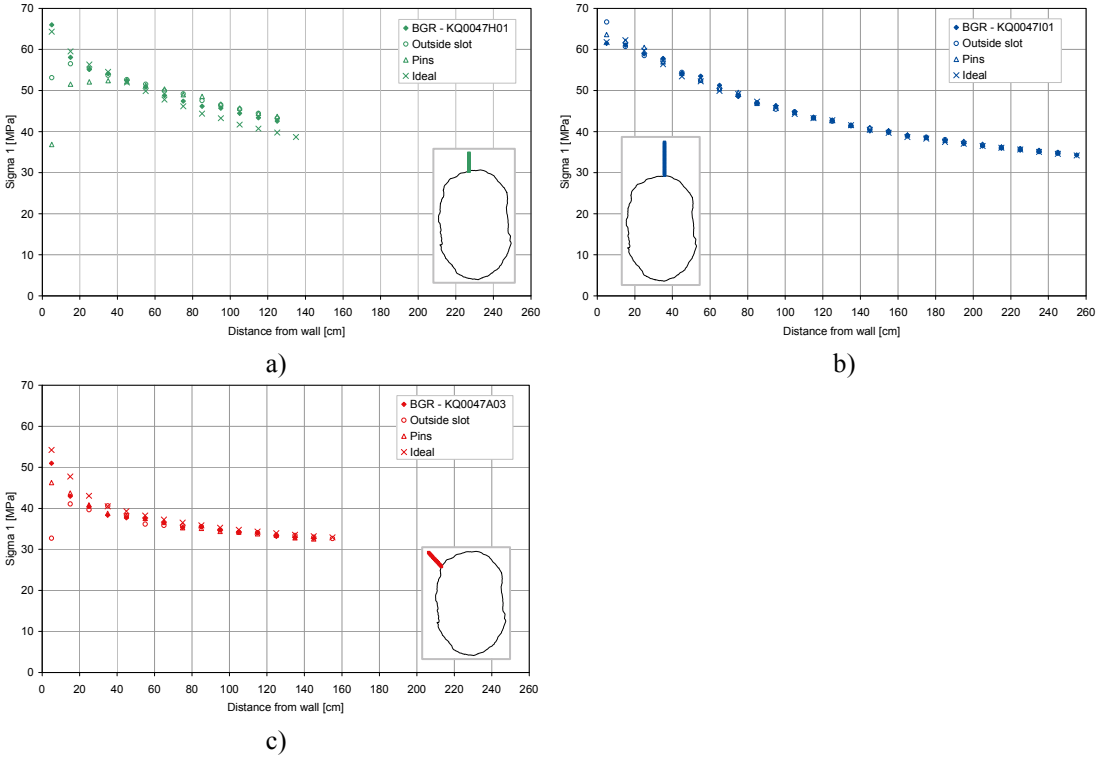

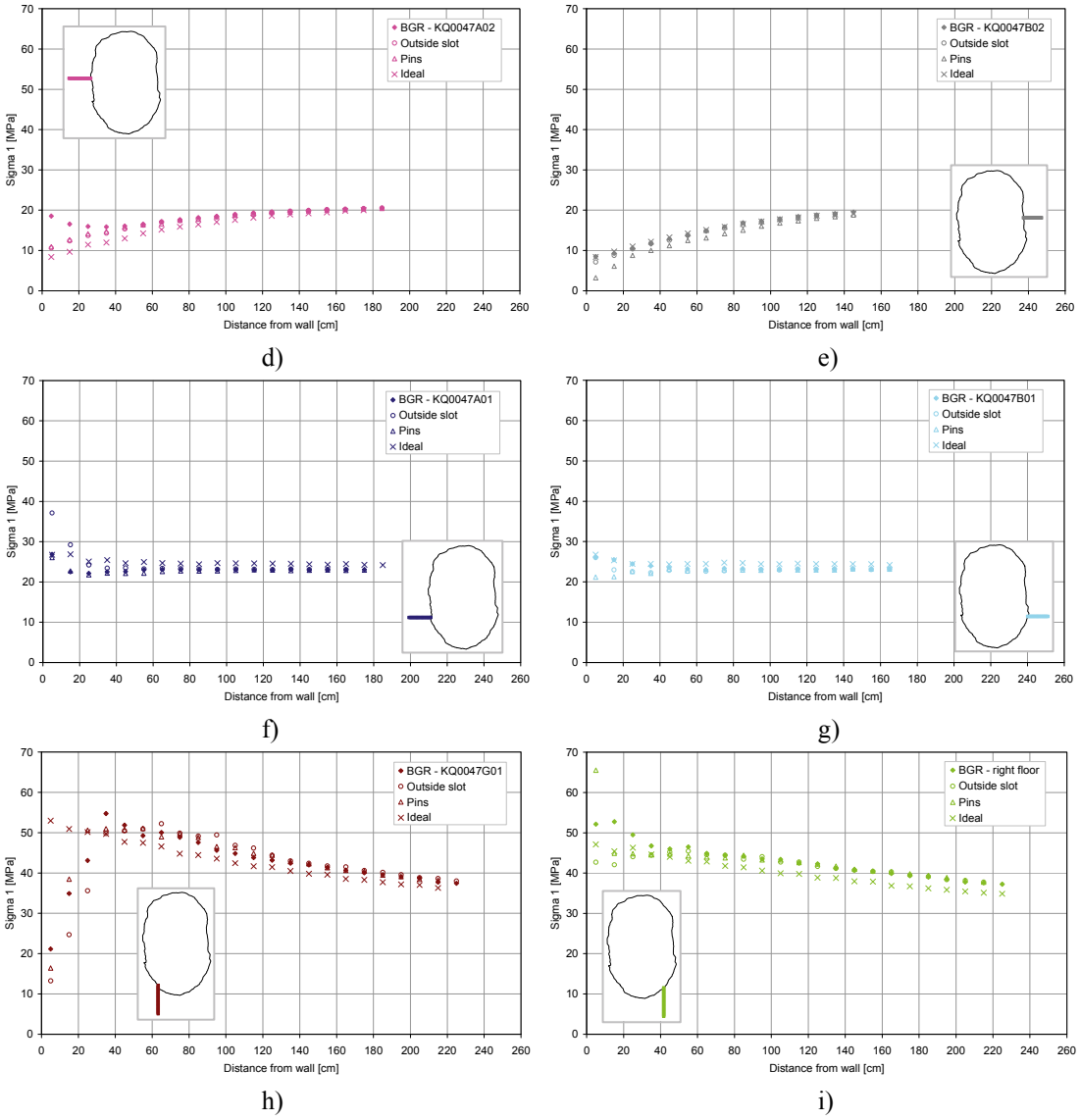

Figure L-5. *Comparison between scanlines of major principal stress when the tunnel bench is excavated for the as-built tunnel at section 47 (BGR), section 48 (outside slot), and section 48.7 (convergence pins) and for the as-planned tunnel shape. The scanlines are taken in each one of the simulated tunnel sections at the approximate location where the boreholes for the ultrasonic measurements were placed at section 47. Models with E = 65 GPa (see Table 9-11).*

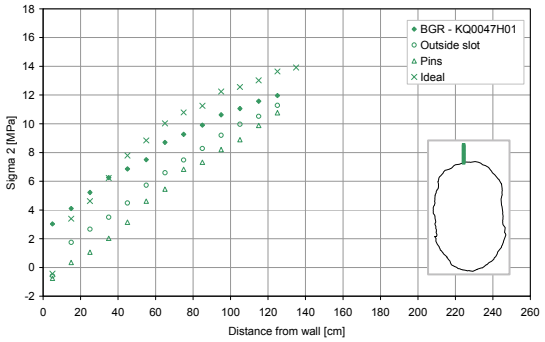
BGR - KQ0047H01
Outside slot
Pins
Ideal
Sigma 2 [MPa]
Distance from wall [cm]

a)

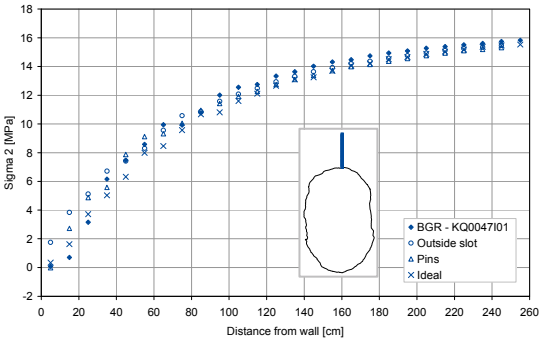
BGR - KQ0047I01
Outside slot
Pins
Ideal
Sigma 2 [MPa]
Distance from wall [cm]

b)

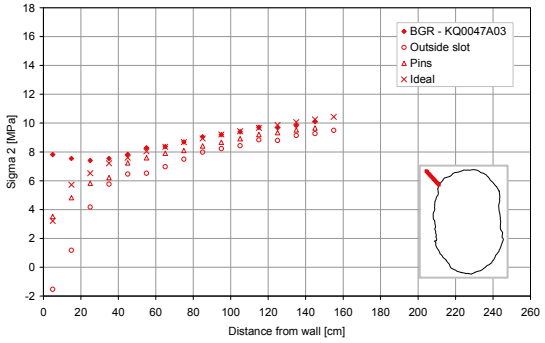
BGR - KQ0047A03
Outside slot
Pins
Ideal
Sigma 2 [MPa]
Distance from wall [cm]

c)

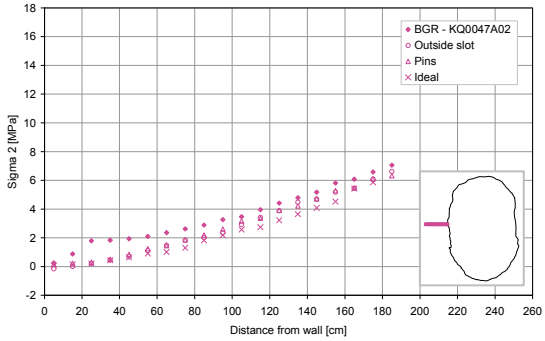
BGR - KQ0047A02
Outside slot
Pins
Ideal
Sigma 2 [MPa]
Distance from wall [cm]

d)

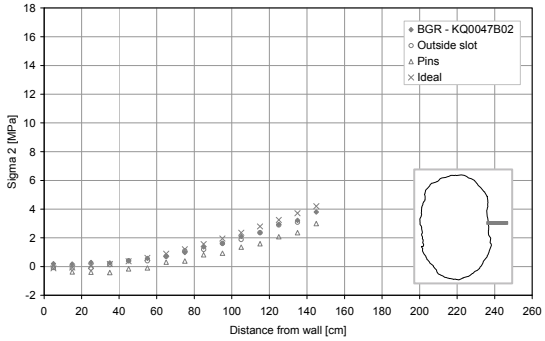
BGR - KQ0047B02
Outside slot
Pins
Ideal
Sigma 2 [MPa]
Distance from wall [cm]

e)

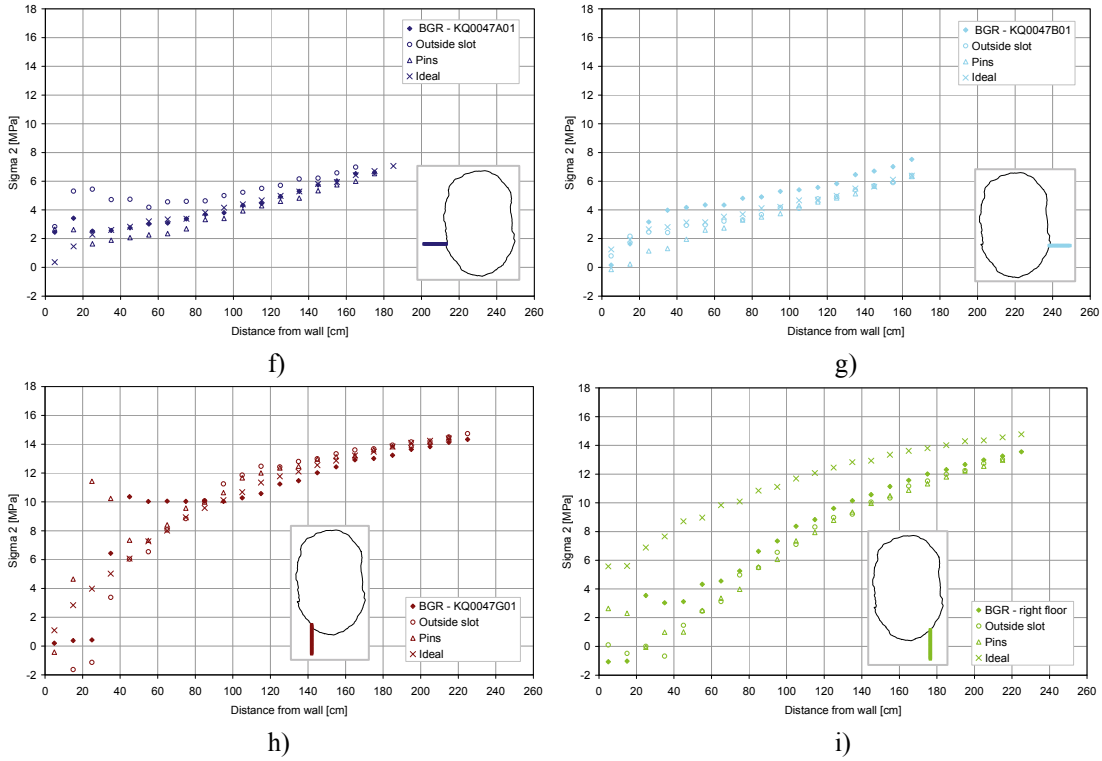

Figure L-6. *Comparison between scanlines of minor principal stress when the tunnel bench is excavated for the as-built tunnel at section 47 (BGR), section 48 (outside slot), and section 48.7 (convergence pins) and for the as-planned tunnel shape. The scanlines are taken in each one of the simulated tunnel sections at the approximate location where the boreholes for the ultrasonic measurements were placed at section 47. Models with E = 65 GPa (see Table 9-11).*

Appendix M

Two-dimensional UDEC models of the TASQ tunnel

Stress tensor plots showing the redistribution of the stress field after the excavation of the heading and the bench on section 47 (where BGR performed the ultrasonic measurements), section 48 (outside the slot) and section 48.7 (convergence pins) in the as-built tunnel. Stress tensor plots showing the redistribution of the stress field after the excavation of the heading and the bench in an ideal (as-planned) tunnel section are also included.

Stress tensor plots of the TASQ tunnel in 3 different sections (BGR, outside slot and convergence pins) with the as-built tunnel shape and the as-planned tunnel shape case after excavating the heading (E = 45 GPa, σ_1 = 30 MPa, σ_1 = 316°).

Ideal tunnel shape

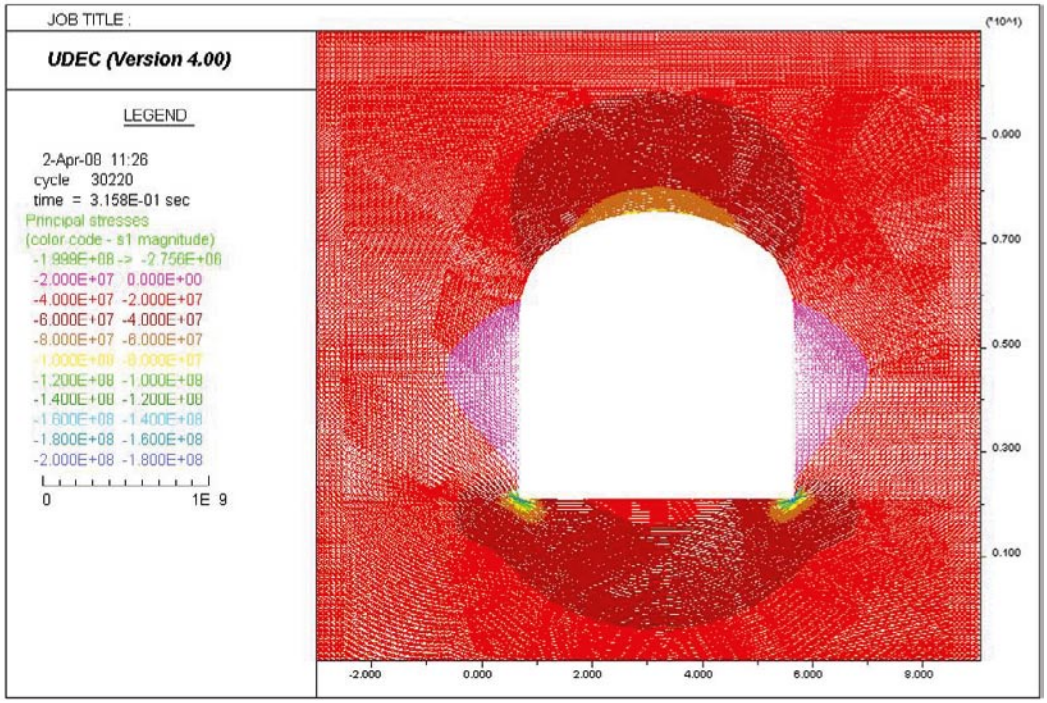

a) Maximum compressive stress = 199.9 MPa

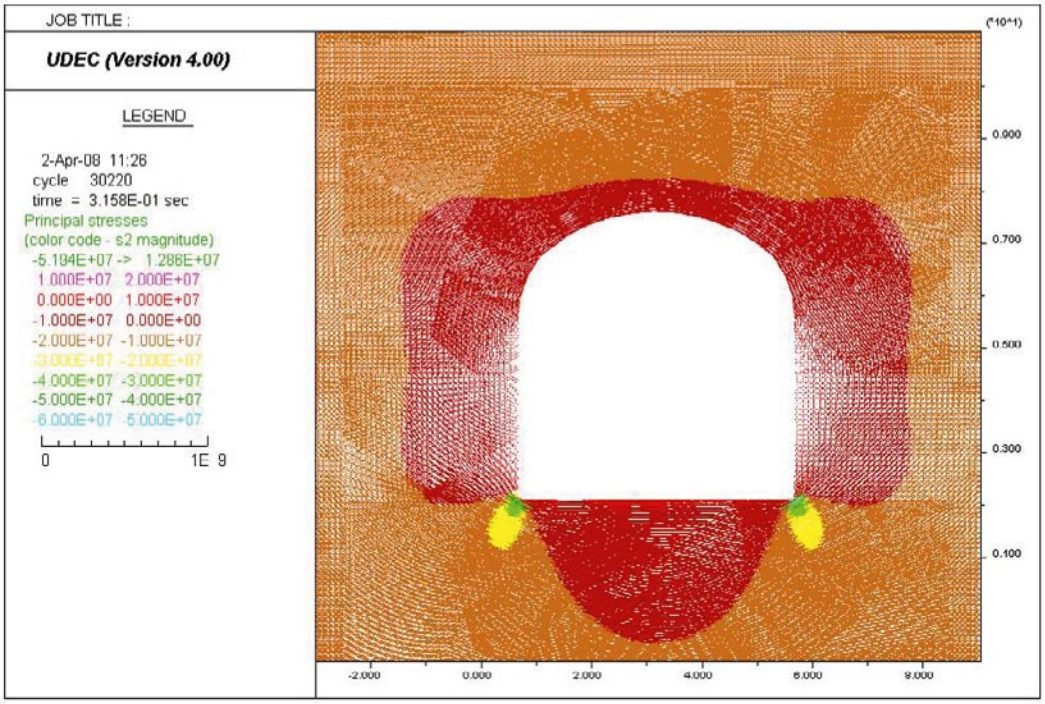

b) Maximum tensile stress = 12.86 MPa

Figure M-1. *Stress tensor plots of the as-planned tunnel shape after excavating the heading; Colors by magnitude of a) Sigma 1 and b) Sigma 2. Model with E = 45 GPa, σ_1 = 30 MPa, σ_1 = 316° (see Table 9-11).*

Ideal tunnel shape

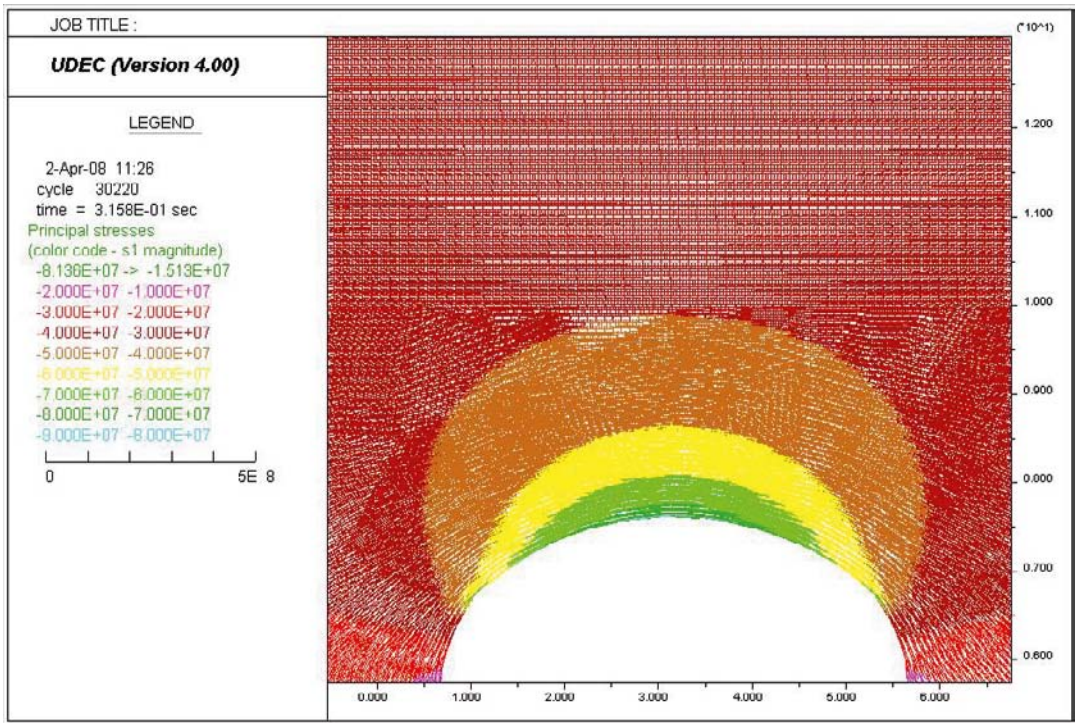

a) Maximum compressive stress = 81.36 MPa

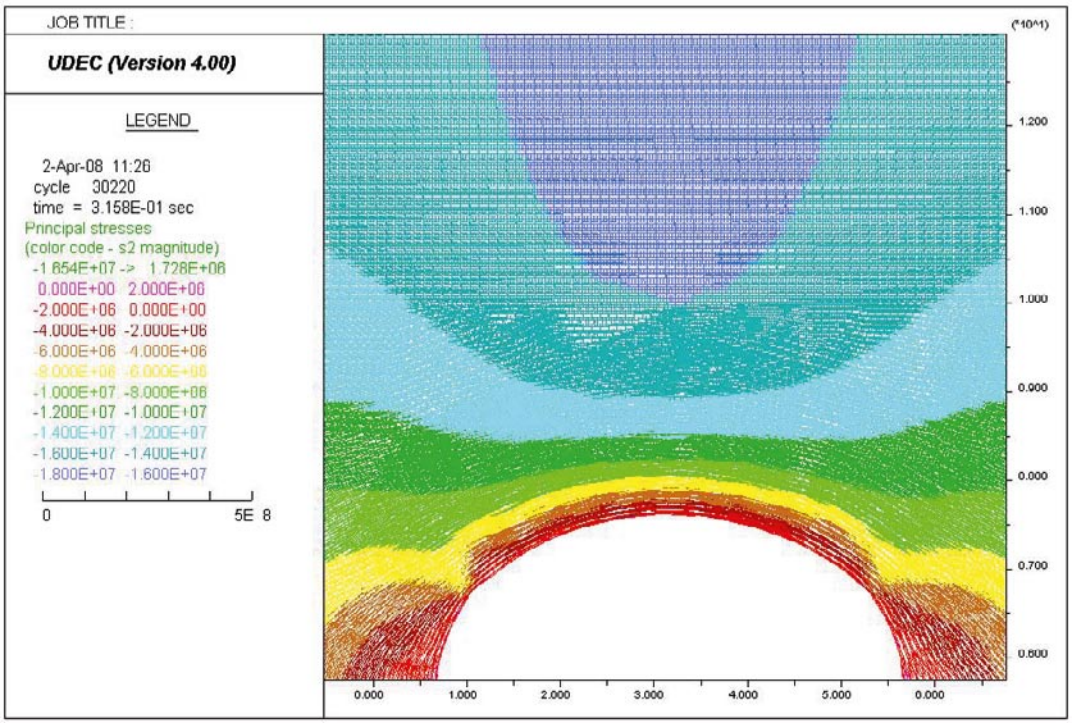

b) Maximum tensile stress = 1.728 MPa

Figure M-2. *Close-up images of the roof. Stress tensor plots of the as-planned tunnel shape after excavating the heading; Colors by magnitude of a) Sigma 1 and b) Sigma 2. Model with E = 45 GPa, σ_1 = 30 MPa, σ_1 = 316° (see Table 9-11).*

Ideal tunnel shape

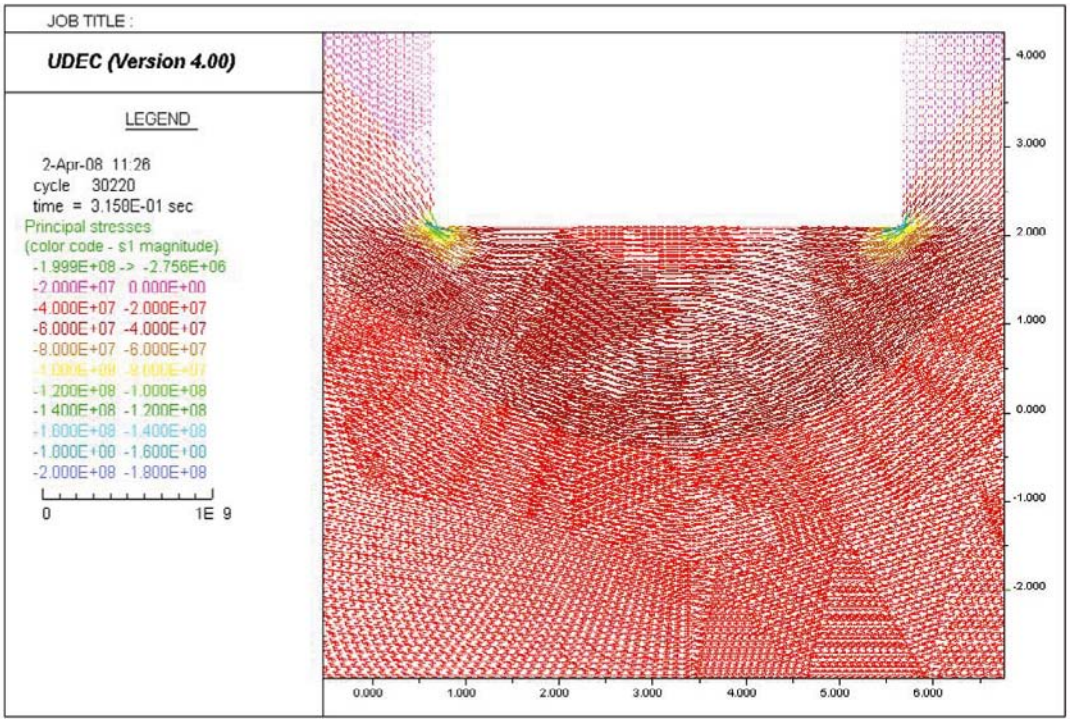

a) Maximum compressive stress = 199.9 MPa

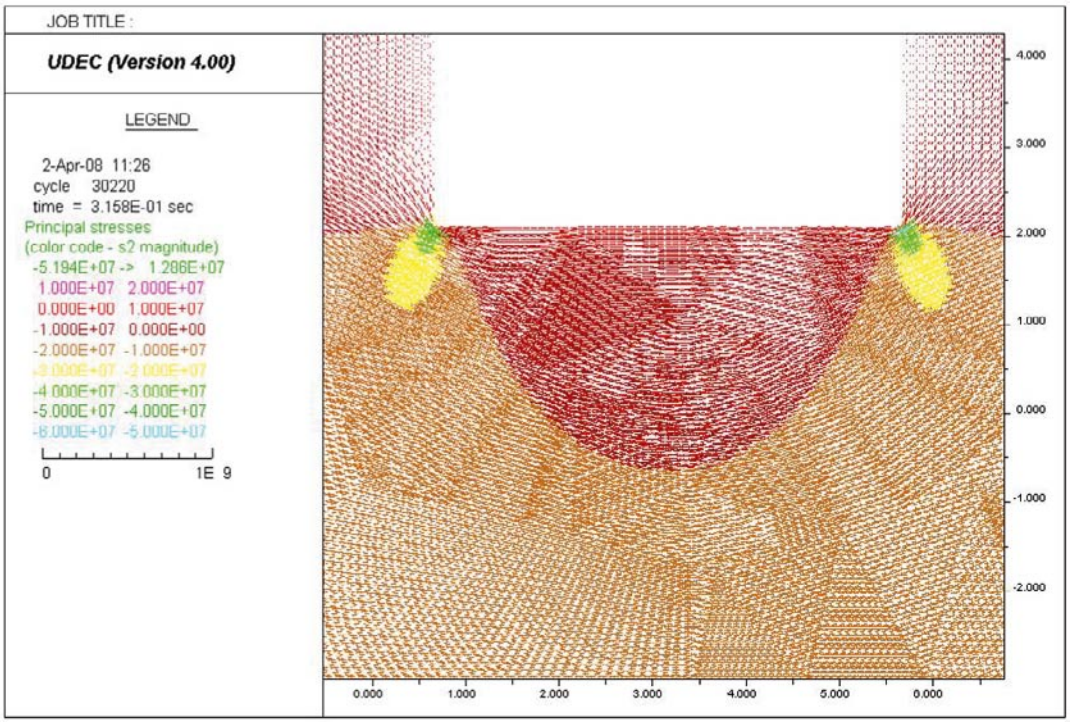

b) Maximum tensile stress = 12.86 MPa

Figure M-3. *Close-up images of the floor. Stress tensor plots of the as-planned tunnel shape after excavating the heading; Colors by magnitude of a) Sigma 1 and b) Sigma 2. Model with E = 45 GPa, σ1 = 30 MPa, σ1 = 316° (see Table 9-11).*

BGR section, as-built tunnel shape

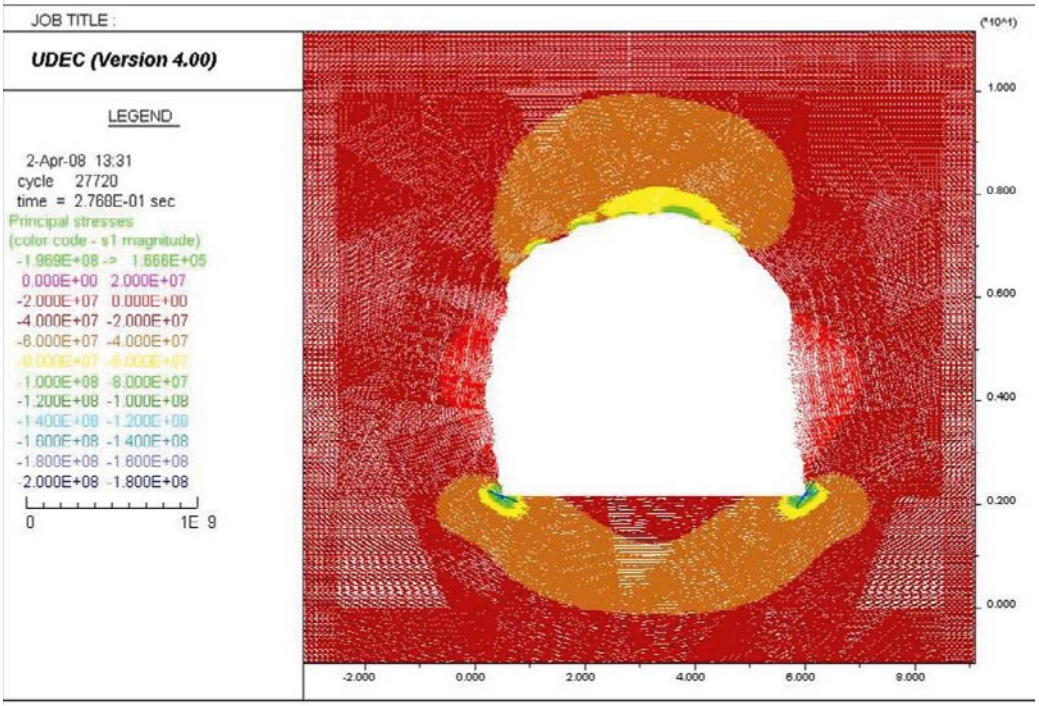

a) Maximum Compressive stress = 196.9 MPa

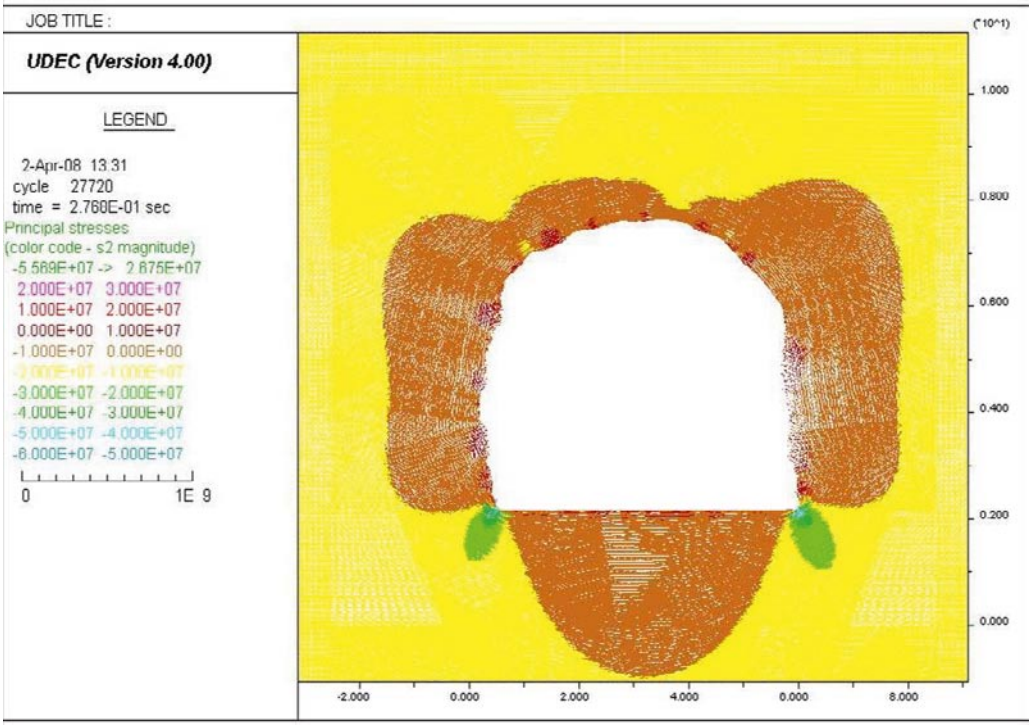

b) Maximum Tensile stress = 26.75 MPa

Figure M-4. *Stress tensor plots at the BGR section after excavating the heading; Colors by magnitude of a) Sigma 1 and b) Sigma 2. Model with E = 45 GPa, σ1 = 30 MPa, σ1 = 316° (see Table 9-11).*

BGR section, as-built tunnel shape

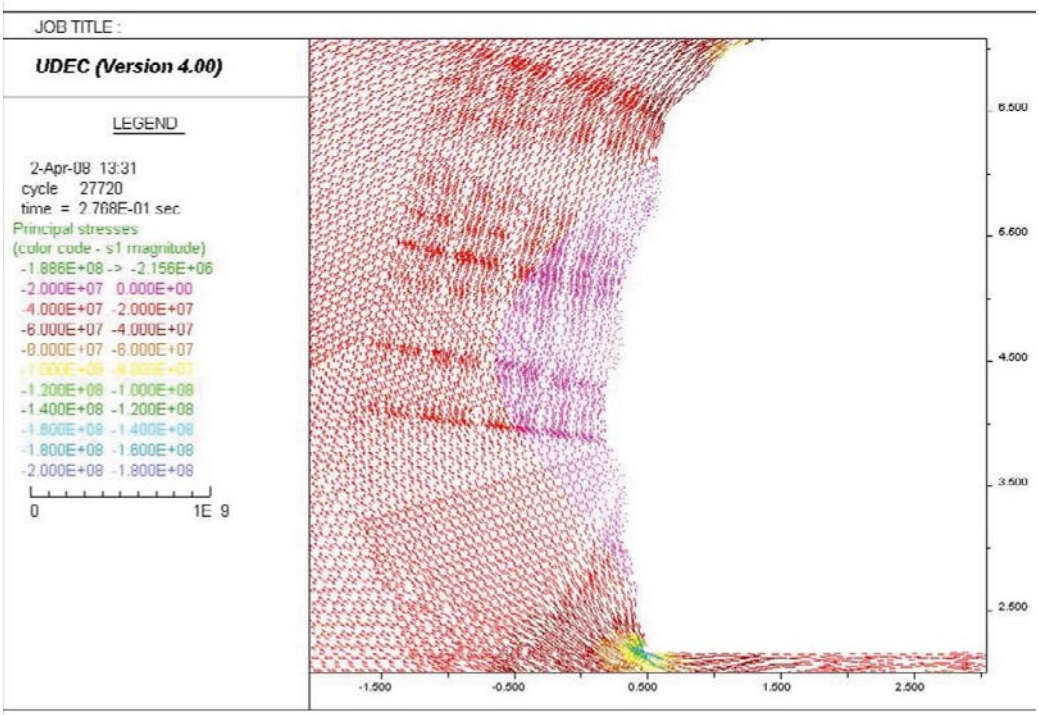

a) Maximum Compressive stress = 188.6 MPa

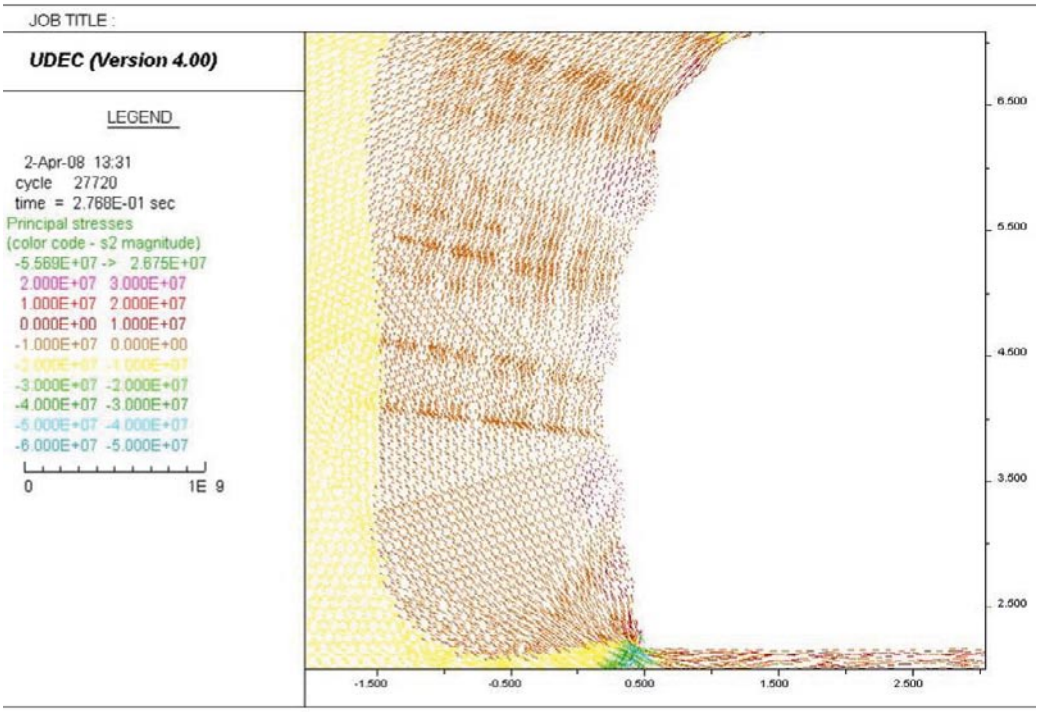

b) Maximum Tensile stress = 26.75 MPa

Figure M-5. *Close-up images of the left side wall. Stress tensor plots at the BGR section after excavating the heading; Colors by magnitude of a) Sigma 1 and b) Sigma 2. Model with E = 45 GPa, σ1 = 30 MPa, σ1 = 316° (see Table 9-11).*

BGR section, as-built tunnel shape

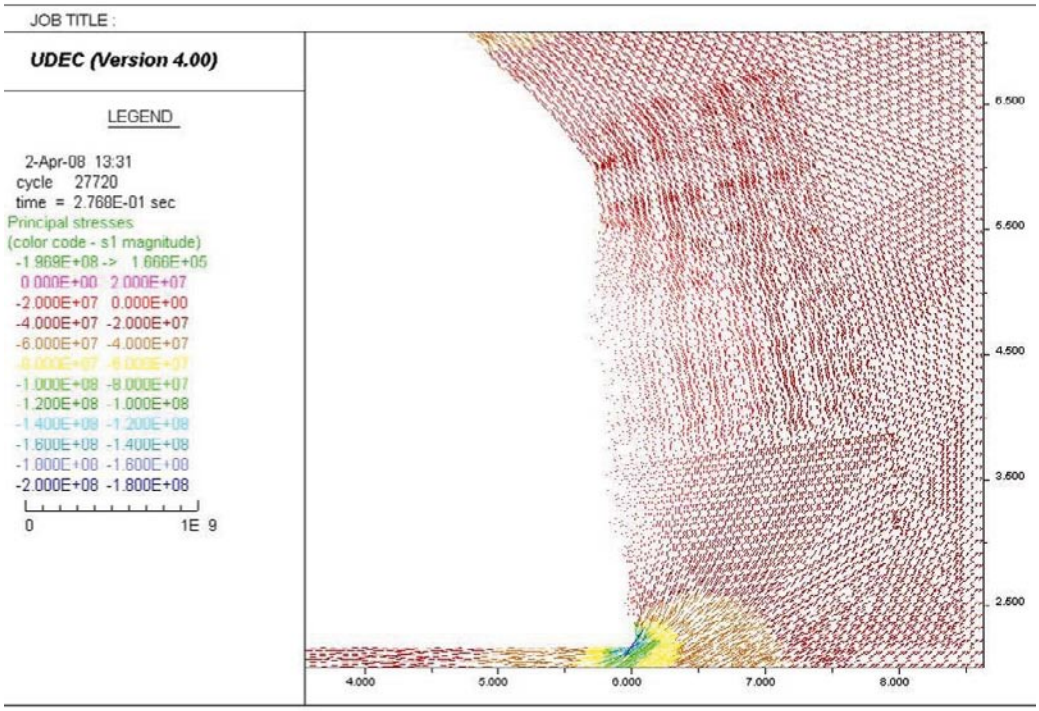

a) Maximum Compressive stress = 196.9 MPa

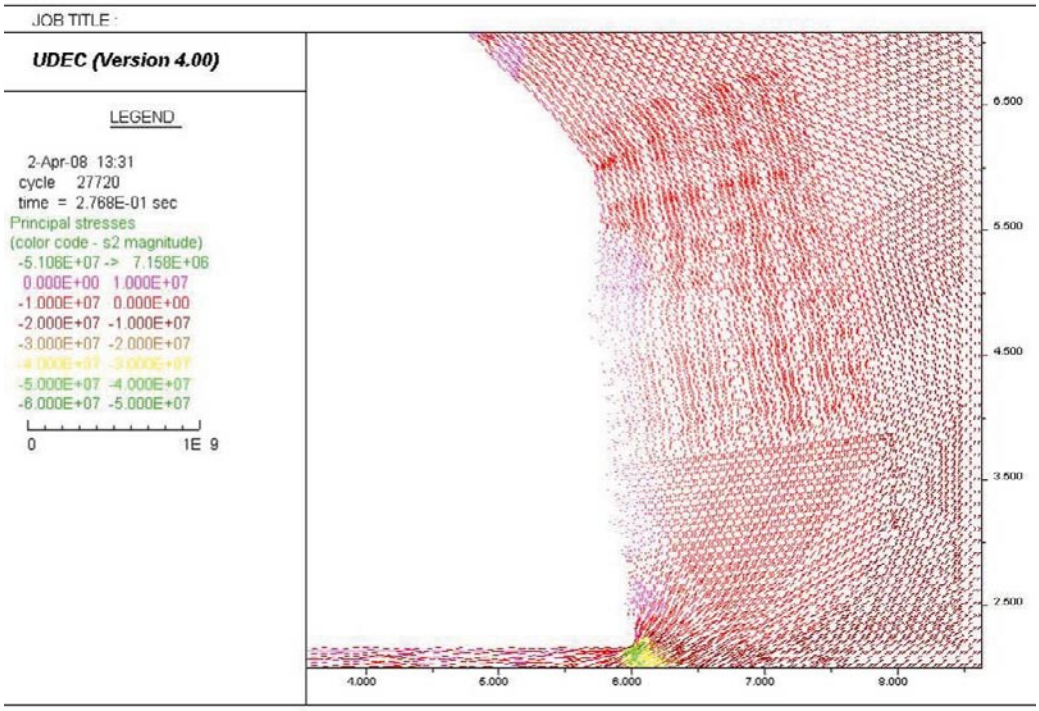

b) Maximum Tensile stress = 7.158 MPa

Figure M-6. *Close-up images of the right side wall. Stress tensor plots at the BGR section after excavating the heading; Colors by magnitude of a) Sigma 1 and b) Sigma 2. Model with E = 45 GPa, σ1 = 30 MPa, σ1 = 316° (see Table 9-11).*

BGR section, as-built tunnel shape

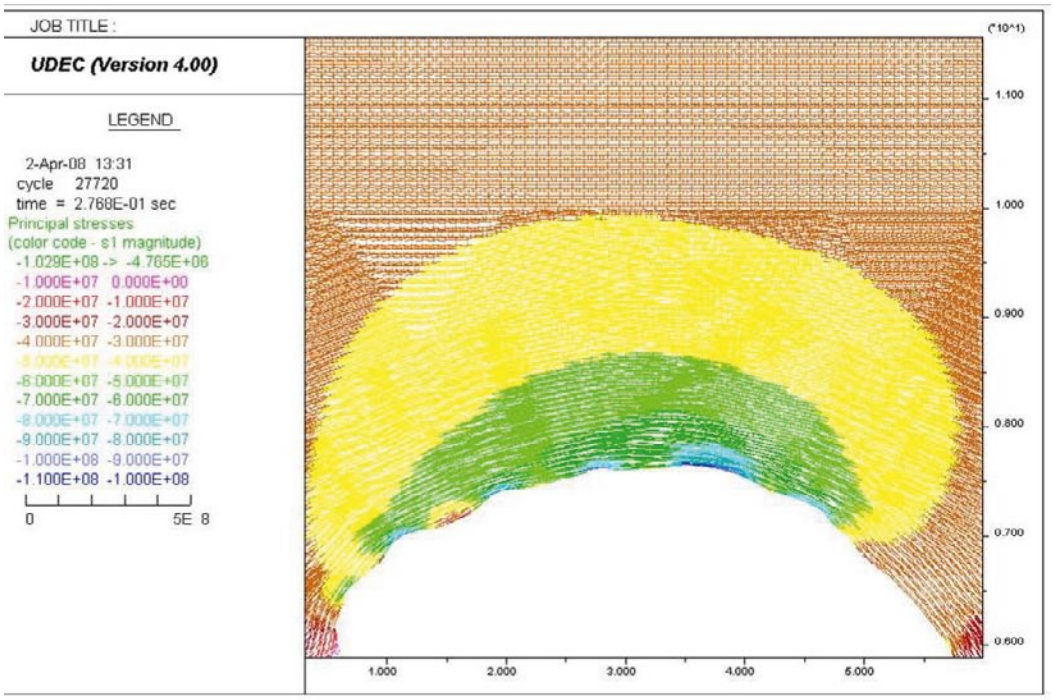

a) Maximum Compressive stress = 102.9 MPa

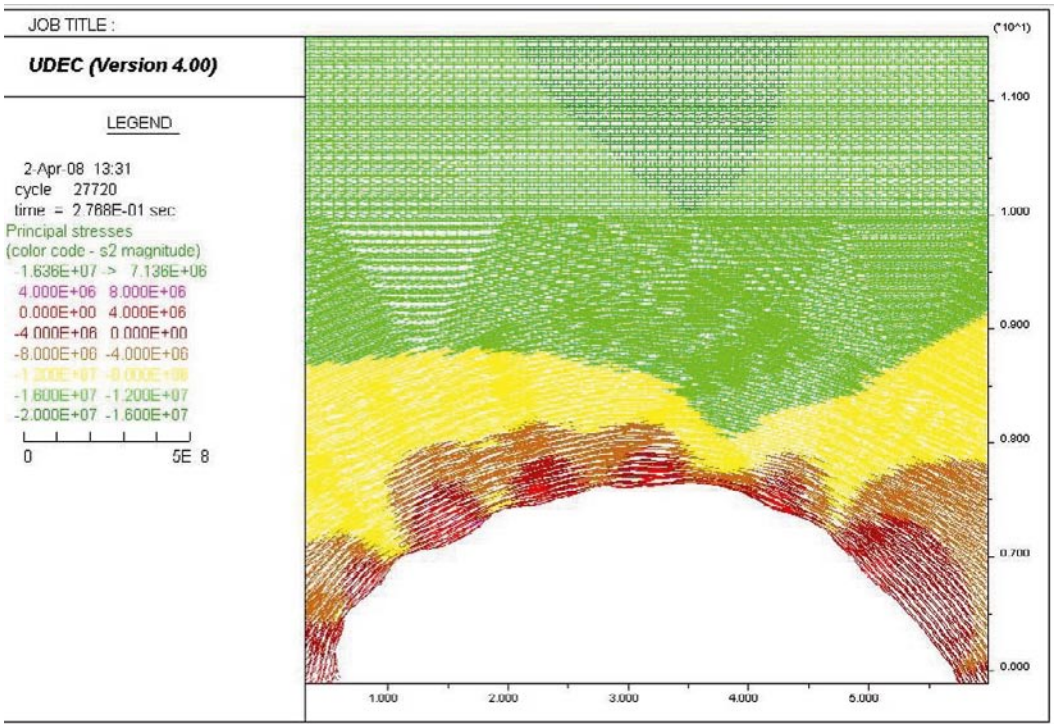

b) Maximum Tensile stress = 7.136 MPa

Figure M-7. *Close-up images of the roof. Stress tensor plots at the BGR section after excavating the heading; Colors by magnitude of a) Sigma 1 and b) Sigma 2. Model with E = 45 GPa, σ1 = 30 MPa, σ1 = 316° (see Table 9-11).*

BGR section, as-built tunnel shape

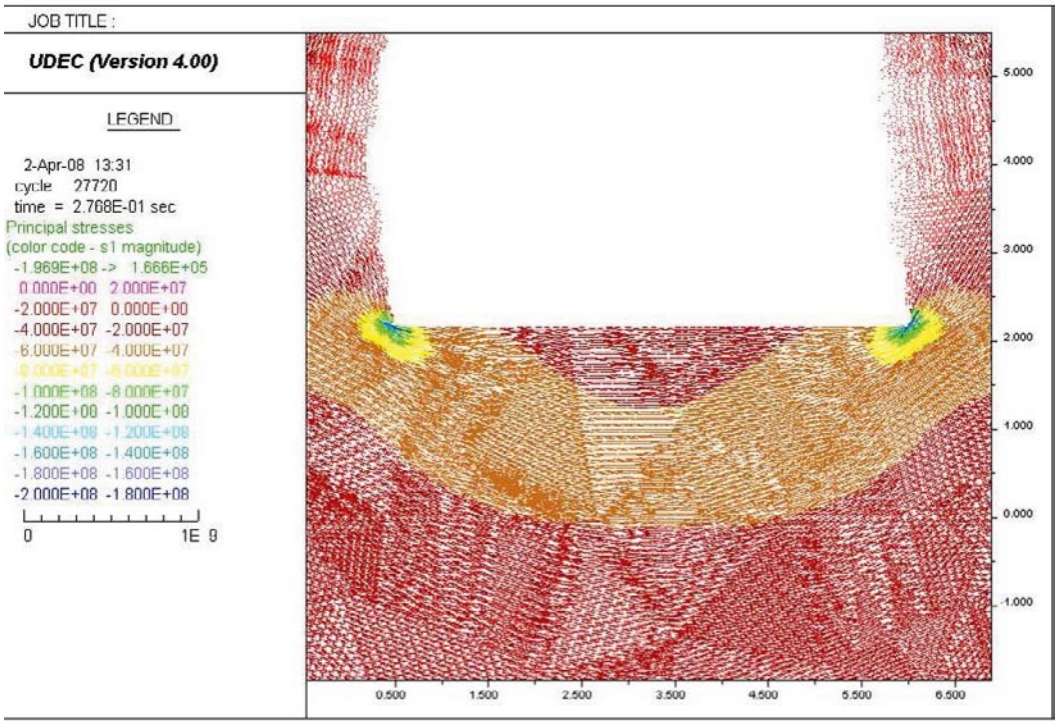

a) Maximum Compressive stress = 196.9 MPa

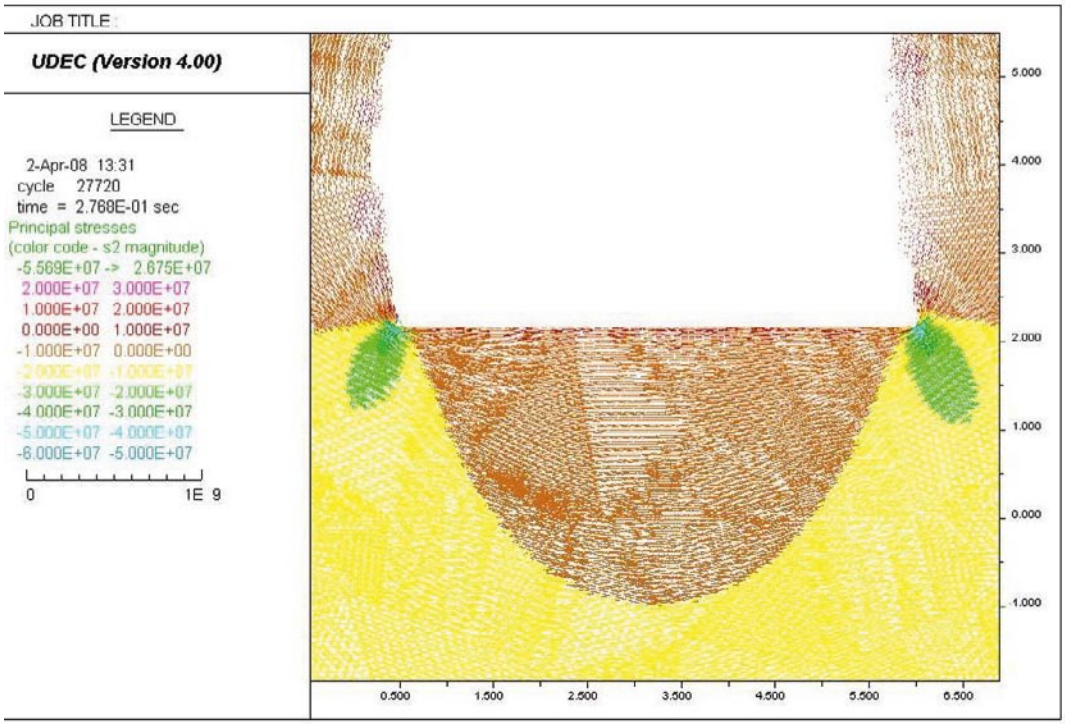

b) Maximum Tensile stress = 26.75 MPa

Figure M-8. *Close-up images of the floor. Stress tensor plots at the BGR section after excavating the heading; Colors by magnitude of a) Sigma 1 and b) Sigma 2. Model with E = 45 GPa, σ1 = 30 MPa, σ1 = 316° (see Table 9-11).*

Outside slot section, as-built tunnel shape

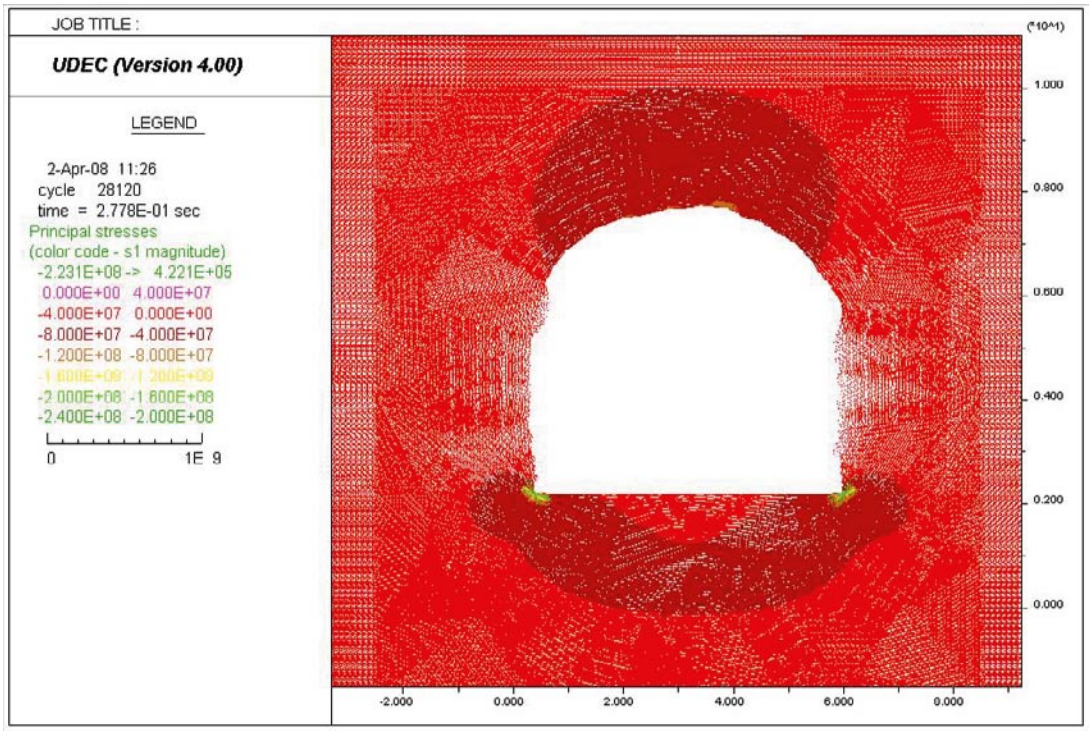

a) Maximum compressive stress = 223.1 MPa

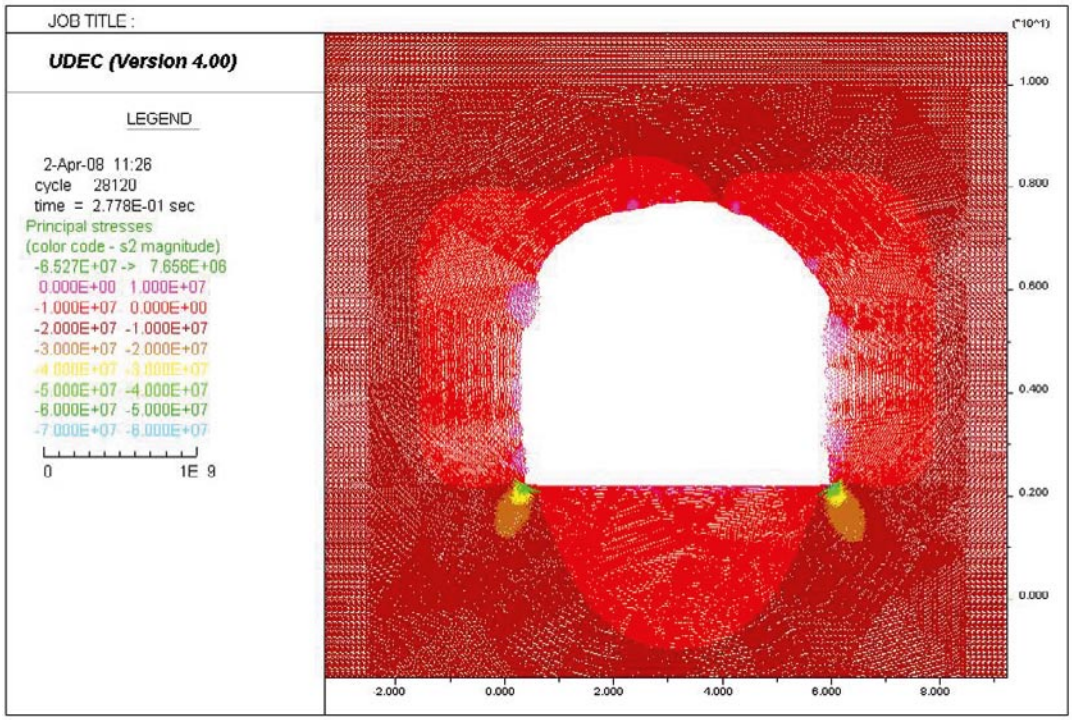

b) Maximum tensile stress = 7.656 MPa

Figure M-9. *Stress tensor plots at a section outside the slot after excavating the heading; Colors by magnitude of a) Sigma 1 and b) Sigma 2. Model with E = 45 GPa, σ1 = 30 MPa, σ1 = 316° (see Table 9-11).*

Outside slot section, as-built tunnel shape

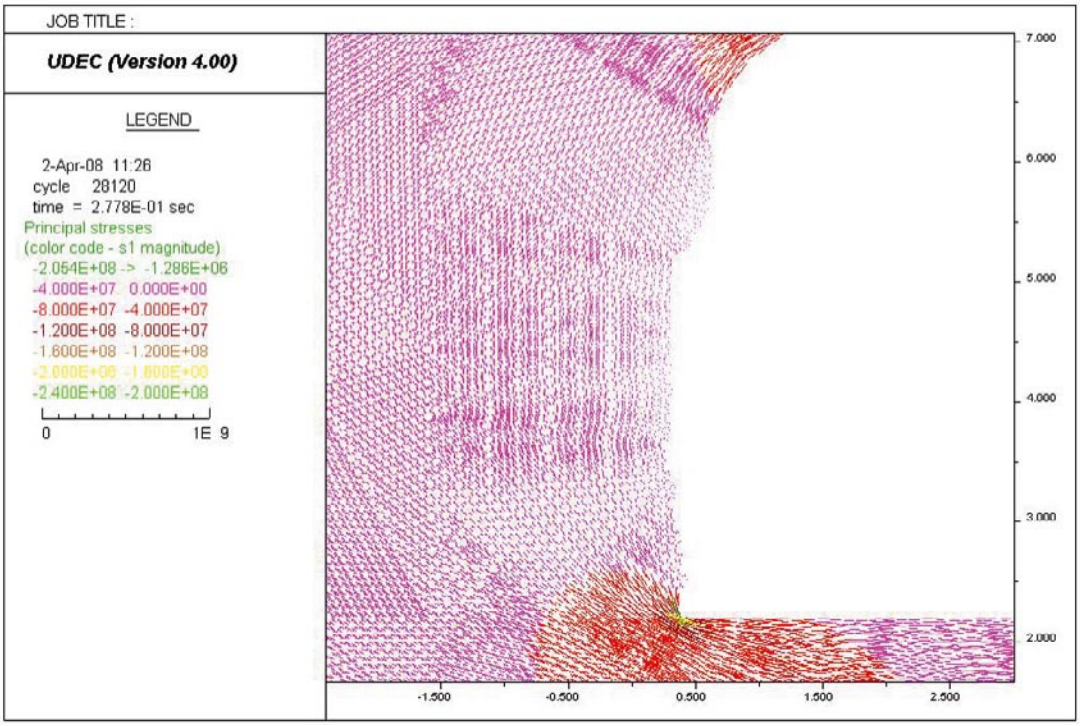

a) Maximum compressive stress = 205.4 MPa

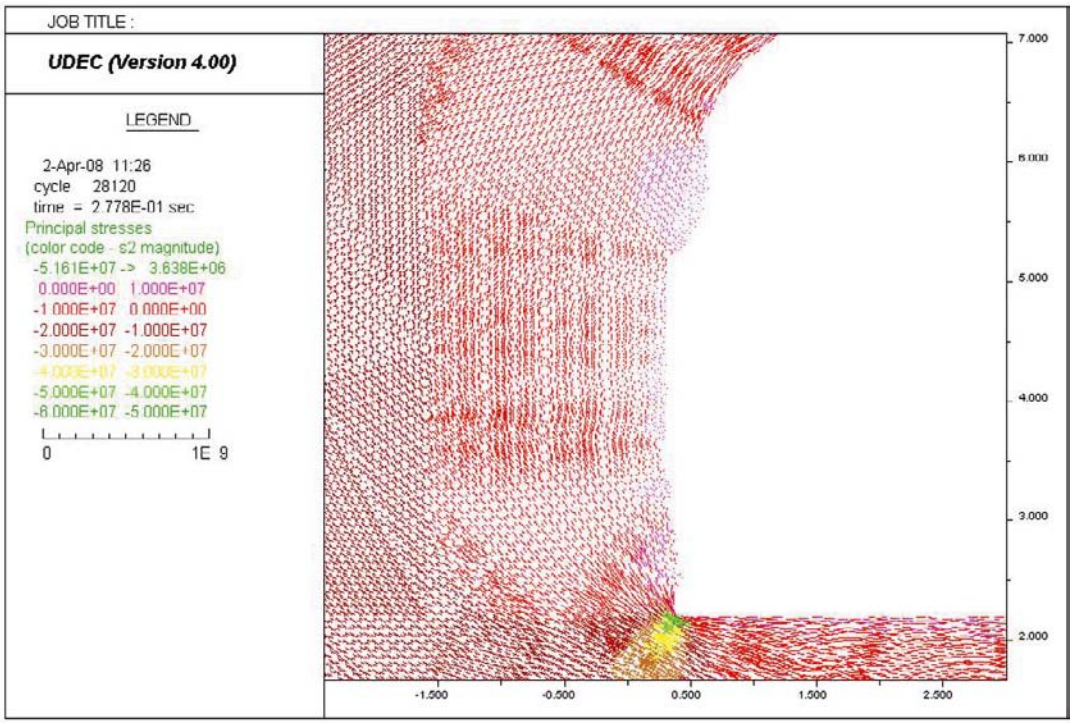

b) Maximum tensile stress = 3.638 MPa

Figure M-10. *Close-up images of the left side wall. Stress tensor plots at a section outside the slot after excavating the heading; Colors by magnitude of a) Sigma 1 and b) Sigma 2. Model with E = 45 GPa, σ1 = 30 MPa, σ1 = 316° (see Table 9-11).*

Outside slot section, as-built tunnel shape

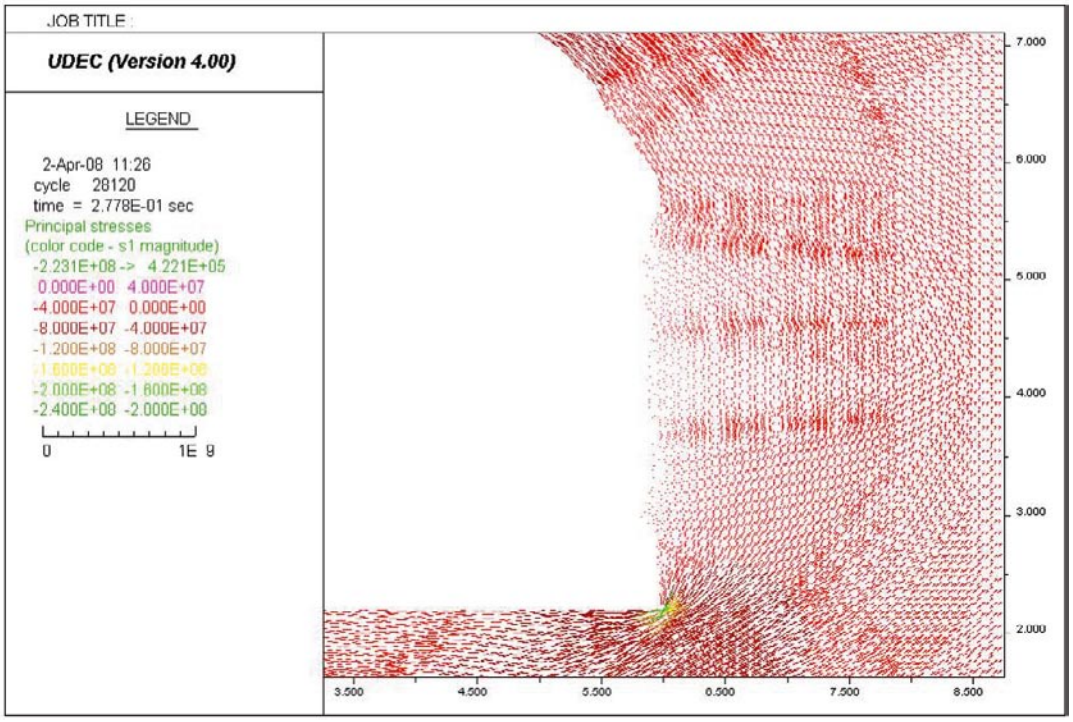

a) Maximum compressive stress = 223.1 MPa

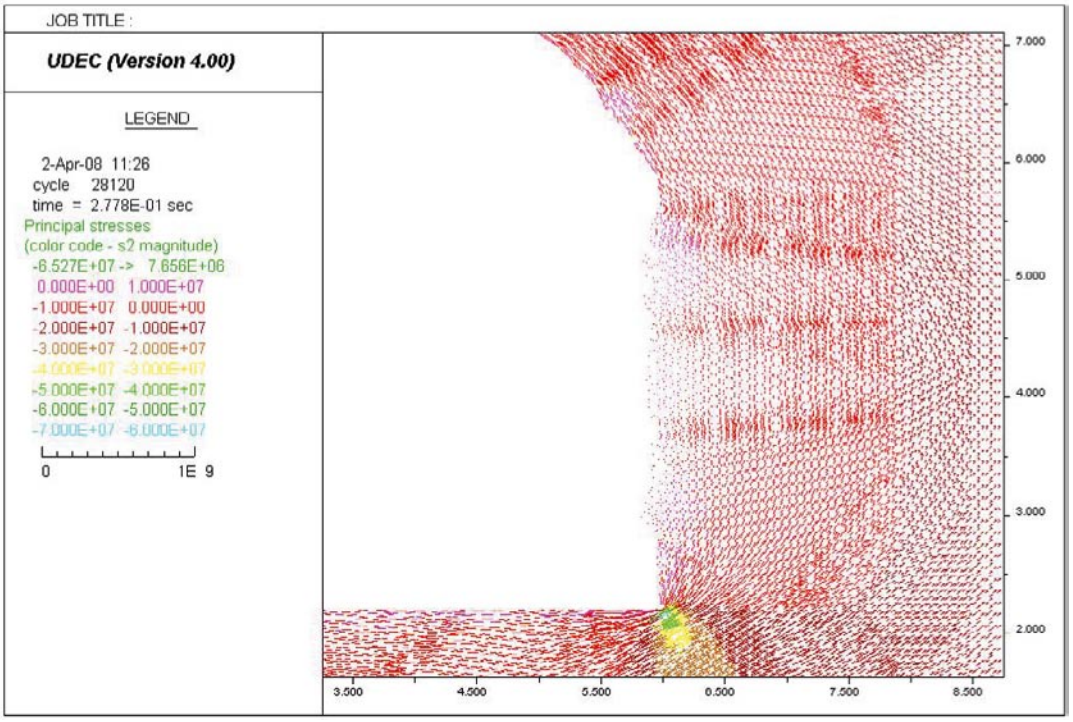

b) Maximum tensile stress = 7.656 MPa

Figure M-11. *Close-up images of the right side wall. Stress tensor plots at a section outside the slot after excavating the heading; Colors by magnitude of a) Sigma 1 and b) Sigma 2. Model with E = 45 GPa, σ1 = 30 MPa, σ1 = 316° (see Table 9-11).*

Outside slot section, as-built tunnel shape

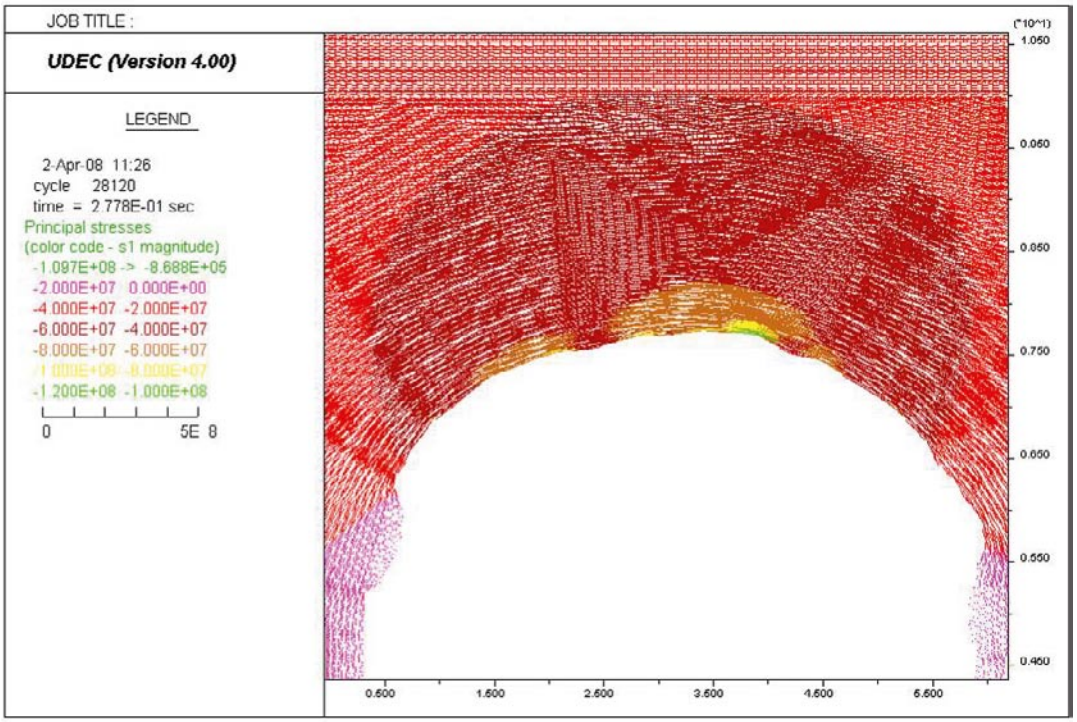

a) Maximum compressive stress = 109.7 MPa

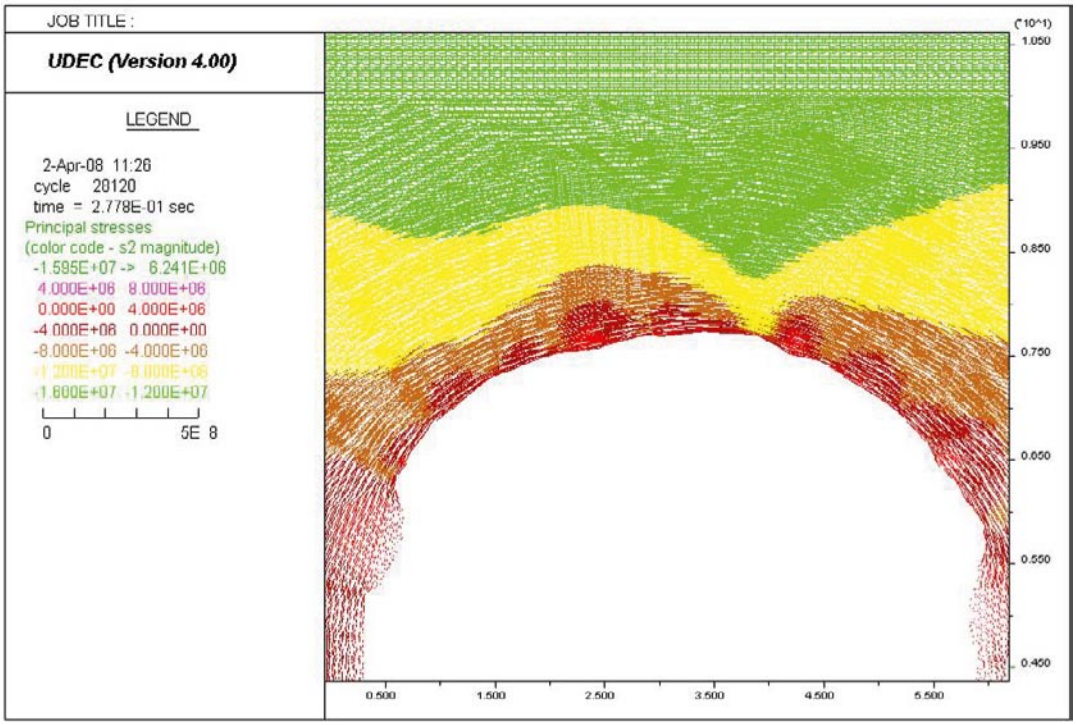

b) Maximum tensile stress = 6.241 MPa

Figure M-12. *Close-up images of the roof. Stress tensor plots at a section outside the slot after excavating the heading; Colors by magnitude of a) Sigma 1 and b) Sigma 2. Model with E = 45 GPa, σ1 = 30 MPa, σ1 = 316° (see Table 9-11).*

Outside slot section, as-built tunnel shape

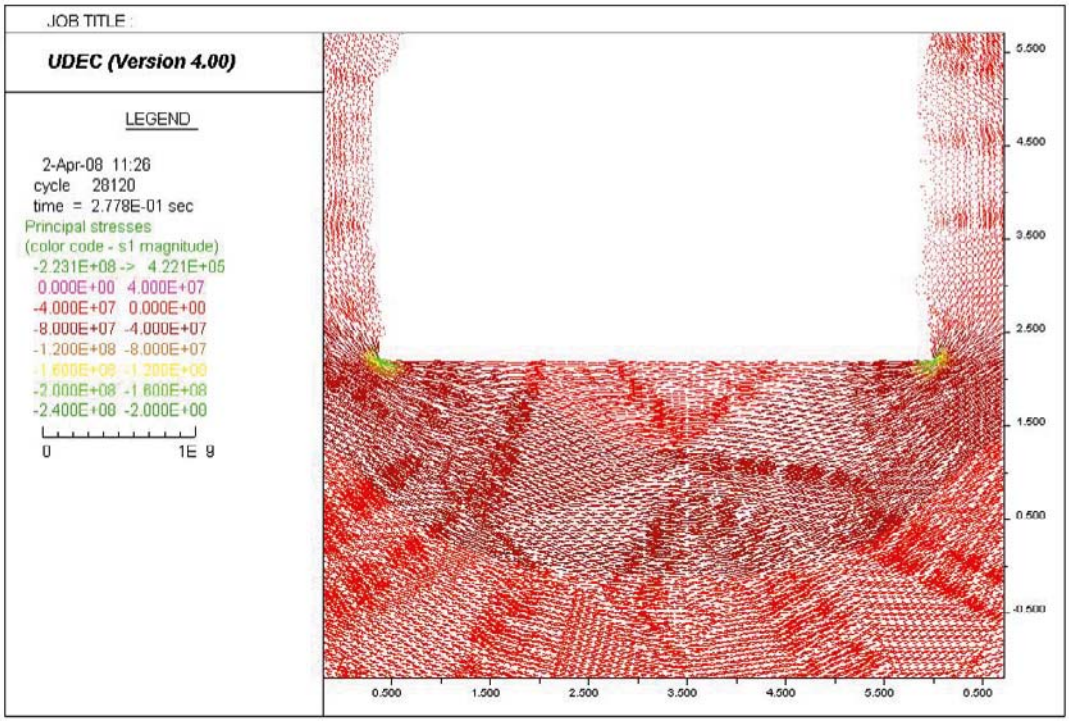

a) Maximum compressive stress = 223.1 MPa

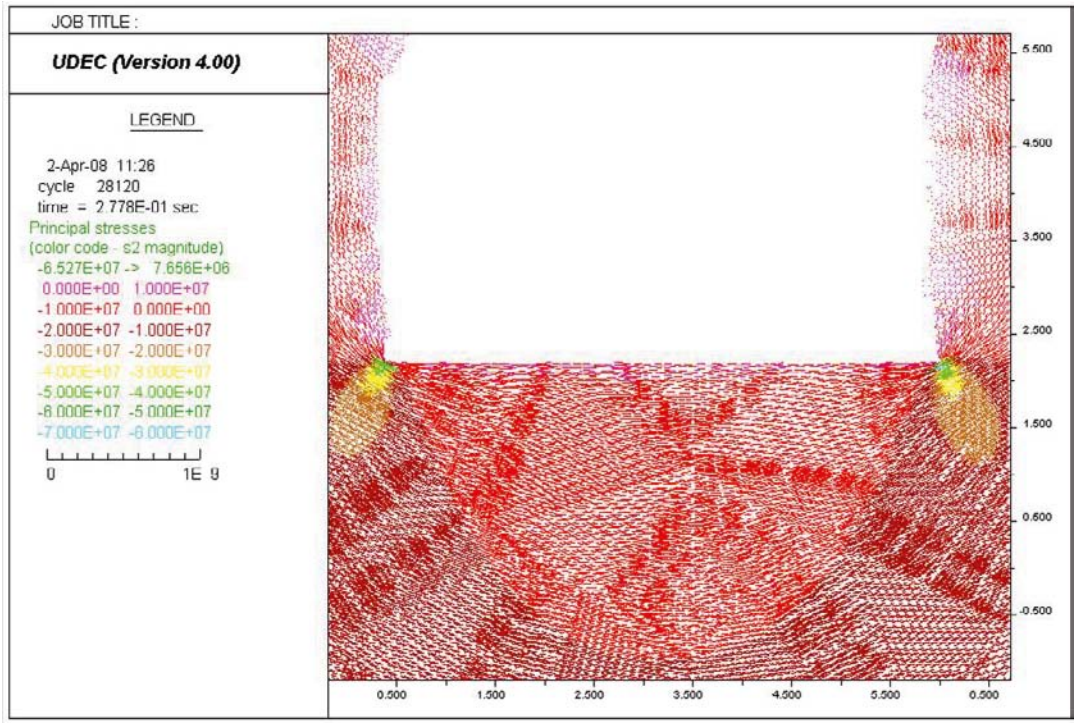

b) Maximum tensile stress = 7.656 MPa

Figure M-13. *Close-up images of the floor. Stress tensor plots at a section outside the slot after excavating the heading; Colors by magnitude of a) Sigma 1 and b) Sigma 2. Model with E = 45 GPa, σ1 = 30 MPa, σ1 = 316° (see Table 9-11).*

Convergence pins section, as-built tunnel shape

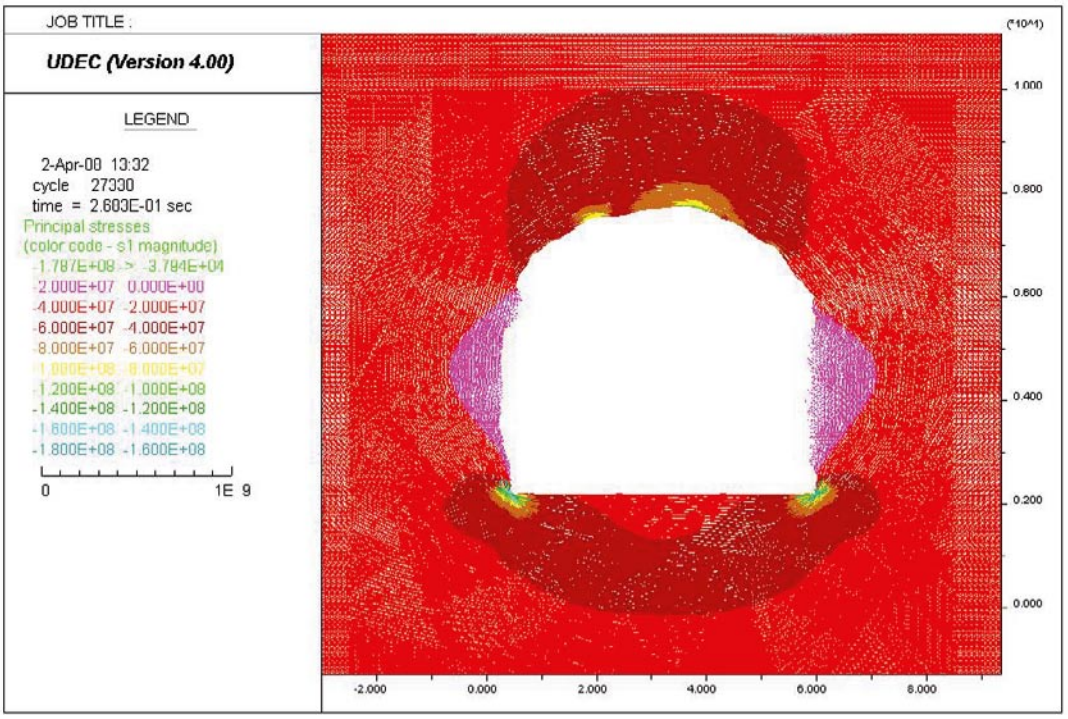

a) Maximum compressive stress = 178.7 MPa

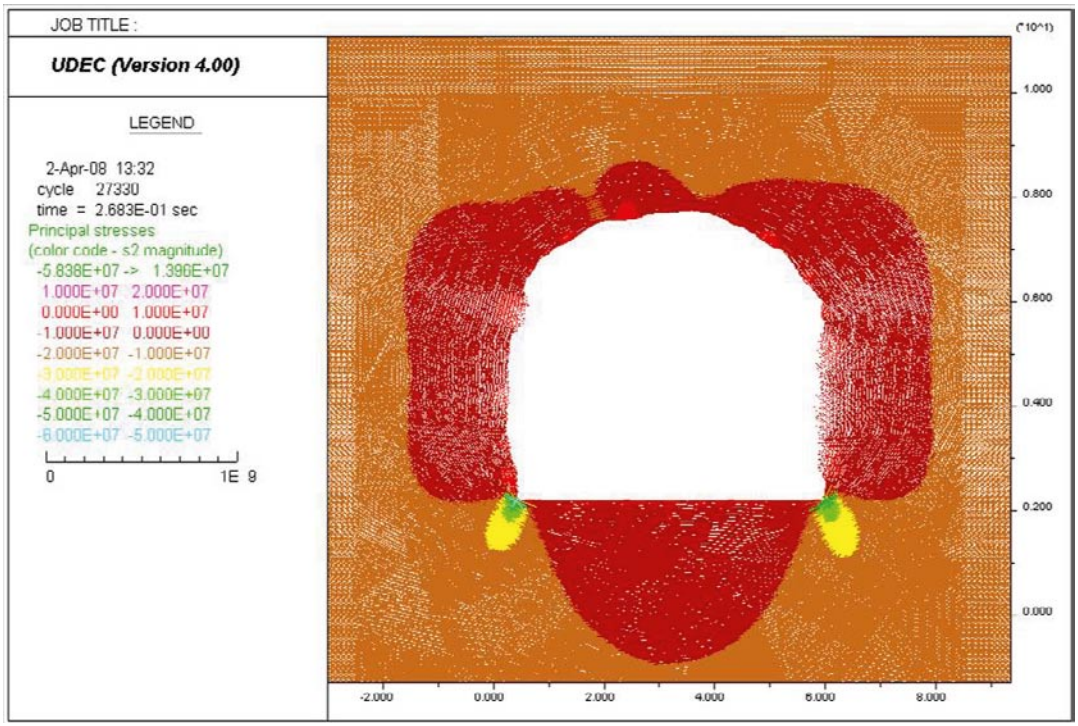

b) Maximum tensile stress = 13.96 MPa

Figure M-14. *Stress tensor plots at the convergence pins section after excavating the heading; Colors by magnitude of a) Sigma 1 and b) Sigma 2. Model with E = 45 GPa, σ1 = 30 MPa, σ1 = 316° (see Table 9-11).*

Convergence pins section, as-built tunnel shape

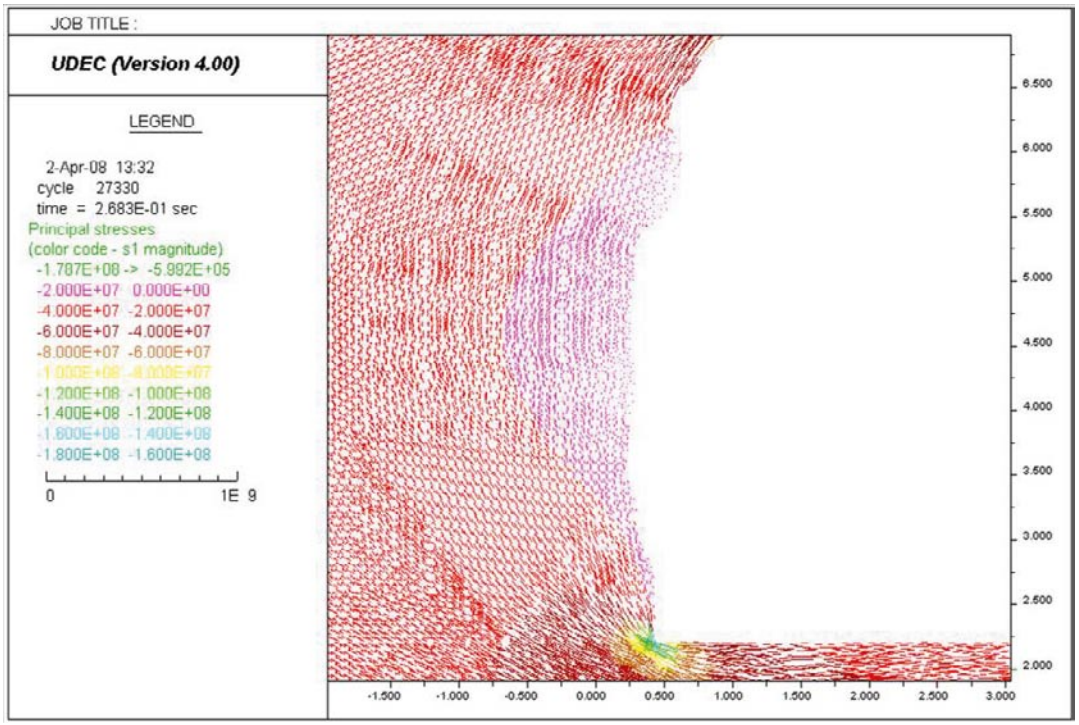

a) Maximum compressive stress = 178.7 MPa

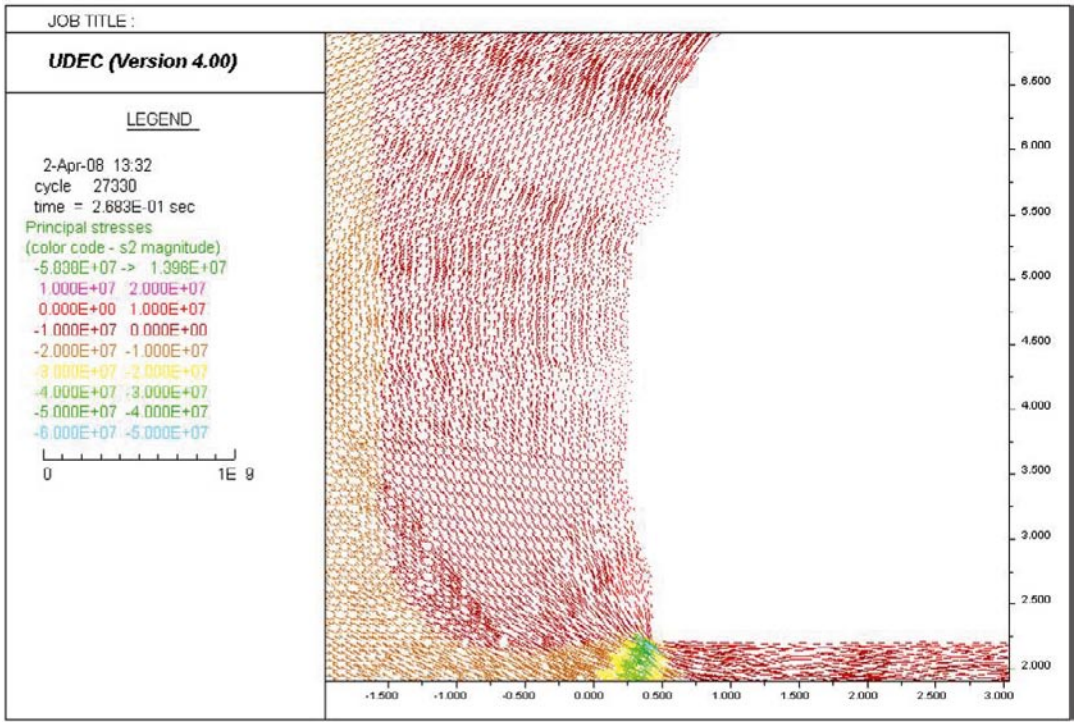

b) Maximum tensile stress = 13.96 MPa

Figure M-15. *Close-up images of the left side wall. Stress tensor plots at the convergence pins section after excavating the heading; Colors by magnitude of a) Sigma 1 and b) Sigma 2. Model with E = 45 GPa, σ1 = 30 MPa, σ1 = 316° (see Table 9-11).*

Convergence pins section, as-built tunnel shape

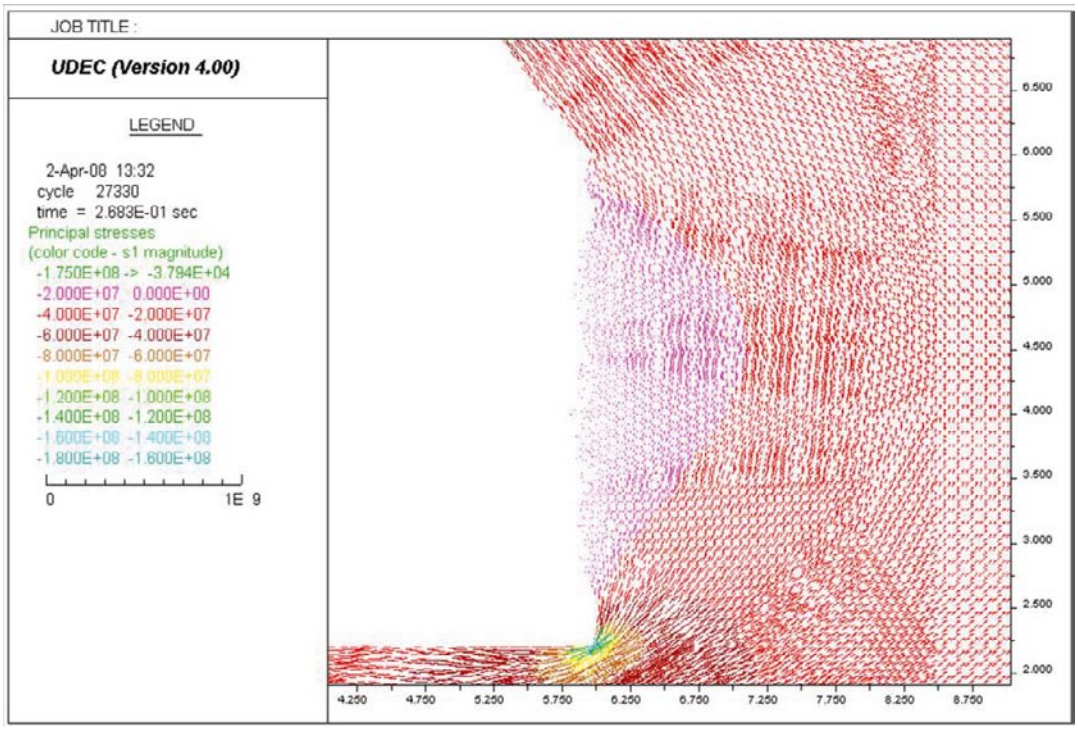

a) Maximum compressive stress = 175.0 MPa

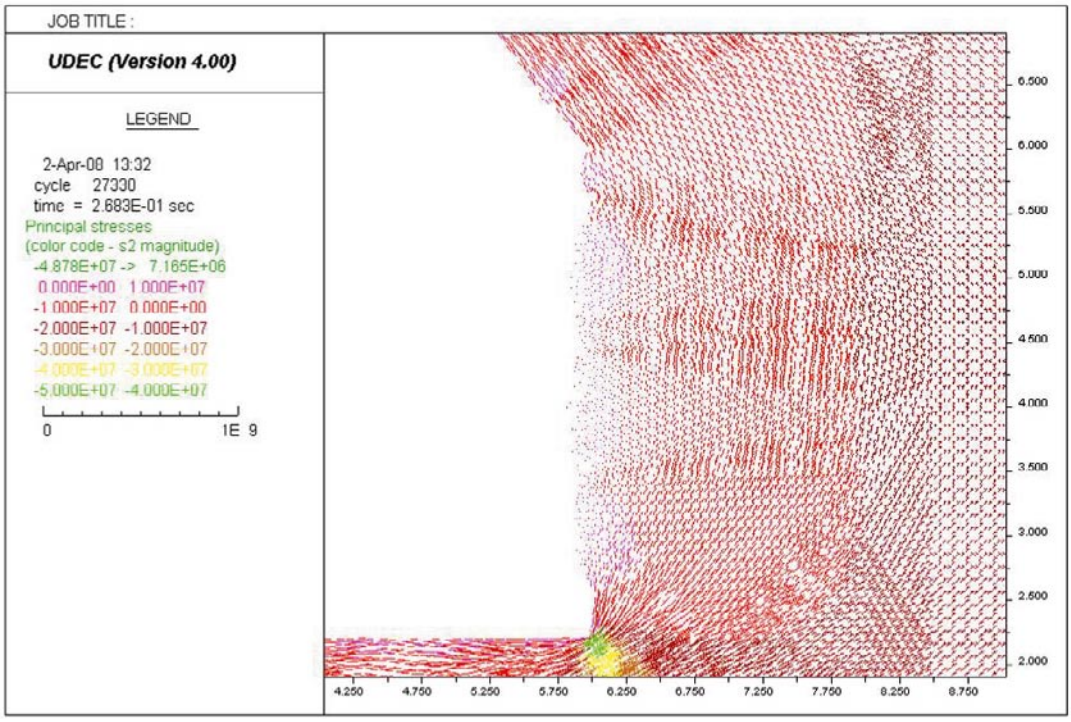

b) Maximum tensile stress = 7.165 MPa

Figure M-16. *Close-up images of the right side wall. Stress tensor plots at the convergence pins section after excavating the heading; Colors by magnitude of a) Sigma 1 and b) Sigma 2. Model with E = 45 GPa, σ1 = 30 MPa, σ1 = 316° (see Table 9-11).*

Convergence pins section, as-built tunnel shape

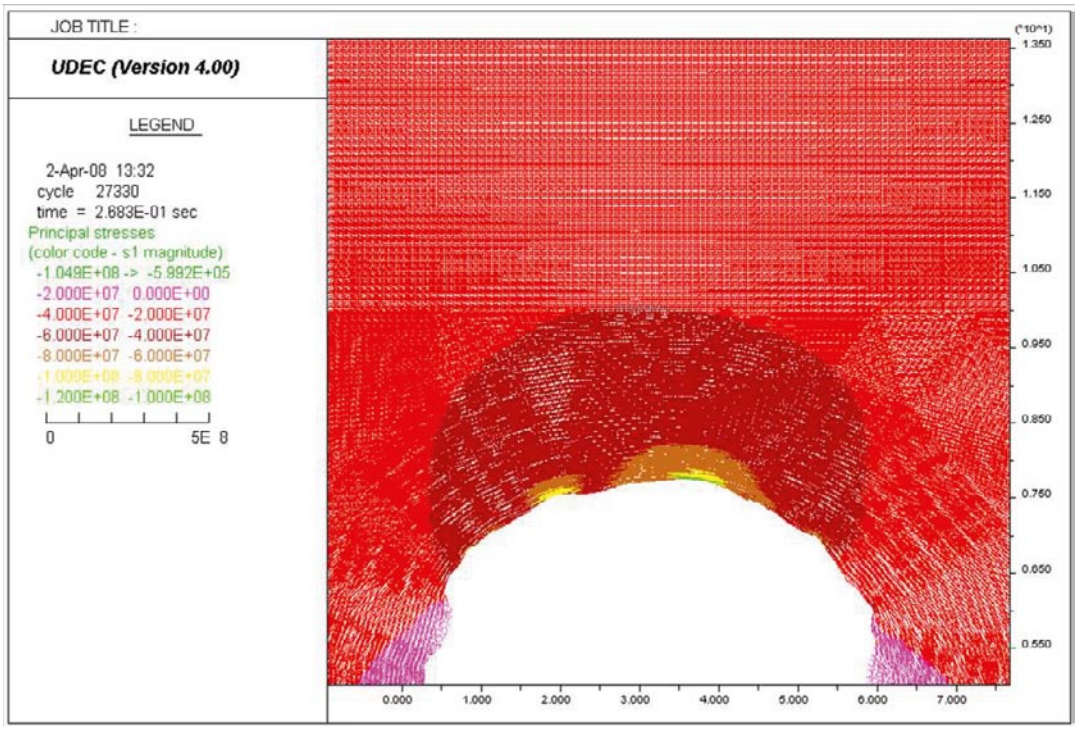

a) Maximum compressive stress = 104.9 MPa

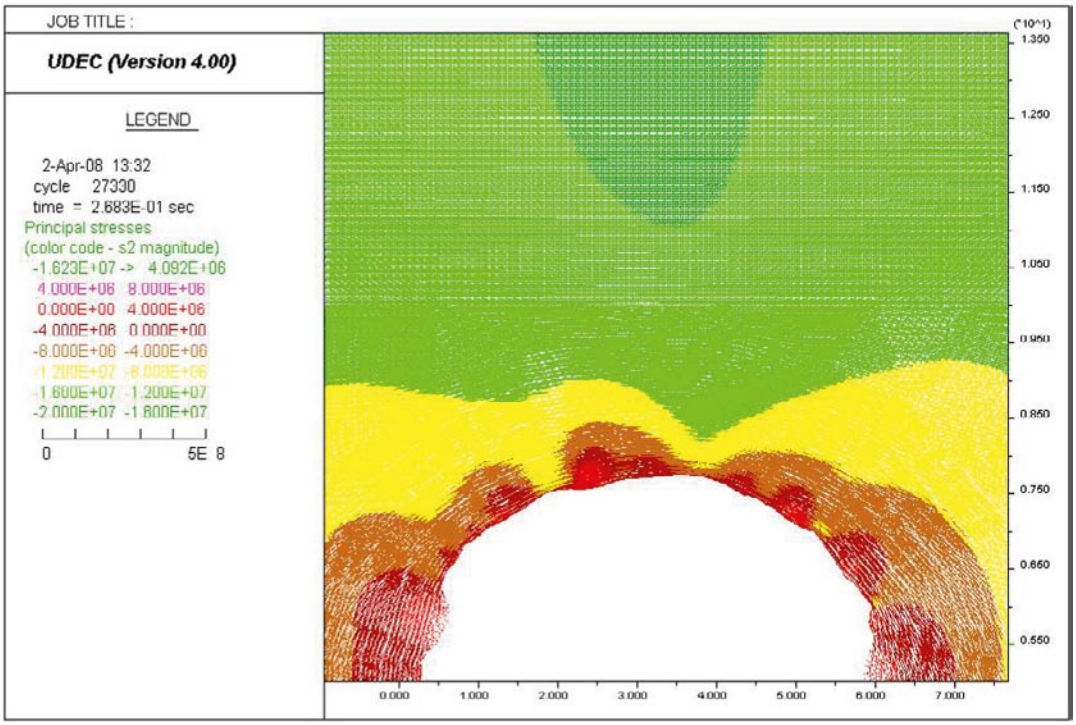

b) Maximum tensile stress = 4.092 MPa

Figure M-17. *Close-up images of the roof. Stress tensor plots at the convergence pins section after excavating the heading; Colors by magnitude of a) Sigma 1 and b) Sigma 2. Model with E = 45 GPa, σ1 = 30 MPa, σ1 = 316° (see Table 9-11).*

Convergence pins section, as-built tunnel shape

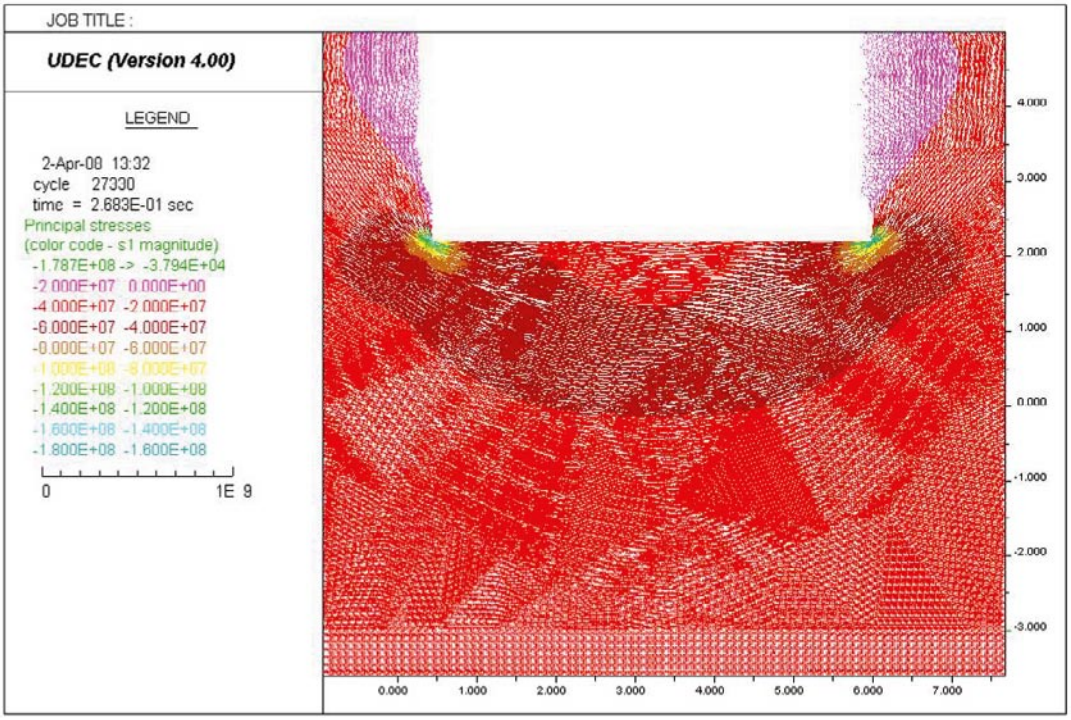

a) Maximum compressive stress = 178.7 MPa

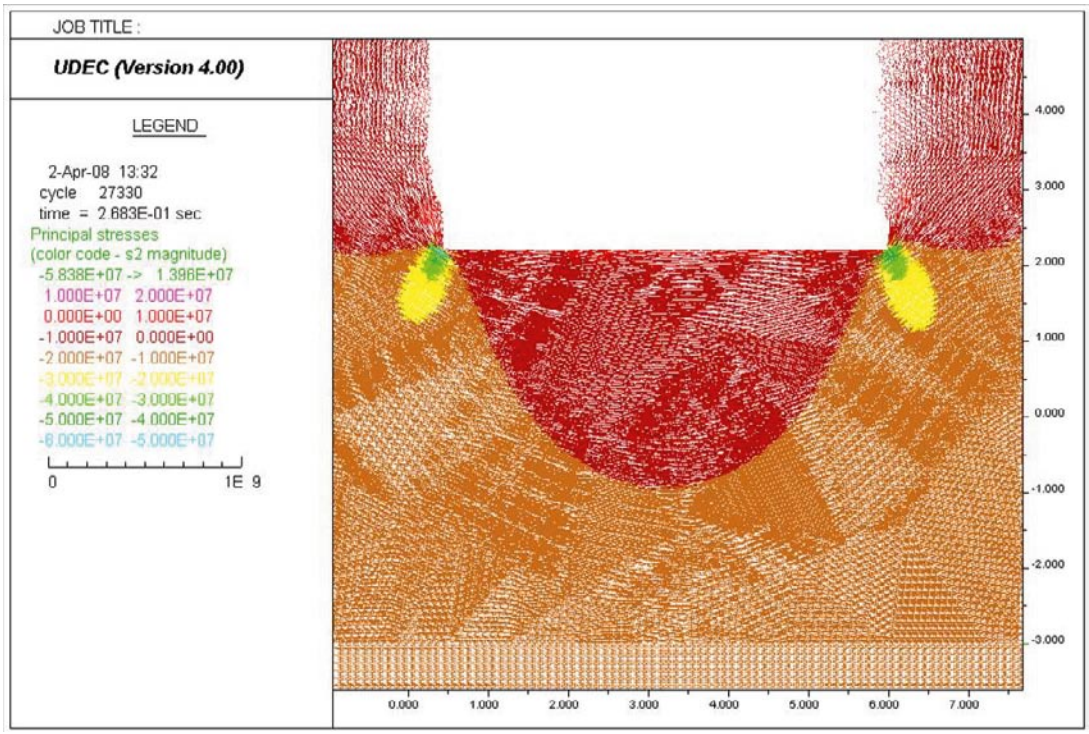

b) Maximum tensile stress = 13.96 MPa

Figure M-18. *Close-up images of the floor. Stress tensor plots at the convergence pins section after excavating the heading; Colors by magnitude of a) Sigma 1 and b) Sigma 2. Model with E = 45 GPa, σ1 = 30 MPa, σ1 = 316° (see Table 9-11).*

Stress tensor plots of the TASQ tunnel in 3 different sections (BGR, outside slot and convergence pins) with the as-built tunnel shape and the as-planned tunnel shape case after excavating the bench (E = 45 GPa, σ_1 = 30 MPa, σ_1 = 316°).

Ideal tunnel shape

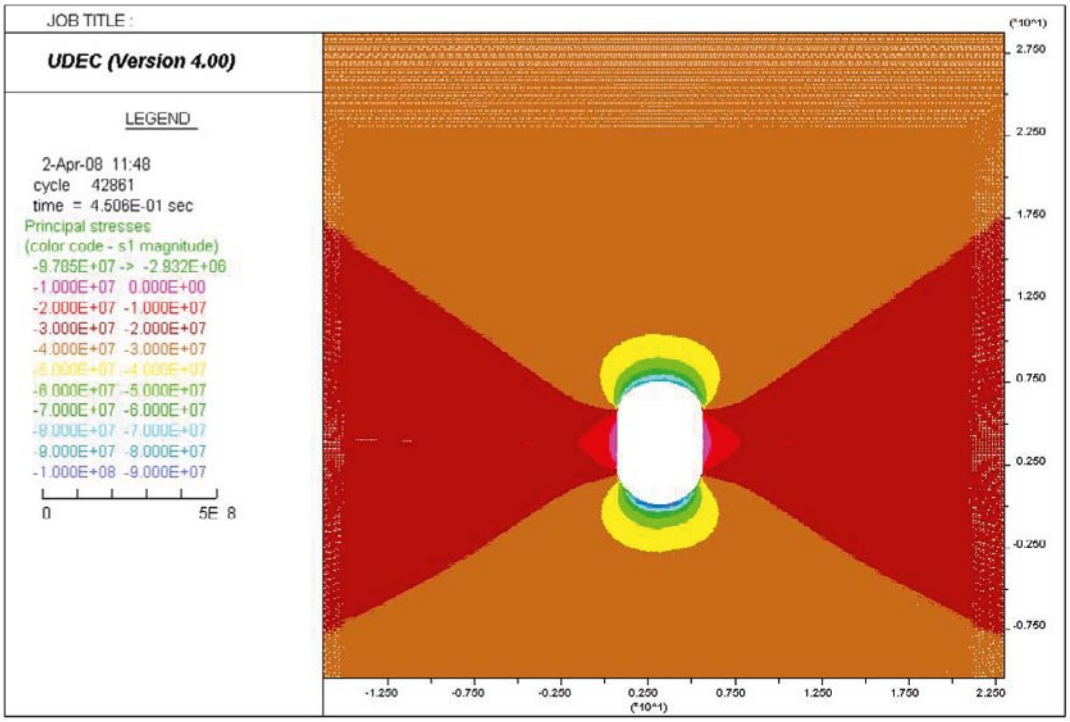

a) Maximum compressive stress = 97.85 MPa

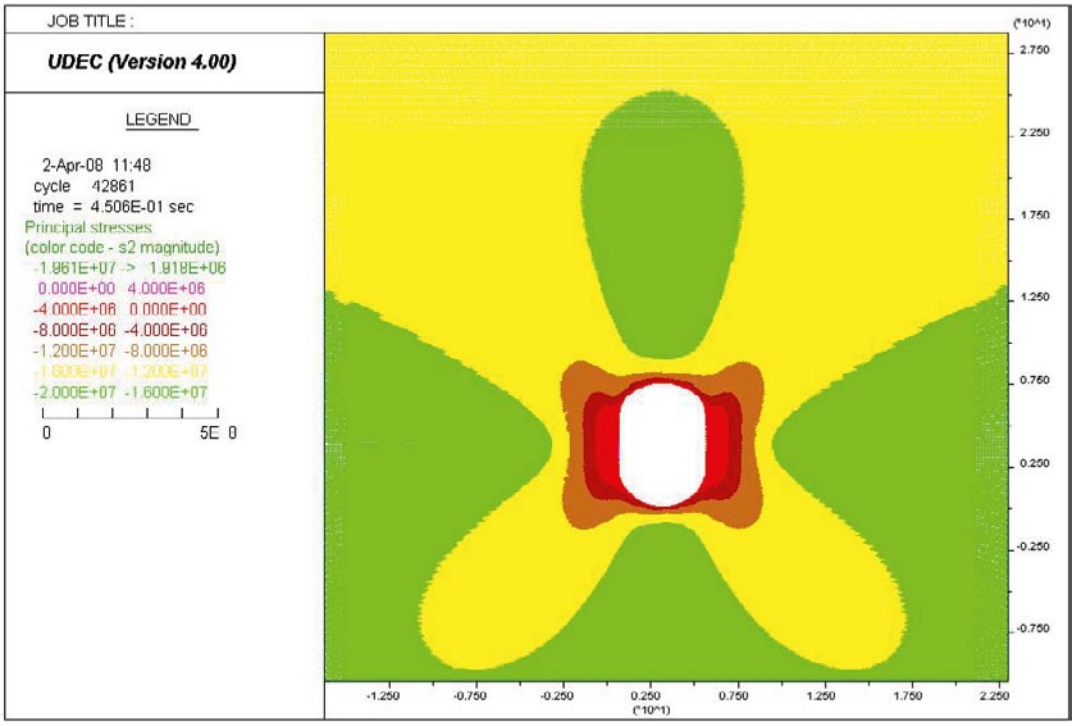

b) Maximum tensile stress = 1.918 MPa

Figure M-19. *Stress tensor plots of the as-planned tunnel shape after excavating the bench; Colors by magnitude of a) Sigma 1 and b) Sigma 2. Model with E = 45 GPa, σ1 = 30 MPa, σ1 = 316° (see Table 9-11).*

Ideal tunnel shape

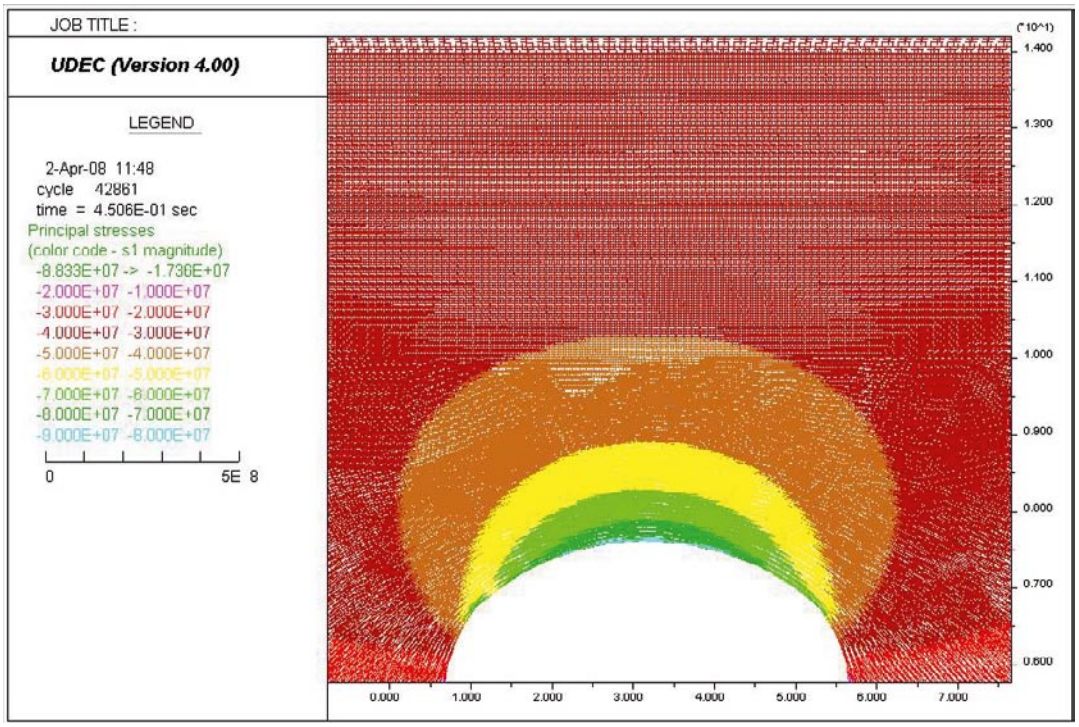

a) Maximum compressive stress = 88.33 MPa

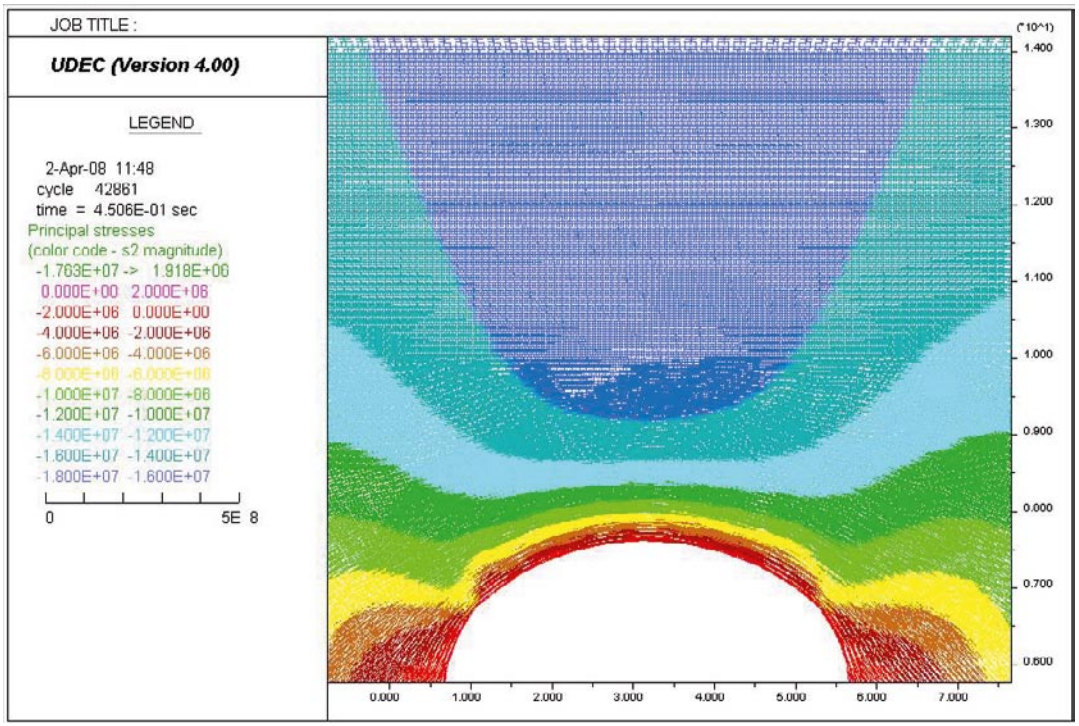

b) Maximum tensile stress = 1.918 MPa

Figure M-20. *Close-up images of the roof. Stress tensor plots of the as-planned tunnel shape after excavating the bench; Colors by magnitude of a) Sigma 1 and b) Sigma 2. Model with E = 45 GPa, σ1 = 30 MPa, σ1 = 316° (see Table 9-11).*

Ideal tunnel shape

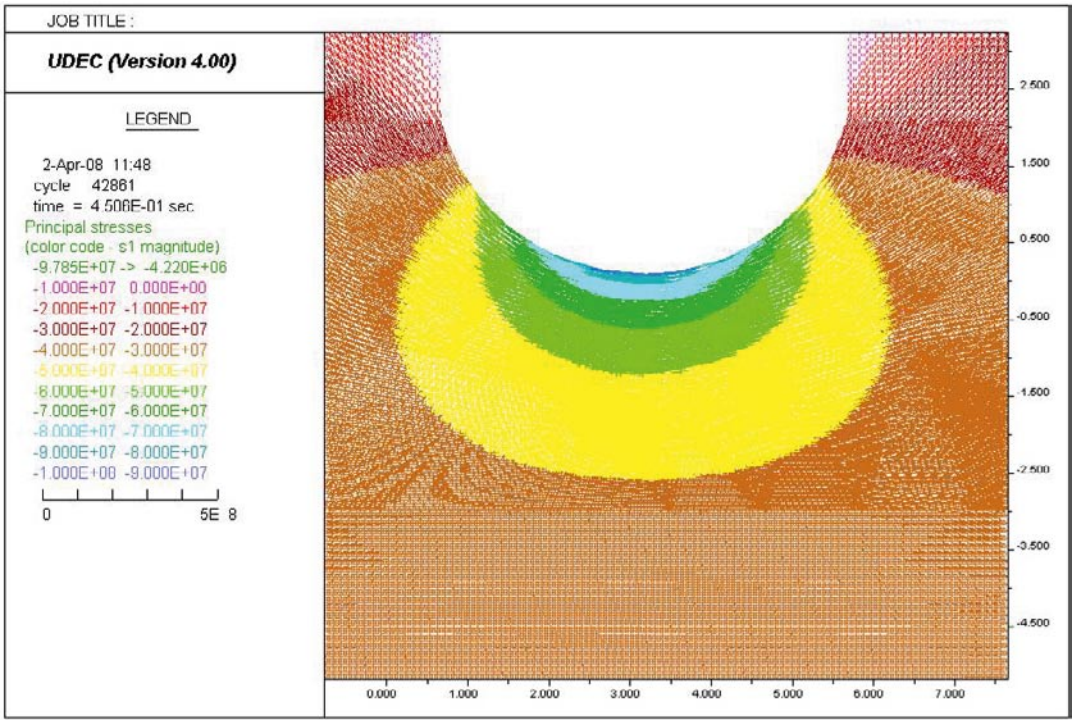

a) Maximum compressive stress = 97.85 MPa

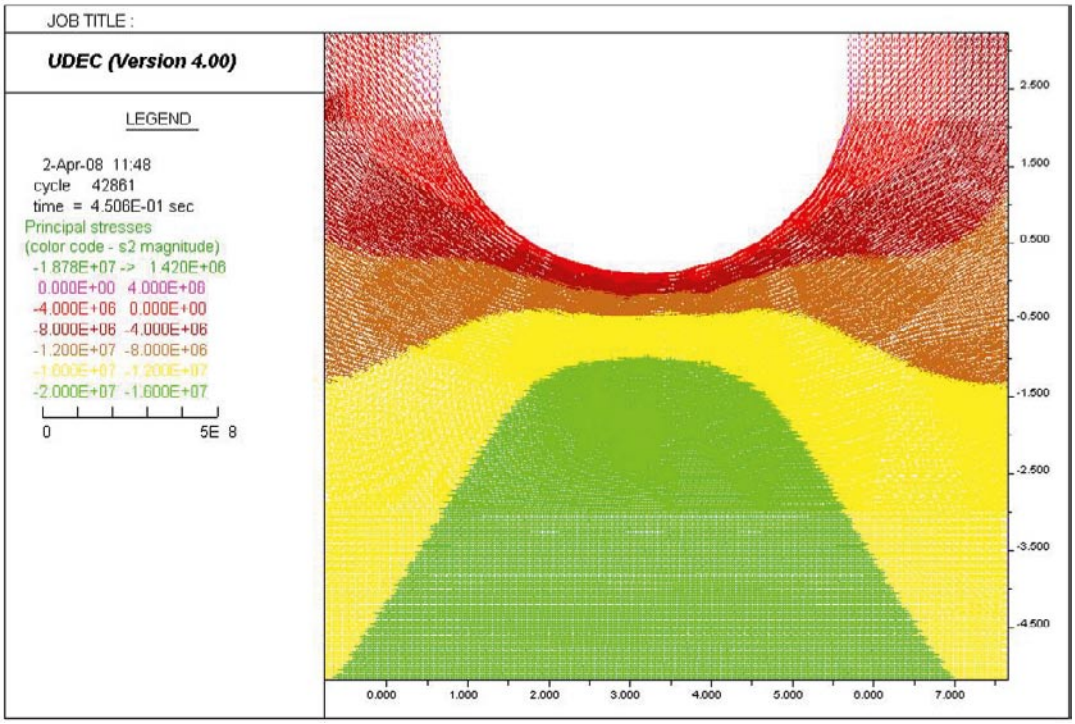

b) Maximum tensile stress = 14.20 MPa

Figure M-21. *Close-up images of the floor. Stress tensor plots of the as-planned tunnel shape after excavating the bench; Colors by magnitude of a) Sigma 1 and b) Sigma 2. Model with E = 45 GPa, σ1 = 30 MPa, σ1 = 316° (see Table 9-11).*

BGR section, as-built tunnel shape

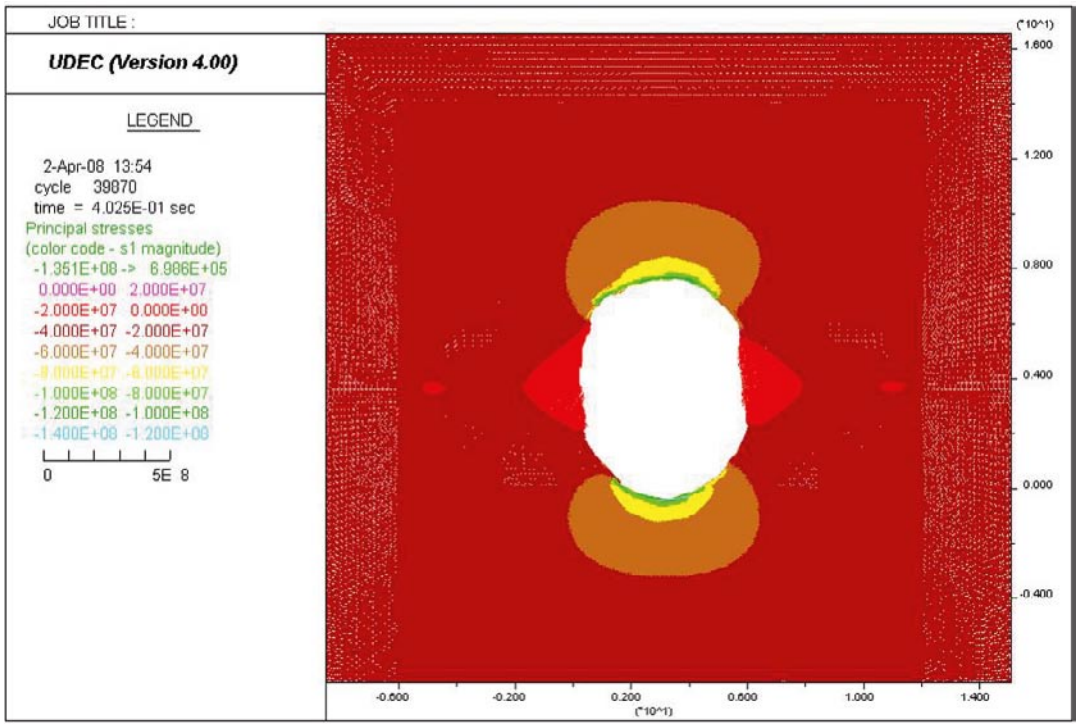

a) Maximum Compressive stress = 135.1 MPa

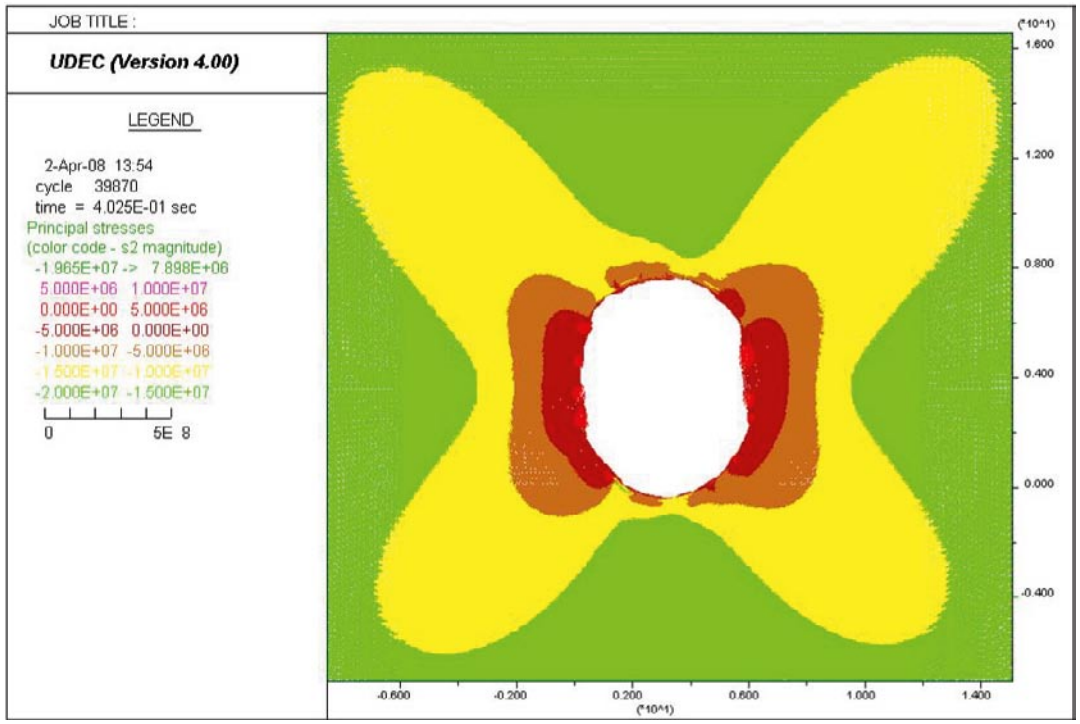

b) Maximum Tensile stress = 7.898 MPa

Figure M-22. *Stress tensor plots at the BGR section after excavating the bench; Colors by magnitude of a) Sigma 1 and b) Sigma 2. Model with E = 45 GPa, σ1 = 30 MPa, σ1 = 316° (see Table 9-11).*

BGR section, as-built tunnel shape

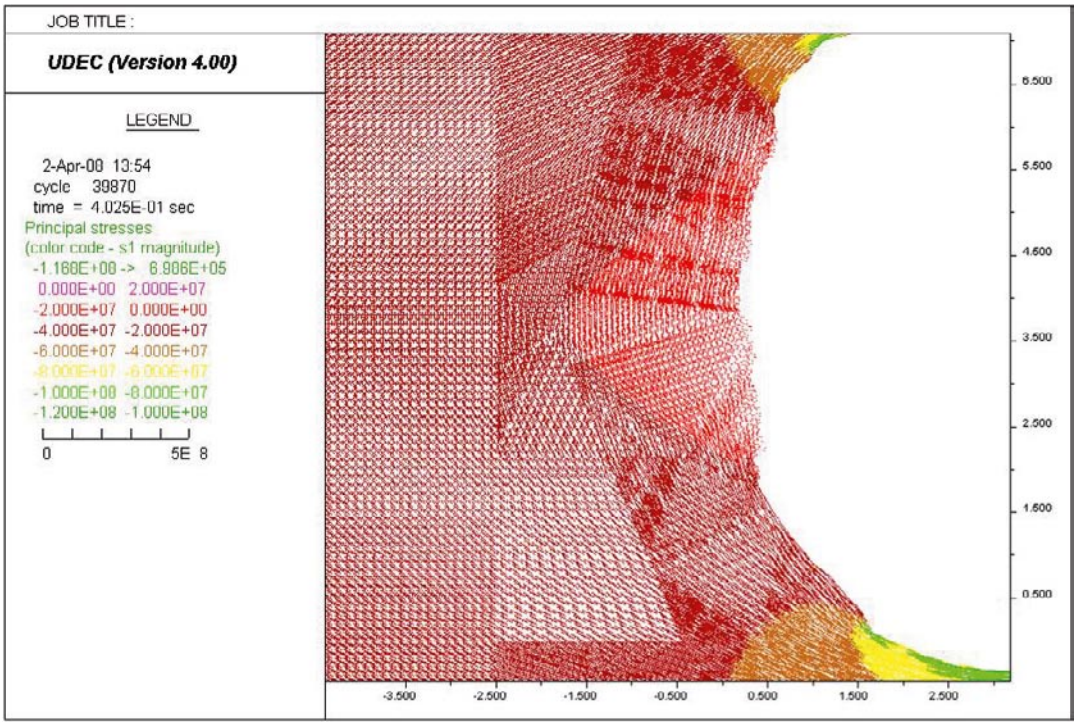

a) Maximum Compressive stress = 116.8 MPa

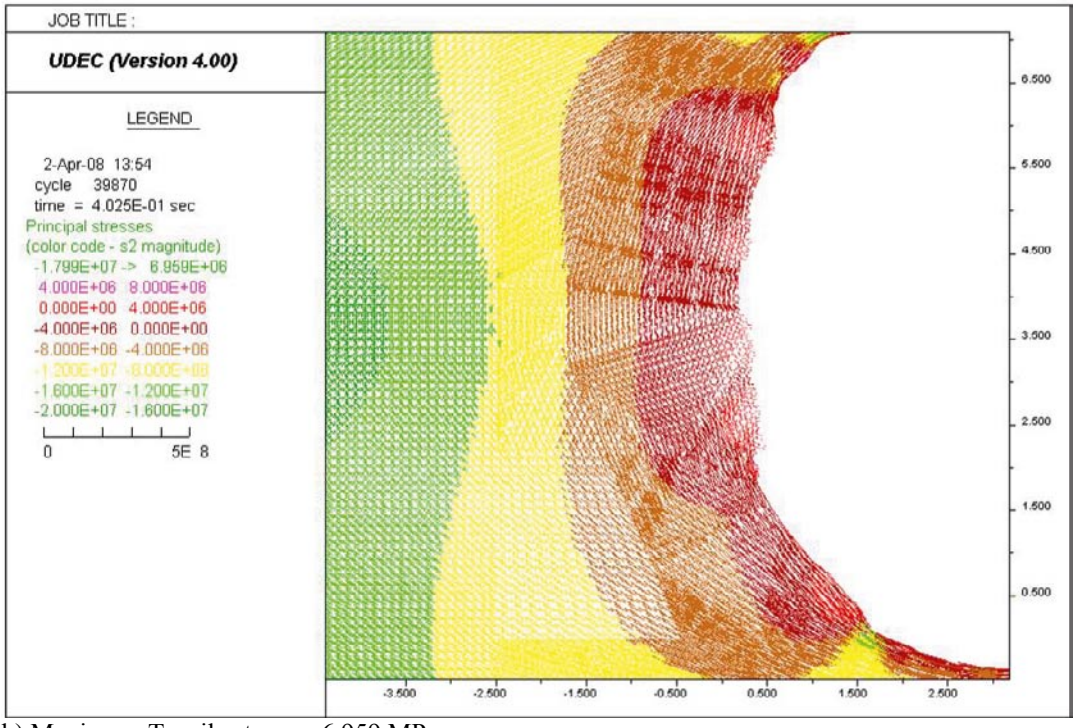

b) Maximum Tensile stress = 6.959 MPa

Figure M-23. *Close-up images of the left side wall. Stress tensor plots at the BGR section after excavating the bench; Colors by magnitude of a) Sigma 1 and b) Sigma 2. Model with E = 45 GPa, σ1 = 30 MPa, σ1 = 316° (see Table 9-11).*

BGR section, as-built tunnel shape

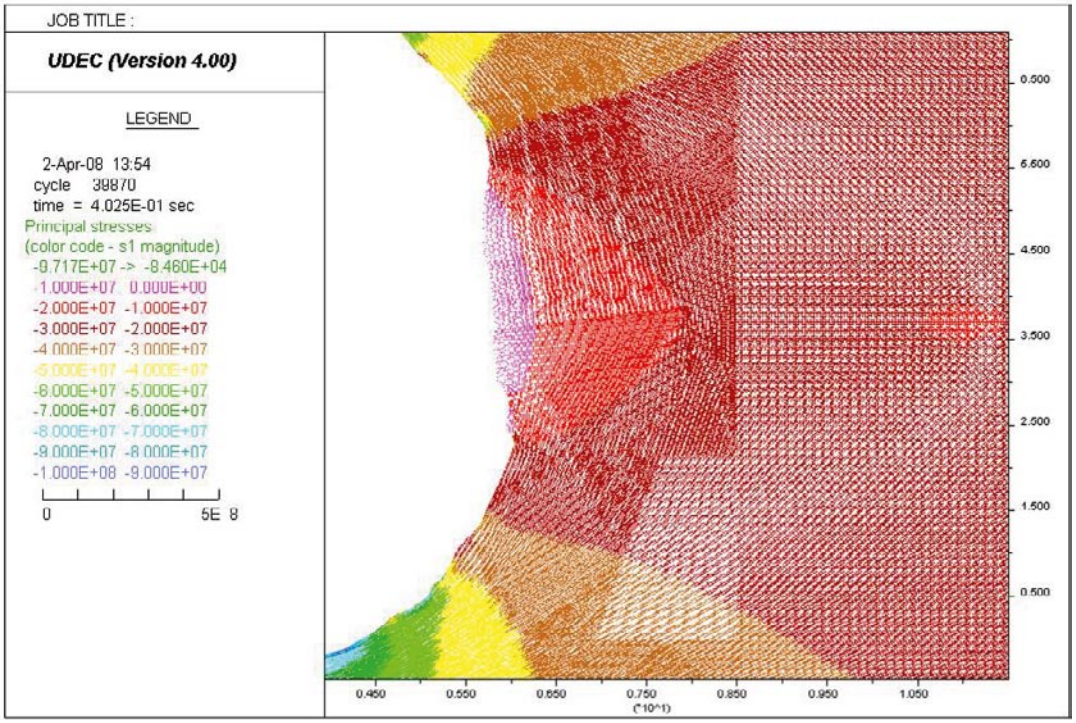

a) Maximum Compressive stress = 97.17 MPa

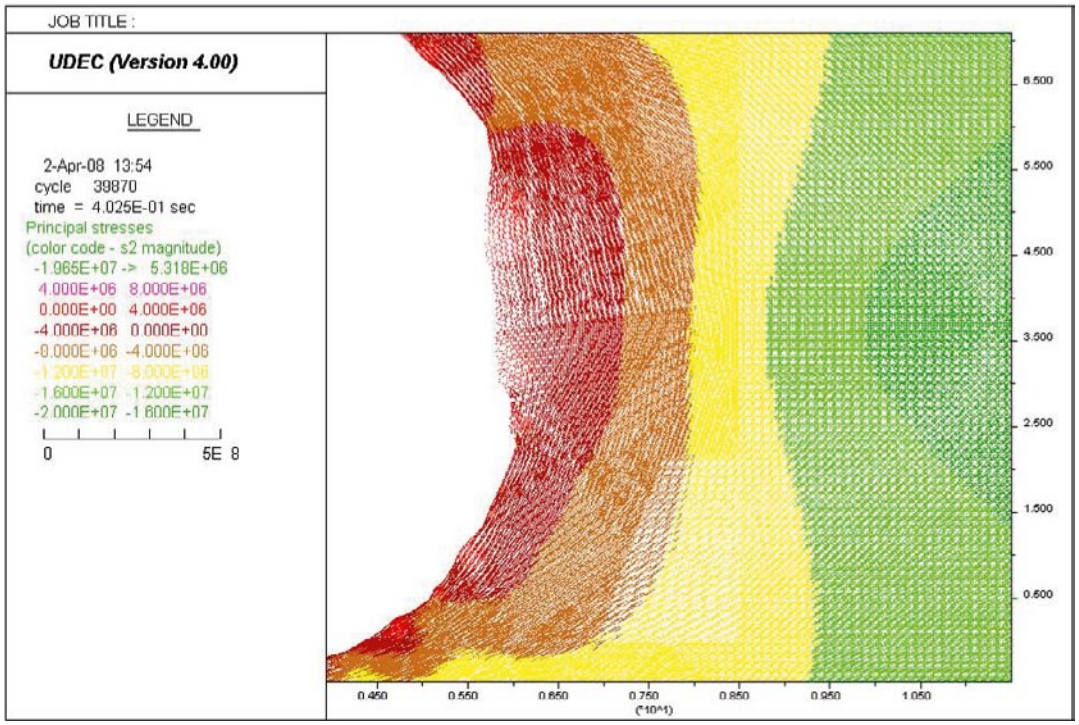

b) Maximum Tensile stress = 5.318 MPa

Figure M-24. *Close-up images of the right side wall. Stress tensor plots at the BGR section after excavating the bench; Colors by magnitude of a) Sigma 1 and b) Sigma 2. Model with E = 45 GPa, σ1 = 30 MPa, σ1 = 316° (see Table 9-11).*

BGR section, as-built tunnel shape

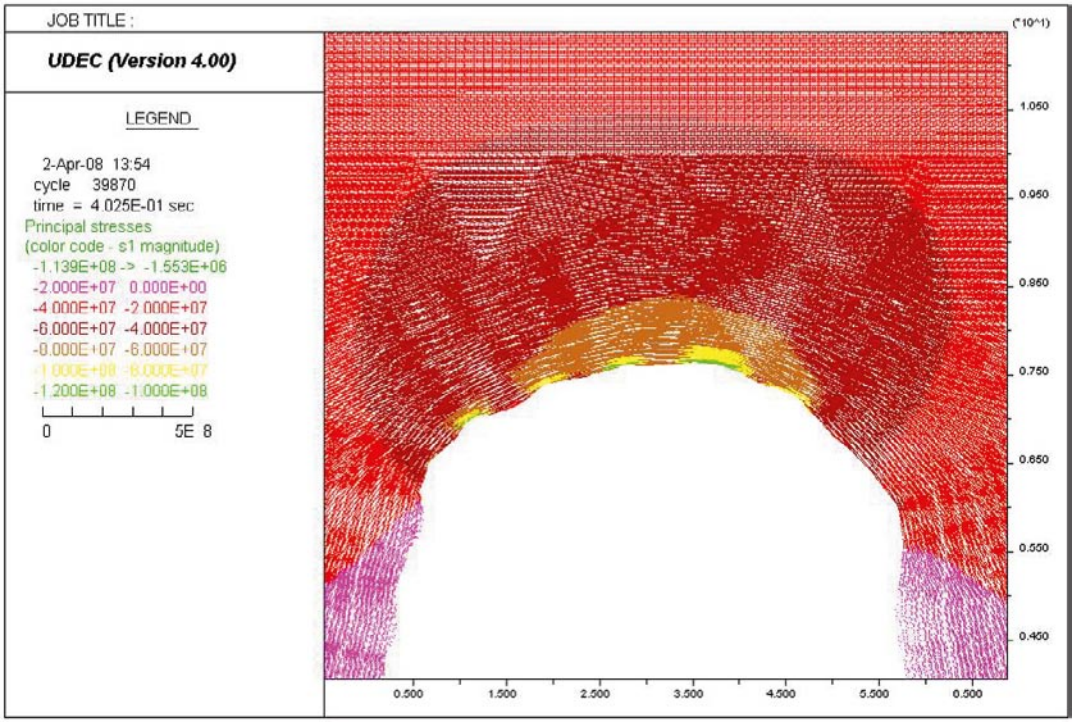

a) Maximum Compressive stress = 113.9 MPa

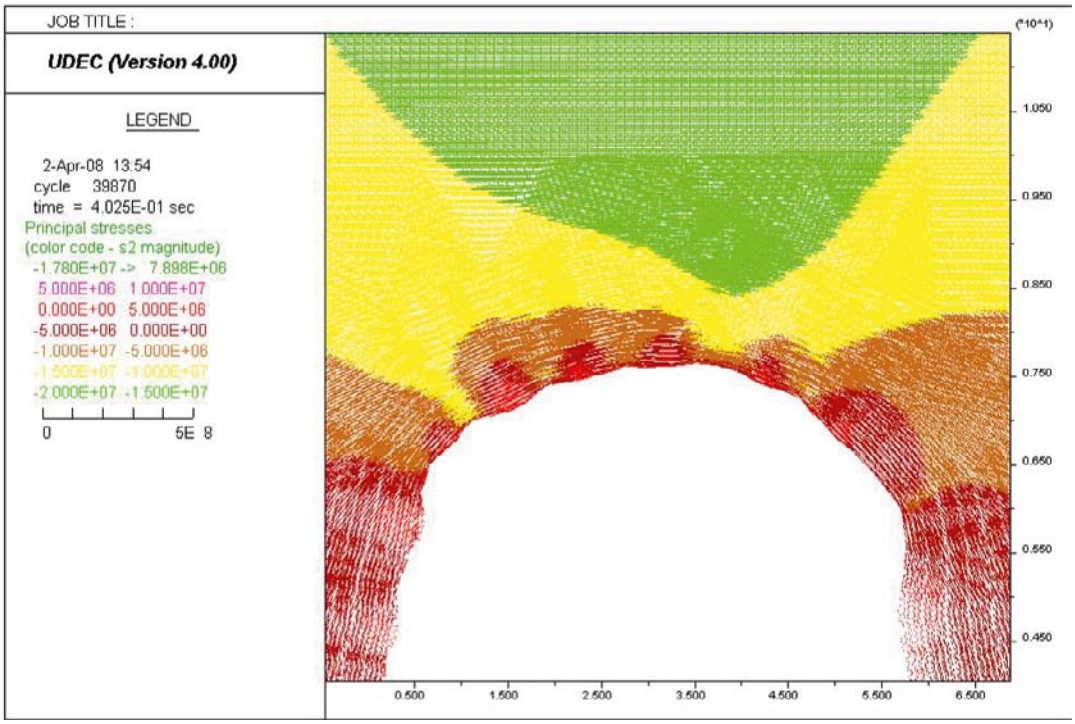

b) Maximum Tensile stress = 7.898 MPa

Figure M-25. *Close-up images of the roof. Stress tensor plots at the BGR section after excavating the bench; Colors by magnitude of a) Sigma 1 and b) Sigma 2. Model with E = 45 GPa, σ1 = 30 MPa, σ1 = 316° (see Table 9-11).*

BGR section, as-built tunnel shape

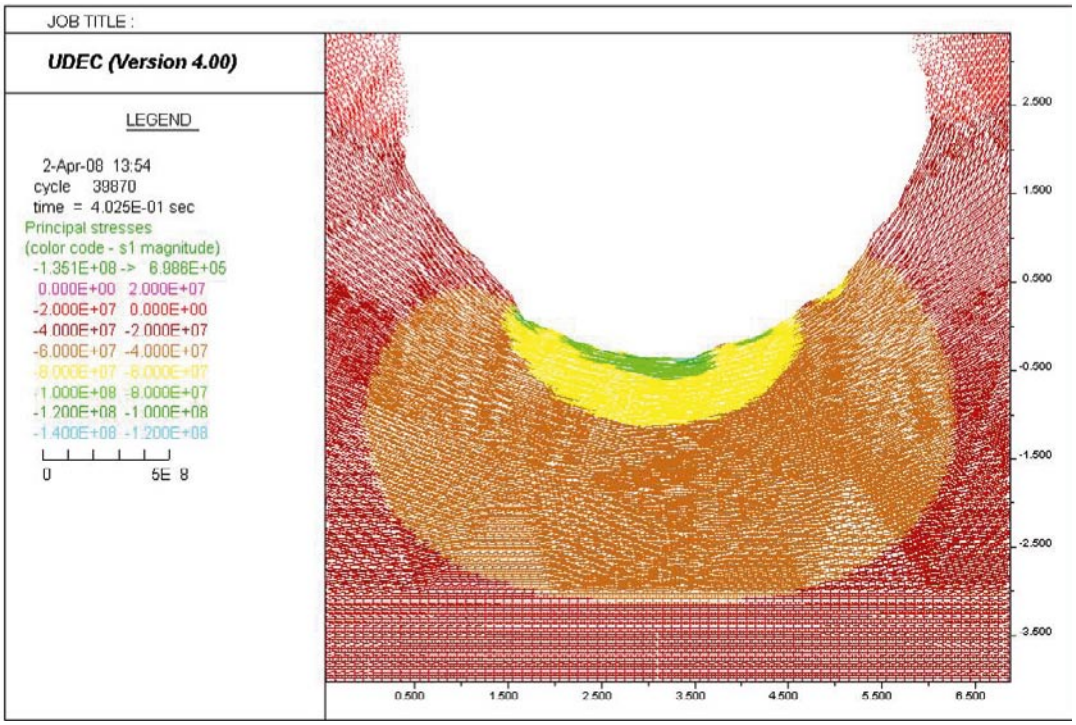

a) Maximum Compressive stress = 135.1 MPa

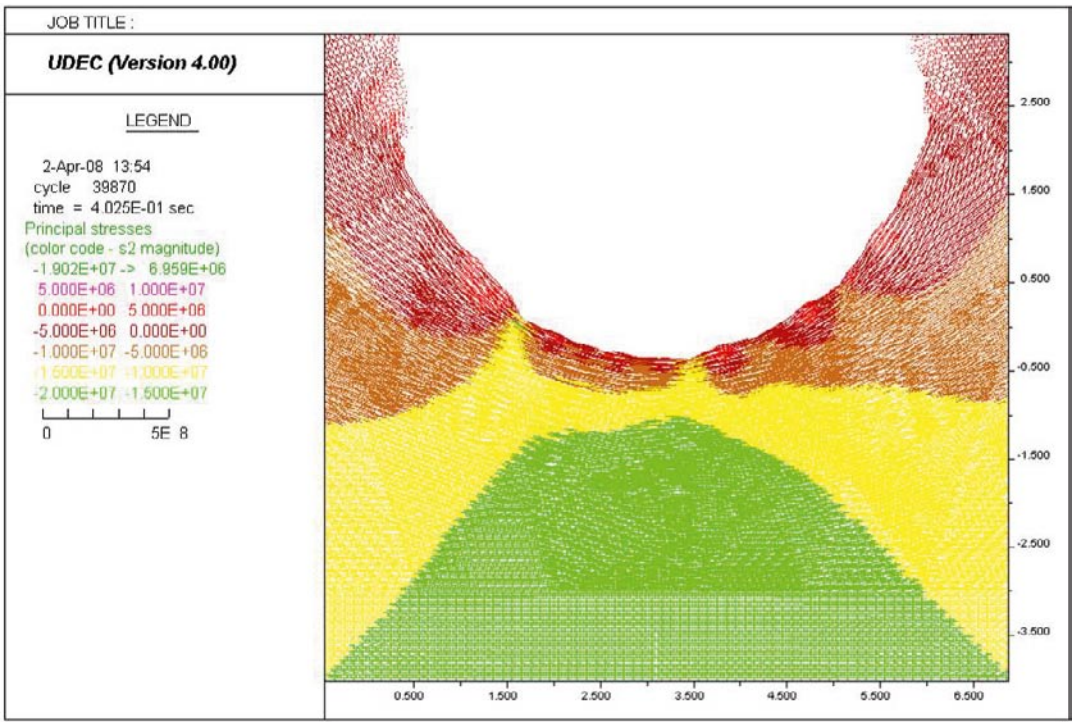

b) Maximum Tensile stress = 6.959 MPa

Figure M-26. *Close-up images of the floor. Stress tensor plots at the BGR section after excavating the bench; Colors by magnitude of a) Sigma 1 and b) Sigma 2. Model with E = 45 GPa, σ1 = 30 MPa, σ1 = 316° (see Table 9-11).*

Outside slot section, as-built tunnel shape

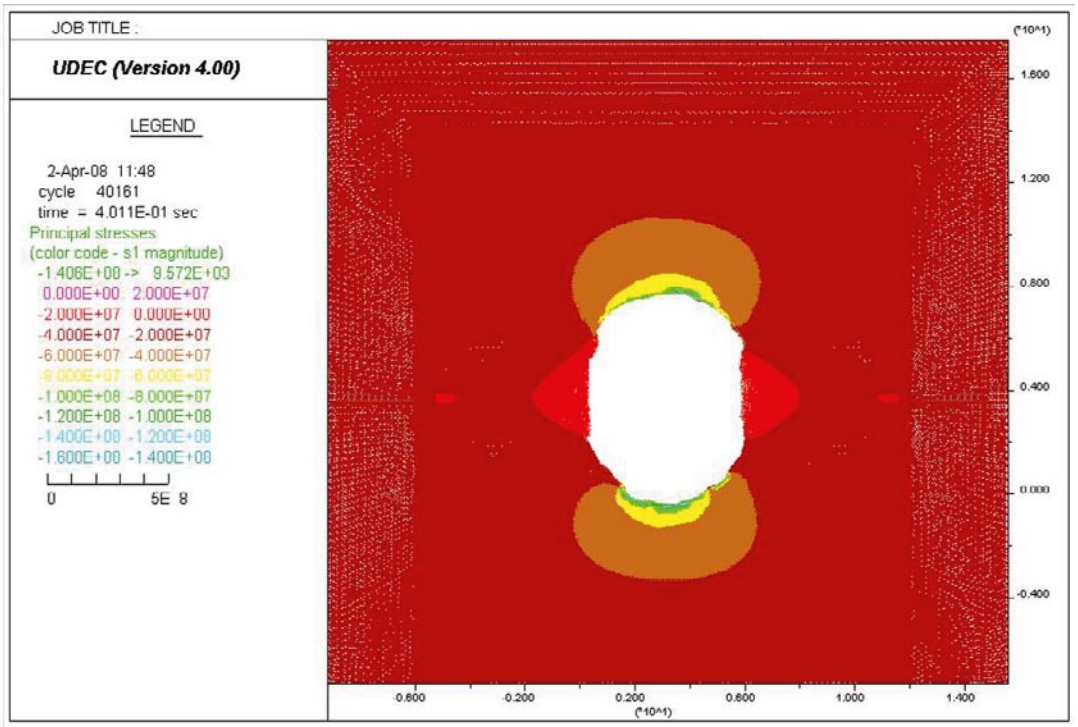

a) Maximum compressive stress = 140.6 MPa

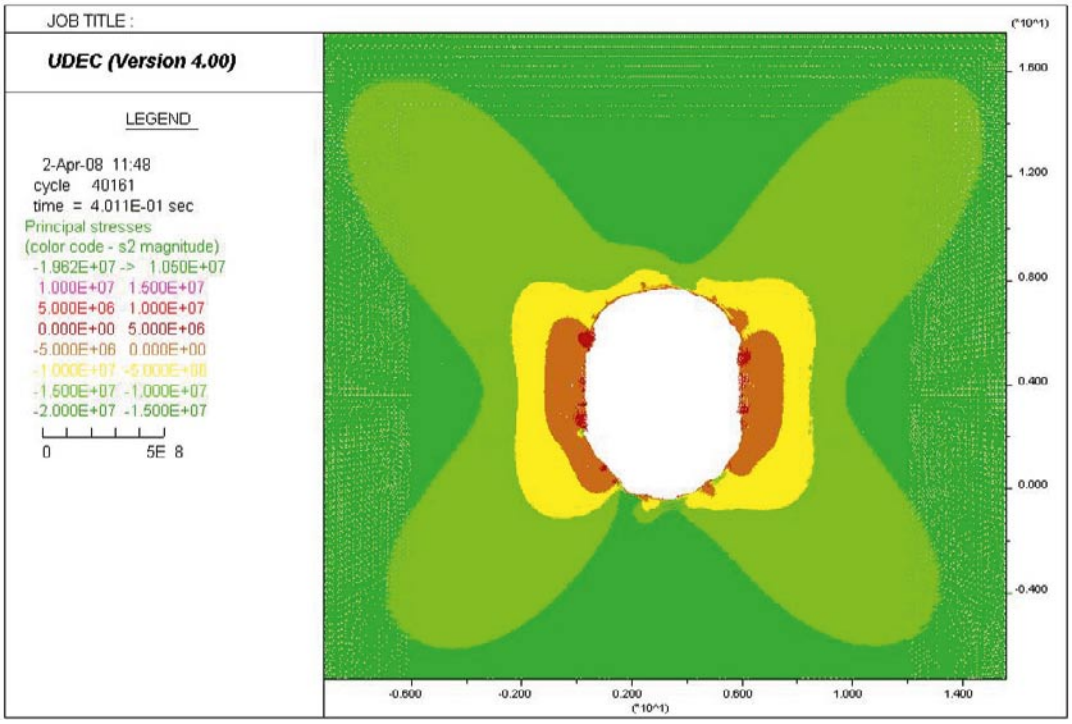

b) Maximum tensile stress = 10.50 MPa

Figure M-27. *Stress tensor plots at a section outside the slot after excavating the bench; Colors by magnitude of a) Sigma 1 and b) Sigma 2. Model with E = 45 GPa, σ1 = 30 MPa, σ1 = 316° (see Table 9-11).*

Outside slot section, as-built tunnel shape

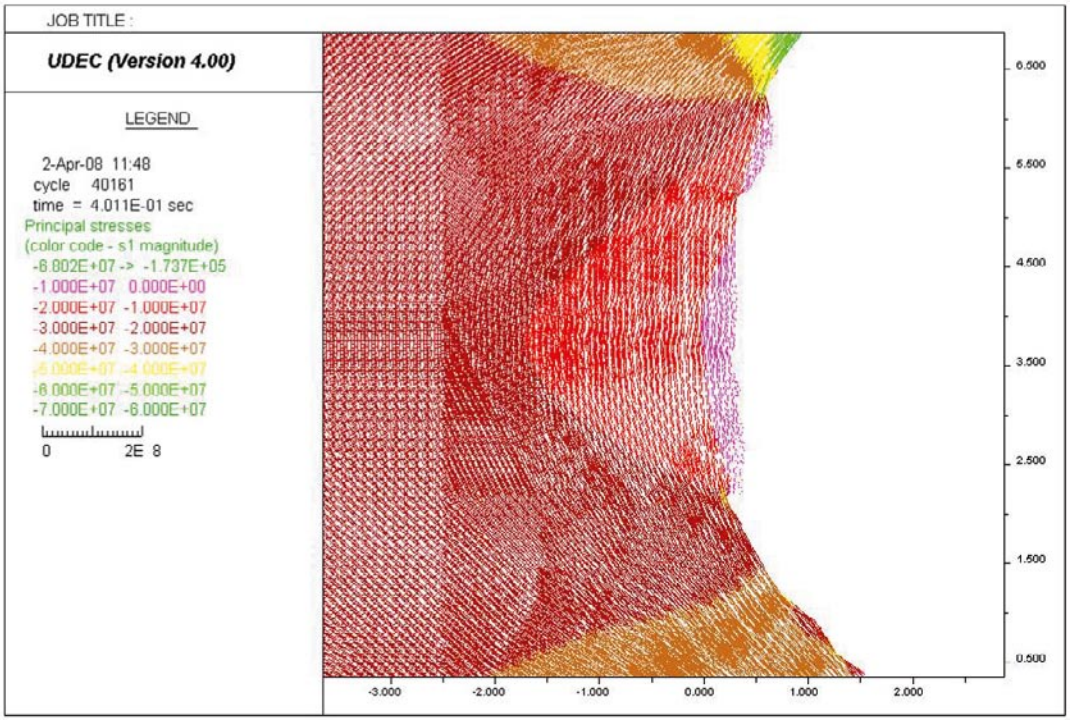

a) Maximum compressive stress = 68.02 MPa

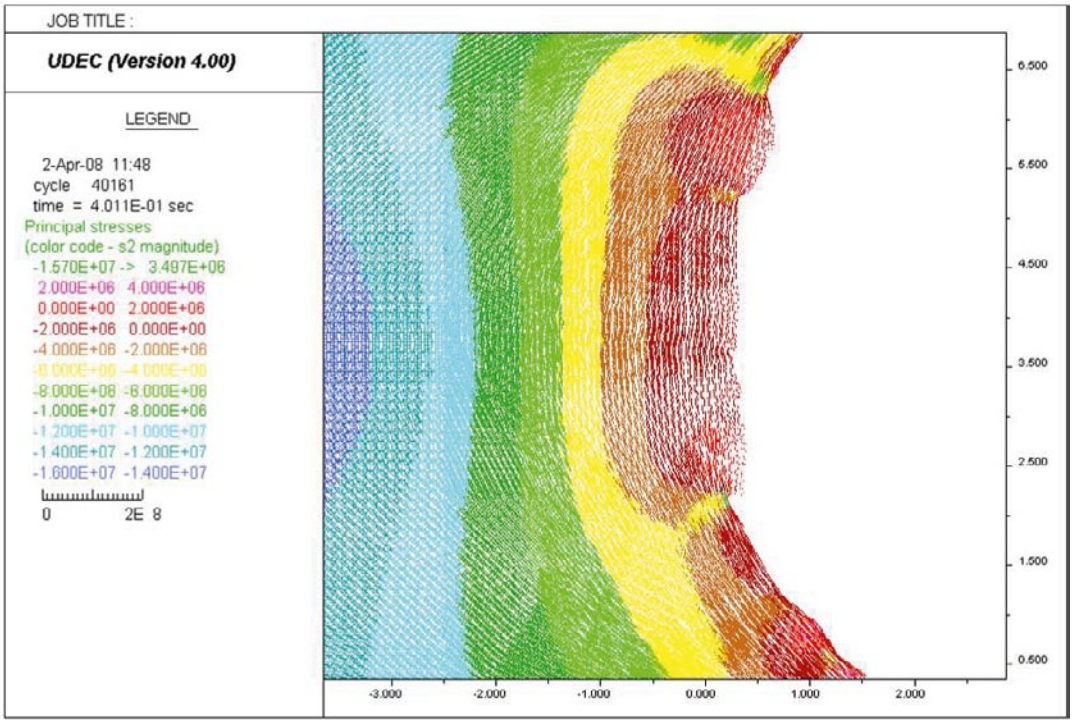

b) Maximum tensile stress = 3.497 MPa

Figure M-28. *Close-up images of the left side wall. Stress tensor plots at a section outside the slot after excavating the bench; Colors by magnitude of a) Sigma 1 and b) Sigma 2. Model with E = 45 GPa, σ1 = 30 MPa, σ1 = 316° (see Table 9-11).*

Outside slot section, as-built tunnel shape

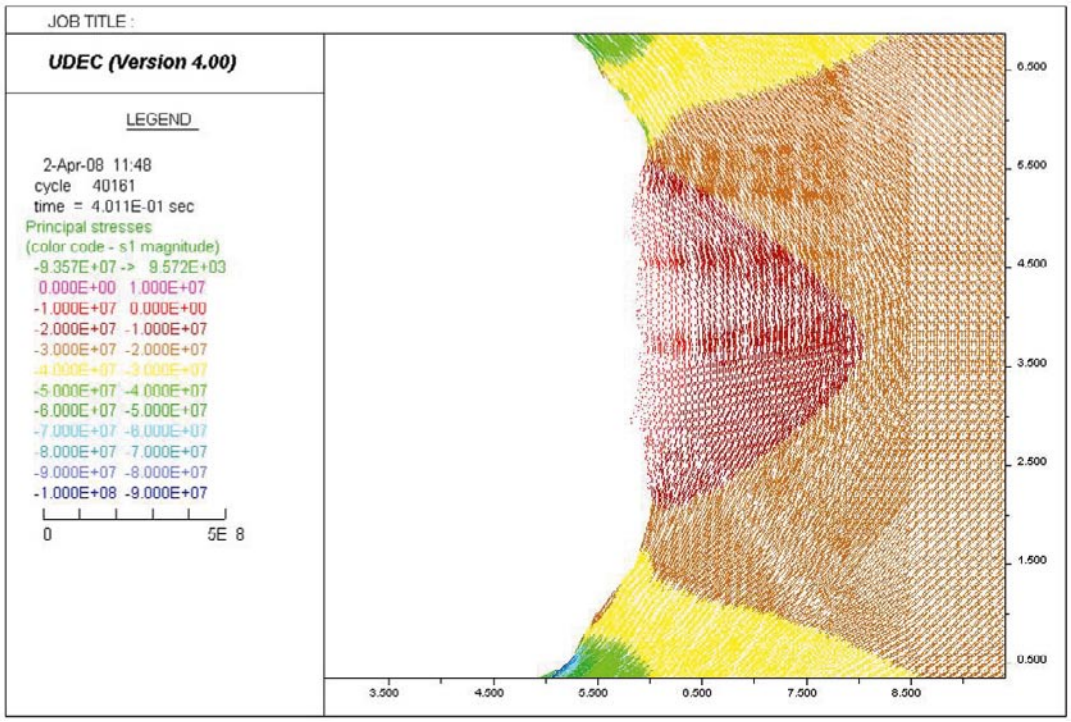

a) Maximum compressive stress = 93.57 MPa

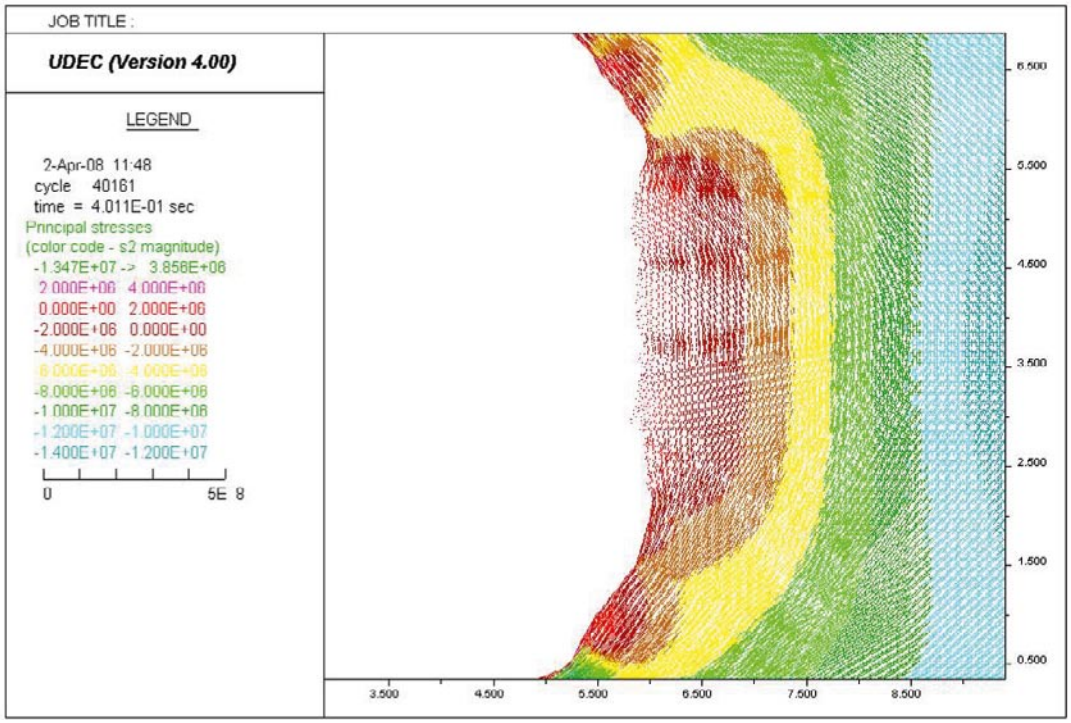

b) Maximum tensile stress = 3.856 MPa

Figure M-29. *Close-up images of the right side wall. Stress tensor plots at a section outside the slot after excavating the bench; Colors by magnitude of a) Sigma 1 and b) Sigma 2. Model with E = 45 GPa, σ1 = 30 MPa, σ1 = 316° (see Table 9-11).*

Outside slot section, as-built tunnel shape

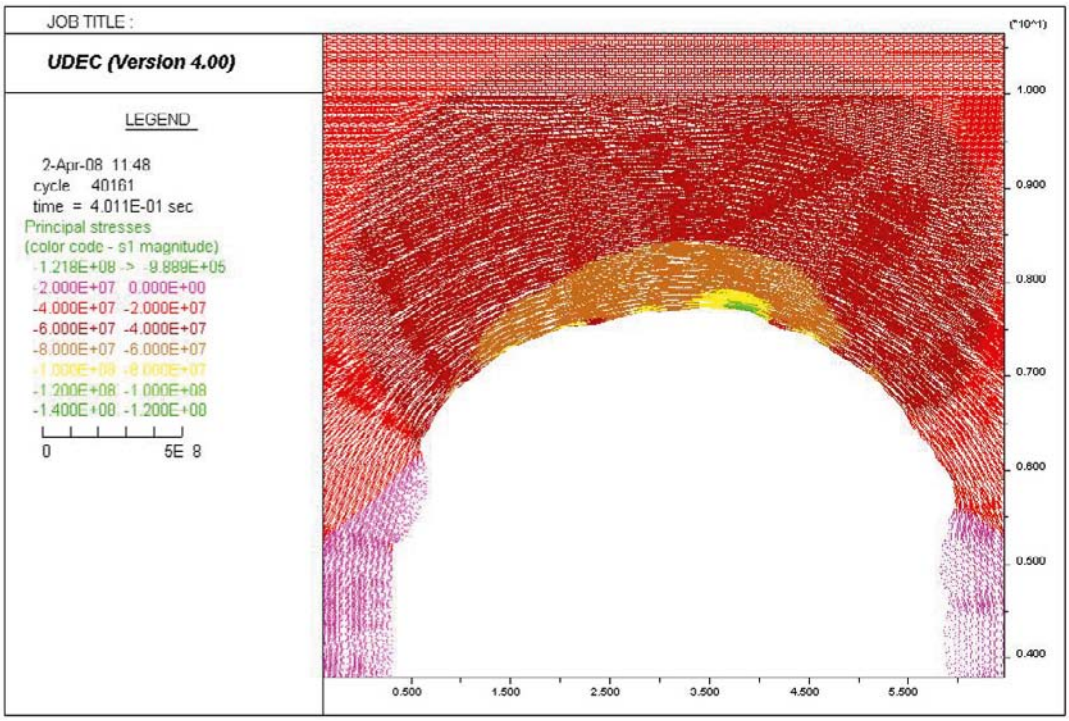

a) Maximum compressive stress = 121.8 MPa

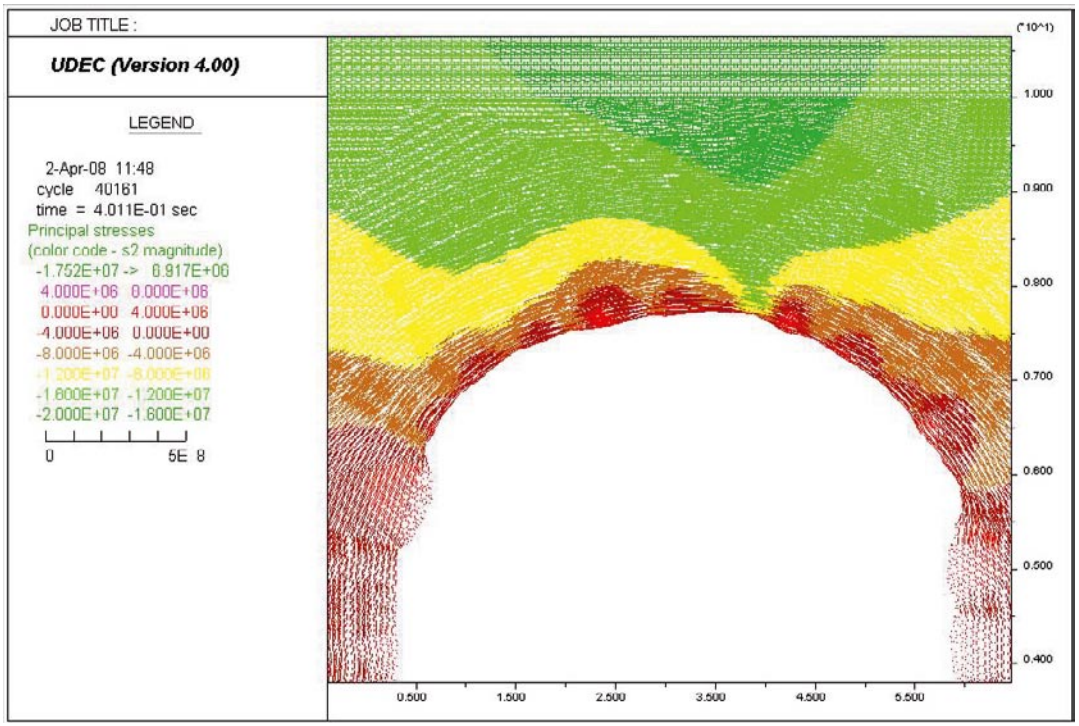

b) Maximum tensile stress = 6.917 MPa

Figure M-30. *Close-up images of the roof. Stress tensor plots at a section outside the slot after excavating the bench; Colors by magnitude of a) Sigma 1 and b) Sigma 2. Model with E = 45 GPa, σ1 = 30 MPa, σ1 = 316° (see Table 9-11).*

Outside slot section, as-built tunnel shape

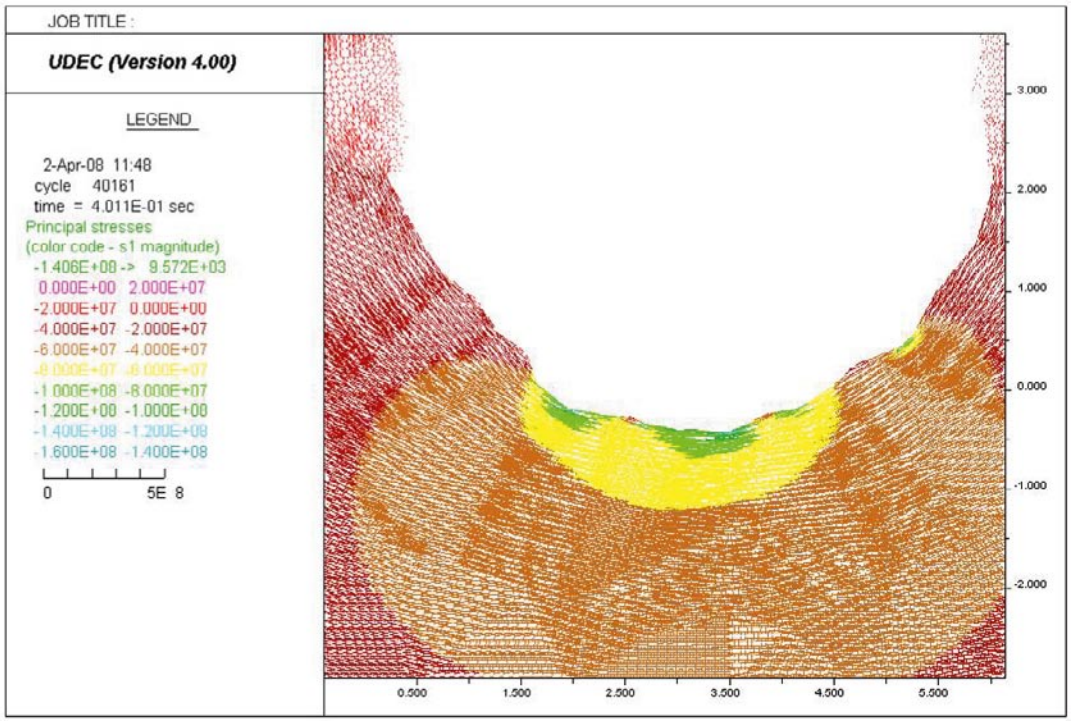

a) Maximum compressive stress = 140.6 MPa

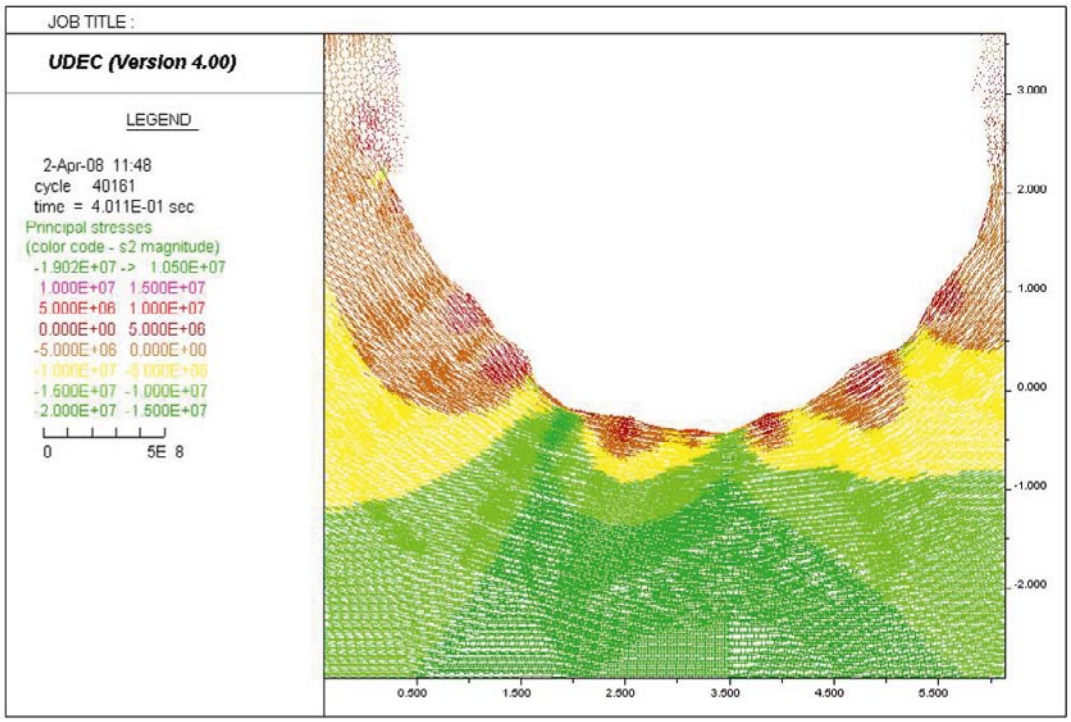

b) Maximum tensile stress = 10.50 MPa

Figure M-31. *Close-up images of the floor. Stress tensor plots at a section outside the slot after excavating the bench; Colors by magnitude of a) Sigma 1 and b) Sigma 2. Model with E = 45 GPa, σ1 = 30 MPa, σ1 = 316° (see Table 9-11).*

Convergence pins section, as-built tunnel shape

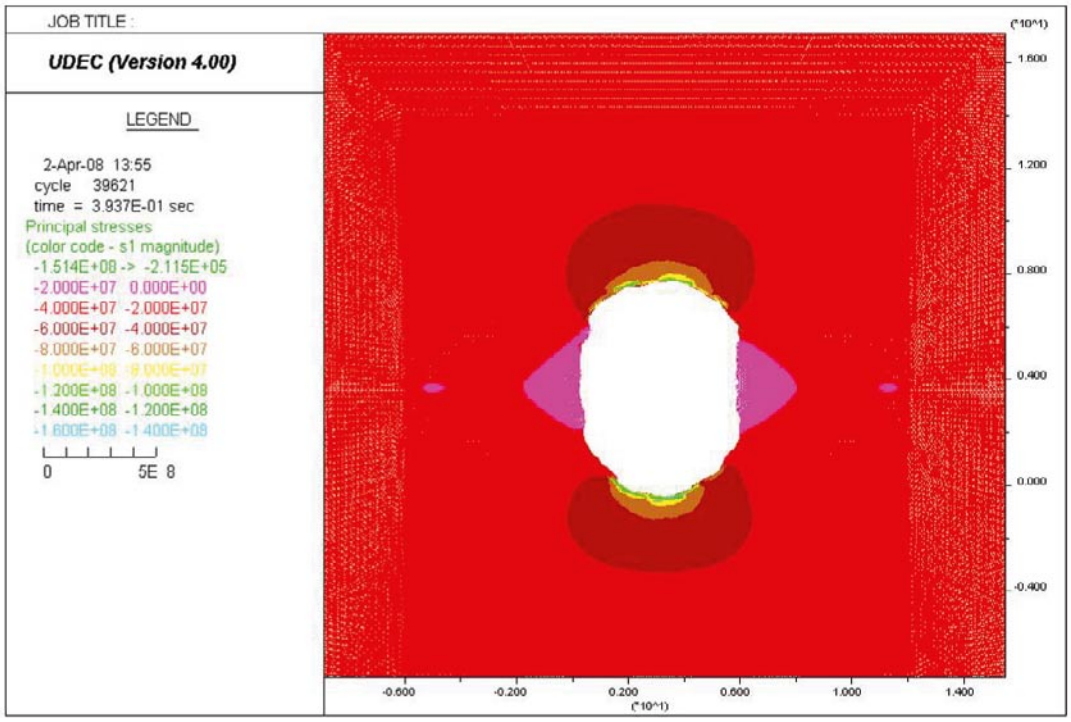

a) Maximum compressive stress = 151.4 MPa

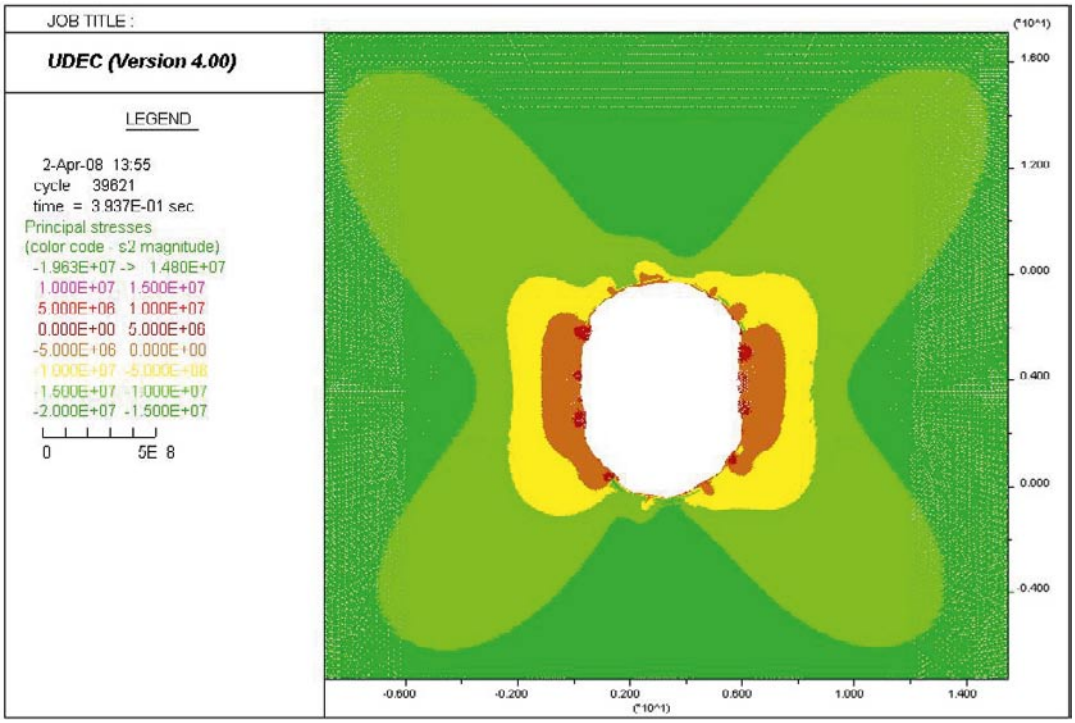

b) Maximum tensile stress = 14.80 MPa

Figure M-32. *Stress tensor plots at the convergence pins section after excavating the bench; Colors by magnitude of a) Sigma 1 and b) Sigma 2. Model with E = 45 GPa, σ1 = 30 MPa, σ1 = 316° (see Table 9-11).*

Convergence pins section, as-built tunnel shape

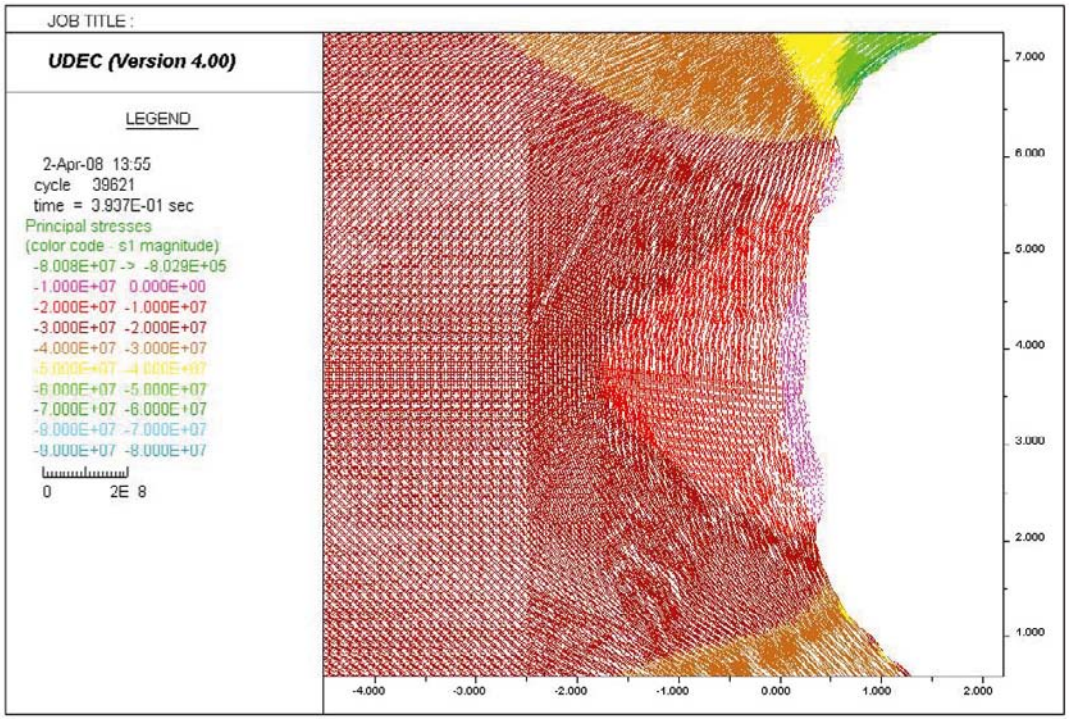

a) Maximum compressive stress = 80.08 MPa

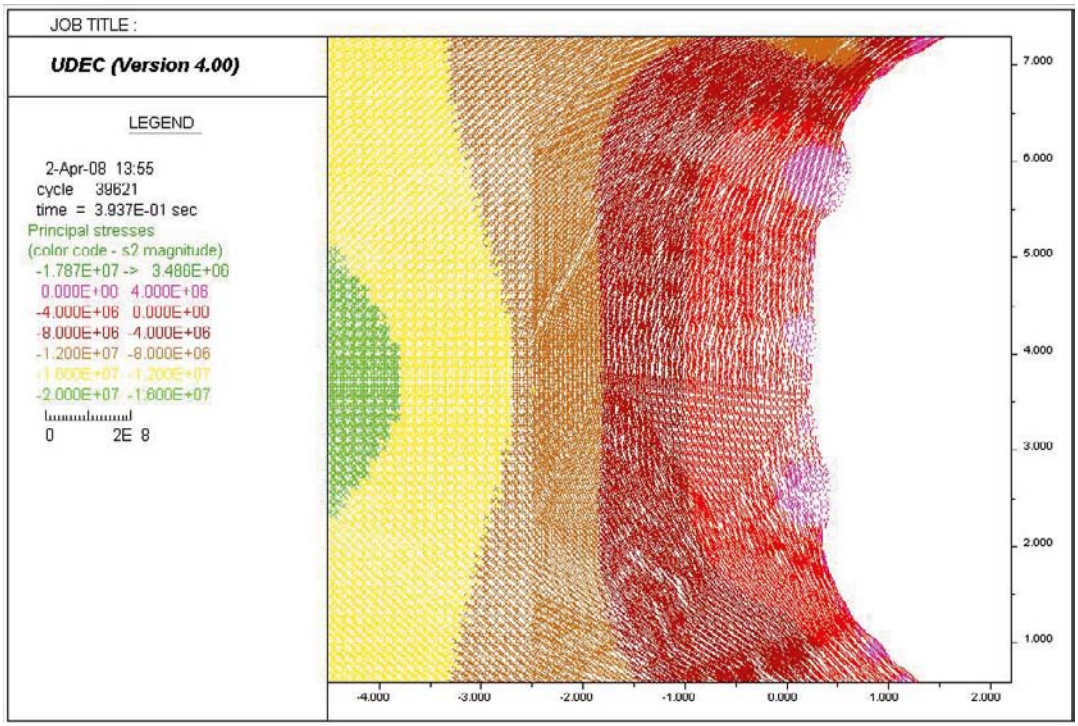

b) Maximum tensile stress = 3.486 MPa

Figure M-33. *Close-up images of the left side wall. Stress tensor plots at the convergence pins section after excavating the bench; Colors by magnitude of a) Sigma 1 and b) Sigma 2. Model with E = 45 GPa, σ1 = 30 MPa, σ1 = 316° (see Table 9-11).*

Convergence pins section, as-built tunnel shape

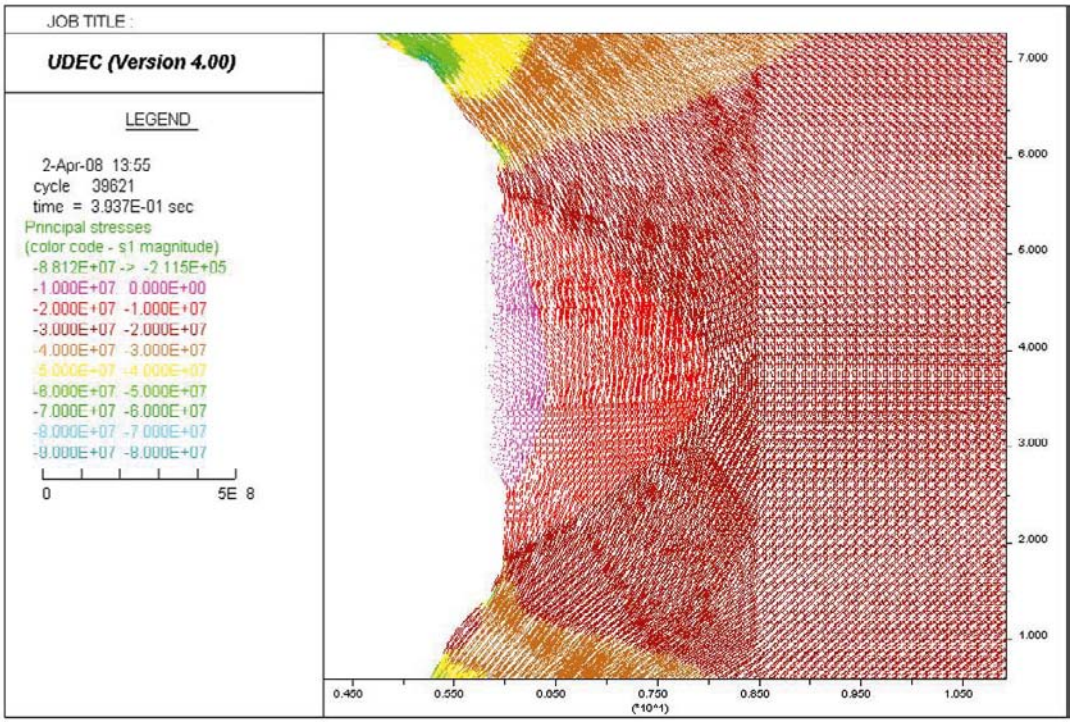

a) Maximum compressive stress = 88.12 MPa

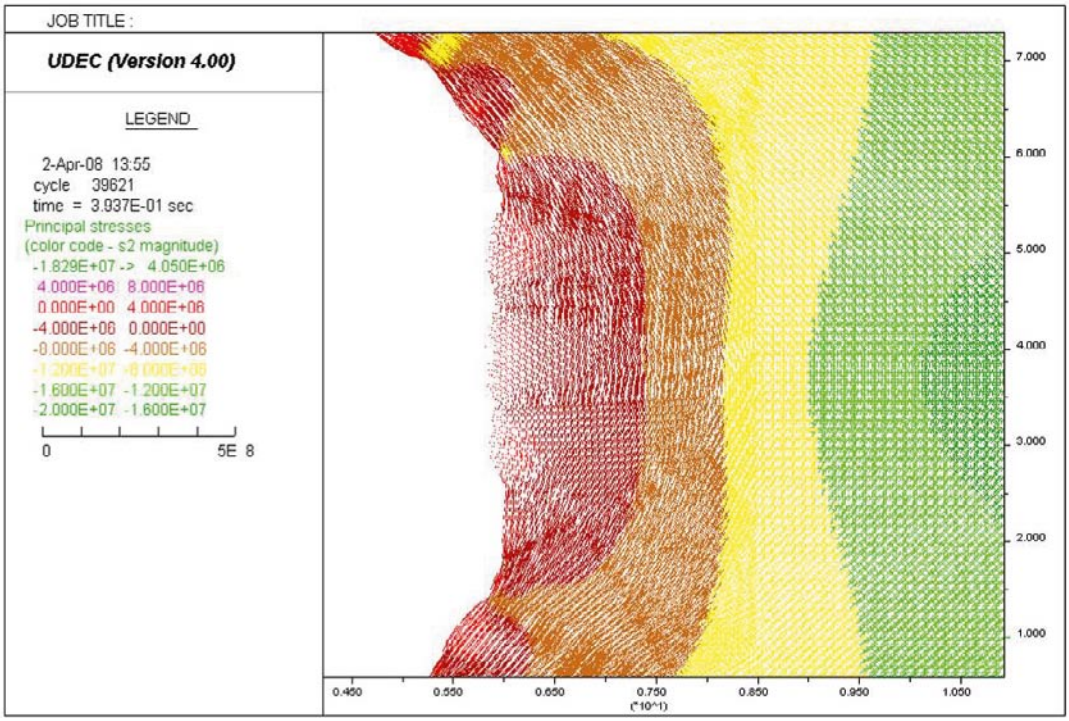

b) Maximum tensile stress = 4.050 MPa

Figure M-34. *Close-up images of the right side wall. Stress tensor plots at the convergence pins section after excavating the bench; Colors by magnitude of a) Sigma 1 and b) Sigma 2. Model with E = 45 GPa, σ1 = 30 MPa, σ1 = 316° (see Table 9-11).*

Convergence pins section, as-built tunnel shape

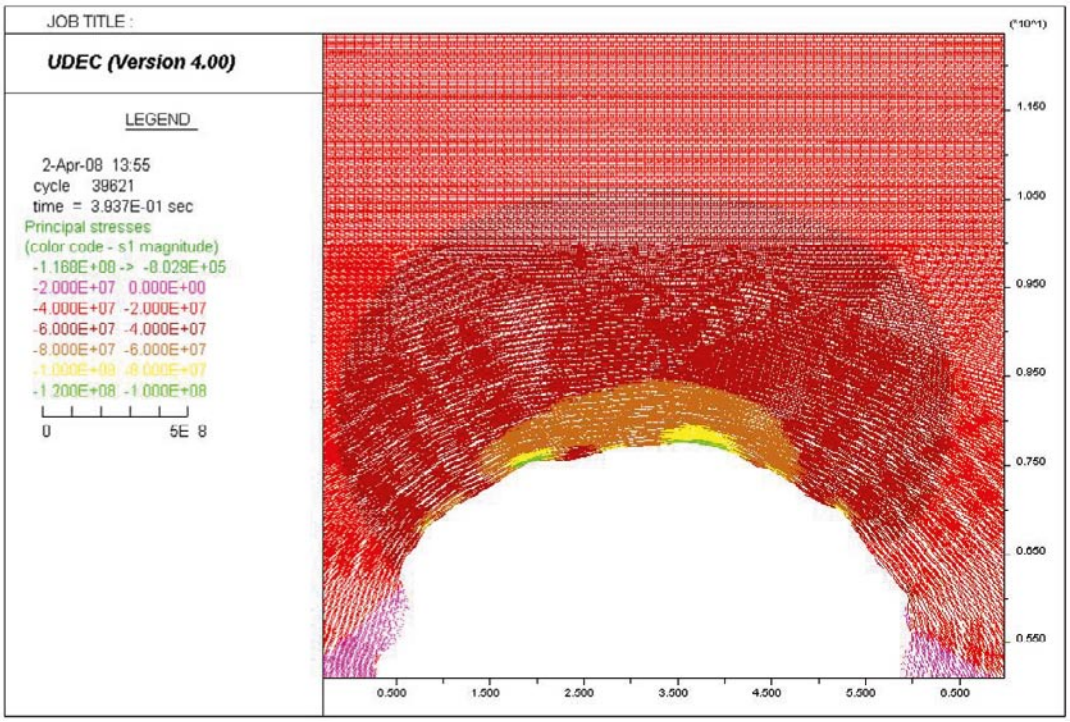

a) Maximum compressive stress = 116.8 MPa

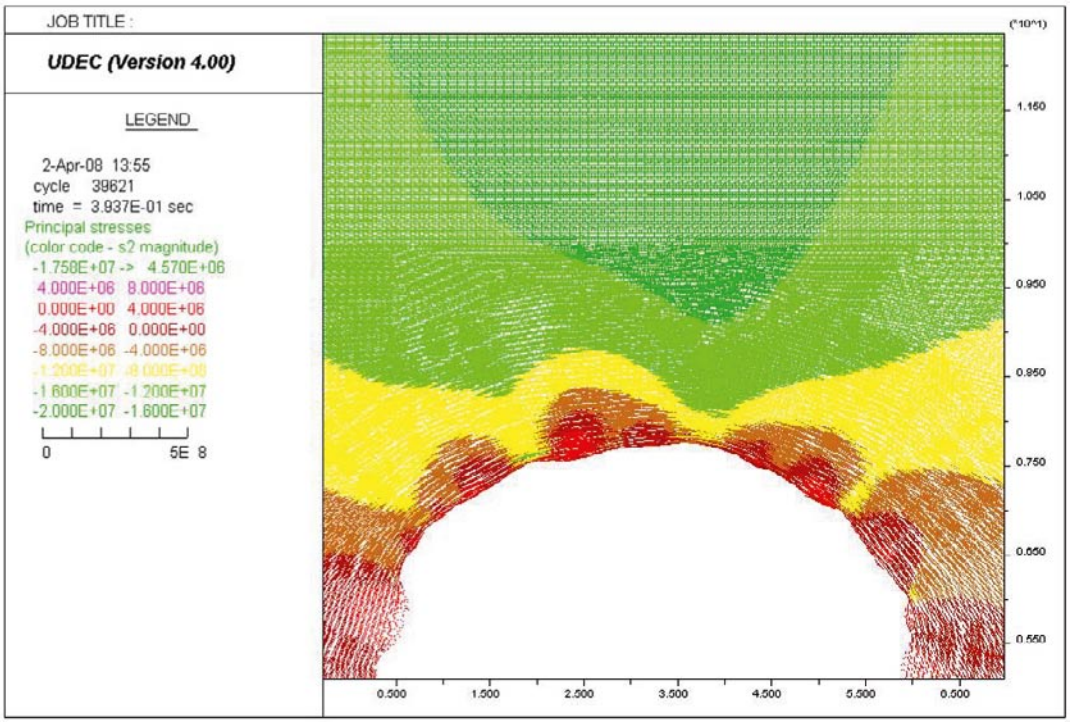

b) Maximum tensile stress = 4.570 MPa

Figure M-35. *Close-up images of the roof. Stress tensor plots at the convergence pins section after excavating the bench; Colors by magnitude of a) Sigma 1 and b) Sigma 2. Model with E = 45 GPa, σ1 = 30 MPa, σ1 = 316° (see Table 9-11).*

Convergence pins section, as-built tunnel shape

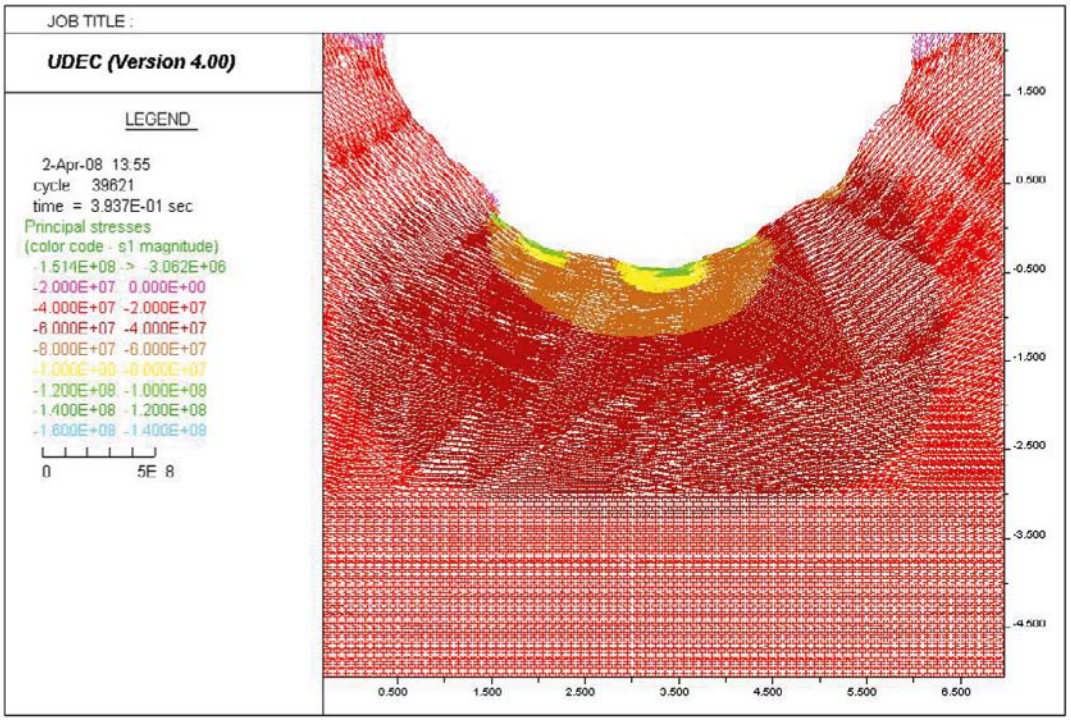

a) Maximum compressive stress = 151.4 MPa

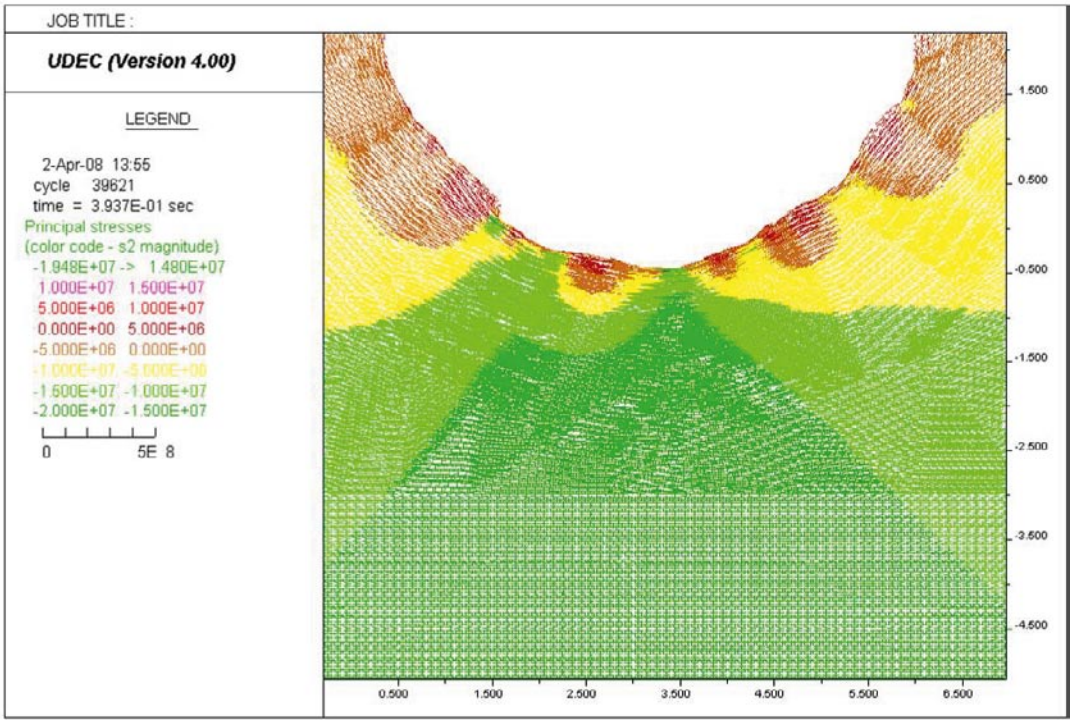

b) Maximum tensile stress = 14.80 MPa

Figure M-36. *Close-up images of the floor. Stress tensor plots at the convergence pins section after excavating the bench; Colors by magnitude of a) Sigma 1 and b) Sigma 2. Model with E = 45 GPa, σ_1 = 30 MPa, σ_1 = 316° (see Table 9-11).*

Stress tensor plots of the TASQ tunnel in 3 different sections (BGR, outside slot and convergence pins) with the as-built tunnel shape and the as-planned tunnel shape case after excavating the heading (E = 65 GPa, σ_1 = 25 MPa, σ_1 = 316°).

As-planned tunnel shape

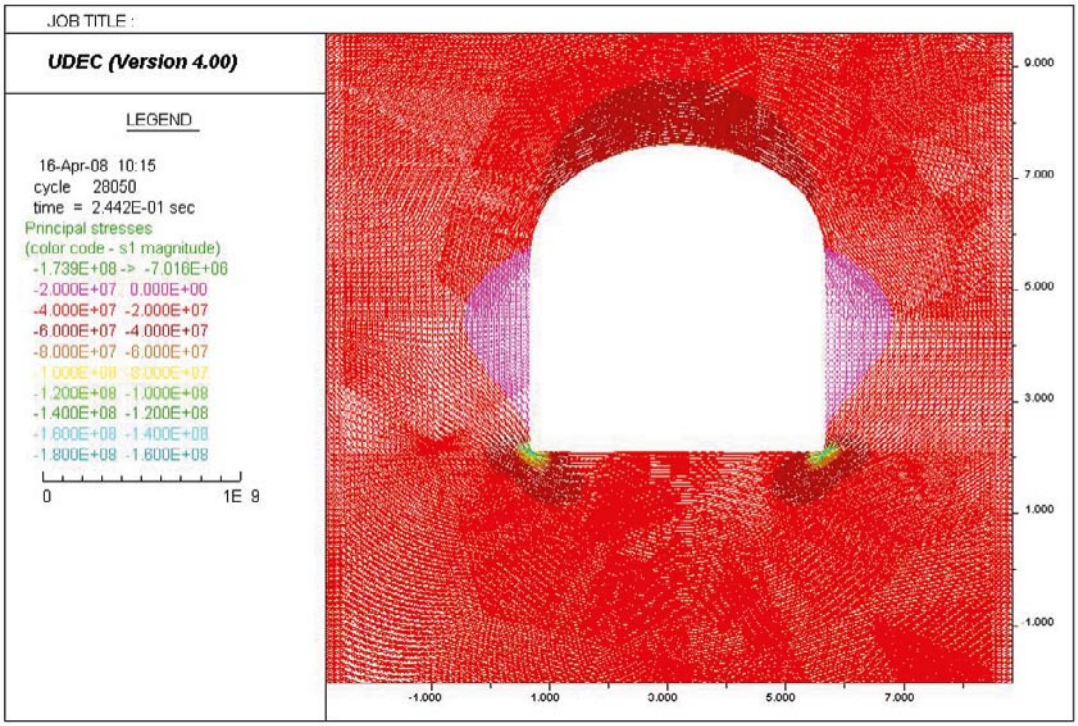

a) Maximum compressive stress = 173.9 MPa

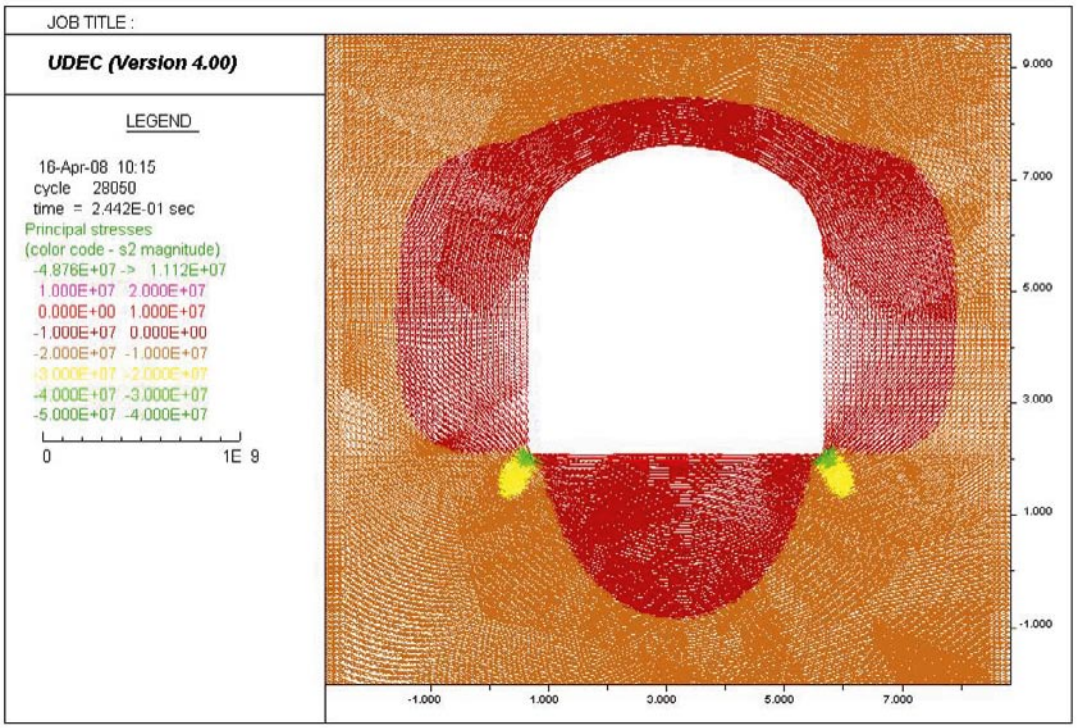

b) Maximum tensile stress = 11.12 MPa

Figure M-37. *Stress tensor plots of the as-planned tunnel shape after excavating the heading; Colors by magnitude of a) Sigma 1 and b) Sigma 2. Model with E = 65 GPa, σ_1 = 25 MPa, σ_1 = 316° (see Table 9-11).*

As-planned tunnel shape

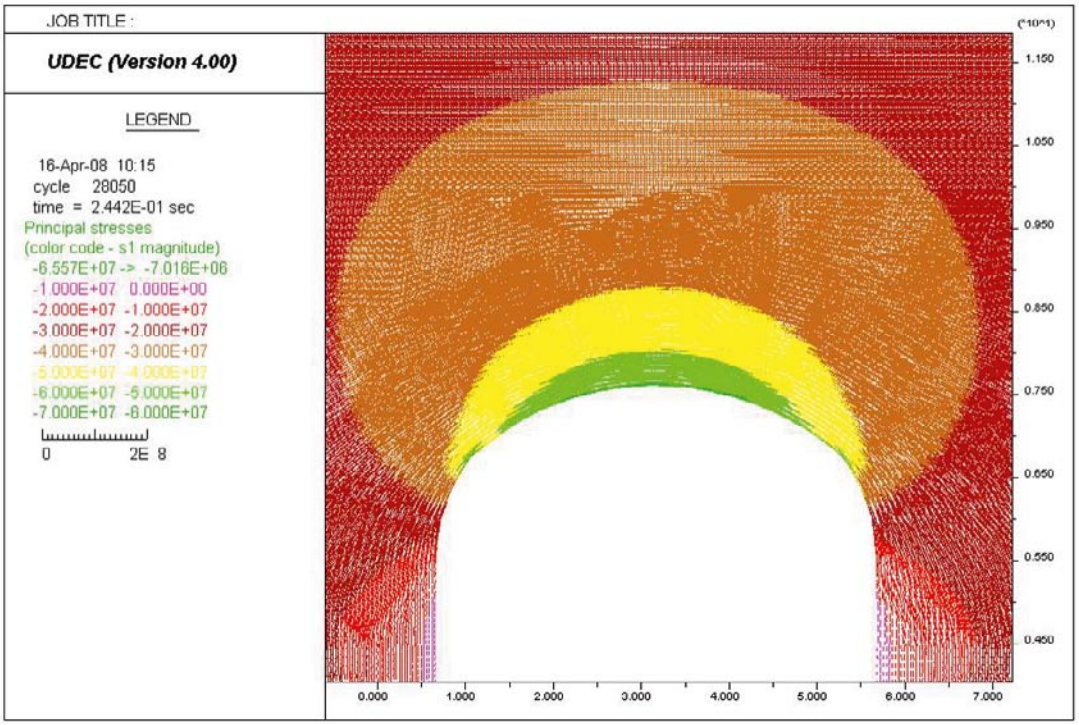

a) Maximum compressive stress = 65.57 MPa

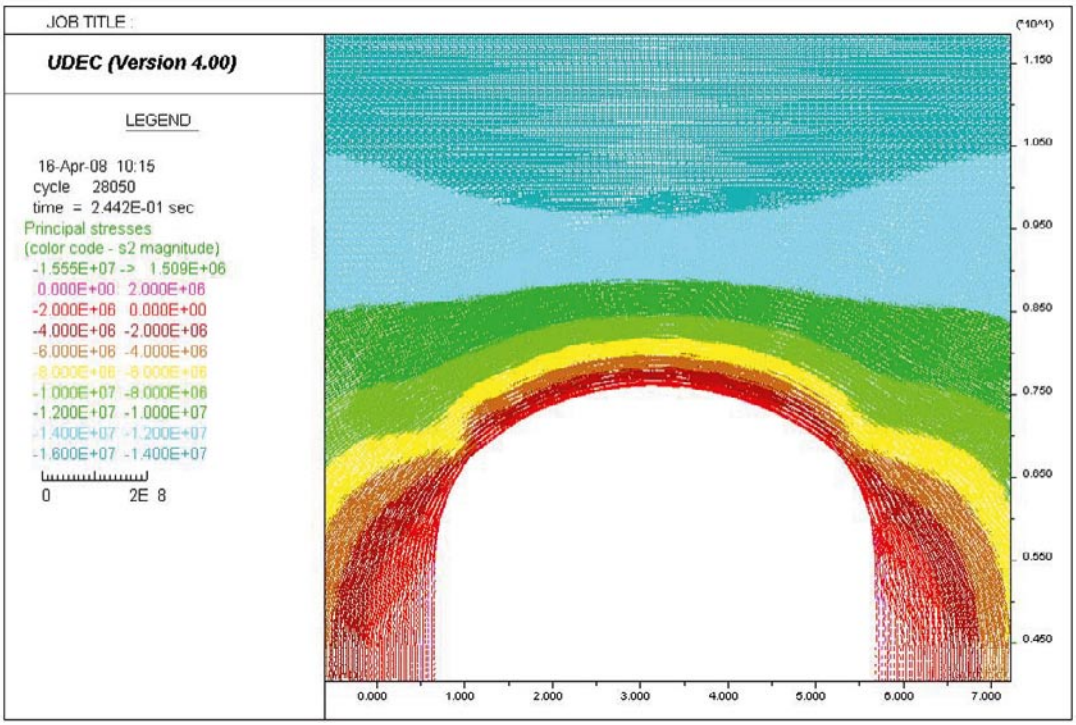

b) Maximum tensile stress = 1.509 MPa

Figure M-38. *Close-up images of the roof. Stress tensor plots of the as-planned tunnel shape after excavating the heading; Colors by magnitude of a) Sigma 1 and b) Sigma 2. Model with E = 65 GPa, σ_1 = 25 MPa, σ_1 = 316° (see Table 9-11).*

As-planned tunnel shape

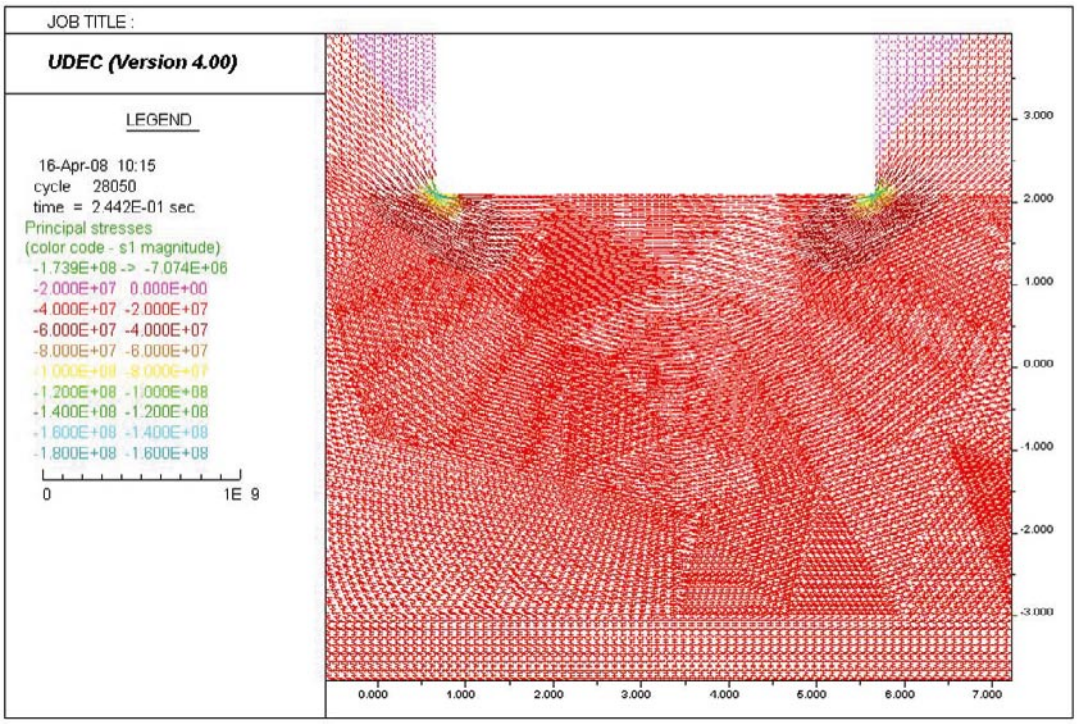

a) Maximum compressive stress = 173.9 MPa

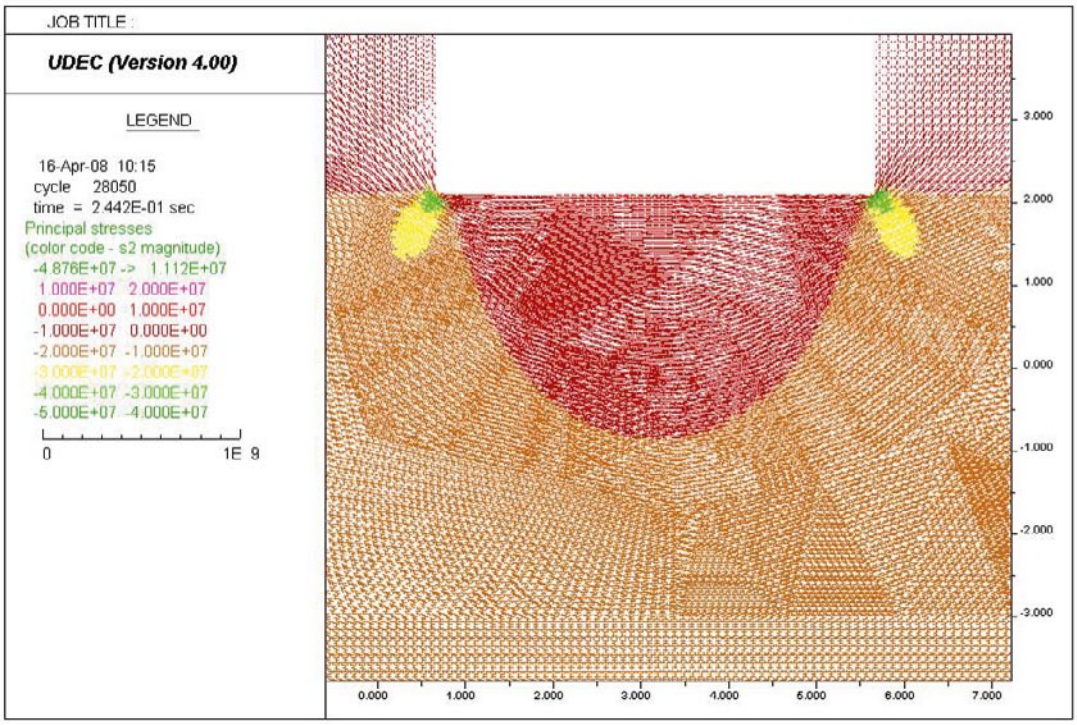

b) Maximum tensile stress = 11.12 MPa

Figure M-39. *Close-up images of the floor. Stress tensor plots of the as-planned tunnel shape after excavating the heading; Colors by magnitude of a) Sigma 1 and b) Sigma 2. Model with E = 65 GPa, σ_1 = 25 MPa, σ_1 = 316° (see Table 9-11).*

BGR section, as-built tunnel shape

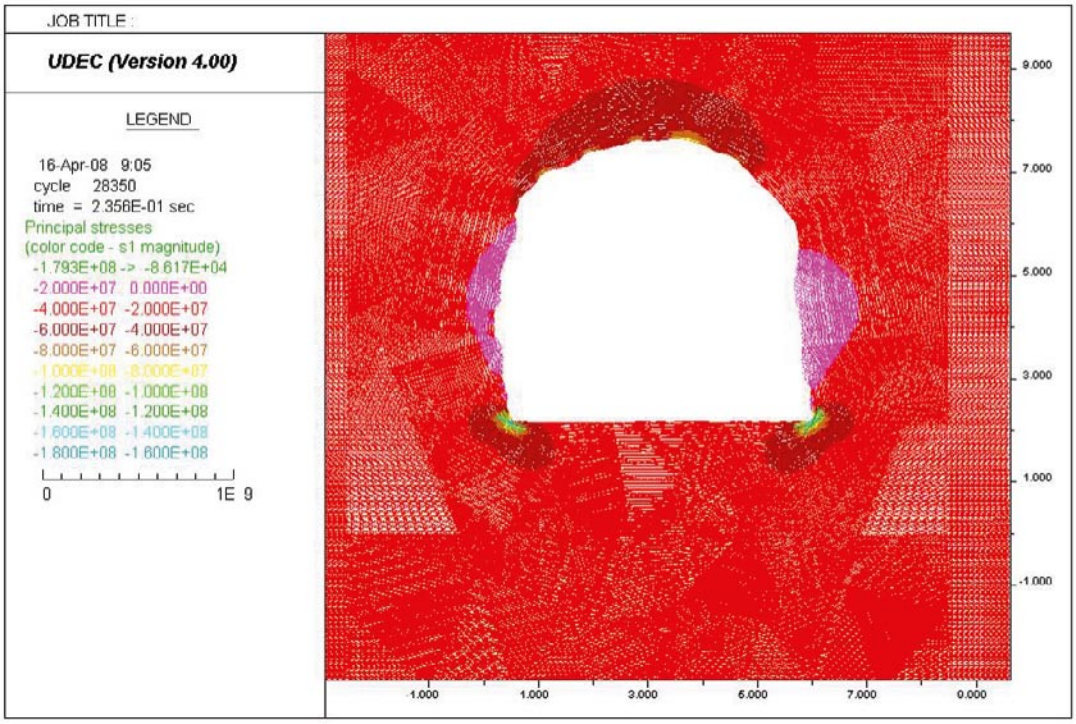

a) Maximum Compressive stress = 179.3 MPa

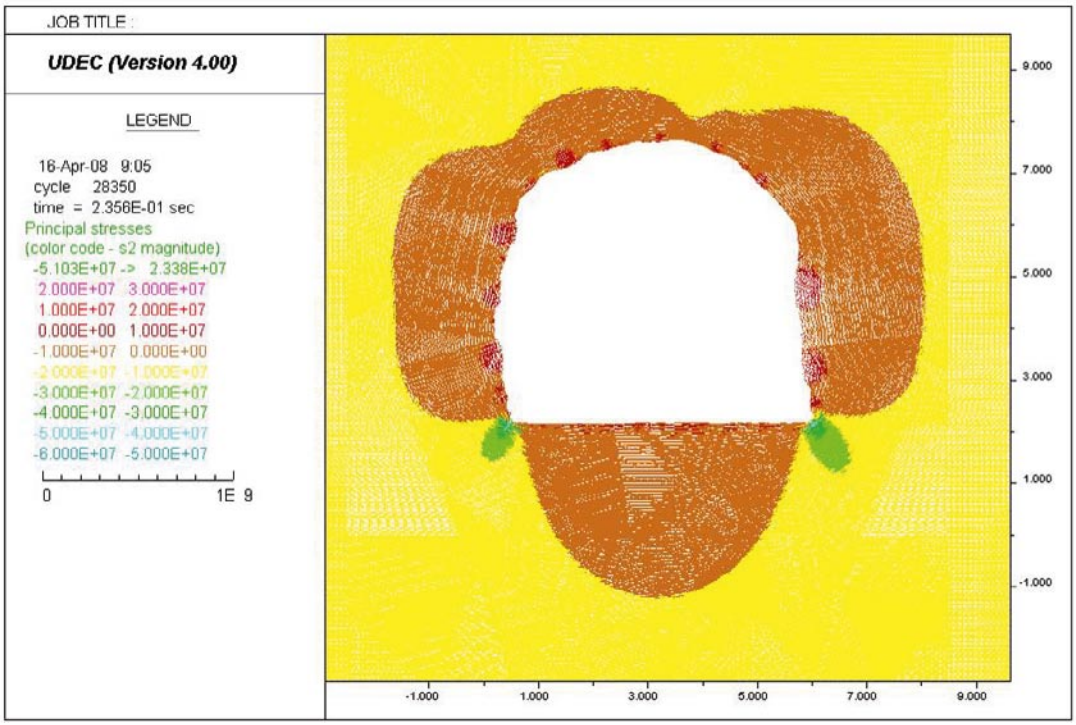

b) Maximum Tensile stress = 23.38 MPa

Figure M-40. *Stress tensor plots at the BGR section after excavating the heading; Colors by magnitude of a) Sigma 1 and b) Sigma 2. Model with E = 65 GPa,* σ_1 *= 25 MPa,* σ_1 *= 316° (see Table 9-11).*

BGR section, as-built tunnel shape

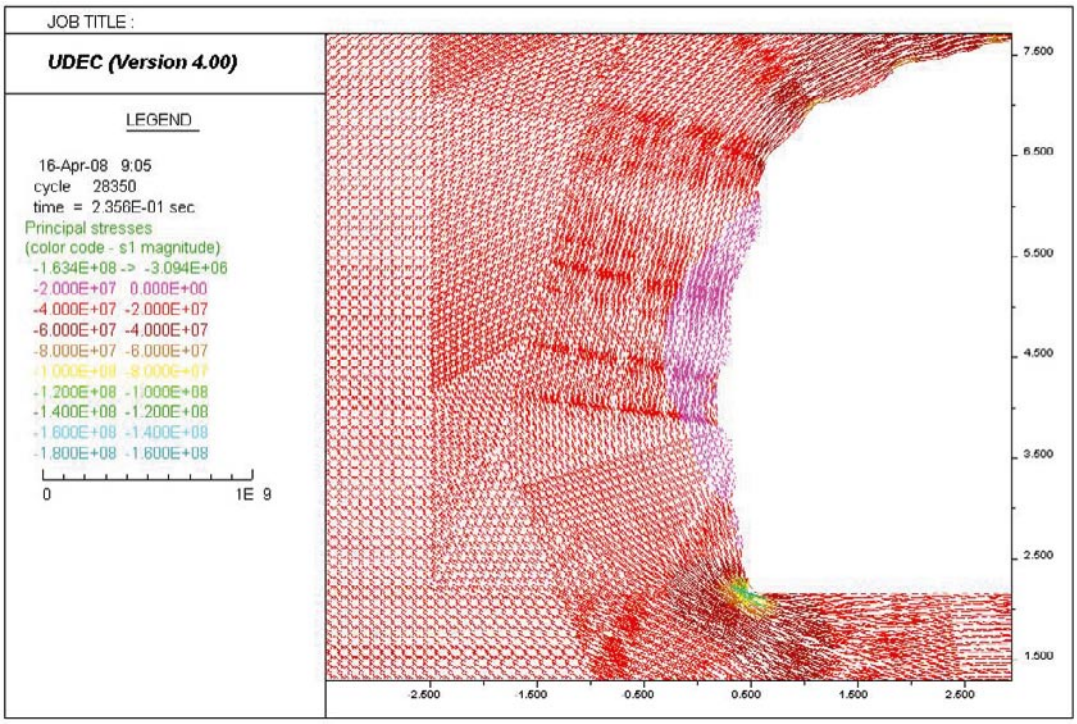

a) Maximum Compressive stress = 163.4 MPa

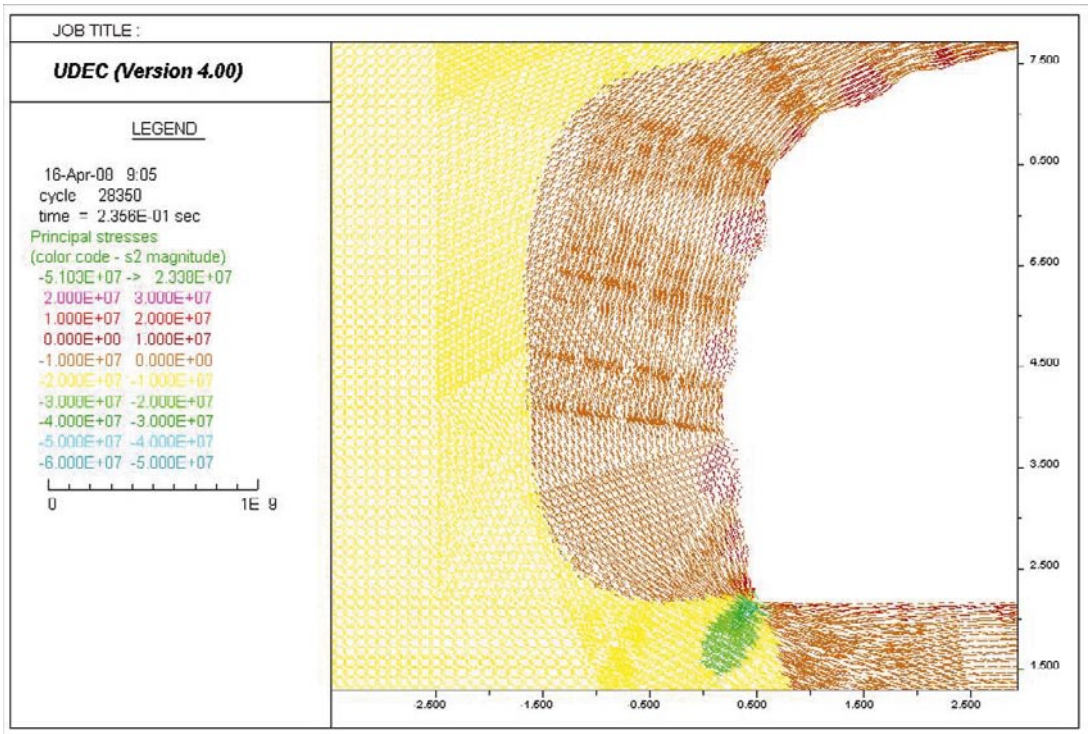

b) Maximum Tensile stress = 23.38 MPa

Figure M-41. *Close-up images of the left side wall. Stress tensor plots at the BGR section after excavating the heading; Colors by magnitude of a) Sigma 1 and b) Sigma 2. Model with E = 65 GPa, σ_1 = 25 MPa, σ_1 = 316° (see Table 9-11).*

BGR section, as-built tunnel shape

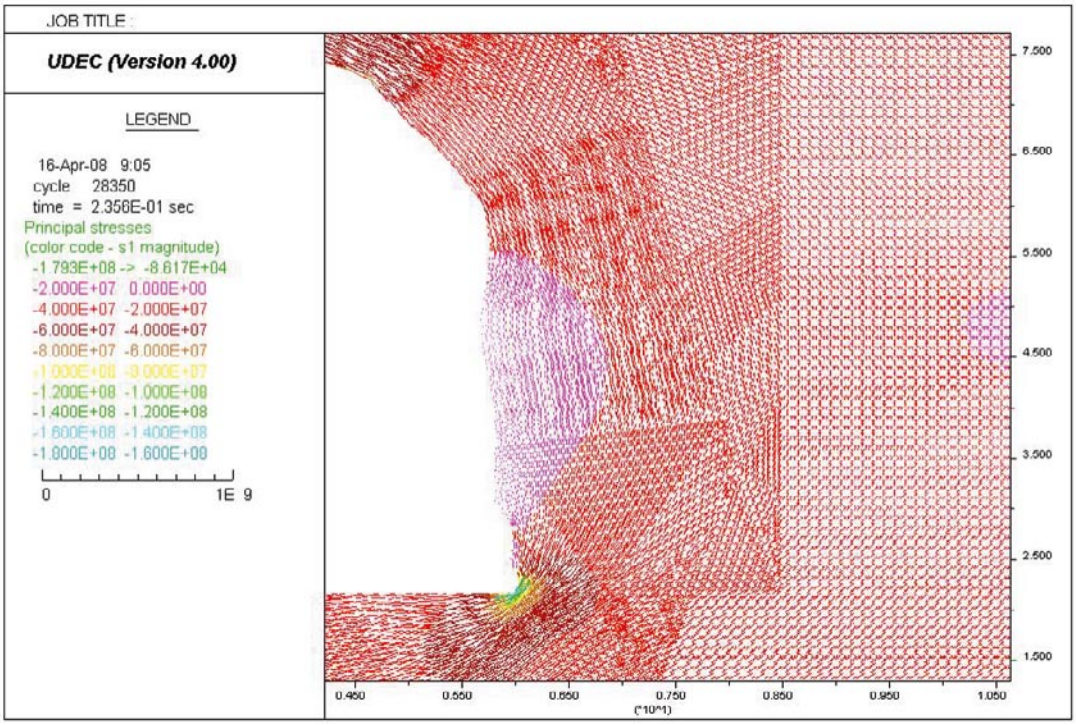

a) Maximum Compressive stress = 179.3 MPa

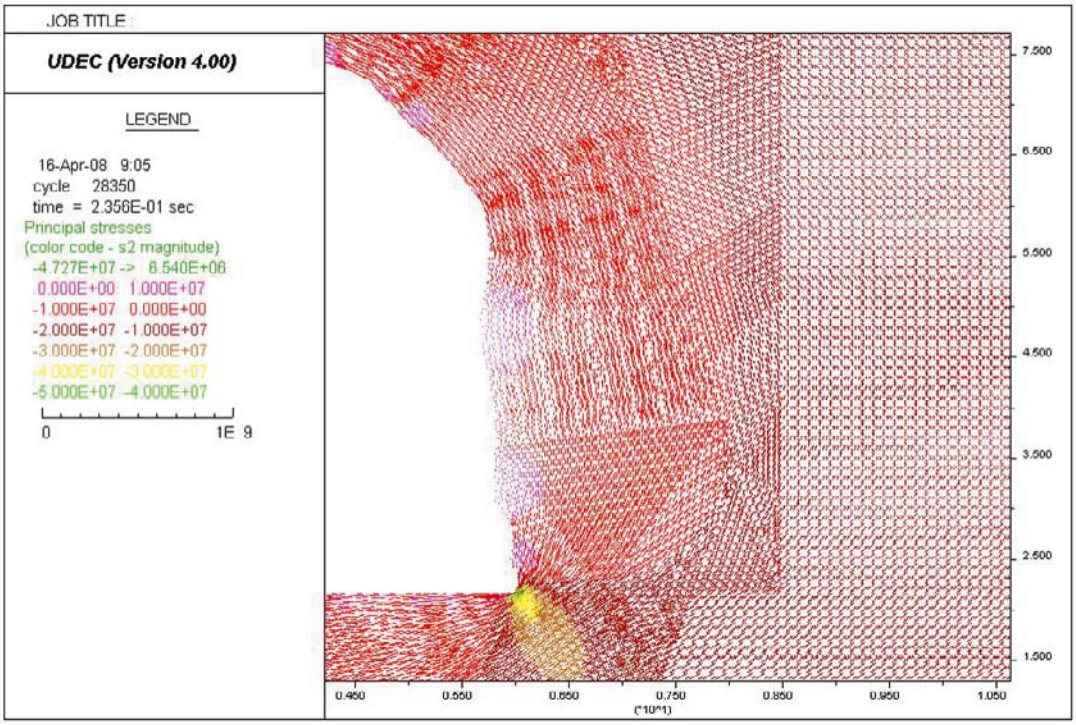

b) Maximum Tensile stress = 6.540 MPa

Figure M-42. *Close-up images of the right side wall. Stress tensor plots at the BGR section after excavating the heading; Colors by magnitude of a) Sigma 1 and b) Sigma 2. Model with E = 65 GPa, σ_1 = 25 MPa, σ_1 = 316° (see Table 9-11).*

BGR section, as-built tunnel shape

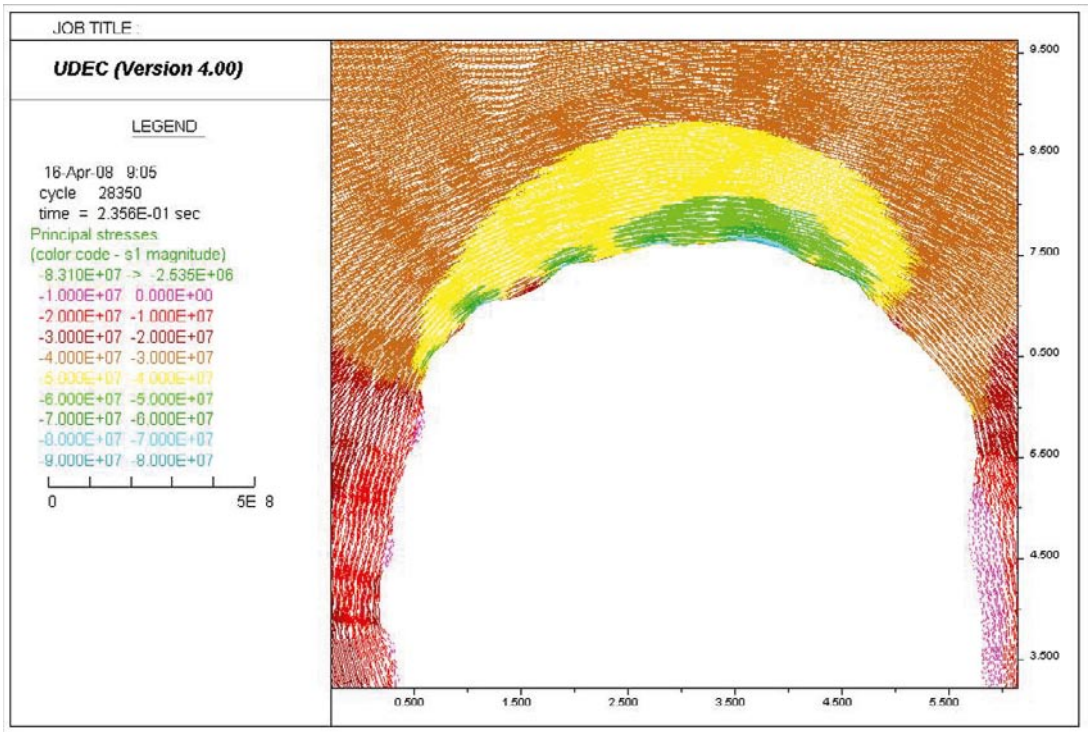

a) Maximum Compressive stress = 83.10 MPa

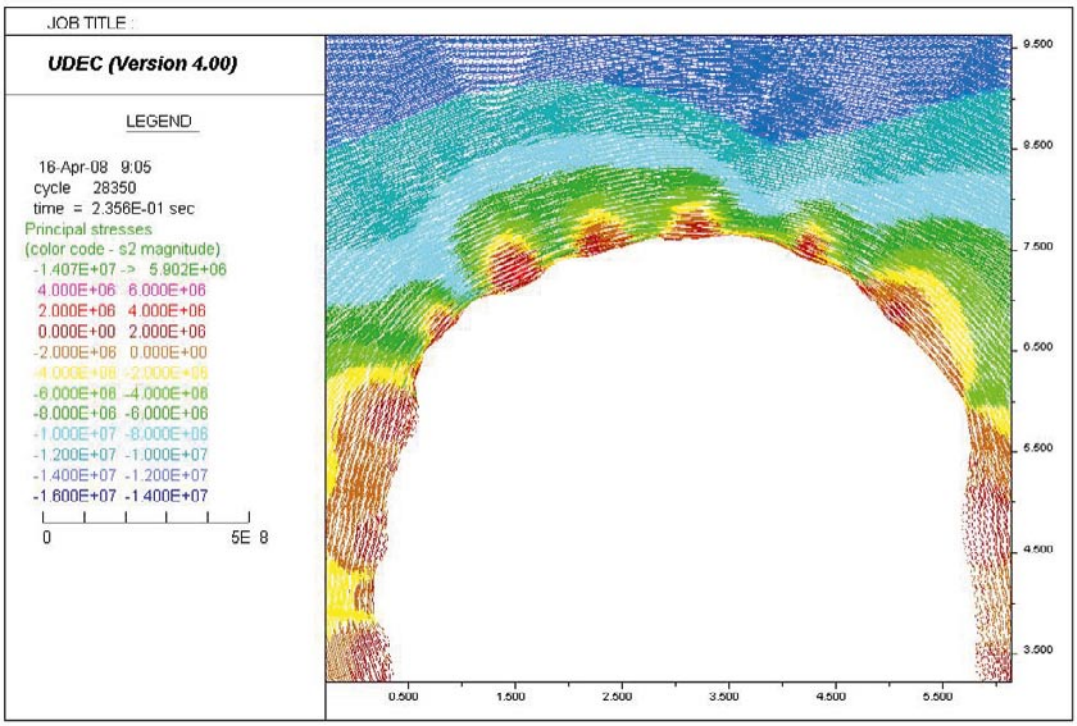

b) Maximum Tensile stress = 5.902 MPa

Figure M-43. *Close-up images of the roof. Stress tensor plots at the BGR section after excavating the heading; Colors by magnitude of a) Sigma 1 and b) Sigma 2. Model with E = 65 GPa, σ_1 = 25 MPa, σ_1 = 316° (see Table 9-11).*

BGR section, as-built tunnel shape

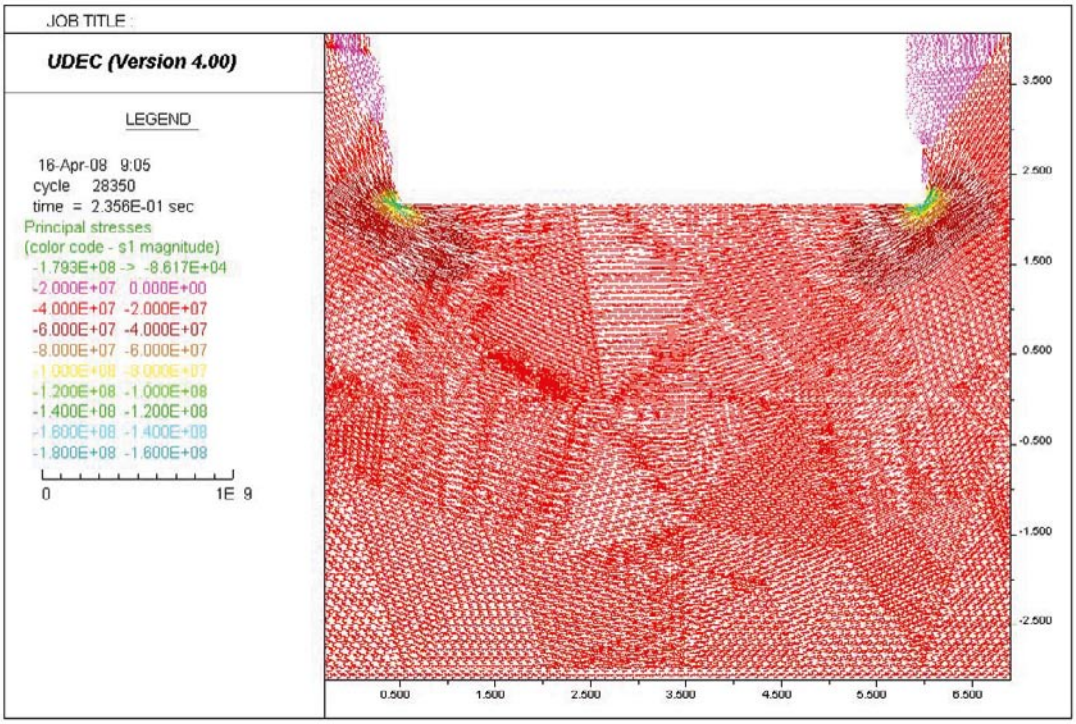

a) Maximum Compressive stress = 179.3 MPa

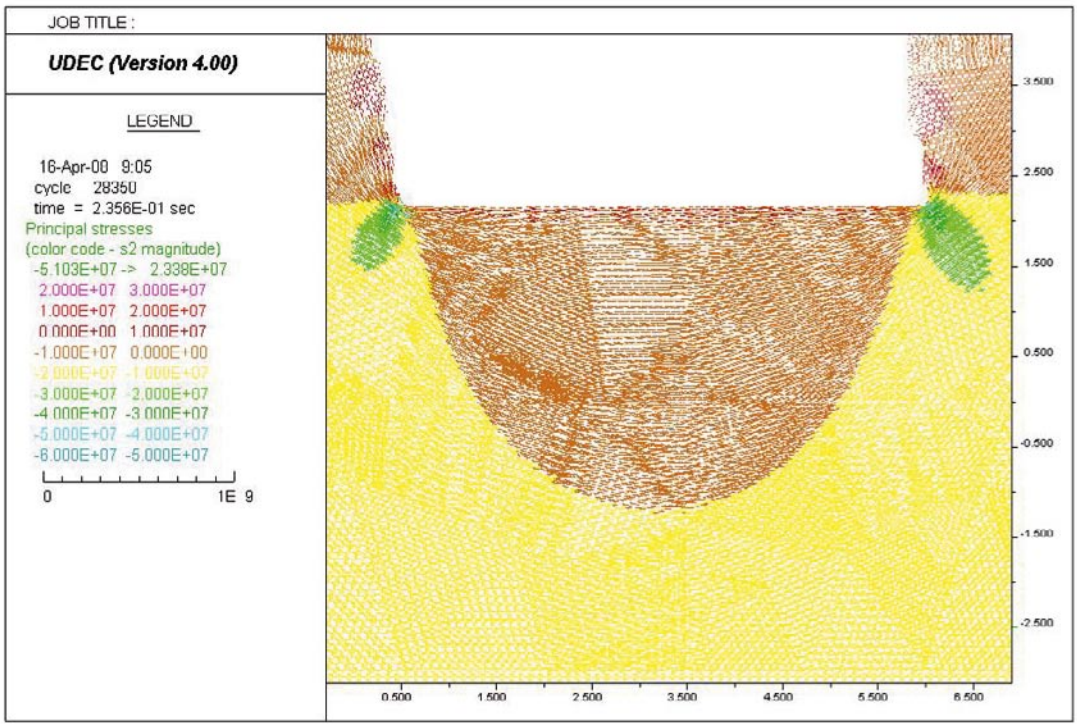

b) Maximum Tensile stress = 23.38 MPa

Figure M-44. *Close-up images of the floor. Stress tensor plots at the BGR section after excavating the heading; Colors by magnitude of a) Sigma 1 and b) Sigma 2. Model with E = 65 GPa, σ_1 = 25 MPa, σ_1 = 316° (see Table 9-11).*

Outside slot section, as-built tunnel shape

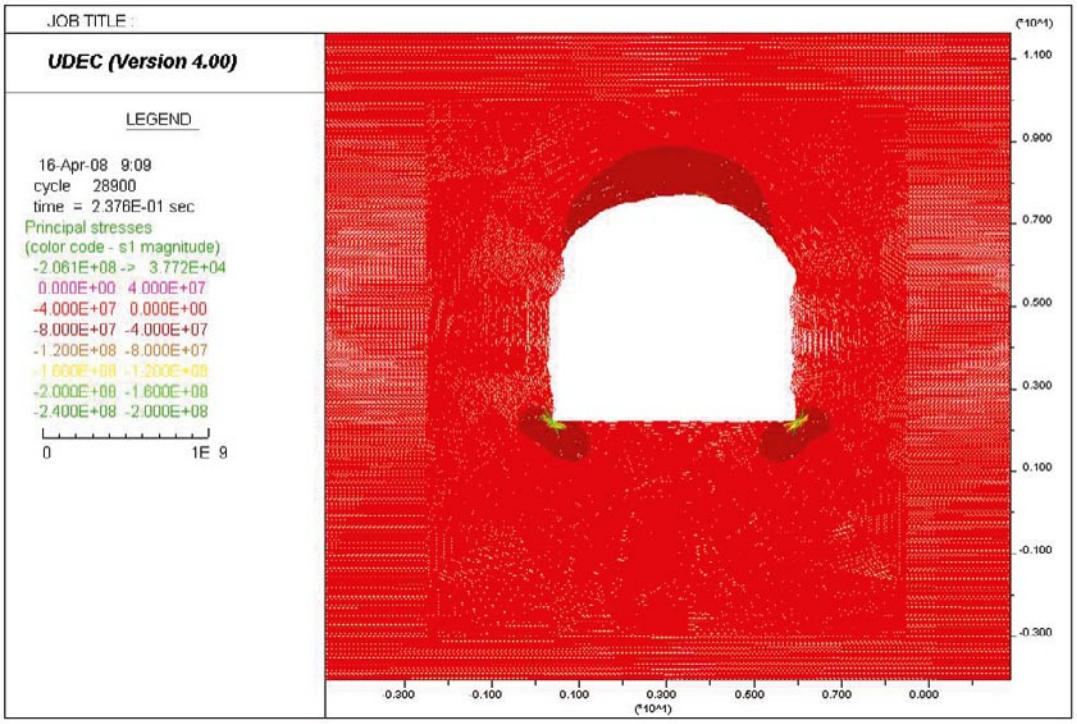

a) Maximum compressive stress = 206.1 MPa

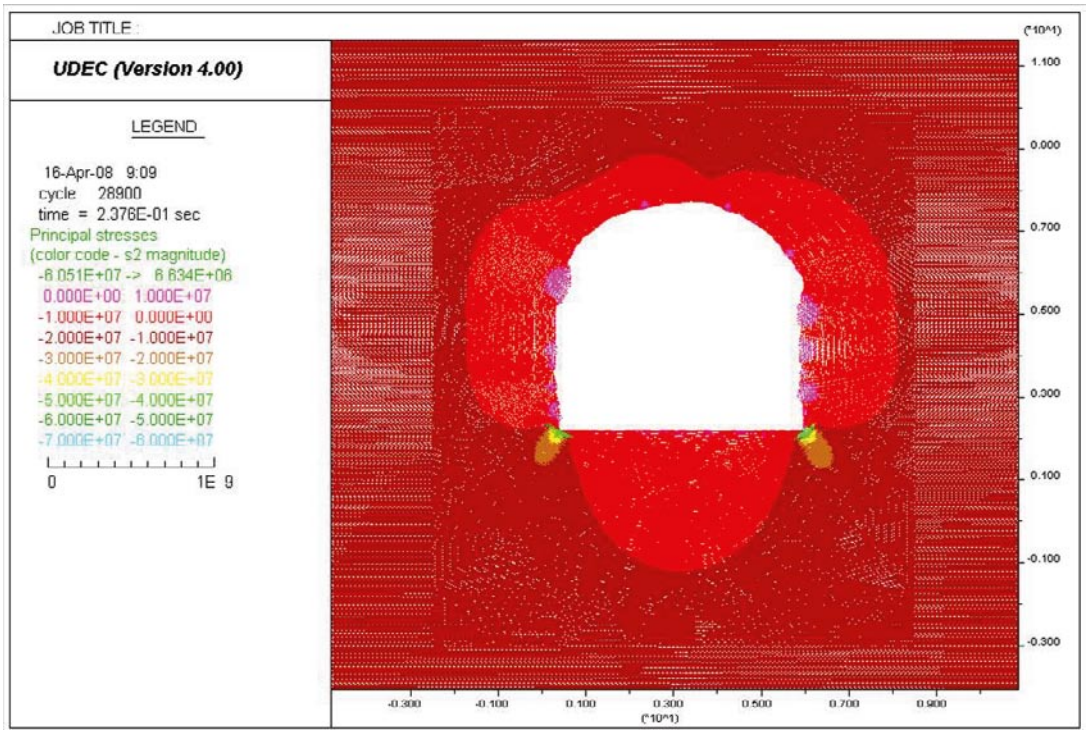

b) Maximum tensile stress = 6.634 MPa

Figure M-45. *Stress tensor plots at a section outside the slot after excavating the heading; Colors by magnitude of a) Sigma 1 and b) Sigma 2. Model with E = 65 GPa, σ_1 = 25 MPa, σ_1 = 316° (see Table 9-11).*

Outside slot section, as-built tunnel shape

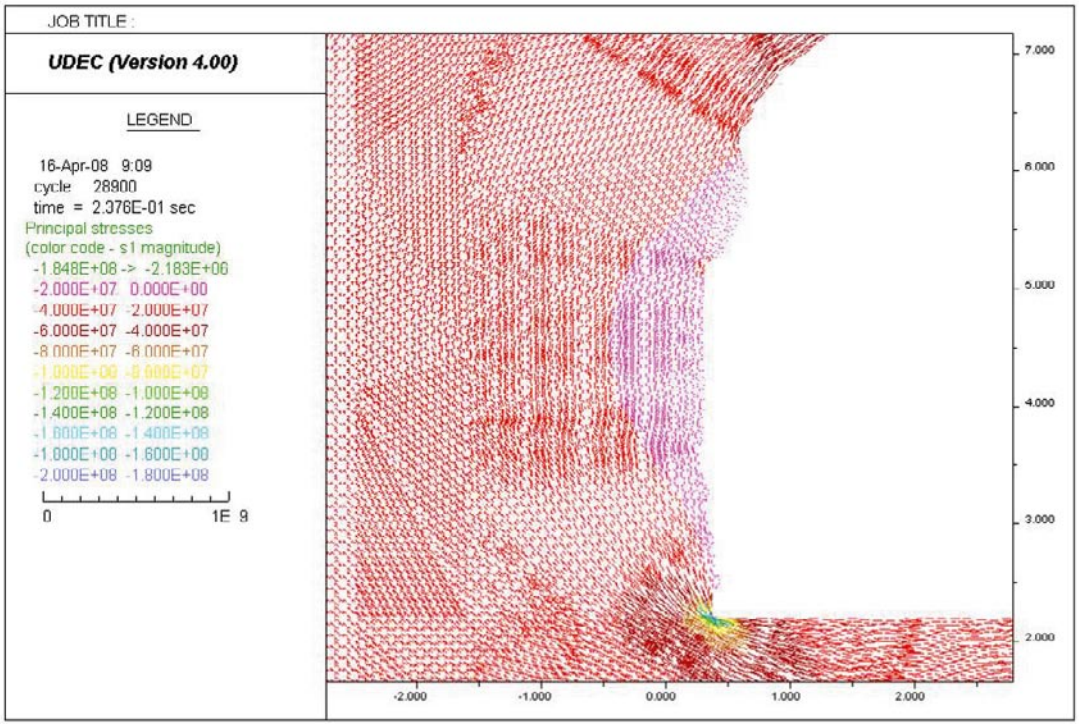

a) Maximum compressive stress = 184.8 MPa

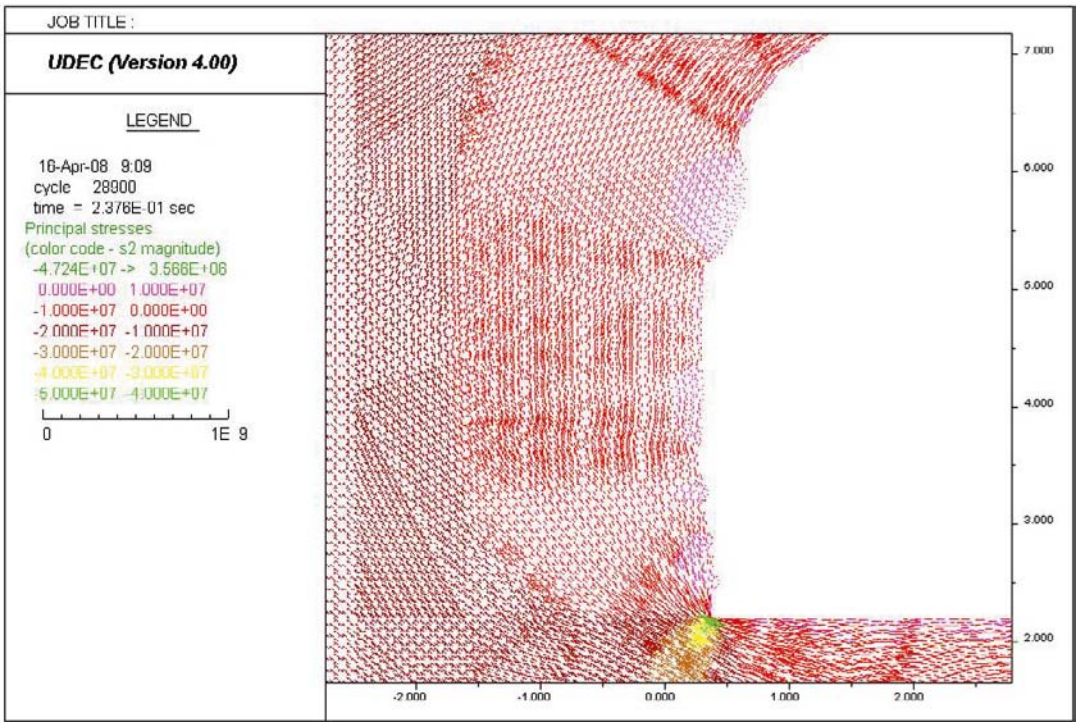

b) Maximum tensile stress = 3.566 MPa

Figure M-46. *Close-up images of the left side wall. Stress tensor plots at a section outside the slot after excavating the heading; Colors by magnitude of a) Sigma 1 and b) Sigma 2. Model with E = 65 GPa, σ_1 = 25 MPa, σ_1 = 316° (see Table 9-11).*

Outside slot section, as-built tunnel shape

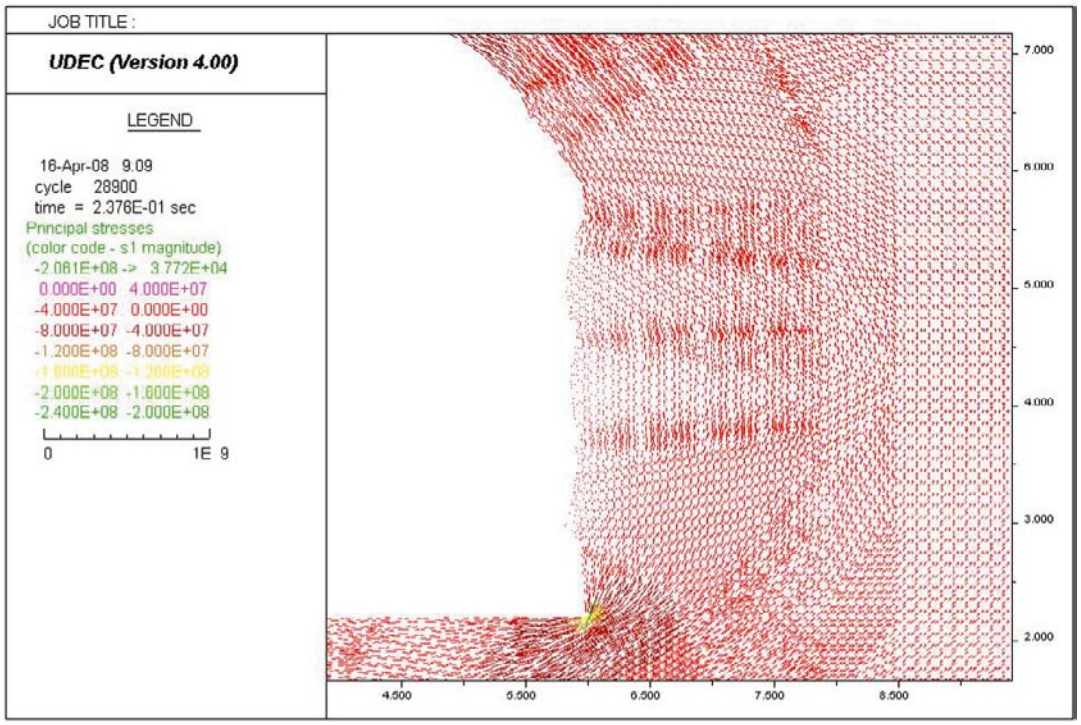

a) Maximum compressive stress = 206.1 MPa

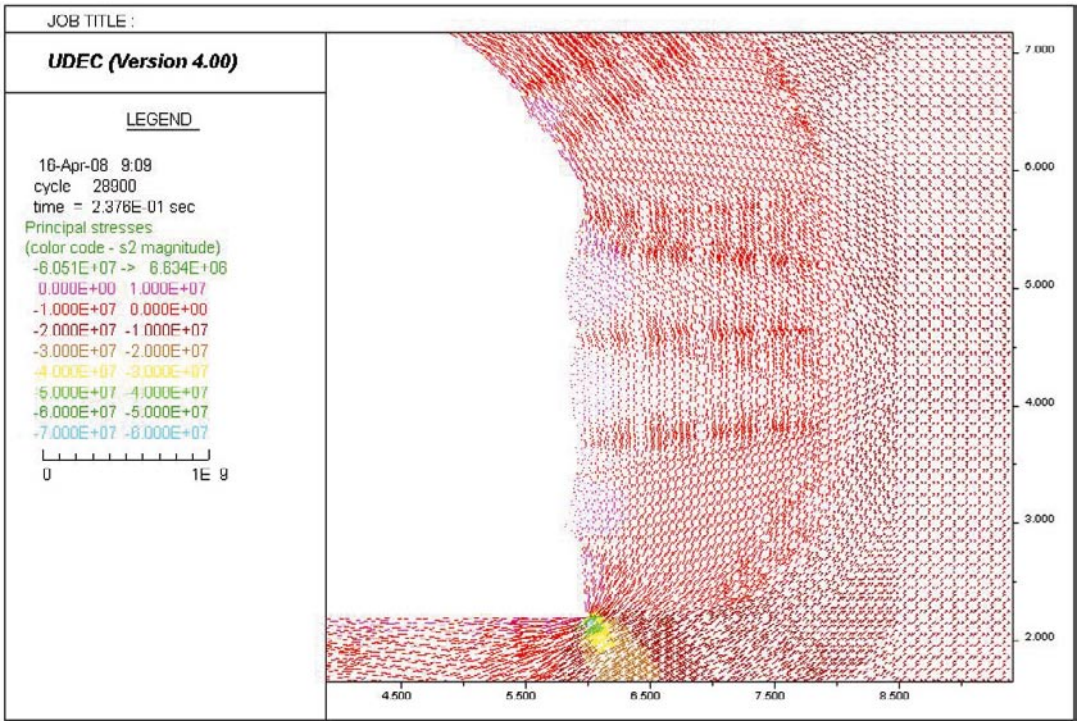

b) Maximum tensile stress = 6.634 MPa

Figure M-47. *Close-up images of the right side wall. Stress tensor plots at a section outside the slot after excavating the heading; Colors by magnitude of a) Sigma 1 and b) Sigma 2. Model with E = 65 GPa, σ_1 = 25 MPa, σ_1 = 316° (see Table 9-11).*

Outside slot section, as-built tunnel shape

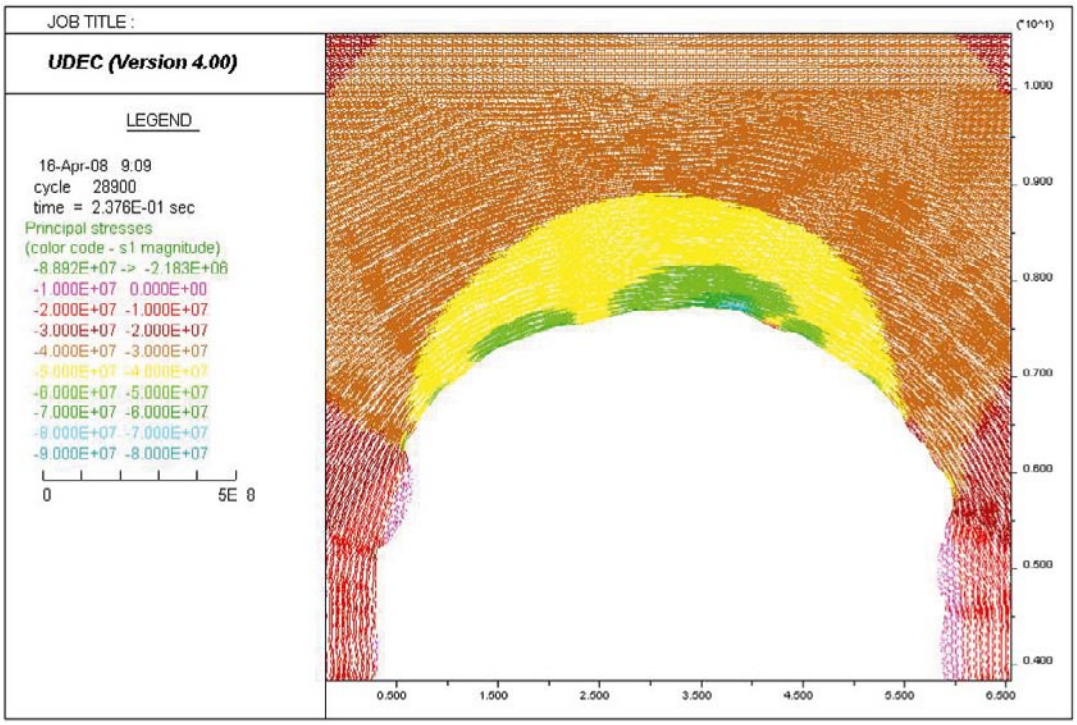

a) Maximum compressive stress = 88.92 MPa

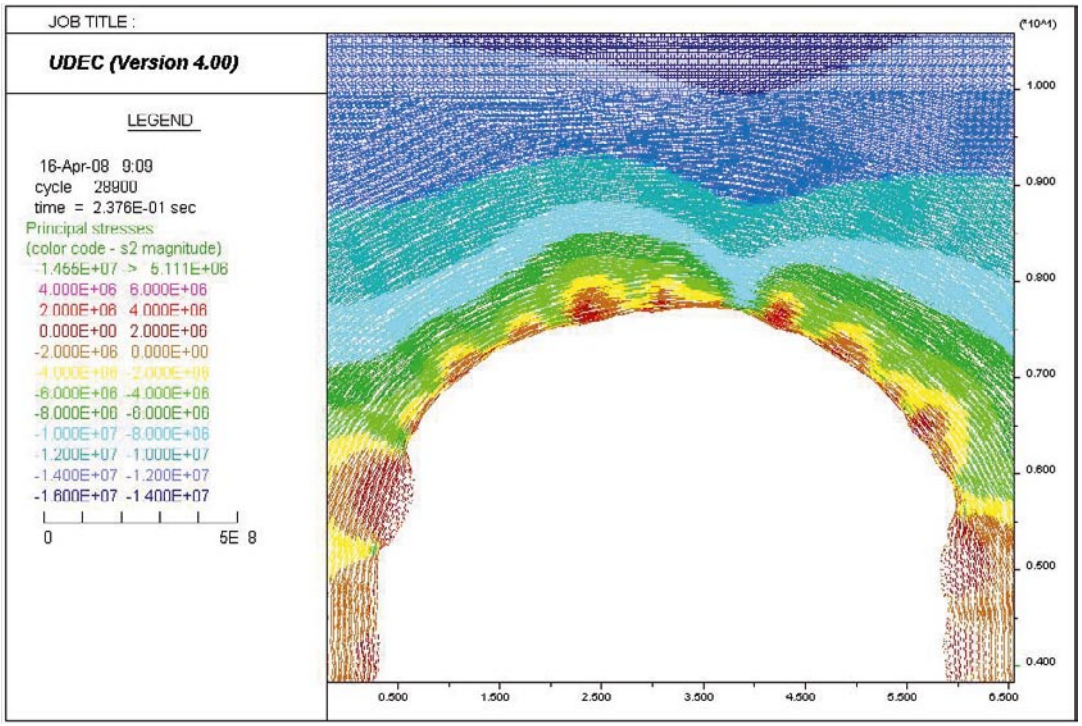

b) Maximum tensile stress = 5.111 MPa

Figure M-48. *Close-up images of the roof. Stress tensor plots at a section outside the slot after excavating the heading; Colors by magnitude of a) Sigma 1 and b) Sigma 2. Model with E = 65 GPa, σ_1 = 25 MPa, σ_1 = 316° (see Table 9-11).*

Outside slot section, as-built tunnel shape

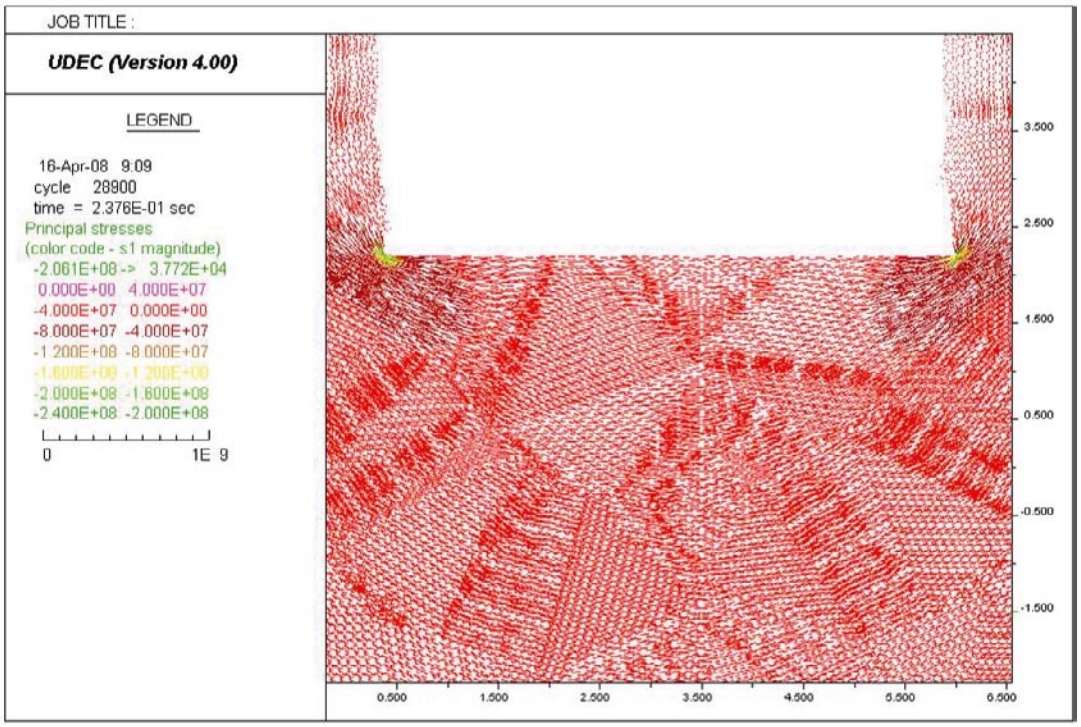

a) Maximum compressive stress = 206.1 MPa

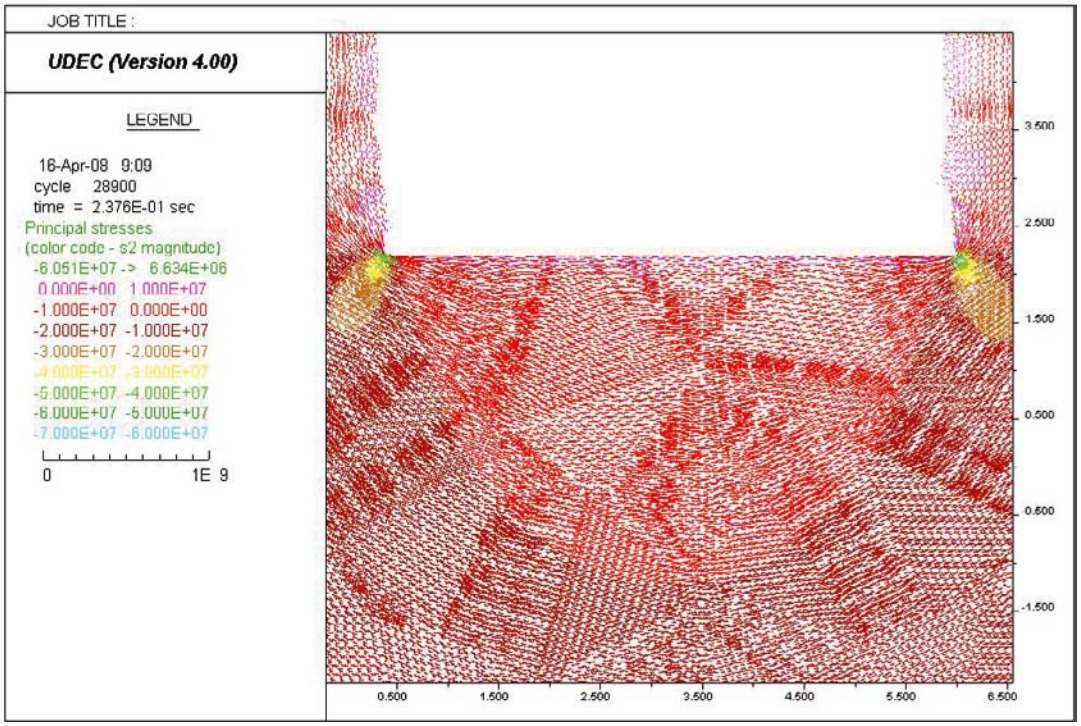

b) Maximum tensile stress = 6.634 MPa

Figure M-49. *Close-up images of the floor. Stress tensor plots at a section outside the slot after excavating the heading; Colors by magnitude of a) Sigma 1 and b) Sigma 2. Model with E = 65 GPa, σ_1 = 25 MPa, σ_1 = 316° (see Table 9-11).*

Convergence pins section, as-built tunnel shape

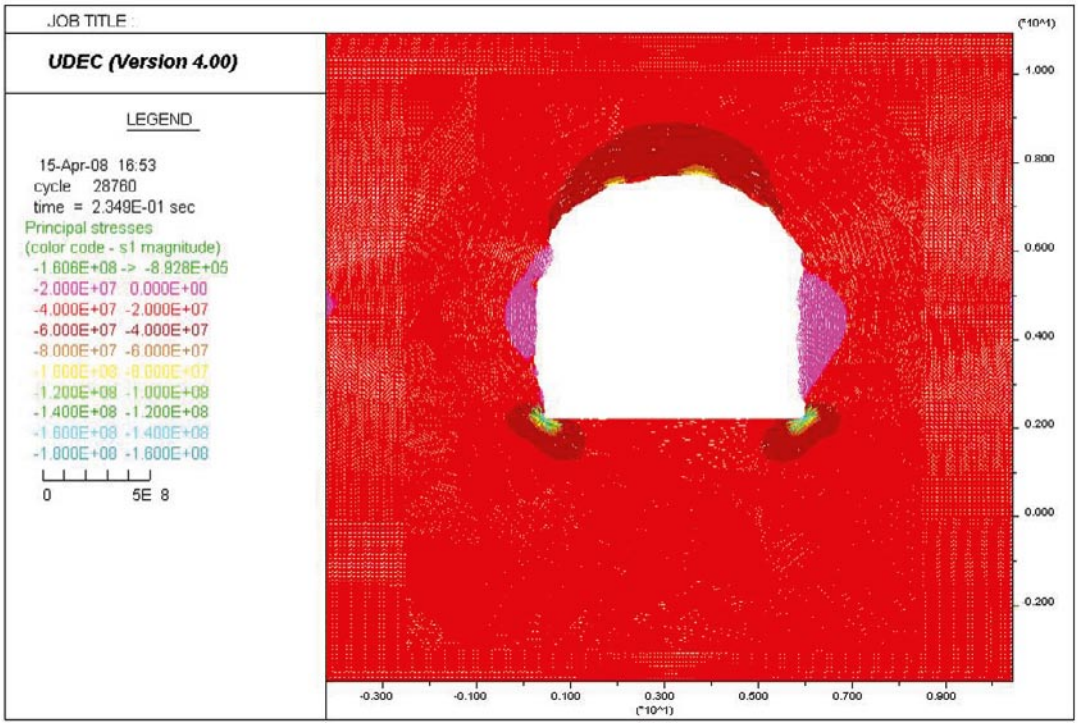

a) Maximum compressive stress = 160.6 MPa

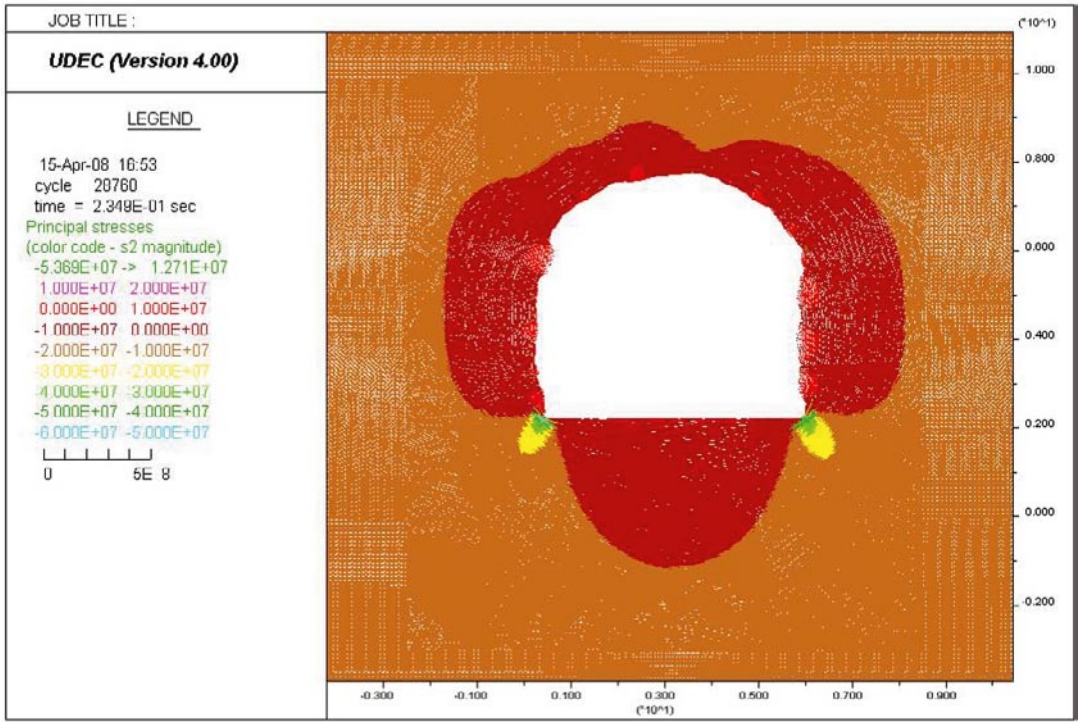

b) Maximum tensile stress = 12.71 MPa

Figure M-50. *Stress tensor plots at the convergence pins section after excavating the heading; Colors by magnitude of a) Sigma 1 and b) Sigma 2. Model with E = 65 GPa, σ_1 = 25 MPa, σ_1 = 316° (see Table 9-11).*

Convergence pins section, as-built tunnel shape

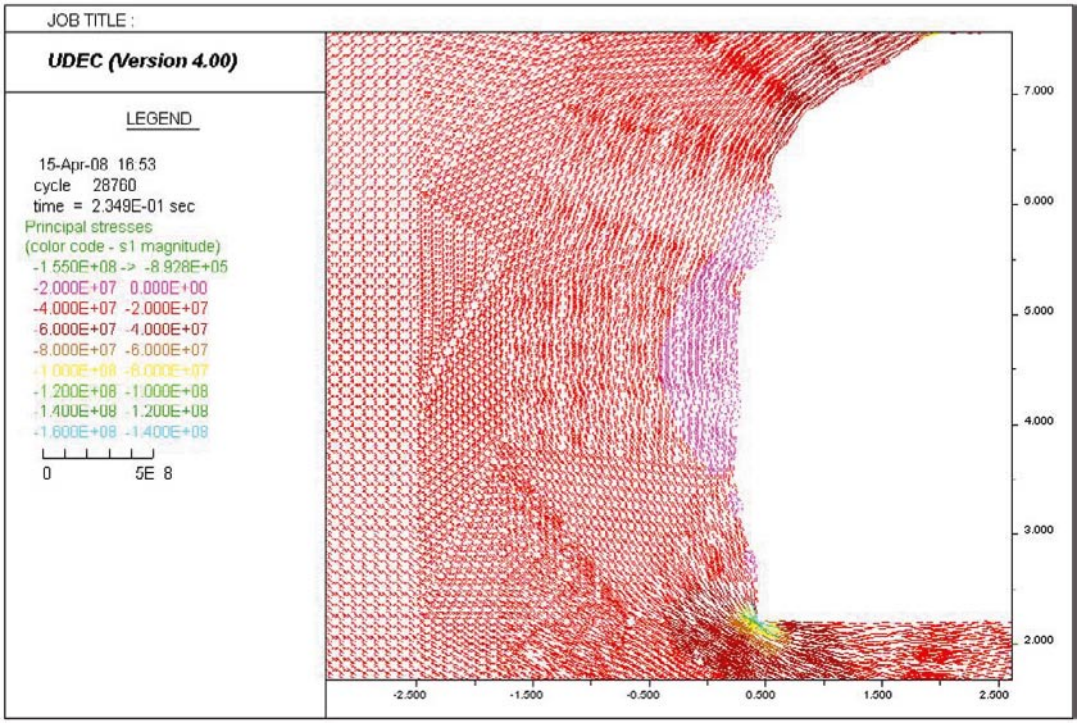

a) Maximum compressive stress = 155.0 MPa

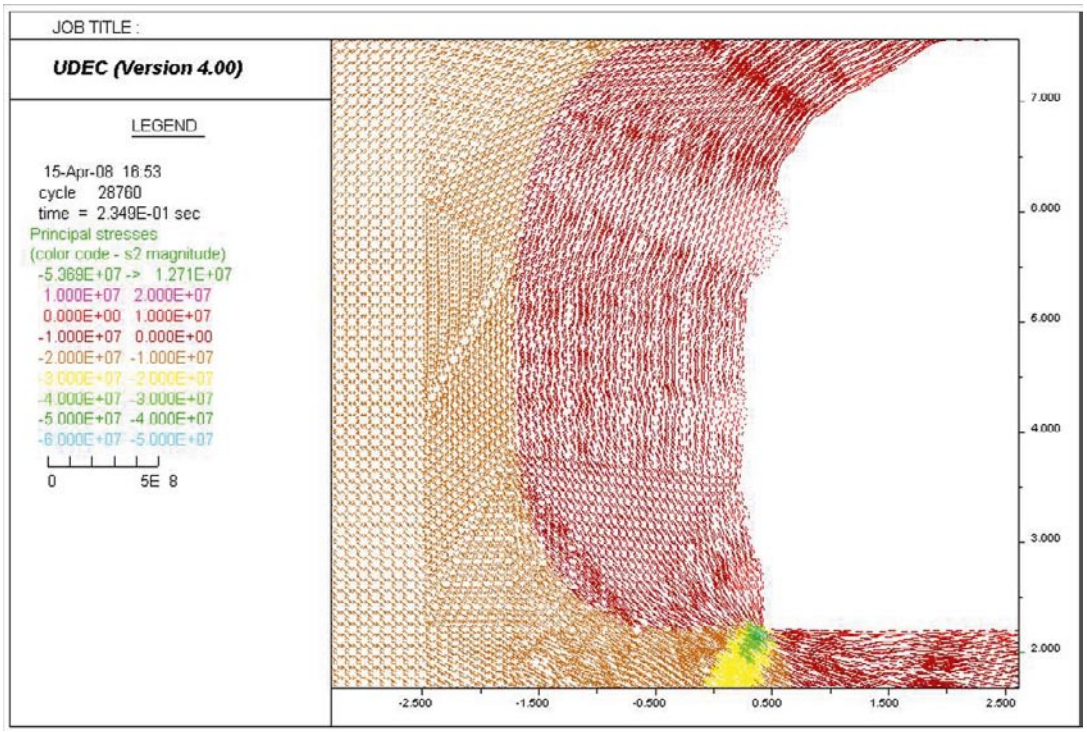

b) Maximum tensile stress = 12.71 MPa

Figure M-51. *Close-up images of the left side wall. Stress tensor plots at the convergence pins section after excavating the heading; Colors by magnitude of a) Sigma 1 and b) Sigma 2. Model with E = 65 GPa, σ_1 = 25 MPa, σ_1 = 316° (see Table 9-11).*

Convergence pins section, as-built tunnel shape

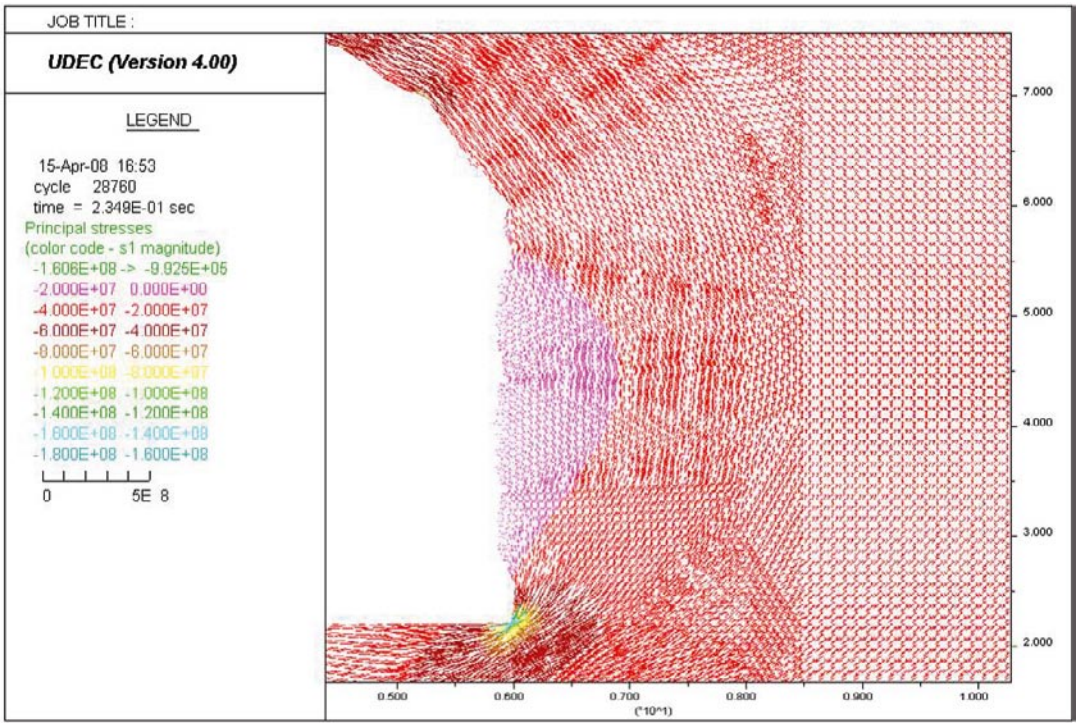

a) Maximum compressive stress = 160.6 MPa

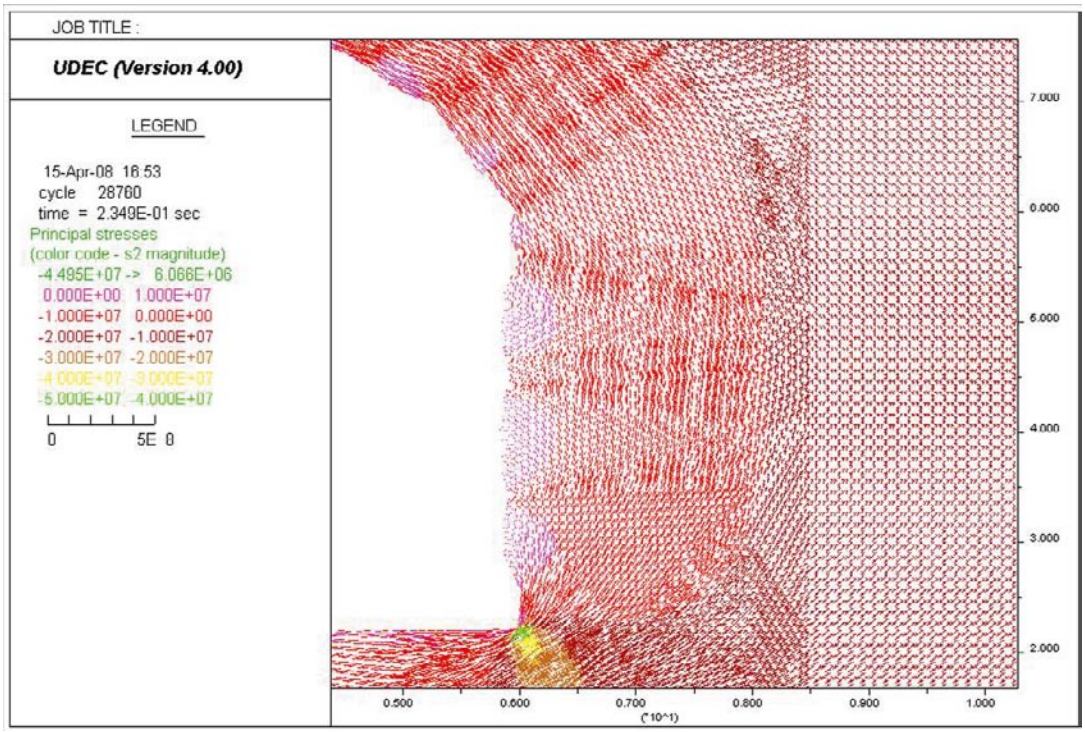

b) Maximum tensile stress = 6.066 MPa

Figure M-52. *Close-up images of the right side wall. Stress tensor plots at the convergence pins section after excavating the heading; Colors by magnitude of a) Sigma 1 and b) Sigma 2. Model with E = 65 GPa, σ_1 = 25 MPa, σ_1 = 316° (see Table 9-11).*

Convergence pins section, as-built tunnel shape

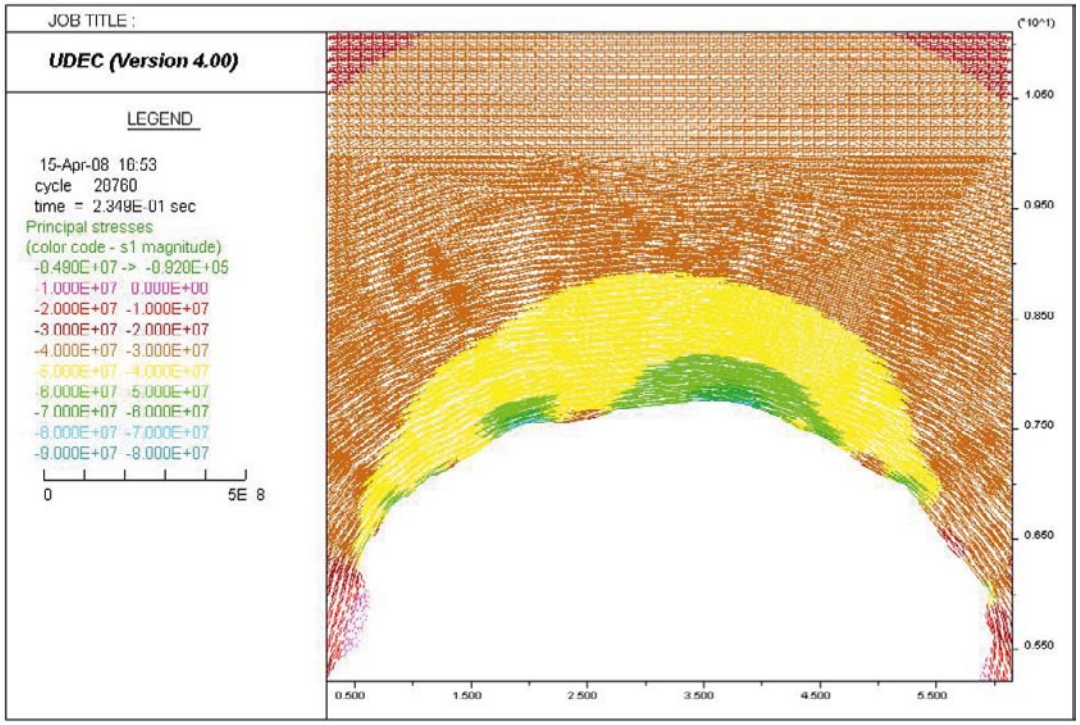

a) Maximum compressive stress = 84.90 MPa

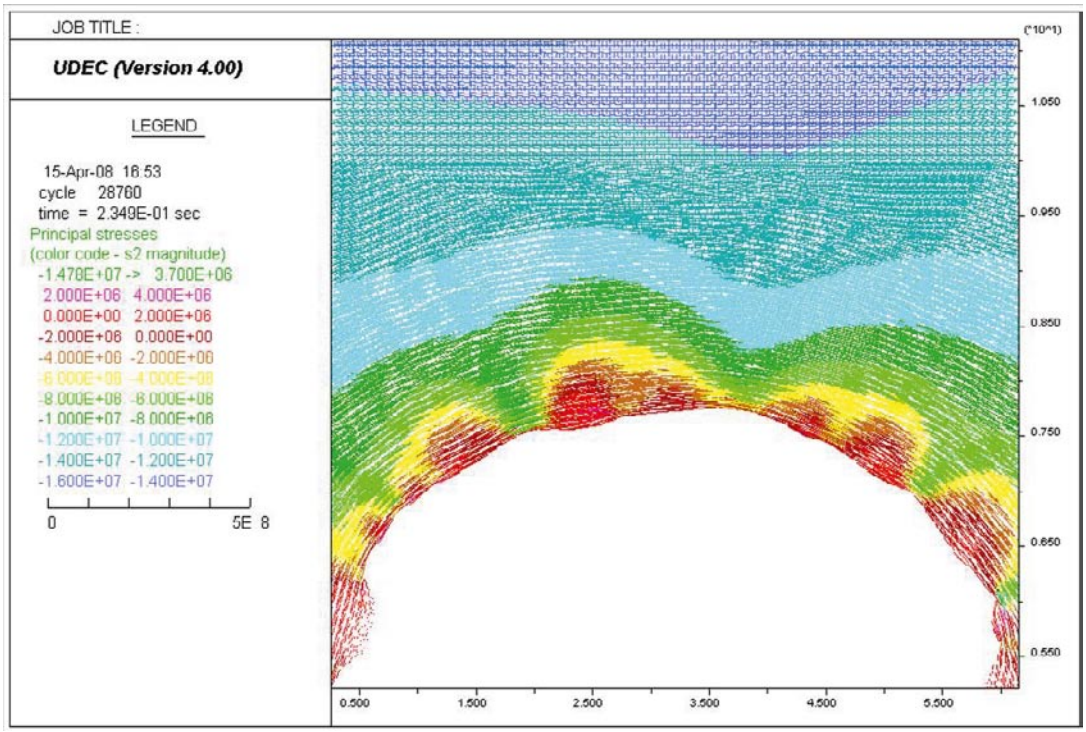

b) Maximum tensile stress = 3.700 MPa

Figure M-53. *Close-up images of the roof. Stress tensor plots at the convergence pins section after excavating the heading; Colors by magnitude of a) Sigma 1 and b) Sigma 2. Model with E = 65 GPa, σ_1 = 25 MPa, σ_1 = 316° (see Table 9-11).*

Convergence pins section, as-built tunnel shape

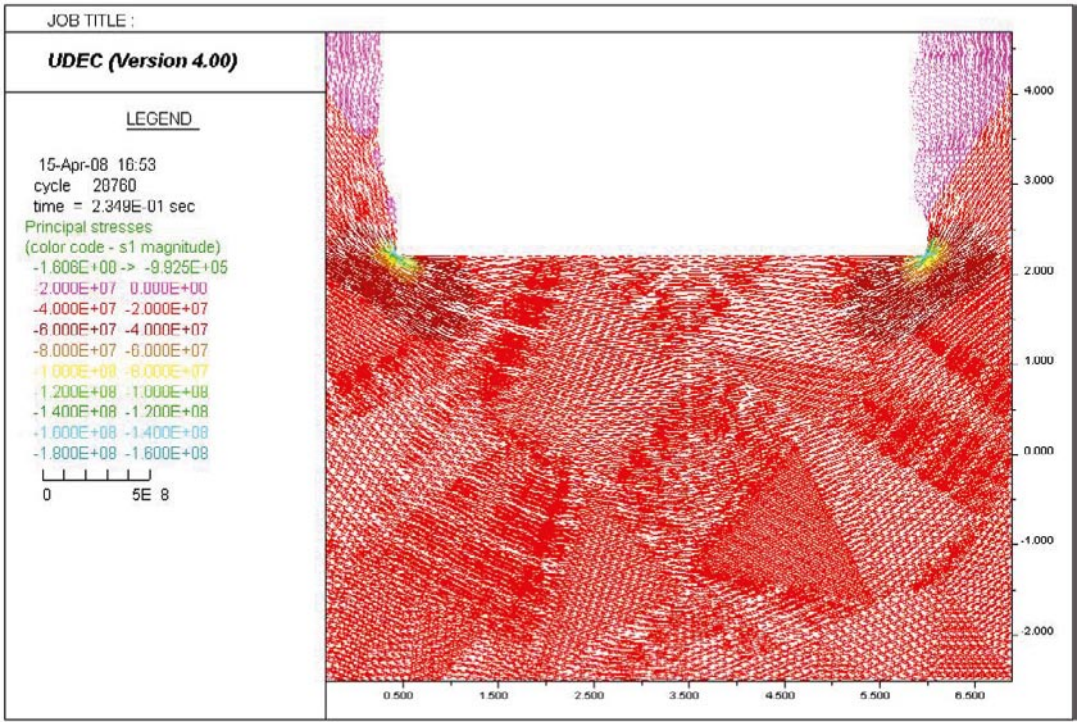

a) Maximum compressive stress = 160.6 MPa

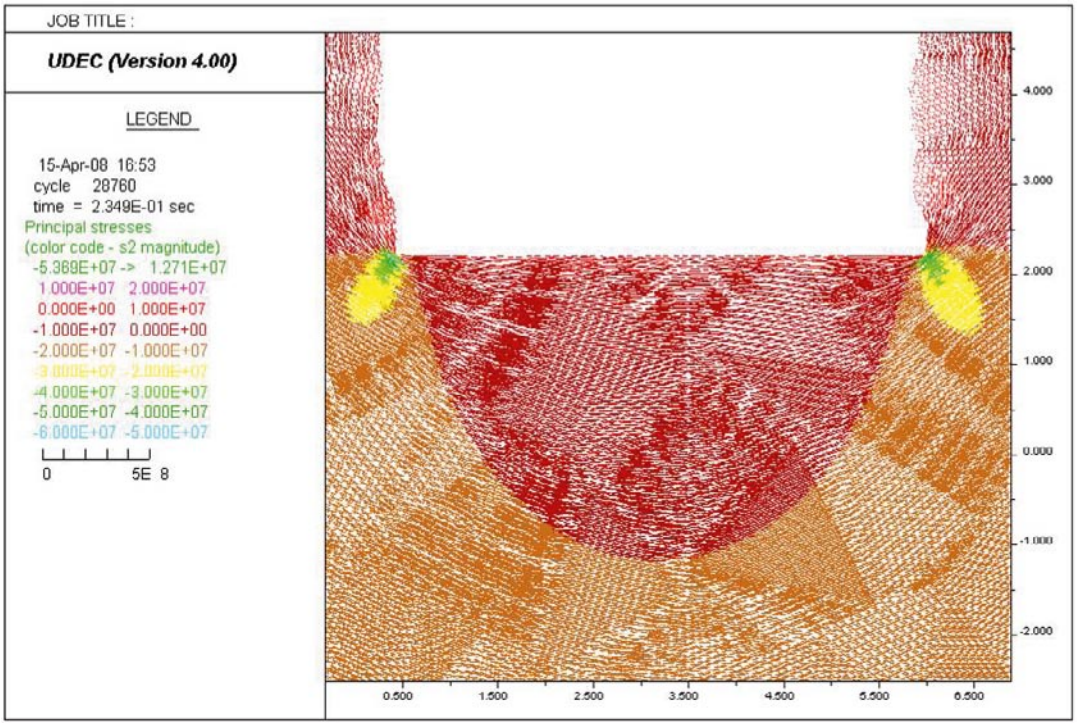

b) Maximum tensile stress = 12.71 MPa

Figure M-54. *Close-up images of the floor. Stress tensor plots at the convergence pins section after excavating the heading; Colors by magnitude of a) Sigma 1 and b) Sigma 2. Model with E = 65 GPa, σ_1 = 25 MPa, σ_1 = 316° (see Table 9-11).*

Stress tensor plots of the TASQ tunnel in 3 different sections (BGR, outside slot and convergence pins) with the as-built tunnel shape and the as-planned tunnel shape case after excavating the bench (E = 65 GPa, σ_1 = 25 MPa, σ_1 = 316°).

As-planned tunnel shape

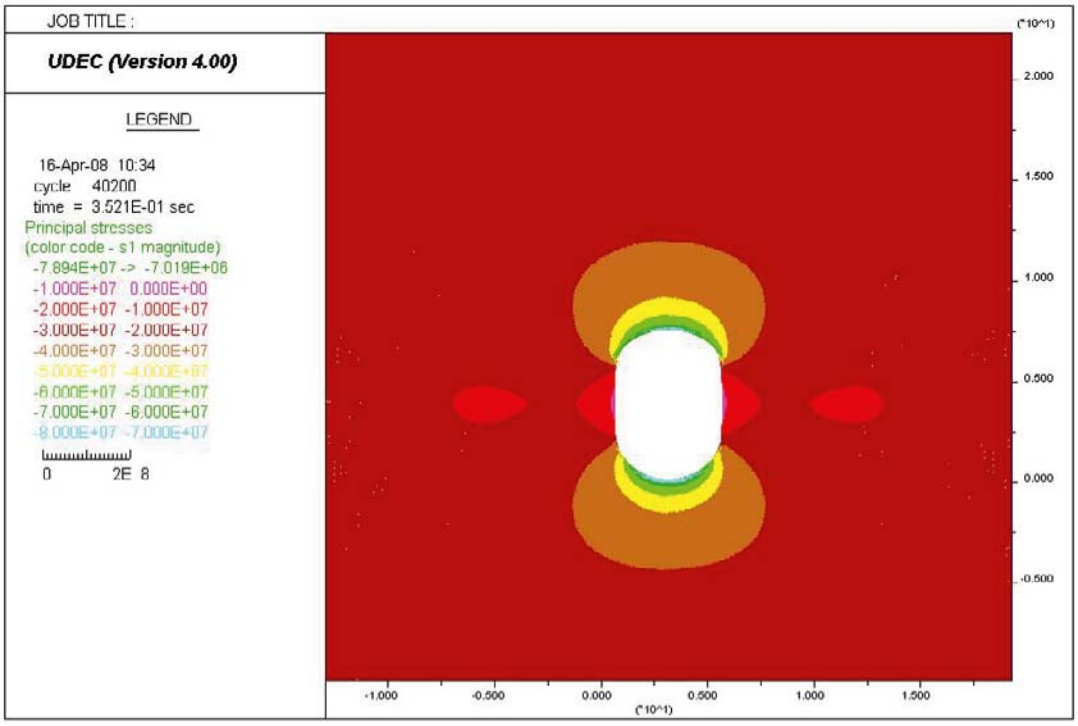

a) Maximum compressive stress = 78.94 MPa

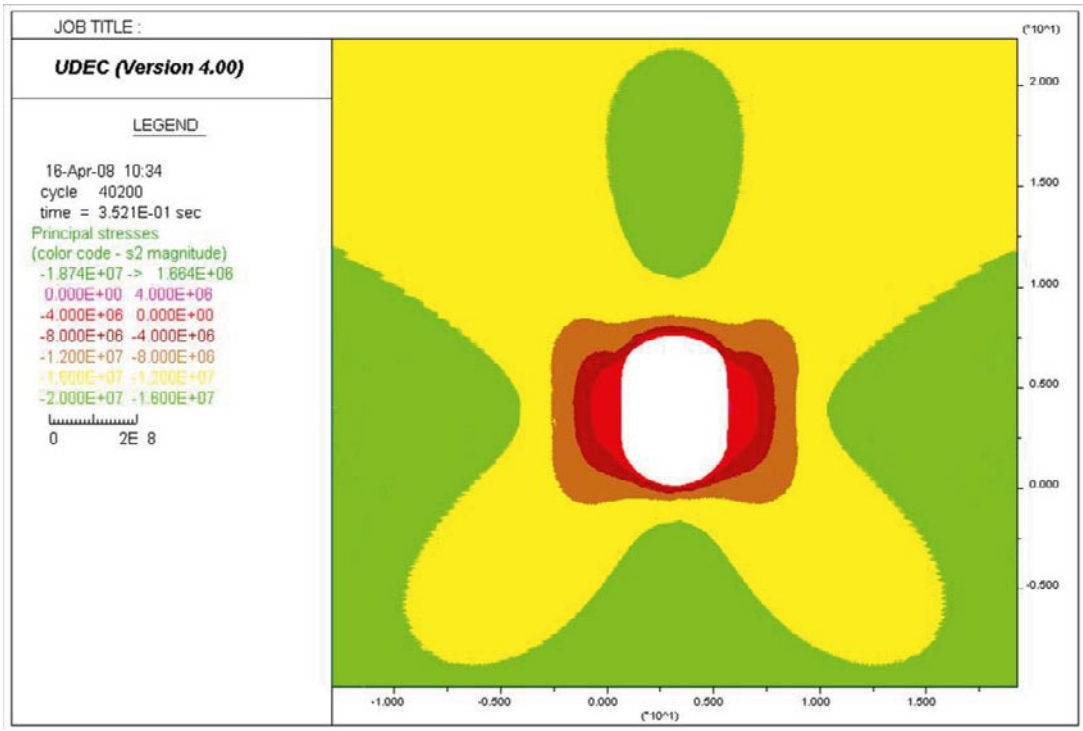

b) Maximum tensile stress = 1.664 MPa

Figure M-55. *Stress tensor plots of the as-planned tunnel shape after excavating the bench; Colors by magnitude of a) Sigma 1 and b) Sigma 2. Model with E = 65 GPa, σ_1 = 25 MPa, σ_1 = 316° (see Table 9-11).*

As-planned tunnel shape

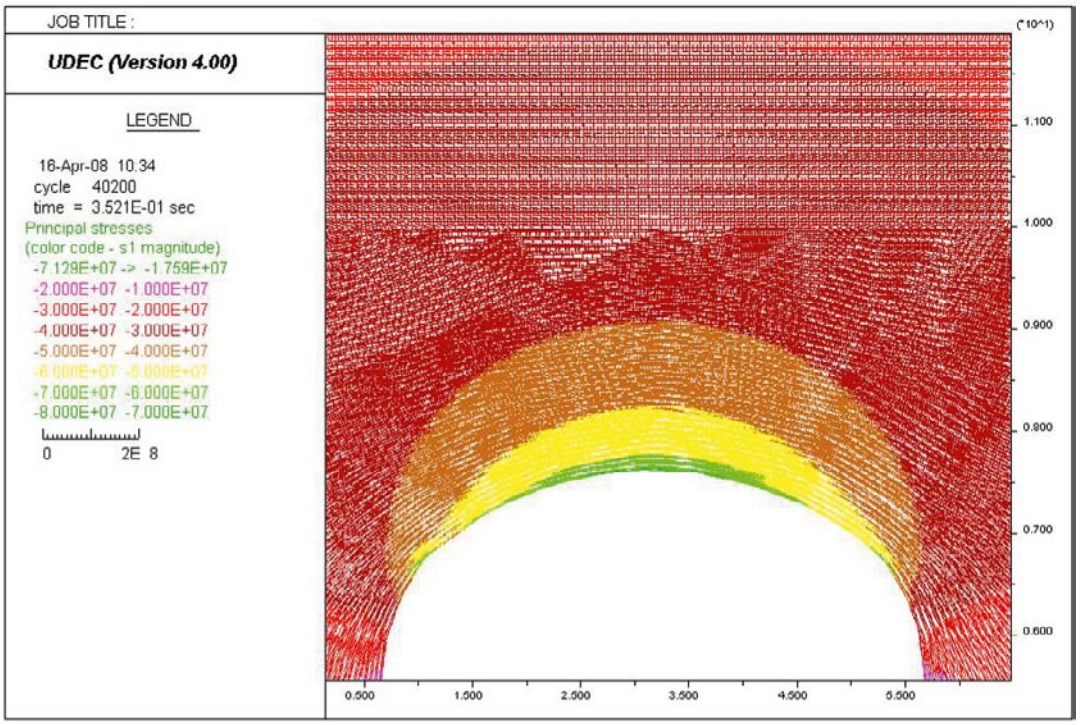

a) Maximum compressive stress = 71.29 MPa

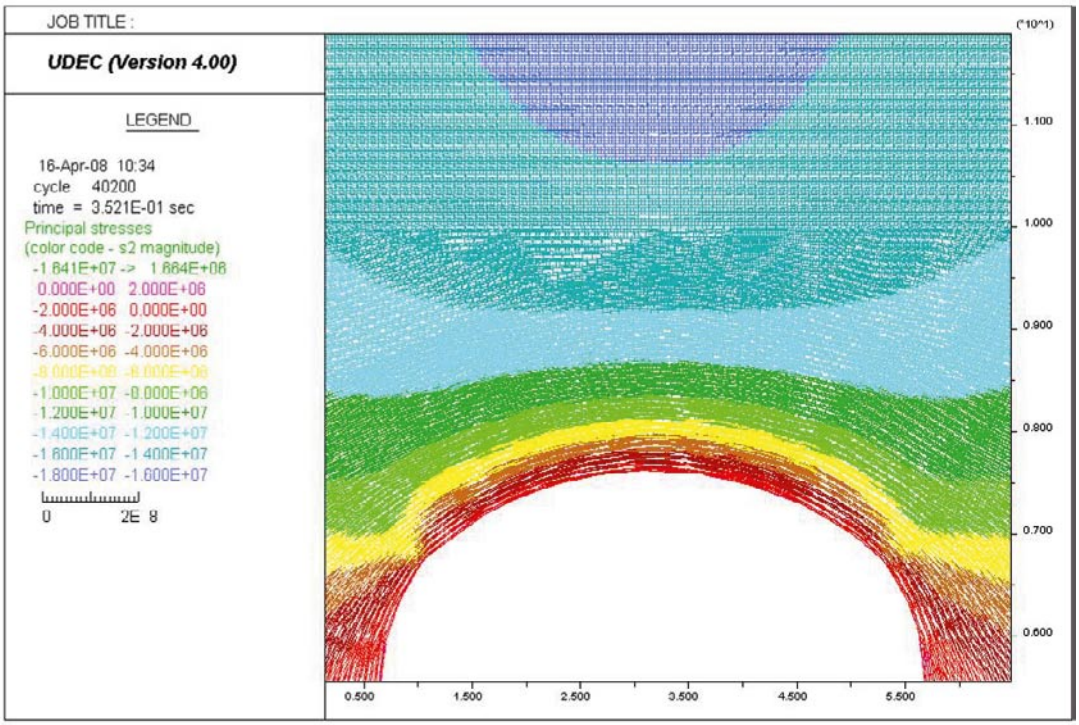

b) Maximum tensile stress = 1.664 MPa

Figure M-56. *Close-up images of the roof. Stress tensor plots of the as-planned tunnel shape after excavating the bench; Colors by magnitude of a) Sigma 1 and b) Sigma 2. Model with E = 65 GPa, σ_1 = 25 MPa, σ_1 = 316° (see Table 9-11).*

As-planned tunnel shape

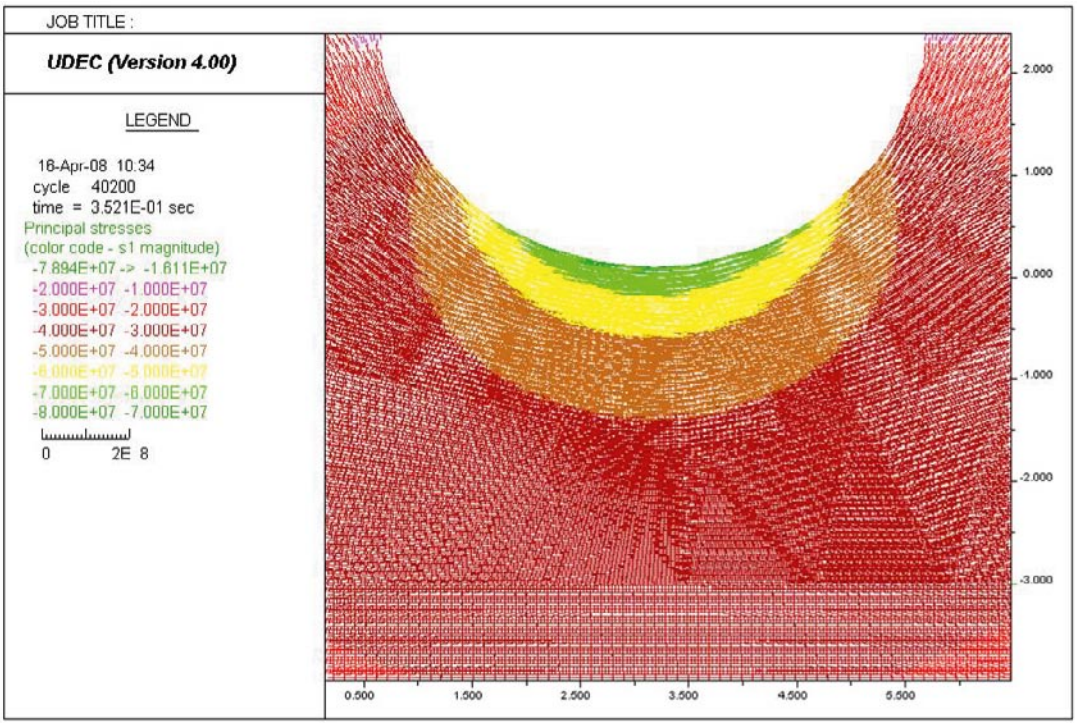

a) Maximum compressive stress = 78.94 MPa

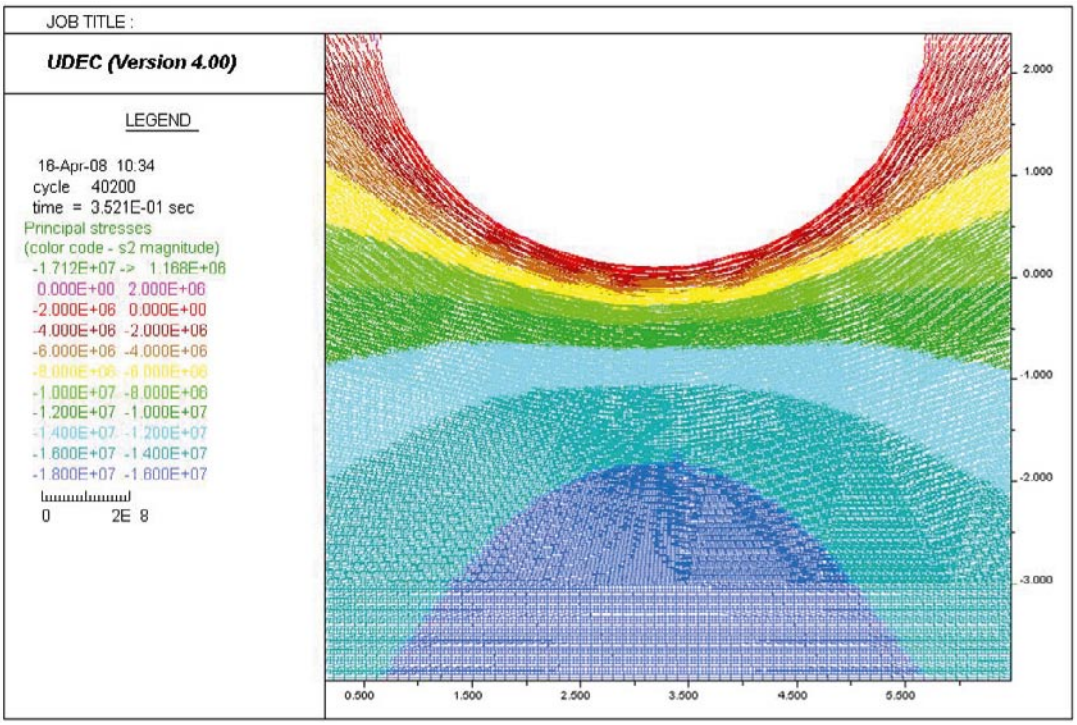

b) Maximum tensile stress = 1.168 MPa

Figure M-57. *Close-up images of the floor. Stress tensor plots of the as-planned tunnel shape after excavating the bench; Colors by magnitude of a) Sigma 1 and b) Sigma 2. Model with E = 65 GPa, σ_1 = 25 MPa, σ_1 = 316° (see Table 9-11).*

BGR section, as-built tunnel shape

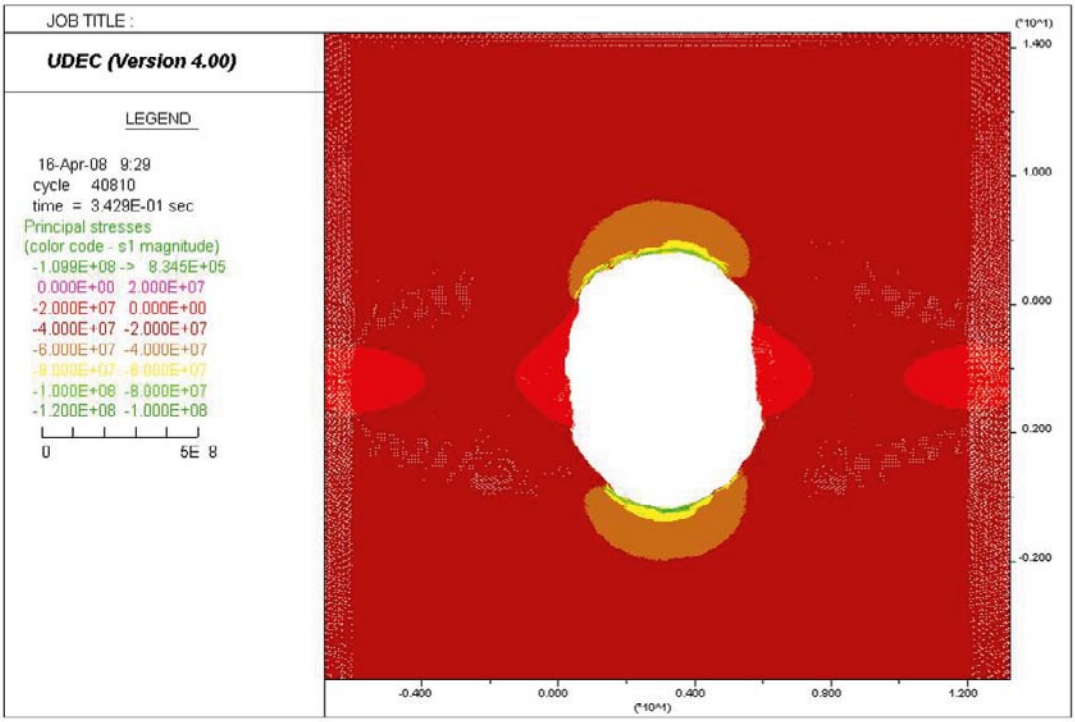

a) Maximum Compressive stress = 109.9 MPa

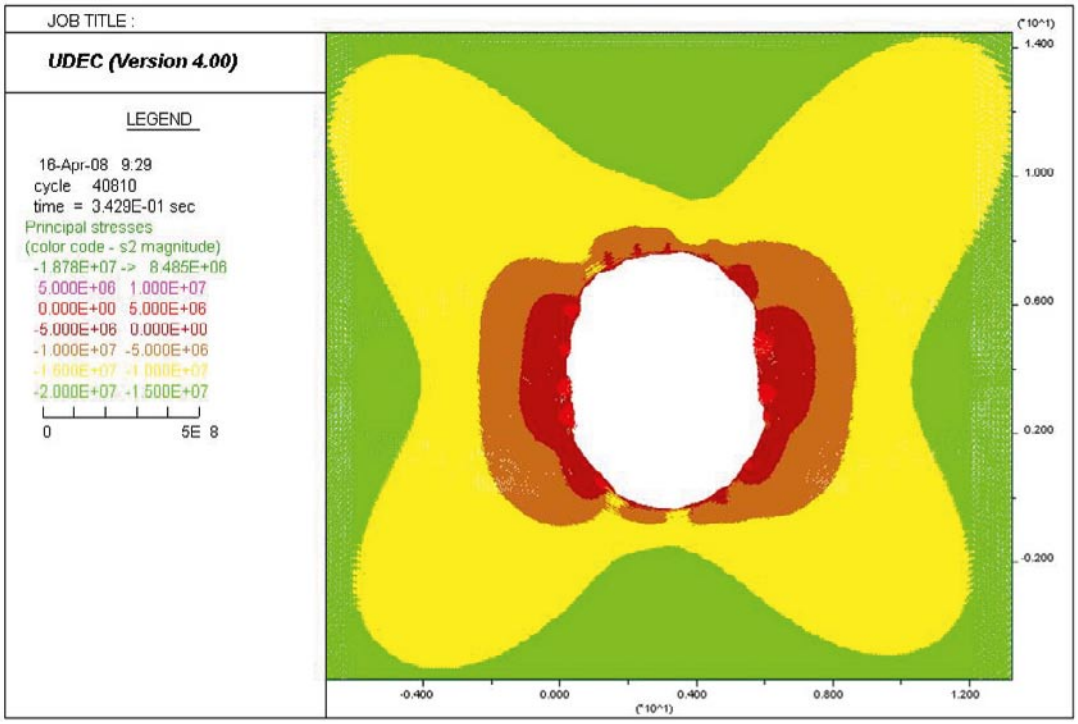

b) Maximum Tensile stress = 8.485 MPa

Figure M-58. *Stress tensor plots at the BGR section after excavating the bench; Colors by magnitude of a) Sigma 1 and b) Sigma 2. Model with E = 65 GPa, σ_1 = 25 MPa, σ_1 = 316° (see Table 9-11).*

BGR section, as-built tunnel shape

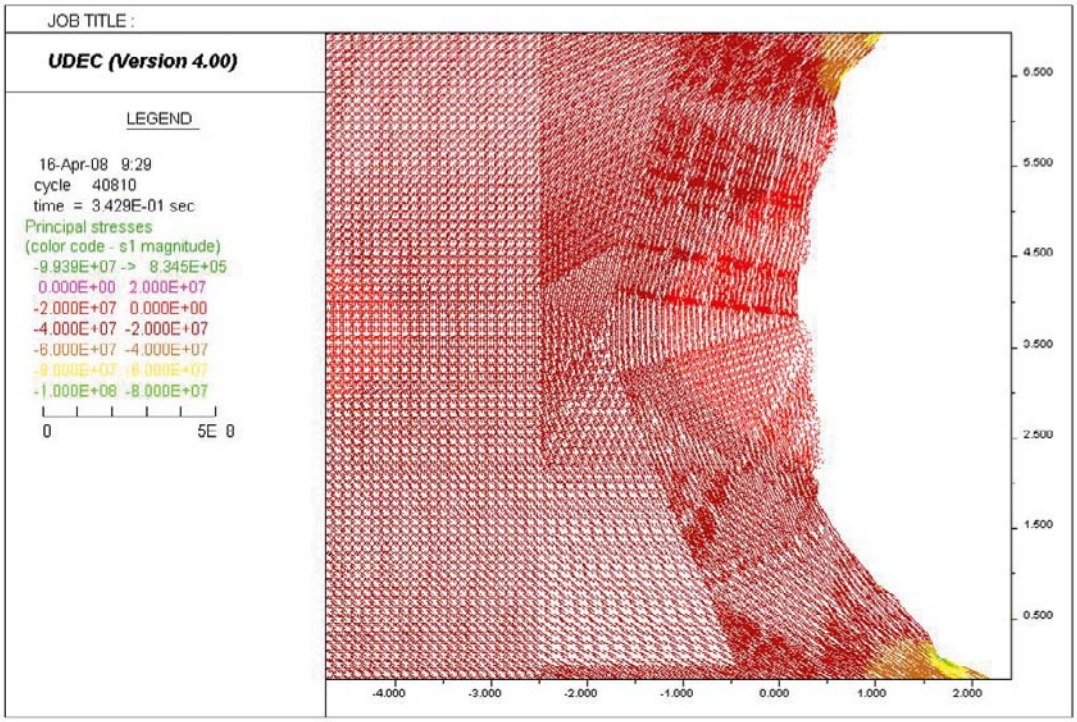

a) Maximum Compressive stress = 99.39 MPa

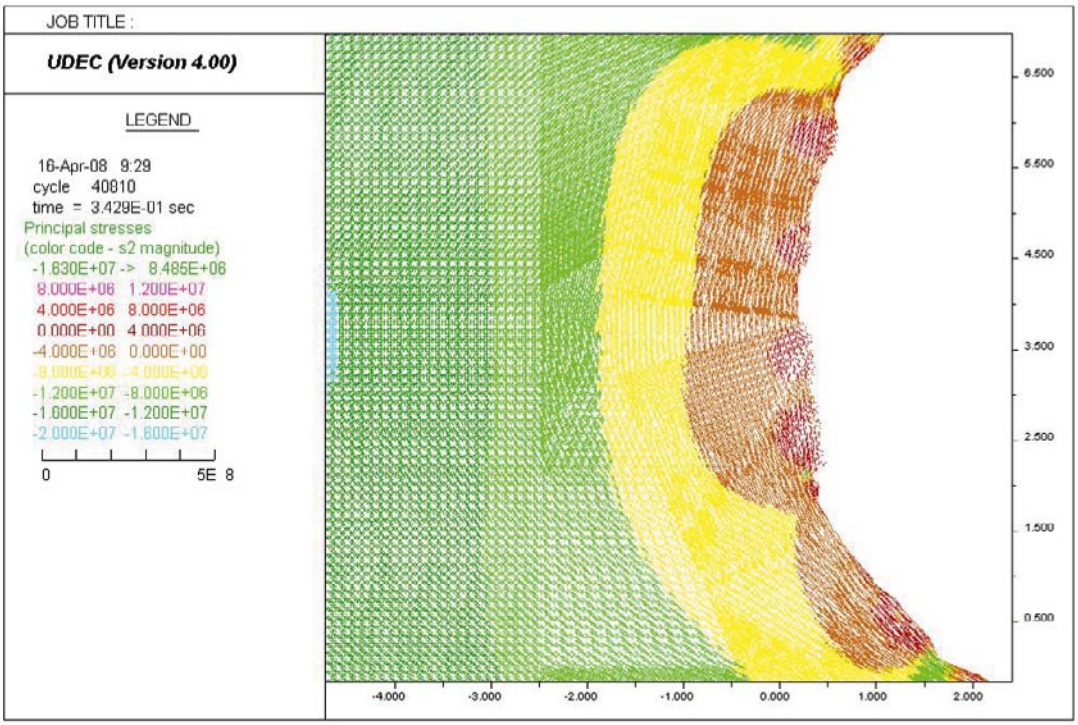

b) Maximum Tensile stress = 8.485 MPa

Figure M-59. *Close-up images of the left side wall. Stress tensor plots at the BGR section after excavating the bench; Colors by magnitude of a) Sigma 1 and b) Sigma 2. Model with E = 65 GPa, σ_1 = 25 MPa, σ_1 = 316° (see Table 9-11).*

BGR section, as-built tunnel shape

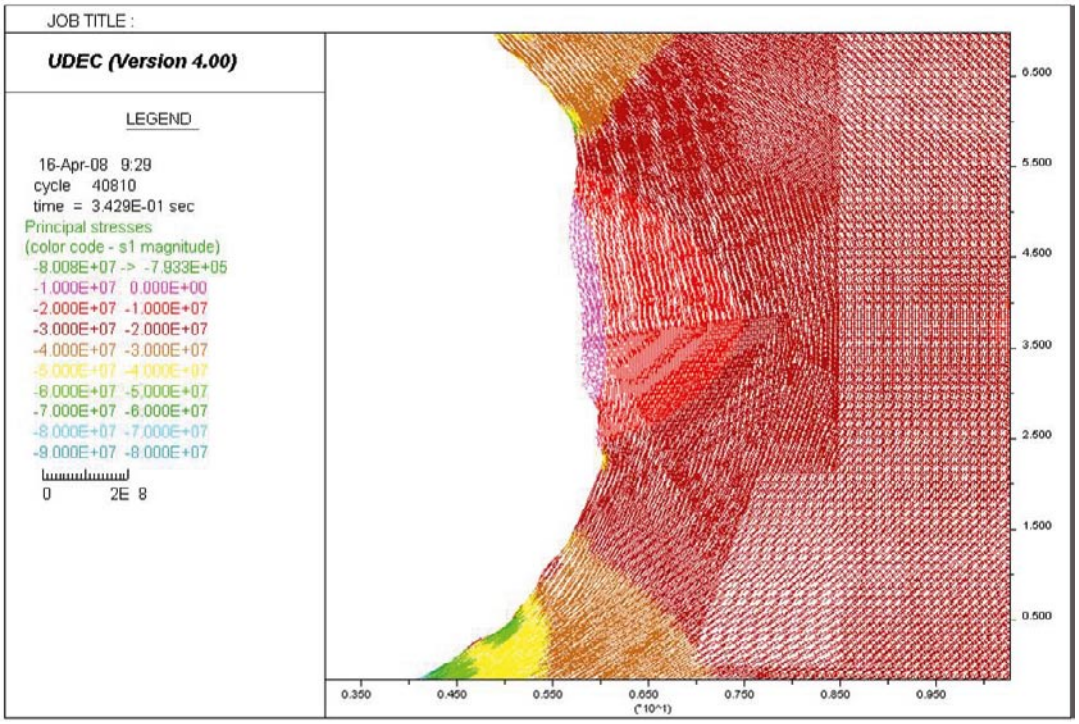

a) Maximum Compressive stress = 80.08 MPa

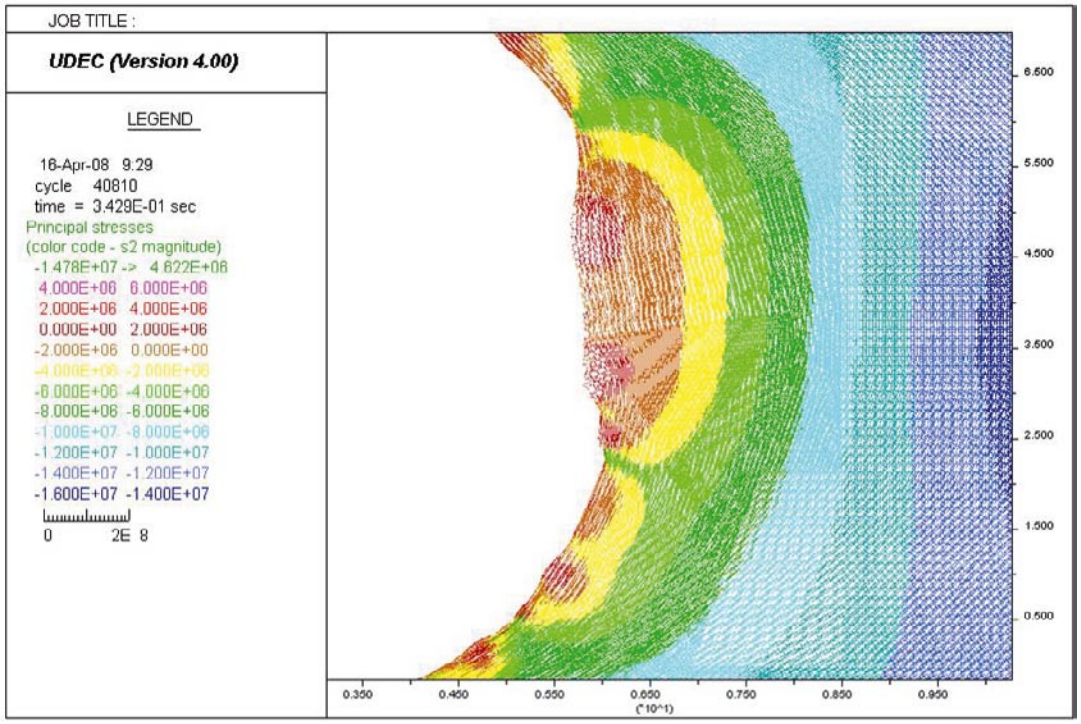

b) Maximum Tensile stress = 4.622 MPa

Figure M-60. *Close-up images of the right side wall. Stress tensor plots at the BGR section after excavating the bench; Colors by magnitude of a) Sigma 1 and b) Sigma 2. Model with E = 65 GPa, σ_1 = 25 MPa, σ_1 = 316° (see Table 9-11).*

BGR section, as-built tunnel shape

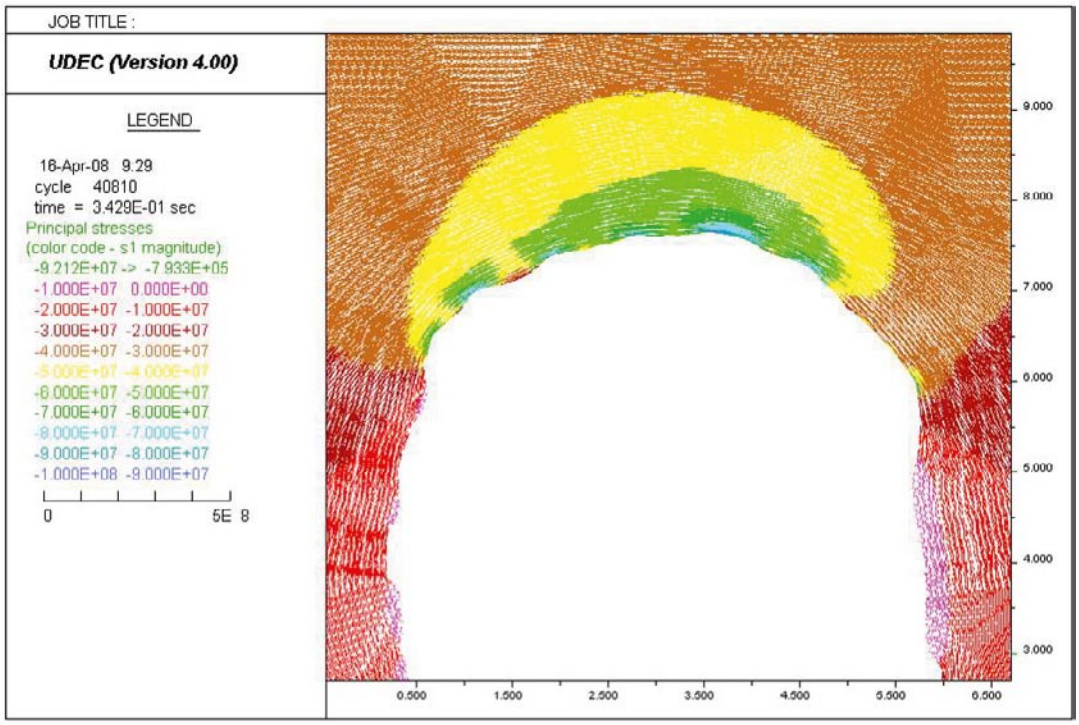

a) Maximum Compressive stress = 92.12 MPa

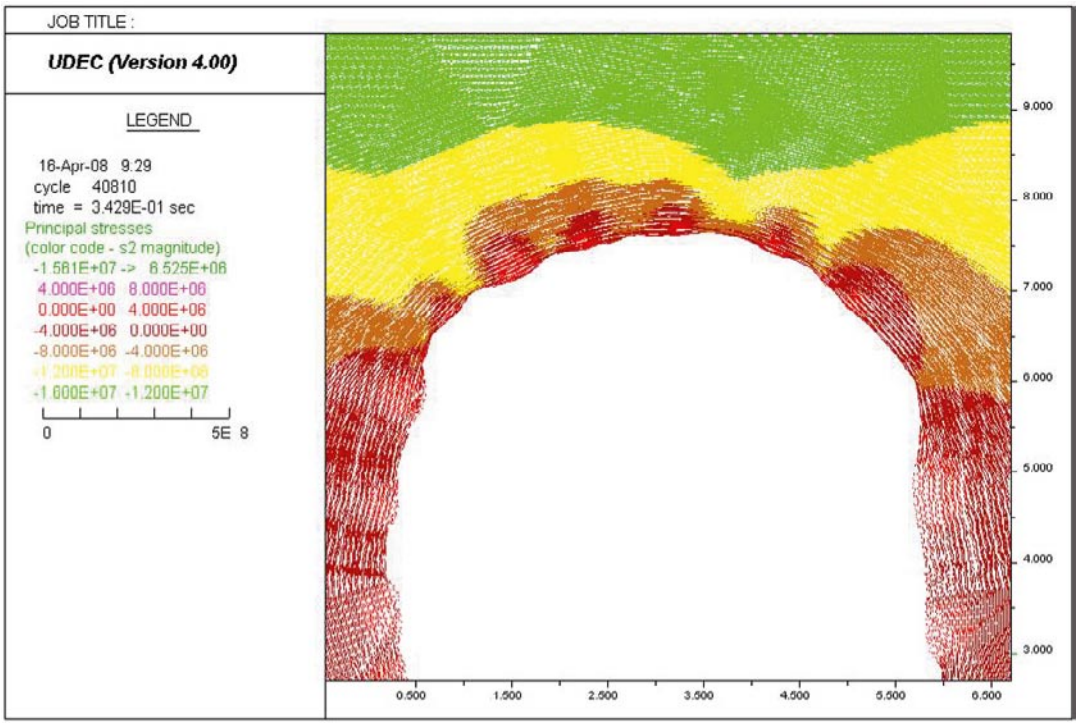

b) Maximum Tensile stress = 6.525 MPa

Figure M-61. *Close-up images of the roof. Stress tensor plots at the BGR section after excavating the bench; Colors by magnitude of a) Sigma 1 and b) Sigma 2. Model with E = 65 GPa, σ_1 = 25 MPa, σ_1 = 316° (see Table 9-11).*

BGR section, as-built tunnel shape

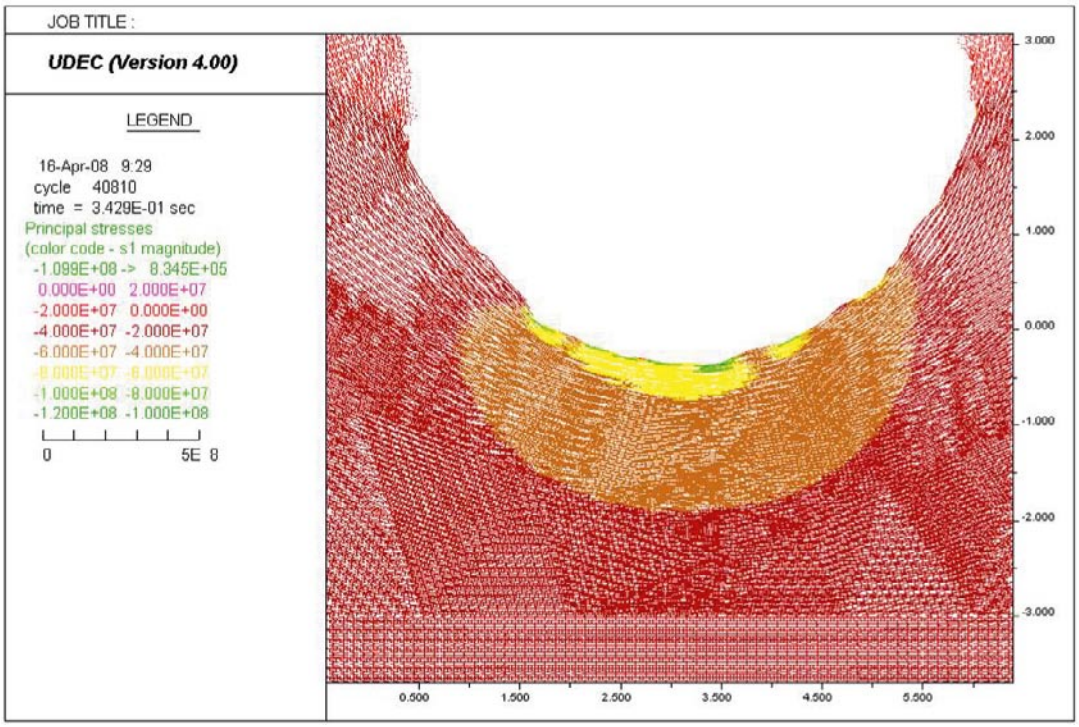

a) Maximum Compressive stress = 109.9 MPa

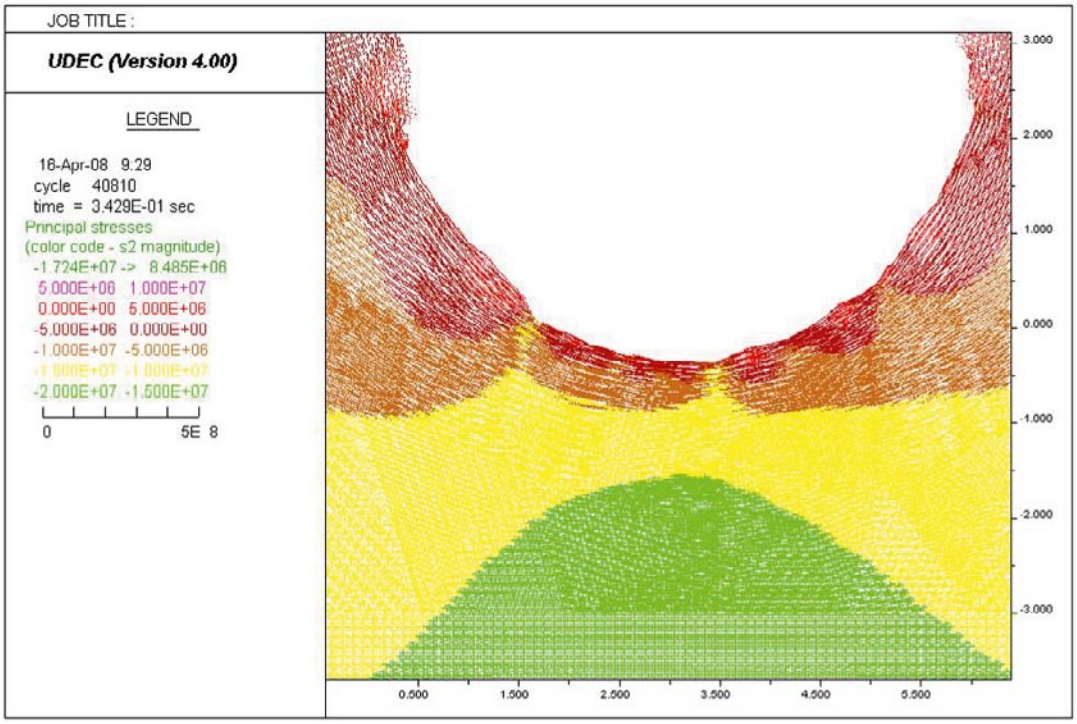

b) Maximum Tensile stress = 8.485 MPa

Figure M-62. *Close-up images of the floor. Stress tensor plots at the BGR section after excavating the bench; Colors by magnitude of a) Sigma 1 and b) Sigma 2. Model with E = 65 GPa, σ_1 = 25 MPa, σ_1 = 316° (see Table 9-11).*

Outside slot section, as-built tunnel shape

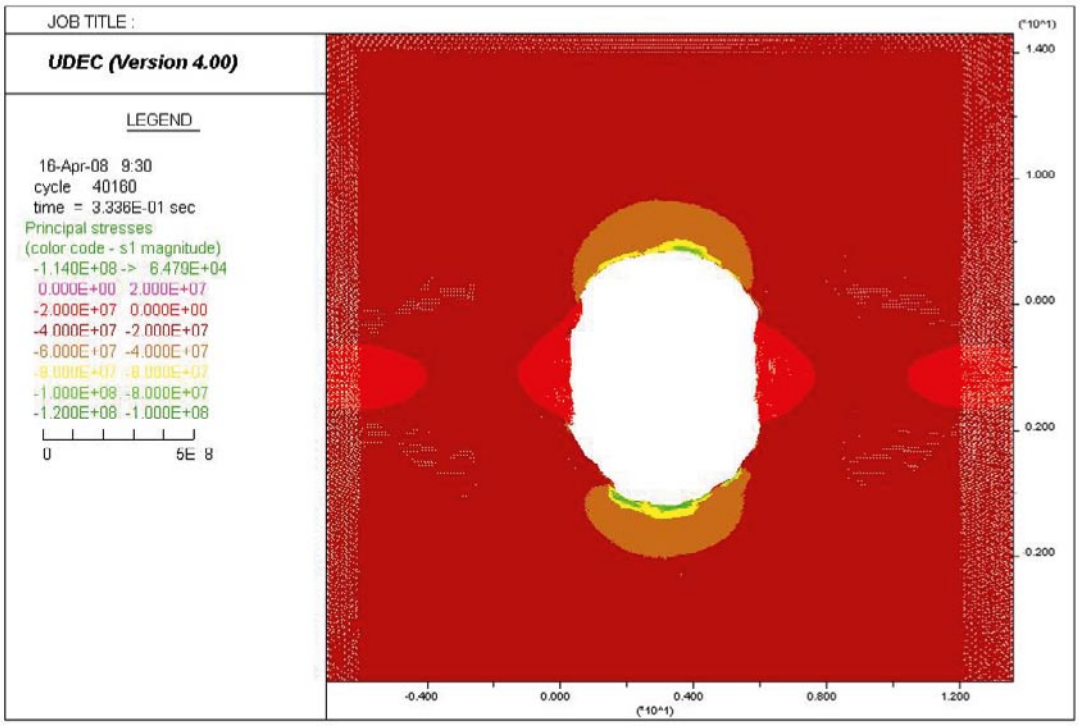

a) Maximum compressive stress = 114.0 MPa

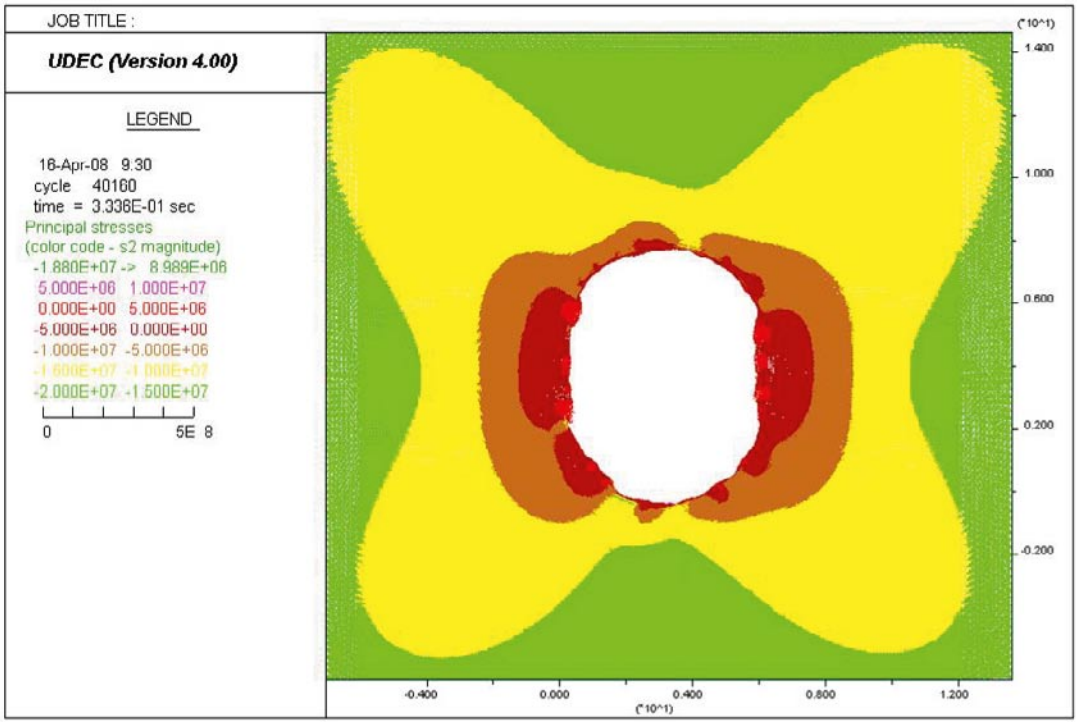

b) Maximum tensile stress = 8.989 MPa

Figure M-63. *Stress tensor plots at a section outside the slot after excavating the bench; Colors by magnitude of a) Sigma 1 and b) Sigma 2. Model with E = 65 GPa, σ_1 = 25 MPa, σ_1 = 316° (see Table 9-11).*

Outside slot section, as-built tunnel shape

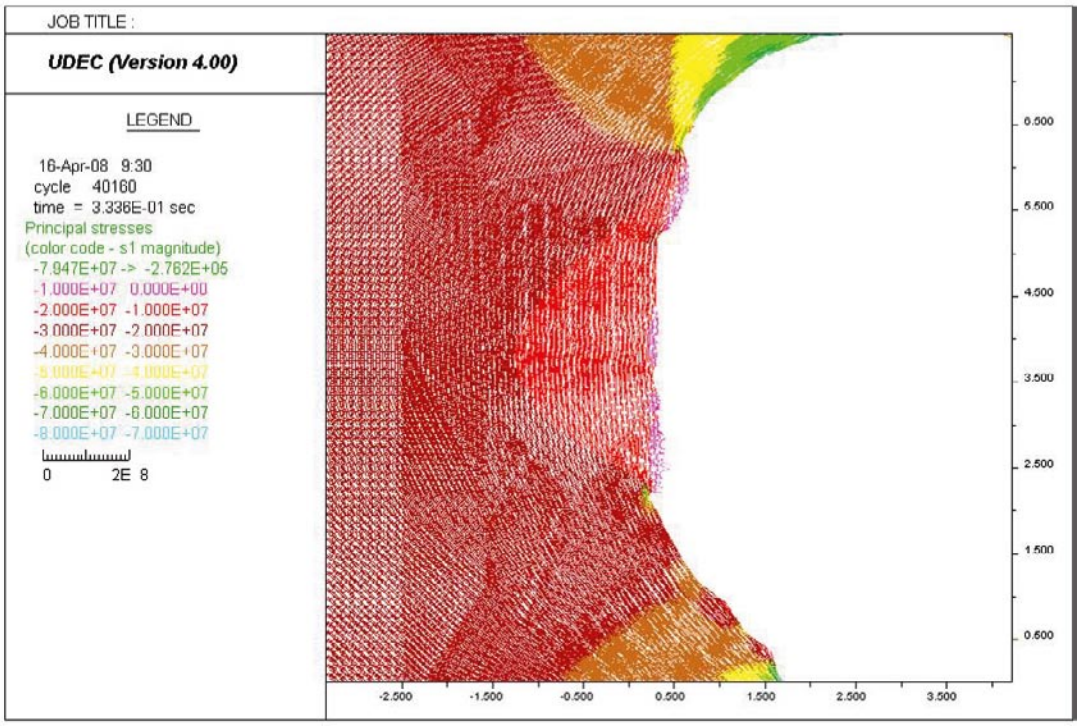

a) Maximum compressive stress = 79.47 MPa

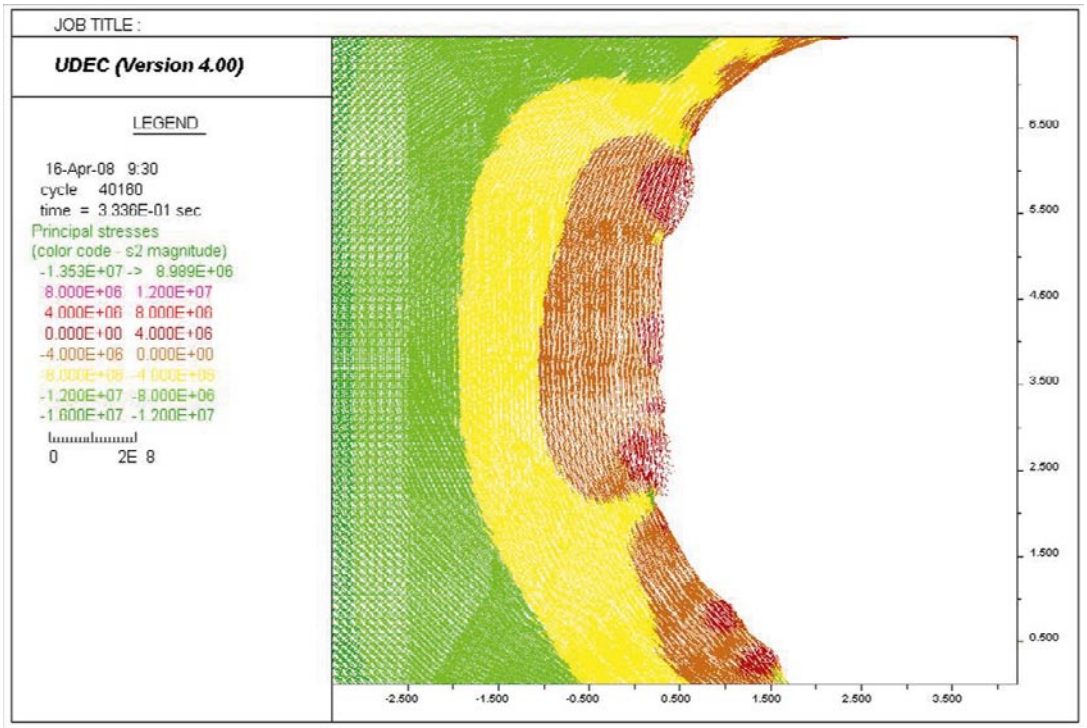

b) Maximum tensile stress = 8.989 MPa

Figure M-64. *Close-up images of the left side wall. Stress tensor plots at a section outside the slot after excavating the bench; Colors by magnitude of a) Sigma 1 and b) Sigma 2. Model with E = 65 GPa, σ_1 = 25 MPa, σ_1 = 316° (see Table 9-11).*

Outside slot section, as-built tunnel shape

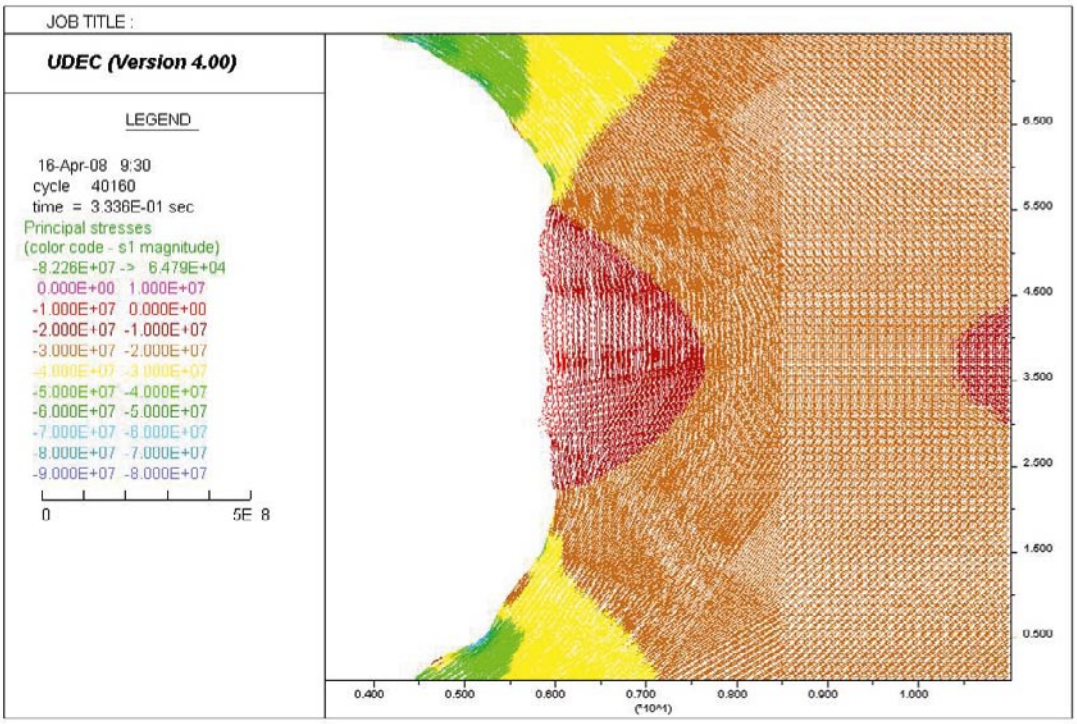

a) Maximum compressive stress = 82.26 MPa

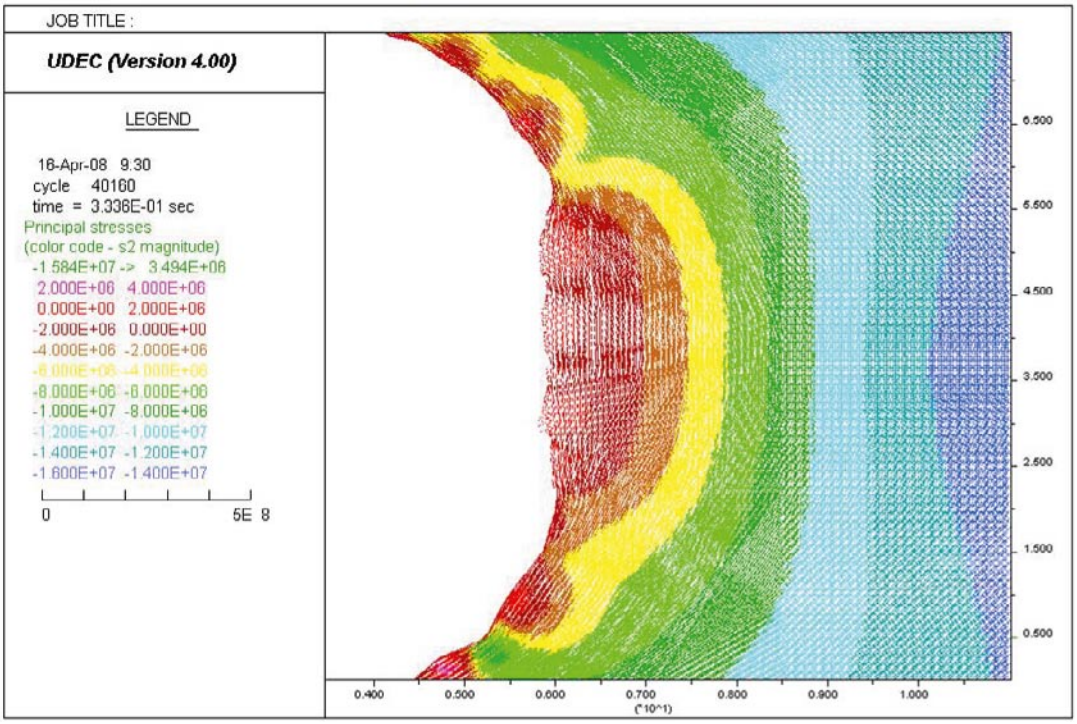

b) Maximum tensile stress = 3.494 MPa

Figure M-65. *Close-up images of the right side wall. Stress tensor plots at a section outside the slot after excavating the bench; Colors by magnitude of a) Sigma 1 and b) Sigma 2. Model with E = 65 GPa, σ_1 = 25 MPa, σ_1 = 316° (see Table 9-11).*

Outside slot section, as-built tunnel shape

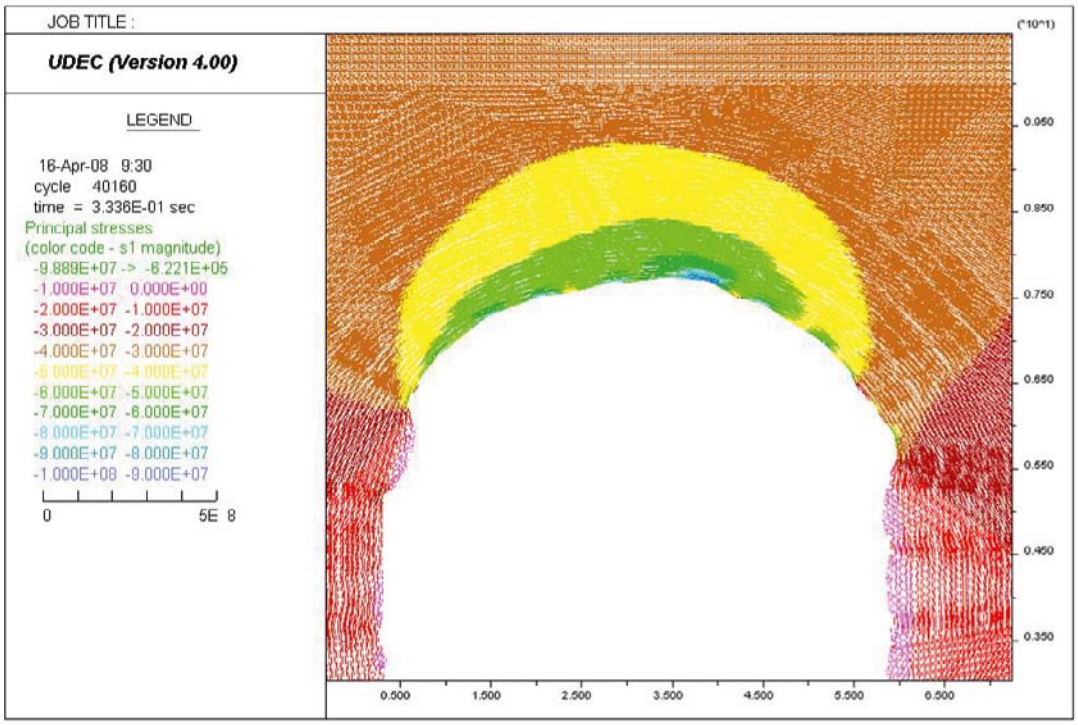

a) Maximum compressive stress = 98.89 MPa

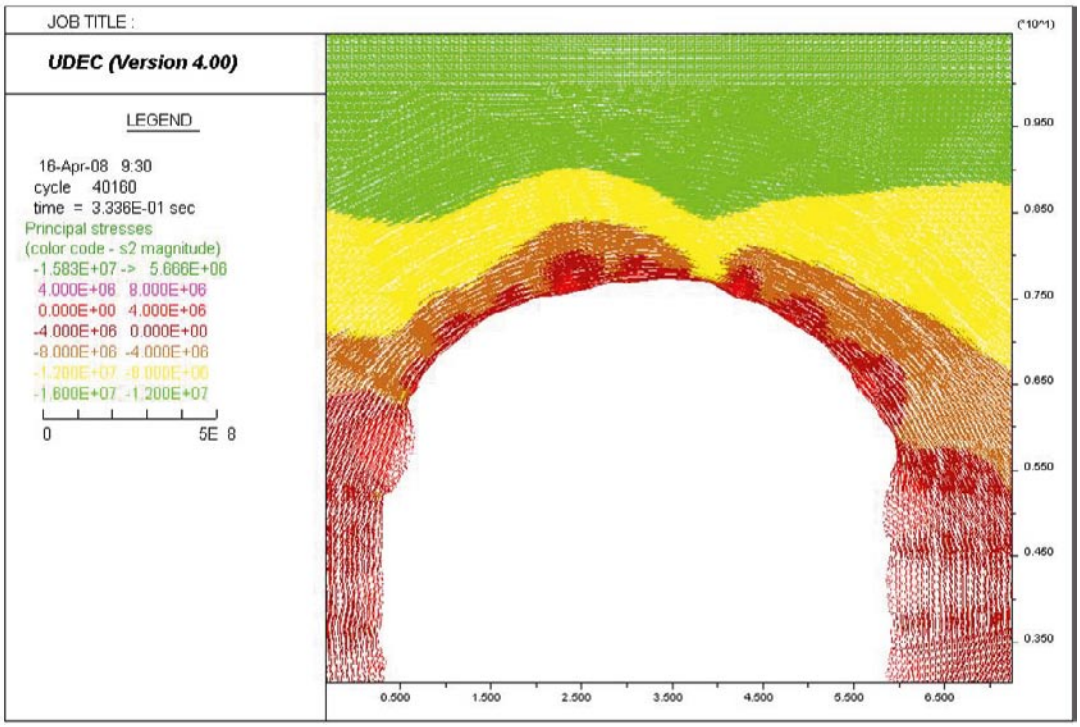

b) Maximum tensile stress = 5.666 MPa

Figure M-66. *Close-up images of the roof. Stress tensor plots at a section outside the slot after excavating the bench; Colors by magnitude of a) Sigma 1 and b) Sigma 2. Model with E = 65 GPa, σ_1 = 25 MPa, σ_1 = 316° (see Table 9-11).*

Outside slot section, as-built tunnel shape

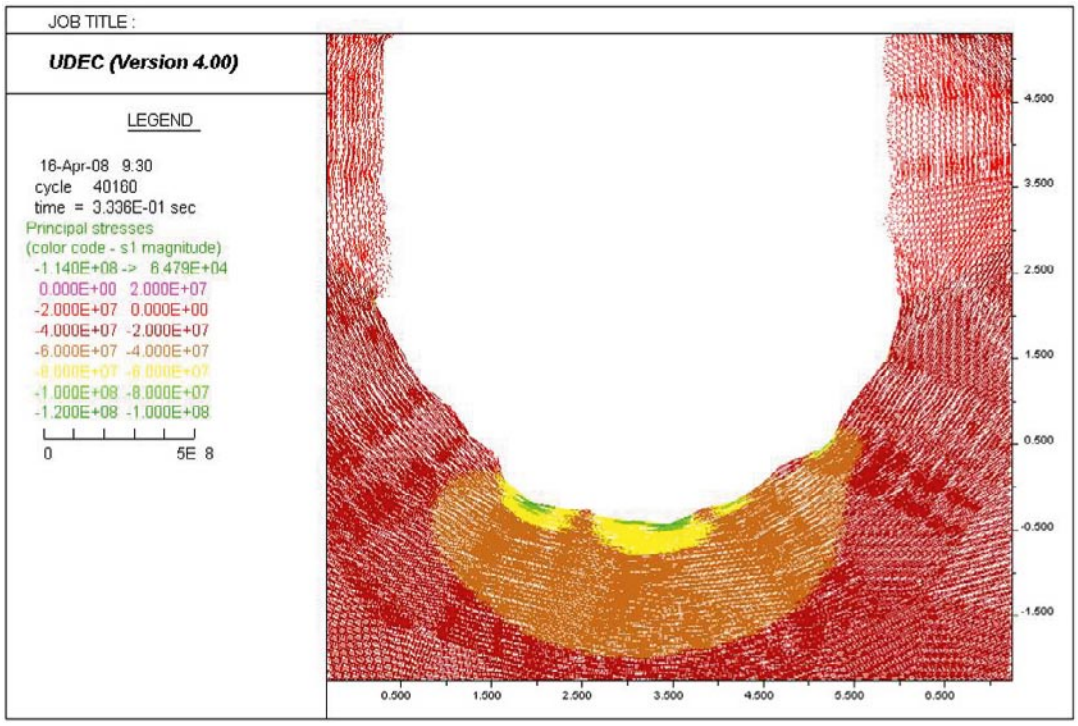

a) Maximum compressive stress = 114.0 MPa

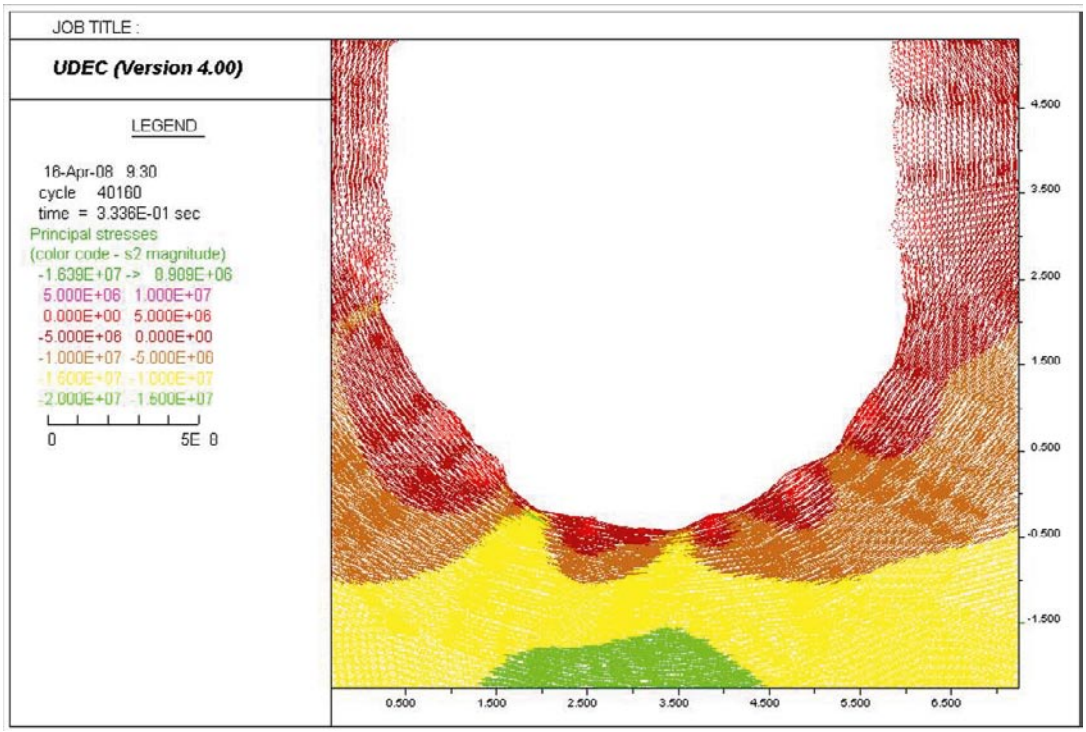

b) Maximum tensile stress = 8.989 MPa

Figure M-67. *Close-up images of the floor. Stress tensor plots at a section outside the slot after excavating the bench; Colors by magnitude of a) Sigma 1 and b) Sigma 2. Model with E = 65 GPa, σ_1 = 25 MPa, σ_1 = 316° (see Table 9-11).*

Convergence pins section, as-built tunnel shape

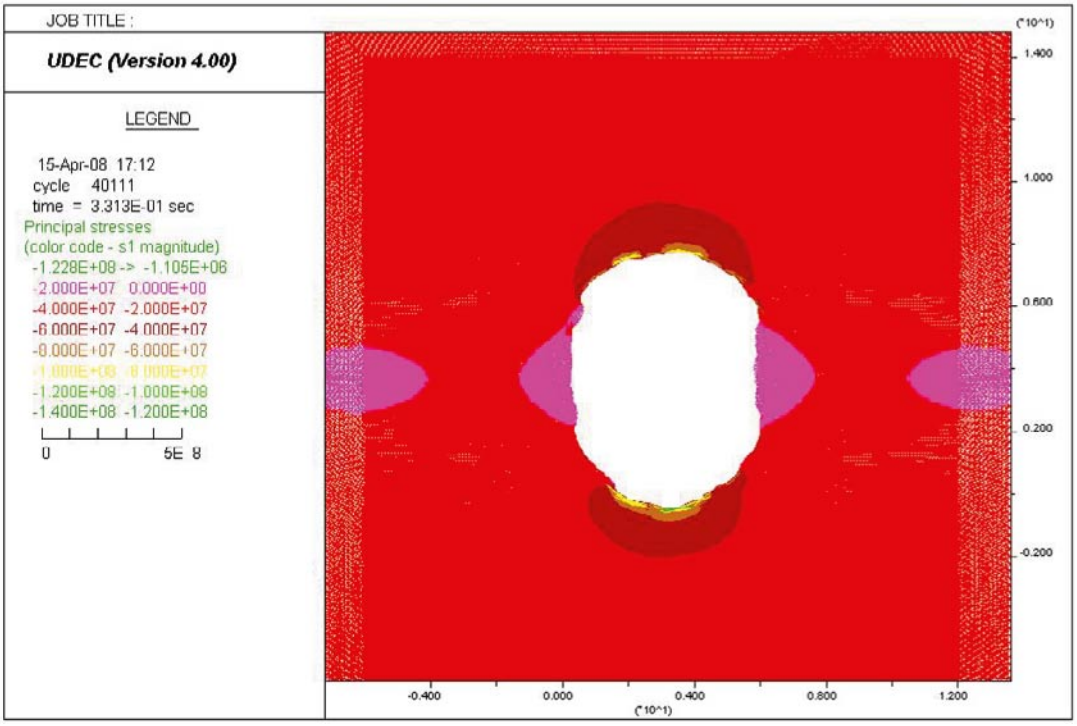

a) Maximum compressive stress = 122.8 MPa

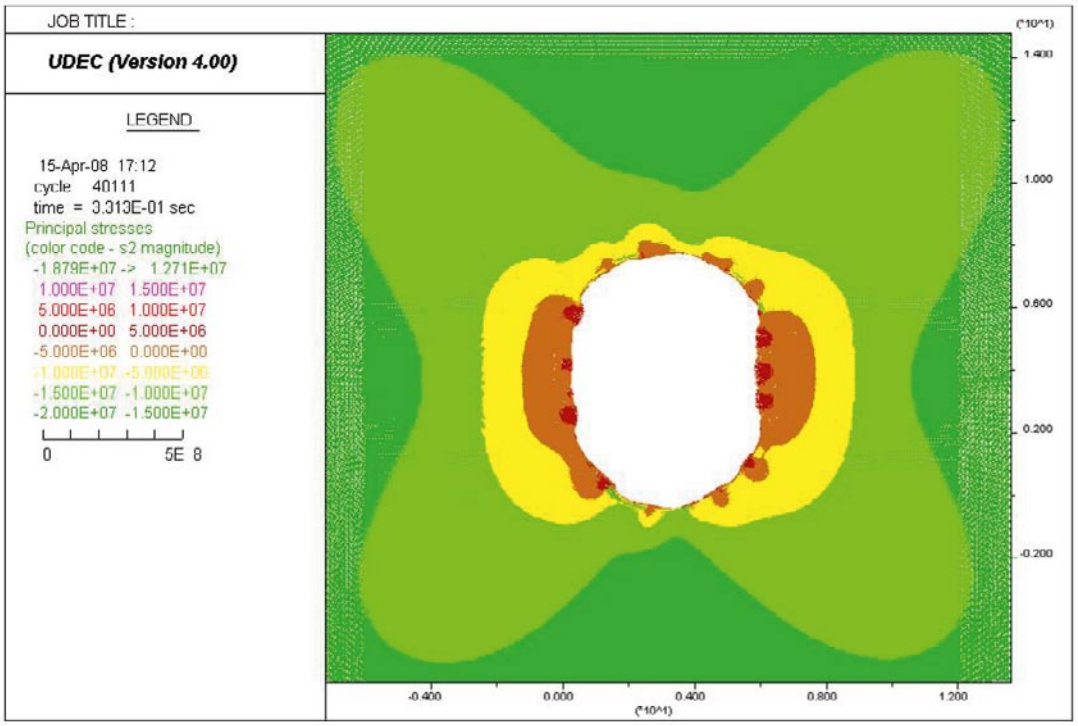

b) Maximum tensile stress = 12.71 MPa

Figure M-68. *Stress tensor plots at the convergence pins section after excavating the bench; Colors by magnitude of a) Sigma 1 and b) Sigma 2. Model with E = 65 GPa, σ_1 = 25 MPa, σ_1 = 316° (see Table 9-11).*

Convergence pins section, as-built tunnel shape

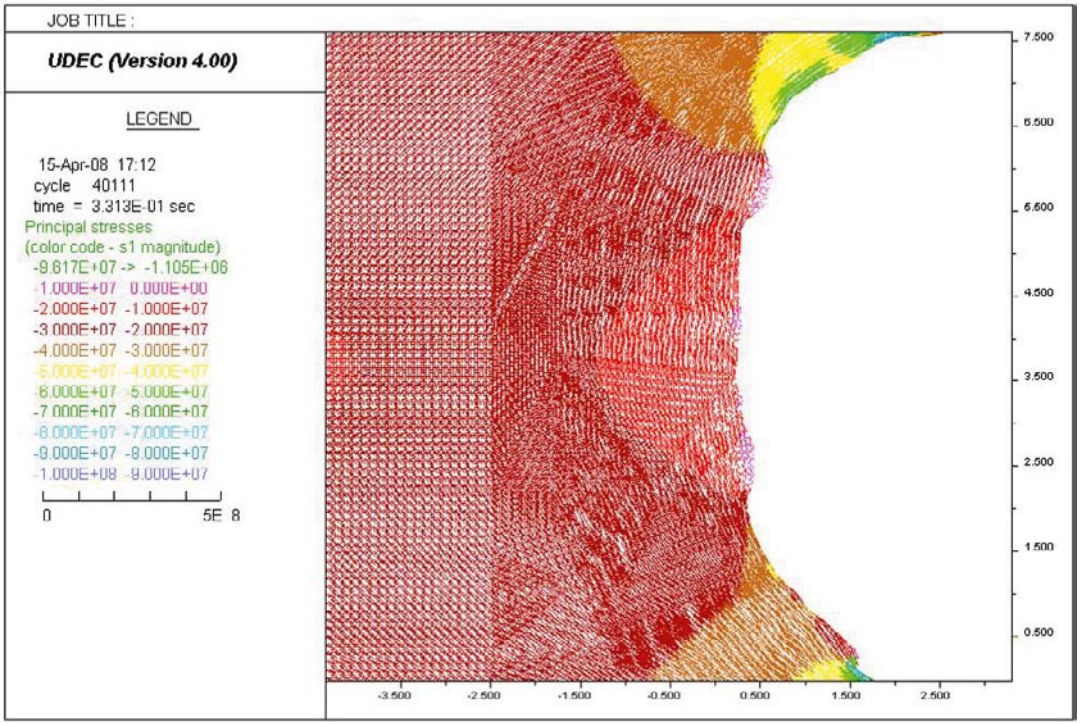

a) Maximum compressive stress = 96.17 MPa

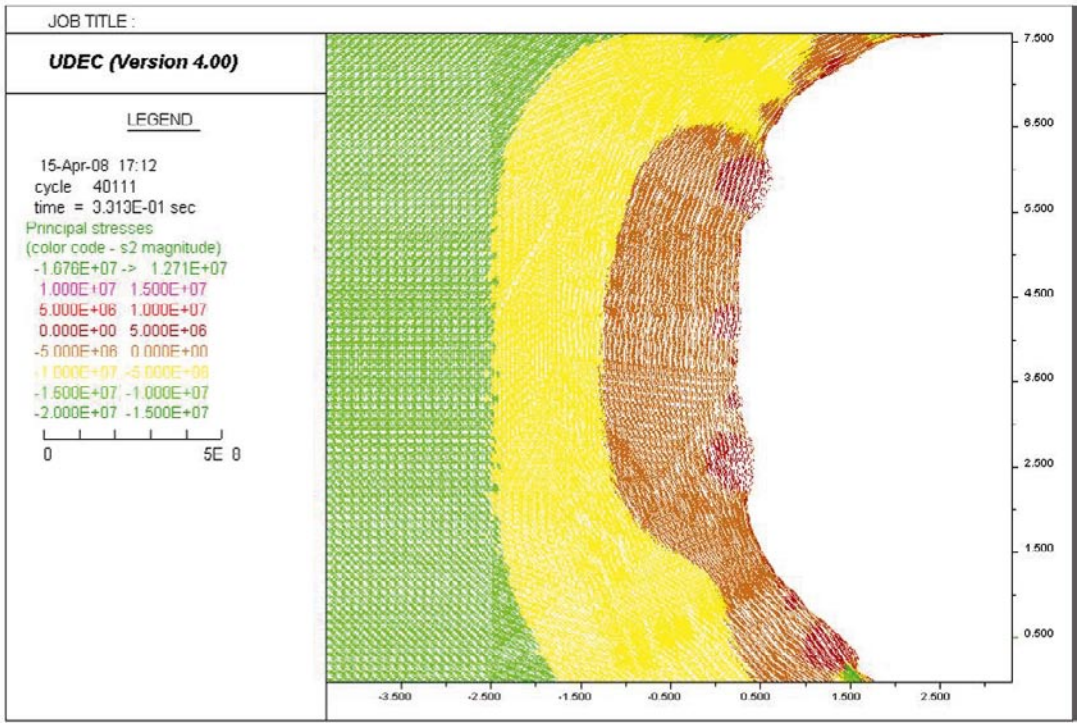

b) Maximum tensile stress = 12.71 MPa

Figure M-69. *Close-up images of the left side wall. Stress tensor plots at the convergence pins section after excavating the bench; Colors by magnitude of a) Sigma 1 and b) Sigma 2. Model with E = 65 GPa, σ_1 = 25 MPa, σ_1 = 316° (see Table 9-11).*

Convergence pins section, as-built tunnel shape

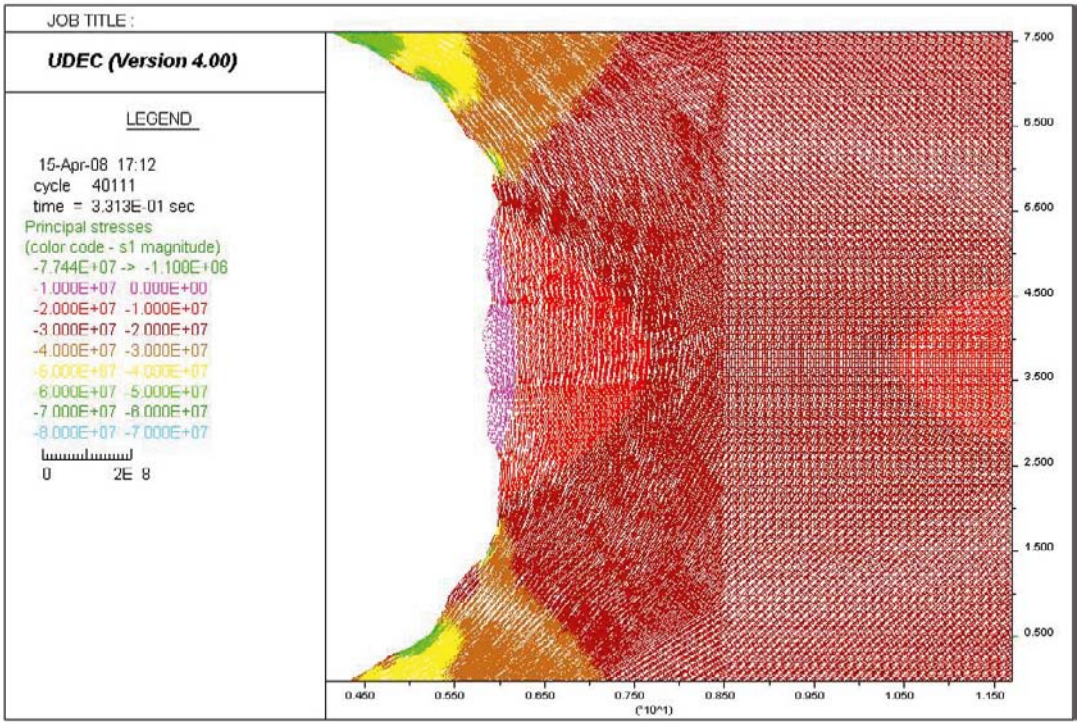

a) Maximum compressive stress = 77.44 MPa

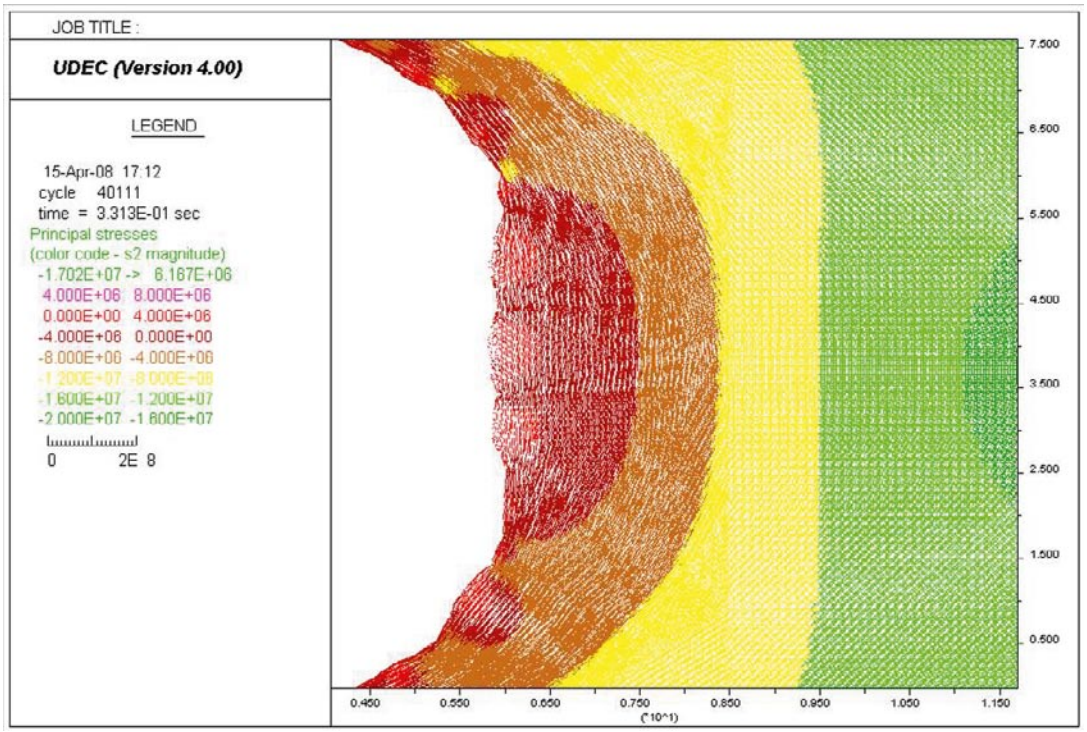

b) Maximum tensile stress = 6.167 MPa

Figure M-70. *Close-up images of the right side wall. Stress tensor plots at the convergence pins section after excavating the bench; Colors by magnitude of a) Sigma 1 and b) Sigma 2. Model with E = 65 GPa, σ_1 = 25 MPa, σ_1 = 316° (see Table 9-11).*

Convergence pins section, as-built tunnel shape

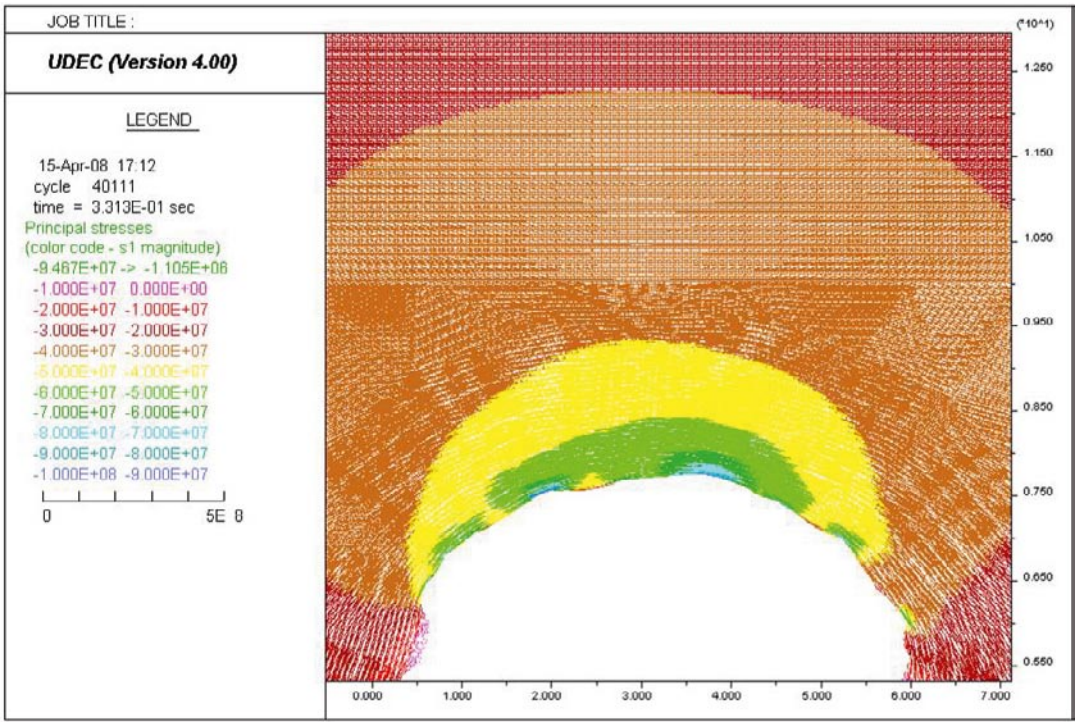

a) Maximum compressive stress = 94.67 MPa

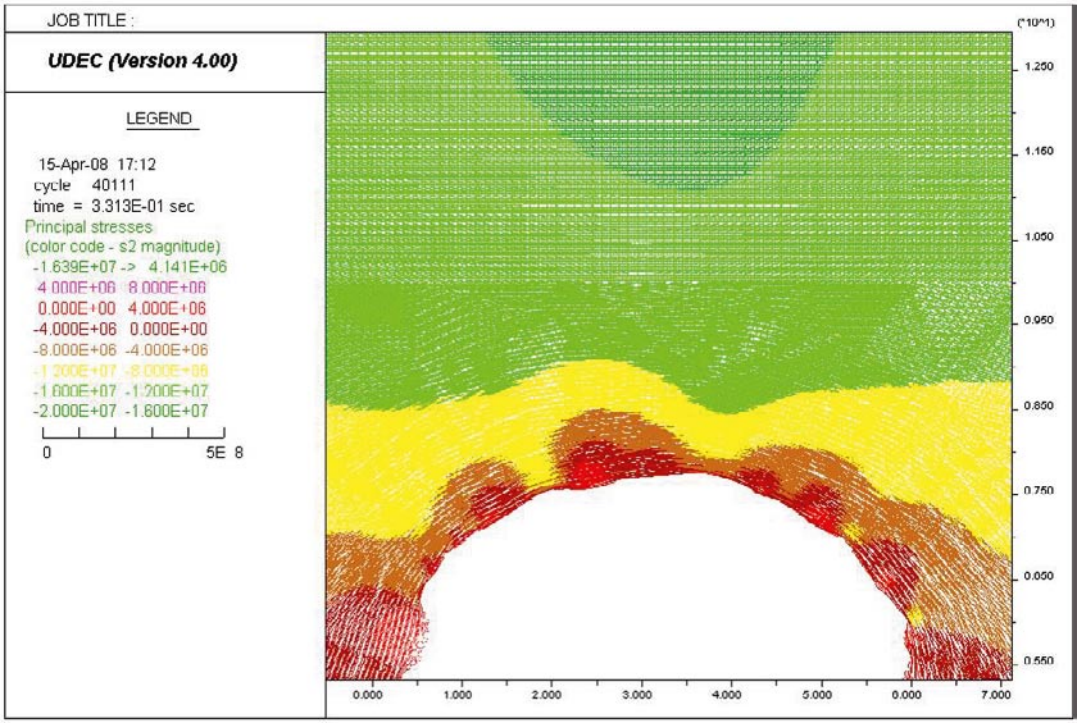

b) Maximum tensile stress = 4.141 MPa

Figure M-71. *Close-up images of the roof. Stress tensor plots at the convergence pins section after excavating the bench; Colors by magnitude of a) Sigma 1 and b) Sigma 2. Model with E = 65 GPa, σ_1 = 25 MPa, σ_1 = 316° (see Table 9-11).*

Convergence pins section, as-built tunnel shape

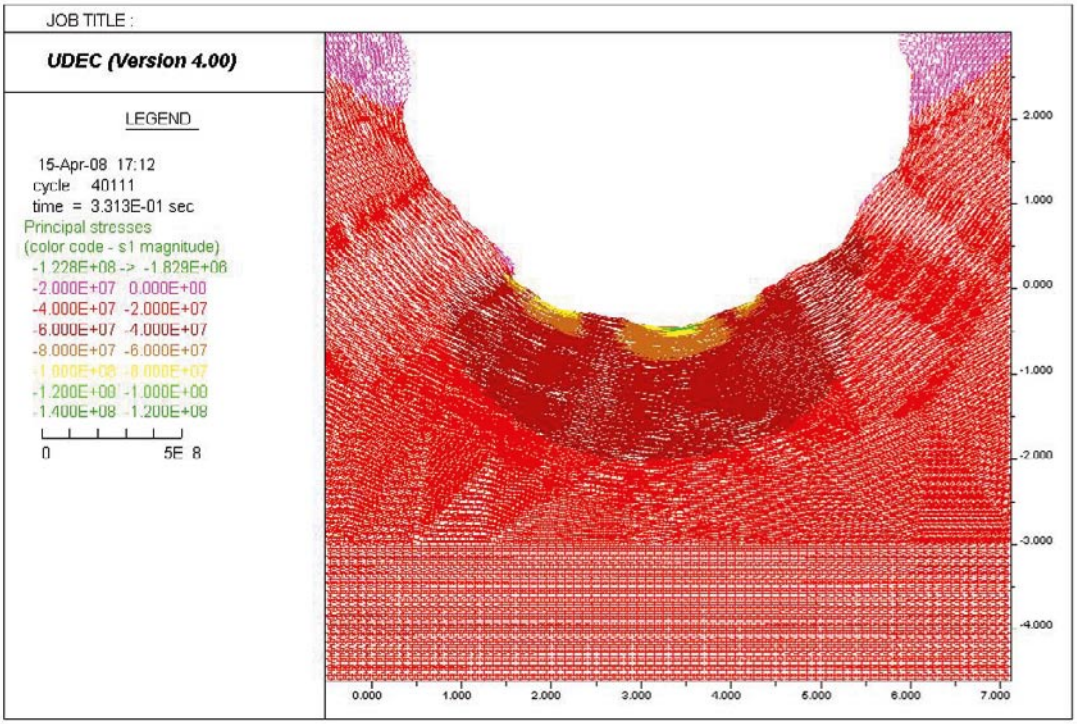

a) Maximum compressive stress = 122.8 MPa

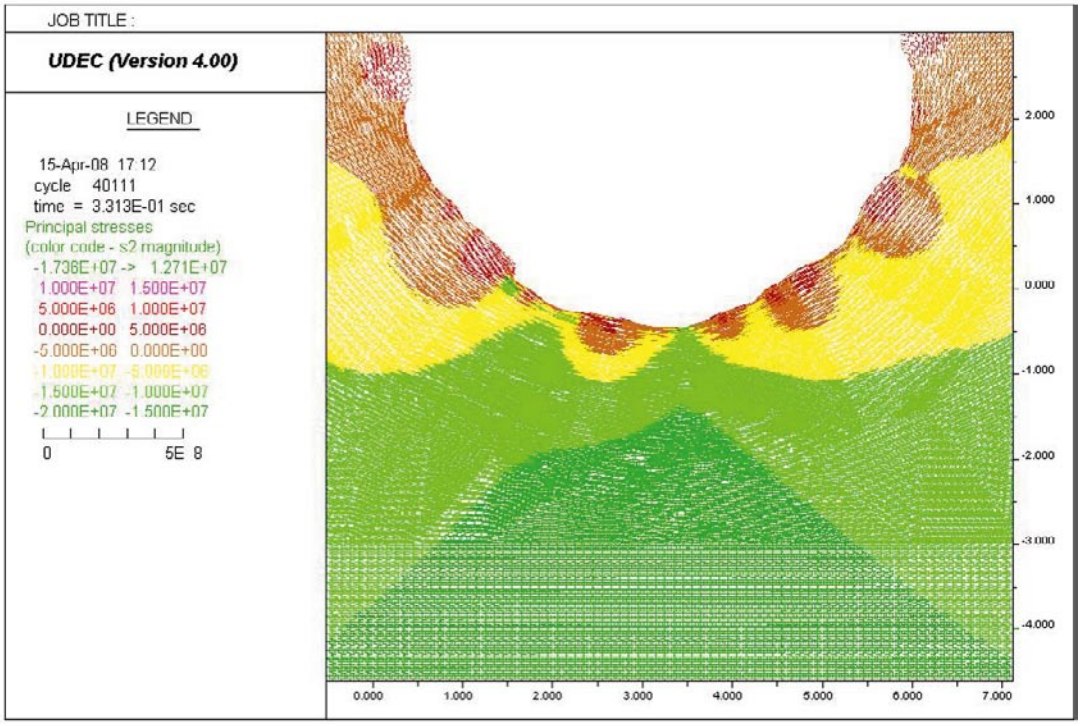

b) Maximum tensile stress = 12.71 MPa

Figure M-72. *Close-up images of the floor. Stress tensor plots at the convergence pins section after excavating the bench; Colors by magnitude of a) Sigma 1 and b) Sigma 2. Model with E = 65 GPa, σ_1 = 25 MPa, σ_1 = 316° (see Table 9-11).*

Appendix N

PM – On the influence of the tunnel shape on the major principal stress in the floor of the Q-tunnel

Margareta Lönnqvist, Clay Technology AB
February 7, 2008

N1 Influence of the shape of the tunnel cross section on the major principal stress

The actual tunnel cross section has been obtained from laser scanning sections of the Q-tunnel at Äspö HRL. Figure N-1 shows a comparison between an idealized tunnel shape and the actual tunnel shape as represented in 3DEC (Diego Mas Ivars, e-mail communication). In tunnel segments 46-49 the floor appears to be rather flat compared with the other sections, which tend to be more like the idealized tunnel floor.

In the following sections, the major principal stress on vertical scan-lines (also provided by Diego Mas Ivars), starting at the floor of the tunnel and extending about 6 m downwards, are compared between the two 3DEC models (and with corresponding Code_Bright results). In every tunnel segment three scan-lines are chosen: One on the tunnel axis (denoted 'middle') and two at positions 1.25 m on either side of the tunnel axis (denoted 'left' and 'right', respectively). Here, zero depth represents the tunnel floor in the centre of the tunnel in each segment.

The results show that there is a very minor influence on the major principal stress, at positions 1 m below the tunnel floor, of the variation in the floor geometry. It seems that there is no strong need now to perform scoping analyses of specific CAPS hole Code_Bright models with a flat floor.

N1.1 Idealized tunnel shape

Figure N-2 shows the idealized tunnel cross sections as represented in Code_Bright and 3DEC. Figure N-3 shows a comparison between the stresses obtained in the idealized models. As seen in the figure, there is an almost perfect agreement between the results.

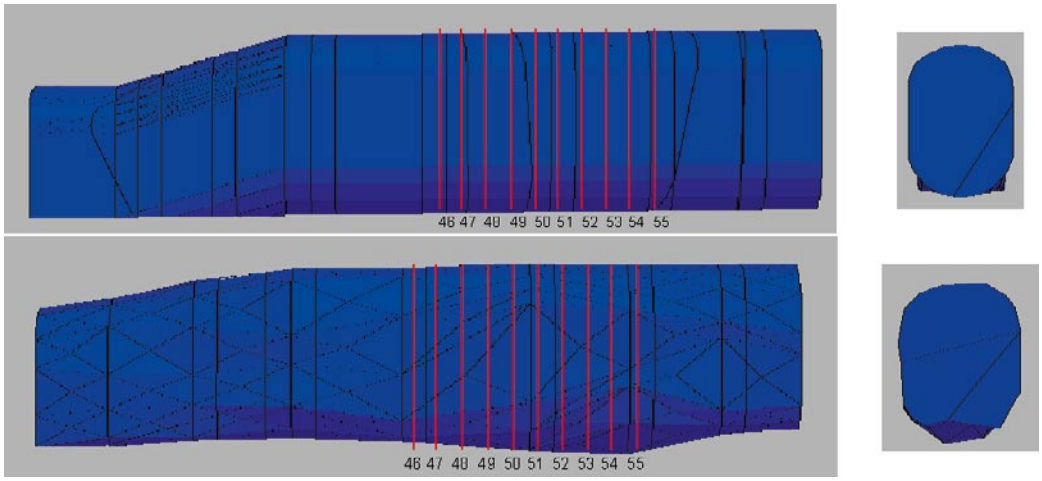

Figure N-1. *3DEC figures by D Mas Ivars – tunnel segments indicated in red. Top: Idealized tunnel shape. Bottom: Laser scanned tunnel shape.*

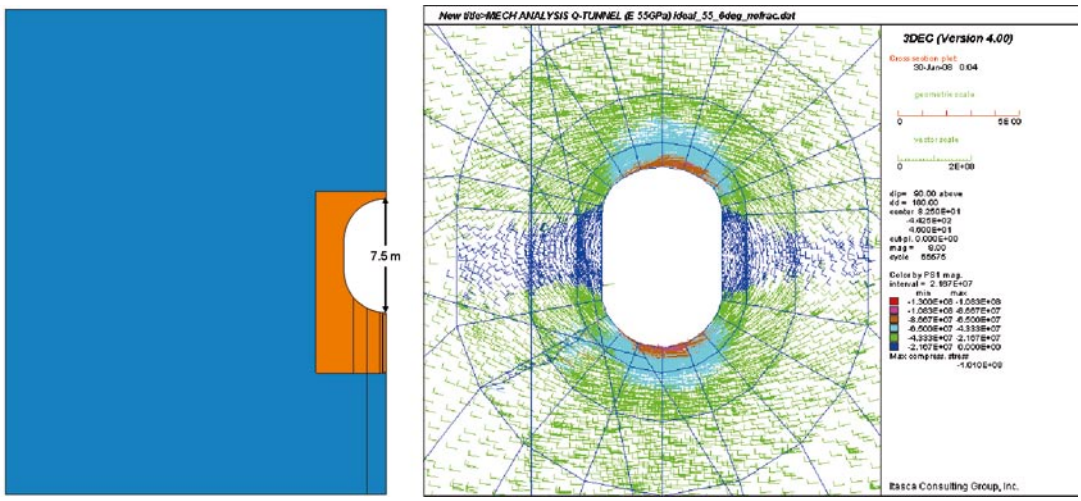

Figure N-2. *Idealized tunnel shape: Representation in Code_bright (left). Representation in 3DEC (right).*

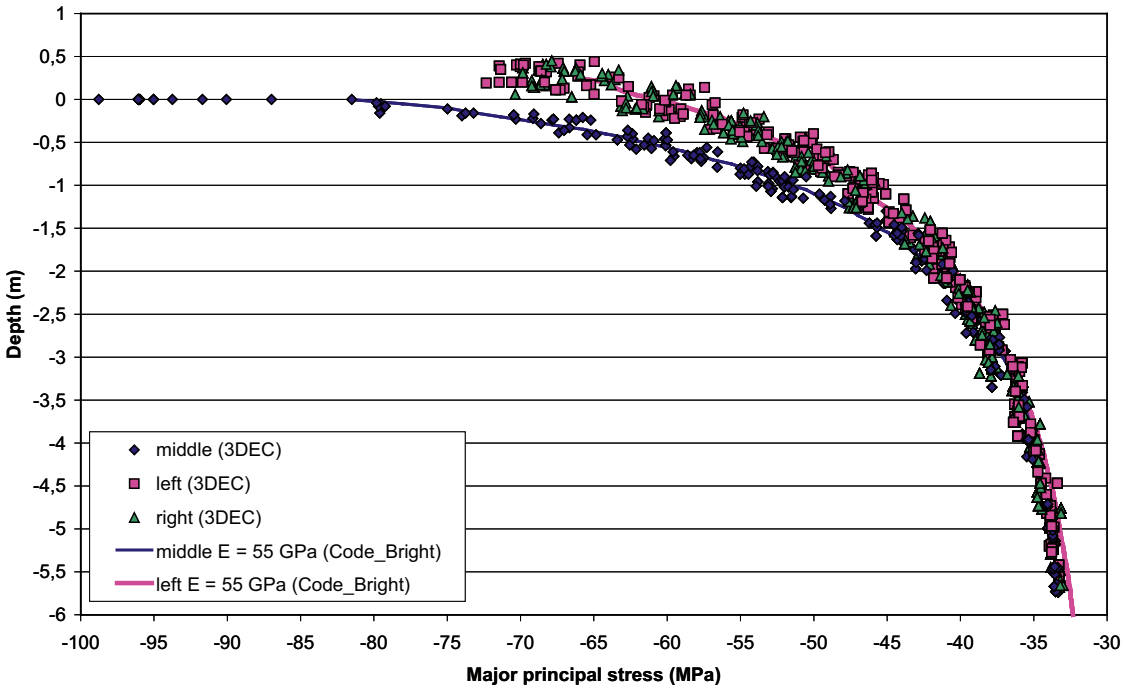

Figure N-3. *Comparison between stress magnitudes in Code_Bright and 3DEC. 3DEC results from (Diego Mas Ivars, e-mail communication).*

N1.2 Real tunnel shape

The major principal stress, along vertical scan-lines, in tunnel sections 46 to 55 is presented in Figure N-4. The stress magnitudes in the laser scanned tunnel cross sections (3DEC models by Diego Mas Ivars) are compared with results from the idealized tunnel (Code_Bright).

As seen in the figures, at positions 1 m below the tunnel floor, the stresses in the idealized Code_ Bright model are in good agreement with the corresponding stresses in the 3DEC model with the laser scanned cross sections.

46 m

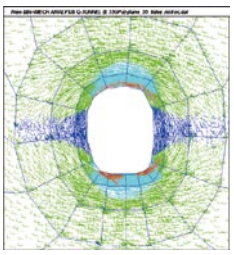

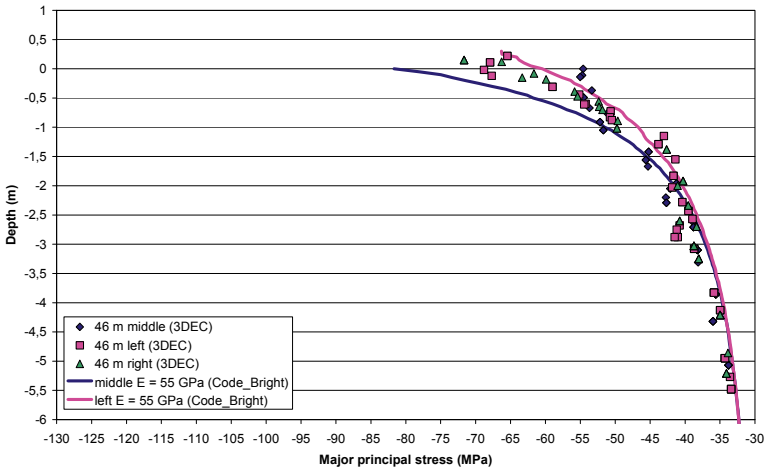
Depth (m)
Major principal stress (MPa)
46 m middle (3DEC)
46 m left (3DEC)
46 m right (3DEC)
middle E = 55 GPa (Code_Bright)
left E = 55 GPa (Code_Bright)

47 m

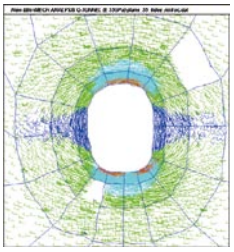

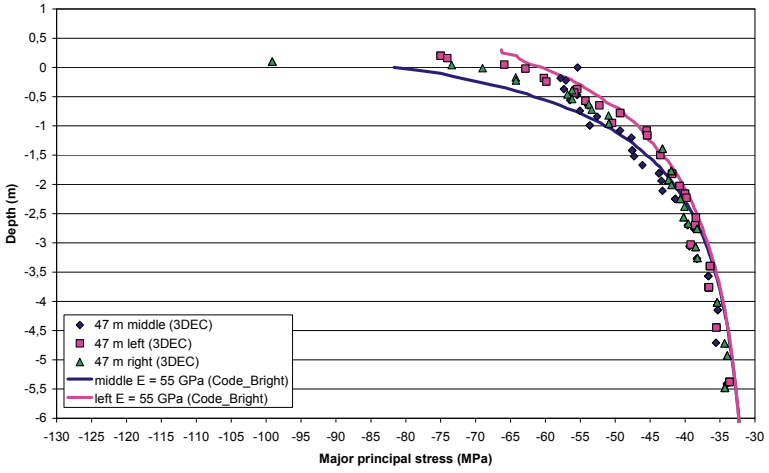
Depth (m)
Major principal stress (MPa)
47 m middle (3DEC)
47 m left (3DEC)
47 m right (3DEC)
middle E = 55 GPa (Code_Bright)
left E = 55 GPa (Code_Bright)

48 m

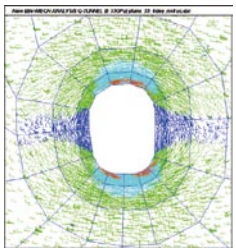

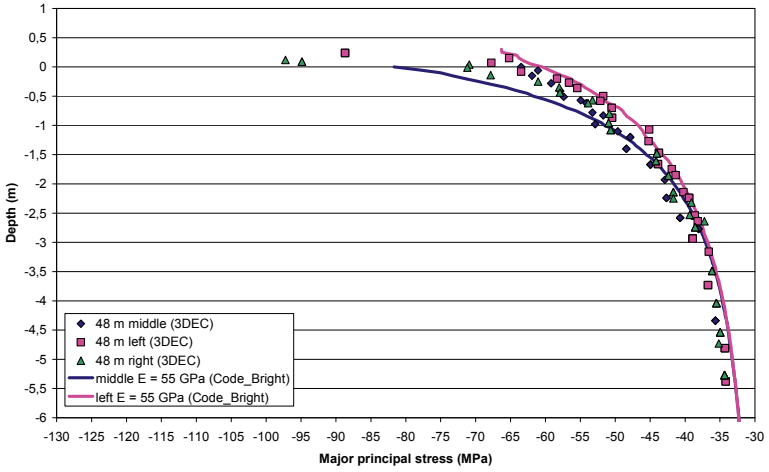
Depth (m)
Major principal stress (MPa)
48 m middle (3DEC)
48 m left (3DEC)
48 m right (3DEC)
middle E = 55 GPa (Code_Bright)
left E = 55 GPa (Code_Bright)

49 m

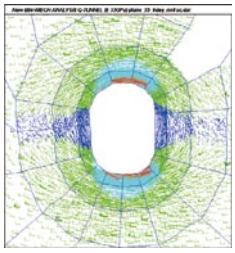

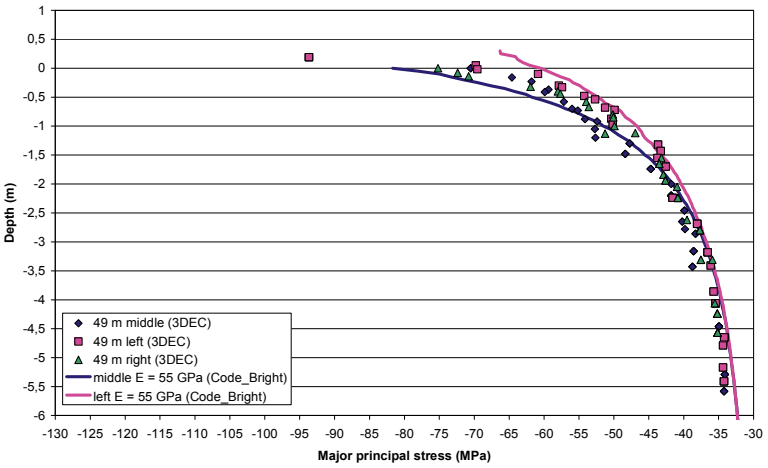
Depth (m)
Major principal stress (MPa)
49 m middle (3DEC)
49 m left (3DEC)
49 m right (3DEC)
middle E = 55 GPa (Code_Bright)
left E = 55 GPa (Code_Bright)

50 m

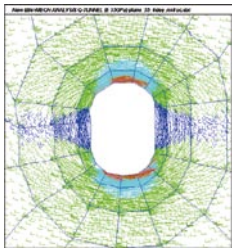

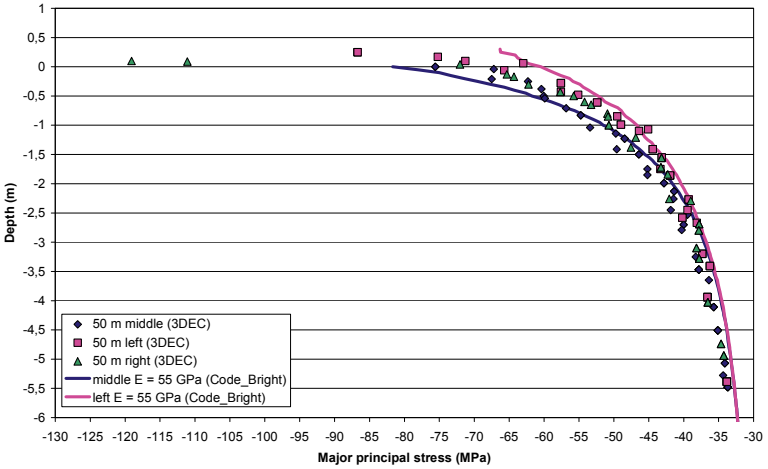
Depth (m)
Major principal stress (MPa)
50 m middle (3DEC)
50 m left (3DEC)
50 m right (3DEC)
middle E = 55 GPa (Code_Bright)
left E = 55 GPa (Code_Bright)

51 m

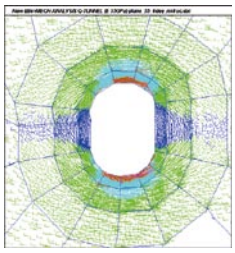

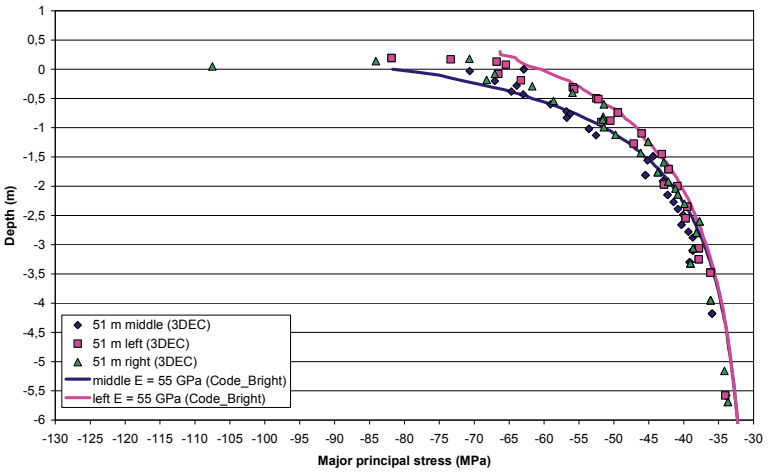
Depth (m)
Major principal stress (MPa)
51 m middle (3DEC)
51 m left (3DEC)
51 m right (3DEC)
middle E = 55 GPa (Code_Bright)
left E = 55 GPa (Code_Bright)

52 m

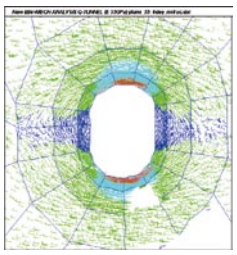

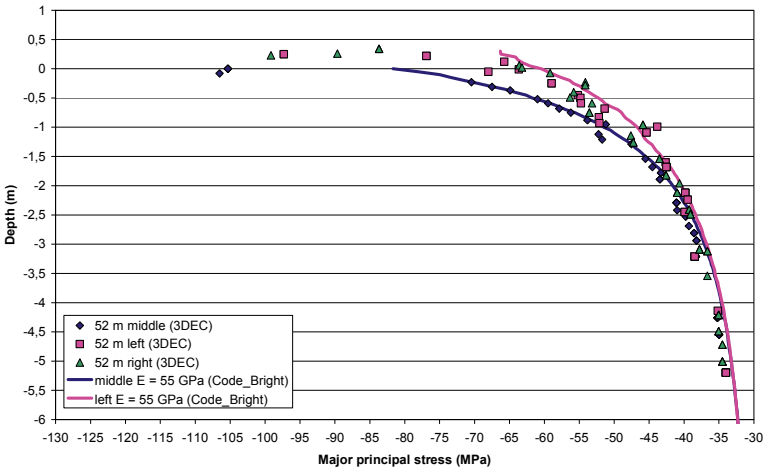
Depth (m)
Major principal stress (MPa)
52 m middle (3DEC)
52 m left (3DEC)
52 m right (3DEC)
middle E = 55 GPa (Code_Bright)
left E = 55 GPa (Code_Bright)

53 m

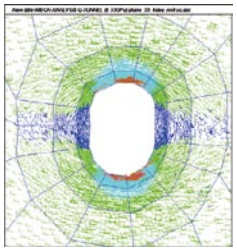

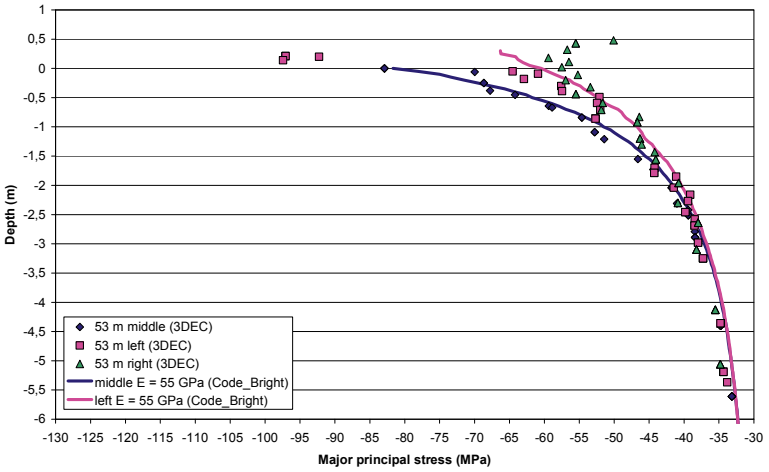
Depth (m)
Major principal stress (MPa)
53 m middle (3DEC)
53 m left (3DEC)
53 m right (3DEC)
middle E = 55 GPa (Code_Bright)
left E = 55 GPa (Code_Bright)

54 m

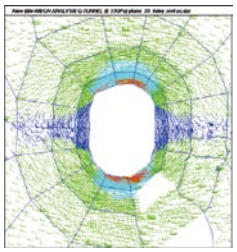

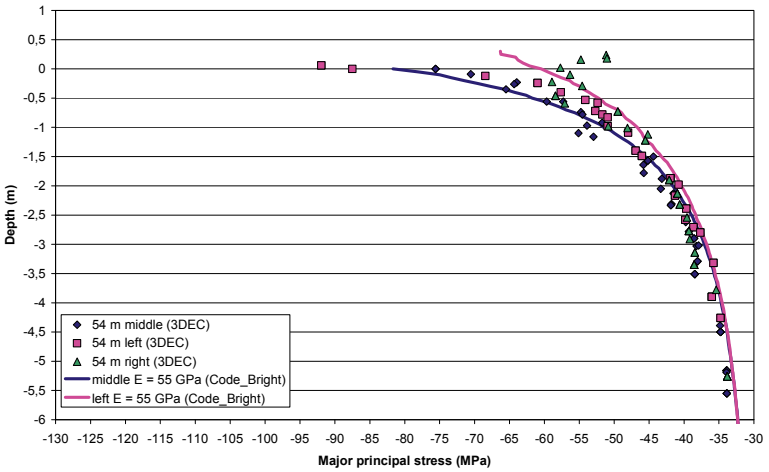
Depth (m)
Major principal stress (MPa)
54 m middle (3DEC)
54 m left (3DEC)
54 m right (3DEC)
middle E = 55 GPa (Code_Bright)
left E = 55 GPa (Code_Bright)

55 m

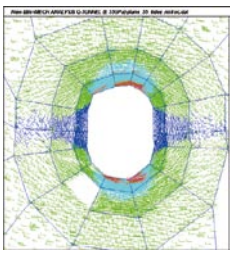

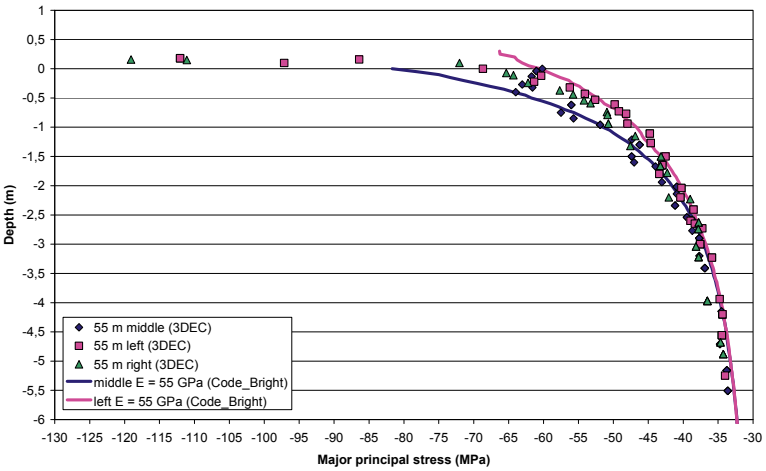

Figure N-4. *Major principal stress along vertical scan lines in tunnel segments 46 to 55 in the Q-tunnel. 3DEC results from (Diego Mas Ivars, e-mail communication).*